

BEHAVIOUR OF REINFORCED EARTHEN EMBANKMENTS DURING EARTHQUAKES

A THESIS

*Submitted in fulfilment of the
requirements for the award of the degree*

of

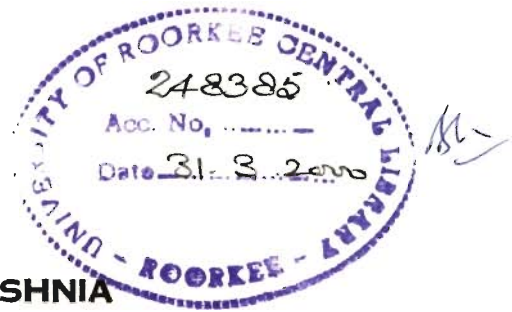
DOCTOR OF PHILOSOPHY

in

EARTHQUAKE ENGINEERING

By

MEHDI SIAVOSHNIYA



**DEPARTMENT OF EARTHQUAKE ENGINEERING
UNIVERSITY OF ROORKEE
ROORKEE-247 667 (INDIA)**

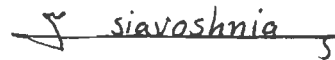
JULY, 1998

Gratis

CANDIDATE'S DECLARATION


I hereby certify that the work which is being presented in the thesis entitled "BEHAVIOUR OF REINFORCED EARTHEN EMBANKMENTS DURING EARTHQUAKES" in fulfilment of the requirement for the award of the Degree of Doctor of Philosophy and submitted in the Department of Earthquake Engineering of the University of Roorkee is an authentic record of my own work carried out during the period from August 1996 to July 1998 under the supervision of Dr. V.H. Joshi and Dr. B.V.K. Lavania.


The matter presented in this thesis has not been submitted by me for the award of any other degree of this or any other University.



(MEHDI SIAVOSHNIYA)


This is to certify that the above statement made by the candidate is correct to the best of our knowledge.



Dr. B.V.K. LAVANIA
Professor
Deptt. of Earthquake Engineering,
University of Roorkee,
Roorkee (U.P.) INDIA



Dr. V.H. JOSHI
Professor
Deptt. of Earthquake Engineering,
University of Roorkee,
Roorkee (U.P.) INDIA

DATE : 23 - 07 - 98

The Ph.D. Viva-Voce examination of **Mr. Mehdi Siavoshnia** Research Scholar, has been held on 24/12/98


24-12-98
Signature of Supervisors


24/12/98
Signature of Professor in Charge
Department of Earthquake Engineering
University of Roorkee
Roorkee


Signature of External Examiner

ACKNOWLEDGEMENT

I wish to express my deepest gratitude and sincerst thanks to **Dr. V.H. Joshi** and **Dr. B.V.K. Lavania**, Professors of Earthquake Engineering, University of Roorkee, Roorkee, for their stimulating supervision of my work. It has been a pleasure to work with them.

I am indebted to **Dr. V.H. Joshi** for sharing with me during the development of the computer program and also for providing excellent computing facility by sparing the personal computer in his office for the present work.

I am specially graceful to **Mr. A.D. Pandey**, Reader, Department of Earthquake Engineering, University of Roorkee, Roorkee for his help and co-operation in my work especially in handling the computer program.

I like to thank Shri J.P. Sharma, S.L.T., Shri Rishi Chand and the others in the workshop, for their help in fabrication of test setup, Shri R.S. Messon, S.L.T., Shri S. Jain, J.L.T. and Shri Rajinder of Soil Dynamics Laboratory, for their help in carrying out experimental studies. Thanks are also due to Mr. A.P. Sharma, S.L.T., Strong Motion Laboratory for his help on operating the recording instrument during shake table tests.

I am grateful to **Dr. M. Mulanajad**, former representative of Ministry of Higher Education, I.R. Iran in India, for his co- operation and encouragement.

Many thanks are due to my friends and colleagues **Mr. Khalid Moin**, **Mr. Hamzehallo** as well as **Mr. Solimani** and **Mr. Khalil** and their families for their kind help and cooperation during different stages of this investigation.

I can not find any words of thanks and gratitude for my father, Late **Mr. Parviz Siavoshnia** for his kind word of encouragement which have inspired me to seek all higher education. His guiding spirit shall remain with me for ever. During my long stay in India for the higher education, I was unable to look after my family in Iran. My mother, **Mrs. Sarieh** has taken care of my family during this period, for which I am greatly indebted to her and I will be never in a position to compensate her for the same. I also thanks my sister, **Mrs. Mahjabin** and **Miss Mahasty** for their understanding through out this period.

Finally, truly unbounded thanks are due to **Hajieh Zahra Sadat**, my wife, who with her encouragement and patience supported me during the course of this study.

MEHDI SIAVOSHIA

ABSTRACT

Ductile reinforced earth (R.E.) capable of taking compression and tension is ideal for use in geotechnical earthquake engineering. This investigation attempts to understand its behaviour in (earthen) embankments during earthquakes. Large R.E. embankments were tested and analyzed under dynamic loads by treating it to be homogeneous and elastic for simplicity.

Objective is to understand dynamic behaviour of R.E. embankments to study: (a) Preparation of test embankments on shake table (b) Embankment response (c) Characterizing factors affecting response and analysis of test data (d) Determination of strain dependent dynamic shear moduli by back analyses of test data (e) Determination of dynamic pullout resistance of fabric from back analyses of frequency-response test data (f) Idealizing R.E. to be homogeneous in FEM analysis to obtain response using shear moduli from tests and by using excitations used in tests (g) Comparison of analytical and experimental embankment responses.

Air dry sand, geotextile reinforcements and sinusoidal excitation were used since seismic excitation may be represented by its sinusoidal equivalent (Seed and Idriss, 1971). This analysis in time domain can also consider earthquake excitation. Following were studied in this study : (a) Forming uniformly dense embankment by using a specifically developed device (b) Developing stress control setup to obtain pullout resistance of fabric (c) Construction of test embankments 1.5 m long and 0.75m wide with different reinforcement arrangements. Developing technique to create plane

strain conditions in transverse section by restraining longitudinal embankment strains (d) Exciting embankments with maximum acceleration up to 0.32g and frequency in range of 5-20 Hz (e) Measuring embankment response at different points (f) Evaluating strain dependent shear moduli for R.E. at different strains (g) Evaluation of dynamic pullout resistance coefficient mobilized along fabric and comparison with static values (h) Analysis in time domain of R.E. embankments with excitation used in tests by FEM by assuming R.E. to be homogeneous to compare with experimental responses (i) Comparing response of plain sand embankments of height, top width and density same as those for R.E. embankments but with different side slopes with R.E. embankment response to highlight merits of R.E.

This study investigated the following :(a) Shear modulus and shear strain (b) Frequency of excitation, natural frequency, and excitation force ratio (c) Shear wave velocity, time lag, phase difference, phase angle and acceleration (d) Inertia at the level of each fabric (e) Coefficient of dynamic pullout resistance for fabrics of each layer and coefficient of average and maximum dynamic pullout resistance (f) Displacement, confining pressure and settlement (g) Response and dynamic shear stress by FEM.

Sand rain apparatus (SRA) developed produced uniform deposits over entire test bed which are better than those from setup reported so far. Strain control setup fails to study time dependent pullout displacement. Stress control setup developed enables such a study also and hence is superior to strain control setup. Lab technique developed for creating plane strain conditions is an important research contribution. Based on analytical and test results, following conclusions were drawn:

- a. Linear variation of shear strain with excitation force ratio for all the three R.E. embankments indicates their elastic behaviour within excitation range employed, even when excited at resonance.
- b. Seismic coefficients recommended by Richardson and Lee (1975) are smaller than those obtained by testing R.E. embankments and fail to predict nonlinear seismic coefficient-base acceleration relationship for stronger excitation and for different embankment stiffnesses.
- c. Values of F_n by method proposed by Richardson et. al. (1977) for R.E. embankments are higher than those obtained from tests. Hence, their expression is not valid for all R.E. embankments.
- d. Continuous reinforcements reduce response near embankment top.
- e. For safety, μ_{advmx} , γ_{avdmx} and dimensionless disturbing force may be obtained for $r_f \leq 1/\sqrt{2}$ at different OME. For stiffer R.E. embankment, these variables are lower than those for weaker R.E. embankment. At resonance, γ_{avdmx} reduces sharply with change in r_f .
- f. Dimensionless disturbing force, μ_{advmx} , γ_{avdmx} at different OME and r_f values remain nearly the same for stiffer embankment and appreciably different for weaker embankment.
- g. R.E. embankments do not fail even when lateral displacements are more than 0.005 H at which plain soil fail.
- h. Maximum displacement occurs at about 0.6H from top which is also reported by other investigators.
- i. Computed post-vibration confining pressures are in agreement with field data of a 15 m high R.E. embankment and with test data reported by Richardson and Lee (1975) and with test data of Fairless (1989). Continuous fabrics not failing in tension are more effective than discontinuous ones designed for pullout resistance.

- j. Post vibration settlements are small even after experiencing resonance.
- k. Damping ratio-shear strain relationship proposed by Seed et.al. (1984) for plain sands is also valid for reinforced earth.
- l. For R.E. embankments, shear strain and damping ratio are of the order of 10^{-3} and 0.18 which are much higher than corresponding values of 10^{-6} and 0.05 respectively for plain sands in elastic domain. Since damping greatly affects shear stress, it helps to reduce peak dynamic shear stress within elastic domain. This is a great advantage of R.E.
- m. For R.E. embankments, response by FEM analysis by idealizing reinforced earth to be homogenous and by using proper damping ratio are comparable to measured response for same excitation. Measured response is closer to computed one with 2-layer idealization which is better.
- n. For same top width, height and excitation, measured response and computed shear stress for R.E. embankment are much smaller than those for plain sand embankments in top 40% of the depth. Maximum dynamic shear stress in plain sand embankments is far more (2.3) than that of R.E. embankment. This highlights advantages of R.E. embankments.

Analytical and test results clearly indicate that responses of R.E. embankment, specially that using continuous reinforcement, is far better than that of plain sand embankment for earthquake conditions. Also it is seen that, for the purposes of analysis, R.E. in (earthen) embankment can be treated to be homogeneous material with improved shear modulus without losing accuracy. It would be better to analyze embankment by considering it as a layered system with appropriate shear modulus for each layer.

LIST OF ABBREVIATIONS

ASCE	American Society of Civil Engineering
Bros.	Brothers
Bull.	Bulletin
Conf.	Conference
Coeff.	Coefficient
Ctr.	Centre
Div.	Division
Earthq.	Earthquake
EERC	Earthq. Engineering Research Centre
Ed.	Edition
Engg.	Engineering
Eq.	Equation
Fig.	Figure
Geotech.	Geotechnical
GTD.	Geotechnical Division
Jl.	Journal
JSSMFE	Japanese Society of Soil Mechanic and Foundation Engg.
ICSMFE Int. Conf.	on Soil Mechanic and Foundation Engg.
Int.	International
IS	Indian Standard
Inst.	Institution
Nat.	National

no.	Number
OME	Oscillator Mass Eccentricity Number
pp.	Page number
Proc.	Proceeding
R.E.	Reinforced Earth
Rep.	Report
Res.	Research
SMFE	Soil Mechanics and Foundation Engg.
SMFD	Soil Mechanics and Foundation Div.
Soc.	Society
Symp.	Symposium
Tech.	Technology
Univ.	University
WCEE	World Conf. on Earthq. Engg.
w.r.t.	With respect to
Vol.	Volume

NOTATIONS

a	Coefficient of the quadratic equation.
a_b	Single amplitude acceleration at the base pickup level of test embankment.
a_m	Single amplitude acceleration at the mid pickup level of test embankment.
a_t	Single amplitude acceleration at the top pickup level of test embankment.
a_{fq}	Single amplitude acceleration for any frequency of excitation.
a_{free}	Single amplitude acceleration from free vibration test at top pickup level of test embankment.
a_{cM1}	Computed maximum absolute acceleration for R.E. embankment M1.
a_{cM3}	Computed maximum absolute acceleration for R.E. embankment M3
a_{cM3}	Computed maximum absolute acceleration for R.E. embankment M3.
a_{c2lM1}	Computed maximum absolute acceleration for R.E. embankment, M1 with two layers idealization.
a_{c2lM3}	Computed maximum absolute acceleration for R.E. embankment, M3 with two layers idealization.
a_{csM1}	Computed maximum absolute acceleration for R.E. embankment, M1 with single layer idealization.
a_{csM3}	Computed maximum absolute acceleration for R.E. embankment, M3 with single layer idealization.
a_{eM1}	Experimentally measured maximum absolute acceleration for M1.

a_{eM3}	Experimentally measured maximum absolute acceleration for M3.
$a_p(t)$	Acceleration at time station (t) at the point p
aP1	Computed maximum absolute acceleration for plain sand embankment P1.
aP2	Computed maximum absolute acceleration for plain sand embankment P2.
$a_{rp}(t)$	Relative acceleration at any point p at time station t.
a_y	Yield acceleration.
a_{ya}	Yield acceleration for positive lobe.
a_{yp}	Yield acceleration for negative lobe.
B	Width of test embankment.
B_r	Width of reinforcement.
B_{cr}	Critical value of width of reinforcement beyond which μ_{avs} reaches constant maximum value.
B_{ry}	Yield width of reinforcement.
B_{rd}	Dimensionless yield width (B_{ry}/B_r).
$(B_{rd})_{max}$	Maximum value of B_{rd} .
$(B_{rd})_{min}$	Minimum value of B_{rd} .
b	Coefficient of quadratic equation.
C	Soil cohesion.
[C]	Damping matrix.
C_s	slope of the relationship between ϕ_m and γ_m (Fig.3.10).
C_μ	Correction factor to be multiplied with μ_{avs} to obtain $\mu_{avsfield}$.
c	Coefficient of quadratic polynomial constant.
[D]	Elasticity matrix
D_p	Perforation diameter.
D_r	Relative density.
D_{ra}	Relative density corresponding to H_{fa} .

D_s	Soil particle diameter.
DP	Damage potential.
DP_a	Positive damage potential.
DP_p	Negative damage potential.
d_m	Maximum displacement at mid pickup level pullout displacement.
d_p	Pullout displacement.
d_{pa}	Plastic displacement in positive direction (outward).
d_{pmax}	Maximum pullout displacement for a given loading increment and pullout force.
d_{pp}	Plastic displacement in negative direction (inward).
d_{fq}	Displacement for any sinusoidal excitation.
d_{free}	Displacement from free vibration test.
d_{pd}	Dynamic pullout displacement.
d_{cM1}	Computed maximum absolute displacement for R.E. embankment, M1.
d_{cM3}	Computed maximum absolute displacement for R.E. embankment, M3.
d_{c2IM1}	Computed maximum absolute displacement for R.E. embankment, M1 with two layers idealization.
d_{c2IM3}	Computed maximum absolute displacement for R.E. embankment, M3 with two layers idealization.
d_{csM1}	Computed maximum absolute displacement for R.E. embankment, M1 with single layer idealization.
d_{csM3}	Computed maximum absolute displacement for R.E. embankment, M3 with single layer idealization.
d_{eM1}	Maximum absolute displacement recorded experimentally for R.E. embankment, M1.
d_{eM3}	Maximum absolute displacement recorded experimentally for R.E. embankment, M3.

d_t	Maximum displacement at top acceleration pickup level of test embankment.
dP1	Computed maximum absolute displacement for plain sand embankment, P1.
dP2	Computed maximum absolute displacement for plain sand embankment, P2.
E	Modulus of elasticity in t/m^2 .
e_c	Eccentricity.
e'	Constant of proportionality.
F_{amx}	Maximum amplitudes of force.
F_{di}	Net disturbing force on i th reinforcing element situated in i 'th element.
F_s	Factor of safety with respect to tension under static case.
F_{sp}	Safety factor w.r.t. pullout resistance under static case.
F_d	Disturbing inertia force.
F_{dk}	Inertia force generated by the mass of k 'th layer.
F_{drag}	Drag force.
F_{dmx}	Maximum inertia force generated by mass of embankment layers for phase angle varying from 0 to 2π .
F_n	Fundamental frequency of excitation in Hz.
F_{rpi}	Restoring force due to shearing mobilized in plain sand in i 'th layer of embankment.
F_{rpmx}	Maximum restoring force due to shearing mobilised due to plain sand of embankment layers.
F_{rq}	Frequency of excitation in Hz.
F_{rri}	Pullout force of resistance due to reinforcement in i 'th layer embankment.

G	Shear modulus in t/m^2 .
G_1	Shear modulus of embankment at mid depth of top layer, when idealized as two layer system in t/m^2 .
G_2	Shear modulus of embankment at mid depth of bottom layer, when idealized as two layer system in t/m^2 .
G_n	Normalised shear modulus.
G_r	Shear modulus of reinforcement earth embankment in t/m^2
G_{rf}	Reference shear modulus in t/m^2 at shear strain of 1×10^{-3} for obtaining normalised shear modulus, G_n .
G_{rn}	Shear modulus at resonance in t/m^2 .
G_s	Shear modulus of plain sand in t/m^2 .
G_{sp}	Specific gravity of sand.
H	Height of embankment.
H_L	Thickness of layers of test embankment.
H_c	Critical height of fall.
H_d	Thickness of soil layer in each operation of SRA.
H_f	Height of fall of soil grain.
H_{fa}	Actual average value of height of fall.
H_t	Height of top pickup position measured from base.
H_m	Height of middle pickup position measured from base.
H_{ri}	Depth from top of the test embankment to the i 'th reinforcement.
[J]	Jacobian matrix.
[K]	Global stiffness matrix.
K	Coefficient of earth pressure.
K_a	Coefficient of active earth pressure.
K_o	Coefficient of at rest earth pressure.
K_p	Coefficient of passive earth pressure.

K_m	Coefficient of mobilised earth pressure.
K_s	Shape factor.
L	Length of the test embankment.
L_a	Initial length of soil element.
L'_a	New position of soil element.
L_e	Effective length of reinforcement which offer pullout resistance.
L_{rci}	Length of i 'th reinforcement if it is continuous from one transverse end to another.
L_{rdi}	Length of i 'th reinforcement if it is discontinues at mid-length of the test embankment.
L_{ri}	Length of i 'th active reinforcement.
L_{reff}	Length of reinforcement extending beyond rupture wedge.
L_{r1}	Length of the test embankment with reinforcement from centre of test embankment towards right side face.
L_{r2}	Length of the test embankment with reinforcement from centre of test embankment towards left side face.
L_s	Length of the test embankment with plain sand (reinforcing element in this segment not active).
l_e	Element length in FEM discretization.
$[M]$	Mass matrix.
M_f	Magnification factor.
m_e	Eccentric mass of mechanical oscillator.
m_i	Mass of i 'th layer of embankments (in the back - analyses).
m_k	Mass of k 'th layer of embankment (in the back- analyses).
N	Shape function
OME	Oscillator mass eccentricity number.
P_s	Pullout force under static condition.

P_r	Force of pullout resistance obtainable for a reinforcement with p_r as pullout resistance per unit width of reinforcement.
P_{rs}	Residual earth force.
P_s	Pullout force under static condition.
P_{sr}	Ratio of P_s/P_{smax} .
P_{smax}	Maximum pullout force under static condition.
P_{rmax}	Maximum force of pullout resistance obtainable for a reinforcement with p_{rmax} as pullout resistance per unit width of reinforcement.
P_{dri}	Dynamic pullout resistance force per unit width.
P_{pri}	Pullout resistance offered by plain sand in ith layer.
P_e	Earth pressure intensity.
p_{rmax}	Maximum static pullout resistance per unit width of reinforcement.
p_{smax}	Maximum intensity of pullout force per unit width of reinforcement generated by pullout test.
p_s	Intensity of applied pullout force per unit width of reinforcement
R_e	Reynold's number.
R_o	Open ratio.
R_p	Perforation ratio.
R_s	Spacing ratio.
r_f	Frequency ratio (F_{rq}/F_n)
r_G	Ratio of shear modulus, defined as (G_r/G_s) of shear modulus of reinforced earth to that of plain sand.
r_a	Ratio of computed maximum absolute acceleration response to that obtained experimentally.
r_{ad}	Percentage discrepancy between r_a and r_{aideal} .
r_{aideal}	Ideal value of r_a .
r_{am}	Ratio of amplification factor.

r_d	Ratio of computed maximum absolute displacement response to that obtained experimentally.
r_{dd}	Percentage discrepancy between r_d and r_{dideal} .
r_{dideal}	Ideal value of r_d .
r_e	Excitation force ratio.
S_{vpmx}	Maximum percentage vertical settlement for the soil obtained from the void ratios at maximum and minimum densities.
S_{are}	Average settlement of R.E. test embankment at top end.
S_{av}	Average settlement of front and rear side of soil sample in pullout test box.
S_{avdp}	Percentage of S_{av} to depth of soil sample in pullout test box.
S_{fs}	Settlement of soil sample in front side of pullout test box.
S_u	Maximum settlement R.E. embankment fill.
S_x	Matrix describing degrees of freedom in x (horizontal) directions
S_y	Matrix describing degrees of freedom in y (vertical) directions
S_{rs}	Settlement of soil sample in rear side of pullout test box.
S_{er}	Differential settlement between the outer end of the reinforcement and its mid length.
T_s	Tension of reinforcement under static conditions.
T	Period of vibration in sec.
t_p	Duration to reach maximum pullout displacement for a given loading increment under consideration.
t_g	Gap between upper and lower part of the box used for pullout resistance test.
t_r	Thickness of reinforcement.
u	Horizontal displacement in Article 5.2.1.
$\{u(t)\}$	Displacement matrix at time t for element in 5.2.2.

$\{\dot{u}(t)\}$	Velocity matrix at time t.
$\{\ddot{u}(t)\}$	Acceleration matrix at time t.
V_s	Shear wave velocity in m/sec.
v	Verticle displacement in Article 5.2.1.
v_t	Terminal velocity of falling particle in m/sec.
v_h	Horizontal velocity of falling Particle in m/sec.
W	Total weight of R.E. test embankment.
W_i	Weight of test embankment acting on the base of the i'h layer.
X	Vertical distance between the two points under consideration.
X_g	Base excitation in horizontal direction
X_b	Distance from top of the test embankment upto the base level of bottom pickup.
X_i	Depth from top of the test embankment upto the base of the i'th layer.
X_m	Distance from top of the test embankment upto position of middle pickup.
X_t	Distance from top of the test embankment upto position of top pickup.
Y_{bt}	Acceleration vector at bottom position of pickup at time t.
Y_k	Acceleration at the mid height of the k'th element.
Y_g	Base excitation in vertical direction
Y_{mt}	Acceleration vector at middle position of pickup at time t.
Y_{tt}	Acceleration vector at top position of pickup at time t.
α_{hav}	Equivalent acceleration response.
α_{hb}	Coefficient of horizontal acceleration at base pickup level.
α_{hm}	Coefficient of horizontal acceleration at middle pickup level.
α_{ht}	Coefficient of horizontal acceleration at top pickup level.

Δ_p	Load increment.
Δt	Time lag.
Δt_p	Particle time of the travel.
$\{\delta\}^e$	Displacement vector for nodes of an element.
$\delta\theta$	Phase difference.
$\delta\theta_b$	Phase difference at base w.r.t. the phase angle at the top end of embankment.
$\delta\theta_m$	Phase difference at middle position of acceleration pickup w.r.t. the phase angle at the top end of embankment.
$\delta\theta_t$	Phase difference at top position of acceleration pickup w.r.t. the phase angle at top end of embankment.
$\{\varepsilon\}$	Strain matrix.
ε_p	Pullout strain under static conditions.
ε_{pmax}	Maximum pullout strain under static conditions.
ε_{th}	Threshold strain.
ϕ	Angle of shearing resistance of plain sand.
ϕ_m	Mobilised angle of shearing resistance of plain sand.
ϕ_p	Angle of pullout resistance of reinforcement.
ϕ_{avpi}	Angle of average pullout resistance developed along the i'th reinforcing element.
ξ	Local coordinate in y direction of a point in isoparametric element.
γ	Shear strain.
γ_{avdmx}	Maximum average shear strain.
γ_d	Unit weight of dry soil.
γ_{dav}	Average unit weight of dry soil.
γ_m	Average mobilised shear strain of plain sand.

γ_r	Average mobilised shear strain at top pickup level of embankment.
γ_{rn}	Average mobilised shear strain at top pickup level of test embankment at resonance.
γ_s	Average mobilised shear strain for plain sand.
γ_{sp}	Specific weight of solid for falling particle.
λ	Wave length in m.
μ_{avd}	Weighted average value of mobilised coefficient of dynamic pullout resistance for the entire test embankment.
μ_{avdi}	Mobilised coefficient of dynamic pullout resistance for i'th reinforcement.
μ_{avdmx}	Maximum weighted average value of mobilised coefficient of dynamic pullout resistance for all phase angles considered for the entire test embankment.
μ_{avs}	Coefficient of static pullout resistance.
$\mu_{avsfield}$	Coefficient of static pullout resistance corresponding to field conditions.
μ_{avsmx}	Maximum coefficient of static pullout resistance.
ν	Poission's ratio
ν_f	Kinematic viscosity of fluid (air).
θ	Phase angle.
θ_b	Phase angle at base pickup level.
θ_m	Phase angle at middle pickup level.
θ_t	Phase angle at top pickup level.
θ_{top}	Phase angle at top end of embankment.
θ_{bt}	Phase angle at the base pickup level at time t.
θ_{mt}	Phase angle at the middle pickup level at time t
θ_{tt}	Phase angle at the top pickup level at time t.

ρ	Mass density of solid of falling particle.
σ_{ov}	Overburden stress.
σ_v	Vertical stress.
σ_2	Normal stress (intermediate principal stress) acting on the transverse plane.
σ_h	Lateral stress.
σ_{oct}	Octahedral stress.
σ_{oct1}	Octahedral stress at mid depth of first layer of embankment when idealized as two layers system.
σ_{oct2}	Octahedral stress at mid depth of second layer of embankment when idealized as two layers system.
σ_{octm}	Octahedral stress at mid depth of embankment when idealized as single layer system.
σ_x	Normal stress in x (horizontal) direction (in FEM analysis).
σ_y	Normal stress in y (vertical) direction (in FEM analysis).
τ	Shear stress.
τ_D	Dynamic shear stress in X-Y plane (in FEM analysis).
τ_{Dmax}	Maximum dynamic shear stress in X-Y plane (in FEM analysis).
τ_p	Pullout stress under static condition
τ_{pmax}	Maximum pullout stress under static condition
τ_{xy}	Shear stress in X-Y plane (in FEM analysis).
ω	Angular velocity per second.
ω_n	Circular frequency at resonance.
ξ	Local coordinate in x direction of a point in isoparametric element.
ζ_1	Damping ratio for fundamental frequency.
ζ_2	Damping ratio for second natural frequency.

LIST OF FIGURES

Figure no.	Description	Page no.
1.2.1	Reinforced Earth Under Static Condition.	3
1.2.2	Stress Strain Curves	3
1.2.3	Stress Strain Curves for Geotextile (Rankilor, 1981)	4
1.2.4	Pullout Resistance.	4
1.3.1	Reinforced Earth Under Earthquake Loading	5
1.5.1	Types of Embankment Failures	6
1.5.2	Cross Section of Reinforced Earthen Embankment.	6
1.6.1	Embankments Type Employed in Geotechnical Engg.	7
2.2.1	Types of Reinforced Earth Embankments.	15
2.2.2	Components of Reinforced Earth Embankments.	16
2.3.1	Reinforced Earth Embankment with Two Side Slopes.	18
2.3.2	Forces Acting on Horizontal Element of R.E. Embankment.	19
2.3.3	Bilinear Idealization of Rupture Surface for Reinforced Earth (Schlosser, 1988; Boyd, 1985; Nagel, 1985 and Tai, 1985).	19
2.3.4	Failure Surfaces and Reinforcement for Embankment with Two Sides.	21
2.3.5	Wedge Analysis with Bilinear Rupture Surface (Romstad et al., 1978).	22
2.3.6	Bi-linear Failure Surface (Bacot and Lareal, 1976)	24
2.3.7	Design Charts for Steep Reinforced Slope (Jewell, 1990).	24
2.3.8	Comparison of Discrete (Homogeneous) and Composite Analysis Results (Herrmann and Al-Yassin, 1978).	27
2.3.9	Depth of Edge Effect and Slippage Zones. (Herrmann and Al-Yassin, 1978).	27
2.3.10	Horizontal Stress Behind Facing (Smith and Segerestin, 1992).	30
2.3.11	Inclination of Failure Surface to the Vertical (Smith and Wroth, 1978).	32

Figure no.	Description	Page no.
2.3.12	Observed and Theoretical Failure Plane (Lee, et. al., 1973).	32
2.3.13	Distribution of Reinforcement Tensions (Schlosser and Long, 1974).	35
2.3.14	Measured Lateral Earth Pressures (Lee, et. al., 1973).	36
2.3.15	Effect of Compaction Operation on Tensile Stresses in Reinforcing Elements (Finlay and Sutherland, 1977).	39
2.3.16	Rankine Failure Wedge within the Reinforced Zone (Lee et. al. 1973).	41
2.3.17	Comparison of Theoretical and Experimental Results (Lee et. al., 1973).	41
2.3.18	Idealized Failure Surface (McKittrick, 1978).	43
2.3.19	Facing Element-reinforcement Connections, the Doe York System (Johnes, 1978).	43
2.3.20	Types of Facing Elements (Tatsuoka, 1992).	45
2.4.1	Static and Dynamic Earth Pressure Behind Vertical Face of R.E. Embankment (Richardson and Lee, 1975).	47
2.4.2	Estimating Peak Dynamic Strains (Richardson, 1978).	47
2.4.3	Estimating the Level of Damping (Richardson, 1978).	47
2.4.4	Design Response Spectra Synthesis (Richardson, 1978).	49
2.4.5	Natural Frequency of Reduction Factor (Richardson, 1978).	51
2.4.6	Stiffness vs Dynamic Earth Pressure (Richardson, 1978).	51
2.4.7	Variation of R_t and R_l with Slope Angle, β , Soil Strength, ϕ , and Seismic Coefficient Bonaparte, et. al., 1986).	54
2.4.8	Active Zone from Japanese Work (Tai, 1985).	59
2.4.9	Static, Dynamic and Inertia Earth Pressures (Tai, 1985).	59
2.4.10	Seismic Design-Displacement Methods(Planar and Biplaner), Jones, 1985.	61
2.4.11	Limiting Equilibrium, Failure Surface Contained (Fairless, 1989).	63
2.4.12	Limiting Equilibrium, Failure, not Contained (Fairless, 1989).	63

Figure no.	Description	Page no.
2.4.13	Rupture Surface For two Step R.E. Structure (Fairless, 1989).	66
2.4.14	Observed and Calculated Displacements Plotted on Lin and Whitman's (1986) Chart of Normalized Conditional Expected Displacement vs Normalized Yield Acceleration (Fairless, 1989).	67
2.4.15	Normalized Conditional Probability of Exceedence of a Permanent Displacement for Sliding Blocks (Fairless, 1989).	67
2.4.16	Slice for a Circular Slip Surface Analysis (Koga, et.al., 1988).	71
2.4.17	Calculation of Tension of Geotextile (Koga, et.al., 1988).	71
2.4.18	Relationship between Mobilized Force and Deformation of Soil Mass (Koga, et.al., 1988).	71
2.4.19	Results of Finite Element Analysis of 12-in (300 mm) Wall for Maximum Seismic Forces Only (Richardson and Lee, 1975).	74
2.4.20	Earthquake Motion Used for Design Example : (a) Accelerograph; (b) Acceleration Response Spectra (Richardson and Lee, 1975).	75
2.4.21	Dynamic Modulus and Damping form Shaking Table Tests (Richardson and Lee, 1975).	75
2.4.22	Results of Model Tests on Reinforced Embankment (Uezawa and Nasu, 1973).	78
2.4.23	Measured Tie Force for Various Accelerations (Richardson and Lee, 1975).	80
2.4.24	Resonance Response of Model Reinforced Earth (Richardson and Lee, 1975).	80
2.4.25	Damping Values and Maximum Dynamic Shear Strains Calculated from the Blast and Forced Vibration Tests (Richardson, et. al., 1977).	82

Figure no.	Description	Page no.
2.4.26	Magnification Factor for Acceleration Pulses (Rea and Wolfe, 1980).	84
2.4.27	Effect of Factor of Safety on Yield Accelerations (Rea and Wolfe, 1980).	85
2.4.28	Effect of Acceleration Intensity on Permanent Displacements (Rea and Wolfe, 1980).	85
2.4.29	Measured and Calculated First and Second Modes Natural Frequencies for Different Height of R.E. Walls (Richardson, et.al., 1977).	87
2.4.30	Field Measured Dynamic Properties of Backfill Soil at UCLA Test Wall Compared with Published Data (Richardson et. al., 1977).	87
2.4.31	Relation of Safety Factor, F_s , with Inclination of Strip Zone, θ (Iwaski and watnable, 1978).	89
2.4.32	Walls after Failure (Nagel, 1985).	92
2.4.33	Typical Acceleration and Displacement Time Histories Late in Test (Nagel, 1985).	93
2.4.34	Maximum Forces Adjacent to the Wall Facing, Test 2 (Fairless, 1989).	98
2.4.35	Failure Geometries, Test 4 and 5 (Fairless, 1989).	100
2.4.36	Distribution of Residual (End of Run) Forces at the Wall Facing, Test 2 (Fairless, 1989).	100
2.5.1	Pullout Resistance of Reinforcement.	104
2.5.2	Variation of Pullout Tests Apparant Friction Coefficient, μ_{avs} , with Height of Fill (after Schlosser and Elias, 1978).	107
2.5.3	Results of Tie Pullout Tests from Middle of Box (Richardson and Lee, 1975).	111
3.2.1a	Relationship between C_D , $F_{drag}/\rho_f v_f^2$ and R_e for Sphere and Disk (Garde and Mirajgaonker, 1977).	121
3.2.1b	Terminal velocity, v_t , Versus Diameter of Spheres Particle, D_s , in Air.	121

Figure no.	Description	Page no.
3.2.2	Velocities of Spheres of Different Diameters with Height of Fall, H_f , in Air.	121
3.2.3	Soil Column Standing on SRA.	127
3.2.4	Improved Sand Rain Apparatus (a) View of SRA When Seen from below (b) Side View of SRA.	130
3.2.5	Suspended SRA Filled with Sand.	131
3.2.6	Close View on SRA with Shutters in Their Open Position.	131
3.2.7	Longitudinal View of SRA with Longitudinal Clamps and Shutters in Their Open Position.	132
3.2.8	Transverse View of SRA with Longitudinal Clamps and Shutters in Their Open Position.	132
3.2.9	Position of Containers on the Test Bed.	134
3.2.10	Variation of Average Mean Density, γ_{dav} , with Height of Fall, H_f .	134
3.2.11	Variation of Relative Density, D_r %, with Height of Fall, H_f .	135
3.2.12	Variation of Void Ratio with Height of Fall, H_f .	135
3.2.13	Variation of Standard Deviation, S_d %, with Height of Fall, H_f .	136
3.2.14	Variation of % Relative Density, D_r , with Depths of Containers.	138
3.2.15	Variation of % Deviation in Relative Density, D_r , with Depths of Containers.	138
3.2.16	Variation of % Change in Relative Density, D_{rpc} , with Average Value of Height of Fall, H_{fa} .	140
3.2.17	Variation of Repetition of Densities of Different Percentage Deviations for Study of Reproducibility.	140
3.2.18	Variation of Mean % Deviation in D_r With Distance from Longitudinal Side, L_{SRA} .	142
3.2.19	Variation of Mean % Deviation in D_r with Distance from Transverse Side, B_{SRA} .	142

Figure no.	Description	Page no.
3.3.1	Details of Shake Table Assembly.	144
3.3.2	Variation of Horizontal Acceleration Coefficient at Base of Shake Table with Square of Frequency When Shake Table Oscillator is Set to Different Position of Its Eccentricity (OME) and Test Embankment Being Mounted on Table.	144
3.4.1	Arrangement for Suspension of SRA.	147
3.5.1	Details of Form Work for Preparation of Test Embankment.	148
4.2.1a	Grain Size Distribution Curve for Solani Sand.	153
4.2.1b	Microscopic View of Solani Sand Grains (Gupta, 1977).	153
4.2.2a	Stress - strain Relationships for Solani Sand (Direct Shear Test).	155
4.2.2b	Mohr Envelop for Solani Sand (Direct Shear Test).	155
4.3.1	Schematic Diagram of Stress Control Type of Apparatus of Apparatus for Static Pullout Resistance.	158
4.3.2	Calibration Chart for Proving Ring (RC.519) in Tension.	160
4.3.3	Calibration Setup for Proving Ring.	161
4.3.4	Lower Half of the Direct Shear Box Filled With Soil and With the Reinforcement With the Grip Placed in Position.	161
4.3.5	The Finished Soil Sample in Direct Shear Box.	163
4.3.6	Test Setup for Pullout Resistance at the Beginning of the Loading.	163
4.3.7	Test Setup for Pullout Resistance with Weights Placed on the Loading Hanger.	164
4.3.8	Results to Establish of Reproducibility of Test Results.	166
4.3.9	Influence of the Time on Pullout Displacement Using Woven Geotextiles Reinforcement (RE1).	167
4.3.10	Effect of Ratio of Pullout Force, P_{sr} , on Time for Reaching Maximum Pullout Displacement, d_p .	168
4.3.11	Influence of the Time on Pullout Displacement Using Nonwoven Geotextile Reinforcement (RE2).	169

Figure no.	Description	Page no.
4.3.12	Influence of the Time on Pullout Displacement Using Nonwoven Geotextile Reinforcement (RE3).	170
4.3.13	Variation of Percentage Pullout Strain, ϵ_p , with μ_{avs} for Woven Geotextile RE1 (295mm x 200mm).	173
4.3.14	Variation of Percentage Pullout Strain, ϵ_p , with μ_{avs} for Nonwoven Geotextile RE2 (295mm x 290mm).	175
4.3.15	Variation of Percentage Pullout Strain, ϵ_p , with μ_{avs} for Woven Geotextile RE3 (295mm x 290mm).	175
4.3.16	Variation of Average Coefficient of Pullout Resistance, μ_{avs} , with Width of Reinforcement, B_r .	177
4.3.17	Idealization Intensity of Pullout Resistance and Applied Pullout Force Considered for Pullout Tests.	179
4.3.18	Different Types of Idealized Variation of Pullout Resistance after Redistribution Along the Width of the Reinforcement.	179
4.3.19	Variation of % Dimensionless Yield Width, B_{rd} , with Relative Density, D_r ,	182
4.3.20	Variation of % Dimensionless Yield Width, B_{rd} , with Normal Stress, σ_v .	185
4.3.21	Variation of Dimensionless Yield Width, B_{rd} , with Width of the Reinforcement, B_r .	186
4.3.22	Variation of % Dimensionless Yield Width, B_{rd} , with Width of Reinforcement, B_r , When B_{rd} is Zero for Smaller Width, $B_r = 100\text{mm}$.	186
4.3.23	Details of Arching Action on Pullout Resistance.	188
4.4.1	Schematic Diagram of R.E. Test Embankment.	191
4.4.2	Details of the Arrangement for Creating Plane Strain condition.	193
4.4.3	View of the Transverse Face of R.E. Test Embankment at the End of Construction after Removal of Form Work.	194
4.4.4	Arrangement for Fixity of the Embankment at the Base.	196
4.4.5	Details of the Hinge at the Base of the Longitudinal Facing.	198

Figure no.	Description	Page no.
4.4.6	Details of Connections Between the Soil Reinforcement, Geotextile Strips Covering Transverse Side and the Facing Element.	200
4.4.7	Details of Measures Taken to Avoid Leakage of Sand at Corner Joints.	201
4.4.8	Schematic Diagram of Details of Top Cover and Top Layer of the Embankment.	201
4.4.9	View of the Setup at the Beginning of Preparation of R.E. Test Embankment.	204
4.4.10	View of the Test Setup after Placing and Connecting the Geotextile Reinforcement.	204
4.4.11	View of R.E. Test Embankment with Form Work in Position at the end of Construction.	205
4.4.12	View of the Longitudinal Face of the Embankment with Acceleration Pickups in Position.	205
4.4.13	A View of the Free Standing R.E. Test Embankment on Shake Table and the Amplifiers and Recorder Just Before the Dynamic Testing.	207
4.4.14	A view of R.E. Test Embankment after the Dynamic Tests is Completed.	207
4.5.1	Schematic Diagrams of Test Embankments.	210
4.5.2	Accelerations and Phase Angles Along the Height of the Embankment.	214
4.5.3	Schematic Diagrams of Embankment Indicating Participating Reinforcements when Subjected to Forward and Reverse Direction Loading.	217
4.5.4	Flow Diagram for the Computer Software 'DYMU'.	222
4.6.1	Frequency-Response Curves for embankment M3 Measured at top Pickup (OME = 6, 9 and 12).	237
4.6.2	Frequency-Response Curves for embankment M3 Measured at top Pickup (OME = 18, 24 and 36).	238
4.6.3	Frequency-Response Curves for embankments M2 and M3 Measured at top Pickup.	239

Figure no.	Description	Page no.
4.6.4	Frequency-Response Curves for embankments M1, M2 and M3 Measured at top Pickup (OME=24).	240
4.6.5	Frequency-Response Curves for embankments M1, M2 and M3 Measured at top Pickup (OME=36).	241
4.6.6	Frequency-Response Curves for embankments M2 and M3 Measured at Middle Pickup.	242
4.6.7	Frequency-Response Curves for embankments M1, M2 and M3 Measured at Middle Pickup (OME=24).	243
4.6.8	Frequency-Response Curves for embankments M1, M2 and M3 Measured at Middle Pickup (OME=36).	244
4.6.9	Variation of Fundamental Frequency of Vibration, F_n , Shear Modulus, G_{rn} , Shear Strain, γ_{rn} , and Magnification Factor, M_f with Excitation Force Ratio, r_e , for R.E. Embankments at Resonance.	245
4.6.10	Variation of Equivalent Design Seismic, α_{hav} , with Coeff. of Base Acceleration, α_{hb} , for R.E. Embankments.	248
4.6.11	Relationship of F_n with Embankment Height, H.	248
4.6.12	Variation of Shear Modulus, G_r , With Shear Strain, γ_r , for R.E. Embankments and Modulus, G_s , and Shear Strain, γ_s , for Plain Sand.	250
4.6.13	Relationship between Shear Strain, γ , and the Ratio, r_G , of Shear Modulus of R.E. to That of Plain Sand.	251
4.6.14	Relationship between Normalised Shear Modulus, G_n , and Shear Strain, γ , for R.E. Embankments for R.E. Specimens by Shewbridge and Sousa (1991).	253
4.6.15	Variation of Shear Modulus, G_r , with Frequency of Excitation, F_{rq} , for R.E. Embankment, M1.	255
4.6.16	Variation of Shear Modulus, G_r , with Frequency of Excitation, F_{rq} , for R.E. Embankment M2.	255
4.6.17	Variation of Shear Modulus, G_r , with Frequency of Excitation, F_{rq} , for R.E. Embankment M3.	256
4.6.18	Variation of Dimensionless Shear Modulus (G_r/G_{rn}) with Frequency Ratio, r_f , for R.E. Test Embankment M1.	256

Figure no.	Description	Page no.
4.6.19	Variation of Dimensionless Shear Modulus (G_r/G_{rn}) with Frequency Ratio, r_f , for R.E. Test Embankment M2.	257
4.6.20	Variation of Dimensionless Shear Modulus (G_r/G_{rn}) with Frequency Ratio, r_f , for R.E. Test Embankment M3.	257
4.6.21	Variation of Acceleration with Dimensionless Depth (X/H) at Different Phase Angle, θ , for R.E. Test Embankment M1.	260
4.6.22	Variation of Acceleration with Dimensionless Depth (X/H) at Different Phase Angle, θ , for R.E. Test Embankment M2.	261
4.6.23	Variation of Maximum Average Shear Strain, γ_{avdmax} , with Frequency Ratio, r_f , for R.E. Test Embankment M1.	262
4.6.24	Variation of Maximum Average Shear Strain, γ_{avdmax} , with Frequency Ratio, r_f , for R.E. Test Embankment M2.	262
4.6.25	Variation of Maximum Average Shear Strain, γ_{avdmax} , with Frequency Ratio, r_f , for R.E. Test Embankment, M3.	263
4.6.26	Variation of Dimensionless Disturbing Force (F_{dmx}/W) with Frequency Ratio, r_f , for R.E. Test Embankment, M1.	263
4.6.27	Variation of Dimensionless Disturbing Force (F_{dmx}/W) with Frequency Ratio, r_f , for R.E. Test Embankment, M2.	264
4.6.28	Variation of Dimensionless Disturbing Force (F_{dmx}/W) with Frequency Ratio, r_f , for R.E. Test Embankment, M3.	264
4.6.29	Variation of Average Coefficient of Pullout Resistance, μ_{avd} , with Phase Angle θ , for R.E. Test Embankment, M1.	266
4.6.30	Variation of Average Coefficient of Pullout Resistance, μ_{avd} , with Phase Angle θ , for R.E. Test Embankment, M1.	266
4.6.31	Variation of Average Coefficient of Pullout Resistance, μ_{avd} , with Phase Angle θ , for R.E. Test Embankment, M2.	267
4.6.32	Variation of Average Coefficient of Pullout Resistance, μ_{avd} , with Phase Angle θ , for R.E. Test Embankment, M2.	267
4.6.33	Variation of Average Coefficient of Pullout Resistance, μ_{avd} , with Phase Angle θ , for R.E. Test Embankment, M3.	268
4.6.34	Variation of Average Coefficient of Pullout Resistance, μ_{avd} , with Phase Angle θ , for R.E. Test Embankment, M3.	268

Figure no.	Description	Page no.
4.6.35	Variation of Average Coefficient of Pullout Resistance, μ_{avd} , with Phase Angle θ , for R.E. Test Embankment, M3.	269
4.6.36	Variation of Average Coefficient of Pullout Resistance, μ_{avd} , with Phase Angle θ , for R.E. Test Embankment, M3.	269
4.6.37	Variation of Maximum Average Coefficient of Dynamic Pullout Resistance, μ_{avdmax} , with Frequency Ratio, r_f , for R.E. Test Embankment M1.	271
4.6.38	Variation of Maximum Average Coefficient of Dynamic Pullout Resistance, μ_{avdmax} , with Frequency Ratio, r_f , for R.E. Test Embankment M2.	271
4.6.39	Variation of Maximum Average Coefficient of Dynamic Pullout Resistance, μ_{avdmax} , with Frequency Ratio, r_f , for R.E. Embankment M3.	272
4.6.40	Sinusoidal Acceleration-Time Response.	272
4.6.41	Variation of Maximum Average Coefficient of Dynamic Pullout Resistance, μ_{avdmax} , with Maximum Shear Strain, γ_{avdmax} , for R.E. Test Embankment M1.	275
4.6.42	Variation of Maximum Average Coefficient of Dynamic Pullout Resistance, μ_{avdmax} , with Maximum Shear Strain, γ_{avdmax} , for R.E. Test Embankment M2.	275
4.6.43	Variation of Maximum Average Coefficient of Dynamic Pullout Resistance, μ_{avdmax} , with Maximum Shear Strain, γ_{avdmax} , for R.E. Test Embankment M3.	276
4.6.44	Variation of Coefficient of Average Dynamic Pullout Resistance, μ_{avdi} , for R.E. Test Embankment, with Dimensionless Depth (X/H).	278
4.6.45	Residual Displacement of R.E. Embankments M3 and M2 at the End of Tests at Different Excitation Frequencies.	280
4.6.46	Net Confining Pressure Distribution along the Dimensionless Depth for Embankments M2 and M3.	285
4.6.47	Residual Force, p_{rs} , in Reinforcement with Dimensionless Depth (X/H) at the End of Dynamic Test on M3 and p_{rs} per reinforcement Reported by Other Investigators.	287

Figure no.	Description	Page no.
4.6.48	Average Settlement, S_{ave} , Profile of R.E. Test Embankments M2 and M3 at Top at End of Dynamic Tests.	289
4.6.49	Maximum Settlement, S_u , and Loss of Contact at Different Reinforcement Levels of Embankment M3.	291
4.6.50	Mechanics of Forces Generated due to Settlement and Earth Pressure.	293
5.2.1	Four Noded Isoparametric Quadrilateral Element and location of Gauss Integration Points.	304
5.3.1	Damping Ratios for Sands (after Seed et.al.,1984).	318
5.3.2	Idealized R.E. Embankment for 2D FEM Analysis.	320
5.3.3	Base Excitation A1 Generated Based on Peak Amplitude of Acceleration Recorded for R.E. Embankment, M1.	323
5.3.4	Base Excitation A3 Generated Based on Peak Amplitude of Acceleration Recorded for R.E. Embankment, M3.	323
5.3.5	Idealized Plain Sand Embankment, P1, for 2D FEM Analysis.	326
5.3.6	Idealized Plain Sand Embankment, P2, for 2D FEM Analysis.	326
5.3.7	Type of Idealization for R.E. Embankments.	328
5.3.8	Flow Diagram of Software FE95.	331
5.4.1a	Computed Relative Acceleration of Embankment M1, Excited at Base Excitation A1 (OME = 24) for $\zeta_1=0.05$.	333
5.4.1b	Computed Relative Acceleration of Embankment M1, Excited at Base Excitation A1 (OME = 24) for $\zeta_1=0.17$.	334
5.4.2a	Computed Relative Acceleration of Embankment M3, Excited at Base Excitation A3 (OME = 24) for $\zeta_1=0.05$.	336
5.4.2b	Computed Relative Acceleration of Embankment M3, Excited at Base Excitation A3 (OME = 24) for $\zeta_1=0.124$.	337
5.4.3	Computed Relative Acceleration of Plain Sand Embankment p1, excited at base excitation A1 (OME = 24).	339
5.4.4	Variation of Damping Ratio, ζ_1 , with Percentage Discrepancy in Acceleration, r_{ad} , at Mid-Depth of R.E. Embankments M1 and M3 Idealized as Homogeneous Single Layer.	340

Figure no.	Description	Page no.
5.4.5	Computed and Experimentally Recorded Maximum Acceleration with Dimensionless Depth (X/H) for R.E. Embankment M1 Excited at Its Fundamental Frequency (OME=24).	342
5.4.6	Variation of Percentage Discrepancy in Acceleration, r_{ad} , with Dimensionless Depth (X/H) for R.E. Embankment M1 Idealized as Homogeneous Single and two Layers.	342
5.4.7	Computed and Experimentally Recorded Maximum Acceleration with Dimensionless Depth (X/H) for R.E. Embankment M3 (OME=24).	344
5.4.8	Variation of Percentage Discrepancy in Acceleration, r_{ad} , with Dimensionless Depth (X/H) for R.E. Embankment M3 Idealized as Homogeneous Single and two Layers.	344
5.4.9	Comparison of Computed Maximum Absolute Acceleration for Plain Sand Embankments P1 and P2 with that of M1 from Tests.	345
5.4.10	Comparison of Computed Amplifications for R.E. Embankment M1 and Plain Sand Embankments P1 & p2.	347
5.4.11	Ratio of Computed Amplification Factor, r_{am} , of Embankments P1 and P2 w.r.t. that of M1.	347
5.4.12a	Computed Relative Displacement of R.E. Embankment M1 Excited at Base Excitation A1 (OME = 24) for $\zeta_1=0.05$.	348
5.4.12b	Computed Relative Displacement of R.E. Embankment M1 Excited at Base Excitation A1 (OME = 24) for $\zeta_1=0.17$.	349
5.4.13a	Computed Relative Displacement of R.E. Embankment M3 Excited at Base Excitation A3 (OME = 24) for $\zeta_1=0.05$.	351
5.4.13b	Computed Relative Displacement of R.E. Embankment M3 Excited at Base Excitation A3 (OME = 24) for $\zeta_1=0.124$.	352
5.4.14	Computed Relative Displacement of Plain Sand Embankment P1 Excited at Excitation A1 (OME = 24).	353
5.4.15	Computed and Experimentally Recorded Maximum Displacement with Dimensionless Depth (X/H) for R.E. Embankment M1 Excited at Its Fundamental Frequency (OME=24).	355

Figure no.	Description	Page no.
5.4.16	Variation of Percentage Discrepancy in Displacement, r_{dd} , with Dimensionless Depth (X/H) for R.E. Embankment M1 Idealized as Homogeneous Single and two Layers.	355
5.4.17	Computed and Experimentally Recorded Maximum Displacement with Dimensionless Depth (X/H) for R.E. Embankment M3 (OME=24).	356
5.4.18	Variation of Percentage Discrepancy in Displacement, r_{dd} , with Dimensionless Depth (X/H) for R.E. Embankment M3 Idealized as Homogeneous Single and two Layers.	356
5.4.19	Comparison of Computed Maximum Absolute Displacement for Plain Sand Embankment P1 and P2 with that of R.E. Embankment M1 from Tests.	357
5.4.20	Variation of Computed Dynamic Shear Stress, τ_D , of R.E. Embankment M1 Excited at Base Excitation A1 (OME =24) for $\zeta_1=0.05$.	359
5.4.21a	Variation of Computed Dynamic Shear Stress, τ_D , of R.E. Embankment M3 Excited at Base Excitation A3 (OME = 24) for $\zeta_1=0.05$.	360
5.4.21b	Variation of Computed Dynamic Shear Stress, τ_D , of R.E. Embankment M3 Excited at Base Excitation A3 (OME = 24) for $\zeta_1=0.124$.	361
5.4.22	Variation of Computed Dynamic Shear Stress, τ_D , of Plain Sand Embankment P1 Excited at Base Excitation A1.	362
5.4.23	Variation of Computed Dynamic Shear Stress, τ_D , of R.E. Embankment M1 :Excited at Base Excitation A1 (OME = 24) for $\zeta_1=0.05$.	363
5.4.24	Variation of Computed Dynamic Shear Stress, τ_D , of R.E. Embankment M3 Excited at Base Excitation A3 (OME = 24) for $\zeta_1=0.05$.	365
5.4.25	Variation of Computed Dynamic Shear Stress, τ_D , of Plain sand Embankment P1 Excited at Base Excitation A1.	366

Figure no.	Description	Page no.
5.4.26	Variation of Computed Maximum Dynamic Shear Stress, τ_{Dmax} , with Dimensionless Depth (X/H) for R.E. Embankment M1.	367
5.4.27	Variation of Computed Maximum Dynamic Shear Stress, τ_{Dmax} , with Dimensionless Depth (X/H) for R.E. Embankment M3.	367
5.4.28	Variation of Computed Maximum Dynamic Shear Stress, τ_{Dmax} , with Dimensionless Depth (X/H) for M1 and Plain Sand Embankments P1 and P2 for $\zeta_1=0.05$.	369
5.4.29	Variation of Computed Maximum Dynamic Shear Stress, τ_{Dmax} , with Dimensionless Distance for R.E. Embankment M1 from Left Transverse End.	369
5.4.30	Variation of Computed Maximum Dynamic Shear Stress, τ_{Dmax} , with Dimensionless Distance for R.E. Embankment M3 from Left Transverse End.	372
5.4.31	Variation of Computed Maximum Dynamic Shear Stress, τ_{Dmax} with Dimensionless Distance from Left Transverse End for Plain Sand Embankments P1 and P2.	372

LIST OF TABLES

Table no.	Description	Page no.
2.4.1	Dimensionless Factors.	55
2.4.2	Calculate and Observed Yield Acceleration k_h and Failure Surface Angles, α , (Fairless, 1989).	69
3.2.1	Details of Data Regarding SRAs and Soil Samples Used.	126
4.2.1	Properties of Solani Sand.	154
4.2.2	Material Properties of Woven Geotextile (RE1).	157
4.2.3	Material Properties of Nonwovens Geotextiles (RE2 and RE3).	157
4.3.1	Values of Δ_p , P_s and t_p From Pullout Tests on Geotextile RE1.	168
4.3.2	Results of Pullout Tests Using Geotextile, RE1.	171
4.3.3	Results of Pullout Tests Using Geotextiles RE1, RE2 and RE3.	172
4.3.4	Maximum Settlement of Soil Samples in Pullout Tests.	177
4.3.5	Dimensionless Yield Width Results From Pullout Tests Considering Linear Pullout Resistance Variation for AIH/DEG Area (RE1 Reinforcement, $B_r = 200$ mm)	184
4.5.1	Percentage Resisting Force Contribution by Plain Sand for R.E. Test Embankment, M3.	218
4.6.1	Parameters for Presentation of Results of Back-Analysis.	224
4.6.2a	Damping Ratios Obtained From Free Vibration Tests on R.E. Embankments.	225

Table no.	Description	Page no.
4.6.2b	Data From Free Vibration Tests on R.E. Embankments.	226
4.6.3	Accelerations, Displacements and Strains at Top Pickup Level of R.E Embankment, M1, Using Shake Table Tests.	228
4.6.4	Accelerations and Displacements at Mid Pickup Level of R.E. Embankment, M1, Using Shake Table Tests.	229
4.6.5	Accelerations, Displacement and Strains at Top Pickup Level of R.E. Embankment, M2, Using Shake Table Test.	230
4.6.6	Accelerations and Displacements at Mid Pickup Level of R.E. Embankment, M2, Using Shake Table Tests.	231
4.6.7	Accelerations, Displacement and Strains at Top Pickup Level of R.E. Embankment, M3, Using Shake Table Tests.	232
4.6.8	Accelerations and Displacements at Mid pickup level of R.E. Embankment, M3, Using Shake Table Tests.	234
4.6.9	Data From Forced Vibration Tests on Embankments at Resonance.	236
4.6.10	Percentage Differences in (G_r/G_{rn}) Values Computed w.r.t. the Mean Value of (G_r/G_{rn}) at Different r_f Values for R.E. Test Embankments.	258
4.6.11	Displacements and Corresponding Coefficient of Earth Pressures at the End of Shake Table Tests.	283
5.3.1	Details of Input data for Single Layer Idealization of Embankments.	321
5.3.2	Material Properties for M1 and M3 With Two Layer Idealization.	328

CONTENTS

	Page no.
Certificate	I
Acknowledgement	II
Abstract	IV
List of Abbreviations	VIII
Notations	X
List of Figures	XXII
List of Tables	XXXVII
1. INTRODUCTION	1
1.1 Preamble	1
1.2 Reinforced Earth Under Static Loading Conditions	2
1.3 Reinforced Earth Under Earthquake Loading	4
1.4 Philosophy of Earthquake Resistant Design	5
1.5 Behaviour of Reinforced Earth Embankments Under Earthquake Loading	5
1.6 Identification of the Problem	7
1.6.1 Investigation under elastic domain	8
1.6.2 Sample preparation and test setup	9
1.7 Objective of the Investigation	9
1.8 Scope of the Investigation	10
1.9 Outline of the Thesis Contents	11
2. REVIEW OF LITERATURE	13
2.1 Preamble	13
2.2 Components of Reinforced Earth Embankments	13
2.3 Investigations Under Static Conditions	17
2.3.1 Analytical investigations	17
2.3.2 Experimental investigations	31

	Page no.
2.4 Dynamic Investigations	46
2.4.1 Dynamic analytical investigations	46
2.4.2 Dynamic experimental investigations	77
2.5 Pullout Resistance of Reinforcements	103
2.6 Rain Fall Method for Preparing Test Embankment	112
2.7 Closure	114
3. EXPERIMENTAL SETUP	119
3.1 Preamble	119
3.2 Sand Rain Apparatus (ARS) for Sample Preparation	119
3.2.1 Theory	119
3.2.2 Factors affecting density obtained by rain fall method.	120
3.2.3 Design consideration for SRA	125
3.2.4 Improved manually operated SRA	128
3.2.5 Performance of SRA	133
3.3 Shake Table Facility	143
3.3.1 The shake table	143
3.3.2 Driving mechanism	143
3.4 Suspension of SRA	146
3.5 Form Work	146
3.6 Measuring Equipment	149
3.7 Closure	149
4. EXPERIMENTAL STUDIES USING SHAKE TABLE AND BACK-ANALYSES	151
4.1 Preamble	151
4.2 Material Properties of the Soil and Geotextiles	152
4.2.1 Material properties of the soil	152
4.2.2 Material properties of reinforcements	156
4.3 Static Pullout Resistance	156
4.3.1 Stress control apparatus for pullout resistance	156
4.3.2 Test procedure	160

	Page no.
4.3.3 Results of pullout resistance tests	165
4.3.4 Theoretical model for stress distribution for pullout tests	178
4.3.5 Effect of arching action on pullout resistance	187
4.4 Test Embankments for Dynamic Investigations	189
4.4.1 Fixing the dimensions of the test embankment	190
4.4.2 Simulation of plane strain conditions for test embankment	191
4.4.3 Components of the test embankment	195
4.4.4 Preparation of test embankments	202
4.4.5 Procedure for dynamic testing of embankments	206
4.5 Processing and Back-Analyses of Experimental Data	208
4.5.1 Fundamental frequency, shear strain and shear modulus	211
4.5.2 Variation of acceleration	213
4.5.3 Disturbing forces	215
4.5.4 Shear resistance due to plain sand	216
4.5.5 Displacement dependent dynamic pullout Resistance of a reinforcement	219
4.5.6 Average dynamic pullout resistance for the whole embankment	220
4.5.7 Computer software 'DYMU' for the back-analyses	221
4.6 Presentation of Results	223
4.6.1 Damping ratios from free vibration tests.	223
4.6.2 Frequency-acceleration response	224
4.6.3 Magnification factor	246
4.6.4 Shear modulus	248
4.6.5 Acceleration variation with phase angle	254
4.6.6 Shear strains	259
4.6.7 Disturbing inertia forces	265
4.6.8 Coefficient of dynamic pullout resistance	265
4.6.9 Lateral Displacements of Longitudinal Faces	279
4.6.10 Settlements	288
4.7 Closure	294

	Page no.
5. DYNAMIC ANALYSIS OF REINFORCED EARTHEN EMBANKMENTS	302
5.1 Preamble	302
5.2 Finite Element Method of Analysis in Time Domain	303
5.2.1 Finite element method.	303
5.2.2 Equation of motion.	312
5.2.3 Solution of equation of motion.	315
5.3 Idealization of Reinforced Earth	317
5.3.1 Details of R.E. embankments analysed.	319
5.3.2 Details of plain sand embankments analysed	325
5.3.3 Embankment analysis using two layer idealization.	327
5.3.4 Computer software 'FE95'.	329
5.4 Results of the Investigation	329
5.4.1 Acceleration response.	330
5.4.2 Displacement response.	346
5.4.3 Dynamic shear stresses.	357
5.5 Closure	371
6. CONCLUSIONS AND SUGGESTIONS FOR FUTURE RESEARCH	376
6.1 Preamble	376
6.2 Conclusions	377
6.2.1 Conclusions from pullout tests	378
6.2.2 Conclusions based on results of shake table tests and back-analyses.	379
6.2.3 Conclusions based on FEM dynamic analysis of embankments	384
6.3 Suggestions for Future Research	387
REFERENCES	390

INTRODUCTION

1.1 PREAMBLE

Earthquake is one of the many natural disasters. Earlier, it did not always lead to catastrophic loss of lives and property due to low population density and less intense economic use of the land. Now a days, earthquakes cause wide spread loss of lives and property. In spite of the progress in earthquake engineering, devastation due to major earthquakes has a unique psychological impact. As such, this problem demands serious attention by earthquake engineers.

Soil improvement by reinforcement is gaining popularity as it offers following significant advantages: (i) Its flexibility enables its construction directly on compressible foundation soil/unstable slopes. This reduces cost of foundations. (ii) It has high static/dynamic strength even though supported by very few investigations with dynamic loading; (iii) Easy to install by using prefabricated facing and reinforcing elements; (iv) Economy of construction materials, time and transportation under certain conditions and (v) Ready for use immediately after construction.

Its common application for road/railway/flood protection embankments and for small earth dams is very important for the economy. As such, their safe design and construction is essential. When situated in earthquake prone areas, it is necessary to know their behaviour under dynamic loading.

This investigation is an attempt in this direction. Only cohesionless fills are considered. Cohesive fills are not included in this study.

1.2 REINFORCED EARTH UNDER STATIC LOADING CONDITIONS

A plain earth element, ABCD, shown in Fig.1.2.1 (a) with vertical stress, σ_1 , and lateral stress, σ_3 , gets deformed to the shape IJKL at failure. Relationship between normal stress, σ , and shear stress, τ , is governed by the strength envelope and Mohr circle-I (Fig.1.2.1(b)). If this element is reinforced, the lateral soil strain induces tension in reinforcement. Traction developed within the element are transmitted to reinforcement through friction generated at interfaces. The net lateral strain will be such that the lateral force exerted on soil element will be equal and opposite to tension in reinforcement. The resulting additional confining stress, $\Delta\sigma_3$, increases effective confining pressure to $(\sigma_3 + \Delta\sigma_3)$ corresponding to circle II in Fig. 1.2.1 which does not touch the failure envelope. To reach failure at $(\sigma_3 + \Delta\sigma_3)$, it is necessary to increase the vertical stress from σ_1 to much larger $(\sigma_1 + \Delta\sigma_1)$ given by circle III. This highlights advantage of reinforced earth. The larger the elasticity modulus of reinforcement compared to that of plain soil, the smaller its lateral strain and deformation indicated by EFGH when compared to that of plain earth with same σ_1 .

Reinforced embankment comprises of three elements : facing element, reinforcements and soil. Steel/aluminium/R.C.C. facing elements are used to contain soil (Schlosser,1982). Strips of galvanized steel or aluminum

magnesium alloy were used in the past and geotextiles are presently in use as reinforcements (Mitchell, 1981; Korner and Welsh, 1980).

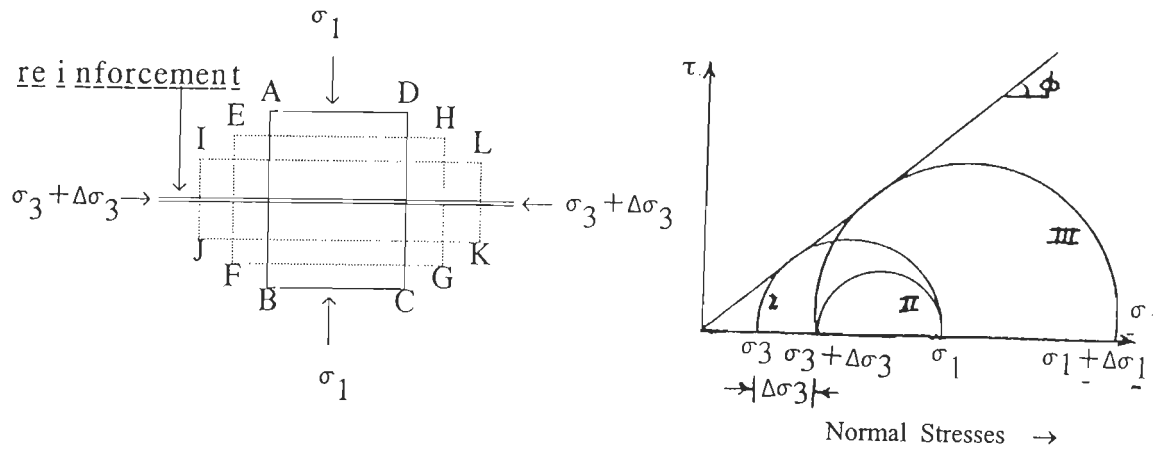


FIG. 1.2.1 REINFORCED EARTH UNDER STATIC CONDITION.

Ductility of materials is helpful in avoiding catastrophic failures due to earthquakes. Figure 1.2.2 shows two ductility behaviours of soils. Reinforcements may fail either in tension or due to excessive pulling out. Reinforcing materials like polypropylene, polyamide etc. exhibit desired ductility in tension (Fig. 1.2.3). To avoid earthquake induced catastrophic failures, tensile failure of reinforcements should be avoided. Pullout resistance of reinforcement (Fig. 1.2.4) exhibits ductility, especially for

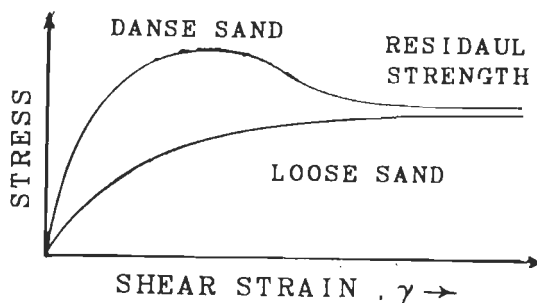


FIG. 1.2.2 STRESS - STRAIN CURVES.

FIG.1.2.2 STRESS STRAIN CURVES

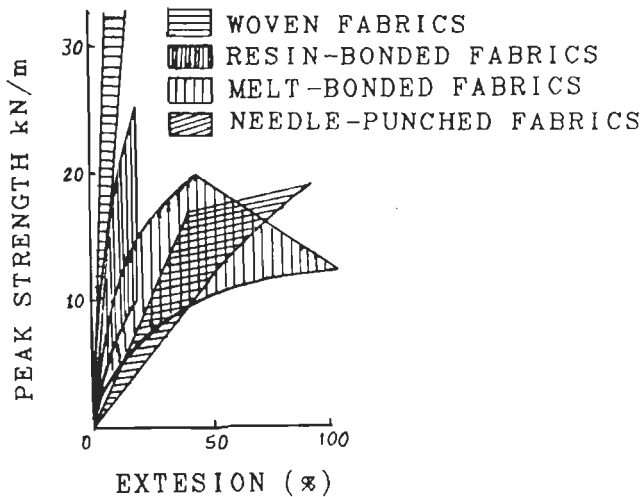


FIG. 1.2.3 STRESS - STRAIN CURVES FOR GEOTEXTILES (RANKILOR, 1981).

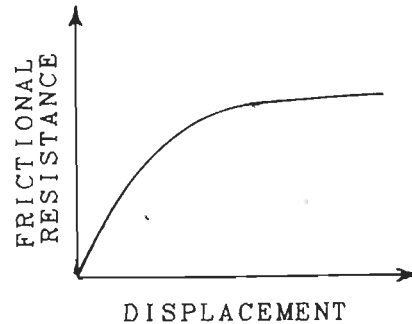


FIG. 1.2.4 PULLOUT RESISTANCE.

geotextiles. As such, it is prudent to allow some pulling out of reinforcements during earthquakes to benefit from associated ductility to avoid catastrophic failures. Therefore, reinforced earth is ductile and ideal for use in geotechnical earthquake engineering.

1.3 REINFORCED EARTH UNDER EARTHQUAKE LOADING

During earthquakes, a plain soil element with shear modulus, G_s , undergoes shear strain, γ_s , (Fig.1.3.1) due to shear stresses, τ , induced by upward propagating shear waves. The γ_s increases with increasing τ and decreasing G_s . Shear modulus of the composite reinforced earth, G_r , is larger than G_s of plain earth. Shear strain, γ_r , of reinforced earth is smaller than the corresponding γ_s for plain earth which is an advantage.

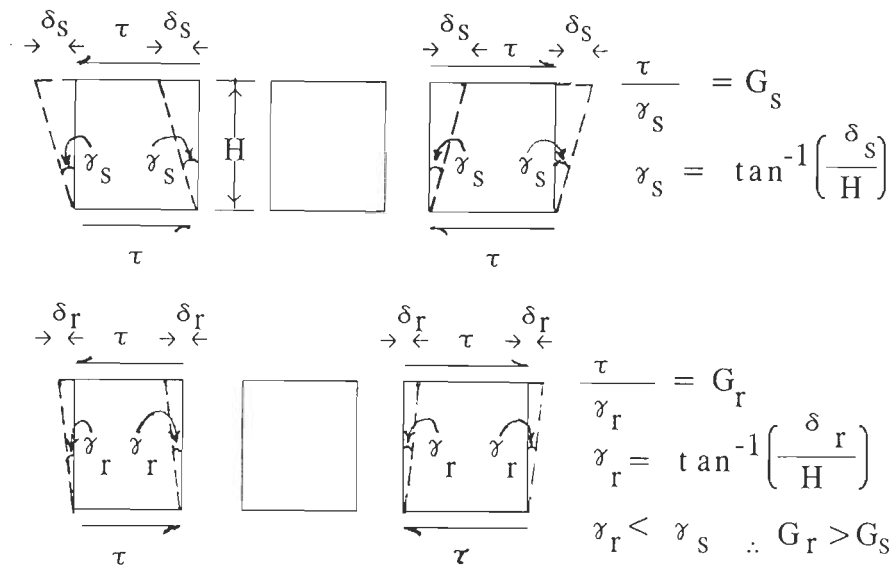


FIG. 1.3.1 REINFORCED EARTH UNDER EARTHQUAKE LOADING

1.4 PHILOSOPHY OF EARTHQUAKE RESISTANT DESIGN

Embankments experiencing operating basis earthquake (OBE) should exhibit elastic behaviour and remain functional. This indicates merit of treating reinforced earth as a composite material for elastic analyses. Dynamic material properties of this composite material in elastic domain may be obtained from tests on large reinforced embankments on shake table.

After experiencing maximum credible earthquakes (MCE), embankments may be allowed to suffer large deformations not resulting into catastrophic failures. Ductile reinforced earth is of considerable help in this regard. Plastic shear parameters for soil and the ultimate pullout resistance for reinforcement may be obtained experimentally.

1.5 BEHAVIOUR OF REINFORCED EARTH EMBANKMENTS UNDER EARTHQUAKE LOADING

Embankment failures due to earthquakes (Fig. 1.5.1) are of four types. Sheet failures occur near sloping surface due to insufficient shear

strength arising out of low confining pressures. This can be prevented by closely spaced reinforcements near the slope (Fig.1.5.2) and which extend to a short length into embankments. Slope failures are likely if soil at shallow depth below the slope is not sufficiently strong. Such failures

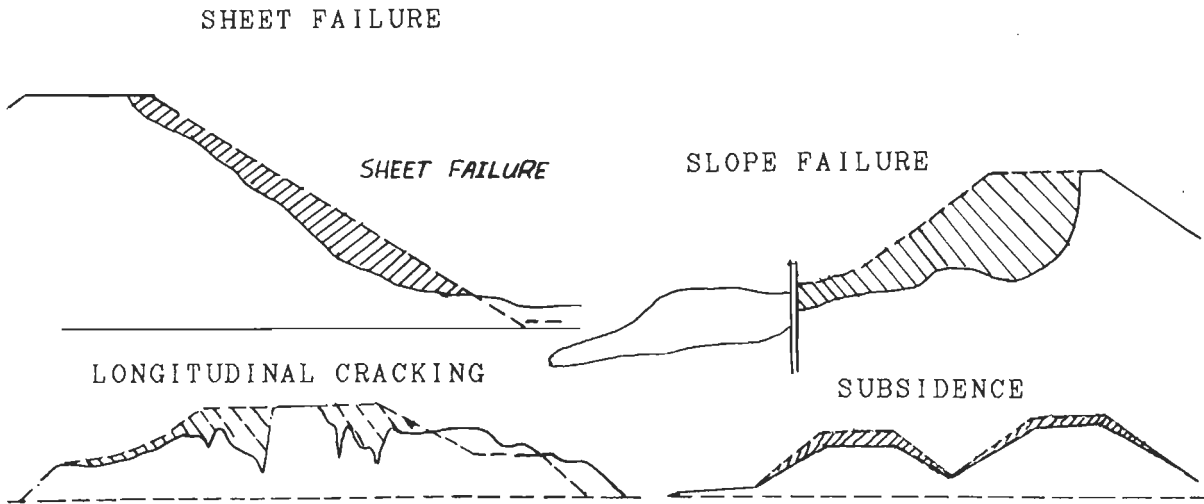


FIG. 1.5.1 TYPES OF EMBANKMENT FAILURES.

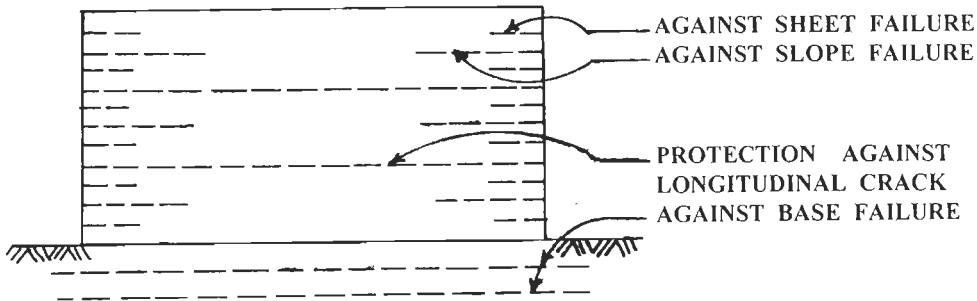


FIG. 1.5.2 CROSS SECTION OF REINFORCED EARTHEN EMBANKMENT.

may be avoided by strengthening the soil in this region (Fig.1.5.2) by reinforcements extending beyond the zone of slope failures. Failure by two sets of intersecting longitudinal cracks may be caused by reversible earthquake loads. Reinforcements extending over the entire embankment width

(Fig.1.5.2) control such failures. Failure by subsidence leads to compaction. Deep seated base failure surfaces extend below embankment base. They are uncommon in recent embankments using efficient compaction and soil improvement methods. Such failures are precluded by placing reinforcements within foundation (Fig. 1.5.2). When spacing between reinforcements is small compared to embankment size, it is called as micro reinforced earth.

1.6 IDENTIFICATION OF THE PROBLEM

Many embankments are employed in geotechnical engineering (Fig.1.6.1). However, due to improved material properties, reinforced earth (R.E.) embankments require lesser width at the ground level compared to embankments of plain earth for a given top width and for a given intensity of loading. This makes them ideal where the land is costly. Often, vertical or near vertical exposed faces are adequate to meet safety needs for R.E. embankments. The R.E. zone behind these faces are some times also referred to as R.E. walls in this presentation.

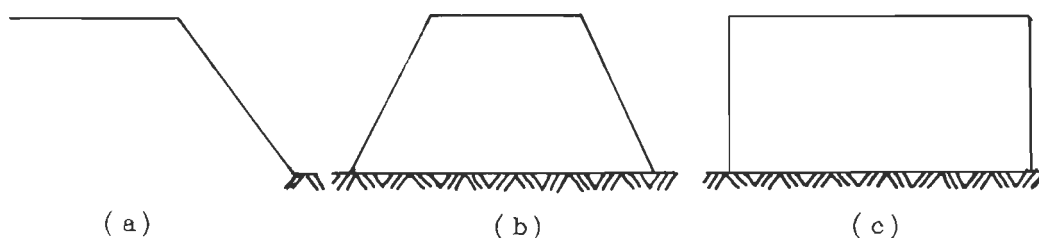


FIG. 1.6.1 EMBANKMENTS TYPE EMPLOYED IN GEOTECHNICAL ENGG.

As of now, the state of art pertaining to R.E. embankments subjected to earthquakes shows vast areas unexplored or underexplored. This article deals with such areas and topics like sample preparation and test setup. Soil is a composite material with three phases - soil grains, water and air. Soil properties depend upon their relative percentages and a variety of other factors. Such a soil body is considered homogeneous, because, the phases repeat at very small intervals. It is desirable to explore possibility of extending this consideration to micro-reinforced earth also. Some research investigators favour this proposition.

1.6.1 Investigations Under Elastic Domain

With above considerations, areas to be explored analytically are:

- i) Extending the concept of homogeneous soil in idealizing composite reinforced earth as homogeneous material.
- ii) Determination of shear modulus of reinforced earth.
- iii) Dynamic analysis of R.E. embankment using finite element method by considering reinforced earth as homogeneous material.

The areas desired to be explored in this context are:

- i) Experimental investigations on large prismatic embankments excited sinusoidally using a shake table to determine shear modulus.
- ii) Influence of different types of soils.
- iii) Effect of moisture content and drainage.
- iv) Effect of different types of reinforcing elements.
- v) Effect of prestretching of reinforcing elements.
- vi) Role of flexible and rigid types facing elements.
- vii) Influence of steep slope angles approaching 90° .

1.6.2 Sample Preparation and Test Setup

Appropriate design and fabrication of set-up and careful testing are important, because, results are strongly influenced by methods of sample preparation and details of test setup used. Hence, preparation of embankments by employing sand rain apparatus needs especial attention.

1.7 OBJECTIVE OF THE INVESTIGATION

The objective of this investigation is to understand the behaviour of reinforced earth in embankments during earthquakes. Only embankments of the type shown in Fig.1.6.1(b) and (c) are considered for this study. Different aspects cited below have been studied :

- i- Preparation of test embankments on shake table and study of response.
- ii- Characterizing factors affecting response and analysis of results.
- iii- Determination of strain dependent dynamic shear moduli by back analyses of test results.
- iv- Determination of dynamic pullout resistance of reinforcements from back analysis of frequency- response test results.
- v- Idealizing the R.E. embankment to be homogeneous in 2D finite element method (FEM) of analysis.
- vi- Obtain response of embankment by FEM analysis using experimentally obtained shear moduli base excitations.
- vii- Comparing measured embankment response with those obtained analytically by idealizing reinforced earth to be homogeneous.

1.8 SCOPE OF THE INVESTIGATION

In this study, air dry cohesionless soil was considered. Woven and nonwoven 100 % polypropylene geotextiles were used as soil reinforcements. Sinusoidal excitation was used since seismic excitation may be represented by its sinusoidal equivalent (Seed and Idriss, 1971). However, this analysis in time domain is capable of considering earthquakes type of excitations also. The following were considered in this investigation:

- i- Placement of uniformly dense soil in test embankments by using a specifically developed device.
- ii- Development of a stress control apparatus for determination of pullout resistance of reinforcing fabric.
- iii- Construction of 3 test embankments, 1.5 m long and 0.75 m wide with different arrangements of reinforcements on shake table.
- iv- Subjecting test embankments to sinusoidal base excitations with peak accelerations upto 0.32 g and frequencies ranging from 5 to 20 Hz.
- v- Observation of acceleration response of R.E. embankments at different locations and excitations.
- vi- Determination of strain dependent shear moduli for R.E. embankments at different excitations.
- vii- Determination of coefficient of dynamic pullout resistance mobilized along reinforcement in test embankments and comparing it with static pullout test results.
- viii- Carrying out analytical study of R.E. embankments for same base excitation using FEM analysis in time domain by considering R.E. embankments as homogeneous.

- ix- Comparing response obtained from analytical and experimental studies.
- x- Analysis of plain sand embankments of same height, top width and density as those for R.E. embankments with different side slope under dynamic conditions and comparing of response of the two to highlight advantages of reinforced earth.

1.9 OUTLINE OF THE THESIS CONTENTS

This research work consists of analytical and experimental investigations for study of "Behaviour of Reinforced Earthen Embankments During Earthquakes". The outline of presentation is given in this article.

In Chapter 2, the state of the art on analytical and experimental investigations on R.E. embankments is reviewed and areas of fresh investigations identified. The state of the art on methods for sample preparation by employing sand rain apparatus has been also reviewed. Chapter 3 deals with design and development of a new sand rain apparatus for this research investigations and results of parametric studies carried out using this equipment. Details of test setup and the shake table used for dynamic investigations have also been discussed. Chapter 4 deals with design and development of the stress control apparatus to obtain pullout resistance of reinforcing fabric. Details of components of R.E. embankments, preparation of test embankments, experimental technique to create plane strain conditions for embankments have also been described. Results of experimental investigations are processed for obtaining shear moduli and shear strains under different excitations. Suitable methods have been developed for this purpose and for obtaining coefficient of dynamic pull-out

resistance of reinforcing fabric by back-analyses of test results. Computer software "DYMU" developed for this purpose is also dealt with. Experimental results obtained have been compared with those reported in the state of the art where ever possible. Chapter 5 deals with 2D FEM analysis in time domain using isoparametric elements to represent R.E. and plain sand embankments. It deals with stiffness, mass, damping matrices, computation of acceleration, velocity, displacement, strain and stress vectors within the embankment analysed. Equation of motion is solved by using Newmark's method of step-by-step integration. Reinforced earth was idealized as a homogeneous material. Computer software "FE95" developed for this purpose has been described. Base excitations assumed for the analysis are the same as those employed for R.E. embankments. Analytical and experimental results obtained are compared to draw conclusions.

REVIEW OF LITERATURE

2.1 PREAMBLE

Reinforcing soils is a methods of soil improvement. Performance of reinforced earth (R.E.) under static loads has been studied and reported in greater detail compared to that under dynamic loads. In this chapter, a brief critical review of analytical and experimental investigations on R.E. embankments under static and dynamic loads is presented though there is very limited information available on this topic for the case of dynamic loading condition. Based on this, research gaps have been identified for better design and construction of R.E. embankments.

2.2 COMPONENTS OF REINFORCED EARTH EMBANKMENTS

Reinforced earth consist of reinforcing elements, facing elements and earth fill which may be cohesive, cohesionless or a $C-\phi$ soil. Generally, cohesionless soil is used as fill material wherever possible.

Reinforcing elements

Reinforcing elements are invariably materials capable of withstanding tension and placed within the fill. Shear resistance along interfaces of reinforcing elements and the fill is useful in transfer of forces from soil

to reinforcing elements. So, tension in reinforcements is transferred to soil in the form of compressive confining pressure as cited in Chapter I. The materials commonly used as reinforcements are :

Metals - Steel, galvanised iron, stainless steel, aluminium alloys etc.

These reinforcements may be in the form of wires, strips or grids.

Geosynthetics : Polyamide (nylon), Polyester, Polythene, Polyvinyl chloride, polypropylene and polystyrene. These may be in the form of geotextiles, geogrids and geomembranes.

Organic materials : Jute, coir, hemp, and other fiber materials. Usually they are spun in the form of coarse threads which are used to manufacture ropes, nets and textiles.

Old auto-tires, rubber, R.C.C. etc. are also occasionally used as reinforcements. Manufactured reinforcements have uniform quality, dependability and available in large quantities. Their material properties are established from tests (Rankilor, 1981). Steel is likely to corrode. Stainless steel resists corrosion but is expensive. Light geosynthetics are relatively inert but may get adversely affected by ultra violet rays of Sun and prone to get attacked by rodents/insects. Bio-degradable organic material reinforcements do not pose environmental problems.

Reinforcements may run to some length into embankment from exposed faces (Fig. 2.2.1(a) and (b)). Some may run continuously from one face to the other (Fig.2.2.1(c)). R.E. embankments need no special foundation. Some times, a very shallow excavation is made below base of exposed face where a thin concrete slab is placed to support the lowest facing element.

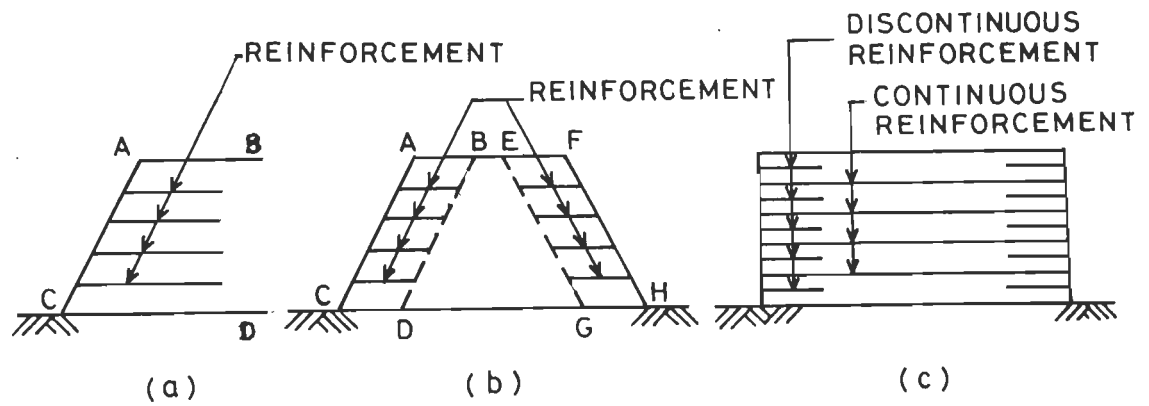


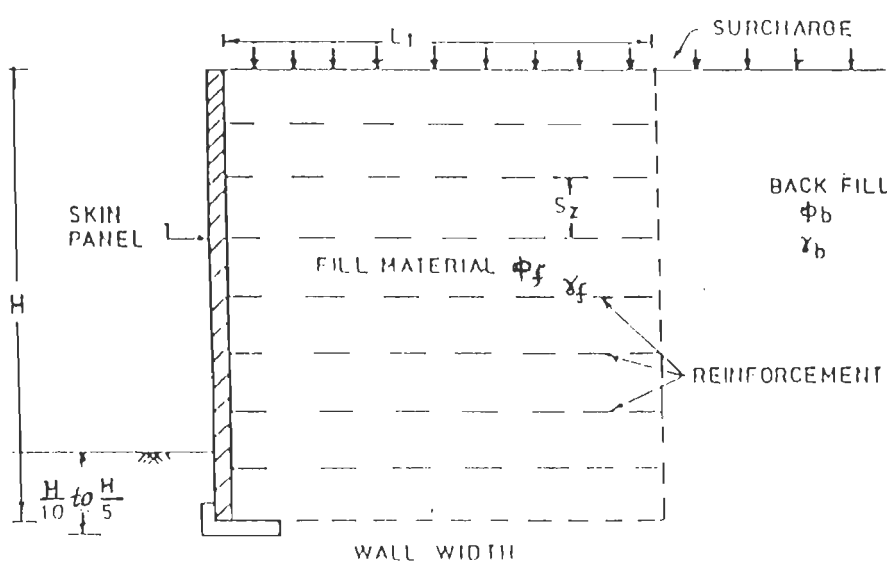
FIG. 2.2.1 TYPES OF REINFORCED EARTH EMBANKMENTS.

Facing elements

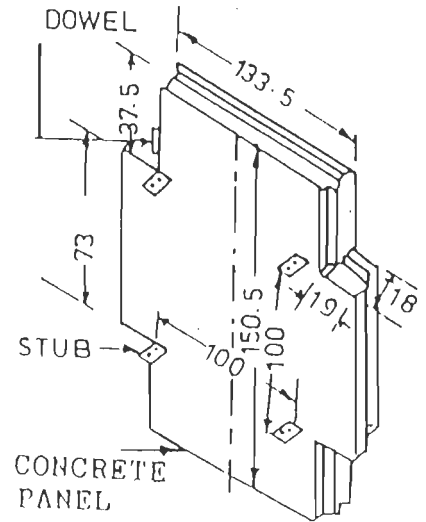
Facing elements contain the earth from spilling. Connecting them to reinforcements is useful in transferring earth pressures exerted on them to reinforcements. Facing elements may be rigid or flexible and in the form of a continuous diaphragm extending to full height of embankments (Fig. 2.2.2). Stiff continuous facing elements when connected to reinforcements are capable of redistributing stresses and strains. They may also be in the form of longitudinal strips hinged to adjacent strips (Fig.2.2.2(b)). Cruciform shaped elements provide flexible facing (Fig.2.2.2(e)). Another variety of flexible facing is in the form of geotextile/geomembranes folded back into the back fill near exposed face of the embankment (Fig.2.2.2(d)).

Connections

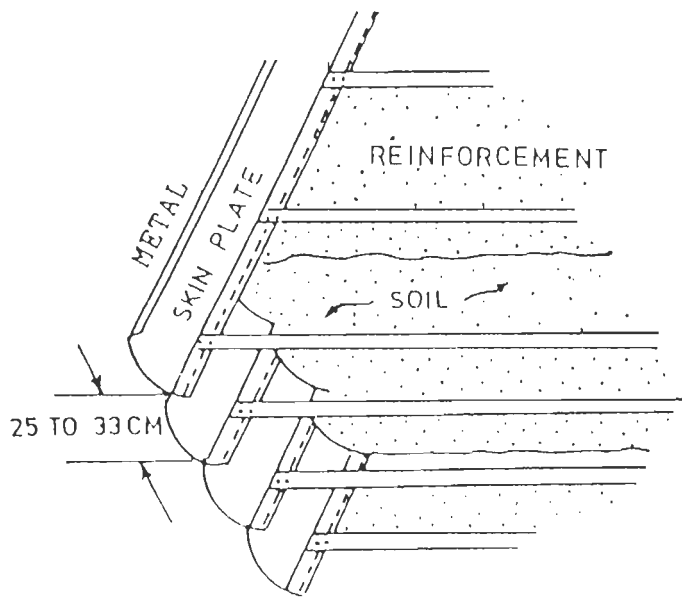
Connections join facing elements to reinforcements. These may be in the form of nuts and bolts, or in the form of welding geosynthetics. In case of geotextiles/geomembranes folded back into the soil (Fig.2.2.1(d)), special connections are unnecessary. Length of geotextiles/geomembranes folded back should be enough to develop interface resistance to withstand forces on



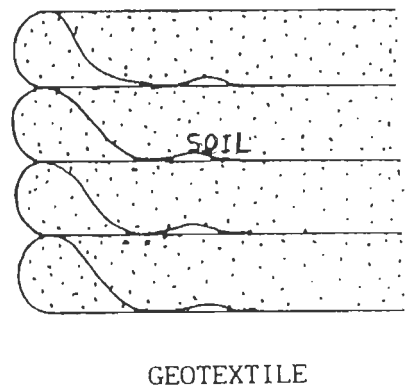
a. Continuous facing elements



c. Cruciform shaped facing elements



b. Longitudinal strip facing elements



d. Geotextile facing elements

FIG. 2.2.2 COMPONENTS OF REINFORCED EARTH EMBANKMENTS.

facing elements (Broms,1988). Connections are designed properly to withstand forces transferred from facing elements to reinforcements.

Connections between facing elements and reinforcements are much more important for embankments under dynamic loads when they are expected to withstand inertia forces and dynamic earth pressures acting on facing elements. Even though they are of critical importance to ensure proper performance of the reinforced earth, they have not been investigated in detail for proper design under static and dynamic conditions.

2.3 INVESTIGATIONS UNDER STATIC CONDITIONS

2.3.1 Analytical Investigations

Henri Vidal (1966) was the first to use R.E. retaining structure. He presented a method for its design which critically depends upon interface shear resistance between the soil and reinforcing element. Research investigations on R.E. embankments may be broadly divided into two groups: the external and the internal stability of embankments. Under external stability, embankments may fail by sliding, spreading, or due to rotational failure, squeezing of foundation soil or inadequate bearing capacity (Rao and Raju, 1990). External stability is analyzed by considering embankments to be monolithic and using static equilibrium conditions. For further details, standard references may be consulted (Rao and Raju, 1990).

Reinforced embankments may have reinforcements close to side slopes (Fig.2.3.1(a)) or may have reinforcements extending from one sloping face to another (Fig.2.3.1(b)). For the latter case, the external stability analysis is sufficient. For embankments cited in Fig.2.3.1(a), in addition to

external stability, it is necessary to examine external stability of reinforced zones such as ABCD and EFGH, because, they may tend to act like separate blocks. Stability of these blocks is also treated similarly.

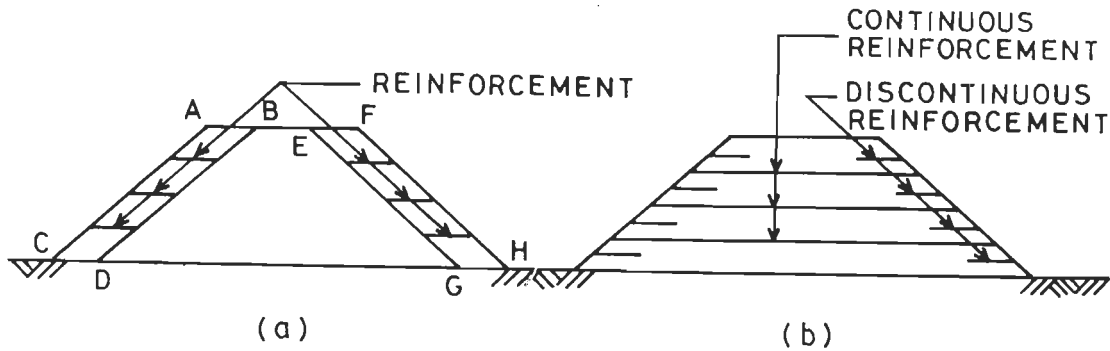


FIG. 2.3.1 REINFORCED EARTH EMBANKMENT WITH TWO SIDE SLOPES.

For internal stability, 4 conditions need be satisfied: reinforcements should not fail in tension; reinforcements should not fail due to inadequate pullout resistance; joints between reinforcements and facing elements should not fail; and facing elements should not fail in shear or bending. Last two conditions are satisfied by using conventional designs.

Tension failure

Figure 2.3.2 shows an R.E. embankment with one exposed face. For equilibrium of element IJKM within the assumed rupture wedge, ABC, we have:

$$T_s = K \cdot \gamma \cdot H_{ri} \cdot H_L \cdot F_{st} \quad (2.3.1)$$

where T_s is tension in reinforcement per unit length of embankment, γ is unit weight of cohesionless fill, H_{ri} is depth of reinforcement from top of embankment, H_L is thickness of layer in which reinforcement is situated, F_{st} is safety factor w.r.t. tension and K is coefficient of earth pressure

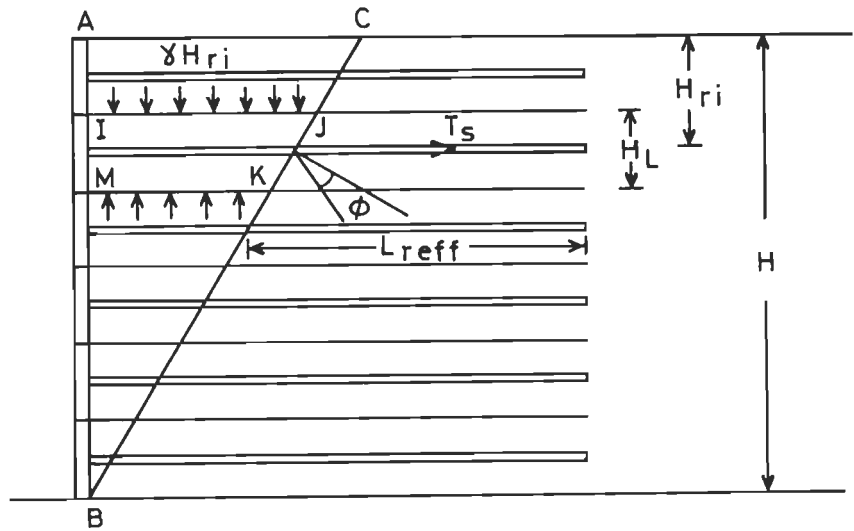


FIG. 2.3.2 FORCES ACTING ON HORIZONTAL ELEMENT OF R.E. EMBANKMENT.

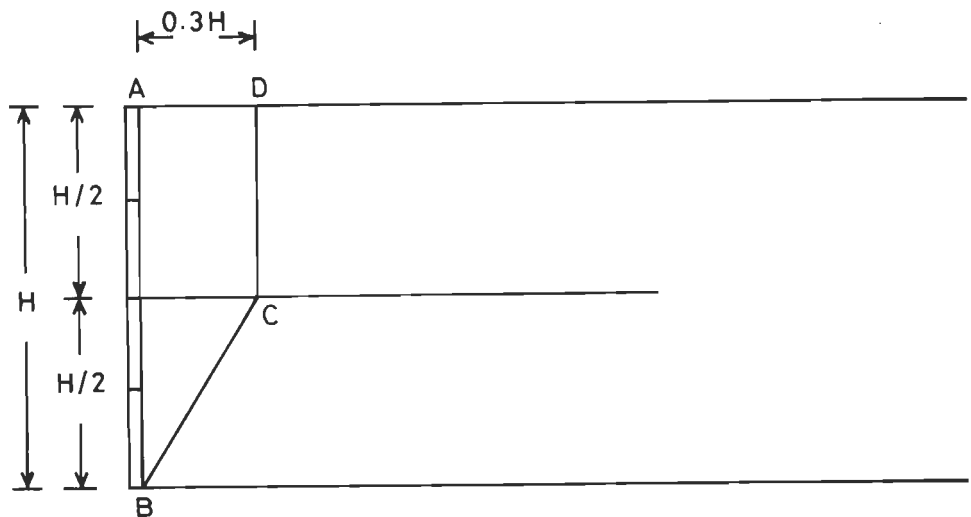


FIG. 2.3.3 BILINEAR IDEALISATION OF RUPTURE SURFACE FOR REINFORCED EARTH (SCHLOSSER, 1990; BOYD, 1985; NAGEL, 1985 AND TAI, 1985).

usually assumed to be Rankine or Coulomb active pressure coefficient (Lee, et. al, 1973; Talwar, 1981; Jones, 1985; Saran, 1990). Rupture surface BC is as predicted by Rankine or Coulomb, whichever is applicable. Failure surface and active earth pressure coefficient given by Rankine appear to be valid for both loose and dense sands when reinforcements fail in tension (Lee et.al., 1973). Reinforcements should be designed to withstand tension, T_s , cited above with desired margin of safety. In this presentation, reinforcements are assumed to extends sufficiently beyond rupture surface to give adequate safety margin. Embankments with reinforcements not extending beyond rupture surface were not included. When failure is due to excessive pullout of reinforcement, rupture surface and active pressure coefficient proposed by Coulomb appears to be valid for both loose and dense sands (Lee et.al., 1973). Some have proposed bilinear rupture surface BCD (Fig.2.3.3) based on loci of points of maximum tension in reinforcements where AD is 0.3H away from exposed face and CD is vertical (McKittrick, 1978; Boyd, 1985; Nagel, 1985 and Schlosser, 1990).

Failure due to inadequate pullout resistance

If reinforcements get pulled out beyond tolerable deformation limit, such a failure occurs. This is due to effective length, L_{reffi} , of the i 'th reinforcement, extending beyond the failure wedge and/or overburden pressure on reinforcement being inadequate. The L_{reffi} is expressed as:

$$L_{reffi} = \frac{T_s \cdot F_{SP}}{2 \cdot \gamma \cdot H_{ri} \cdot \mu_s} \quad (2.3.2)$$

where F_{sp} is factor safety w.r.t. pullout resistance, μ_s is coefficient of static pullout resistance and H_{ri} is soil depth above the reinforcement.

When failure surface such as BE (Fig. 2.3.4) extends beyond mid points M1, M2 or M3 of layers under consideration, it is logical to run the reinforcement continuous from one end to the other. Such a continuous reinforcement should be designed to withstand tension equal to earth force on facing element connected to it. In this case, its pullout resistance evaluation is unnecessary. It is prudent to preclude tensile failure of reinforcement to avoid catastrophic failures. Tensile strength of reinforcements is supplied by manufacturer or may be obtained experimentally. Literature review on pullout resistance of reinforcements will be dealt with in Chapter 4.

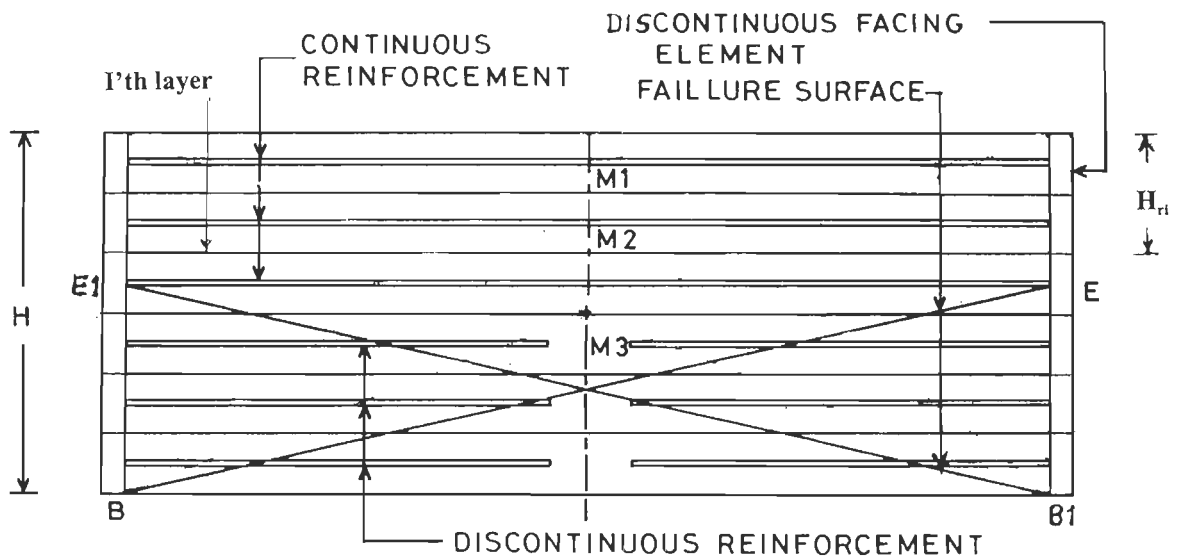


FIG. 2.3.4 FAILURE SURFACES AND REINFORCEMENT FOR EMBANKMENT WITH TWO SIDES.

Analysis using bilinear failure surface

As cited earlier, loci of points of maximum tension indicate bilinear failure surfaces. Romstad, et. al. (1978) carried out FEM analysis of R.E.

embankments with vertical side (Fig. 2.3.5). They concluded that idealization of failure surface, BCD, to be bilinear may be employed in stability analysis of embankments by using wedge analysis. Equilibrium conditions were used to establish critical height of embankment for a given length of reinforcements by varying rupture surface slopes θ_1 and θ_2 .

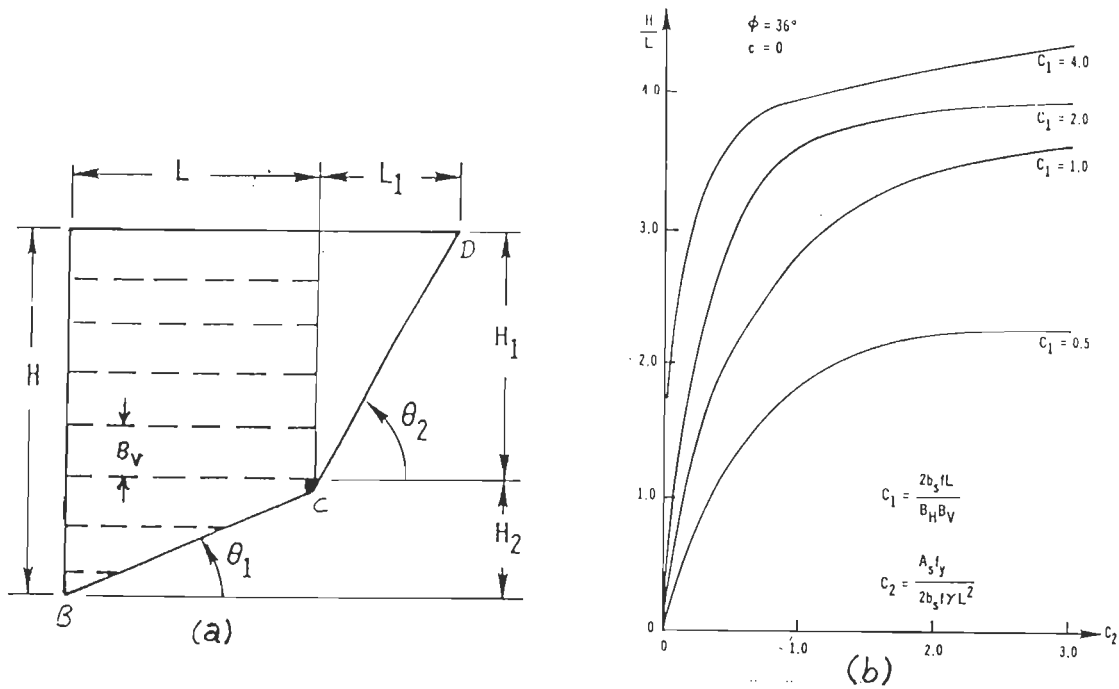


FIG. 2.3.5 WEDGE ANALYSIS WITH BILINEAR RUPTURE SURFACE (ROMASTAD ET. AL., 1978).

Results of analysis are expressed in term of dimensionless height, H/L , and constants C_1 and C_2 expressed as:

$$C_1 = \frac{2b_s f L}{B_H \cdot B_V} \quad (2.3.3)$$

$$C_2 = \frac{A_s f_y}{2b_s \cdot f \cdot \gamma \cdot L^2} \quad (2.3.4)$$

where B_H and B_V are horizontal and vertical spacing, L is reinforcement length, b_s is strip width, f is friction coefficient between soil and strip,

A_s is cross-sectional area of strips, f_y is yield stress of strips and γ is unit weight of soil. Figure 2.3.5 indicates that for a given C_1 there is a critical C_2 beyond which H/L remains very nearly constant. Critical heights predicted by them agree reasonably with failure heights obtained experimentally by Lee et.al., (1973).

Bacot and Lareal (1976) stated that Rankine method grossly under estimates failure height of embankment for uniform or Meyerhof type base pressures. To overcome this, bilinear failure surface BCC' (Fig. 2.3.6) was used to examine equilibrium of wedge $ABCC'$ with reinforcements of length L each. With earth force on CC' due to $CC'D$, expression for C is given as:

$$C = R_T \sqrt{k_p} (1 - \cot \theta) / S_Z \quad (2.3.5)$$

where C is average apparent cohesion, S_Z is vertical spacing, R_T is tensile force and k_p is passive earth pressure coefficient. They concluded that when $L \leq kH_c$, Critical height, H_c , is given by $(L + h')$ where h' is induced height.

Jewell (1990) stated that design of R.E. embankment slope is similar to that of earth retaining structure. Using a log spiral failure surface and equilibrium conditions, point of application and resultant earth force, P_{rm} , is given by :

$$P_{rm} = k_{req} \gamma H^2 / 2 \quad (2.3.6)$$

where k_{req} is equivalent earth pressure coefficient, γ is unit weight and H is embankment height. By approximating the log spiral to be bilinear for wedge analysis of assumed rupture wedge, he obtained disturbing forces for destabilising slope and hence the length, L_r , and spacing of reinforcements

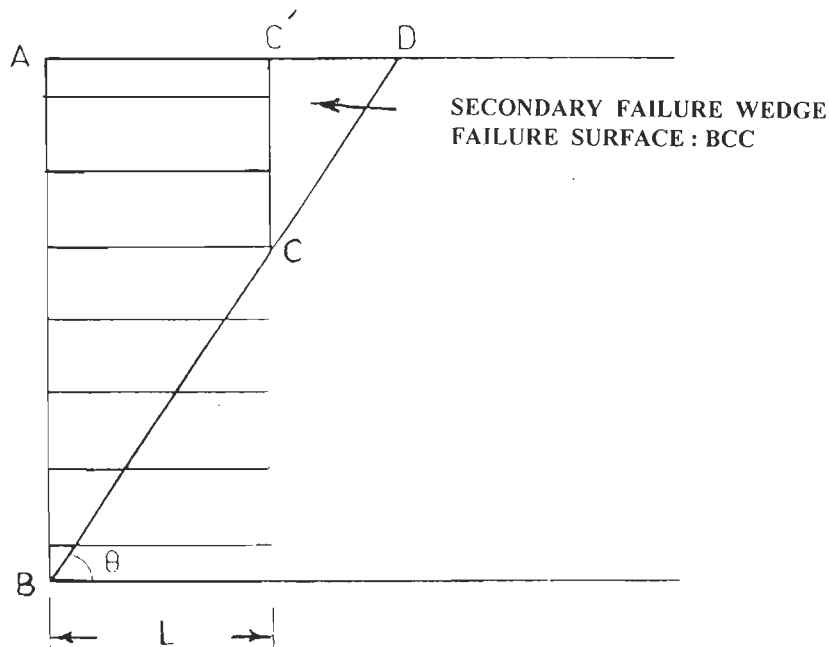


FIG. 2.3.6 BI-LINEAR FAILURE SURFACE (BACOT AND LAREAL, 1976).

Minimum Required Force, K_{Req}

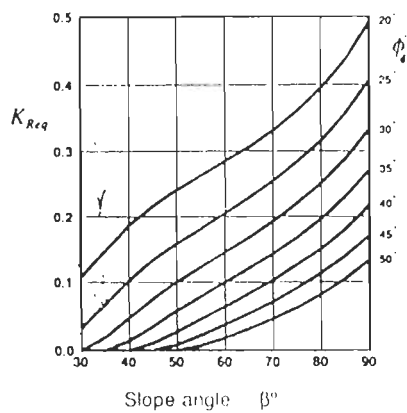
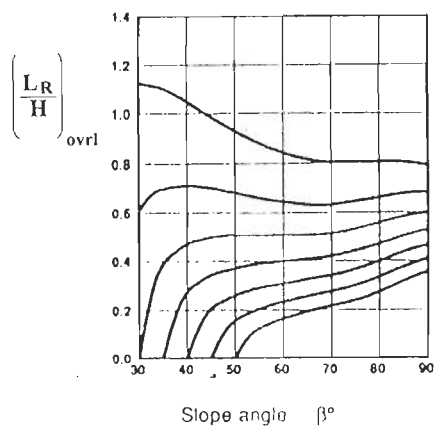


CHART 1

$$r_u = u / \gamma z = 0.0$$

Minimum Required Length
Overall Stability $(L_R/H)_{ovrl}$



Minimum Required Length
Direct Sliding $(L_R/H)_{ds}$

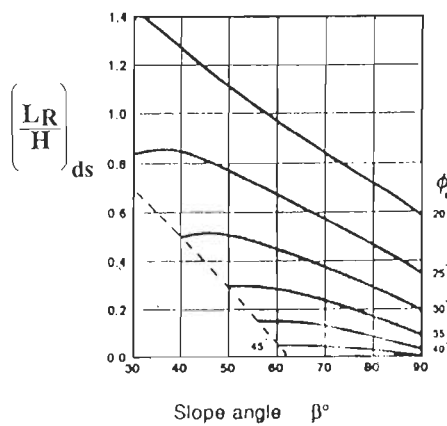


FIG. 2.3.7 DESIGN CHARTS FOR STEEP REINFORCED SLOPE (JEWELL, 1990).

for a stable slope. He also considered pore pressures in his analysis. Results of analysis are presented in form of design charts (Fig. 2.3.7) for obtaining k_{req} , minimum dimensionless reinforcement length for overall stability, $(L_r/H)_{Ovr1}$, and minimum dimensionless reinforcement length to overcome direct sliding failure, $(L_r/H)_{ds}$, as functions of slope angle, β , and angle of shear resistance, ϕ_d . His observation that bond between reinforcement and soil is usually insufficient near embankment crest and hence the need for extra reinforcement length in this zone is reasonable. His presentation using dimensionless factors is an advantage.

Slip circle method of analysis

Phan et.al. (1979) analyzed stability of embankments by the method of slices and also by global equilibrium of slipping mass which gave different factors of safety. Critical failure surface predicted by slice method closely resembled locus of points of maximum tension in reinforcements obtained experimentally. Koga, et.al. (1988) also carried out similar investigation under static/dynamic conditions. Their conclusion that safety factor reduces with increasing embankment slope is reasonable.

Finite element method of analysis

Banerjee (1975) carried out FEM analysis of R.E. wall to predict dimensionless tension coefficient which may have a maximum value of 0.35 only. This coefficient (analogous to lateral earth pressure coefficient) makes some of his equations independent of angle of shear resistance, ϕ .

Al-Hussaini and Johnson (1978) carried out FEM analysis for plain strain condition. Reinforcement strips at one level were represented by an

equivalent reinforcement extending over the entire wall length by reducing interface friction suitably. This simplifies the 3D problem into a 2D problem. Nonlinear hyperbolic stress-strain behaviour of the foundation and fill material was assumed. Reinforcement was assumed to be linear elastic upto yield point and plastic thereafter. Results predicted the tension variation and soil pressure in the back fill to be in reasonable agreement with results obtained experimentally for a test wall.

Hermann and Al-Yassin (1978) analysed R.E. embankment with a single vertical slope by using FEM. Strip reinforcements in four layers embedded in sand were used. Effect of construction was accounted for by considering four stages of construction. Two types of FEM idealizations were considered. In the first idealization, the R.E. was considered as composite material with interface between the reinforcement and sand represented by frictional resistance. They gave a procedure for computing stiffness to represent interface behaviour. In the second idealization, R.E. is assumed to be a homogeneous material with equivalent properties. Figure 2.3.8 shows computed forces in bottom strips and lateral stress variations obtained by the two idealizations which are practically identical. Hence, they conclude idealization of R.E. as homogeneous material is reasonable within the elastic domain. They extended the consideration of soil with many phases to be homogeneous to be valid for R.E. also which is very important. They further reported that use of simple 4 noded quadrilateral isoparametric elements with four Gaussian points is adequate to represent R.E. which is an advantage. Eight noded isoparametric elements with nine gaussian points may be used when bending predominates.

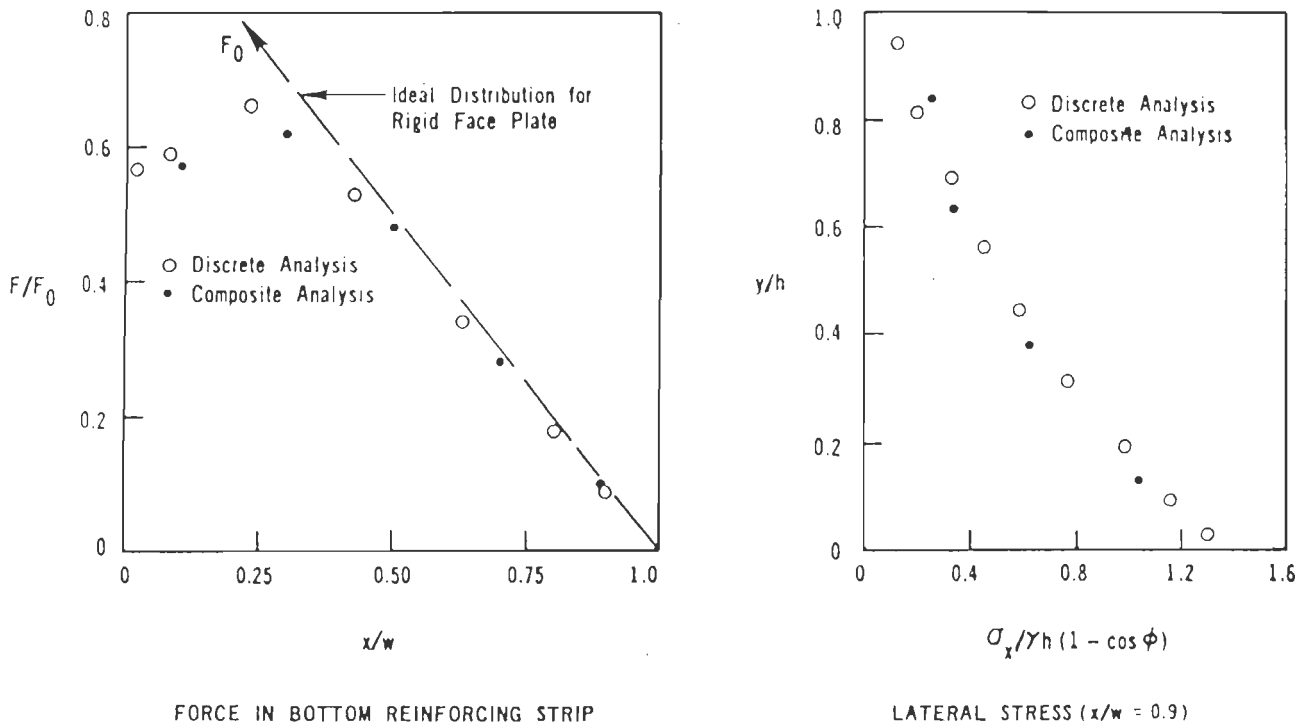


FIG.2.3.8 COMPARISON OF DISCRETE (HOMOGENEOUS) AND COMPOSITE ANALYSIS RESULTS (HERMANN AND AL-YASSIN, 1978).

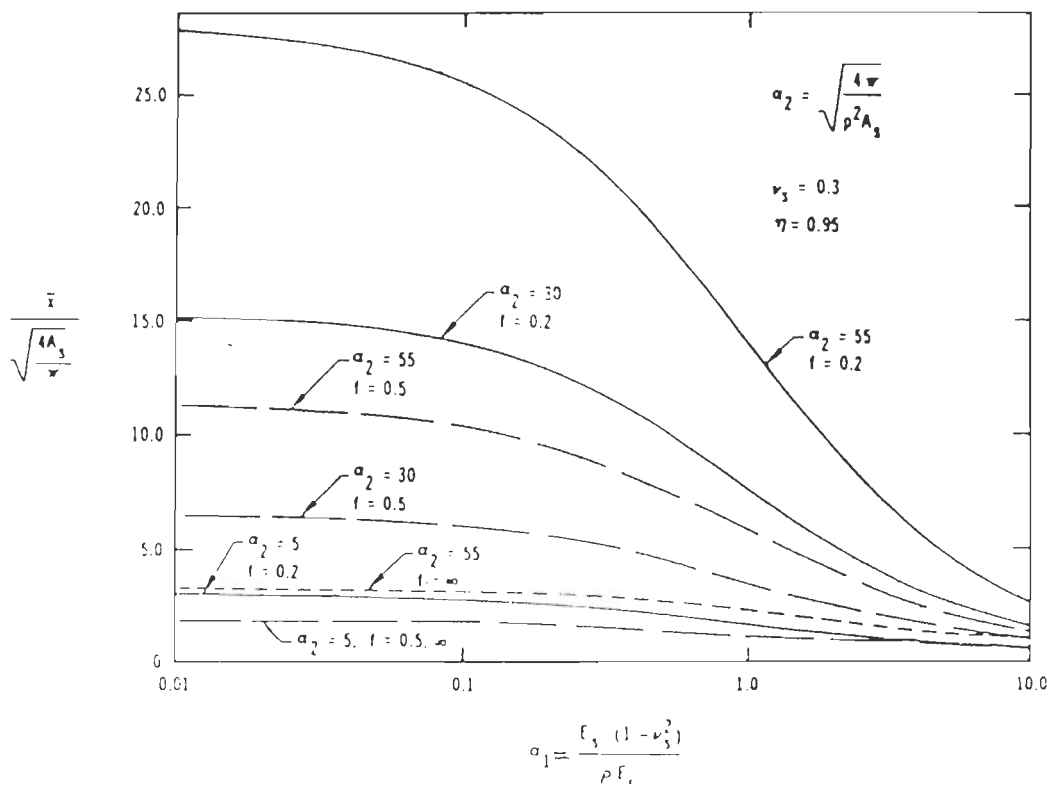


FIG.2.3.9 DEPTH OF EDGE EFFECT AND SLIPPAGE ZONES (HERMANN AND AL-YASSIN, 1978).

They reported that computational effort is significantly more for FEM analysis when R.E. is represented as a composite material than for the same analysis when R.E. is idealized as a homogeneous material. For 3D analysis, computational effort needed may be 50 to 100 times more compared to that for FEM analysis assuming homogeneous R.E. As such they recommend idealization of R.E. as homogeneous material.

Hermann and Al-Yassin (1978) also reported that it is necessary to consider edge effect when free ends of reinforcements are not connected to facing elements. It is more prominent when perimeter of cross section of reinforcement is large and when interface friction coefficient, f , is small for reinforcement and soil is small. The total of edge effect and slippage effect, denoted by \bar{X} , has been computed as :

$$\bar{X} = \sqrt{\frac{4A_s}{\pi}} \frac{\left[-\ln\left(\frac{1-\eta}{a^*}\right) + \left(\frac{1}{b^*} - 1\right) \right]}{\sqrt{\frac{4(1-\nu_s)(\alpha_1 + 1)}{\ln \alpha_2 - 3/4}}} \quad (2.3.7)$$

which is expressed as a function of α_1 , α_2 and f where :

$$a^* = \begin{cases} 1 & b^* \geq 1 \\ b^* & b^* < 1 \end{cases}, \quad b^* = \frac{f \sqrt{4(1-\nu_s)(\ln \alpha_2 - 3/4)(\alpha_1 + 1)}}{\nu_s \alpha_2} \quad (2.3.8)$$

$$\alpha_1 = \frac{1}{\rho} \frac{E_s}{\left(\frac{1-\nu_s^2}{E_r} \right)}, \quad \alpha_2 = \sqrt{\frac{4\pi}{p^2 A_s}} \quad (2.3.9)$$

When f ranges from 0.5 to ∞ , the edge effect and slippage effect are practically negligible (Fig. 2.3.9). When many reinforcements of same

length appear one over the other, their combined edge effect could be large if cross sectional area of each reinforcement is large. Therefore, thin reinforcements are of advantage.

Romstad et.al. (1978) in FEM analysis idealized R.E. as homogeneous material with stress-strain relationship based on perfect bond between soil and reinforcement making strains in composite material identical to those in soil in planes transverse to length of reinforcing strips. Computed soil stresses and horizontal movements compared well with test results for a field wall. Tension distribution pattern in reinforcements compare well with measured tension. However, magnitudes of tension do not agree.

Smith and Segrestin (1992) analysed 7.5 m high R.E. embankment with one vertical side slope reinforced with ten 6 m long strips of high adherence steel (HAS) or oriented polyethylene grids (OPG) rigidly connected to facing elements. The sand behind R.E. and in foundation has ϕ equal to 30° and that in R.E. has ϕ equal to 36° . The 3-D FEM analysis treated reinforcements as linearly elastic and soil as linearly elastic-cohesionless Mohr-Coulomb plastic solid. Isoparametric brick elements with 20 and 14 nodes were used to represent fill, foundation, reinforcements and facing elements. Construction sequence was considered using 1.5 m stages.

Their results show that maximum outward displacement of facing was only 3.5 mm for embankment with HAS compared to 92.5 mm for embankment with OPG because of larger strength and elasticity modulus of HAS. When grid reinforcements are employed, locus of maximum tension points is bilinear with near-vertical upper segment of locus being at a distance of 0.25 H from exposed embankment face upto mid-height, H being height of fill. For

embankment with HAS, reinforcements over their entire length had nearly same tension indicating redistribution of stresses within reinforcement and that no failure surface is developed though a small region close to foot of slope reached plastic state. As such, stress concentration may occur in foundation there affecting internal stresses. This shows importance of embankment-foundation interaction in analysis and need of a suitable foundation slab in that region to take care of such stress concentrations.

For HAS and ORG, computed horizontal stresses behind facing were close to Coulomb active pressures (Fig. 2.3.10) for fill upto 0.75H from top. top. Near base, pressures were closer to at rest pressures. Pressure in case of HAS was larger than that in case of ORG in view of negligible movement at base and larger modulus of HAS compared to that of ORG. It is also clear that use of steel is better if small outward embankment movement is tolerable. Full strength of steel may not be realized due to its high

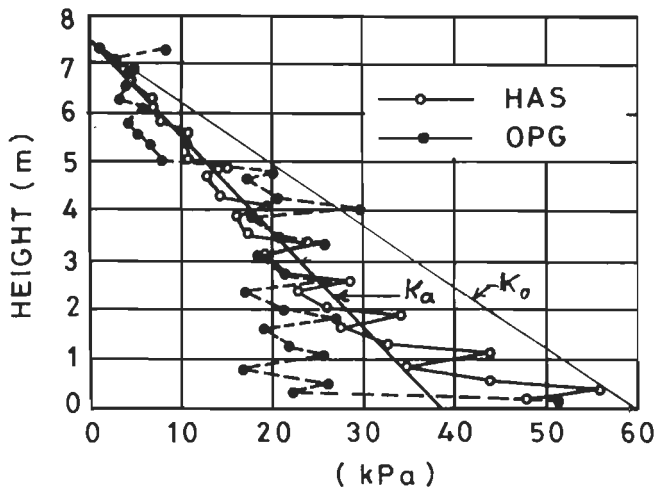


FIG. 2.3.10 HORIZONTAL STRESS BEHIND FACING (SMITH AND SEGERESTIN, 1992).

strength and low strain levels leading to low mobilization of reinforcing action which makes use of steel costly. When larger outward embankment movements are allowed (like in case of roads and railways), extensible reinforcement are cheaper due to larger mobilization of soil resistance.

2.3.2 Experimental Investigations

Experimental studies are needed to understand mechanics of the problem under study. A better understanding of the same is helpful in formulating better analytical methods for further improvement of test results. As such, analytical and experimental investigations compliment to each other.

Most experimental studies reported employ tests on small R.E. embankments as they are easy to perform, economical and frequently due to resources crunch. Measurement errors may greatly affect such results. Besides, simulation laws for prototypes are never fully satisfied for scaled models. As such, extrapolation of results of model investigations may not be possible for much larger prototypes. This necessitates tests on largest possible model which are expensive, difficult and time consuming.

Failure surfaces

Earth pressures induce stresses and strains in side the R.E. and the backfill behind. This may lead to formation of rupture surface at failure. This is a function of properties of fill, strip reinforcements and (L/B) ratio of strips where L and B are length and width of strips respectively. Figure 2.3.11a shows failure surface approximated to be bilinear with strips of short (L/B) ratio (Smith and Wroth, 1978). Rupture surface AE, at an angle θ_1 to vertical, is close to Coulomb failure surface for cohesionless

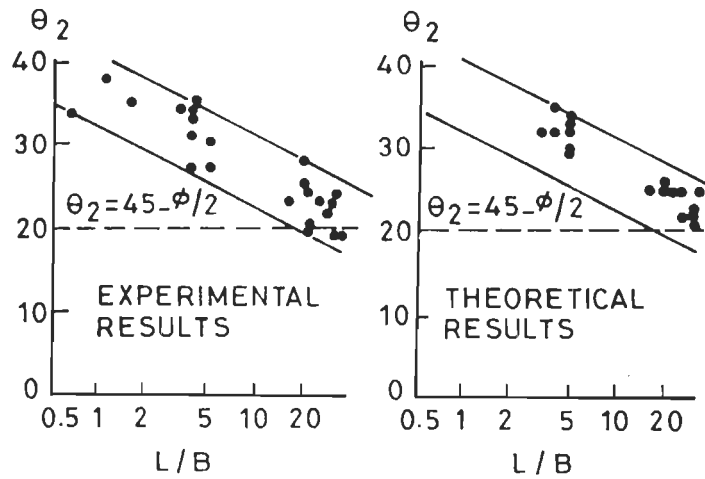


FIG. 2.3.11 INCLINATION OF FAILURE SURFACE TO VERTICAL (SMITH AND WORTH, 1978).

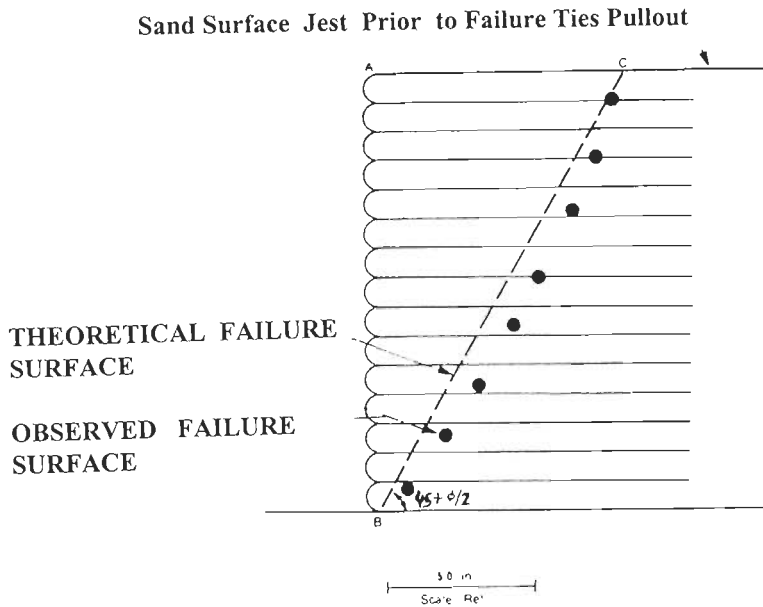


FIG. 2.3.12 OBSERVED AND THEORETICAL FAILURE SURFACES (LEE, ET. AL., 1973).

soil. Rupture surface DE, making an angle θ_2 with vertical in R.E. zone, is usually flatter than AE in plain backfill, because, strains within R.E. zone are smaller due to reinforcing action. Consequently, mobilised value of angle of shear resistance, ϕ_m , along DE is much smaller than ϕ and, as such, θ_2 is usually greater than $(45-\phi/2)$. Smith and Wroth (1978) reported that as (L/B) ratio increases, θ_2 reduces and ultimately reaches $(45-\phi/2)$ at (L/B) \geq 20 indicating very insignificant contribution of reinforcements (Fig. 2.3.11b). For smaller (L/B) ratio, the reinforcing action is significant leading to smaller mobilisation of shear strains and corresponding value of smaller ϕ_m leading to larger θ_2 . This is supported by similar observations reported by John (1979).

When wall fails due to tensile failure of reinforcements, the observed failure plane (Fig. 2.3.12) is close to Rankine active failure surface (Lee et.al., 1973). Such tensile failure occurs in under-reinforced embankments only and be avoided to preclude catastrophic failures. The other failure mode is due to lack of pullout resistance leading to bilinear failure surface partly within the R.E. and partly extending into fill behind if reinforcement is short (Smith and Wroth, 1978 and John 1979).

Over reinforced embankment with reinforcements longer than the height, the R.E. zone behaves almost like a rigid body (Schlosser and Vidal, 1969; Smith and Bransby, 1976). This result into very small strains in R.E. zone and no failure surface develops within R.E. zone. However, if displacement of R.E. zone is large, a clear Rankine failure surface may develop within fill behind R.E. zone (Smith and Wroth, 1978; John, 1979). This is revealed by radiographic recording of R.E. embankment (laiden with a grid of lead shots) taken before and after failure (Smith and Brainsby, 1976).

When R.E. zone behaves almost like a rigid body, stress concentrations occur near lower end of exposed face which is supported by analytical results (Smith and Segrestin, 1992). As such, associated large shear strains initiate rupture surface formation at that point. This zone is very small if R.E. zone is nearly rigid leading to non-formation of rupture surface. As flexibility of R.E. zone increases, possibilities of formation of rupture surface originating from foot of the vertical face extending into R.E. zone increase. The extent of its penetration into backfill ranges from $0.23H$ (Naresh et.al., 1989) to $0.3H$ (Tai, 1985). For relatively over reinforced wall very small outward movement of facing is expected. For an embankment which is more flexible (due to a small L_T/H ratio, use of flexible reinforcements and/or facing elements) a greater degree of outward movement is expected (Bolton et al., 1978; Schlosser, 1978, Ingold, 1982 and Smith and Segrestin, 1992). Measurement of tension in reinforcements indicates that the Locus points of maximum tension is curvilinear which may be approximated to be bilinear originating from the foot of the facing and with a vertical leg extending from mid height upto the top end (Schlosser, 1978, AL-Hussaini and Perry, 1978a and Naresh et. al., 1989). Similar results (Fig. 2.3.5) have been obtained analytically also (Schlosser and Long, 1974; Romstad et. al., 1978 and Smith and Segrestin, 1992). When the facing elements are rigid and secured to reinforcements, the maximum tension appears to occur at the facing itself (Bolton and Pang, 1982).

Schlosser and Long (1974) based on test results reported that at point, F, on a typical reinforcement where maximum tension occurs, shear stress is zero (Fig. 2.3.13). Along, FG, on fill side, pullout resistance along interfaces is directed towards fill side. Along, EF, interface resistance is

directed towards facing. Locus, BCD, of points of maximum tension is considered as failure wedge for design. Figure 2.3.3 cited earlier shows some bilinear idealization of such failure surfaces.

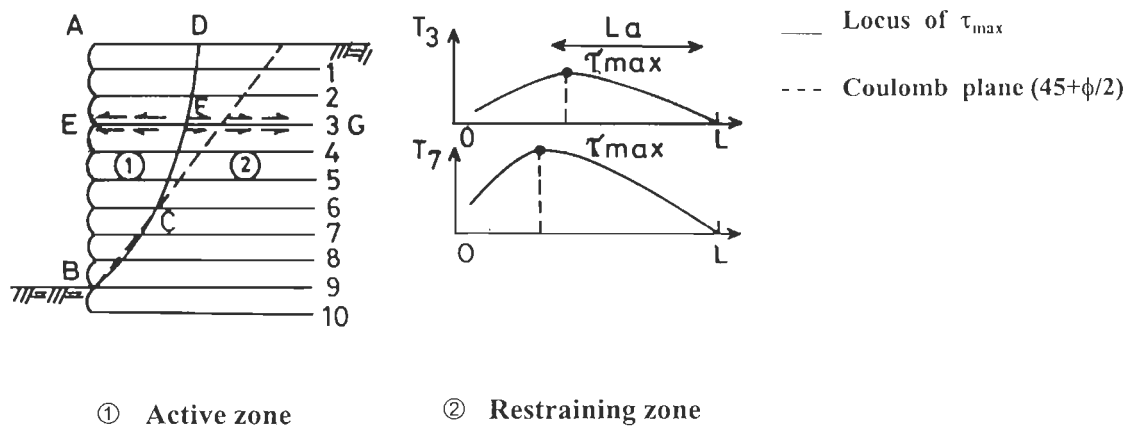


FIG. 2.3.13 DISTRIBUTION OF REINFORCEMENT TENSIONS.
(SCHLOSSER AND LONG, 1974)

Earth pressures

Earth pressures are displacement depend. Usually, lateral displacement of facing to the tune of 0.25% to 0.5% of height, H , is required at the embankment top to reach active state for dense to medium dense cohesionless fills. Lee et. al. (1973) reported that measured static earth pressures are very close to Rankine active pressures for R.E. embankments failing due to tensile failure of reinforcements (Fig. 2.3.14). They also established from test results that active state is mobilized throughout the depth.

Hoshiya (1978) reported that design of R.E. embankment by using Coulomb force/ moment leads to conservative design when compared with experimental values. It appears that actual earth pressures were a bit lower than active earth pressures suggesting realization of active state throughout the depth.

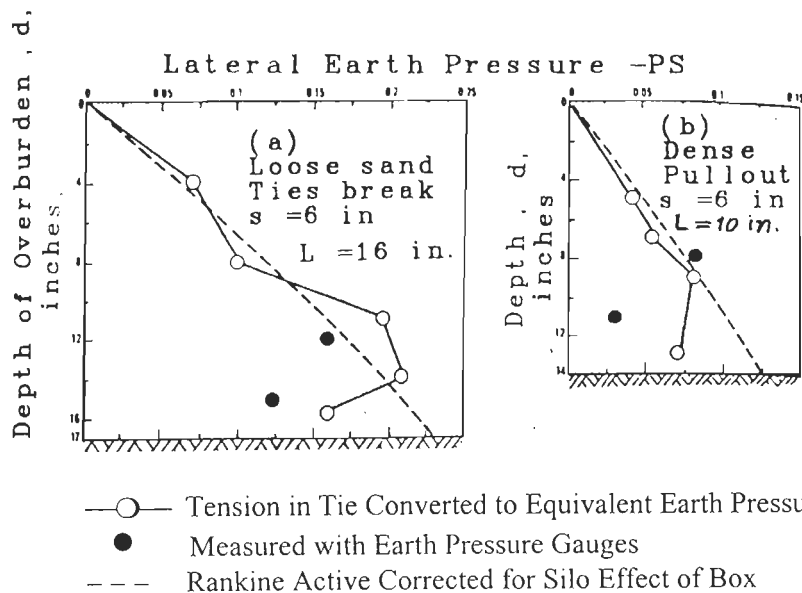


FIG. 2.3.14 MEASURED LATERAL EARTH PRESSURES.
(LEE ET. AL., 1973)

Al-Hussaini and Perry (1978a) tested R.E. wall which failed on reaching a height of 2.75m. Lateral embankment movement was about 10 cm (3.6% of H), i.e., large enough to reach active state. Measured earth pressures were comparable to Rankine active pressures from top end upto mid-height. At lower depths below, measured pressures were smaller than Rankine values and reach a value equal to 50% of Rankine value at the base. It may be noted here that Rankine theory overestimates active earth pressures. As such, the comparison of measured pressures near the base will be less unfavourable than what is cited above. Movements of under-reinforced walls are large enough to realize active state. Al-Hussaini and Perry (1978b) reported pullout failure of R.E. retaining wall on reaching a height of 2.74m. The corresponding wall displacement at top was 5.7 cm (2.08% of H) which is adequate to reach active state. Measured pressures were close to Rankine active pressures upto a depth of about (H/6) from top. Further below, pressures were lower than Rankine pressures. Heavy duty nylon fabric coated

with 2 mm (0.08") thick neoprene, 101 mm (4") wide and 3.05 m (10') long spaced at 609.6 mm (2') vertically and 1219 mm (4') horizontally. Failure occurred due to breakage of reinforcement as well as due to failure of connections at facing elements. Test results, indicated that estimation of lateral pressure in R.E. wall without surcharge by Rankine theory may be considered conservative.

Naresh et. al. (1989) carried out field testing of R.E. embankment, 4.2m high. Reinforcements were designed with a safety factor of 1.8 w.r.t. tension failure and 1.4 w.r.t. pullout failure. Recorded end of construction earth pressures were 1.2 to 1.4 times active earth pressures inspite of observed wall movements being of the order of 2% to 2.5% of H, large enough to reach active state. This was attributed by them to non-snug fit of adjacent/skin elements, method of compaction, creep effects and time lag due to installation of instruments. However, on application of surcharge load on top of embankment, the measured earth pressures were in the range of 1.1 to 1.15 times the Rankine active earth pressures. Field measurements on R.E. Wall with concrete panels as facing elements at Granton (Finlay, 1977) have also shown a horizontal tilt of 2.4% of H with out failing. From this discussion, it may be concluded that large wall movements need not be considered as failure of R.E. Walls as this does not impair their satisfactory performance. For highway and railway embankment, large outward displacements of the order of 1 to 2% of H can be allowed. As such, design of reinforcements assuming Rankine failure surface and nominal factors of safety may be considered adequate for static case. Creep in the soil may increase the active earth pressure to larger pressures which may be close to at rest conditions after certain duration of time. As such, it may

be necessary to consider higher earth pressure or larger safety factors w.r.t. effective length of reinforcement (Al-Hussaini and Perry, 1978c).

Talwar (1981) studied R.E. embankment, 1.75 m high with cruciform shaped facing elements. Aluminium strips were used as reinforcements, 0.6H to 1.33H long, with horizontal spacing of 278mm - 556mm and vertical spacing of 250mm. Rupture surface is similar to log spiral. Measured earth pressures ranged between Rankine active and Jaky's at rest pressures in lower half of wall. In the upper half, they were either closer to at rest pressures or larger. Earth pressures reduced with increasing length of reinforcement and vice versa. Dimensionless factor, D_p , was defined as :

$$D_p = \frac{f_o w H^2}{S_X S_Z L_1} \quad (2.3.10)$$

where f_o is the friction coefficient in pullout resistance, w , S_X , S_Z and L_1 are width, horizontal spacing, vertical spacing and effective length of reinforcing strips and H is the depth of the fill. This D_p is used to define intensity of reinforcement. He recommends 0.6 H as the length of optimum reinforcement for D_p values in practical range.

Locked-in-stresses due to stress history also influence lateral earth pressures. In the field, compaction by tampers and rollers may cause very large vertical stress causing conditions close to passive pressures at the end of compaction. However, as the surcharge pressure due to layers above increase, the earth pressure gradually approach at rest or active pressure depending upon displacements (Naresh et al., 1989). Figure 2.3.15 shows effect of compaction on earth pressures (Finlay and Sutherland, 1977).

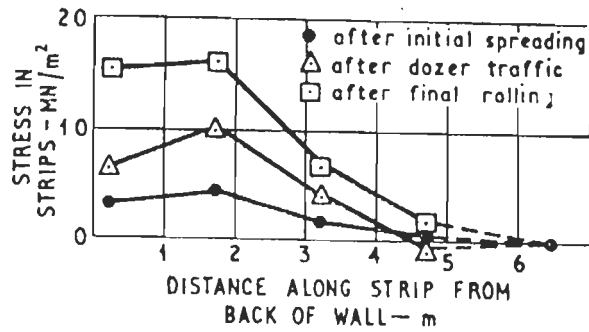


FIG. 2.3.15 EFFECT OF COMPACTION OPERATION ON TENSILE STRESSES IN REINFORCING ELEMENTS (FINLAY AND SUTHERLAND, 1977)

Length of reinforcing element

Schlosser and Vidal (1969) stated that effective length of the reinforcement, L_{rb} , is that extending beyond the rupture surface and into the backfill for mobilising pullout resistance to keep the embankment stable. This also assumes no tension failure of reinforcements. Schlosser (1972) proposed a method of analysis for R.E. by considering a single layer of strip type of reinforcement containing N strips of width, b_r , per unit length of wall and with a vertical spacing, S_v . The effective length, L_{rb} , is the length of reinforcement extending beyond rupture surface. Average coefficient of pullout resistance, μ_{avs} , is obtained by dividing the shear force, T , by effective area under shear and effective normal stress (distributed uniformly) at the level of reinforcement. Therefore, the expression for L_{rb} is given as :

$$L_{rb} = \frac{K_a S_v}{2N b_r \mu_{sav}} \quad (2.3.11)$$

where K_a is the Rankine coefficient of active earth pressure. The above expression shows that L_{rb} is independent of level of reinforcing layer.

Subsequently, Schlosser proposed a more meaningful calculation considering distribution of vertical stress along the length of reinforcement. Meyerhoff type of vertical stress distribution was applied to give expression for L_{rb} as :

$$L_{rb} = \frac{K_a S_v}{2N b_r \mu_{sav} [(1-K_a H^2/3L^2)]} \quad (2.3.12)$$

Comparison of the theoretical results with results obtained from models and full scale walls showed poor agreement (Ingold, 1982). It may be noted that no safety factor appears in this computation of L_{rb} .

Lee et.al. (1973) assumed Rankine failure wedge within the R.E. zone (Fig. 2.3.16). Total reinforcement length, L_r , is expressed as :

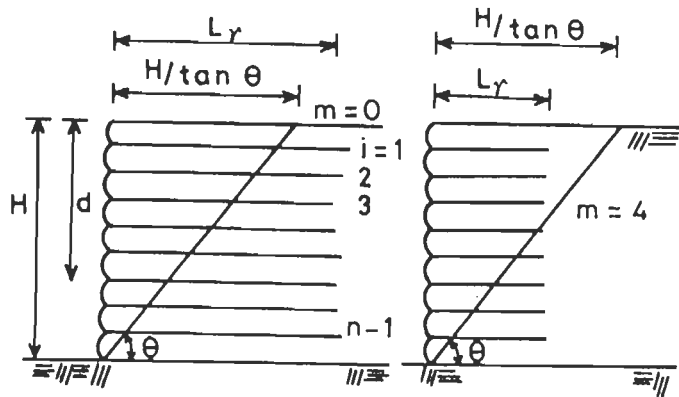
$$L_r = \frac{H}{\tan \theta} + F_b L_{rb} \quad (2.3.13)$$

$$L_r = \frac{H}{\tan \theta} + \frac{k_a S_v F_b}{2N b_r \mu_{avs}} \quad (2.3.14)$$

where F_b is safety factor w.r.t. L_{rb} . Comparison of embankment height at failure by Coulomb force method, Coulomb moment method and Rankine method (Fig.2.3.17) with test results showed that Rankine method predicts longest and Coulomb force method predicts the shortest reinforcement length.

Schlosser (1978) compiled variation of earth pressure coefficient, K , for 7 R.E. walls with over burden height ranging from 0 to 15 m. For depth, $z < 6$ m, $K < K_a$ was given by:

$$K = K_o + z (K_a - K_o)/6 \quad (2.3.15)$$



$$\theta = 45 + \phi/2 = \text{RANKINE ACTIVE FAILURE SURFACE}$$

FIG. 2.3.16 RANKINE FAILURE WEDGE WITHIN THE REINFORCED ZONE (LEE ET. AL., 1973).

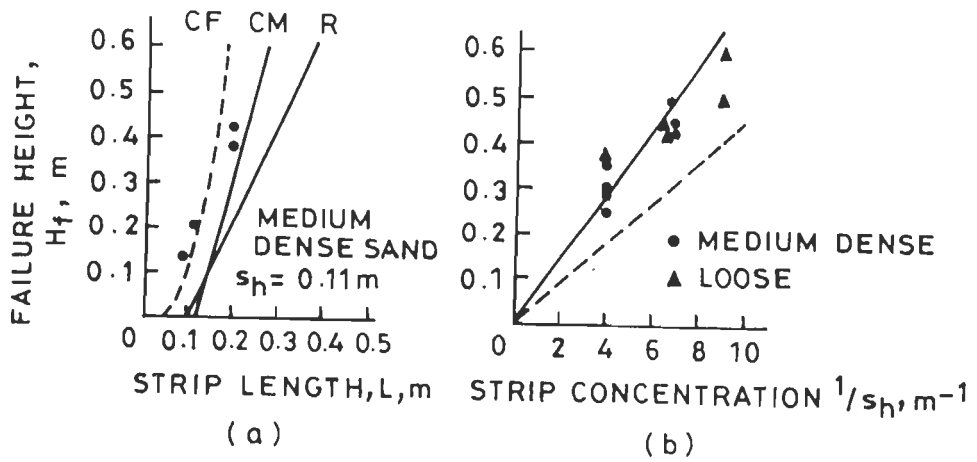


FIG. 2.3.17 COMPARISON OF THEORETICAL AND EXPERIMENTAL RESULTS (LEE ET. AL., 1973).

For $z > 6$ m, $K = K_a$. Figure 2.3.18 shows idealized failure surface proposed by McKittrick (1978) for designing against bond failure with bond length, L_{rb} , extending beyond the assumed rupture surface. Schlosser and Elias (1978) proposed following expression for L_{rb} :

$$L_{rb} = 1.5 T/2 b_r \mu_{sav} \gamma H_r \quad (2.3.16)$$

where 1.5 stands for factor of safety w.r.t. L_{rb} and H_r is depth of reinforcement from top surface. Coefficient of pullout resistance is taken to be 0.4 for plain strips and $\tan \phi$ for ribbed strips, where ϕ is the angle of shear resistance of backfill.

Johns (1978) recommended a system connection for facing elements and strip reinforcements (Fig. 2.3.19) which will be explained in detail later. For such a system, μ_{sav} is assumed to be $(\alpha \tan \phi)$ where reduction factor, α , ranges from 0.46-0.5 for plain strips and 0.9 for ribbed strips. He recommended a minimum length of 5 m or 0.8H which ever is larger.

Facing elements

Facing elements are required for R.E. embankments to contain and stop soil from spilling out. Facing elements primarily takes earth pressures due to fill and transfers it to reinforcements. In this process, they develop bending moments and shear forces which they have to withstand.

In the earlier years, strip reinforcements were placed at smaller vertical and horizontal spacings. As such, bending and shear stresses within facing elements were relatively small. Therefore, metal panels of semi-elliptical form running along the length of embankment (Fig. 2.2.1 b) were

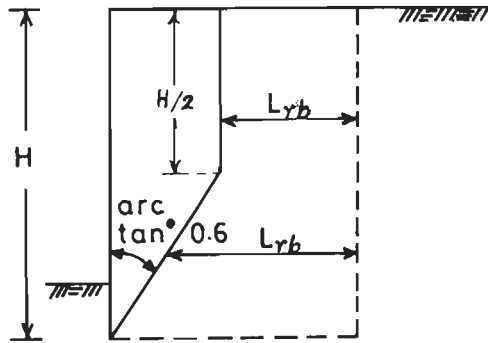


FIG. 2.3.18 IDEALISED FAILURE SURFACE (MCKITTRIC, 1978).

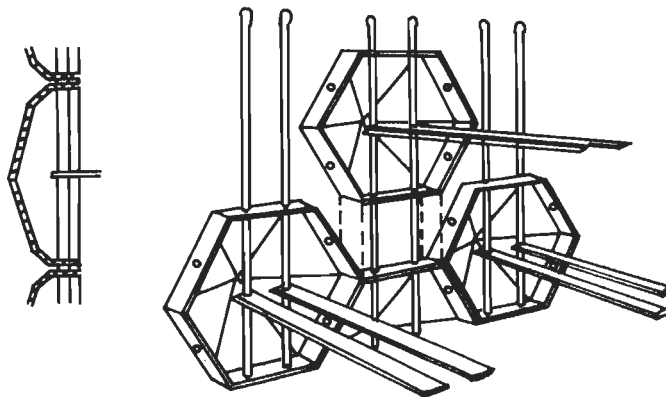


FIG. 2.3.19 FACING ELEMENT-REINFORCEMENT CONNECTIONS, THE DOE YORK SYSTEM (JOHNES, 1978).

used as facing elements (Vidal, 1978). Cruciform shaped precast concrete panels as facing elements (Fig. 2.2.1 c) are easy to handle during construction (Vidal, 1978). More recent geosynthetic fabrics/membranes are folded back into the earth to contain soil (Fig. 2.2.1 d). The soil enclosed within such fabric (marked A in Fig. 2.2.1 d) is confined by fabric and acts as a relatively stronger material to gain some strength to act as facing element. However, when the backfill of R.E. settles down, it does so along with the reinforcements embedded within it. This necessitate downward movement of facing elements also. Some vertical gap between adjacent facing elements is needed to allow such movements. Jones (1978) proposed Hexagonal facing elements with vertical poles passing through the horizontal flanges of facing element. Strip reinforcements are connected to facing elements (Fig. 2.3.19). The system, known as DOE York system, allows free vertical movement of reinforcements which is an advantage.

In the recent past, role of facing elements was studied in a greater detail to examine its ability to contribute to a more favourable stress distribution within the R.E. zone for a better performance (Gutierrez and Tatsuoka, 1988; Tatsuoka et.al., 1989 and Tatsuoka, 1992). Some of the arrangements investigated (Fig. 2.3.20) are :

- (a) Gabions connected to reinforcements.
- (b) Gabions cited above provided with external shotcrete facing.
- (c) Gabions cited in (a) with a relatively stiff continuous concrete facing capable of redistributing bending moment and shear forces.
- (d) Rigid continuous covering element extending from top to some depth.

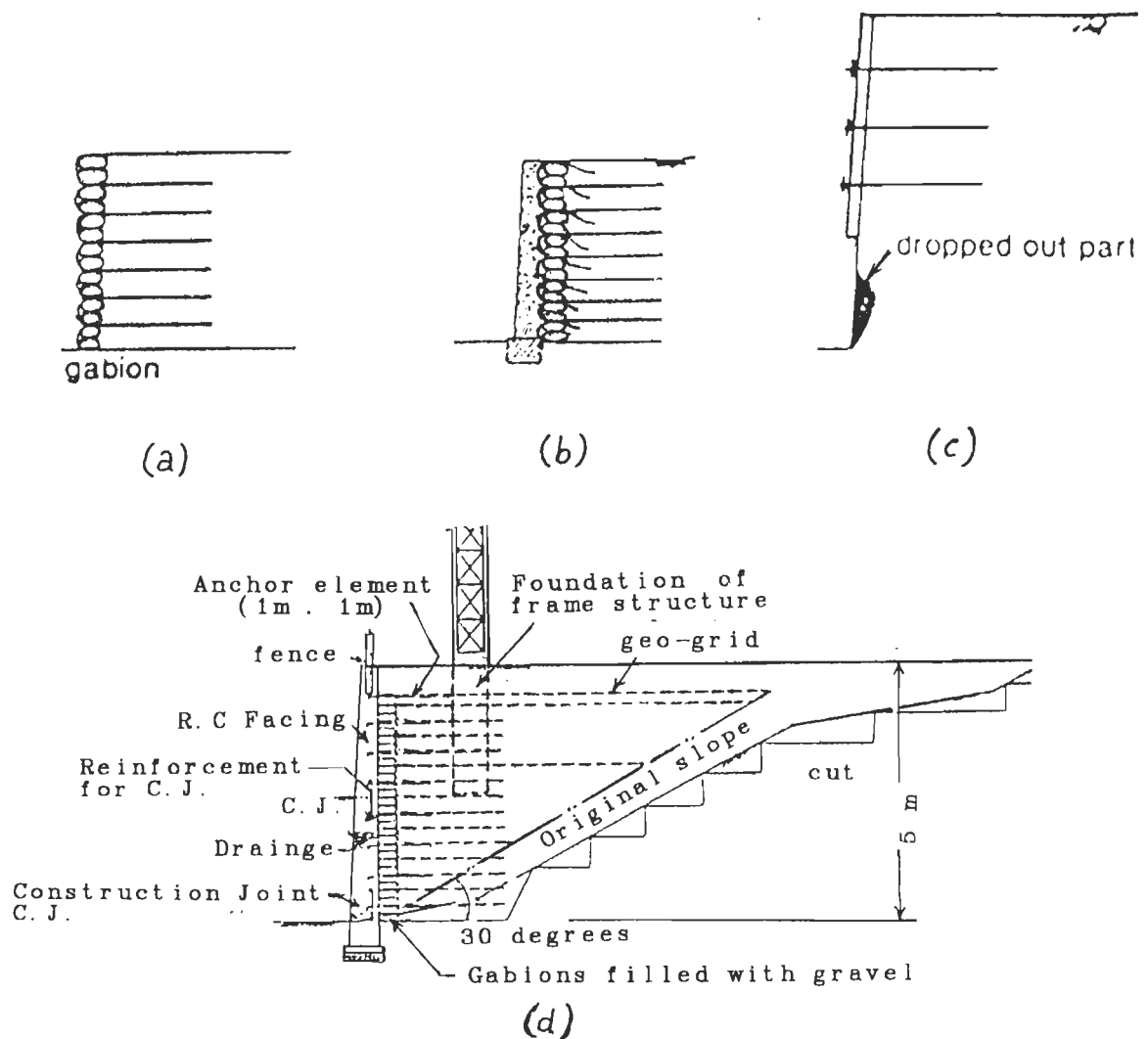


FIG.2.3.20 TYPES OF FACING ELEMENTS (TATSUOKA, 1992).

Tatsuoka (1992) reported that stiffness of facing element and its continuity significantly influences redistribution of stresses with the R.E. zone. A stiff and continuous facing element, therefore, is useful in avoiding high stress concentrations which is an advantage. Applied loads on embankment top often lead to larger stresses near top end. Therefore, continuous facing element extending at least upto some depth from top end are of advantage. With increasing stiffness of facing element its redistribution capacity also increases. It will be necessary to account for it in the embankment analysis by using FEM or other methods.

When facing elements are rigid and secured to reinforcements, the maximum tension appears to occur at the facing itself (Bolton and Pang, 1982). Facing elements are often adequate to avoid sheet failures and/or slope failures of embankments (cited in Article 1.5) penetrating upto a shallow depth below the sloping surface (Gutierrez and Tatsuoka, 1988).

2.4 DYNAMIC INVESTIGATIONS

In Article 2.3, soil improvement using reinforcement for static case was dealt with. Very limited dynamic investigations on R.E. embankments have been carried out and reported. In this article, dynamic analytical and experimental investigations have been critically reviewed.

2.4.1 Dynamic Analytical Investigations

Analysis using plane failure surfaces

Based on experimental studies, Richardson and Lee (1975) recommended static and dynamic earth pressure distribution behind vertical face of R.E. embankments (Fig. 2.4.1). Knowing input base acceleration, magnification factor, M_f , equal to 1.4 was recommended to estimate design seismic coefficient for computing earth pressure distribution to be used for design of R.E. embankments. However, this value of M_f is arbitrary and may be considered valid for only the model and test parameters employed by them. Value of M_f depends on geometry of model tested, its material properties (including type and intensity of reinforcements provided) and excitation parameters (frequency, amplitude, dynamic load etc.). Richardson (1978) reported that reinforcement design based on earth pressure distribution

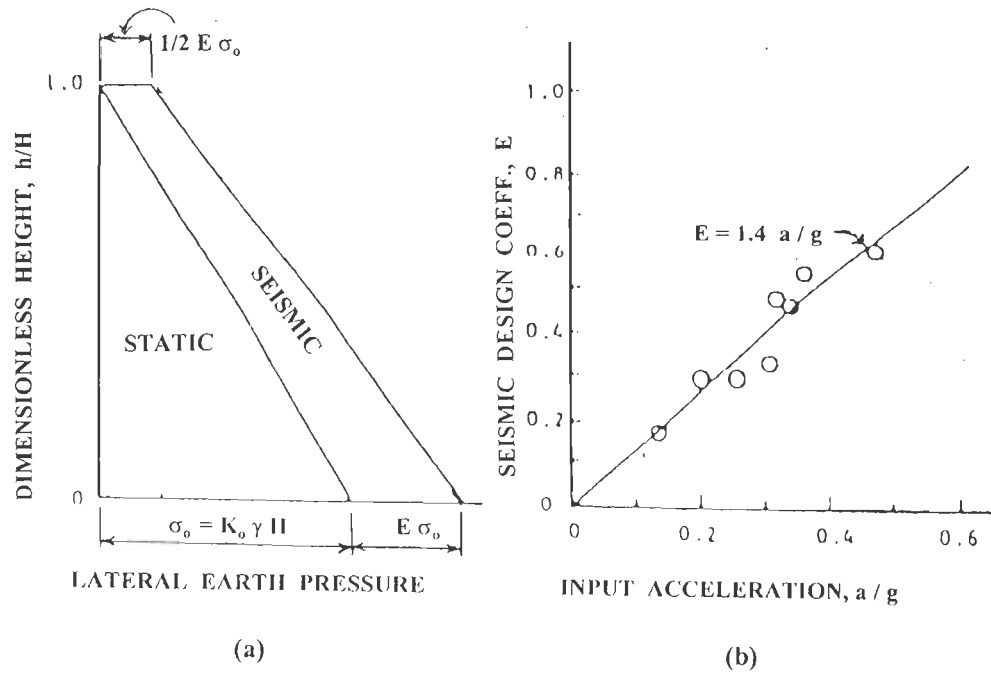


FIG. 2.4.1 STATIC AND DYNAMIC EARTH PRESSURES BEHIND VERTICAL FACE OF R.E. EMBANKMENT (RICHARDSON AND LEE, 1975).

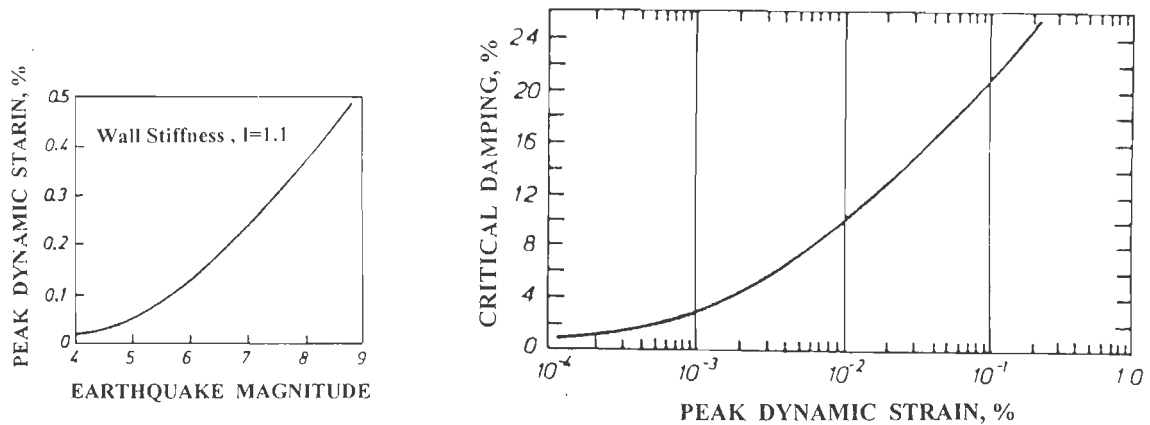


FIG. 2.4.2 ESTIMATING PEAK DYNAMIC STRAINS (RICHARDSON, 1978).

FIG. 2.4.3 ESTIMATING THE LEVEL OF DAMPING (RICHARDSON, 1978).

recommended by Richardson and Lee (1975) was grossly conservative when applied to a 6.1m high test embankment (Richardson et.al., 1977).

The elaborate design method proposed by Richardson (1978) for R.E. embankment subjected to earthquake loading is explained below:

- a) From Fig. 2.4.2, peak strain, ϵ , may be evaluated from known magnitude, M , of design earthquake.
- b) Using Fig. 2.4.3, design damping, λ , may be obtained knowing ϵ .
- c) Using Fig. 2.4.4, design response spectra may be developed using M , and λ cited above.
- d) First and second natural frequencies, F_1 and F_2 , in Hz may be evaluated for an embankment of height, H , in m by using empirical expressions:

$$F_1 = 38/H \quad (2.4.1)$$

$$F_2 = 100/H \quad (2.4.2)$$

- e) From Fig. 2.4.5, obtain frequency correction factor, FCF_ϵ , knowing ϵ .
- f) Obtain strain dependent natural frequencies F'_1 and F'_2 as:

$$F'_1 = F_1 \cdot FCF_\epsilon \quad (2.4.3)$$

$$F'_2 = F_2 \cdot FCF_\epsilon \quad (2.4.4)$$

- g) Using the design response spectrum obtained in step (c) above, obtain spectral acceleration S_{a1} and S_{a2} using F'_1 and F'_2 . The dynamic force ΣF , and effective mass of the embankment, M_{eff} are given by :

$$\Sigma F = (S_{a1} + 0.2 S_{a2}) M_{\text{eff}} \quad (2.4.5)$$

$$M_{\text{eff}} = 0.75 K_0 \cdot \rho \cdot H^2 \quad (2.4.6)$$

where K_0 is at rest pressure coefficient and ρ is mass density of soil.

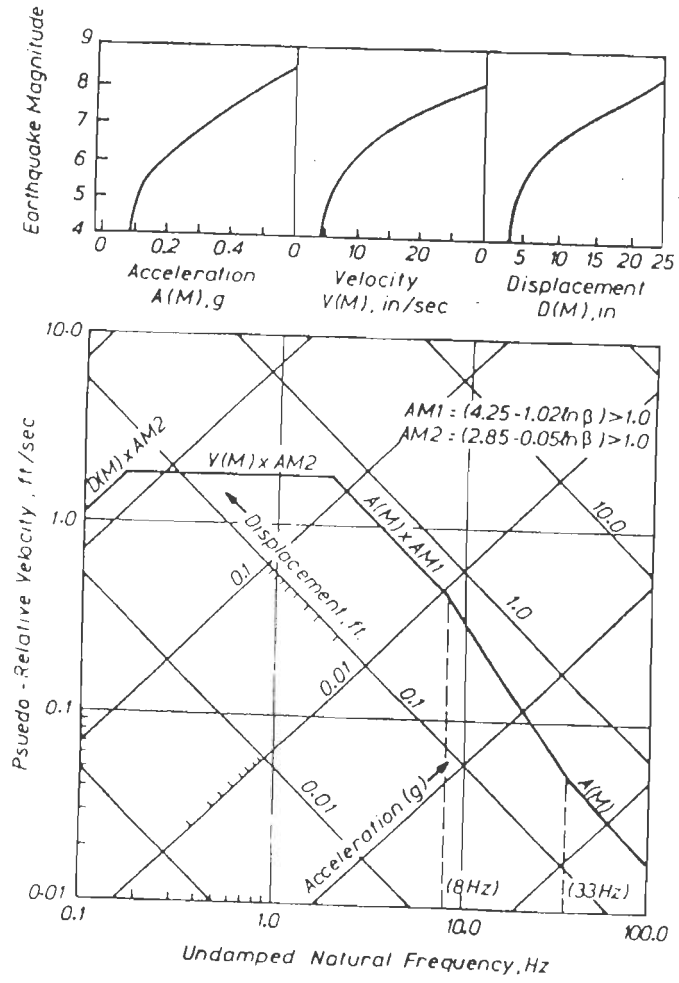


FIG. 2.4.4 DESIGN RESPONSE SPECTRA SYNTHESIS (RICHARDSON, 1978).

h) The stiffness coefficient, I , is defined as :

$$I = \sum_{i=1}^N d_i^2 F_i \quad (2.4.7)$$

where d_i is height of i 'th reinforcement from base, F_i is minimum yield strength force in i 'th reinforcement either in tension or in pullout and N is number of strips. Value of I computed for a 6.1m high reference wall reinforced with $0.8H$ long strips provided at uniform horizontal and vertical spacing (by assuming static safety factor of unity) and tested with blast vibrations is termed as, I_{ref} . For reference wall, dynamic earth pressure distribution, P , over the height of embankment is assumed to be uniform and that for a wall with different stiffness coefficient, I , is obtained on lines indicated in Fig. 2.4.6 where $I < 2$.

i) The stiffness of design wall, I' , is given by :

$$I' = \sum_{j=1}^m d_j^2 \cdot F_j \cdot (S/S_j) \quad (2.4.8)$$

where S is horizontal reinforcement spacing in reference wall, S_j is that in j th layer in the design wall and m is number of strips in the design wall. Based on this, normalised stiffness, I , is given by :

$$I = I' / I_{reff} \quad (2.4.9)$$

Relationship between ϵ and M (Fig. 2.4.2) is derived from F.E.M. study using program 'LEVSFC' given by Idriss and Seed (1978). Displacements obtained from tests for blast tests at UCLA are compared with results obtained analytically by the procedure cited above. Based on this, the following empirical relationship is arrived at :

248385.



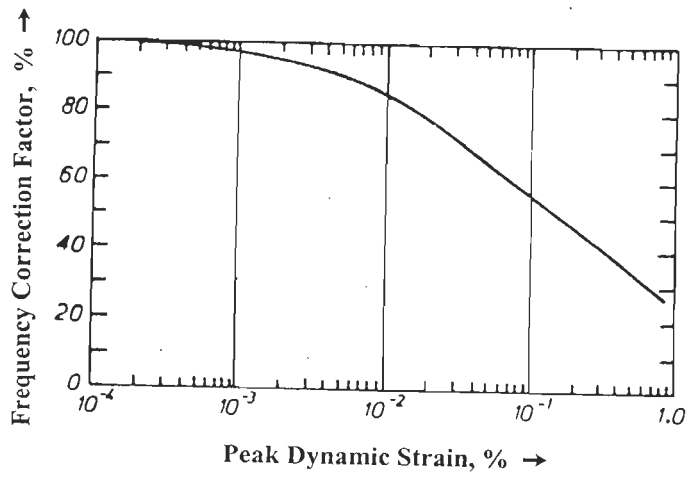


FIG. 2.4.5 NATURAL FREQUENCY REDUCTION FACTOR (RICHARDSON, 1978).

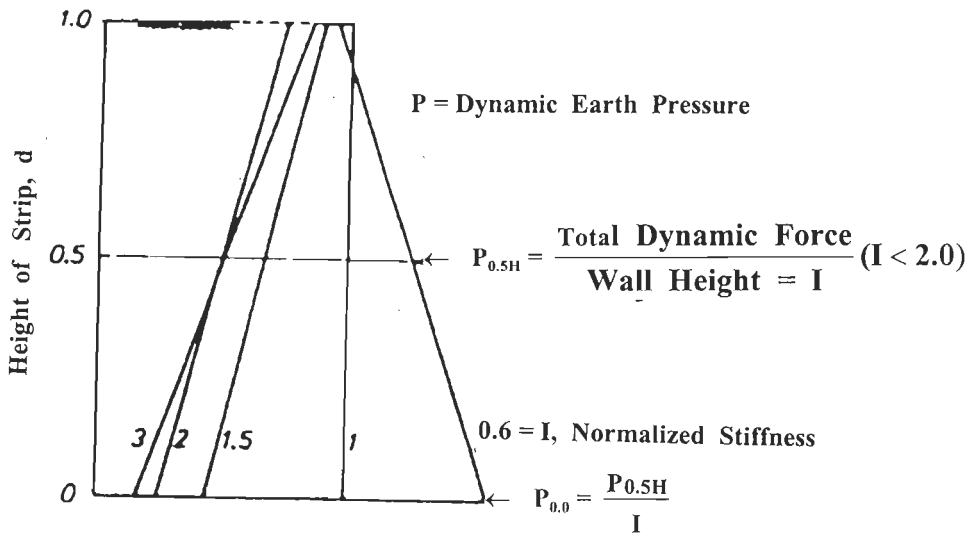


FIG. 2.4.6 STIFFNESS VS DYNAMIC EARTH PRESSURE (RICHARDSON, 1978).

$$\varepsilon = \frac{1.1}{I} \varepsilon_{\text{LEVSFC}} \quad (2.4.10)$$

where ε is peak dynamic strain of design wall, I is normalized stiffness and $\varepsilon_{\text{LEVSFC}}$ is predicted embankment displacement using 'LEVSFC' program. Embankments of H ranging from 5m to 16.75m were analysed.

The earthquake record input for program LEVSFC was obtained by scaling amplitudes in the light of magnitude of design earthquake. However, the scaling method used has not been clearly explained. Figure 2.4.3 and Fig. 2.4.5 were both derived by Richardson (1978) from the method of Seed and Idriss (1970) to account for change in dynamic ε . Blast tests (Richardson et. al. 1977) showed a nonlinear decrease of the first mode natural frequency of the embankment with increasing dynamic ε . Fairless (1989) made following comments on analyses of Richardson (1978):

-It is overdependent on LEVSFC in relating earthquake magnitude and peak dynamic strain whereas Breacegirdle (1979) has indicated notable influence of input soil parameters on results. Similarly attenuation law used and not defined by Richardson (1978) also has significant influence on results obtained. Besides, LEVSFC is extremely sensitive to boundary conditions as indicated by Bracegirdle (1979).

-The Eq. 2.4.10 based on blast tests is not representative of seismic loading particularly when its predominant vibration period is small.

-Earth pressure is difficult to predict even for static case and even more so for dynamic case. Locked in stresses due to stress history during placement and compaction may affect earth pressures for active state if enough time is allowed (AL-Hussaini and Perry, 1978c).

-Richardson's analysis is within elastic domain and hence valid for analysis with operating basis earthquakes. For larger earthquakes, it is not applicable and more rigorous analysis is needed.

-Based on results of FEM analysis Aggour and Brown (1974) concluded that earthquakes are affected by geometry of the model as well as its material properties. So, prediction of earth pressure as function of only stiffness appear to be unreasonable.

-Expression for M_{eff} recommended by Richardson (1978) is arbitrary.

-Boyd (1985) pointed out that this method makes no distinction between dynamic earth pressure forces and the inertia of wall itself, though the method is valid for internal stability. Because of the arbitrary recommendations assumed, it is complicated and difficult to justify.

Besides above limitations cited by Fairless (1989), more draw backs may be pointed out. Dynamic earth pressures are functions of wall movement realised, angle of shear resistance of soil, embankment geometry, rigidity of facing elements and length of reinforcements. As such, the dynamic earth pressure distribution based on stiffness coefficient only is incorrect.

Bonaparte et.al. (1986) performed pseudo-static stability analysis of R.E. embankments of sand subjected to earthquakes assuming Coulomb's active rupture wedge and rigid plastic stress-strain characteristics. Ratio of reinforcement, R_T , was defined as tensile force ratio, T_e , for seismic case to tensile force, T_s , for static case. Reinforcement length ratio, R_L , was defined as ratio of reinforcement lengths L_e and L_s for seismic and static cases respectively. Variations of R_T and R_L with slope angle β and

horizontal seismic coefficient k for angle of shear resistance of fill, $\phi=25^\circ$ (Fig.2.4.7) showed that as k increase R_T and R_L increase which is reasonable. However, use of Coulomb's static failure wedge for dynamic cases is incorrect. Size of dynamic rupture wedge is larger than that of static wedge and increases considerably with increasing k .

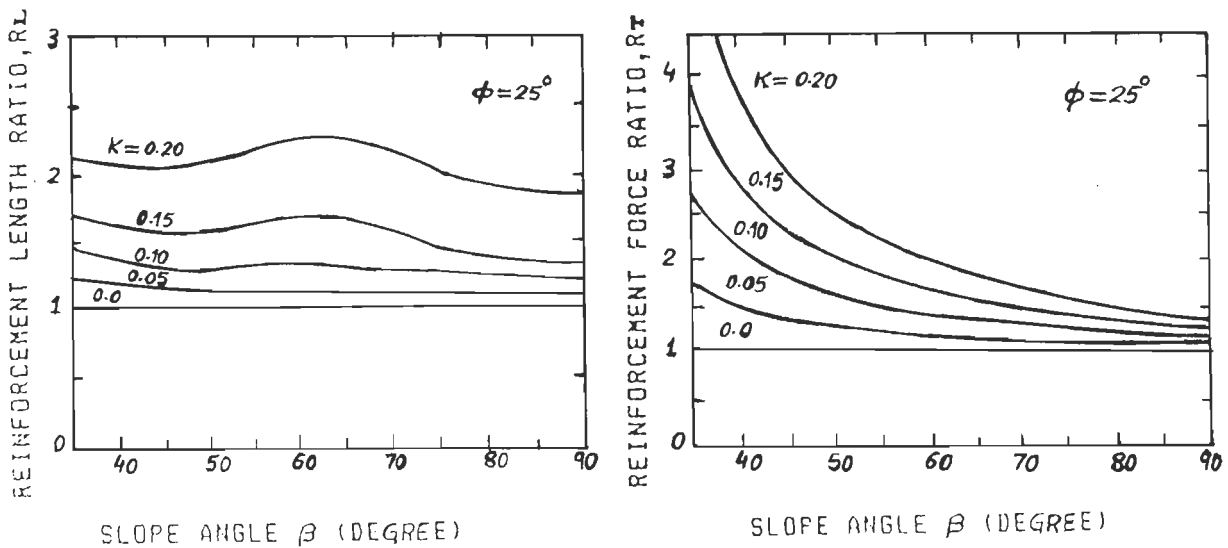


FIG.2.4.7 VARIATION OF R_T AND R_L WITH SLOPE ANGLE, β , SOIL STRENGTH, ϕ , AND SEISMIC COEFFICIENT. (BONAPARTE ET.AL.,1986).

Verma (1991) analysed R.E. walls with vertical facing and level cohesionless fill assuming Mononobe-Okabe rupture wedge for dynamic case and that of Coulomb for static case. Embankment face was assumed to rotate about base to reach active state. Tension in reinforcements was obtained using these pressures. Reinforcement length is worked out by considering pullout resistance in that reinforcement length which extends beyond static/dynamic rupture surfaces into the fill. Extensive parametric studies were carried out and results presented in terms of dimensionless factors (Table 2.4.1). The length factor increases with increasing distance from

embankment base and with increasing, α_h , as expected. The maximum length factor obtained is about 1.6 for $\alpha_h = 0.3$ and $\phi = 30^\circ$. Variation of vertical reinforcement spacing does not appear to greatly influence length factor for any α_h . This important finding indicates economy and advantage of using

Table 2.4.1 : Dimensionless Factors

Sl. No.	Factor	Symbol	Definition
1.	Length factor	C_L	L/H
2.	Length factor for the i 'th horizontal slice.	C_{LHi}	L_i/H
3.	Length factor for initial width of wall	C_{Lini}	L_{ini}/H
4.	Length factor for safety against overturning	C_{LO}	(Width of wall safe in overturning)/H
5.	Length factor for safety against sliding	C_{LS}	(Width of wall safe in sliding)/H
6.	Length factor for safety against compression at base	C_{LC}	(Wall width safe against bearing pressure)/H
7.	Length factor for safety against tension at base	C_{LT}	(Width of wall safe against tension at base)/H
8.	Height factor at the base of slice i 'th	C_{hi}	h_i/H
9.	Static skin friction factor	C_{Fs}	$\tan \phi_{Fs}/\tan \phi$
10.	Dynamic skin friction factor	C_{Fd}	$\tan \phi_{Fd}/\tan \phi$

longer reinforcements with larger vertical spacing which is in agreement with test results of Fairless (1989). Length factor reduces sharply with increasing ϕ for static/dynamic cases as expected. As such, use of sands at higher density is better. Increasing values of skin friction factor or

coefficient of pullout resistance reduce length factor sharply. However, at coefficient of pullout resistance of 0.4, length factor assumes very nearly constant value for α_h equal to 0.4. This constant value of length factor increases appreciably with increasing α_h . This is reasonable, because, higher values of α_h induce larger inertia forces. Coulomb/Mononobe-Okabe wedge may be realised for underreinforced embankments. As the degree of reinforcement and length of reinforcement increase, test results indicate that rupture surface gets flatter. As such, the design based on Mononobe-Okabe rupture surface may not be realistic. It is more realistic to obtain the critical value of α for the plane rupture surface by maximising the active earth force.

Saran and Khan (1990) analysed a vertical R.E. wall with level fill using pseudo-static approach. Reinforcement length was obtained by using external stability of R.E. zone in sliding and under bearing pressures. Suitable safety factors were also incorporated. Reinforcement length is further checked against tensile failure by equating tension to active earth force predicted by Coulomb/Mononobe-Okabe. Length was also checked against failure by pullout by equating earth force to pullout resistance mobilised along length of reinforcements extending beyond rupture surface. This analysis is similar to that proposed by Verma (1990). Hence, limitations of Verma's method of analysis are applicable to results of Saran and Khan.

Pseudo-dynamic earth pressure theory of Steedman and Zheng (1990) accounts for influence of phase difference over height, H , of a vertical retaining wall with plain fill. Base excitation propagates upward through fill with shear velocity, V_s , of soil. This was extended to nailed soil

slopes with sand assuming planar failure surface by Sabhahit et.al. (1996). For interface friction angle, δ , and vertical acceleration coefficient, $k_v=0$ horizontal acceleration at depth, z , and time, t , is given by:

$$a(z,t) = a_0 \sin [\omega (t-(H-z)/V_s)] \quad (2.4.11)$$

where ω is angular frequency and a_0 is peak base acceleration. Horizontal slices of assumed failure wedge with plane failure surface at angle, α , slope angle, ψ , soil density, γ , and acceleration due to gravity, g , have incremental mass, $m(z)$, total active earth force is $p_{AE}(t)$ and equivalent dynamic active earth pressure coefficient, K_{AE} , are given by:

$$m(z) = \gamma/g (H-z)(\cot\alpha-\tan\psi) dz \quad (2.4.12)$$

$$p_{AE}(t) = \frac{Q_h(t) \cos(\alpha-\phi)}{\cos(\delta-\alpha+\phi)} + \frac{W \sin(\alpha-\phi)}{\cos(\delta-\alpha+\phi)} \quad (2.4.13)$$

$$K_{AE} = 2p_{AE}/\gamma H^2 \quad (2.4.14)$$

$$\text{where } Q_h = \int_0^H m(z) a(z,t) dz \quad (2.4.15)$$

When $V_s \rightarrow \infty$, $p_{AE}(t)$ by pseudo-dynamic approach tends to value predicted by Mononobe-Okabe theory. Pseudo-dynamic approach allows location, H_d , of dynamic force increment Δp_{dyn} to be determined numerically for a range of base motion frequencies, which is welcome. Solution for H_d and Δp_{dyn} is independent of ϕ and γ , but depends on V_s and period, T , of assumed sinusoidal horizontal base acceleration. Results presented in dimensionless terms (H_d/H) and (H/TV_s) show that for low excitation frequency, $H_d=H/3$

above base and increases to 0.4H to 0.7H at higher frequencies. It appears Mononobe-Okabe method is conservative for overturning/base eccentricity design calculation for a wide range of base motion frequencies.

In above investigation, analytical/experimental evaluation of V_s as a function of length, vertical and horizontal reinforcement spacing and properties of backfill has not been given.

Analysis using bilinear failure surface

Tai (1985) described pseudo-static method of analyses of Seed and Mitchell (1980) for R.E. with seismic loading. Figure 2.4.8 shows assumed rupture wedges for static and dynamic cases. Inertia and the dynamic earth force may not reach peak values simultaneously. However, their separate minimization did not give appreciably different results when compared with those obtained when they act simultaneously (Antia and Whitman, 1982). Dynamic active earth force, E_{ae} , is given by Mononobe-Okabe as :

$$E_{ae} = (0.5 \gamma H^2) (0.75 a/g) = 0.375 \gamma H^2(a/g) \quad (2.4.16)$$

where a stands for peak seismic ground acceleration and H is the height of the embankment. This is assumed to act at a distance of 0.6H above the base. It is assumed that inertia of the R.E. wall, E_I , is given by :

$$E_I = 0.5 \gamma H^2 a/g \quad (2.4.17)$$

where width of wall and that of active zone are 0.5H. Width of active zone is wider for higher accelerations. However, Tai preferred Japanese practice for fixing width of active zone, L_a , (Fig. 2.4.8). Expressions for L_a and E_I assumed to act at a distance of H_a from base are given by:

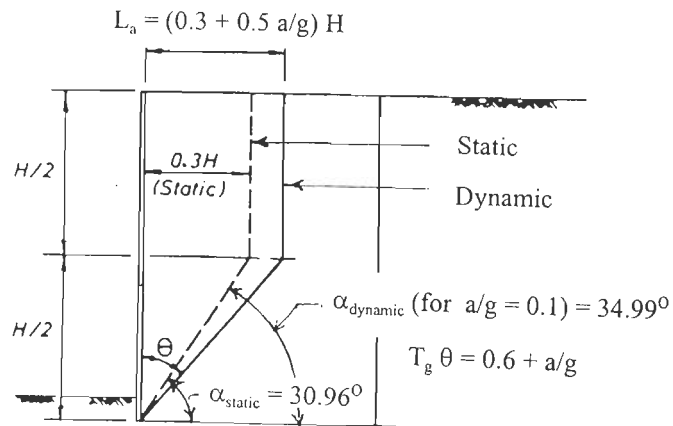
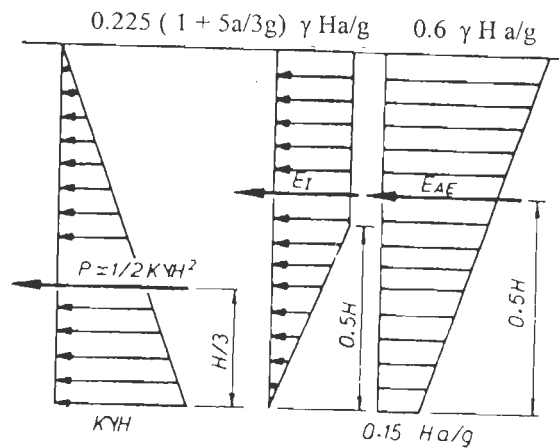


FIG. 2.4.8 ACTIVE ZONE FROM JAPANESE WORK (TAI, 1985).



Inertia Force $E_I = 0.15 \gamma H^2 a/g (1 + 5a/3g)$

Dynamic Earth Pressure $E_{AE} = 0.375 \gamma H^2 a/g$

FIG. 2.4.9 STATIC, DYNAMIC AND INERTIA EARTH PRESSURES (TAI, 1985).

$$L_a = [0.3 + 0.5 (a/g)]H \quad (2.4.18)$$

$$E_I = 0.75H[(0.3 + 0.5a/g)]H\gamma(a/g) = 0.225 \gamma H^2(a/g)(1 + 5a/3g) \quad (2.4.19)$$

$$H_a = \frac{1}{3} \cdot \frac{H}{3} + \frac{2}{3} \cdot \frac{3H}{4} = 0.61 H \quad (2.4.20)$$

This E_I and E_{ae} act at the same level. To account for nonoccurrence of E_I and E_{ae} simultaneously, a reduction factor is introduced so that :

$$(E_{ae} + E_I) \leq 0.7 \gamma H^2 \cdot (a/g) \quad (2.4.21)$$

Seed and Mitchell suggest reducing E_I by 35 % while holding E_{ae} to be the same. Tai choose to reduce E_I , by 1/3 and this results into :

$$E_I = 0.15 \gamma H^2 (a/g) (1 + 5a/3g) \quad (2.4.22)$$

Figure 2.4.9 shows resultant earth pressures. Seed and Mitchell (1980) also concluded that for all practical purposes $S_{a1} \approx S_{a2} \approx a$. Combining above equation and using Jacky's $K_0 = 0.412$ for $\phi = 36^\circ$ and Richardson's stiffness coefficient, $I = 1.5$, the internal force, E_d , is given by :

$$E_d = 0.25 \gamma H^2 \cdot (a/g) \quad (2.4.23)$$

Seed and Mitchell preferred to limit dynamic stresses in strips to lower values and hence revised arbitrarily values of, E_d , (Fig. 2.4.9) as:

$$E_d = 0.3 \gamma H^2 \cdot (a/g) \quad (2.4.24)$$

By assuming $E_I = \{0.2(1 + 5a/3g) \gamma H \Delta h (a/g)\}$, dynamic earth pressure force $E_{ae} = \{0.6 \gamma H \Delta h (a/g) - (0.5)(0.45) \gamma \Delta h^2(a/g)\}$ and static earth force, $P = \{(0.5)(0.3) \gamma \Delta h^2\}$ (for $\phi = 35^\circ$, $k_a = 0.3$) for slices of $\Delta h \leq H/2$, and comparing the sum to shear resistance (mass $\cdot \tan\phi$) at base of slice, Seed and Mitchell gave :

$$(a/g)^2 + (2.4 - 0.675 \Delta h/H)(a/g) + (0.45 \Delta h/H - 1.5) = 0 \quad (2.4.25)$$

Based on results, they concluded that risk of permanent deformation of wall is not there if all strips are longer than $0.7H$ and $a \leq 0.5g$. This is valid for top half of wall. No analysis was carried out taking slice as greater than $H/2$ deep.

This method neglects flexibility of R.E. walls. Forces in reinforcements (which are very important for design) are assigned arbitrary values. The stress is mainly on internal stability, evaluation of E_I and E_{ae} . Determination of forces in reinforcements was given lesser attention.

Analysis Using planar and bilinear failure surface

Jones (1985) recommended use of planar or bilinear rupture surfaces passing through R.E. zone only or passing partly through R.E. zone and partly through plain soil (Fig.2.4.10). He employed a numerical approach and examined equilibrium of horizontal slices of rupture wedge to obtain

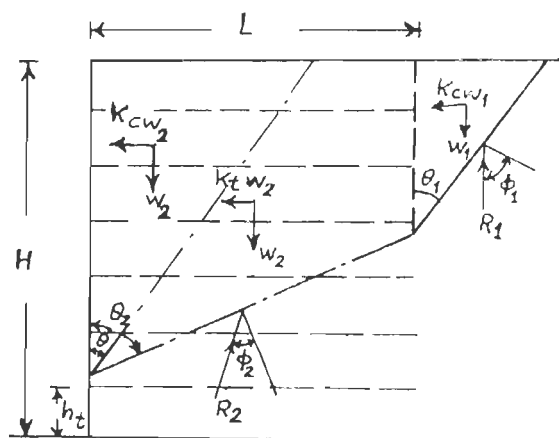


FIG. 2.4.10 SEISMIC DESIGN-DISPLACEMENT METHODS: PLANAR AND BIPLANAR (JONES, 1985).

length of reinforcements at different elevations. Though this is a step in the right direction, it fails to provide plastic displacements. Without this quantitative information, it is impossible to assess pullout resistance of reinforcements. Nevertheless, the idea of considering different failure modes to obtain critical surfaces is reasonable.

Fairless (1989) adopted Pseudo-static analysis to determine critical rupture wedge of R.E. embankments. Figure 2.4.11 and 2.4.12 show types of rupture wedges considered. The following assumptions were made:

- (i) Plane strain conditions are valid
- (ii) No change in pore pressure within the embankment
- (iii) No vertical acceleration
- (iv) Horizontal acceleration in the longitudinal direction of the embankment has negligible influence.
- (v) Smooth and weightless vertical embankment facing.
- (vi) Horizontal surface with no surcharge.

For embankment (Fig.2.4.11) of height, H , reinforcements of uniform length, L , plane rupture surface at an angle α with horizontal fully situated within R.E. zone, the resultant, R , of tensile forces in reinforcements, weight of rupture wedge, Mg , horizontal inertia ($k_h \cdot Mg$), normal reaction, N , and shear force ($N \tan\phi$) on rupture surface are shown in figure. Gravitational acceleration is g . For equilibrium of wedge:

$$k_h \cdot Mg = R + N \tan\phi \cos\alpha - N \sin\alpha \quad (2.4.26)$$

$$Mg = N \tan\phi \sin \alpha + N \cos \alpha \quad (2.4.27)$$

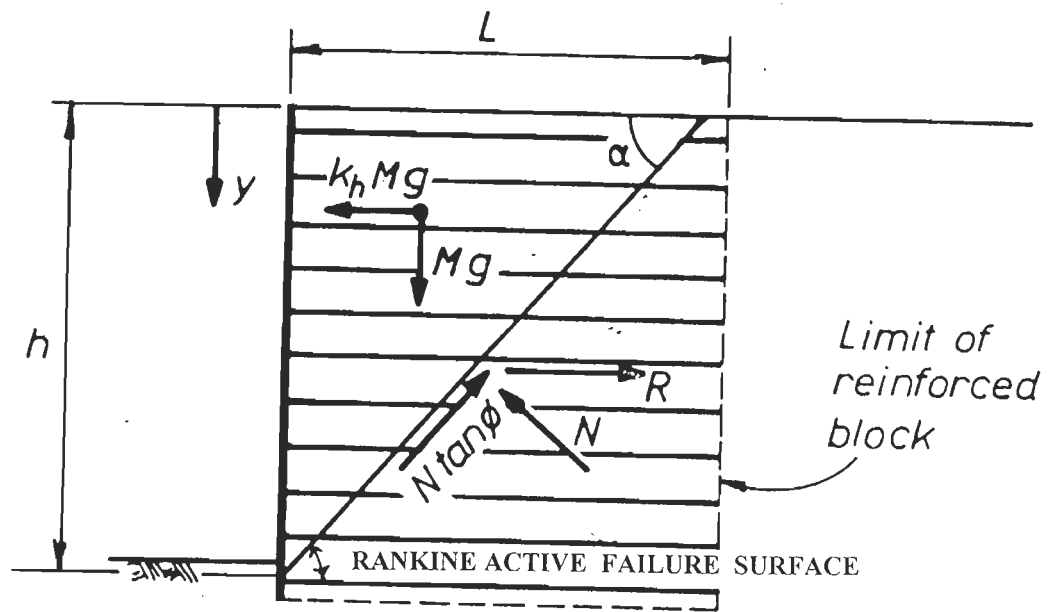


FIG. 2.4.11 LIMITING EQUILIBRIUM, FAILURE SURFACE CONTAINED (FAIRLESS, 1989).

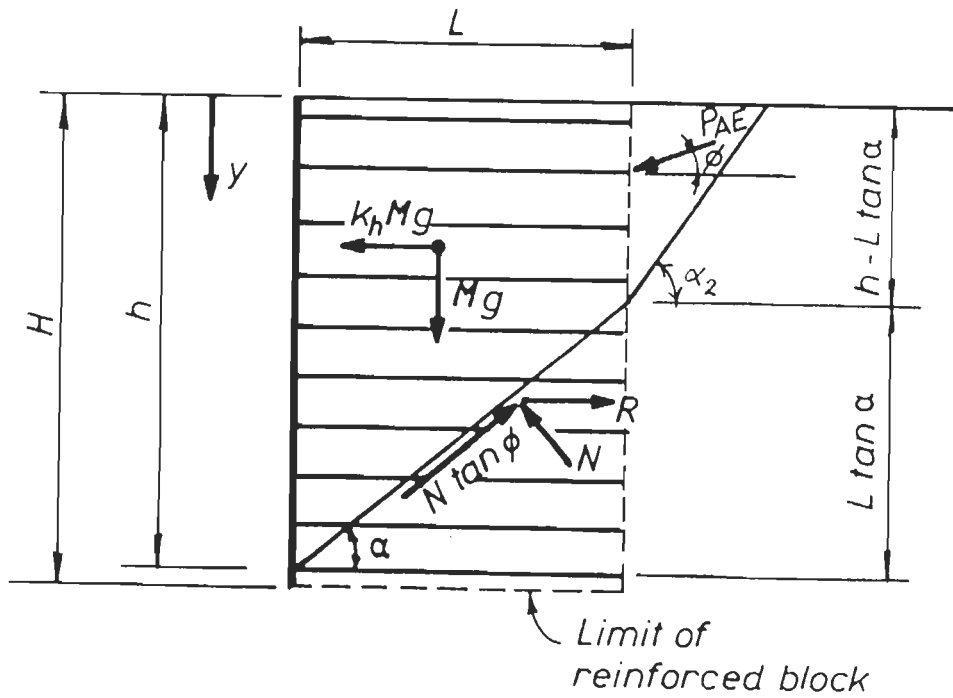


FIG. 2.4.12 LIMITING EQUILIBRIUM, FAILURE, NOT CONTAINED (FAIRLESS, 1989).

Solving these two equations, the yield acceleration coefficient, k_h , at the failure and the weight of rupture wedge, Mg , are obtained as:

$$k_h = \tan(\phi - \alpha) + (R/mg) \quad (2.4.28)$$

$$Mg = \rho gh^2 / \tan \alpha \quad (2.4.29)$$

where ρ is mass density of embankment material. Expression for resultant, R , of tension in reinforcements at the failure is:

$$R = \sum F_y = \sum_{i=1}^m [\{L - (h - y_i) / \tan \alpha\} 2bn\rho gy_i f_i^*] \quad (2.4.30)$$

where b is strip width, f_i^* is apparent friction coefficient, n is number of strips per meter run of wall, F_y is force in strip at depth y below top of wall and y_i is depth of i th reinforcement. If f_i^* is independent of depth,

$$R = 2bn\rho g f^* [(L - h / \tan \alpha) \sum_{i=p}^m y_i + (1 / \tan \phi) \sum_{i=p}^m y_i^2] \quad (2.4.31)$$

where p is layer number in which rupture surface meets vertical embankment face with m layers. From Eq. 2.4.29 and Eq. 2.4.31, k_h is given as:

$$k_h = \frac{2bnf^* \tan \alpha [(L - h / \tan \alpha) \sum_{i=p}^m y_i + (1 / \tan \phi) \sum_{i=p}^m y_i^2]}{h^2} + \tan(\phi - \alpha) \quad (2.4.32)$$

Value of k_h is minimised to obtain α for critical rupture wedge.

It may be noted that Fairless assumed f^* to be independent of depth in obtaining k_h given in Eq. 2.4.32 which is unnecessary. Infact f^* varies with depth and can be obtained experimentally. Yield acceleration k_h may be evaluated by assuming trial values of α to obtain R and Mg values by using Eq. 2.4.29 and 2.4.30 which in turn is substituted in Eq. 2.4.28 to get k_h by trial and error. This is easily achieved by using a computer program.

Consider an embankment with bilinear rupture surface partly passing through R.E. zone and partly in plain earth behind (Fig.2.4.12). Dynamic earth pressure, P_{AE} , acts at an angle ϕ to the vertical interface between plain soil and R.E. zone as shown in the figure. Expressions for P_{AE} and Mononobe-Okabe dynamic active earth pressure coefficient, k_{AE} , are:

$$P_{AE} = \frac{1}{2} \rho g h_w^2 \cdot k_{AE} \quad (2.4.33)$$

$$k_{AE} = \frac{\cos^2(\phi - \theta)}{\cos\theta \cos(\delta + \theta) \left[1 + \sqrt{\frac{\sin(\delta + \phi) \sin(\phi - \theta)}{\cos(\delta + \theta)}} \right]^2} \quad (2.4.34)$$

where h_w is depth at which plain rupture surface meets vertical interface between plain earth and R.E. zone. Notation δ and β in Eq. 2.4.34 stand for wall friction angle and surcharge angle which are taken to be zero for the problem under consideration. Symbol θ stands for $\tan^{-1}\{k_h/(1 \pm k_v)\}$, k_v being vertical acceleration coefficient assumed to be zero for problem under consideration. From equilibrium of rupture wedge within R.E. zone we have:

$$k_h Mg = R + N \tan \phi \cos \alpha - N \sin \alpha - P_{AE} \cos \phi \quad (2.4.35)$$

$$Mg + P_{AE} \sin \phi = N \tan \phi \sin \alpha + N \cos \alpha \quad (2.4.36)$$

Eliminating N we obtain :

$$k_h Mg = R + [(Mg + P_{AE} \sin \phi) (\tan \phi \cos \alpha - \sin \alpha) / (\tan \phi \sin \phi + \cos \alpha)] - P_{AE} \cos \phi \quad (2.4.37)$$

where weight of active wedge, Mg , within R.E. zone is:

$$Mg = \rho g L \{h - (L \tan \alpha) / 2\} \quad (2.4.38)$$

Substituting this Mg in Eq. 2.4.37, expression for k_h is obtained which is

minimised to get α for critical rupture wedge on the lines cited earlier. Above procedure may be extended to embankments with stepped R.E. zone shown in Fig. 2.4.13 on similar lines to obtain a critical rupture wedge.

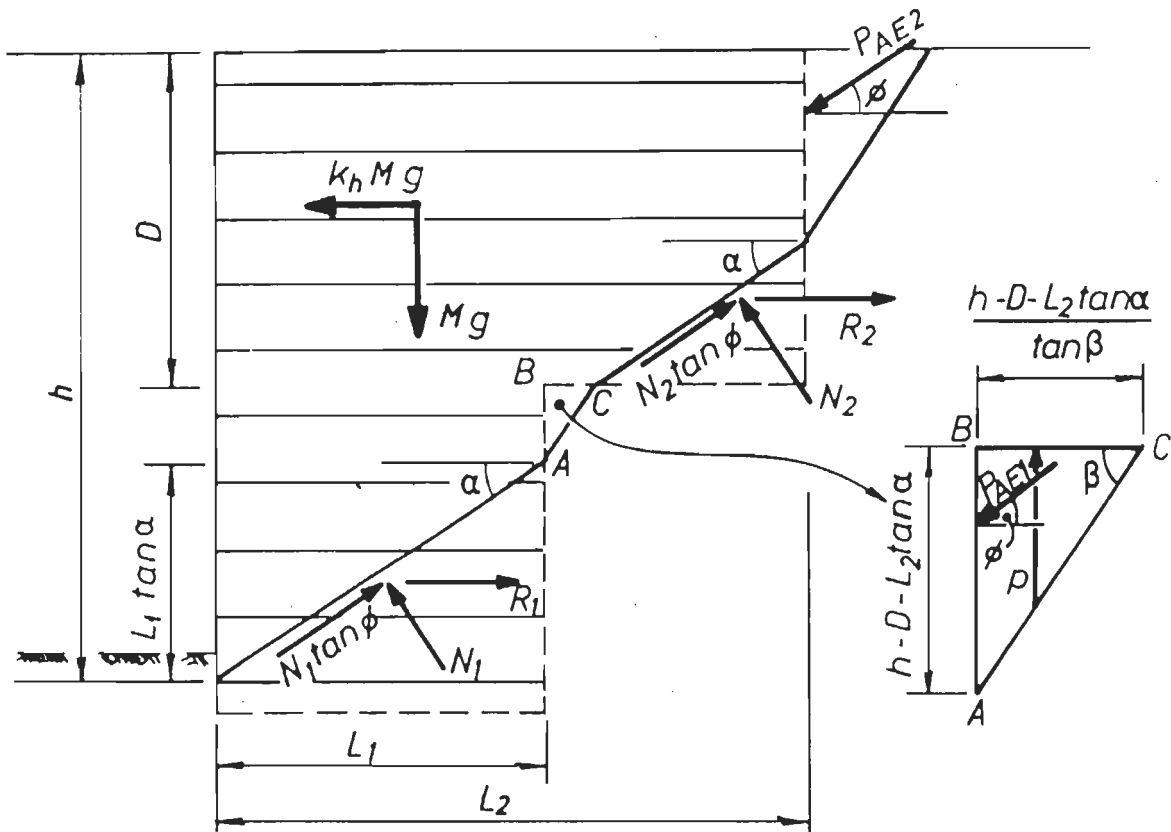


FIG.2.4.13 RUPTURE SURFACE FOR TWO STEP R.E. STRUCTURE (FAIRLESS, 1989).

In above derivation, rupture wedge deformations are neglected. Fairless obtained seismic plastic displacement of rupture wedge by using method of Newmark (1965) further improved by Sarma (1975) and by Lin and Whitman (1986). Fairless favours Lin and Whitman approach to get expected conditional displacements for comparison of analytical and observed results

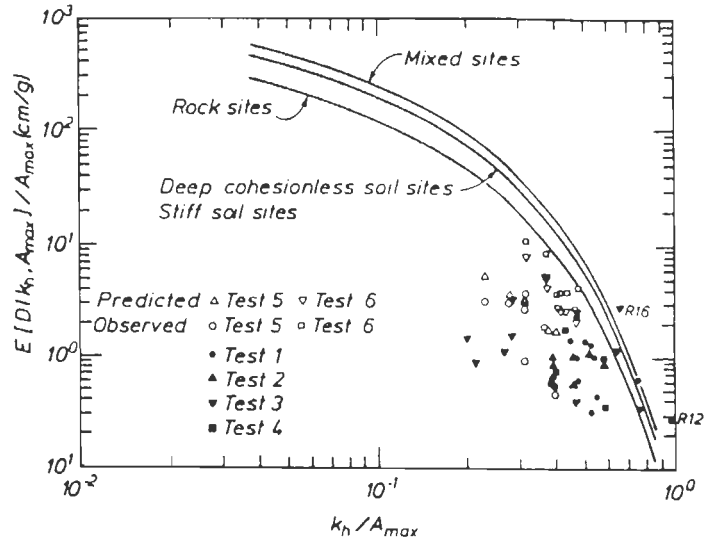


FIG. 2.4.14 OBSERVED AND CALCULATED DISPLACEMENTS PLOTTED ON LIN AND WHITMAN'S (1986) CHART OF NORMALIZED CONDITIONAL EXPECTED DISPLACEMENT VS NORMALIZED YIELD ACCELERATION (FAIRLESS, 1989).

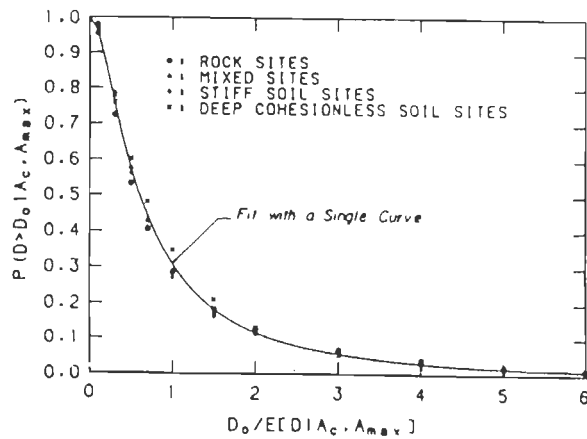


FIG. 2.4.15 NORMALIZED CONDITIONAL PROBABILITY OF EXCEEDENCE OF A PERMANENT DISPLACEMENT FOR SLIDING BLOCKS (FAIRLESS, 1989).

(Fig.2.4.14 and Fig.2.4.15). It may be observed from figures that computed and observed points are below enveloping curves of Lin and Whitman (1986).

From Table 2.4.2, it is seen from Set A and B that computed values of α are larger than those observed from tests. In Set C, these show better agreement. Computed values of k_h are not always comparable and may be higher or lower than observed values. These discrepancies in computed and observed values of α and k_h obtained by Fairless appear to be due to his incorrect assumption that value of ϕ mobilised, i.e. ϕ_m , along rupture surface within the R.E. zone is independent of wedge displacement and is always equal to ϕ at failure. In reality, ϕ_m is displacement dependent and increases with displacement from zero to ϕ . These displacements and α in turn depend on accelerations, length and horizontal/vertical spacing of reinforcements; relative density and shear parameter of the backfill as well as the pullout resistance and extensibility of reinforcements. Relationship between these parameters was not obtained by him which would have been useful. Nevertheless, his results show that reinforcement length has more effect on α than vertical/horizontal spacing. As reinforcement length increases α decreases other condition being same which is expected.

Fairless provided 8.5% of embankment height as foundation depth for R.E. embankment as per recommendations of MWD (1973). As such, 85% of the lowest facing element was buried into the foundation soil. The passive resistance due to this buried portion has not been accounted for in his analysis which is in error and leads to over-estimation of computed mobilized pull out resistance of reinforcements near the base. This may be one of the reasons why observed earth pressures on facing elements decrease after reaching peak values as we go towards the bottom end.

Table-2.4.2 Calculated and Observed Yield Acceleration: k_h and Failure Surface Angles, α (Fairless, 1989)

Test	k_h (g)		α (degrees)	
	Calculated	Observed	Calculated	Observed
Set A : $\phi = 45^0$ and $f^* = 0.85$				
1	0.24	0.24	47.0	36.7
2	0.30	0.21	47.0	33.2
3	0.16	0.09	54.4	43.0
4	0.23	0.21	44.7	41.8
5	0.23	0.20	44.7	36.7
6	0.24	0.22	47.8	39.5
Set B : $\phi = 40^0$ and $f^* = 0.85$				
1	0.16	0.24	47.0	36.7
2	0.21	0.21	48.7	33.2
3	0.06	0.09	54.4	43.0
4	0.14	0.21	47.0	41.8
5	0.14	0.20	47.0	36.7
6	0.16	0.22	47.0	39.5
Set C : $\phi = 38^0$ and $f^* = 1.40$				
1	0.26	0.24	35.5	36.7
2	0.34	0.21	32.7	33.2
3	0.18	0.09	43.0	43.0
4	0.21	0.21	36.7	41.8
5	0.21	0.20	36.7	36.7
6	0.26	0.22	35.5	39.5

Sabhahit and Madhav (1996) gave a method of analysis of R.E. walls. They considered Coulomb wedge for static case and Mononobe-Okabe wedge for dynamic case with plane failure surface to obtain reinforcement length for a

given safety factor, F_s . By employing bilinear failure surface using same reinforcement length, F_s is re-calculated. Dimensionless reinforcement length (L/H) varies linearly with F_s for $K_h=0$ and 0.1 for typical walls for plane and bilinear surfaces. Overall error in plain failure analysis was of the order of 11% w.r.t. that for bilinear failure analysis.

At $L/H=0.71$ and 0.94 errors in F_s are 15% and 7.22% respectively which are small. For dynamic case, $L/H>0.94$ is not uncommon and for which error could be $< 7.22\%$. Hence, no significant advantage results by using bilinear failure surface. Limitations of the method are similar to those for method of analysis of Verma (1991) and by Saran and Khan (1990).

Slip circle method of the analysis

Koga et.al. (1988) carried out pseudo-static stability analysis of R.E. embankment for dynamic case using slip circle type of rupture wedge (Fig.2.4.16 and 2.4.17). Stress-strain relationship was idealized to be elastic upto failure strain and rigid plastic there after (Fig. 2.4.18). The following were assumed :

- (i) Slip circle has a slip band of constant thickness and shear strain.
- (ii) Reinforcing element deforms with the adjoining soil and can not be separated from the soil.
- (iii) Shear strain in slip band generates tensile strain in reinforcement intersecting the slip band.
- (iv) Tension in reinforcement is adequate to hold the slipping mass.

The tensile strain, ϵ_g , of the reinforcement (Fig.2.4.17) is :

$$\epsilon_g = (cd-bd)/bd = \{\cos i - \cos(i+\gamma')\} / \cos(i+\gamma') \quad (2.4.39)$$

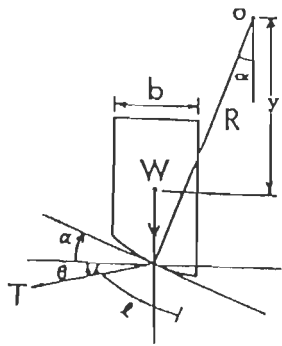


FIG. 2.4.16 SLICE FOR A CIRCULAR SLIP SURFACE ANALYSIS (KOGA, ET.AL., 1988).

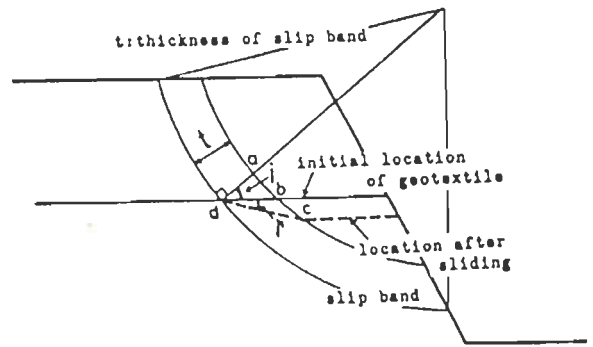


FIG. 2.4.17 CALCULATION OF TENSION OF GEOTEXTILE (KOGA, ET.AL., 1988).

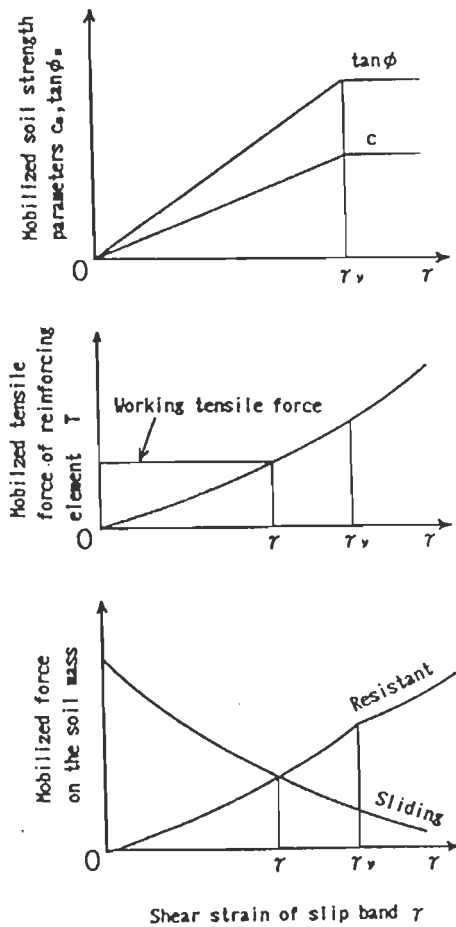


FIG. 2.4.18 RELATIONSHIP BETWEEN MOBILIZED FORCE AND DEFORMATION OF SOIL MASS (KOGA, ET.AL., 1988).

where i is angle between reinforcing element and normal to slip surface at d and γ' is corrected shear strain of soil generally not equal to shear strain in slip band. From equilibrium of wedge, factor of safety, F_s , is:

$$F_s = \frac{\sum R [C_m l + \{W \cos\alpha - k_h W \sin\alpha + T \sin(\alpha+\theta)\} \tan\phi_m]}{E [R W \sin\alpha + y.k_h W \cos\alpha - R T \cos(\alpha+\theta)]} \quad (2.4.40)$$

where C_m is mobilised cohesion, ϕ_m is mobilise angle of shear resistance, T is tension in the reinforcement, W is weight of the slice, θ is angle between the horizontal and the direction of the tension, α is angle between the horizontal and the tangent to the slip circle at the base of the slice under consideration, R is the radius of the circle, l is length of arc of base of the slice and k_h is coefficient of horizontal acceleration. The analysis is carried out for a given geometry and arrangement of reinforcement to obtain minimum F_s . Analysis is continued till desired F_s is obtained. Their result showed that F_s reduces sharply with increasing k_h for different slope angles of embankment which is reasonable.

In the above analysis, Koga et.al. (1986) have not indicated a method for determination of shear zone, AD. The thickness of shear zone depends on shear parameters and stress-strain characteristics of soil, load extension characteristics of reinforcement, the rotational movement of the rupture wedge etc. which will change from one set of conditions to another. As such, the evaluation of the thickness of shear zone is rather difficult. On the other hand, the tension in reinforcement, T , contributes significantly in improving the F_s given by Eq. 2.4.40 which in turn depends on the assumed thickness of shear zone. As such, in absence of a reliable method for estimating the thickness of shear zone, results of this analysis are of

questionable advantage. Besides, there is room for improving the analysis by accounting for inter slice forces. The contention of the authors that the F_s may be further improved by considering the confining effect of reinforcement at the sloping face of embankment is incorrect, because, the tension, T , already accounts for the same. There may be additional forces induced by the reinforcement to account, provided deformations within rupture wedge (excluding shear zone) are to be considered. Moreover, in Fig.2.4.16, y is indicated as the vertical distance between centre of rotation, O , and the centre of gravity (c.g.) of vertical slice whereas in deriving Eq.2.4.40 for F_s , y is treated as the radial distance between centre of rotation and c.g. of vertical slice. This discrepancy needs to be clarified.

Finite element method of analysis

Richardson and Lee (1975) analysed a R.E. test embankments, 304.8 mm (12 in) high and 914.4 mm (36 in) long using FEM analysis by employing QUAD-4 program modified to include elastic compression/tension bar elements to represent reinforcements. Sinusoidal excitation with 11.6 Hz had 0.1g single acceleration amplitude. Figure 2.4.19 shows maximum dynamic tie forces obtained by analysis by using Seed and Idriss damping data and by using modulus and damping obtained experimentally. It may be observed that values obtained by using experimental data are much larger. Based on these results, they have recommended design envelope for tie forces (Fig.2.4.19). These dynamic tie forces are reported to be in good agreement with tie forces obtained experimentally.

Richardson and Lee (1975) also analysed R.E. wall, 6.4 m (21 feet) tall using QUAD-4 programme cited above. A synthetic design accelorogram

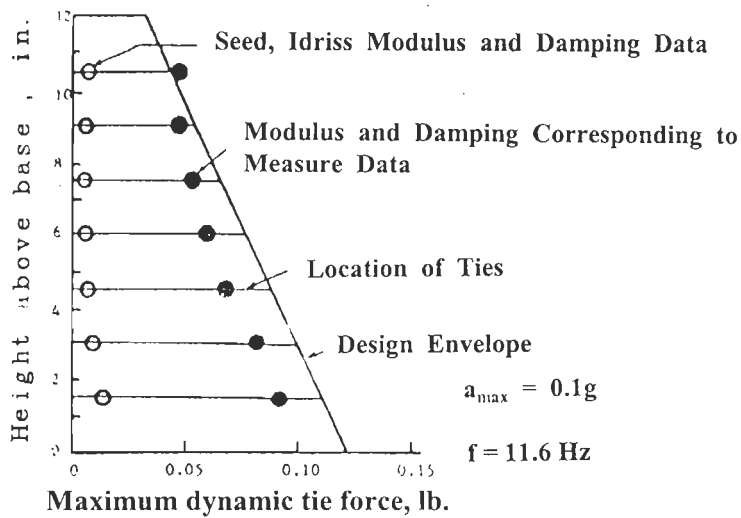
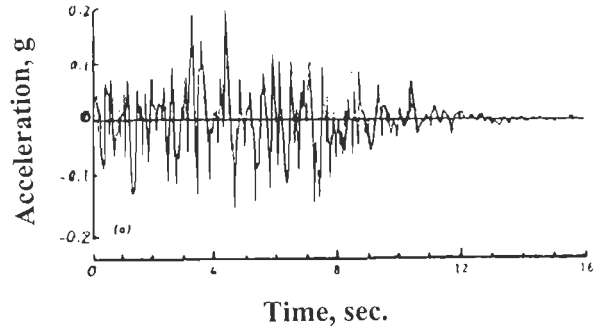


FIG. 2.4.20 EARTHQUAKE MOTION USED FOR DESIGN EXAMPLE (RICHARDSON AND LEE, 1975).

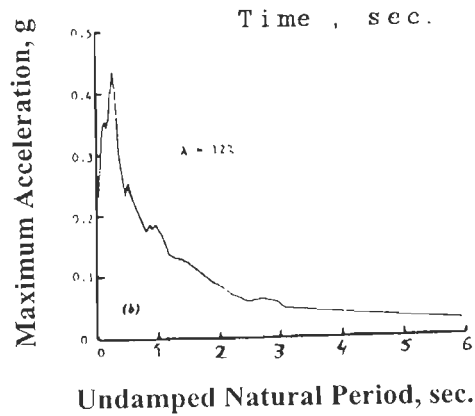
(Fig. 2.4.20a) was base excitation. Modified damping values recommended by Seed and Idriss (Fig.2.4.21) were employed. Tie forces computed are added to additional tie forces due to at rest earth pressures to get total earth forces. Two sets of results were obtained; one for fixed backfill and the other for free backfill. Based on results, the design envelope diagram for tie forces is given. Wall was also analysed by response spectrum method using acceleration response spectra (Fig. 2.4.20b). Backfill was represented by 10 lumped masses. Only first two modes were considered using modal participation factor, Γ_1 equal to 1.25 and Γ_2 equal to half. Therefore, design acceleration, A_{des} , is obtained as:

$$A_{des} = 1.25 S_{a1} + 0.5 S_{a2} \quad (2.4.41)$$

where S_{a1} and S_{a2} are spectral accelerations for the first and second modes. Based on results of the analysis, they recommend approximate empirical



(a) Accelerograph



(b) Acceleration Response Spectra

FIG. 2.4.20 EARTHQUAKE MOTION USED FOR DESIGN EXAMPLE (RICHARDSON AND LEE, 1975)

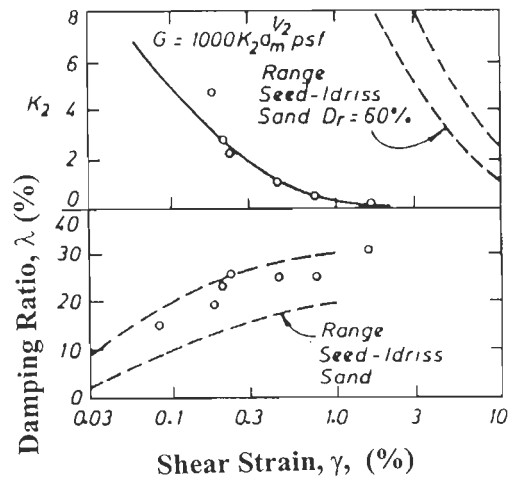


FIG. 2.4.21 DYNAMIC MODULUS AND DAMPING FROM SHAKING TABLE TESTS (RICHARDSON AND LEE, 1975).

values of periods of vibrations (in seconds) T_1 and T_2 for the first two modes which are given by:

$$T_1 = (0.006 - 0.001)H \quad (2.4.42)$$

$$T_2 = T_1/3 \quad (2.4.43)$$

where H is height of the backfill in feet. The expression for T_1 cited above appears to be in error and is probably given by:

$$T_1 = 0.006 - 0.001H \quad (2.4.44)$$

Richardson and Lee (1975) have also given a number of special design considerations cited below:

- (i) In addition to calculating tie forces, it is necessary to decide size, spacing and length of all ties with appropriate F_s .
- (ii) Skin element must be designed with allowance for corrosion. The foundation stability must also be checked.
- (iii) Ties and connections should be sufficiently strong to avoid tensile failure.
- (iv) If mild steel ties are used, F_s of 2 for yield strength seems appropriate which results into an additional hidden factor of safety of about 1.9 on ultimate strength.
- (v) Failure by tie pullout be prevented by providing sufficient horizontal surface area of ties. A factor of safety of 4 on coefficient of the peak soil-tie sliding friction is recommend.
- (vi) The effective length of ties be measured from an assumed rupture plane sloping at an angle of 60° with horizontal for static case. The actual failure plane for seismic case is a bit flatter and may lead to a little more actual deformation during earthquakes but will not lead to a catastrophic collapse.

(vii) Quantity of steel required for seismic design was twice the quantity required for static case. However, this leads to cost increase of only 5 to 10% of total cost of R.E. wall for the static case.

2.4.2 Dynamic experimental investigations

Uezawa and Nasu (1973) tested large scale R.E. embankment models, 1.5 m high, with 1:1.5 side slopes, mounted on shake table excited with sinusoidal vibrations at 7 Hz for a duration of 10 sec. at 0.1 g followed by another excitation for 2 sec. at 0.2g which in turn was followed by another shaking at 0.3g extending for a longer duration. In the first model, 3 layers of nets of nylon wire of 3.2 mm dia. were placed close to embankment base. In the second model, 12 layers of the same net were placed at uniform vertical intervals. In the third model, 7 reinforcement layers of Vinyl sheets extending upto full width of embankment but discontinuous at the middle, were employed (Fig. 2.4.22). From test results, they concluded that no catastrophic embankment failure took place. Settlements and deformations increased with duration of shaking.

Richardson and Lee (1975) carried out static/dynamic studies on R.E. embankments, 0.3m high and 0.76 m wide with vertical face. Mylar magnetic recording tapes were used as reinforcements. Eight thin aluminum strips, 37.5 mm high, were used as facing. Sinusoidal base excitations at 11.6 Hz with 0.05 to 0.5g single acceleration amplitude were used. Accelerations, displacements and strip forces were measured using strip chart recorders. In one of their tests with reinforcement fold back into the embankment with 11 layers, the embankment failed catastrophically with second and third reinforcements from the bottom end failing in tension near the facing.

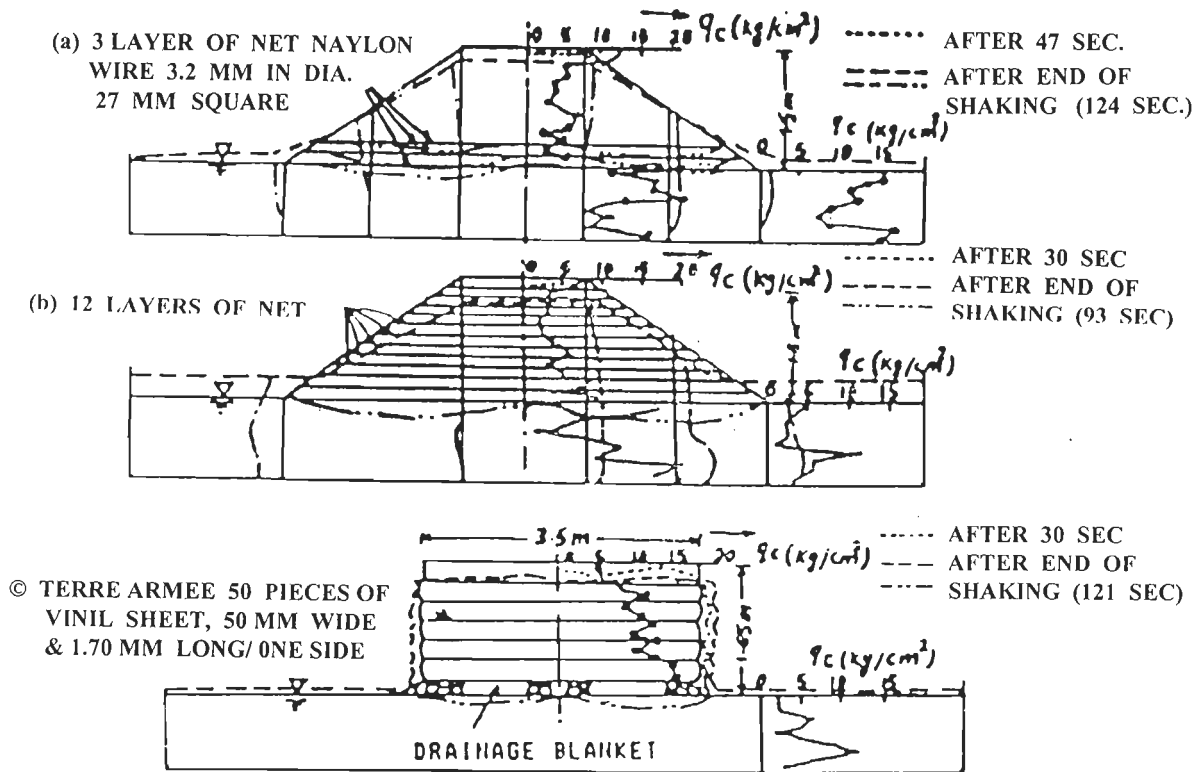


FIG. 2.4.22 RESULTS OF MODEL TESTS ON REINFORCED EMBANKMENT.
(UEZAWA AND NASU, 1973)

Before tension failure, the wall moved as if it was rotating about the base initially and then followed by gradual formation of bulge near the lower third point and then ultimately failed. They strongly recommend avoidance of tensile failure of reinforcements.

In another test, an embankment with 8 layers provided with facing elements hinged to adjacent elements was tested. The lowest facing element was hinged to base plate. Initially, the wall moved as if rotating about the base. This was followed by relatively larger outward displacement of top two layers and significant rotational outward displacement of the lowest facing element. After sometime, the lowest facing element rested flat on the shake table. Then onwards, the behaviour of the second facing element from the

bottom end was similar to that of the bottom most facing element. This clearly indicates that rotational moments acting on facing elements near the bottom end are significant. The embankment did not fail catastrophically, because, there was no tension failure. Figure 2.4.23 shows measured tie forces at various accelerations. It may be observed from these results that the tension in ties reduces after reaching the peak as we approach the base. This is due to relatively stiffer foundation (shake table plate form) of the model which offers greater resistance to outward movement of layers near the bottom. This is supported by test results of Fairless (1989) also. Based on this, a simplified version of earth pressure diagram (Fig. 2.4.1) recommended by them for the design of reinforcements.

Fairless (1989) commented that use of the earth pressure distribution diagram (Fig. 2.4.1) leads to conservative design of reinforcements. It may further be observed that, the design seismic coefficient, $E = 1.4 a/g$, is arbitrary and not valid for all base excitations and for all embankments with different heights and reinforcements. It is a function of the stiffness of the embankment. Besides, the shape of the earth pressure diagram (particularly for the portion of the diagram representing the dynamic increment) is quite arbitrary.

Richardson and Lee have also obtained frequency-response curves for R.E. embankment using experimental data (Fig. 2.4.24). As base excitation increases, the resonant frequency and magnification factors reduce and shear strain levels increase as expected. From one dimensional wave propagation theory, shear modulus, G , of homogeneous embankment of height, H , fundamental period T and mass density, ρ , is given by :

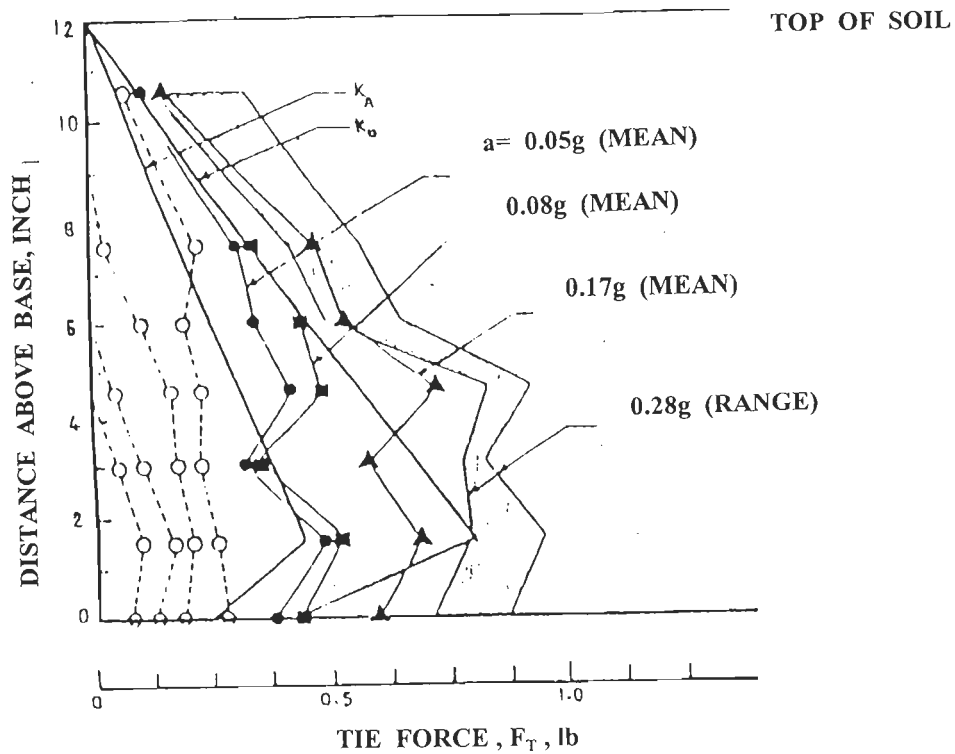


FIG. 2.4.23 MEASURED TIE FORCE FOR VARIOUS ACCELERATION (RICHARDSON AND LEE, 1975).

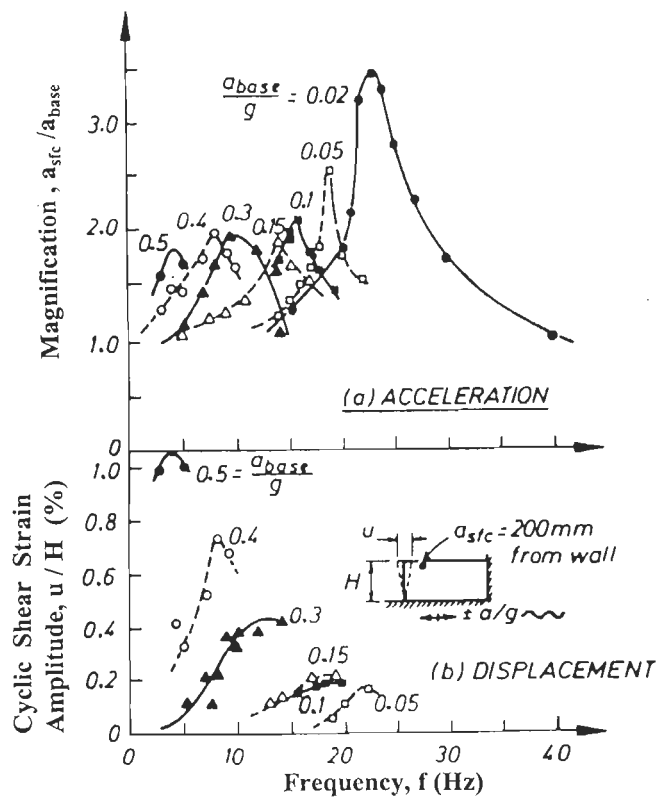


FIG. 2.4.24 RESONANCE RESPONSE OF MODEL REINFORCED EARTH (RICHARDSON AND LEE, 1975).

$$G = 16H^2 \rho/T^2 \quad (2.4.45)$$

Expression for G (expressed in psf) proposed by Seed and Idriss (1970) is :

$$G = 1000 K_2 (\sigma_{oct})^{1/2} \quad (2.4.46)$$

Using T, ρ and H obtained from tests on R.E. embankments, G obtained from Eq. 2.4.45 and k_2 for R.E. was evaluated using Eq. 2.4.46 which were lower than K_2 recommended by Seed and Idriss (1970) for plain sand (Fig. 2.4.21). This finding is unreasonable, because, K_2 of R.E. is expected to be larger than k_2 of plain sand. Richardson and Lee have not indicated whether additional confinement induced by reinforcements was accounted for in computing octahedral stress, σ_{oct} . Besides, they have not indicated value of σ_2 , considered in computation. Moreover, k_2 values as well as shear strains for $D_r=60\%$ reported by Seed and Idriss (1970) do not match with those cited in above figure and attributed to Seed and Idriss (1970). Richardson and Lee also computed critical damping ratio, λ , given by:

$$\lambda \approx 1/2M_f \quad (2.4.47)$$

where magnification factor, M_f , is ratio of response at the top of the embankment to the maximum response due to base excitation. Figure 2.4.25 shows variation of percentage damping ratio as a function of shear strain (Richardson et.al., 1977). It may be observed that with increasing shear strain the damping increases as expected.

Additional short comings of work reported by Richardson and Lee (1975) were given by Wood (1982) (as reported by Nagel, 1985) as cited below :

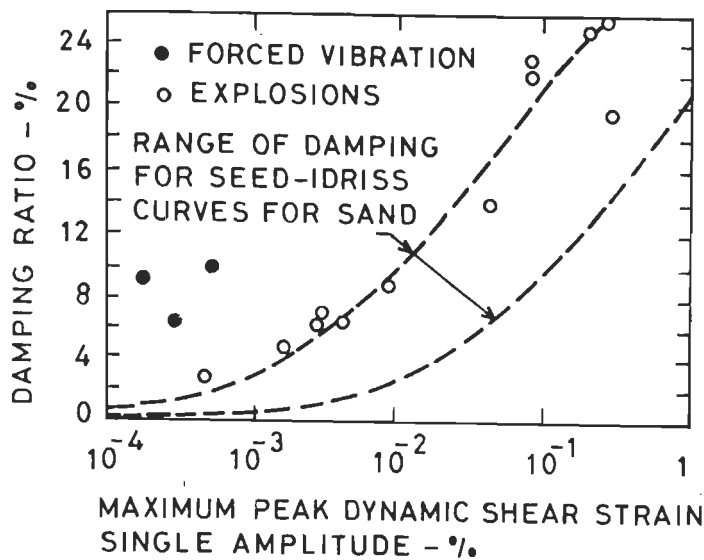


FIG. 2.4.25 DAMPING VALUES AND MAXIMUM DYNAMIC SHEAR STRAINS CALCULATED FROM THE BLAST AND FORCED VIBRATION TESTS (RICHARDSON, ET. AL., 1977).

- i) Mylar tape has low friction angle with sand and is not typical of actual reinforcements.
- ii) This low friction angle resulted into requirements of longer ties w.r.t. height which is not indicative of reinforcement length requirements of actual walls.
- iii) Only limited failure surface information reported.
- iv) Very limited information on wall displacement reported.

Wolfe et.al., (1978) tested 610 mm high R.E. walls with clean fine sand backfill at the same density, reinforced with 12.7 mm wide strips of fiber glass screen mesh (16 threads/inch) and also with mylar recording tape of same length and width. Mesh strips were more extensible and more like those used for commercial walls than mylar tapes. Horizontal and vertical spacing of strips/tapes was same for all walls. Base excitations were horizontal, vertical or combined horizontal/vertical. Sinusoidal excitations had $\pm 0.2g$

acceleration amplitude at 30Hz to 5Hz frequencies at 1 Hz decrements. Taft earthquake vibrations (1952) scaled to 0.5g horizontal and 0.35g vertical at a time scale factor of $\sqrt{6}$ (approximately equal to 2.5) were also used as base excitation. They measured some horizontal response of the embankment eventhough excitation was only in the vertical direction. Similarly, vertical response was measured even when base excitation was only horizontal. For combined horizontal and vertical excitation, the system responded primarily to horizontal excitation and forces in strips for such cases were slightly higher than those obtained with horizontal component only of same excitation. Vertical harmonic excitations showed some influence only for the first mode. Larger earthquake excitations showed much less influence from vertical excitation than the lower level vertical harmonic vibrations. Hence, they recommend to ignore vertical components of ground excitation in design.

Rea and Wolfe, (1980) carriedout shake table experiments on walls, 305 mm, 457 mm and 610 mm high, with mylar tapes as strip reinforcements. Plexiglass facing panels were 6mm thick, 76 mm wide and 762 mm long. Horizontal spacing of strips was 152 mm at mid height of panels and 305 mm at top and bottom levels of panels. Vertical spacing of strips alternated between 38 mm and 76 mm. For different tests only length of strips was varied from 305 to 762 mm. The minimum length was 168 mm ($F_s=1$) and actual safety factor, F_s , varied from 1.8 to 4.5 for static case. N-E component of Taft earthquake (1952) with time scale factor of 2 and with sub-4 Hz frequencies filtered out was used as base excitation. The low strain first mode fundamental frequency, f_1 , was 24 Hz. Accelerations and displacements were measured at the embankment top. Displacements were relative to the

base. Maximum input base excitation was 0.9g. Magnification factor, M_f , obtained for different accelerations (Fig. 2.4.26) show that M_f reduces with increasing acceleration as expected provided excitation is not at resonance. The M_f falls below unity for inward table acceleration at about 0.5g acceleration whereas it is never below unity even at 0.8g outward table acceleration (passive case) which is reasonable. Their test results also

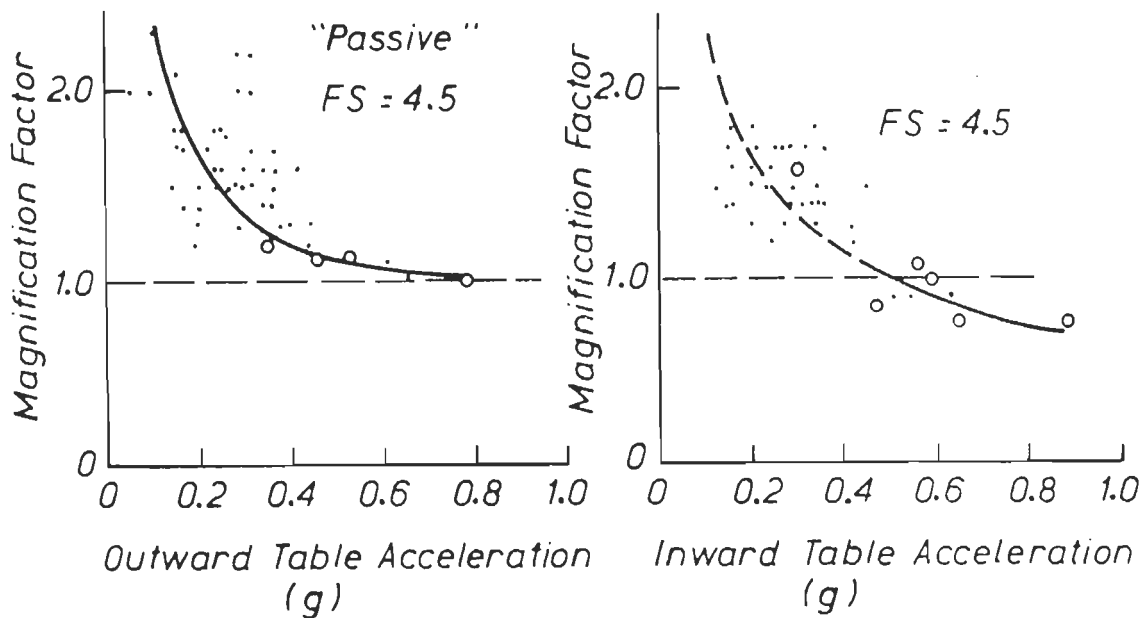


FIG.2.4.26 MAGNIFICATION FACTOR FOR ACCELERATION PULSES (REA AND WOLFE, 1980).

indicate that yield acceleration is affected by F_s used and increases with increasing F_s which is also reasonable (Fig. 2.4.27). The permanent displacement expressed as a percentage of wall height increases with increasing peak inward acceleration for any value of F_s used (Fig. 2.4.28).

Richardson et.al. (1977) tested a number of R.E. walls using blast type of loading from one point. The wall at UCLA, 6.08 m (20 feet) tall, was

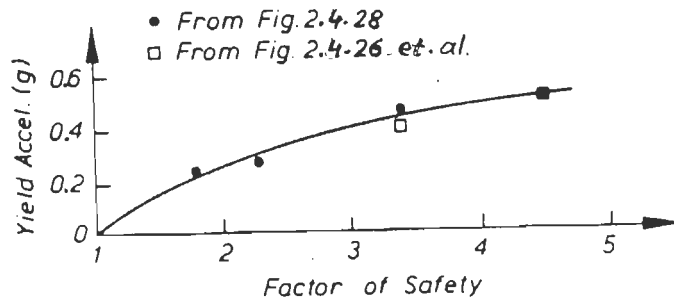


FIG. 2.4.27 EFFECT OF FACTOR OF SAFETY ON YIELD ACCELERATIONS (REA AND WOLFE, 1980).

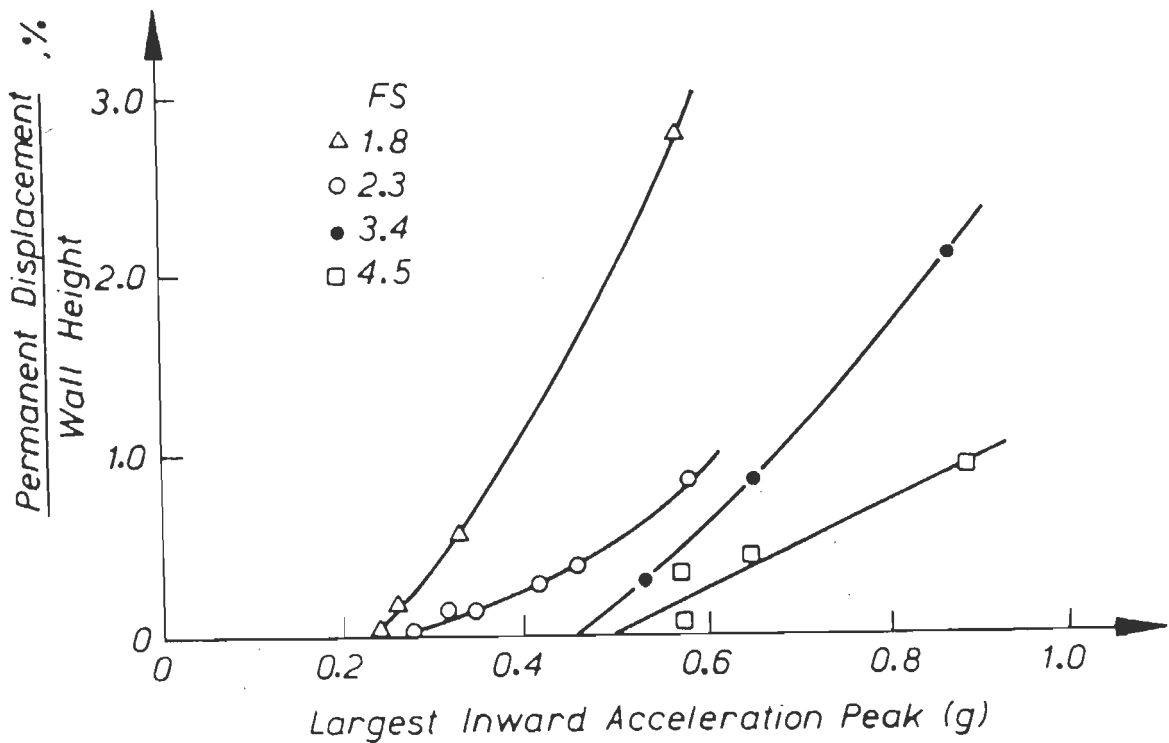


FIG. 2.4.28 EFFECT OF ACCELERATION INTENSITY ON PERMANENT DISPLACEMENTS (REA AND WOLFE, 1980).

designed for the design envelope for maximum seismic earth pressure recommend by Richardson and Lee (1975). Acceleration of 1.46g at the toe (and 1.52 g at wall top in the same blast) was the largest measured. It was essentially a single cycle with vibration period < 0.1 sec. This shock also caused the largest displacement (95 mm) of wall facing at a distance of 1.9 m below the embankment top. The wall after all tests developed an outward accumulated tilt of 5.5% of wall height giving a displacement of 210 mm at 1.9 m below top. They are silent about displacements at the base.

Measured first and second natural frequencies for different R.E. walls and based on many frequency-response curves obtained from tests agree reasonably with corresponding values obtained by using empirical Eq. 2.4.1 and 2.4.2 proposed by them (Fig. 2.4.29).

Peak values of single amplitude of percentage dynamic shear strain varies nonlinearly with first mode frequency, f_1 , for plain strain case (Fig. 2.4.30). Besides, data obtained from forced vibration tests and from explosion tests fit well into the curve given by Seed and Idriss (1970) for relative density, D_r , of 65% and for $f_1 = (V_s/4H)$ where V_s is shear wave velocity. Therefore, it is reasonable to consider that $f_1 = (V_s/4H)$. This was also supported by tests on small R.E. walls (Richardson and Lee, 1975). Variation of peak values of single amplitude of percentage dynamic shear strain with percentage damping ratio obtained from force vibration and blast testing does not fit well with that obtained by Seed and Idriss (1970) for sands (Fig. 2.4.25), particularly for forced vibration test data. It appears that material damping dominates in studies of Seed and Idriss (1970) whereas geometric damping (radiational damping) dominates in studies of Richardson and Lee (1975) and Richardson et.al. (1977).

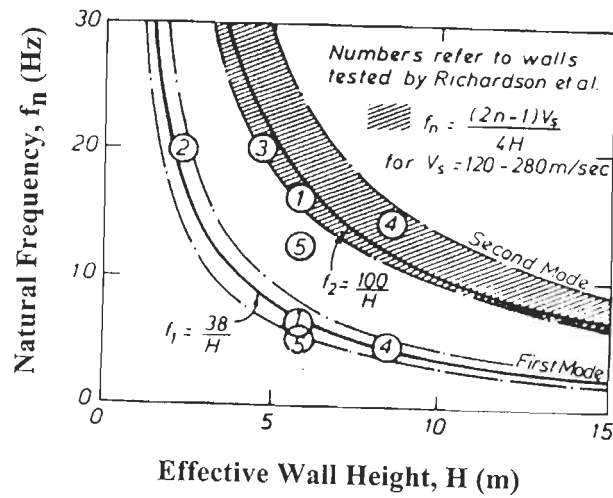


FIG. 2.4.29 MEASURED AND CALCULATED FIRST AND SECOND MODE NATURAL FREQUENCIES FOR DIFFERENT HEIGHTS OF R. E. WALLS (RICHARDSON ET. AL., 1977).

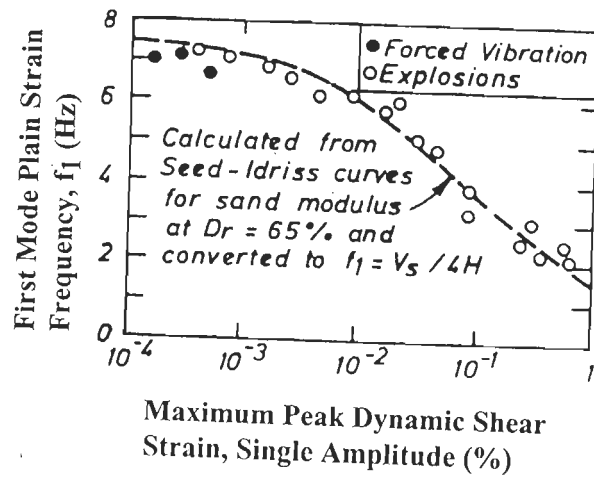


FIG. 2.4.30 FIELD MEASURED DYNAMIC PROPERTIES OF BACKFILL SOIL AT UCLA TEST WALL COMPARED WITH PUBLISHED DATA (RICHARDSON ET.AL., 1977)

No catastrophic failure of any wall occurred in this study. Even walls not designed to withstand seismic forces, withstood them but moved outward by about 5% of the wall height near top end. As such, they observed that walls designed for static loads only have reasonable capacity to withstand seismic forces also. They also observed that tie forces and deformations are related to seismic load intensity, wall geometry and placement of reinforcements. Shorter ties may lead to larger outward wall displacements and seismic forces on R.E. zone. On the other hand, use of longer ties results into shorter wall displacements smaller seismic forces.

Iwaski and Watanabe (1978) reported that R.E. embankment of $H=3$ m and width of 5 m, suffered no residual deformation after experiencing Tokachioki earthquake of 1968 though they did not report accelerations induced. However, computed accelerations using attenuation laws proposed by Donovan (1973), Orphal and Lahond (1974) and by McGuire (1977) are low and range from 7 to 10 gals. Hence, embankment with reinforcements $1.16H$ long is likely to behave in elastic domain for such low excitations. Embankment vibrated by mechanical oscillator mounted on top showed resonant frequency in 17 to 20 Hz range associated with 200 gals amplitudes at top which was nearly twice the amplitude of 110 gals at base. Maximum dynamic displacement (5.2 mm) observed was 0.173 % of H , which is less than about 0.5% of H required to reach active state. Hence, earth pressures closer to at rest pressures occurred during tests. It is further supported by occurrence of no residual displacements (i.e. behaviour in elastic domain only). Reasons for using $1.16 H$ long reinforcements for dynamic case compared to $0.8 H$ long ones needed for static design was not explained.

Iwasaki and Wantabe (1978) also studied safety factor, F_s , obtained from tests and compared them with F_s computed by using the relationship :

$$F_s = (R_s + R_w)/(E_a + E_w) \quad (2.4.48)$$

where R_s and R_w denote withdrawal resistance of strips due to weight of fill material and the load on the embankment (surcharge) respectively, E_w is earth pressure due to load on embankment and E_a is active earth force by Coulomb. Computed and test results are reported to agree reasonably. Reinforcement has maximum effect on F_s when it runs normal to Rankine active rupture surface (Fig. 2.4.31). This makes contribution of resisting moment of reinforcements for a given tension maximised, when wall tends to rotate about base. However, use of inclined reinforcements is precluded by practical difficulties associated with their construction.

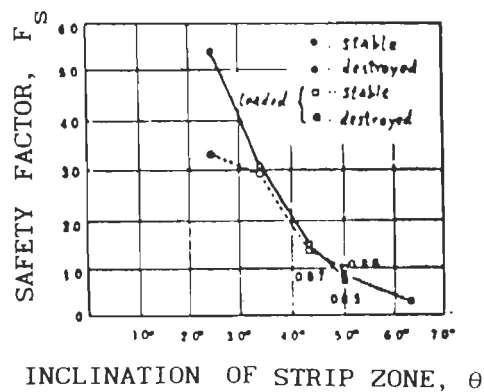


FIG.2.4.31 RELATION OF SAFETY FACTOR, F_s , WITH INCLINATION OF STRIP ZONE, θ (IWASKI AND WATNABE), 1978).

Fang (1978) tested sand embankments reinforced with bamboo mats/strips treated with sulphur compounds placed in the form of vertical curtains or horizontal mats extending from sloping surface into the embankments. They

were subjected to sinusoidal base excitations of 2, 3 and 7 gals using a shake table. Time to reach failure defined by a specific deformation was considered as a performance parameter which decreases with increasing level of excitation as expected. He also reported that the time for failure for a given excitation level is more for a reinforced embankment compared to that for unreinforced embankment which is also reasonable.

Fang (1978) also obtained theoretical potential failure planes by using conventional limit equilibrium methods. He worked out length of bamboo reinforcements either in vertical or horizontal direction extending slightly beyond failure surfaces to penetrate into the soil mass behind R.E. zone. However, length of reinforcements computed in this way are shorter than those predicted by conventional theories even for static conditions for three of the cases he investigated. For the fourth case, computed reinforcement length was in excess of that predicated by conventional methods. It is clear from this discussion that it is not possible to work out reinforcement length effectively. However, even if reinforcements extend marginally beyond rupture surface into the fill behind R.E. zone, time to reach failure for R.E. embankments is substantially higher than that for plain embankments. This is due to significantly enhanced rupture wedge rigidity. Moreover, marginal penetration of reinforcement beyond the critical failure surface shifts failure surface to a position away from critical surface of failure which increases resistance to slope failure.

Sommers and Wolfe (1984) tested R.E. embankments similar to those of Rea and Wolfe (1980). Input base excitation was N21-E component of Taft (1952) and N-S component of EL-Centro (1940) earthquakes, both scaled to

different time scale factors and with two bands of limited white noise. Accelerations and displacements at base and top were monitored during tests. They pointed out that Richards and Elms (1979) ignored amplification of motion in backfill which is incorrect. Amplification factor of the order of 3 or more are possible. Richards and Elms assumed no passive fill in their analysis which is a hypothetical case whereas passive displacements were observed by Sommers and Wolfe (1984) during tests. Wall displacements at top depended on type of input motion, level of base excitation and minimum yield acceleration level needed to induce permanent displacements. Yield acceleration was relatively insensitive to frequency and type of base excitation. It could be determined from F_s proposed by Rea and Wolfe (1980). They concluded that allowable deformation criteria were appropriate for R.E. walls design. They also pointed out that F_s , peak base excitation and ratio of fundamental frequency of wall to predominate frequency of base excitation proposed by Rea and Wolfe (1980) are important. However, different motions induced different responses even with same values of peak acceleration, F_s and frequency ratio.

For base excitations with frequencies smaller than fundamental frequency of embankment, similar response was seen for each excitation level. When input frequencies were similar to wall frequency, displacement of wall was greatly influenced by specific motion. There is no information, however, given about magnification factors at or near resonance and how they changed with changing frequency of excitation.

Nagel (1985) tested seven embankments, 320 mm high and 810 mm long, using 6 mm wide satin ribbon for reinforcements and 8 vertical facing

elements of aluminum panels(40 mm high and 0.45 mm thick) numbered serially from bottom to top end. Accelerations were measured at top, middle and base of embankment. Displacements relative to base were measured at centers of panels 1 and 8 . Tie forces were measured at all panels at their respective central tie. Sides of embankment were provided with glass sheets for clear visibility of failure surfaces which was recorded photographically.

Failure surface formation initiated from base and progressed with continuing shaking to reach the ground surface eventually. Rupture surfaces were linear when situated totally within R.E. zone and were bilinear when the surface was partly within R.E. zone and partly within plain sand behind (Fig.2.4.32). Angle of rupture surface with horizontal within R.E. zone was smaller than that given by Mononobe-Okabe for plain sand and was affected by length, vertical/horizontal reinforcement spacings and particularly the length. Recorded accelerations at top clearly indicate acceleration levels reaching fairly constant values when yield displacement was initiated (Fig. 2.4.33). This supports yield acceleration concept of Newark (1965).

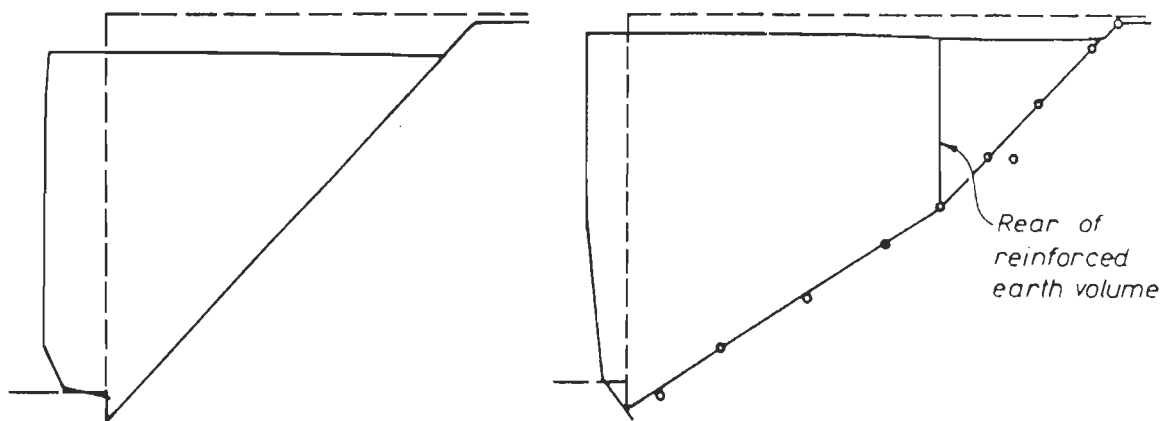


FIG. 2. 4. 32 WALLS AFTER FAILURE (NAGEL, 1985).

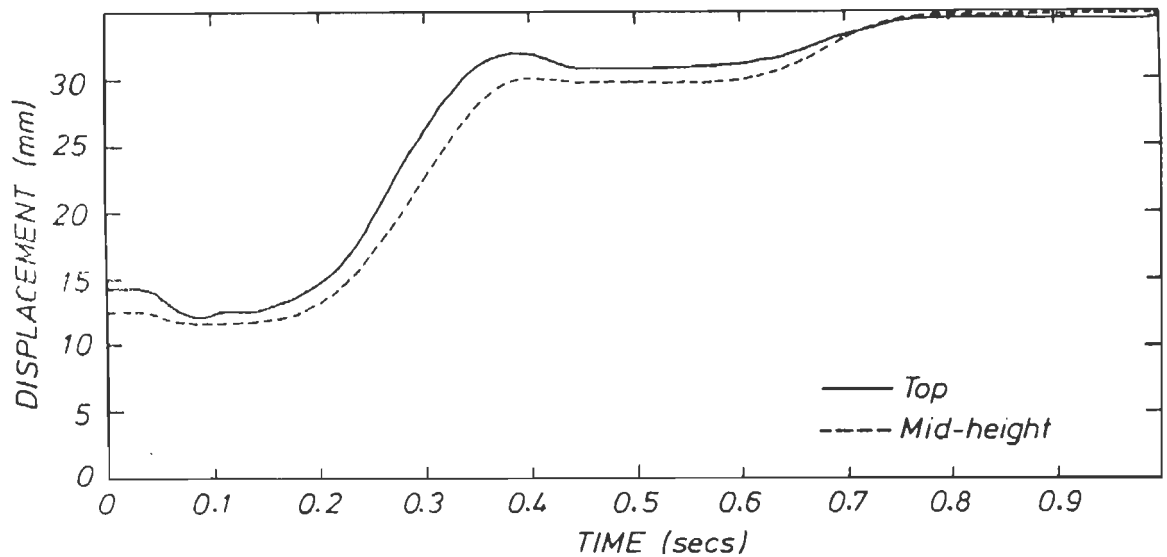
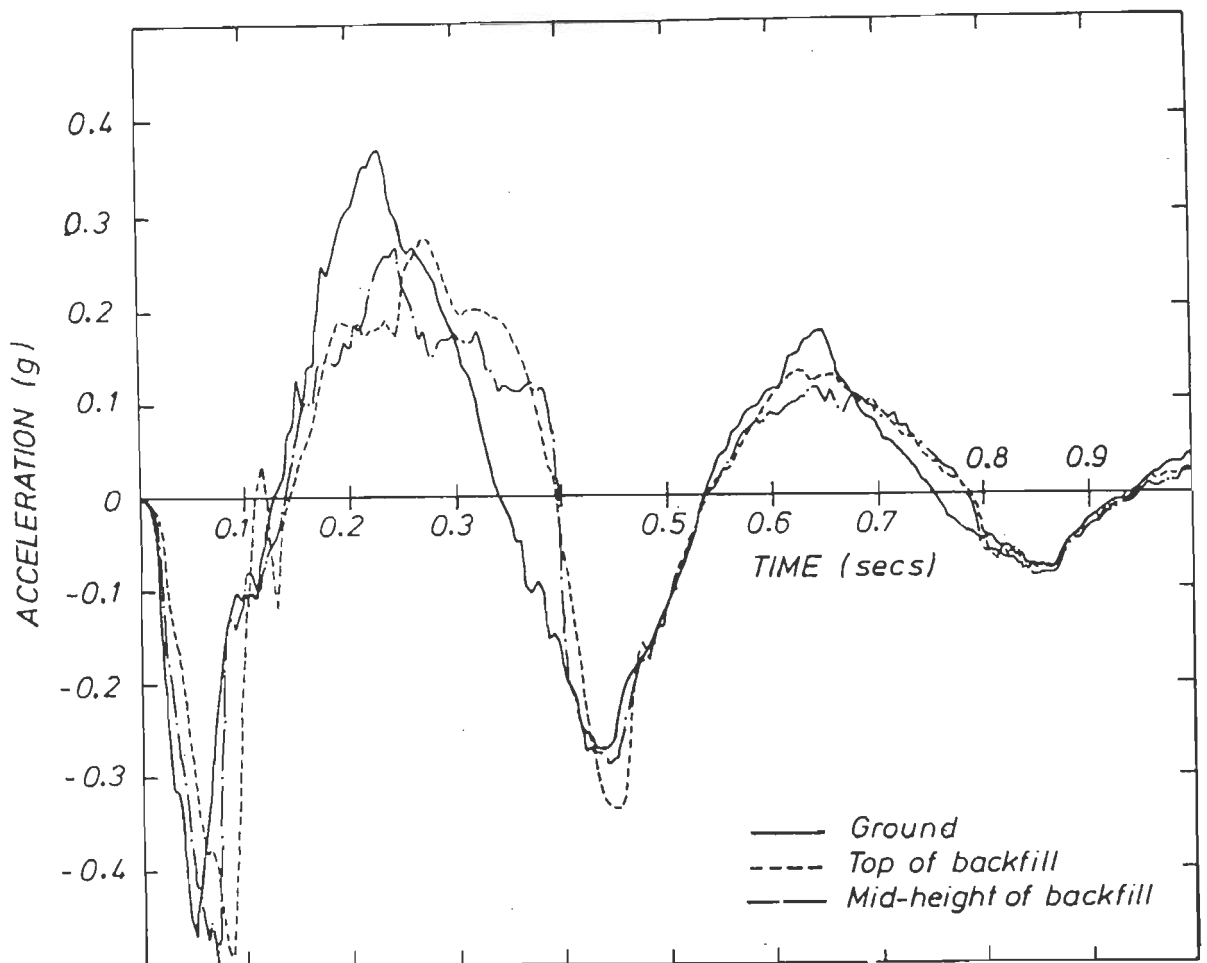


FIG. 2.4.33 TYPICAL ACCELERATION AND DISPLACEMENT TIME HISTORIES LATE IN TEST (NAGEL, 1985).

As yield displacement builds up, wall begins to bulge outward with bottom most facing element experiencing significant rotational displacement and eventually making that element rest flat on shake table. Plastic displacement of the order of 10% of wall height were allowed to occur which were associated with significant settlement of rupture wedge (Fig. 2.4.32).

Koga et.al. (1986) tested a small R.E. embankment subjected to horizontal sinusoidal loading using a shaking table. They studied many test parameters like length of reinforcements, number of reinforced layers, slope of the face and different reinforcing materials. Their results showed an important finding that R.E. embankment acted as one block and resisted earth pressure like a gravity retaining wall. This shows that pressure in R.E. area is distributed uniformly. When driving force exceeds resistance force of R.E. section, the whole block moves together. This favours checking external equilibrium of R.E. zone in usual way by considering sliding along the base and bearing pressures at the base.

Koga et.al. (1988) initially constructed plain sand embankments, 1 m high, with gentle slopes on shake table. Reinforced shoulder fills were added on sides to produce R.E. embankments with steeper slopes. Different side slopes and intensities of reinforcements were employed. Sand bags were used as facing elements. In certain cases, horizontal reinforcements were nailed to plain earth embankment using 150 mm deep nails and anchored to steel bar penetrating 300 mm deep into the plain earth. Settlements were measured at top end. Reinforcements were in the form of nonwoven fabrics and plastic nets. Plain sand and R.E. embankments were subjected to sinusoidal accelerations ranging from 100 to 800 gals with frequency of 4 Hz for a

duration of 10 sec. They reported that settlements of plain sand embankment were larger than those of R.E. embankments. Settlements decrease with increasing degree of reinforcement. Nailing and anchoring of reinforcements increased their effectiveness and improved performance. However, no explanation was given in support of it. It appears that passive resistance offered by plain earth to rotation of nails and anchors resulted into restricted lateral movement of reinforcements to compel them to perform in tension instead of in pullout. Reinforcements perform better in tension and, hence, help to restrict lateral embankment displacements which is desirable. In case reinforcements are to perform in tension only, their failure in tension should be precluded with adequate safety margin.

Nakamura et.al. (1988) studied R.E. embankments of height, $H=5$ m, with different facing elements. Fabric folded back into the fill, gabions with reinforced shotcrete facing and precast R.C. slabs were facing elements used. These embankments experienced an earthquake in 1987 with peak ground acceleration of 0.33 g. Deformation at the embankment top was about 1% of H for facing with folded back geotextile. This was much higher than that of 0.127% of H for embankment with facing of gabions with R.C. shotcrete finish and 0.145% of H for embankment of precast R.C. panel facing. As such, the latter two types of facing elements with adequate stiffness to redistribute earth pressures lead to much better performance compared to more flexible facing with fold back geotextile.

In this investigation, it appears embankment were provided with gabions of 0.5 m width which contributed about 12.5% of the total bearing capacity of R.E. wall. This is insignificant in view of the short gabion width. So,

for embankments of $H \geq 3$ m, contribution of bearing capacity by 0.5 m wide gabions is negligible. Use of wider gabions compared to H is advantageous as they contribute significantly larger bearing capacity.

Fairless (1989) carried out extensive experimental studies on R.E. embankments of height, $H=1$ m, using a shake table. Sinusoidal as well as N-S component of El Centro earthquake of 1940 were used as base excitations. Aluminum strips, 0.45 mm thick and 10 mm wide, were used as reinforcements with lengths varying from $0.5 H$ to $1 H$ which were placed at vertical interval 100 mm and horizontal spacing ranging from 250 mm to 330 mm. Transverse embankment sides were provided with transparent glass sheets to photograph failure surfaces. Displacements and accelerations were measured at top and mid-height of embankments constructed with 10 layers of 100 mm thickness each. Forces were measured in each strip at several points along length. Earth pressures also were measured at each facing element.

He observed rupture surface initiating at some point on facing near base and progressing towards top end as shaking continued. The surface was planar when located totally within R.E. zone and bilinear when partly within R.E. zone and partly in plain sand behind. Its orientation, θ_1 , with horizontal within R.E. zone was smaller than that for Coulomb/ Mononobe-Okabe rupture surfaces for plain sand under static/dynamic cases. With increasing degree of reinforcement, θ_1 decreases. Length of reinforcements was more effective in decreasing θ_1 than their vertical/ horizontal spacing which is expected. However, they could neither predict successfully θ_1 as a function of degree of reinforcement, embankment geometry, properties of backfill material, types of facing elements and peak excitation employed nor

explain why θ_1 decreases with increasing degree of reinforcement. It appears that this is due to resistance of R.E. for near vertical propagation of rupture surfaces due to ability of R.E. to force rupture surface to flatter orientations. This is also supported by study of propagation of vertical cracks in material with horizontal reinforcements (Rao and Raju, 1990).

Magnification factor (M_p) for accelerations is about 3 at top and about 2 at mid height. Outward displacement appeared to predominate compared to rotation about base. Accelerations were larger initially and as rupture wedge displacement increased to reach its maximum value, the yield acceleration reduced to reach the minimum value. Recorded displacements indicated that wall basically moved outward in translation with relatively small rotation and with some bulge near mid height. Large displacements of about 0.1 H indicated possibility of precluding catastrophic failure if tensile failure is avoided. Definition of displacement dependent failure of R.E. embankments is, therefore, more logical in earthquake engineering. Wall deformation is very severe where rupture surface meets facing near the base where high localised strain occur. The rupture wedge behaves nearly like a rigid body. The thickness of rupture zone along the rupture surface is rather thin. When inertia of the rupture wedge acts in outward direction, the wedge moves with greater ease because of near absence of resisting passive fill. When such inertia is directed towards the fill, full passive resistance over the entire embankment height resists wall movements to negligibly small values and leads to intermittent movement of the wedge. This is expected and reported by many others (Nagel, 1985).

For first load pulse, wall moved out at the base inducing maximum force in the lowest tie. At this juncture, failure surface got initiated. Then

onwards, this tie experienced no additional force, because, it was situated below rupture wedge. Most severe lateral strain occurred near lower end of wedge (covering 2nd and 3rd strips) leading to higher mobilisation of pullout resistance for these strips. Very high vertical overburden stresses acting at these strips induced high lateral earth pressures leading to high pullout resistance also as indicated by large forces measured for these ties (Fig. 2.4.34). With increasing distance from base, mobilised pullout resistance reduces due to reducing vertical stress indicated by decreasing measured tie forces as expected (Fig.2.4.34).

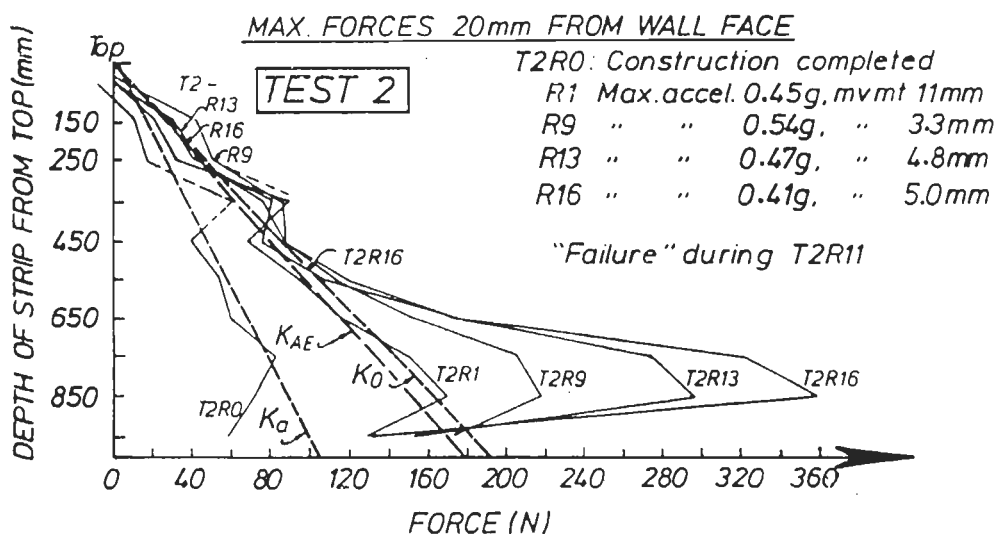


FIG. 2.4.34 MAXIMUM FORCES ADJACENT TO THE WALL FACING, TEST-2 (FAIRLESS, 1989)

Recorded tie forces increase with depth below top and then reduce to form a neck and then again increase near the base. Mononobe-Okabe and Coulomb's theory fail to predict earth pressure distributions. However, static/dynamic earth pressure distribution may be obtained using method of Joshi and Parajupati (1982), further modified by Parasad (1989) for active case and by Pandey (1995) for at rest case with due regard to failure wedge

deformation and its variation along height of wedge. They successfully predicted formation of neck in pressure distribution near top end. For ties with uniform length, tie forces reach a maximum value and then decrease as we approach base due to increase in resistance due to sliding mobilised. It is also affected by structure- foundation interaction.

Measured tie forces for R.E. wall and forces computed using Coulomb static active coefficient, Jaky at rest coefficient and Mononobe-Okabe Dynamic coefficient of earth pressures for ties are shown in Fig. 2.4.34. Tie forces computed by using earth pressure coefficients are much smaller than those measured experimentally.

Size of rupture wedge situated within R.E. zone or passing through R.E. zone is larger than that for plain earth behind a gravity wall of same height. Hence for same acceleration, the wedge of R.E. generates larger inertia forces resulting into larger earth pressures. It is obvious that a much larger force is required to push a given weight of rupture wedge when wedge is sitting on a flatter slope of rupture surface than the force required to push same weight of the rupture wedge sitting on a steeper slope of rupture surface. Because of these two reasons, a much larger dynamic force is exerted by the rupture wedge of a reinforced wall when compared with that by the wedge of plain earth. This explanation has not been clearly brought out by Fairless (1989) and many other investigators.

For stepped wall (Fig. 2.4.35), stiffness of lower part of R.E. with shorter reinforcements is less than what it would be if all reinforcements were as long as those in upper portion. This leads to smaller pullout resistance mobilisation in ties in lower R.E. zone and a relatively larger

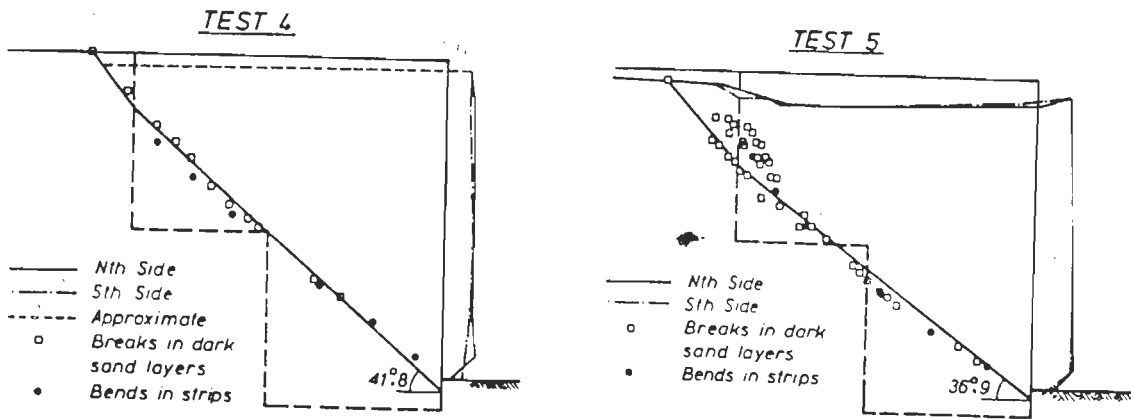


FIG. 2.4.35 FAILURE GEOMETRIES, TEST 4 AND 5 (FAIRLESS, 1989).

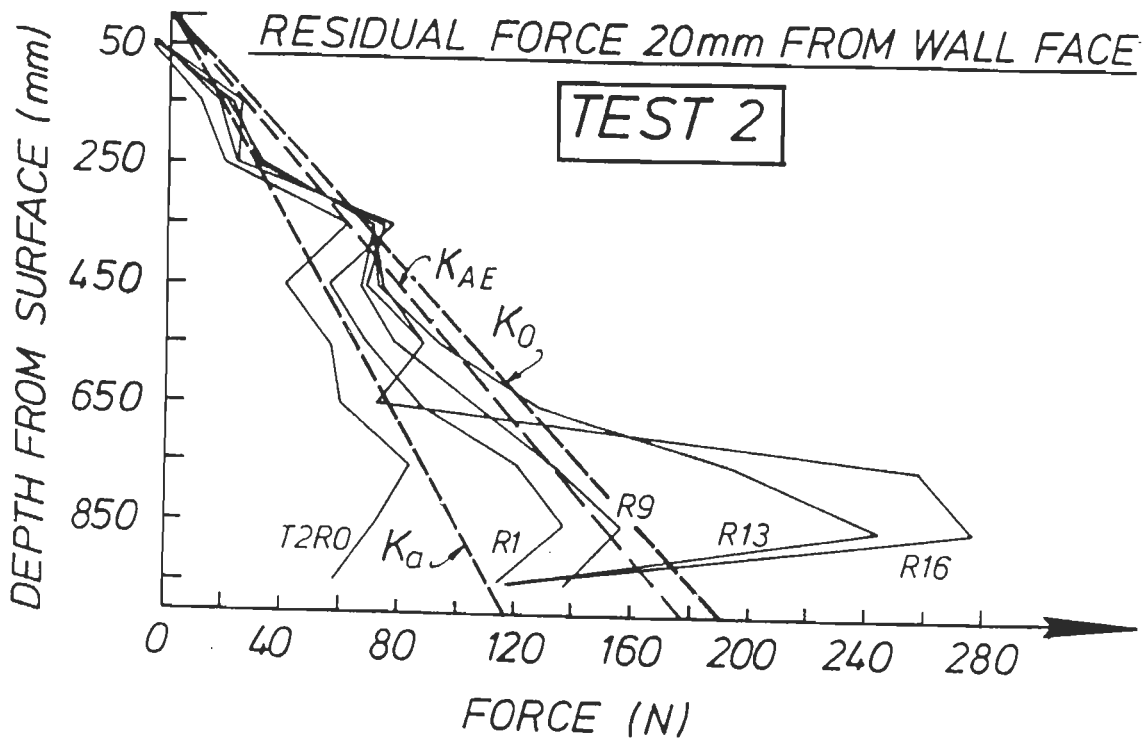


FIG. 2.4.36 DISTRIBUTION OF RESIDUAL (END OF RUN) FORCES AT THE WALL FACING, TEST 2 (FAIRLESS, 1989).

mobilisation of resisting force in fill behind R.E. zone. This appears to be responsible for smaller measured tie forces in lower portion. Fairless observed no change in rupture surface orientation in R.E. zone (Fig. 2.4.35) at the steeped portion but gave no supporting explanation.

Recorded residual tie forces are smaller but form a significant percentage of peak dynamic tie forces (Fig. 2.4.36) indicating that a major portion of dynamic strains induced during the loading gets locked up in the form of large residual stresses and residual tie forces. Residual forces are much larger than those attributable to initial at rest tie forces due to initial at rest earth pressures. This is contrary to statement of Richardson (1978) that strip forces return to pre-earthquake static levels at end of shaking. Pattern of residual forces variation is similar to that for recorded dynamic peak strip forces. Maximum tension along ties occurs close to facing for lower ties where rupture surface meets ties. With increasing distance of tie from base, point of maximum tension gradually moves away from facing upto embankment mid height. For all ties in upper portion, distance from facing to point of maximum tension is roughly the same and is larger than the corresponding distance for static case. This is due to larger width of dynamic rupture wedge and correspondingly large deformations of rupture wedge in the upper portion of R.E. compared to that for static wedge. It is desirable to account for this factor in study of point of maximum tension which was not done by Fairless (1989).

Fairless (1989) did study resonance of R.E. embankments as he used a single excitation frequency of 3 Hz, which is an important shortcoming.

Chakrabarty (1989) tested R.E. walls of height $H=650$ mm on shake table using sinusoidal excitation single amplitude accelerations of 0.125 to 0.25 g with frequencies of 5 to 10 Hz. Fine sand at $\gamma_d=1.81$ t/m³ corresponding to relative density, $D_r=80\%$. Steel plate, 16 mm thick, as wide as test tank and secured at top end to sides of tank was the continuous facing element not connected to reinforcements (bamboo strips and aluminium strips, 3 mm thick and 25 mm wide and 0.6 m long). Test were also carried out with plain sand fill. Static and dynamic earth pressures were measured at 5 points along wall height. Results indicated that largest static and dynamic earth pressures occurred at a depth of about $H/3$ from top for bamboo and aluminium reinforcements. The corresponding distance was $0.54 H$ from top for plain earth fill.

Chakrabarty (1989) did not give displacements of facing element. About 25% of the displacement of wall required to reach active state at mid height where facing element undergoes maximum displacement due to beam action. Besides, he does not specify displacements for assumed at rest conditions. As such, it is difficult to critically review his results. His observation of peak dynamic at rest pressure acting at a distance of $0.38H$ from the top end is not supported by results of any other investigation. Moreover, advantage of continuous facing element was not fully utilized because it was not connected to reinforcements.

Murata et.al. (1992) tested on shake table R.E. wall of height $H=1$ m with geogrid as reinforcement connected to rigid continuous and to discrete facing elements. Geogrids were of $0.4 H$ and $0.6 H$ length. Wall performance was expressed in terms of displacement measured at 100 mm below wall top. At

about 0.4 to 0.45 g excitation, walls failed by a displacement $> 0.1H$. Longer geogrid lead to better stability and a continuous rigid facing element resulted into to smaller outward wall displacement compared to displacements with discontinuous facing element, as expected.

Tatsouka (1992) reported results of tests carried out by Koga et.al., 1992 (Original paper in Japanese). Test embankments had clay core flanked by sandy shells. Plain earth embankment with gabion facing and embankments with reinforcements connected to gabions were tested on shake table. Settlement of R.E. embankment at top of the shoulder was less than that for plain earth embankment, as expected.

Sakaguchi et.al. (1992) tested sand embankment of height $H=1.5$ m on shake table to study effect of weight of facing elements which were light weight rectangular blocks of expanded polystyrene foam/other synthetic materials as well as sand bags. Geogrid and geotextile reinforcements were $0.8 H$ long. Outward displacement at top was smaller for embankment with lighter facing compared to that for embankment with heavier facing. Scholsser (1995) also agrees with this. Accelerations amplification along length/height of embankment indicated acceleration amplification increase with increasing distance from base as expected and supported by many others (Fairless, 1989). Acceleration increases with distance from centre towards facing at any level under consideration. This is also expected as confining effect is much smaller near the facing in comparison with interior points.

2.5 PULLOUT RESISTANCE OF REINFORCEMENTS

Static/dynamic design and performance of R.E. are critically influenced by pullout resistance of reinforcements. However pullout resistance is

difficult to determine by laboratory/field investigations as many parameters influencing it are difficult to control or to assess. Many methods proposed for its determination are critically reviewed here.

Figure 2.5.1 shows a reinforcement of length, L_r , under effective normal soil pressure, σ_v , and subjected to a static pullout force, P_s ,

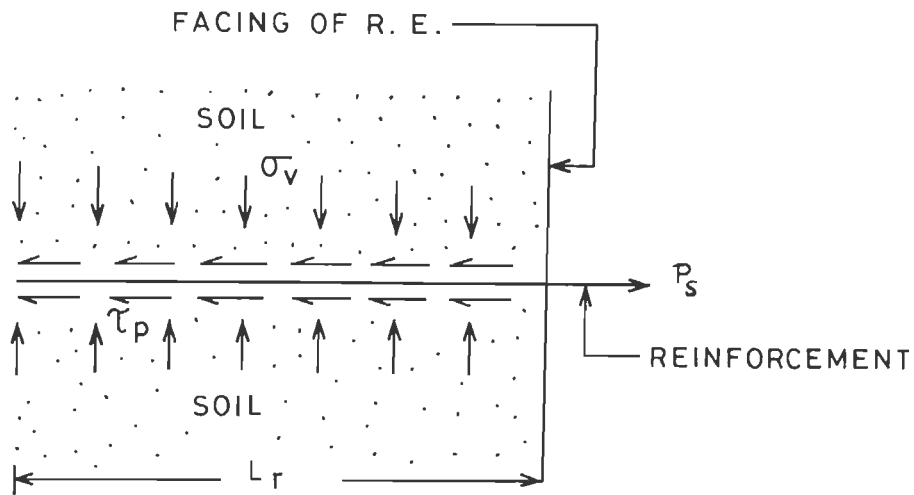


FIG. 2.5.1 PULLOUT RESISTANCE OF REINFORCEMENT

resisted by stresses along the soil-reinforcement interface giving rise to the resultant resisting pullout force, P_r , which is equal and opposite to P_s . From static equilibrium conditions, coefficient of average pullout resistance, μ_{avs} , is given by:

$$\mu_{avs} = P_s / (2b_r L_r \sigma_v) \quad (2.5.1)$$

where b_r is reinforcement width. Pullout resistance stress along L_r is not uniform. Value of μ_{avs} is reflective of the net mobilised pullout resistance, P_r . Various factors affecting the P_r are:

Soil parameters :Density, percentage of fines and overburden stress

Reinforcement properties:Length, width, thickness (edge effect), nature of interface, stress - strain relationship of reinforcement in tension

Test parameters :Stress control (ratio of loading), strain control (rate of pulling out), pullout displacement and dynamic loading characteristics (frequency, acceleration and nature of loading.)

Factors affecting pullout resistance, P_r , are discussed below:

Soil parameters

For sands, angle of ultimate shear resistance, ϕ , strongly influences P_r . However, ϕ is a function of mobilised strain, γ_m . As such, mobilised angle of shear resistance, ϕ_m , has to be related to γ_m . As density of sand increases, ϕ increases and corresponding shear strain reduces. Soils with angular grains results into higher value of ϕ and hence, larger P_r .

Alimi et. al. (1977) reported that when pullout tests are carried with low density (loose) soils, P_r reaches peak value at low strains followed by a fall in P_r (Ingold, 1982) due to collapse of soil structure in the vicinity of reinforcement leading to arching action in soil which shields reinforcement to some extent from overburden pressure, σ_{OV} , resulting into reduced effective normal stress, σ_v , on reinforcement and correspondingly reduced P_r . Such reinforcements mobilize nearly uniform friction over full length and μ_{avs} as well as actual pullout resistance coefficient mobilized at different points along length are identical. For dense soils, as pullout displacement, d_p , and additional confining pressure resulting from

reinforcing action increase. This in turn increases mobilisation of P_r . Dilatancy effect of dense soil is prominent and further contributes to increasing P_r (Guilloux et. al. (1979).

Percentage of fines in soils causes reduction of ϕ and hence P_r . As such, it is prudent to specify percentage of fines in sands of R.E. fills. A value of 15 μm or less has been recommended as the grain size to define finer fraction of the soil (Schlosser and Elias, 1978).

Without arching action, $\sigma_{OV} = \sigma_v$. With increase in density/depth of soil, σ_{OV} increases at reinforcement level leading to increase in P_r which reduces due to arching action, if any. Schlosser and Elias (1978) reported high μ_{avs} at low σ_{OV} due to lesser arching action. As σ_{OV} increases, μ_{avs} reduces and for $\sigma_{OV} = 100 \text{ KN/M}^2$ (6 m depth for most soils), μ_{avs} gets stabilized and stops increasing with additional pressure (Fig.2.5.2).

Reinforcement properties

Reinforcement properties strongly influence P_r . Stiff reinforcements like steel and concrete as well as fabrics or sheets with relatively large modulus of tension when placed in loose soils undergo very little tensile elongation resulting into near uniform mobilisation of pullout resistance stress, τ_p , along length. For large d_p , relative movement between soil and reinforcement is the largest near R.E. wall face and reduces progressively towards buried end leading to larger τ_p near outer end and reduces slowly towards buried end. So, reinforcements with higher tension modulus have advantage of mobilizing large τ_p and P_r with small outward movements.

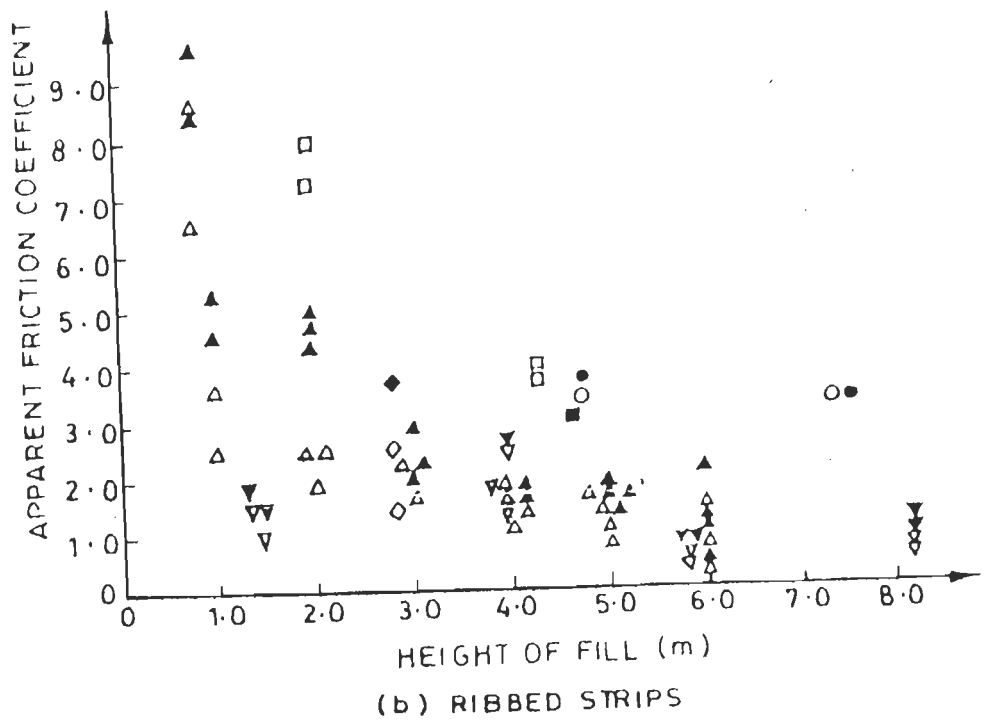
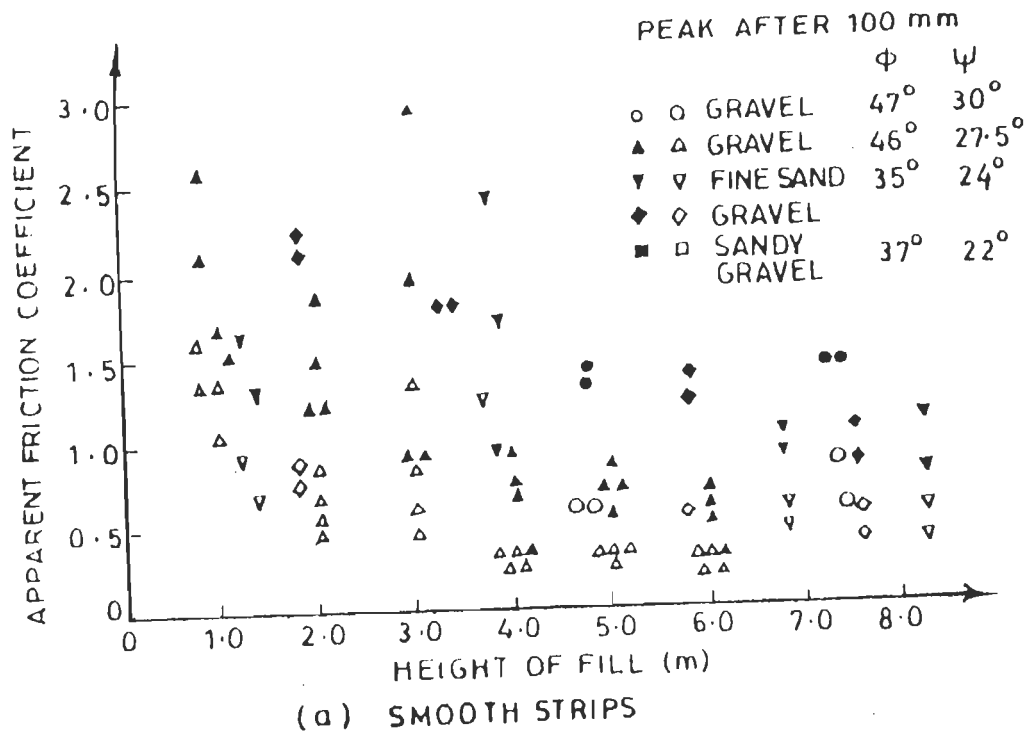


FIG. 2.5.2 VARIATION OF PULLOUT TESTS APPARANT FRICTION COEFFICIENT, μ_{avs} , WITH HEIGHT OF FILL (AFTER SCHLOSSER AND ELIAS, 1978).

Smoother surfaces of reinforcements mobilize smaller P_r (Fig. 2.5.2). Rougher surfaces mobilize larger P_r and shorter d_p (Schlosser and Elias, 1978 and Yourmann, 1978). As such, ribbed metal strips, rough textured geotextiles and geogrids are preferable to smooth ones.

Larger reinforcement length, L_r , gives larger area and larger P_r . However, for very long L_r , stress due to pullout resistance, τ_p , reduces with larger distance from outer end of L_r which reduces μ_{avs} . This is more pronounced for reinforcement with low tension modulus (Schlosser and Elias, 1978 and McKittrick, 1978). By testing mylar tape and glass fiber as ties, Tso (1988) concluded that ratio of peak to residual P_r was independent of L_r . But this should be interpreted in light of tension modulus of ties, relative density of soil and σ_{ov} on ties. Besides, useful P_r is realized on the portion of reinforcement which extends beyond rupture surface into backfill. Its length inside rupture wedge contributes no P_r . Reinforcement length is, therefore, more effective than the width in generating P_r .

With larger L_r , μ_{avs} reduces and μ_{avs} from tests by outward rotation of rigid wall about base and with reinforcing strip attached to wall was different from μ_{avs} got from setup similar to direct shear test (Yourmann, 1978). So, these tests do not truly represent R.E. wall-fill system. Value of μ_{avs} obtained by rotating rigid wall about base was larger than that obtained by using direct shear type setup (Hausmann and Lee, 1978).

Reinforcement should be thin. Geotextiles, thin aluminum strips etc. are examples. When pullout, they create lesser void behind buried end which helps in reducing arching action leading to associated increase in P_r which is desirable. Thick reinforcements of R.C. slabs, metal plates, rods etc.

be discouraged as they create large voids at buried ends leading to more arching action and reduced P_r . Theoretical aspects of edge effects were discussed in detail earlier in this chapter (Romstad et.al., 1978). Increasing reinforcement width causes larger void at its buried end due to d_p leading to more arching action and associated decrease in P_r .

Parameters related to testing

Type of tests carried out, dimensions of soil sample and reinforcement used affect P_r . There are two types of tests: strain control type and stress control type. For strain control type, reinforcement is pulled out at a constant rate. Value of P_r and corresponding d_p are measured to obtain μ_{avs} . With increasing rate of pulling reinforcement, P_r increase, because, the P_s at any d_p is not allowed sufficient time to realize full displacement. Values of P_r thus obtained are comparable only when the rate of pull and other test details are standardised. Most of test setup reported in the state of the art to obtain μ_{avs} are of strain control type and are easy to design and operate (Fairless, 1989; Khan, 1980 etc.).

For stress control apparatus, P_s applied to reinforcement is allowed enough time to realize full d_p and also fully account for short term creep and progressive failure, if any. Such determination of P_r is superior and may be expected to be smaller than that obtained by strain control setup. However, this type of stress control apparatus is not presently available.

For lab tests with small reinforcements and soil samples, P_r tend to be larger than those for field tests with longer reinforcements (Ingold, 1982) mainly due to reduction in μ_{avs} with increasing L_r . Lab results are also

affected by edge effect, arching action and void created by pulling out of reinforcements which may greatly affect stress environment within R.E. test sample when compared with field conditions. Short reinforcement widths in lab may cause stress distribution in reinforcement, soil sample and along interface of the two which may be very different from in-situ plain strain conditions. For tests using direct shear type setup, clearance between upper and lower halves of box is slightly larger than thickness of reinforcement tested. Increasing clearance w.r.t. reinforcement thickness and effective soil grain size affects P_r to an greater extent. However, if clearance is close to reinforcement thickness, the effect may be neglected.

With increasing d_p , the P_r increases to reach the peak value, P_{rmax} . Thereafter, with further increase in d_p , the P_r may remain the same or reduce slightly to reach residual P_r for dense/medium dense fill. For loose fill, reduction from the peak P_r to residual P_r may be large due to arching action. So, R.E. in such test exhibits ductility and residual P_r is always dependable. This is important in geotechnical earthquake engineering to preclude catastrophic failure. Effect of stress-strain relationship of reinforcing elements on d_p has already been discussed earlier.

Pullout resistance under dynamic loading

Under dynamic loads, P_r has not been studied in detail. Two investigation are reported. Richardson and Lee (1975) tested embankments on shake table with sinusoidal excitations using mylar magnetic tapes as reinforcements. Values of μ_{avs} , before and after the dynamic testing was comparable. It was higher than coefficient of dynamic pullout resistance, μ_{avd} , during dynamic loading. This was true for peak as well as residual

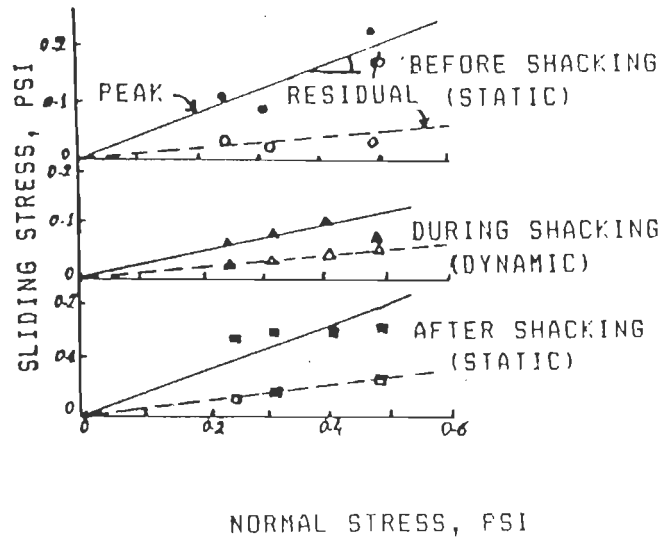


FIG. 2.5.3 RESULTS OF TIE PULLOUT TESTS FROM MIDDLE OF BOX. (RICHARDSON AND LEE, 1975).

values of μ_{avs} and μ_{avd} (Fig. 2.5.3). They did not relate the coefficient to d_p and other dynamic load parameters. Wood (1982) indicated that smooth mylar tapes do not represent rough reinforcements used in the field. Besides, he feels that this coefficient should be related to length, L_r .

Fairless (1989) tested embankments on shake table using sinusoidal excitation and aluminum strip, 10 mm wide and 0.4 mm thick. Effective grain size of sand was 0.3 mm. Strip tension in dynamic tests was measured. With known σ_{ov} at strip level, μ_{avd} was evaluated which ranged from 0.62 to 1.7 (angle of pullout resistance, ϕ_{pd} , ranging from 31.79° to 59.5°). Value of ϕ obtained from shear tests on sand was 40° ($\tan \phi = 0.83$). He concluded that $\phi_{pd} < \phi$ or $\phi_{pd} \geq \phi$, but did not give supporting reasons. His contention that single grain thick (0.3 mm) soil layer gets rigidly attached to strip to increase its effective width to 10.6 mm fails to explain phenomenon fully.

Above phenomenon may be explained using dynamic pullout displacement, d_{pd} . When disturbing inertia of a layer is larger than P_{rmax} for static case, mobilisation of plastic slippage occurs between reinforcement and soil. Actual slippage depends upon the damage potential of dynamic loading. Disturbing force larger than P_{rmax} for static case does not always cause failure and should not be interpreted as a μ_{avd} larger than μ_{avs} . It is faulty interpretation of μ_{avd} which makes it apparently look larger than μ_{avs} . Since dynamic disturbing force is a function of frequency, base excitation level, elastic moduli etc., μ_{avd} changes with these parameters.

2.6 RAIN FALL METHOD FOR PREPARING TEST EMBANKMENT

For reliable lab test results, it is essential to prepare reliable test specimens. Uniformity of density at different points within the same layer of specimen in horizontal and vertical directions and reproducibility of density in different trials is needed to assess reliability. Percentage errors and standard deviations of densities with large sample strength of readings are essential to assess quality of test embankments. Conventional method like compaction of soil by mechanical means (Proctor mould, etc.) are not capable of producing uniform density and are unsuited to prepare large test specimens (Mulilis, et.al., 1975). Rain fall method is considered to approximate natural deposition process. Nature of anisotropy and soil fabric obtained by this method has been found to simulate those observed in natural alluvial environment (Oda et. al. 1978).

A free falling particle accelerating under gravity, decelerates due to air resistance. Its velocity depends on height of fall, H_f , of the particle (Housner and Hudson, 1963; Garde and Mirajgaonker, 1977 and Vaid and

Negusse, 1984). When deceleration equals gravitational acceleration, particle attains constant or terminal velocity, v_t , on falling through critical height, H_c . After impacting on soil surface below, its kinetic energy compacts sand. By choosing H_f from zero to H_c , different densities of soil are obtained. Largest density is reached with H_c . Larger diameter particles give higher density compared to smaller diameter particles, because, air resistance increases with decreasing particle diameter. Temperature's effect on air resistance may be neglected for all practical purposes. Soil densification by kinetic energy of falling soil grains has been used to prepare cohesionless test specimens. It gives good control on density. Equipment for this purpose may be put into two groups: manually operated equipment and motorised equipment.

Older manually operated equipment employed hoppers with opening as wide as width of test tank. Hopper was moved manually along length of tank on guides for distributing soil raining through hopper (Sharda, 1975; Talwar, 1981). Sud (1984) used a tray with perforated base plate and mounted on rails. Tray was moved manually along the length of the tank for depositing sand passing through perforations. Another version consisted of a single tray with perforated base plate covering the entire tank. Soil of known weight was spread manually over tray using buckets (Garg, 1988, Khan, 1991 and Youssef, 1995). Height of fall is decided by the desired density. Hopper is raised intermittently to maintain constant height of fall.

Manually operated equipment cited above have many disadvantages. It is difficult to move trolley with uniform speed manually. Height of fall has to be adjusted frequently which slows down the speed of preparation. Spatial variation of densities obtained within the test specimen has not been

reported together with percentage deviations and standard deviations to establish the degree of uniformity of density.

Motorised equipment rain sand through a nozzle scanning tank width by using a constant speed motor on transverse rails. This assembly scans length bit by bit on longitudinal rails at end of each scan of width to cover complete area of tank. The setup is rised continually to maintain H_f (Matyas and Davis, 1982 and Passalacqua, 1991). Percentage deviation of $\pm 1\%$ and mean standard deviation in density of 1.47% were obtained by Passalacqua (1991). Another equipment used hopper with nozzle length very nearly equal to tank width. Hopper scans the length on longitudinal rails at uniform speed and is rised continually to maintain H_f (Fairless, 1989). Percentage error in density in layer near tank base was 0.42% and that for a layer, 200 mm above the base, was 0.65%. Error in reproducibility of densities for six test specimens was 2.163% and standard deviation was 2.39%. Deposition of sand at transverse ends of tank was more than that over remaining length. This is due to momentary stoppage of trolley at transverse ends where travel direction reverses. This extra soil is removed manually. Level of fill close to longitudinal sides of tank was slightly lower than that over the remaining width, because, nozzle length is always a bit shorter than tank width. As such, some nonuniformity of densities is inevitable, which may be avoided by raining soil over entire area of tank simultaneously.

2.7 CLOSURE

This critical review of the state of the art reveals many important theoretical and experimental research findings as well as research gaps for further investigation. An attempt is made here to summarize them.

Rainfall method is ideal for preparing large specimen of sands of uniform density with good reproducibility. Equipment raining sand over entire area of test specimen are preferred for better quality control.

Reinforcing earth is a recent important concept of soil improvement. It increases stress range with elastic behaviour, improves shear strength and drainage. It is ductile and has vast potential for use in geotechnical earthquake engineering. Very few investigations in this field are reported. Tensile reinforcement failures be avoided to preclude catastrophic failure.

Microreinforced earth with small gaps between reinforcements compared to embankment height may be idealized as homogeneous in linear analysis. It is logical and desirable. Embankment design for operating basis earthquake uses simple and quick linear analysis. This is a significant advantage eventhough such a R.E. embankment may be relatively under stressed.

Under severe dynamic loading due to M.C.E., the behaviour is nonlinear and wedge analysis with linear/bilinear rupture surface using methods like that proposed by Newmark (1965) [[predicts seismic displacements of rupture wedge.]] Most methods of wedge analysis neglect wedge deformation. For sands, considering rupture wedge deformation in static/dynamic earth pressure study proposed by Joshi and Parajapati (1982) and improved by Parasad (1989) and Pandey (1994) is useful in this regard.

Tests on R.E. embankments show increasing acceleration amplification with increasing distance above embankment base and with increasing horizontal distance from the centre of width. Amplification increases with increasing base excitation level, embankment height and with decreasing

shear modulus. On reaching yield acceleration, further amplification stops and large sliding displacements occur. It is supported by test results.

As reinforcement length increases, shear modulus and safety against embankment failure increase. Only that length of reinforcement which extends beyond rupture surface contributes pullout resistance for stability.

It is difficult to reinforce embankments with small top width and two sets of intersecting rupture surfaces because of lack of enough space to place design length projecting beyond rupture surface for discontinuous reinforcements designed for pullout resistance. Continuous reinforcements running from one side slope to other and connected to stiff facing elements act in tension to stabilize such embankment, particularly it is expected to withstand earthquake. This is also supported by test results.

Reinforcement, when pulled out, creates void equal to volume of its portion pulled out leading to stress redistribution and arching action in soil which increases with increasing reinforcement thickness and reduces pullout resistance. So, use of thin reinforcement is more desirable.

Embankments with reinforcements tied to facing are far better than those with untied reinforcements specially for dynamic case. Flexible facing elements like geotextile folded back into embankment lead to relatively larger outward embankment movements. Rigid facing able to redistribute disturbing forces is preferred. Discontinuous elements make embankment face flexible. For better redistribution of localised disturbing forces (particularly for dynamic case), stiffer elements like concrete panels and gabions with a continuous interconnecting R.C. slab would be

useful. Light and strong synthetic facing elements are better than heavy ones because of reduced disturbing inertia due to lighter weight. Above observations are supported by test results.

For embankments, dynamic loading is more severe compared to static loading and horizontal excitation is far more critical compared to vertical excitation. As such, vertical excitation may be often neglected.

Excitation frequency has a very strong influence on the response of embankments. However, detailed investigations are needed to clearly highlight the effect of excitation frequency on response. It would be interesting to see if there is a frequency range in which the response of embankments may be considered to be frequency independent. At resonance, the acceleration amplification is very high.

For severe excitation, visible rupture surfaces are developed. Test results indicate a plane rupture surface if formed totally within the R.E. zone and a bilinear rupture surface if it is partly in R.E. zone and partly in plain sand behind. As degree of reinforcement increases, rupture surface within R.E. zone becomes flatter, because, horizontal reinforcements strongly resist formation of near vertical rupture surfaces.

Tension is very large in reinforcements situated within lower third height of embankment. As the base is approached, tension in reinforcements reduces due to embankment-foundation interaction. Variation in tension of reinforcements with depth is very similar to that of earth pressures.

Well reinforced zone of embankment behaves like a monolithic block which is supported by test results. External stability of reinforced zone is

checked against sliding and bearing using equilibrium conditions. Stress concentrations may occur below the outer edge of R.E. zone at the base. Provision of light R.C. slabs below outer edge may be needed to overcome bearing pressures. Providing a small passive fill of 8.5% of embankment height further improves performance in bearing and in sliding (MWD, 1980).

Embankments perform under plain strain conditions. It is difficult to create them in lab. Smooth glass sheets are often provided at transverse ends of embankments leading to friction at their interfaces which vitiates plain strain conditions. So, better testing techniques are needed.

To obtain shear modulus of idealized homogeneous R.E., size of R.E. block used should be fairly large compared to length/spacing of reinforcements. Use of smaller blocks may lead to appreciable errors.

Design seismic excitations are random in nature and standard methods are available in the state of the art to find out equivalent sinusoidal excitation which make analysis easier. It is easier to carryout parametric studies w.r.t. frequency for tests with sinusoidal excitations for which facilities are easier and cheaper to obtain. Sinusoidal accelerations are more severe than seismic accelerations of same peak.

For design of R.E. embankments pullout resistance is important. For its determination under static case, strain control type of equipment are most commonly available which are inferior to stress control type apparatus which need be developed urgently employing as large a reinforcement as possible. Dynamic pullout resistance is worked back from results of dynamic tests and which may be smaller than the static value. Some times it is computed to be larger than the static value due to faulty interpretation.

EXPERIMENTAL SETUP

3.1 PREAMBLE

For reliable test results, good test facilities and measuring equipment for various test parameters are essential. Rain fall technique is the best for sample preparation (Oda et.al., 1978). A manually operated equipment capable of raining sand over entire test bed has been developed which performs better than other equipment reported in the state of the art. Details of the test set up has been dealt with in this chapter.

3.2 SAND RAIN APPARATUS (SRA) FOR SAMPLE PREPARATION

3.2.1 Theory

Dynamics of an idealized spherical particle of diameter, D_s , with specific weight, γ_{sp} , falling through a fluid of specific weight, γ_f , and kinematic viscosity, ν_f , has been theoretically analysed (Housner and Hudson, 1963; Garde and Mirajgaonkar, 1977 and Vaid and Negusse, 1984). When the sphere begins its downward journey, it accelerates under the influence of gravity. Its velocity increases with time of free fall. However, the particle velocity gets retarded by drag force (fluid resistance), F_{drag} , which increases with velocity. When deceleration due to drag completely overcomes gravitational acceleration, g , the sphere attains a constant or terminal velocity, v_t . Height of fall, H_f , of the particle at

that instant is termed as critical height, H_c . Expression for F_{drag} and relationship between v_t , ν_f , D_s and Reynold's number, R_e , for the fluid is:

$$F_{\text{drag}} = \{\pi D_s^3 (\gamma_{\text{sp}} - \gamma_f)\}/6 \quad (3.2.1)$$

Relationship between v_t , ν_f , D_s and Reynold's number, R_e , for the fluid is:

$$R_e = v_t D_s / \nu_f \quad (3.2.2)$$

Reynold's number is a function of $(F_{\text{drag}}/\rho_f \nu_f^2)$ where ρ_f is mass density of fluid (Fig. 3.2.1a) from which v_t is obtained. Relationship between v_t and D_s for D_s upto 4.75 mm is nonlinear (Fig. 3.2.1b) which may be assumed to be linear for D_s up to 1 mm as reported by Vaid and Negussey (1984) also.

Figure 3.2.2 shows relationship between velocities of particles of 0.1, 0.4 and 1 mm diameters as functions of H_f (Vaid and Negussey, 1984). In the same figure is shown similar data for 0.21 mm diameter particle with specific gravity, G_{sp} , of 2.59 obtained for Solani sand used in this investigation and showing similar variation. Variation of velocity of this particle for different values of H_f were obtained by trial and error solution of equation of motion of the particle and by knowing the initial velocity to be zero (at rest condition). Details are given in standard texts on fluid mechanics. With decreasing D_s , H_c reduces. So, rainfall technique is unsuitable for very fine grained soils.

3.2.2 Factors Affecting Density Obtained by Rain Fall Method

Factors affecting the density obtained by rain fall method are discussed in this article:

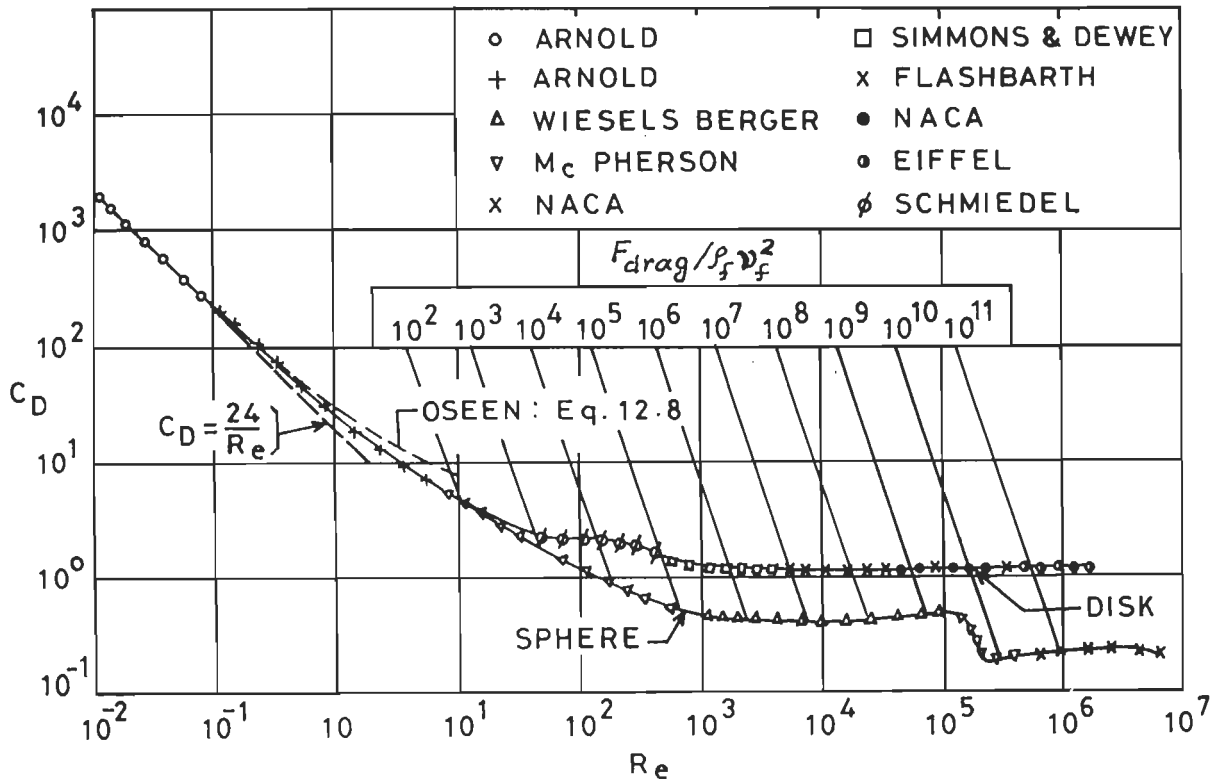


FIG. 3.2.1a RELATIONSHIP BETWEEN C_D , $F_{drag} / \rho_f v_f^2$ AND Re FOR SPHERE AND DISK (GARDE AND MIRAJGAONKAR, 1977).

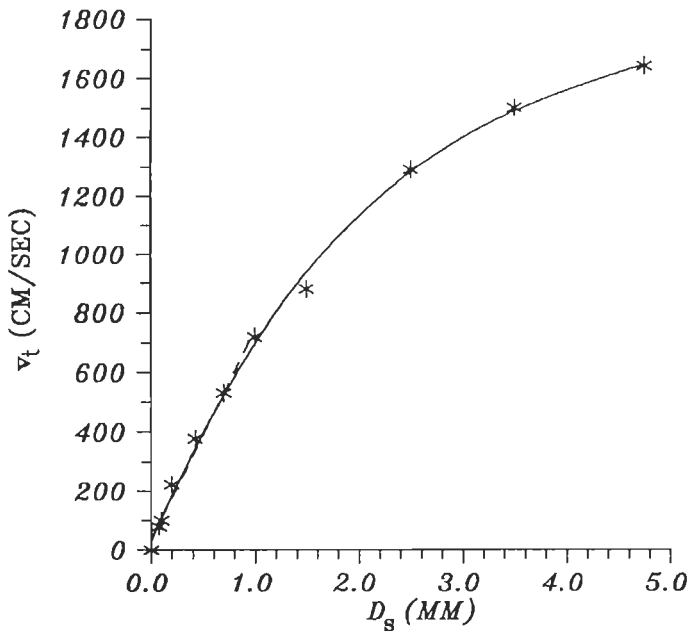


FIG.3.2.1b TERMINAL VELOCITY, v_t , VERSUS DIAMETER OF SPHERE PARTICLE, D_s , IN AIR.

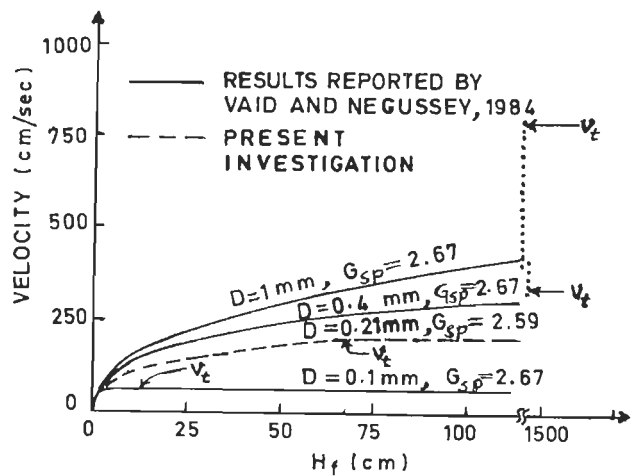


FIG.3.2.2 VELOCITIES OF SPHERES OF DIFFERENT DIAMETER WITH HEIGHT OF FALL, H_f , IN AIR.

Diameter and shape of particle

As cited earlier, with D_s increasing, v_t increases which leads to higher relative density, D_r , of soil. Diameter of particle, D_{60} , corresponding to 60% finer fraction of soil (obtained from grain size distribution curve) is considered to represent the cohesionless soil used for this study. Though, particles are idealized as spheres, actually their shapes may be described as angular, subangular or rounded. Any shape other than spherical leads to higher resistance to free fall and hence lower v_t and D_r . Besides, particle shape also affects soil structure and hence D_r . These are specific to the soil under study and can not be generalized. So, the soil type is not considered as a parameter in this investigation.

Size of perforations of SRA

Perforation diameter, D_p , should be larger than largest dimension of particles to allow free flow of soil. Perforation ratio, R_p , is defined as ratio of D_p to D_{60} of soil. Larger R_p is desired to facilitate easier, smoother and quicker flow of soil and to reduce blockage of perforations due to interlocking soil grains.

Open ratio of SRA

Open ratio, R_o , is defined as the ratio of total area of perforations to overall area of SRA. It should be large enough to allow free flow of soil. Upper limit of R_o is unity and not achievable.

Spacing ratio of SRA

Spacing ratio, R_s , is defined as the ratio of D_p to mean C/C spacing of perforations in two orthogonal directions. Minimum value of R_s is zero for

plate with no perforations. Larger R_s is desired to reduce gap between perforations leading to a more desirable even deposition of sand.

Collision of free falling soil grains

When soil placed on SRA falls through perforations (circular holes), it is ideally expected to fall vertically. However, only particles standing directly above holes may do so. When soil particles above a hole fall through, adjoining particles slide down to occupy their place. This continues till a small amount of soil (residual soil) stands on gap between holes. Slope of this residual soil is at an angle ϕ to the horizontal, ϕ being angle of repose of soil. As such, smaller R_s is desired to reduce residual soil. Particles in the initial soil column on solid portion of SRA slide along the slope at an angle, ϕ , giving them a small horizontal radial velocity component, v_h . Due to radial symmetry, such particles collide and their v_h get cancelled leading to the desired near-vertical fall. This does not affect their predominantly vertical velocity responsible for soil densifications. Due to nonuniformity of size and shape of particles, v_h may not always be nullified fully. The residual horizontal velocity results into some lateral scatter of sand. As such, some sand rains on soil surface directly below gaps between holes which reduces unevenness of soil surface generated by sand rain. Details about the maximum possible v_h for particles will be given later.

Height of fall

As explained earlier, increasing height of fall, H_f , increase velocity till terminal velocity, v_t , is reached. The kinematic energy of falling

particle impacting on soil surface below densifies soil. Impacting particles may slightly rebound or shift a bit laterally depending upon many factors like the shape of particles etc. This lateral shift and vibrations of surface particles increase D_r . It is known from tests that horizontal excitations are more effective than vertical excitations and a simultaneous vertical and horizontal excitations is even more effective in soil densifications. Hence, presence of small v_h of particles is beneficial in getting higher densities.

Thickness of soil layer deposited in one operation

For a motorized SRA scanning the entire test bed, the thickness of soil layer formed in each scanning is small. As such, H_f is not altered much. However, in manually operated SRA, each operation of pouring soil forms a layer whose thickness may be significant compared to H_f . This results into continuous decrease in effective H_f as soil rains down, if SRA is stationary. This decreases density and leads to nonuniformity of density which is undesirable. It has to be ascertained for each soil and each setup. The nonuniformity may be reduced by continually raising the SRA through a distance equal to the depth of soil layer formed below to maintained a constant H_f as far as possible. Besides, forming a thinner layer in each operation helps in reducing this source of nonuniformity.

Sample containers

To assess degree of uniformity of soil layer formed by SRA, it is necessary to measure densities of samples taken by placing containers at different locations of that layer. The containers displace soil of volume

equal to volume of side walls and base of containers which should be as thin as possible. Some falling sand particles on hitting top edge of container walls get dispersed. Therefore, top edge of the container wall should be chamfered with sloping chamfer dipping away from container. Besides, the container base should be large enough to cover a large number of perforations (holes) of SRA to reduce the relative position of container and holes. At the same time, container should be small enough to attribute the measured density to be represented by a point in soil sample prepared. Above two requirements conflict with each other and, hence, need some compromise solution. All falling particles should ideally impact on soil surface below, but, may hit container walls instead. Soft walls may absorb some energy to alter energy level of falling particles which may lead to some undesirable change in the density. Hard container container walls reflect particles hitting them with negligible energy absorption leaving magnitudes of vertical and horizontal velocity nearly unchanged. It, therefore, leads to negligible change in density. Another factor to be studied experimentally is the depth of containers, though it appears that depths may not be a significant parameter.

3.2.3 Design Consideration for SRA

Specifying performance parameters is required for design of SRA. It is desirable to rain sand over the entire test bed simultaneously for more uniform density. The R.E. Embankment required for testing was 1.5 m long, 0.75 m wide and 0.9 m tall formed by 12 layers of 75 mm thickness. As such, the SRA should be 1.5 m long, 0.75 m wide and 75 mm deep. Suitable mechanism should be provided to allow instantaneously start of sand rain.

Air dry Solani river sand of Roorkee, which is a fine sand with D_{60} equal to 0.23 mm, was used for testing. As per Indian Standard code of practice (IS: 1948-1970), it is a fine sand classified as SP with G_{sp} of 2.59, minimum density of 1.39 t/m^3 , maximum density of 1.75 t/m^3 , uniformity coefficient of 1.53, coefficient of curvature of 1.04 and particle sizes D_{10} , D_{30} , D_{50} , D_{60} and D_{100} are 0.15, 0.19, 0.21 and 0.23 mm respectively. Table 3.2.1 gives data regarding the SRAs and soil samples used by Garg (1988), Khan (1991) and Youssef (1995). These investigators reported satisfactory performance of their respective SRAs as far as free flow of sand is considered. Hence, $R_p \geq 12$ may be considered adequate w.r.t. D_{60} . However, to rationalise the design, it is desirable to provide $R_p=6$ w.r.t. D_{100} . As such, circular perforations of 3 mm diameter were adopted giving R_p equal to 13.04 w.r.t. D_{60} and equal to 6 w.r.t. D_{100} .

Table 3.2.1 Details of Data Regarding SRAs and Soil Samples Used

Investigator	Type of soil	D_{60}	D_{100} (mm)	Dia. of perforation (mm)	Spacing perforation (mm)	R_p	R_o	R_s
Garg (1988)	Fine sand	0.20	0.26	3.0	25.00	15.00	0.0013	8.33
Khan (1991)	Fine sand	0.25	1.0	3.0	25.00	12.00	0.0113	8.33
Youssef (1995)	Fine sand	0.25	1.0	3.0	25.00	12.00	0.0113	8.33
Proposed SRA	Fine sand	0.23	2.0	3.0	10.00	13.04	0.0707	3.33

Open ratio, R_o , of SRA should be large enough for a quick deposition of sand layer of 75 mm thickness in 1 to 2 minutes. Trials showed that it could do so in 60 seconds when R_o was 0.07068 which compares favourably with R_o used by above investigators (Table 3.2.1).

Spacing ratio, R_s , should be small and $R_s=8.33$ has been employed by above investigators which lead to a relatively larger amount of residual sand standing on SRA. To reduce this and to improve evenness of soil surface formed, $R_s=3.33$ was adopted. Hence, holes of 3 mm diameter at 10 mm C/C in lateral/longitudinal directions of SRA were proposed.

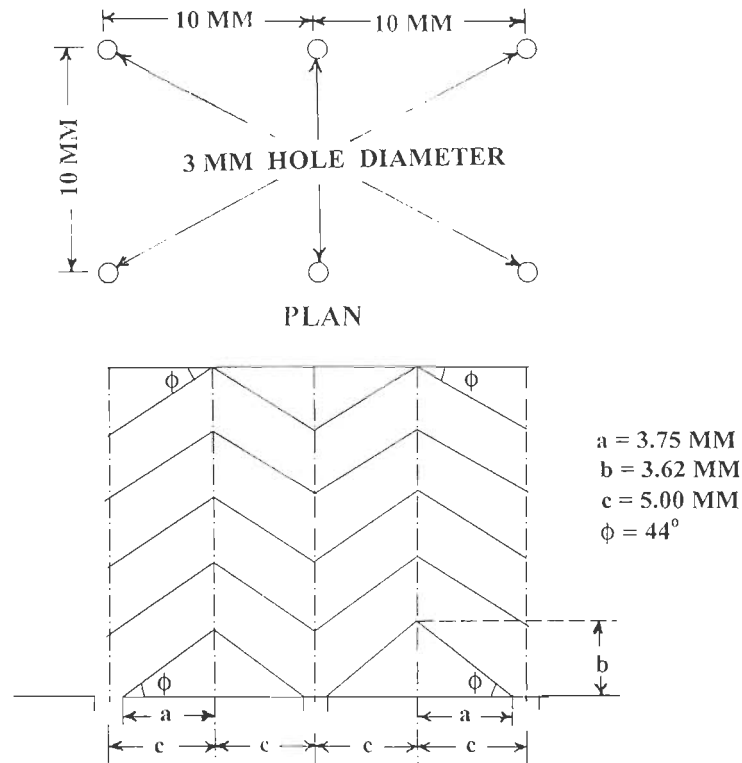


FIG. 3.2.3 SOIL COLUMN STANDING ON SRA.

Figure 3.2.3 shows soil column standing on SRA. When sand rain begins, level of soil falls on each hole till surface slope reaches angle of repose. Then, the whole surface moves down vertically with same surface configuration. Its vertical velocity may be computed knowing volume of the typical prismatic soil column, cross sectional area of hole and duration in which it rains down and is computed as 17.6 mm/sec. Its component resolved parallel to sloping soil surface is 12.28 mm/sec. whose horizontal

component, v_h , is 8.83 mm/sec., with which falling particles disperse. Travel time, Δt_p , needed for the soil particle fall through H_c is given by:

$$\Delta t_p = H_c / (0.5 v_t) \quad (3.2.3)$$

where $(0.5v_t)$ is the mean velocity of travel and v_t is the largest velocity. Air resistance is neglected for simplicity. For soil used in tests, $\Delta t_p=0.67$ sec. in which lateral scatter of particle is obtained as 5.71 mm. Radially symmetrical scatter of about 10 mm in each radial direction was measured experimentally from the point directly below the centre of circular hole. Difference between observed and computed scatter is due to assumption of spherical particles which really are angular. Nevertheless, this computed v_h works out to be 0.42% of v_t which is considered tolerable though it is possible to reduce the initial horizontal velocity of particle scatter by adopting smaller R_s .

Whenever falling particles collide, their horizontal velocity tend to get cancelled leading to near vertical fall for all practical purposes resulting into reduced scatter. For each operation, thickness of sand layer, H_d , deposited by SRA is 75 mm or a significant 11.53 % of $H_c=650$ mm obtained from tests. Hence, raising SRA continually to maintain a constant value of H_f is desirable.

3.2.4 Improved Manually Operated SRA

The proposed SRA incorporates desired feature of raining sand over entire test bed. Motorised SRA with electronic/electrical controls are

intricate, costly and difficult to operate/maintain. The proposed manually operated SRA is rugged, inexpensive and simple to operate/ maintain.

The developed SRA has a length, L_{SRA} , of 1.8 m and a width, W_{SRA} , of 0.75 m (Fig. 3.2.4) for preparing R.E. embankments of same size. It eliminates the need to move SRA along length and width of the test bed. The SRA with depth, D_{SRA} , of 75 mm has base plate, P_b , with holes of 3 mm diameter, 10 mm C/C in either direction. Eighteen shutters, S_s , 750 mm long and 100 mm wide hinged to base plate are moved to horizontal position by pulling them with flexible steel wires, S_w , to close holes while pouring sand on SRA. These wires, attached to free ends of shutters, are pulled up by turning longitudinal pipe, P_{SRA} , around which wires get wound up. Two longitudinal clamps, L_{CSRA} , hinged to SRA sides hold shutters in closed position by transverse clamps, T_{CSRA} , at each end of longitudinal clamps.

The assembly is hung from a beam supported by two A-frames by using chain pulley block to control drop height of sand. Steps involved in using this SRA are: (i) A predetermined quantity of sand is poured on SRA with shutters and clamps in closed position and hung at the desired height. Figure 3.2.5 shows the suspended SRA filled with sand. (ii) Plastic sheets are hung around SRA to control escape of dust clouds. (iii) The handle, H_{SRA} , (Fig. 3.2.5) is rotated to pull out transverse clamps, T_{CSRA} , which release longitudinal clamps, L_{CSRA} . Springs attached to L_{CSRA} assist in opening these clamps instantaneously. This in turn releases 18 shutters, S_s , which are moved to open position quickly with the help of attached springs. The whole process takes places instantaneously and sand starts pouring down on test bed. The minimum H_f of this SRA is 200 mm. To maintain a constant H_f throughout the duration of rain, the SRA was gradually pulled

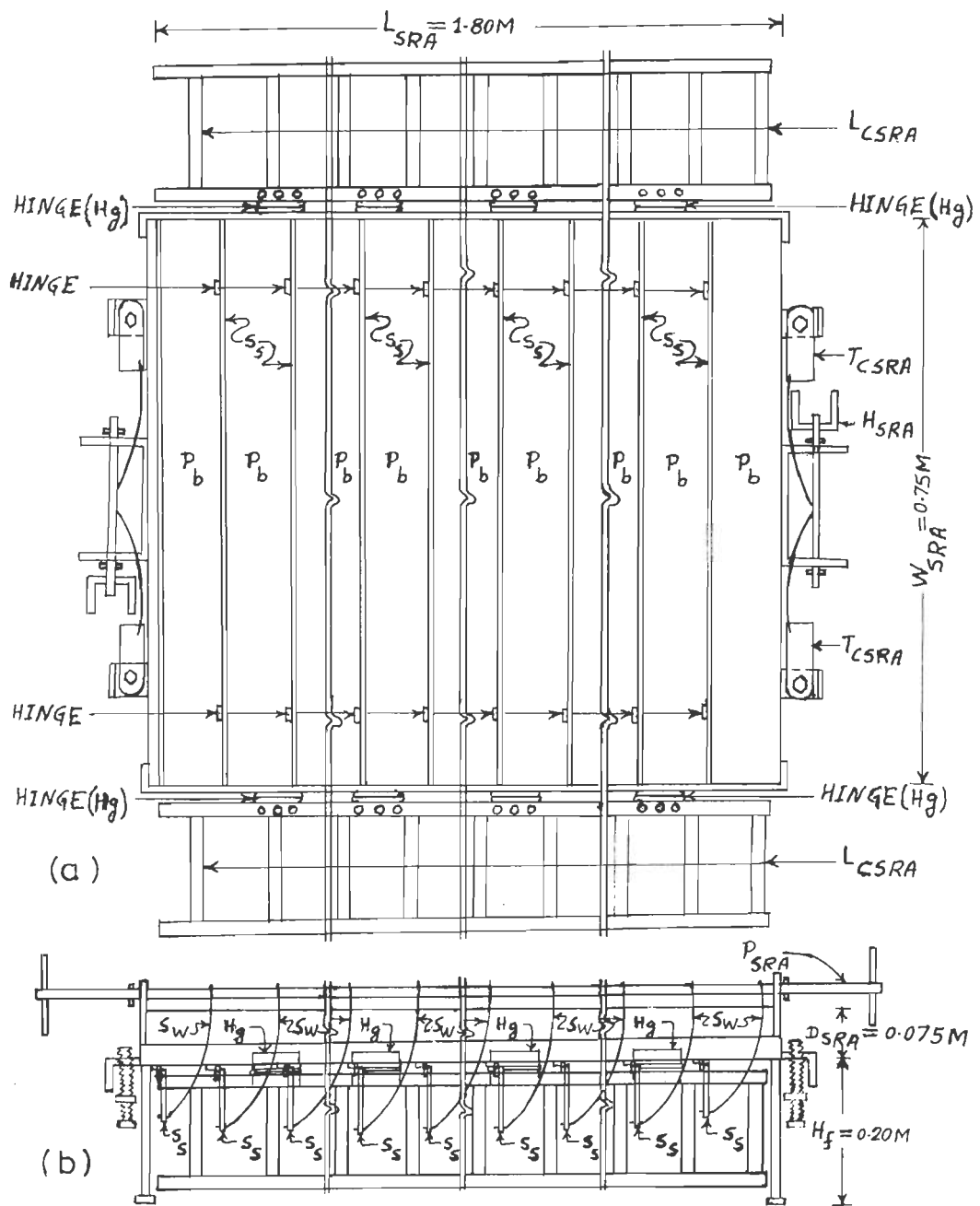


FIG. 3.2.4 IMPROVED SAND RAIN APPARATUS (a) VIEW OF SRA WHEN SEEN FROM BELOW (b) SIDE VIEW OF SRA.



FIG.3.2.5 SUSPENDED SRA FILLED WITH SAND.



FIG.3.2.6 CLOSE VIEW OF SRA WITH SHUTTERS IN THEIR OPEN POSITION.

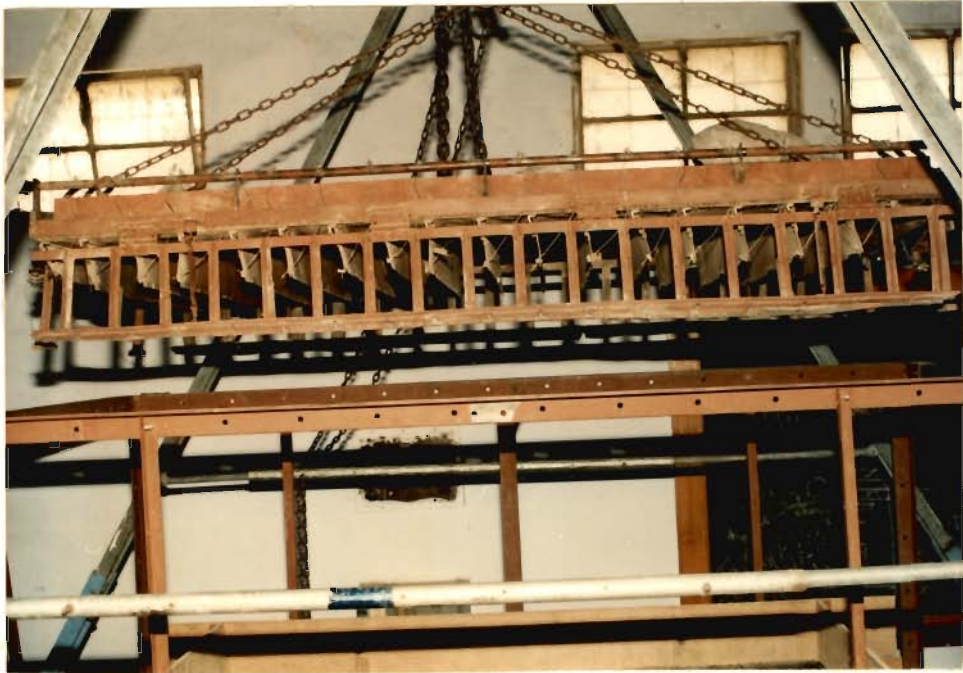


FIG. 3.2.7 LONGITUDINAL VIEW OF SRA WITH LONGITUDINAL CLAMPS AND SHUTTERS IN THEIR OPEN POSITION.

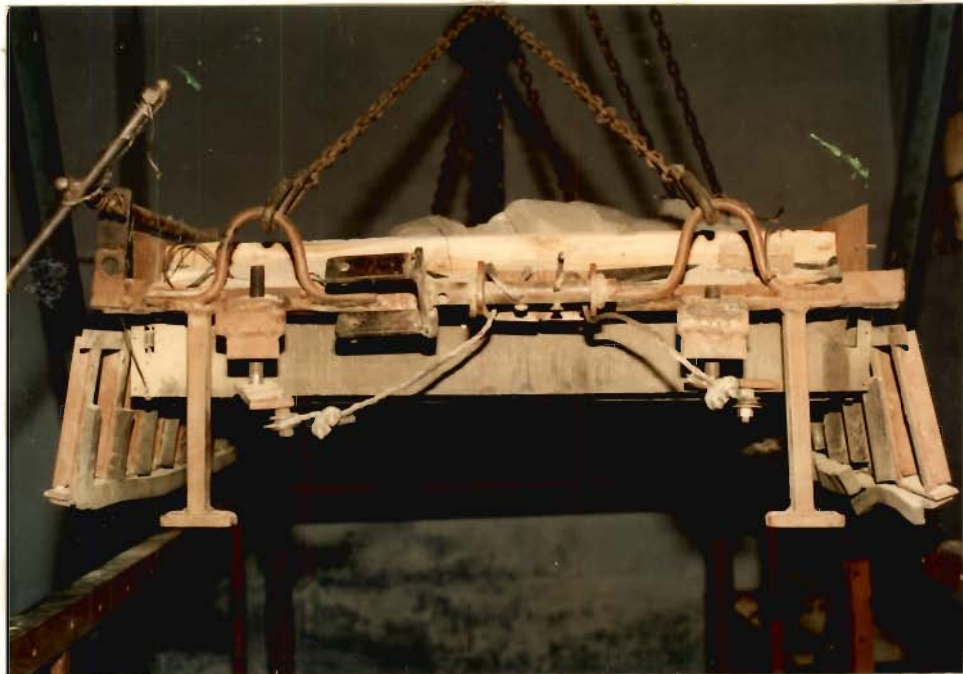


FIG. 3.2.8 TRANSVERSE VIEW OF SRA WITH LONGITUDINAL CLAMPS AND SHUTTERS IN THEIR OPEN POSITION.

up manually by a distance of H_d by using chain pulley block. Figure 3.2.6 shows shutters, S_s , in open position. Figure 3.2.7 and 3.2.8 show longitudinal clamps, L_{CSRA} , and shutters, S_s , in open position.

3.2.5 Performance Of SRA

Tests were conducted using Solani sand. Results of various parametric studies carried out is presented in this article.

Effect of height of fall on density

Tests were performed using H_f ranging from 250 to 950 mm with 75 mm deep sand layer in SRA. Figure 3.2.9 shows fourteen containers of 80 mm diameter placed on the test bed to obtain soil samples to measure density. For each H_f , tests were repeated three times. The average of three densities, γ_{dav} , for each H_f is shown as a function of H_f (Fig. 3.2.10). It may be observed that γ_{dav} increases linearly with H_f from 250 to 680 mm. For H_f larger than $H_c = 680$ mm, γ_{dav} remains the same. The maximum γ_{dav} attained was 1.6505 t/m^3 which corresponds to a relative density of 76.64 % (Fig. 3.2.11). This is considered adequate. The terminal velocity, v_t , of particle size D_{50} of 0.21 mm for Solani sand, idealized to be a sphere works out to be 2.007 m/sec. The corresponding H_c obtained from tests is 680 mm. Figure 3.2.3 also shows values of v_t and H_c . It may be observed that the data obtained for Solani sand shows characteristics similar to those reported by Vaid and Negussey (1984). Figure 3.2.12 shows variation of void ratio of the soil as a function H_f . As H_f increases the void ratio reduces and ultimately reaches the minimum value at H_c . The data reported by Vaid and Negussey (1984) for Ottawa sand with D_{50} equal 0.4 mm (shown in the same figure) also shows similar characteristics.

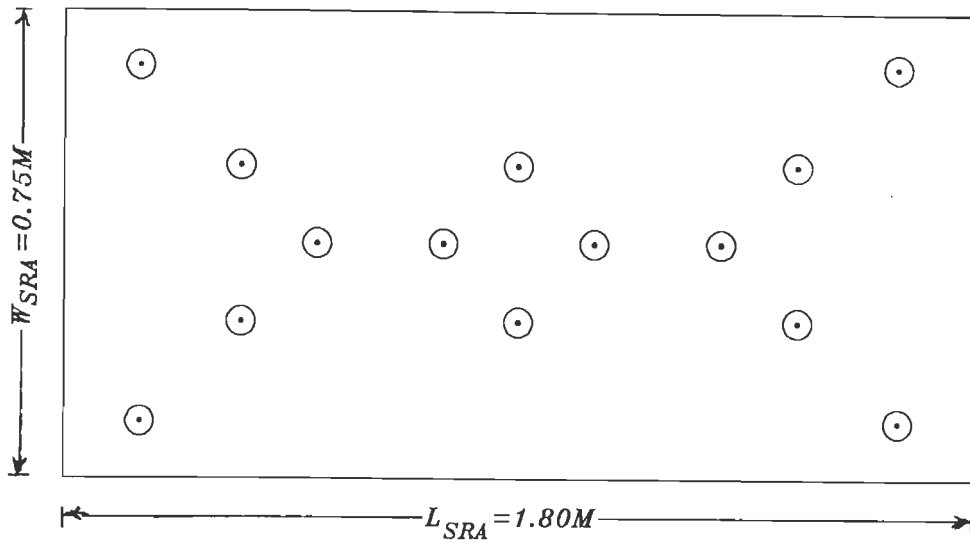


FIG.3.2.9 POSITION OF CONTAINERS ON TEST BED.

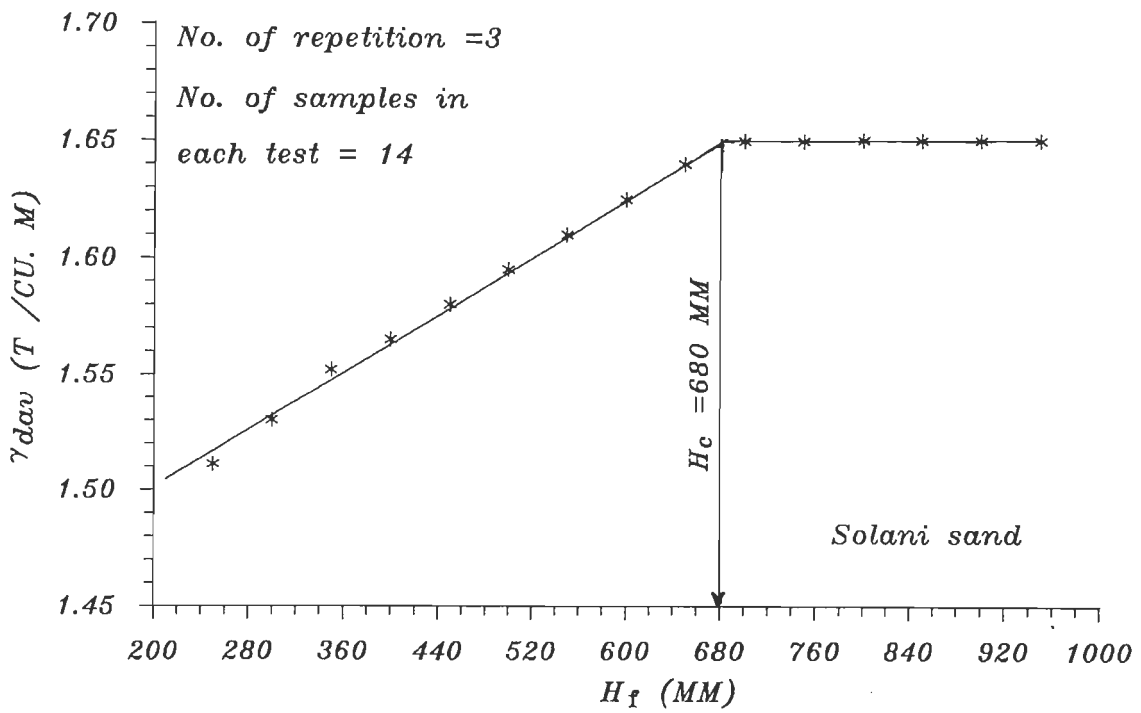


FIG.3.2.10 VARIATION OF AVERAGE DENSITY, γ_{dav} , WITH HEIGHT OF FALL, H_f .

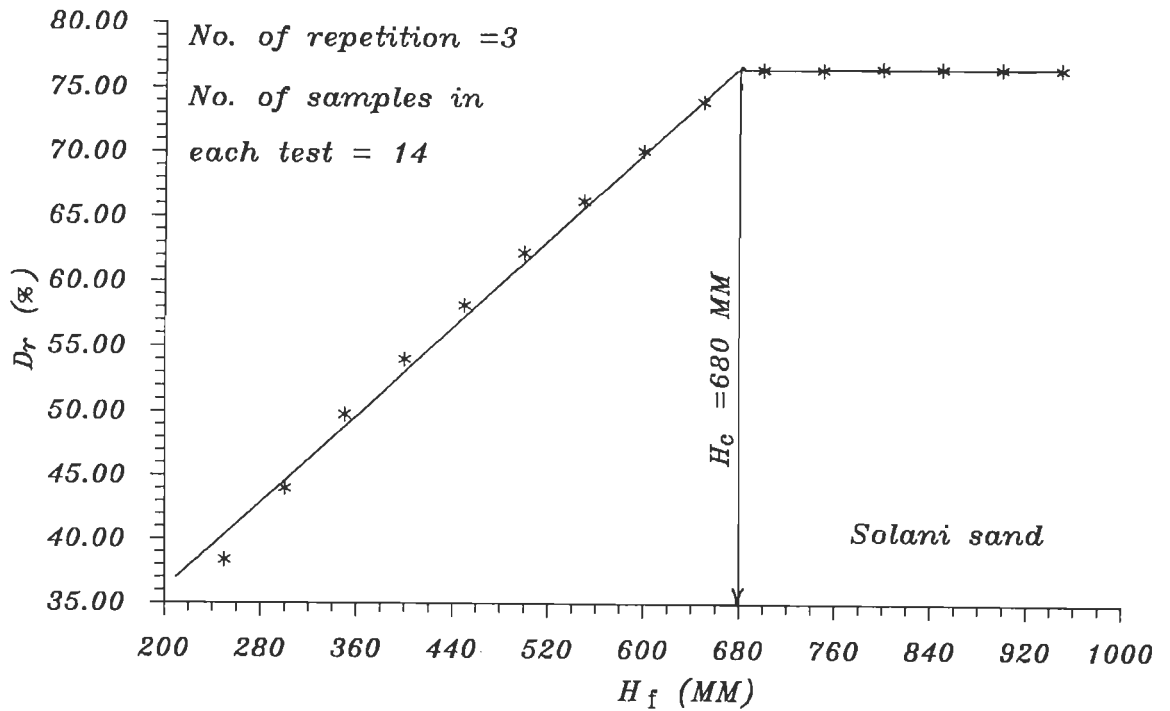


FIG.3.2.11 VARIATION OF RELATIVE DENSITY, D_r %, WITH HEIGHT OF FALL, H_f .

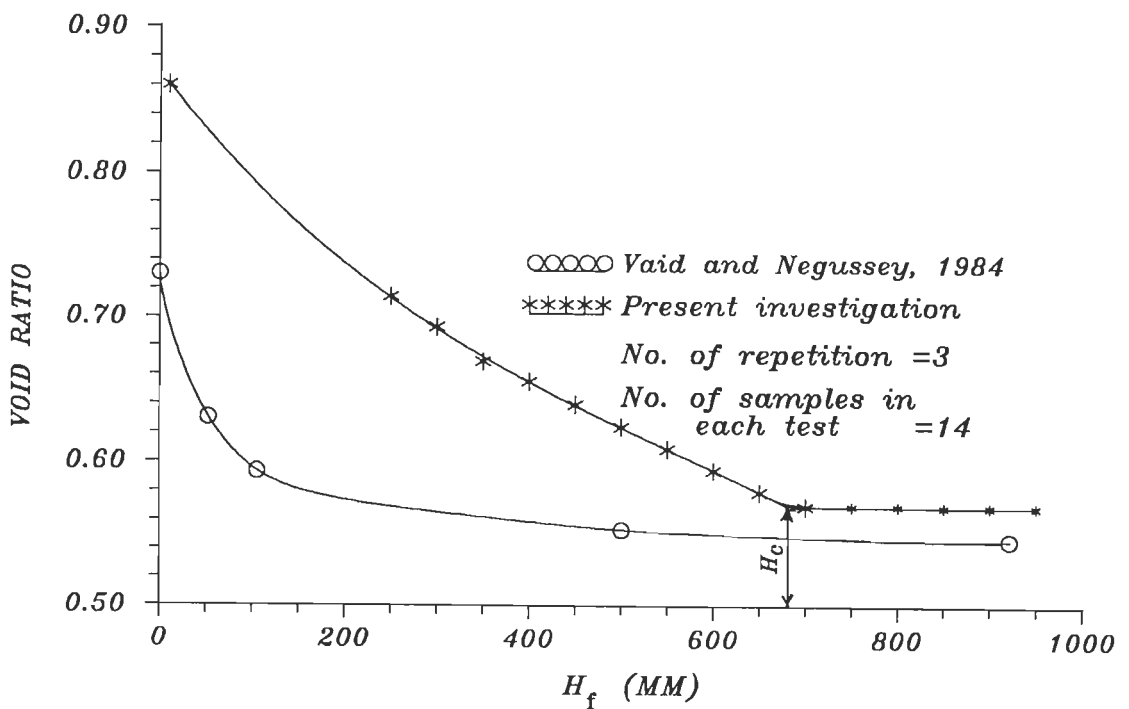


FIG.3.2.12 VARIATION OF VOID RATIO WITH HEIGHT OF FALL, H_f .

For each H_f , three tests were performed and 14 samples of densities obtained for each test, thus giving 42 samples to obtain percentage standard deviation, S_d , for each H_f and shown in Figure 3.2.13 as a function of H_f . It may be noted that S_d increases with increasing H_f and gets stabilized at about 1.12% at $H_c=680$ mm. Mean standard deviation is 1.08% which is better than that of 1.47% reported by Passalacqua (1991) and 2.39% worked out for results of Fairless (1989).

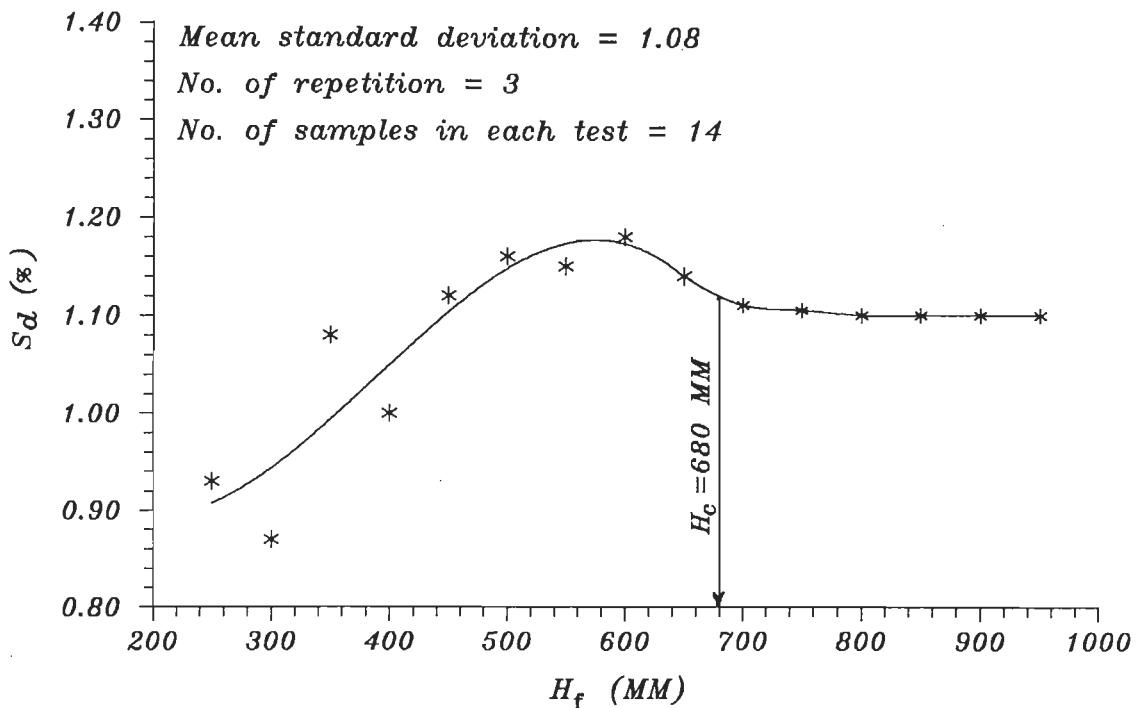


FIG.3.2.13 VARIATION OF STANDARD DEVIATION, S_d (%), WITH HEIGHT OF FALL, H_f .

Sample container

Cross sectional area of container of 80 mm internal dia. is 5026 mm^2 which is large enough to cover 47 perforations of 3 mm diameter at 10 mm C/C in either directions. Number of perforations falling on the edge of

container is limited to 2 only which forms 4.25% of the 47 perforations which fall totally within the container area. As such, the relative position between container and perforations is not expected to have much influence. Cross sectional area of containers, being only 0.447% of the area of soil sample under preparation, is quite small.

Total volume of solids wall and bases of all 14 containers adds up to be 311354 mm^3 which is a negligible 0.37% of the volume of sand poured in one operation. Increase in average thickness of finished soil layer due to volume of soil displaced by volume of solids of buried containers is a 0.27 mm which is a negligible 0.108% of minimum $H_f = 250 \text{ mm}$ and much less for larger H_f . A change of 0.27 mm in H_f leads to 0.024% error D_r which is negligible. Controlling H_f with an accuracy of 0.27 mm is difficult. Hence, presence of 14 containers has no noticeable adverse effect tests.

These 14 containers used have six different depths ranging from 25 to 50 mm to study effect of their depth. The six densities obtained for these six container depths for each H_f are presented in Fig. 3.2.14 for the ten different H_f . It may be noted that density increases very slightly as container depth increases from 25 to 50 mm for H_f equal 250 mm. The increase gradually reduced to insignificance as H_f increased from 250 to 800 mm. Upper and lower bounds of % deviation in D_r w.r.t. mean of all the 14 density obtained are 0.62 and -0.73 for the entire range of H_f (Fig. 3.2.15) which are quite small deviations. Best fit line for these points indicates that % deviation in D_r is within ± 0.21 which is even smaller. From above discussion, it may be concluded that D_r is independent of container depth for all practical purposes and for range of H_f used.

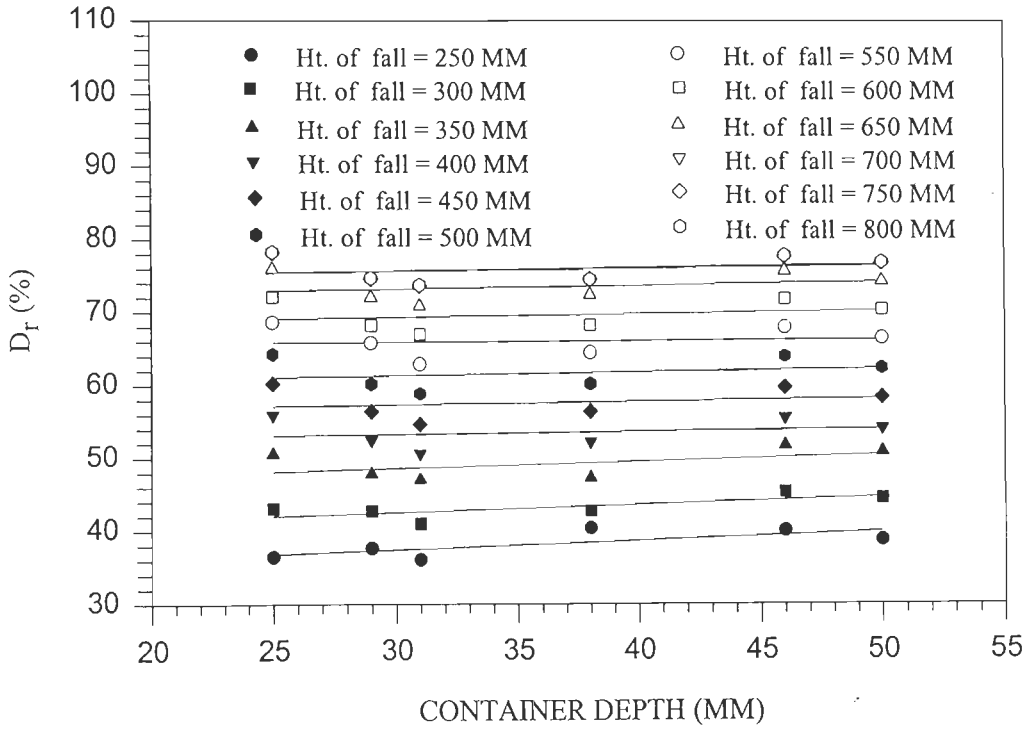


FIG. 3.2.14 VARIATION OF % RELATIVE DENSITY, D_r , WITH DEPTH OF CONTAINERS.

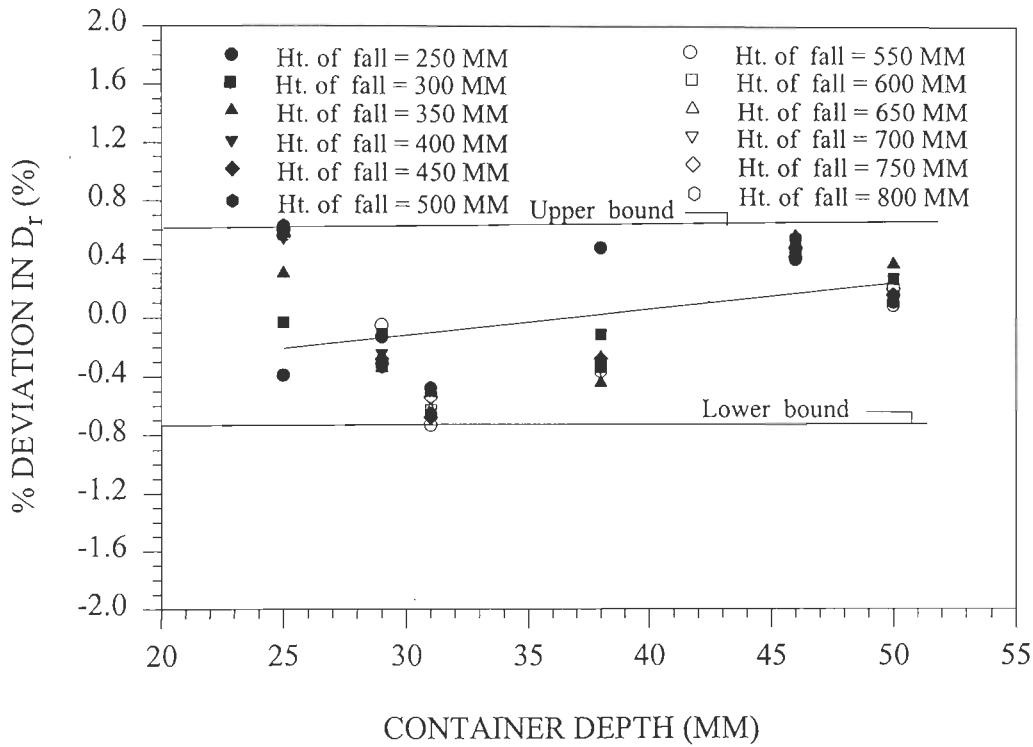


FIG. 3.2.15 VARIATION OF % DEVIATION IN RELATIVE DENSITY, D_r , WITH DEPTH OF CONTAINERS.

Thickness of layer formed in one operation

In this study, depth of soil layer formed in one operation is 75 mm. A constant H_f is maintained for each operation by continually raising level of SRA by pulling the chain of pulley block. Figure 3.2.11 shows D_r as function of H_f . The change in % D_r per mm of H_f worked out to be 0.088 for the rising flank of the relationship. If SRA is not raised continually to maintain constant H_f , the actual H_f decreases continuously from initial H_f to final $H_f=(H_f-75)$ mm at the end of operation. Therefore, actual average H_f , denoted by H_{fa} , works out to be $[H_f+(H_f-75)]/2 = (H_f -37.5)$ mm. For $H_f=H_{fa}$, corresponding relative density, D_{ra} , may be obtained by using data from Fig. 3.2.11 and which would be lesser than D_r obtained for initial H_f , if H_f were held constant. Percentage change, D_{rpc} , in D_r w.r.t. D_{ra} is:

$$D_{rpc} = 100 (D_r - D_{ra})/D_{ra} \quad (3.2.4)$$

Figure 3.2.16 shows D_{rpc} as a function of H_{fa} computed for four assumed thickness, H_d , of 25, 50, 75 and 150 mm per operation. It may be observed that when H_d is 25 mm, the D_{rpc} varies in an narrow range of 1.5 to 3 percent. However, as H_d increases from 25 to 50, 75 and 150 mm, the D_{rpc} shoots up to unacceptably high range from 6 to 21.5 percent. When H_{fa} approaches critical height of fall, H_c , these curves drop sharply to reach $D_{rpc}=0$ sharply, because, $H_f > H_c$ no more increases density. Hence, it is concluded that raising SRA continually to maintain a constant H_f is highly desirable. In case this is not implemented for each operation, $H_d \leq 25$ mm should be adopted which would be very cumbersome and slow process to prepare test samples.

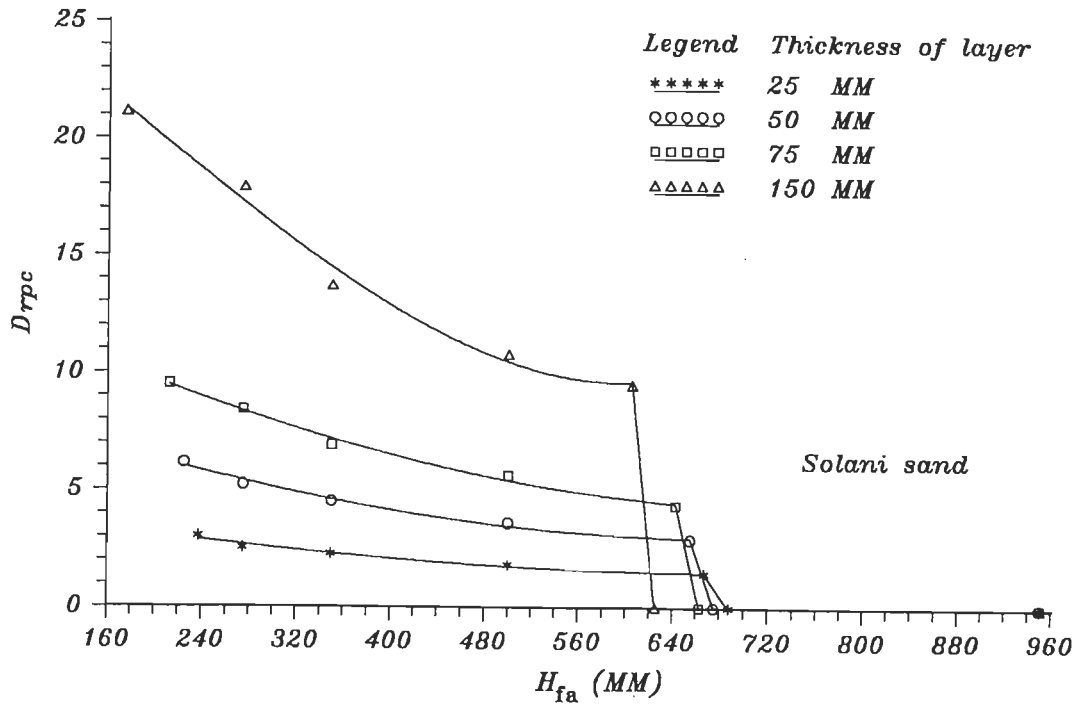


FIG. 3.2.16 VARIATION OF %CHANGE IN RELATIVE DENSITY, D_{rpc} , WITH ACTUAL AVERAGE VALUE OF HEIGHT OF FALL, H_{fa} .

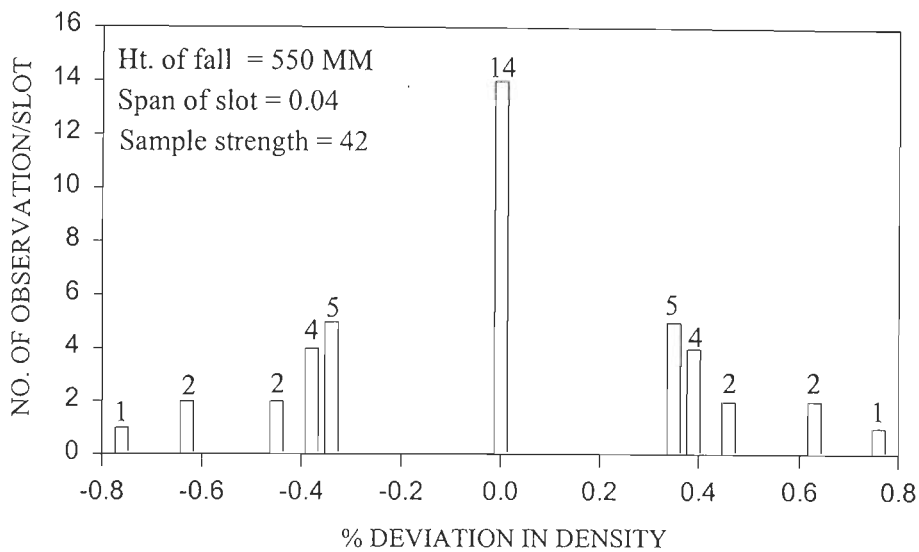


FIG. 3.2.17 VARIATION OF REPETITION OF DENSITIES OF DIFFERENT % DEVIATION FOR STUDY OF REPRODUCIBILITY.

Reproducibility of density

To evaluate spatial and temporal reproducibility of density, three tests were performed for the same H_f with 14 density samples obtained from each test to give a total of 42 samples. Figure 3.2.17 shows % deviation and number of observations for density obtained for $H_f = 550$ mm. It may be observed that 14 observations were obtained with zero % deviation which accounts for one third of the total observations. Besides, 86.7% of observed densities were obtained with an error of $\pm 0.47\%$ or less. The largest percentage deviation of $\pm 0.76\%$ was associated with only 4.76% of observed densities. This is much better than error margin of 1% reported by Passalacqua (1991) and 2.163% worked out for results of Fairless (1989).

Uniformity of density in a horizontal layer

To ascertain uniformity of density distribution in a horizontal layer, average values of densities obtained along various strips of layer for longitudinal and transverse directions have been considered. Percentage deviations and mean % deviations based on these densities are plotted as functions of distance from the longitudinal side in Fig. 3.2.18 and from transverse side in Fig.3.2.19 for various H_f . It may be observed that the maximum % deviation from mean value is + 0.78 % and -0.88 % for variation along the longitudinal side and + 0.45 % and -0.17 % for the transverse side. These % deviations are much smaller and considered reasonable. Results reported in other investigations have not been presented in a style to enable such a quantitative comparison with results of this study.

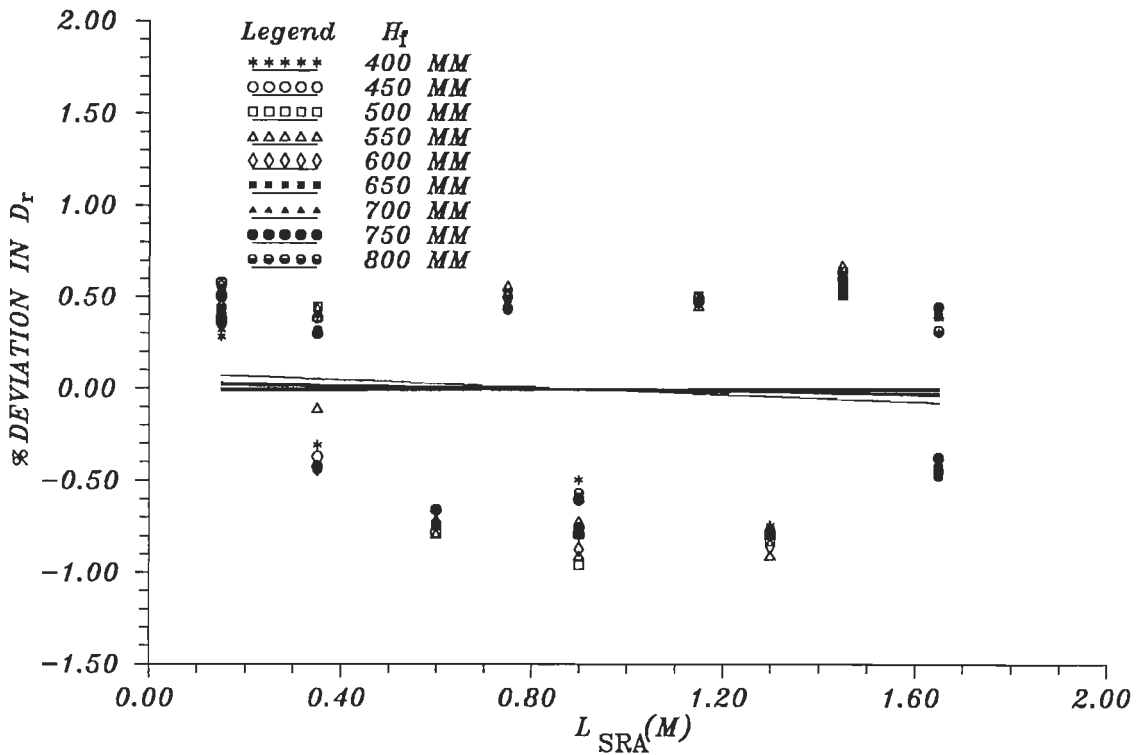


FIG.3.2.18 VARIATION OF MEAN % DEVIATION IN D_r WITH DISTANCE FROM LONGITUDINAL SIDE, L_{SRA} .

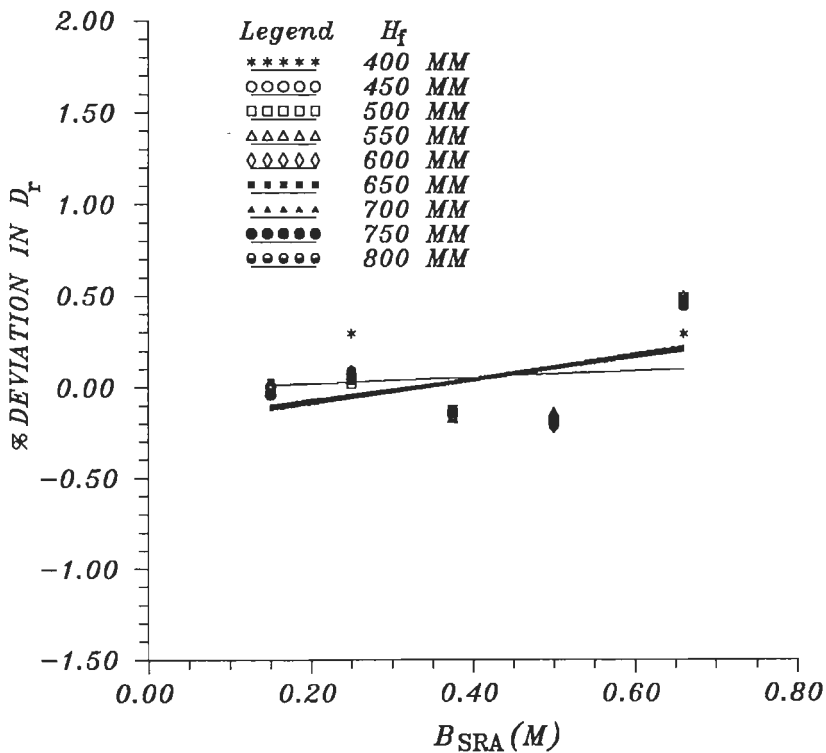


FIG.3.2.19 VARIATION OF MEAN % DEVIATION IN D_r WITH DISTANCE FROM TRANSVERSE SIDE, B_{SRA} .

3.3 SHAKE TABLE FACILITY

Shake table with sinusoidal excitation at various frequencies and dynamic force levels was used for testing embankments placed on the table. Details of excitation facility, geometry of table etc. are discussed here.

3.3.1 The Shake Table

Shake table is 2 m long and 1 m wide. The M.S. Steel plate of the table is 10 mm thick welded to a channel of 100 mm x 50 mm size on each side along the length. Eight I-beams of the same height and same flange width are provided at equal C/C spacing along the length. The table is provided with two wheels on knife edge supports along each longitudinal support to facilitate its movement in longitudinal direction (Fig. 3.3.1).

The table is provided with a rectangular frame, 1.5 m deep, running along the periphery of table (Fig. 3.3.1). The frame is strengthened with suitably designed vertical, horizontal and diagonal members connected by nuts and bolts to the table. Corner joints of the frame are welded. Frame is stiff enough to make its natural frequency much larger than the range of excitation frequencies used. The frame is used to hold the form work of the test embankment during its preparation.

3.3.2 Driving Mechanism

The table is excited by a mechanical oscillator driven by DC motor (Fig. 3.3.1). The oscillator consists of eccentric masses driven by two axes rotating in opposite directions. Vertical components of centrifugal forces

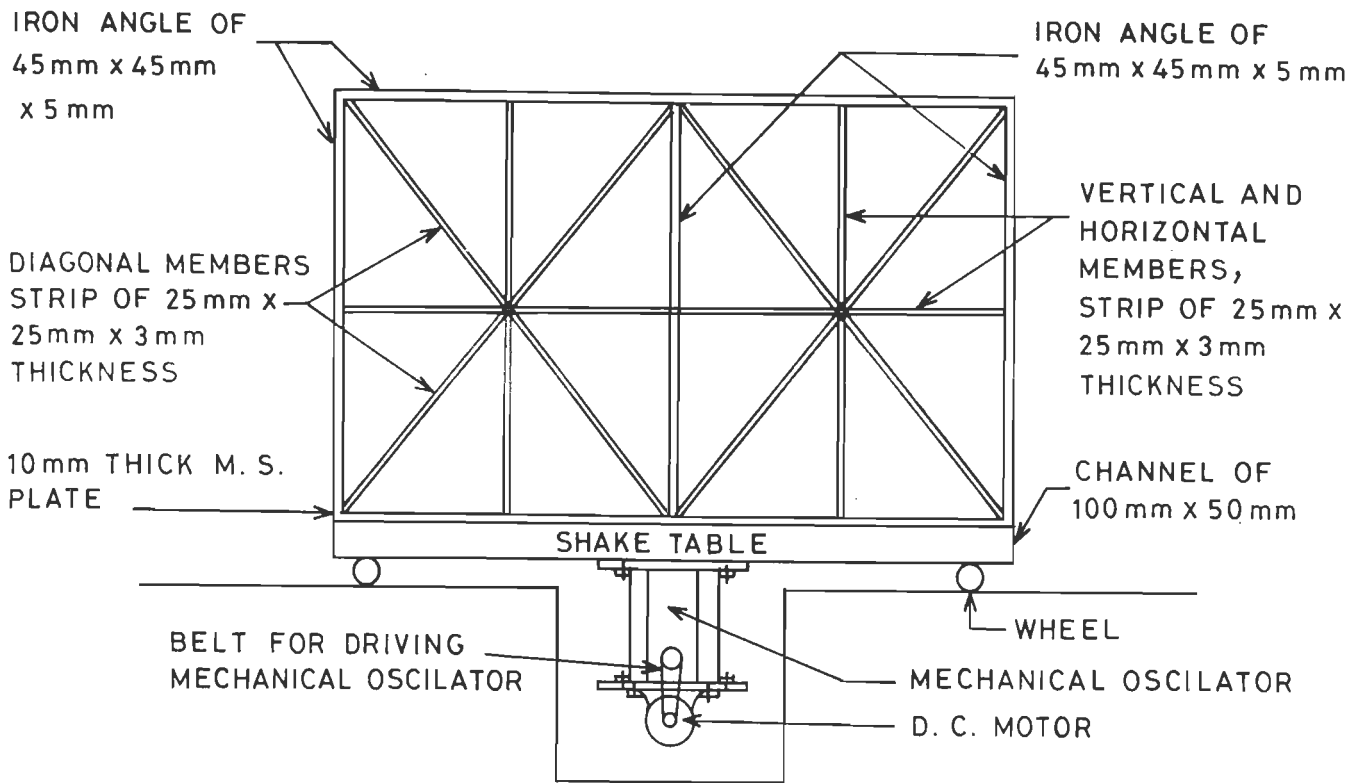


FIG.3.3.1 DETAILS OF SHAKE TABLE ASSEMBLY.

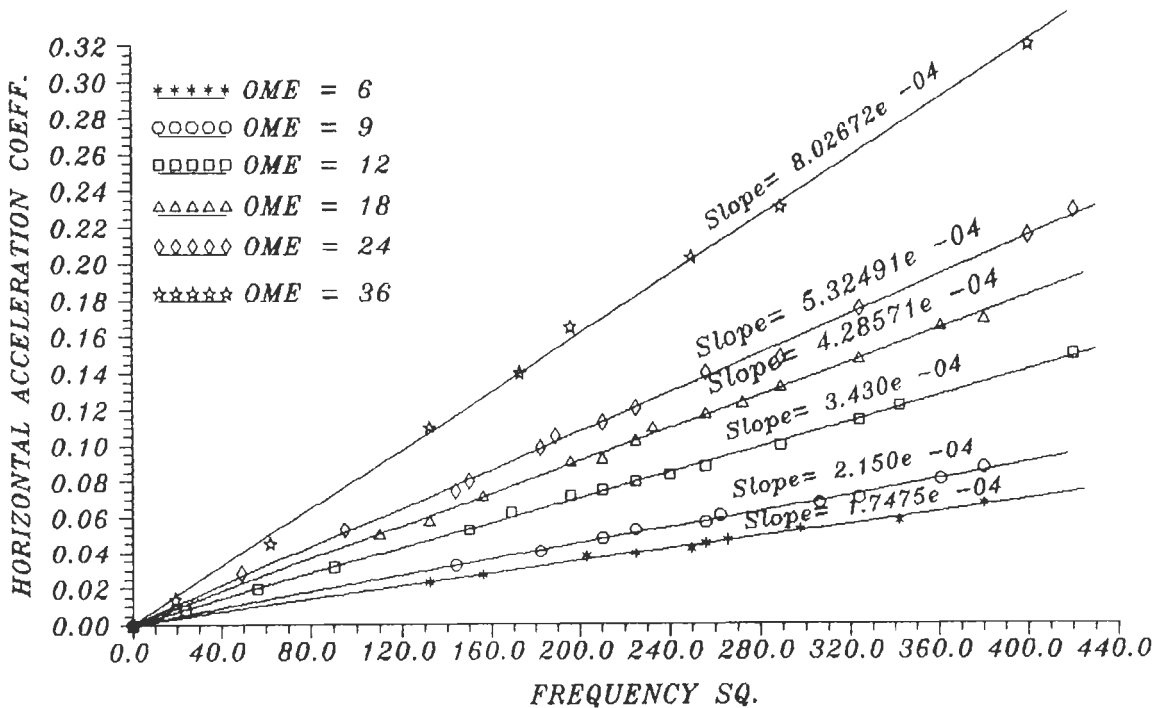


FIG.3.3.2 VARIATION OF HORIZONTAL ACCELERATION COEFFICIENT AT BASE OF SHAKE TABLE WITH SQUARE OF FREQUENCY OF SHAKE TABLE OSCILATOR IS SET TO DIFFERENT POSITION OF ITS ECCENTRICITY NUMBER (OME) AND REINFORCED EARTH TEST EMBANKMENT BEING MOUNTED ON TABLE.

generated by rotating masses get cancelled and horizontal components get vectorially added to generate sinusoidal forcing. The eccentricity of masses can be varied from 0 to maximum by turning a lever. The eccentricity range is divided into 36 equal intervals. Level of eccentricity of oscillator is increased/decreased in simple multiples of these intervals and denoted by Oscillatory Mass Eccentricity (OME) from 0 to 36.

The power axis of Oscillator is driven by a 5 HP, 3 phase DC compound motor by using a belt drive. Operating range of RPM of DC motor is from zero to 1500 which is more than adequate for tests in this study. Varic type of speed control unit to controls the motor speed. By using different motor speeds and different OME values, it is possible to obtain different levels of forces at the same frequency and different levels of forces at the same OME value.

For an oscillator with a pair of eccentric masses totalling to m_e and with an eccentricity e_c rotating with angular velocity ω per second, the maximum amplitudes of force, F_{amx} , generated is given by :

$$F_{amx} = M_e e_c \omega^2 \quad (3.3.1)$$

From above equation, it may be noted that the force increases linearly with ω^2 for any OME. Figure 3.3.2 shows coefficients of accelerations of shake table (obtained from its recorded accelerations from tests with embankment mounted on table) at different frequencies and OME. It may be observed that horizontal acceleration coefficient of table varies linearly with square of frequency for each OME as indicated by the equation cited above.

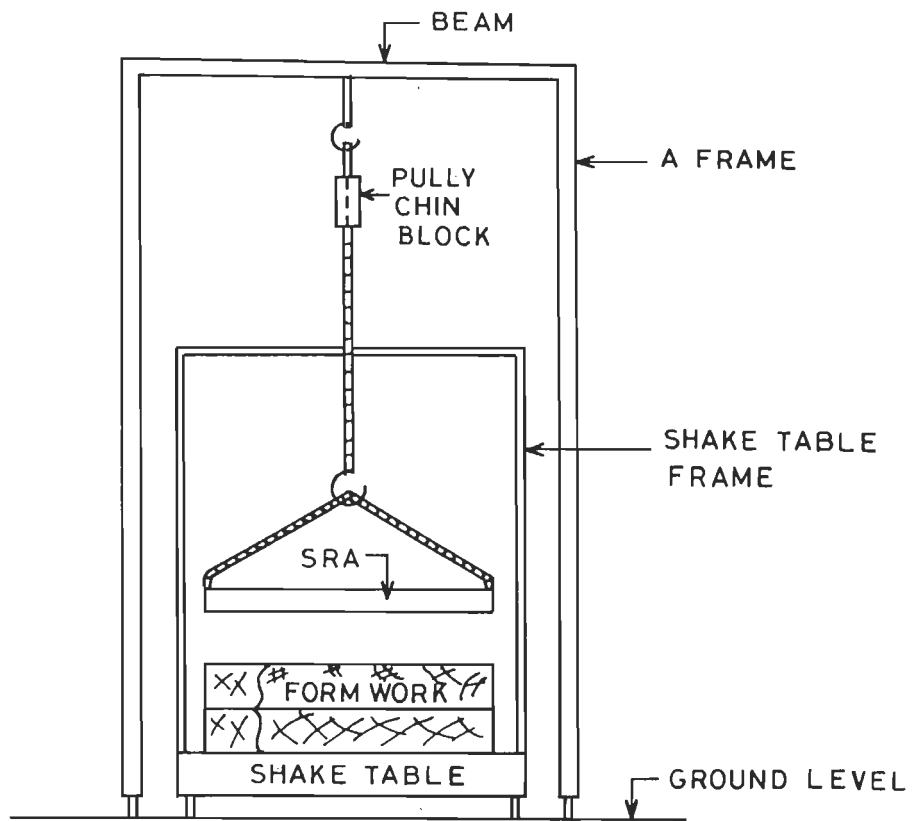
3.4 SUSPENSION OF SRA

The SRA is positioned directly above the test bed by suspending it from the horizontal beam using a chain pulley block to adjust its height above test bed to desired value. The horizontal beam is supported by two A-frames (one on each side of the table) mounted on wheels to move in longitudinal direction. Height of the horizontal beam can be varied by controlling the length of adjustable horizontal connecting members. Enough clear space is provided between A-frames and the table (Fig. 3.4.1). After suspending SRA at desired height, it is tied to legs of A-frame by using steel wires to prevent its horizontal oscillations.

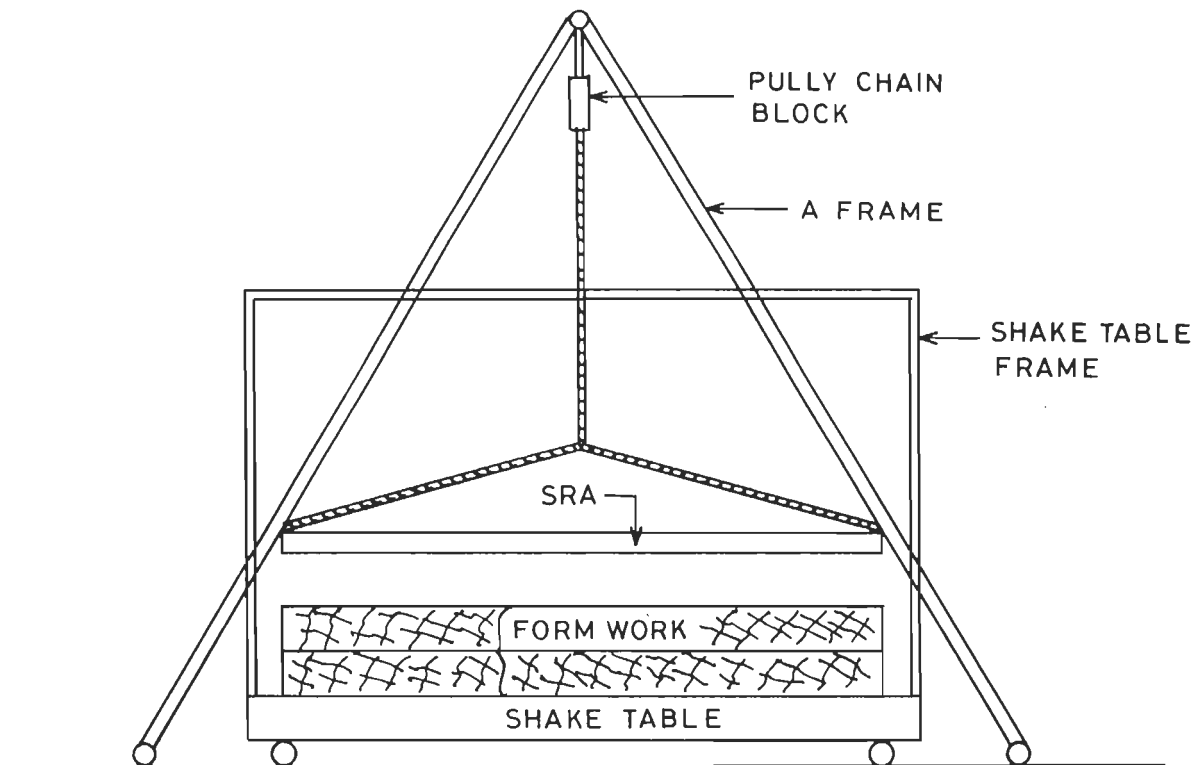
3.5 FORM WORK

The construction of embankment is made by using six layers. Form work for constructing and supporting test embankments is also provided with six separate frames, one for each layer. Plywood planks (12 mm thick, 150 mm high) form sides of each frame. Longitudinal planks are stiffened along length by screwing them to m.s. angles. Longitudinal and transverse planks are connected at corner junctions by using 150 mm long vertical m.s. angles screwed to them to form rectangular frames. Frames are positioned properly by bolted connections to rectangular steel frame of table (Figure 3.5.1). Shorter sides of form work (750 mm long), suitably connected to reinforcements, also work as facing elements of test embankments. Further details in this regard are given in Chapter IV.

A dummy frame similar to frames of form work is placed on top of usual form work to stop sand raining from SRA from falling out side the test bed



SIDE VIEW



FRONT VIEW

FIG. 3.4.1 ARRANGEMENT FOR SUSPENSION OF SRA.

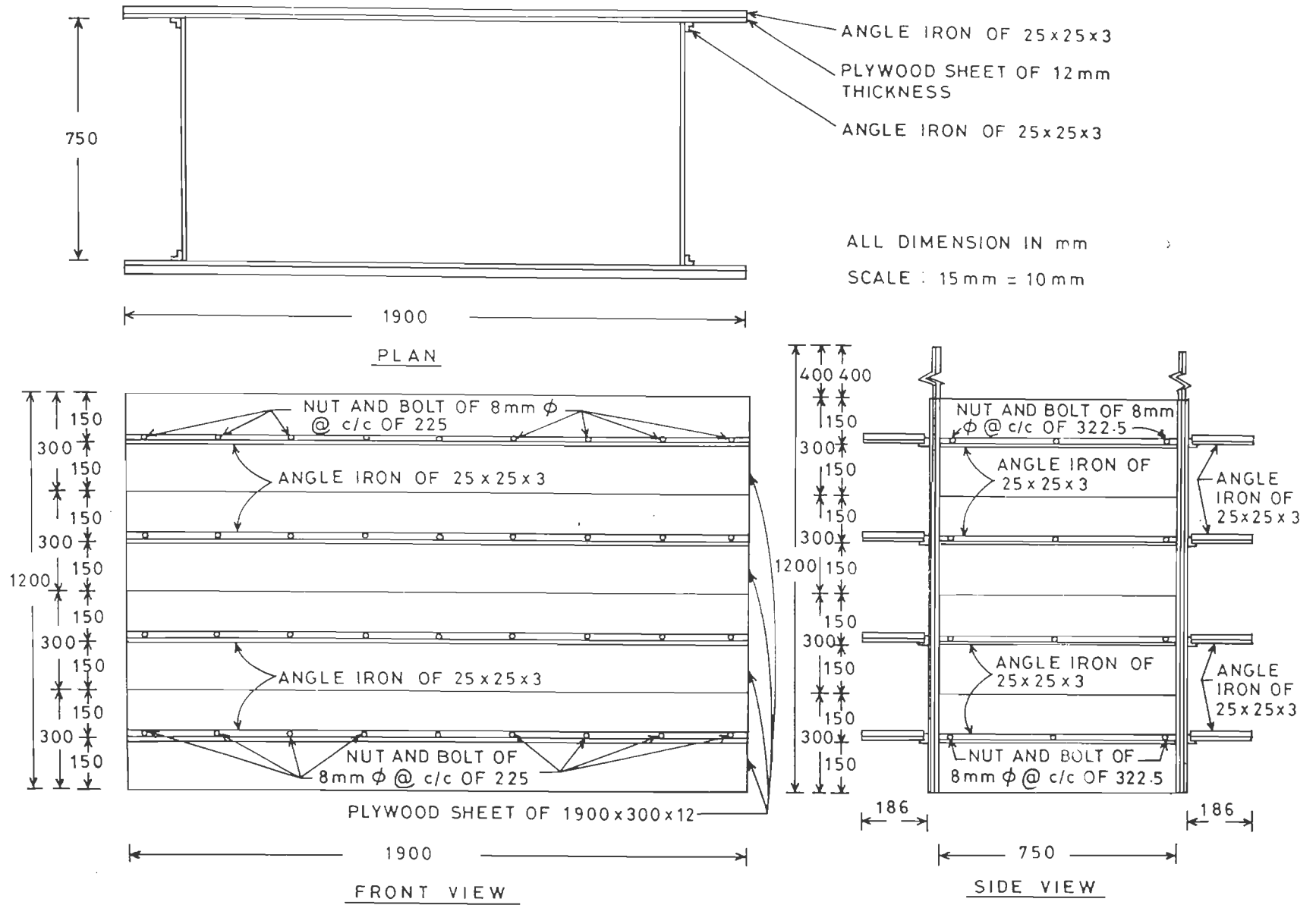


FIG. 3.5.1 DETAILS OF FORM WORK FOR PREPARATION OF TEST EMBANKMENT.

and to stop dust clouds from escaping out side. This is further assisted by plastic sheet suspended inside form work by securing to base of SRA.

Transverse sides of embankment should be in plane strain condition. Transverse planks of form work ensure it during construction. On removing these planks at the end of construction, transverse embankment sides are maintained in plain strain condition by enclosing these sides by using geotextiles reinforced by G.I. sheet panels connected to opposite panels on other transverse face by steel wires described in detail in Chapter IV.

3.6 MEASURING EQUIPMENT

Embankment behaviour under dynamic loads was studied from tests by measuring horizontal acceleration of table and embankments on longitudinal facing elements at 425 and 875 mm above table. Reluctance type acceleration pickups were used whose output was recorded by using universal amplifiers and ink type of strip chart recorders with speeds of 5, 25 and 125 mm/sec.

3.7 CLOSURE

Details of test setup have been dealt with in this chapter. A manually operated sand rain apparatus has been developed using which tests were performed to study its performance. Important points summarized are:

- i) The developed SRA is capable of raining sand over the entire test bed to obtain relative densities upto 76.64% for the Solani Sand.
- ii) Mean standard deviation as a function of H_f was 1.08%.

- iii) Maximum percentage deviation from mean is +0.78 and -0.88% along length and +0.45% and -0.17% along width of bed. Density reproduction with $\pm 0.47\%$ deviation was possible for 86.7% of density observations.

Above performance is better than that of more sophisticated SRA with electrical/electronic controls reported in the state of art and, hence, useful for preparation of R.E. test embankments for this investigation.

EXPERIMENTAL STUDIES USING SHAKE TABLE AND BACK-ANALYSES

4.1 PREAMBLE

Experimental studies were carried out on sandy fill to establish its material properties. Material properties of geotextiles supplied by manufacturers were used. A stress control apparatus for obtaining static pullout resistance was developed and a number of tests were carried out to obtain pullout resistance of three geotextiles. Parametric studies have been carried out to study the effect of different widths of reinforcement and different densities of the soil on pullout resistance. Based upon the results obtained, choice of the geotextile for dynamic investigations has been made.

It is proposed to study response of R.E. embankments vibrating in shear mode. Embankment dimensions were chosen to ensure this behaviour. Embankments were prepared on shake table. Suitable devices were developed to ensure plane strain behaviour in longitudinal direction. Embankments acceleration response and base excitations were measured to study effect of different types of reinforcements and different base excitation parameters on amplification of response. Back-analyses of results of dynamic tests were carried out to obtain relationships between shear modulus, shear strain, frequency, phase angle, horizontal acceleration, disturbing force and coefficient of average dynamic pullout resistance of reinforcements.

In this chapter, details of experimental studies and back-analyses of results are dealt with and results compared with those reported by other investigators in the state of the art.

4.2 MATERIAL PROPERTIES OF SOIL AND GEOTEXTILES

4.2.1 Material Properties of Soil

Cohesionless soil used for this study is air dried, clean, angular and fine grained Solani sand of Roorkee. Tests were carried out to determine its material properties.

Sieve analysis

Sieve analysis was performed as per Indian standard code of practice (IS:2720-IV, 1975) to obtain grain size distribution curve (Fig.4.2.1a), from which particle sizes D_{10} , D_{30} , D_{50} , D_{60} corresponding to 10,30,50 and 60% finer fractions as well as uniformity coefficient and coefficient of curvature were obtained (Table 4.2.1). The sand is classified as poorly graded sand (SP) as per IS classification of soils (IS:1948; 1970). The photograph of sand (Fig. 4.2.1b) shows that its grains are angular.

Specific gravity test

The specific gravity of the mineral of soil grains has been determined as per Indian Standard Code of Practice (IS:2720-III 1964). Table 4.2.1 indicate the value of the specific gravity obtained.

Density

Minimum density of soil was obtained by using method of Kolbuzewski (1948) with air dried sand. Maximum density was determined by using CBR mould on shake table. Table 4.2.1 shows these densities and void ratios.

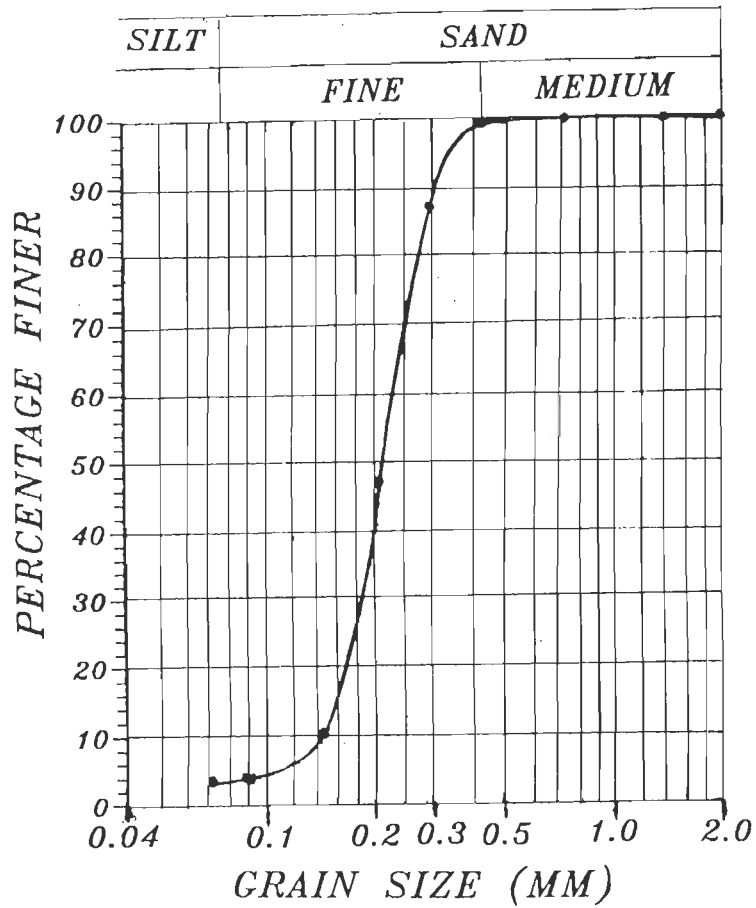


FIG. 4.2.1a GRAIN SIZE DISTRIBUTION CURVE FOR SOLANI SAND.



FIG. 4.2.1b MICROSCOPIC VIEW OF SOLANI SAND GRAINS (GUPTA, 1977).

Table 4.2.1 - Properties of Solani Sand

S.NO.	ITEM	VALUE
1.	Soil type	SP
2.	Effective size, D_{10}	0.15 mm
3.	Gram size, D_{30}	0.19 mm
4.	Grain size, D_{50}	0.21 mm
5.	Grain size, D_{60}	0.23 mm
6.	Uniformity coefficient, C_u	1.53
7.	Coefficient of curvature, C_c	1.04
8.	Specific gravity	2.59
9.	Minimum voids ratio	0.48
10.	Maximum voids ratio	0.86
11.	Minimum density of the sand	1.39 t/m ³
12.	Maximum density of the sand	1.75 t/m ³
13.	Angle of shearing resistance, ϕ for	
	Relative density 54%	33.42°
	Relative density 62.2%	35.44°
	Relative density 70%	44.44°

Direct shear-test

Angle of shear resistance, ϕ , was obtained by performing direct shear tests as per Indian standard code of practice (IS:2720-XIII, 1972) at relative densities, D_r , of 54%, 62.2% and 70%. Figure 4.2.2(a) shows stress strain relationships obtained for tests with 70% D_r . Mohr Envelope obtained (Fig. 4.2.2b) from test results gave $\phi = 44.44^\circ$ for this D_r . Similar plots were obtained for other densities. Table 4.2.1 shows values ϕ obtained.

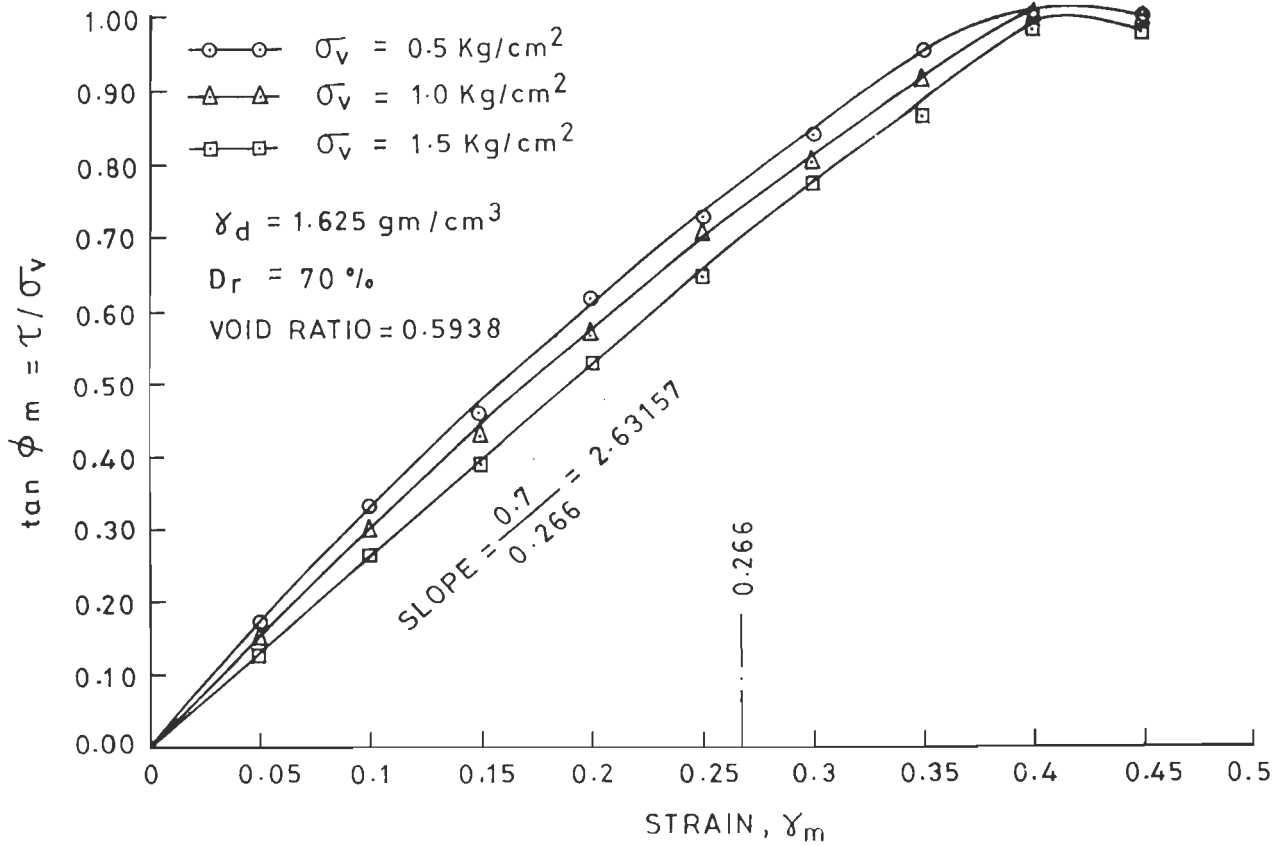


FIG. 4.2.2a STRESS-STRAIN RELATIONSHIPS FOR SOLANI SAND. (DIRECT SHEAR TESTS)

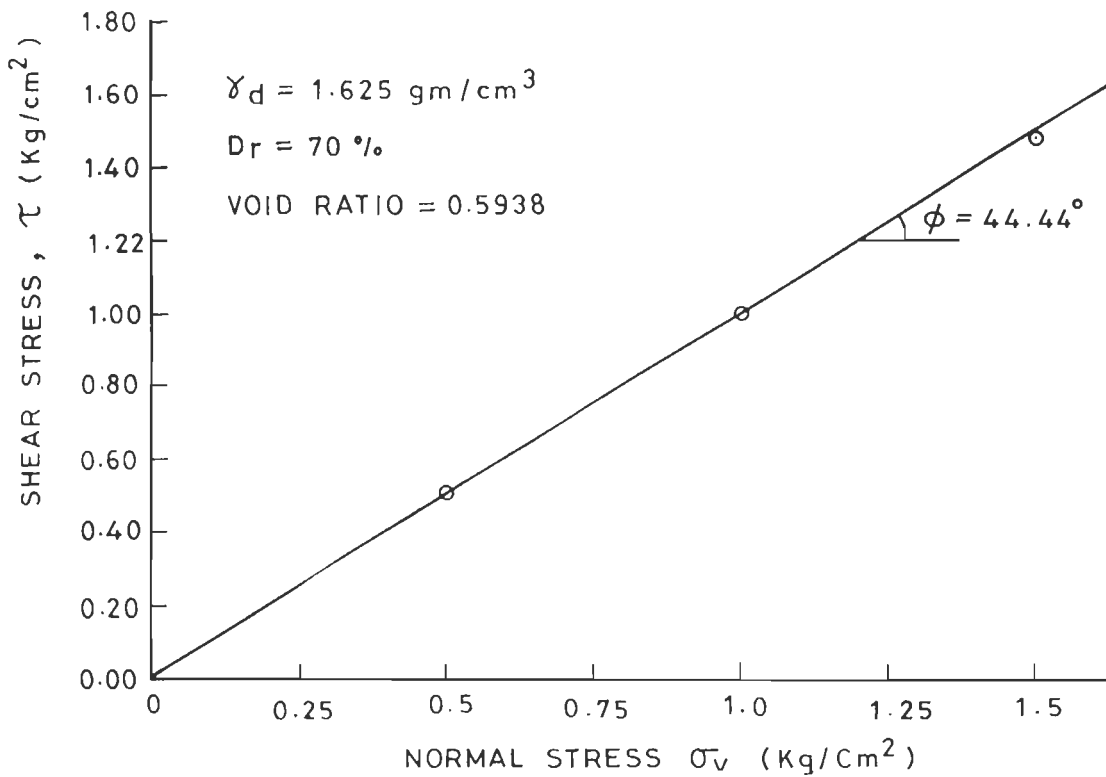


FIG. 4.2.2b MOHR ENVELOPE FOR SOLANI SAND (DIRECT SHEAR TESTS).

4.2.2 Material Properties of Reinforcements

One woven and two nonwoven geotextiles were used in this study. Material properties like grab strength and percentage elongation etc. for these materials were supplied by manufactures. Table 4.2.2 and Table 4.2.3 show these material properties which were used in this study.

4.3 STATIC PULLOUT RESISTANCE

Reinforcement, while being pulled out from fill, resists pullout force due to resistance developed along the soil-reinforcement interface. As such, pullout resistance is basic design data for design of R.E. structures and obtained by using a test setup similar to direct shear box or by pulling reinforcement out from large test/prototype R.E. embankments. However, the latter methods are difficult to carryout, time consuming and costly. Moreover, strain control equipment used for its determination are inferior to stress control type of facility which allows enough time for applied load to facilitate occurrence of full pullout displacements. Hence, development of a stress control type of test facility for this purpose is warranted.

4.3.1 Stress Control Apparatus for Pullout Resistance

Stress control type of apparatus developed for determination of pullout resistance employs direct shear type of box housing 300 mm x 300 mm x 100 mm deep soil sample (Figure 4.3.1). The geotextile embedded within soil sample is pulled out through the small gap between upper and lower parts of box. The thickness of gap is controlled by placing adequate number of 0.5 mm thick G.I. strips between the parts so that the gap is slightly larger than thickness of geotextile. Ribbed plates were placed at top and bottom of soil sample for good grip. Normal reaction was applied by using a yoke connected

Table 4.2.2 Material Properties of Woven Geotextile RE1

Quality no. Specification	PD 380/B
1. Material	100% Polypropylene
2. Specific gravity	0.91
3. Weight/sq. metre in grams	276.00
4. Thickness in mm	0.68
5. Breaking strength (5x20 cms) (IS-1969-1963)	
Warpway (kg)	245.7
Weftway (kg.)	182.0
6. Elongation at break percentage (IS-1969-1963)	
Warp	46.9
Weft	27.8
7. Grab strength test (3" x 1" strip) (ASTM-D-1682)	
Warpway (kg)	214.8
Weftway (kg)	152.8
8. Elongation % (Grab test) (ASTM-D-1682)	
Warpway	45.3
Weftway	30.3
9. Tear strength (single rip) (ASTM-D-2261)	
Warpway (kg)	21.2
Weftway (kg)	18.0
10. Water Permeability (Liters/sec/metre) at 10 cm water head)	4.2
11. Pore size in microns	
Mean	25.0
Max.	69.0

Table 4.2.3 Material Properties of Nonwovens Geotextile (RE2 and RE3)

Quality No. Specification	CNPP-1(8)	CNPP-4(5)
1. Material	100% polypropylene	100% polypropylene
2. Weight (gms/sq.mtr.)	150	450
3. Thickness (mm)	1.8	3.7
4. Pore size	63	< 63
5. Tensile strength		
M/D kgf	20	80
C/D kgf	24	95
6. Elongation %		
M/D	80	75
C/D	85	70
7. Mullen Bursting Strength kg/sq.cm.	13	35

to a beam with reaction type of loading which is superior to the set up employing reaction type of loading using hydraulic jacks, because, jacks

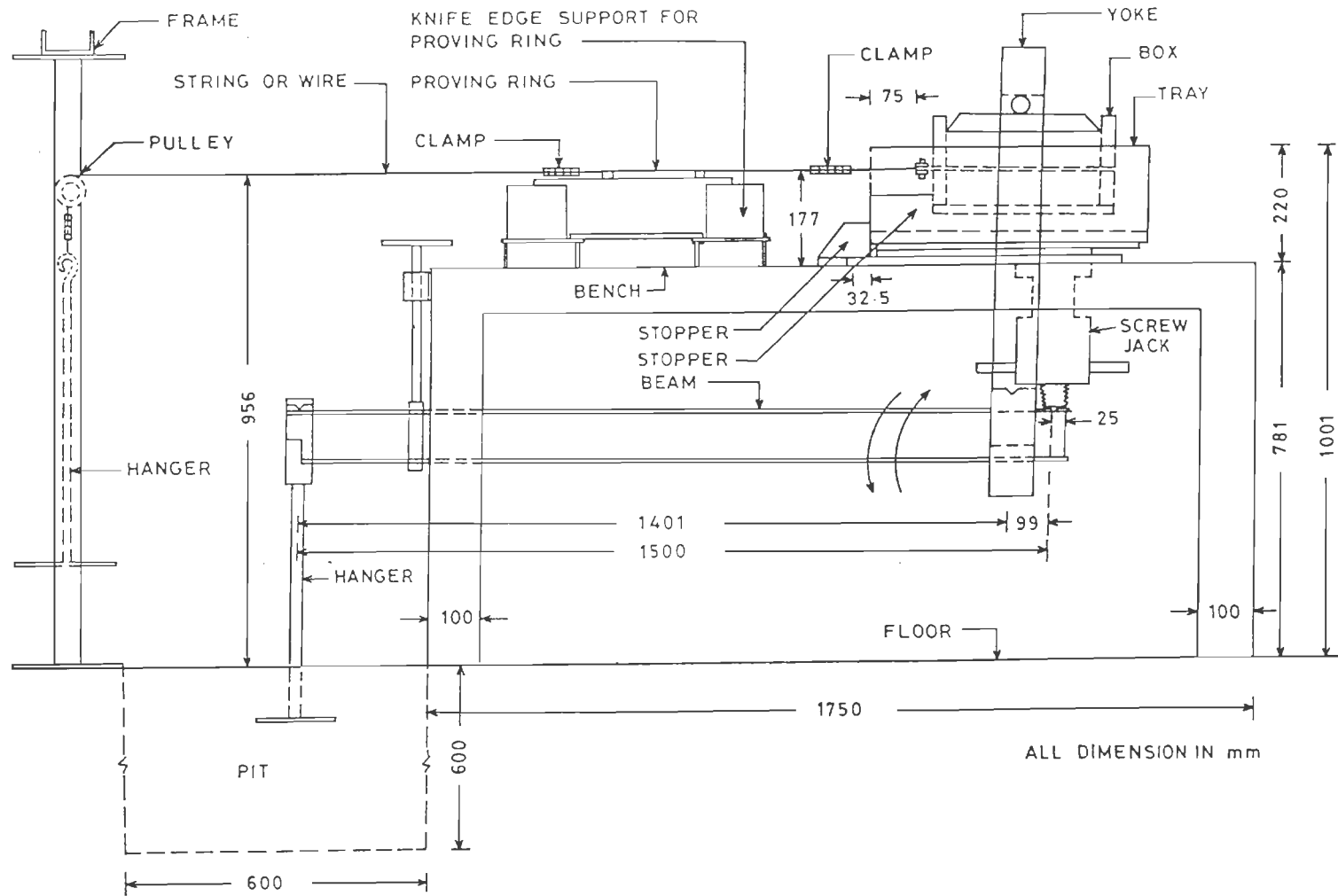


FIG. 4.3.1 SCHEMATIC DIAGRAM OF STRESS CONTROL TYPE OF APPARATUS FOR STATIC PULLOUT RESISTANCE.

need continuous adjustment to maintain constant normal loading in view of settlements. The box is housed inside a large tray (Fig. 4.3.1). Weights are placed on the hanger at the free end of beam having a lever arm ratio of 1:14 to obtain the desired normal stress σ_v . reaction type of loading with gravity weights used in this set up

Geotextiles of initial embedded length of 295 mm and widths of 100, 200 and 290 mm were used. Outer free end of the geotextile was gripped between two rough M.S. strips, 25 mm wide, 5 mm thick and 300 mm long, held together by four bolts of 6.35 mm (0.25 inch) nominal diameter. Pullout force was applied to fabric through grip designed to take 400 kg force applied through two flexible clutch wires (1.5 mm dia.) tied to grip. These wires passing over a pulley were tied to a hanger which receives weights to apply desired pullout force (Fig. 4.3.1). A proving ring on knife edge support, placed close to box, measured tension in wire. Suitable M.S. clamps held wires tightly wherever necessary. Dial gauge of 0.01 mm least count, fitted on bench by using magnetic base, measured horizontal pullout displacements. Tip of dial gauge rod butted against a vertical metal plate attached to grip to measure pullout displacements. Two dial gauges with 0.01 mm least count, mounted on box top using magnetic base and placed at opposite diagonal ends of box measured vertical settlements.

Calibration of proving ring

Proving ring (RC 519) of 500 kg capacity was hung from a frame using clutch wires. A hanger suspended to lower end of proving using clutch wires received incremental weights and corresponding proving ring dial gauge readings noted in three cycles of loading and unloading. Calibration chart

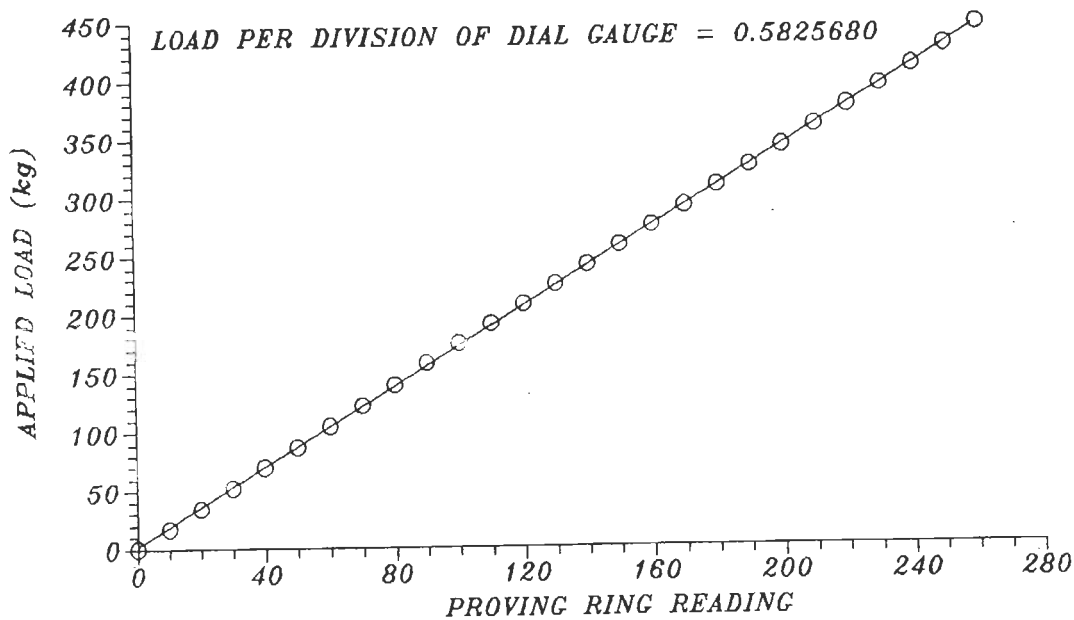


FIG.4.3.2 CALIBRATION CHART FOR PROVING RING (RC. 519) IN TENSION.

thus prepared for proving ring (Fig. 4.3.2), shows elastic behaviour of ring upto maximum load of 260 kg. Figure 4.3.3 shows test set up used.

4.3.2 Test Procedure

Lower half of the direct shear box was placed in a tray, butting against rear tray wall. Movement of box transverse to loading direction was restrained by four stoppers within the tray. Tray was fixed to the bench suitably. Solani sand of pre-determined weight was rained in the lower half by using a funnel with a pipe of required length to give the desired drop height. Length and width of the box were scanned manually by moving the lower square end of vertically held pipe of the funnel. After filling lower half, soil surface was levelled by using a straight edge. Geotextile held by grip at one end was then placed on soil surface (Fig. 4.3.4). Required number of G.I. packing strips were then placed along longitudinal and rear sides of lower half. The top half was then placed, positioned and



FIG. 4.3.3 CALIBRATION SETUP FOR PROVING RING.

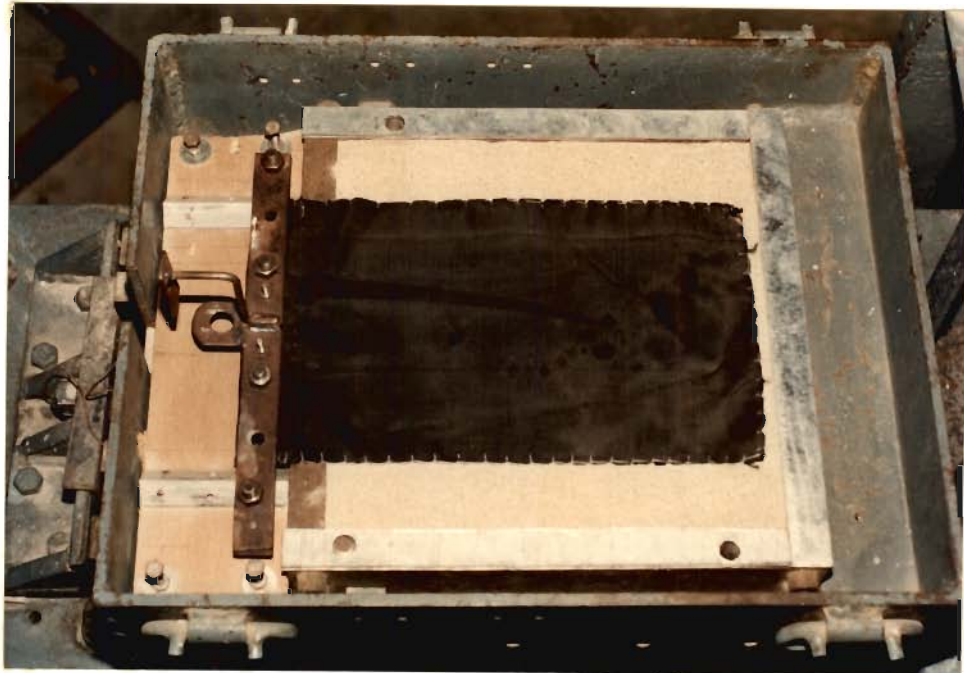


FIG. 4.3.4 LOWER HALF OF THE DIRECT SHEAR BOX FILLED WITH THE REINFORCEMENT WITH THE GRIP PLACED IN POSITION.

screwed firmly to lower half. Sand was again rained to fill upper half as usual to obtain 108.5 mm high sample. The surface was then levelled. Finished sample inside the box is shown in Fig. 4.3.5. Top plate of the box was then placed in position and its level checked by using a spirit level.

Dial gauges for measurements of settlements of top plate and pullout displacements were placed in position. Loading yoke was placed on top of steel ball on top plate. Beam for reaction loading was positioned and weights were placed on hanger of the beam to obtain desired normal stress on soil sample. Clutch wire assembly together with proving ring was secured to the grip. A hanger was suspended at its other end (Fig. 4.3.6).

A rough estimate of ultimate pullout resistance, P_{rmax} , was the product of normal force on soil and $\tan \phi$, ϕ being known angle of shear resistance of soil. Initially, to obtain pullout resistance at that displacement when slackness in fabric is overcome, small increments of 1.5% of estimated P_{rmax} were placed on hanger for 15 minutes. Most of the pullout displacement, d_p , occurred in about 1 minute duration and the maximum d_p was reached well within 15 minutes. After reading all dial gauges, next load increment was applied. This was repeated at such loading increments to reach about 6 % of estimated P_{rmax} . Then, load increment was doubled and the procedure repeated till applied load was about 13 % of the estimated P_{rmax} . Then, loading increment was further doubled and procedure repeated till the applied load was about 84 % of estimated P_{rmax} . At this stage, the applied load being close to P_{rmax} , a smaller increment of 3 % of the estimated P_{rmax} to obtain more accurately P_{rmax} and the associated pullout displacements. Figure 4.3.7 shows the test setup.

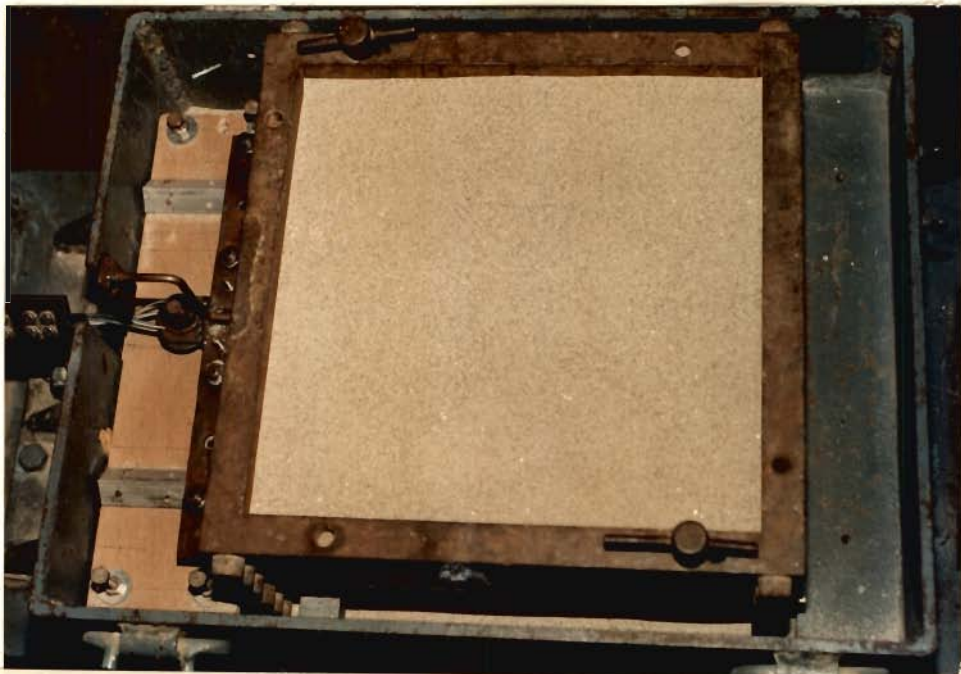


FIG. 4.3.5 THE FINISHED SOIL SAMPLE IN DIRECT SHEAR BOX.

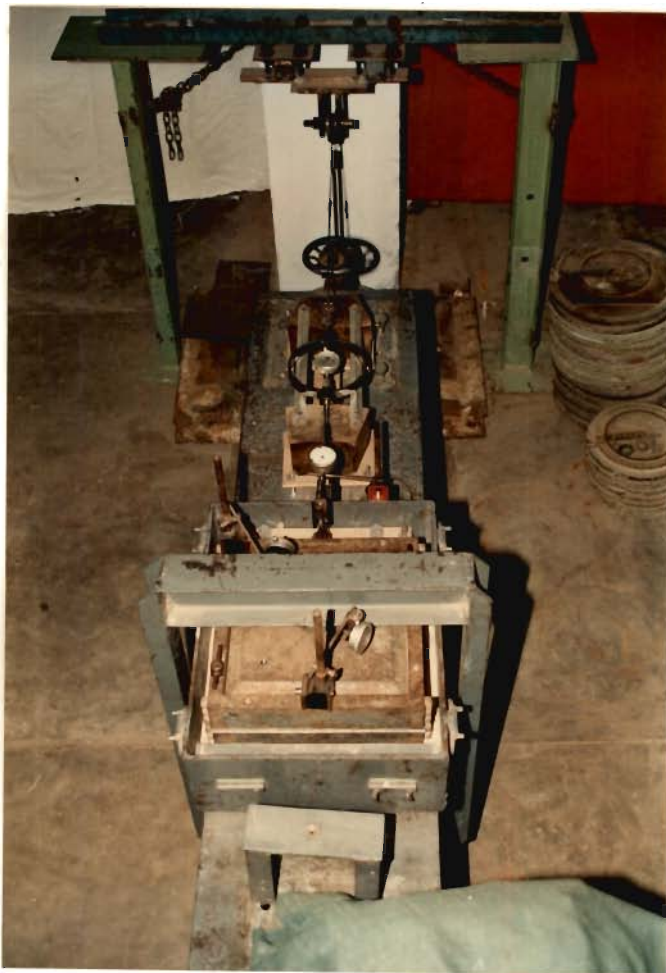


FIG. 4.3.6 TEST SETUP FOR PULLOUT RESISTANCE AT THE BEGINNING OF THE LOADING.



FIG. 4.3.7 TEST SETUP FOR PULLOUT RESISTANCE WITH WEIGHTS PLACED ON THE LOADING HANGER.

4.3.3 Results of Pullout Resistance Tests

Tests were performed using this setup to study pullout strain, time duration, type and width of geotextiles, soil density and normal stresses.

Reproducibility of results was studied by repeating each test twice using the woven geotextile, RE1, and Solani sand with relative density of 70% and subjected to normal stress of 0.435 kg/cm^2 . Figure 4.3.8 shows results from the two tests from which it may be noted that upto 63.5% of the P_{rmax} , results are identical. Beyond that, the maximum difference in pullout resistance obtained from two tests at any displacement is 6.22% only and the two P_{rmax} values differ by 1.79% only. Hence, it is concluded that reproducibility of results obtained by using this set up is good.

As cited earlier, stress control setup has advantage of allowing enough time, t_p , for each load increment, Δ_p , to cause full pullout displacement, d_p . Figure 4.3.9 shows effect of t_p on d_p for various Δ_p . During the first minute of application of Δ_p , d_p increases very rapidly for all Δ_p . After that, rate of increase of d_p with time reduces and the maximum pullout displacement, d_{pmax} , for that Δ_p is reached after a duration t_p ranging from 3 to 30 minutes. Values of t_p is 3 minutes for $\Delta_p=5 \text{ kg}$ till pullout force, $P_s=20 \text{ kg}$ is reached. Table 4.3.1 gives Δ_p , P_s and t_p obtained from tests for P_s ranging from zero to $P_{smax}=310 \text{ kg}$. It may be concluded that for smaller Δ_p and smaller ratio, P_{sr} , defined as (P_s/P_{smax}) , values of t_p are smaller. As Δ_p and P_{sr} increase, t_p also increases to reach its maximum at P_{smax} (Fig. 4.3.10). This is reasonable, because, plastic displacements near P_{rmax} are large and require large time durations to get mobilised. On the other hand, for smaller values of Δ_p and P_{sr} , contribution of plastic

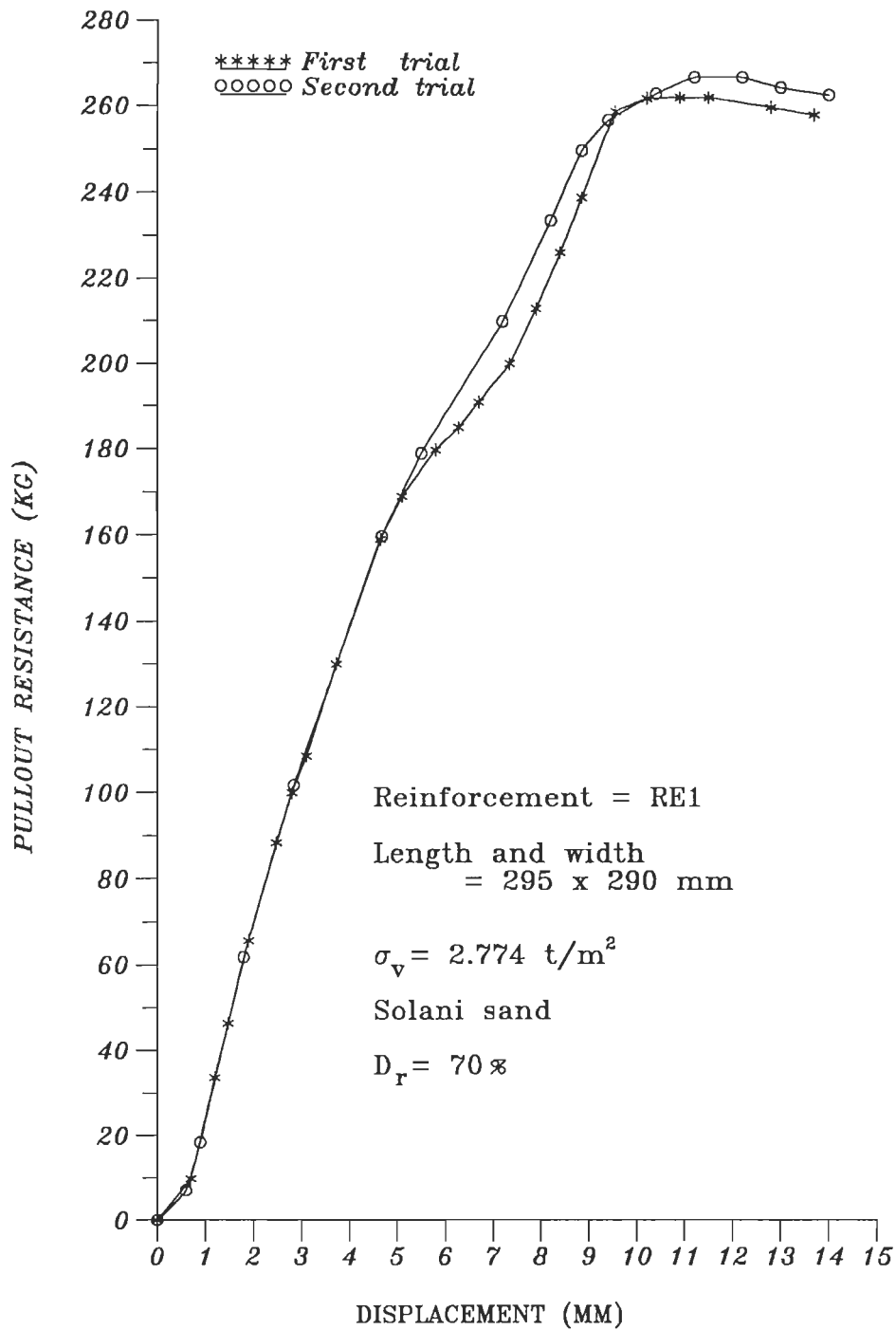


FIG. 4.3.8 RESULTS TO ESTABLISH OF REPRODUCIBILITY OF TEST RESULTS.

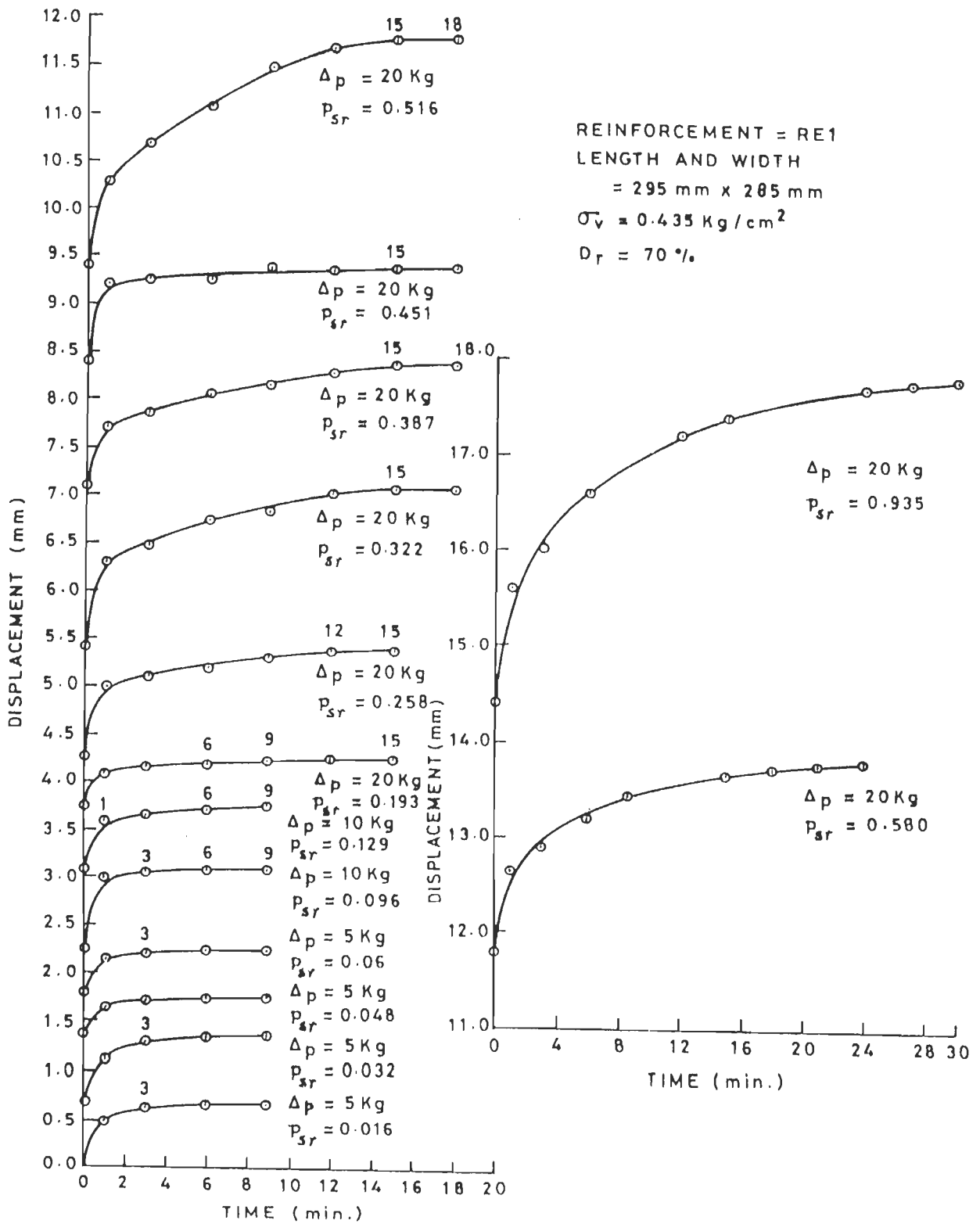


FIG.4.3.9 INFLUENCE OF THE TIME ON PULLOUT DISPLACEMENT USING WOVEN GEOTEXTILES REINFORCEMENT (RE1).

behaviour is negligible and larger contribution by elastic behaviour is mobilised in a relatively short time. Similar behaviour was observed during tests on woven fabric with different values of σ_v and D_r .

Similar tests were performed using nonwoven geotextiles RE2 and RE3 (Table 4.2.3). Figure 4.3.11 and 4.3.12 show pullout displacements as a function of time for different Δ_p for RE2 and RE3 respectively.

Table 4.3.1 Values of Δ_p , P_s and t_p from Pullout Tests on Geotextile RE1

Load increment, Δ_p , in kg.	5	10	20	10
Range of pullout force, P_s , in kg	20	20-40	40-260	260- $P_{smax}=310$
Time for full pullout displacement, t_p , in minute	0-3	9	15-25	26-30

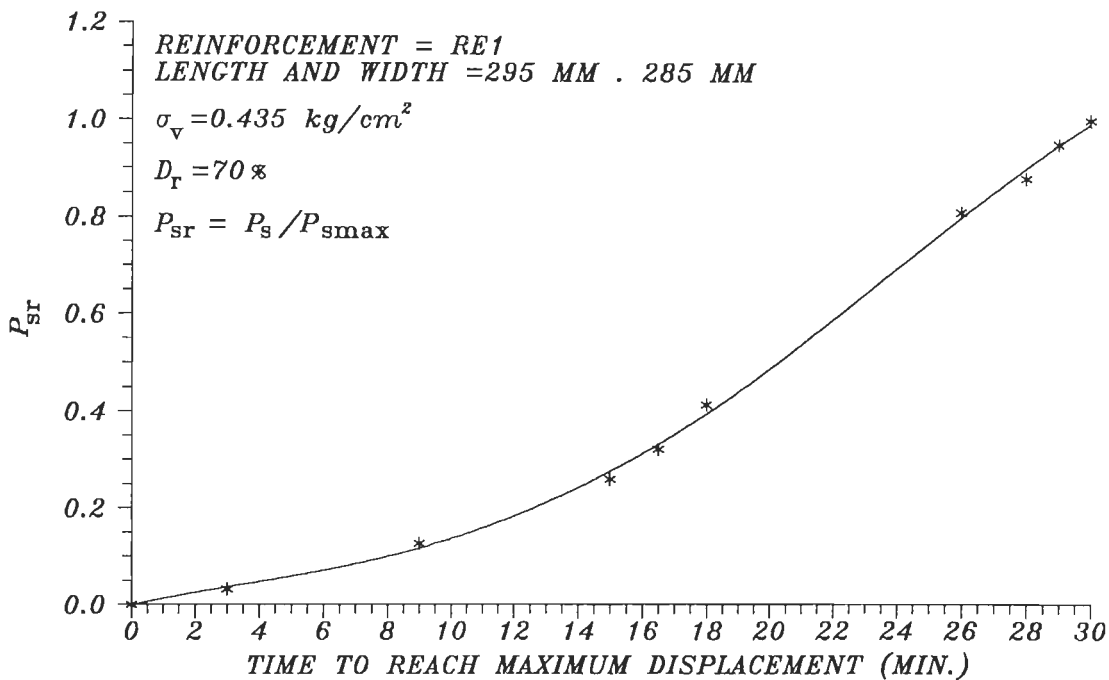


FIG.4.3.10 EFFECT OF RATIO OF PULLOUT FORCE, P_{sr} , ON TIME FOR REACHING MAXIMUM PULLOUT DISPLACEMENT, d_p .

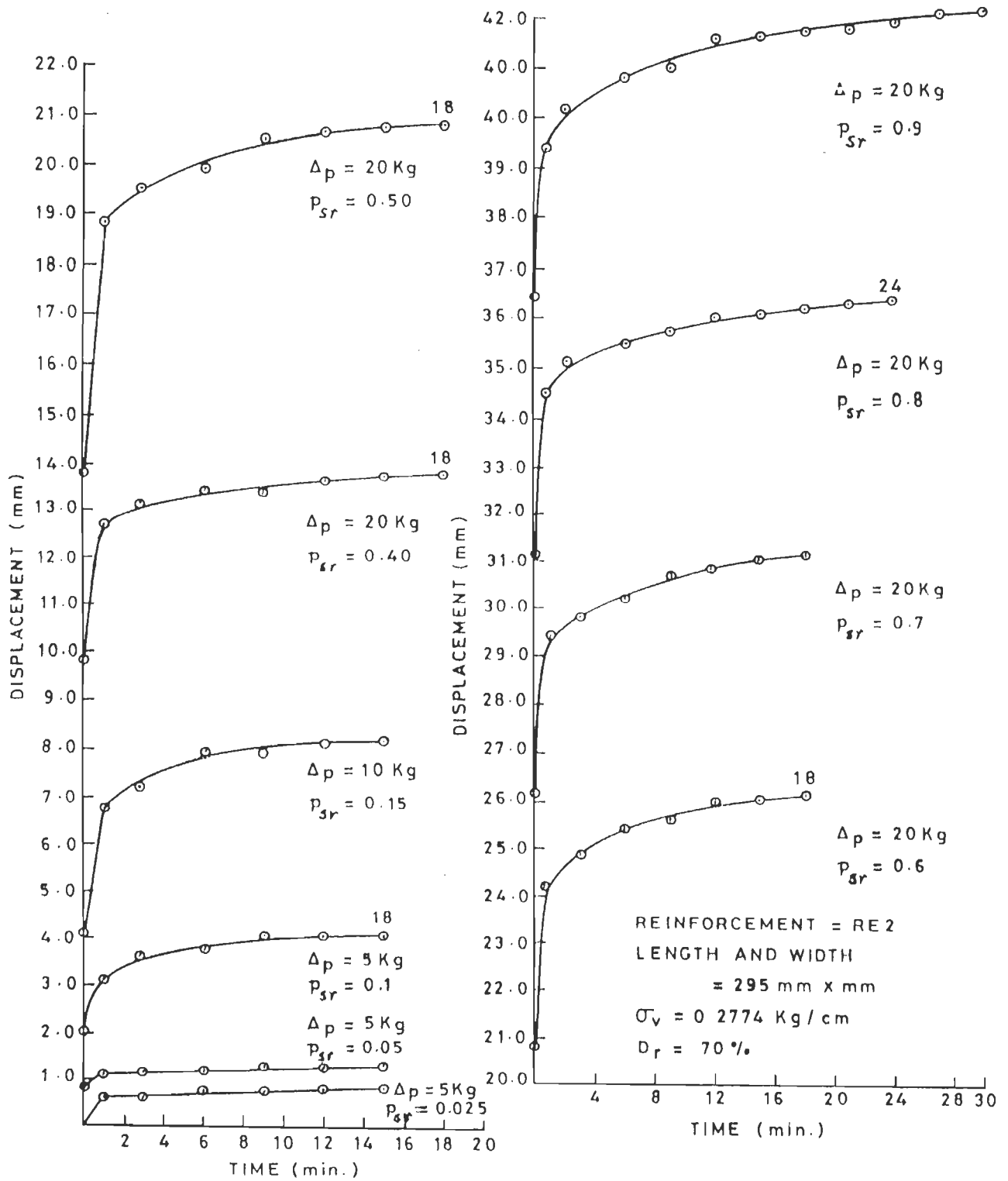


FIG.4.3.11 INFLUENCE OF THE TIME ON PULLOUT DISPLACEMENT USING WOVEN GEOTEXTILES REINFORCEMENT (RE2).

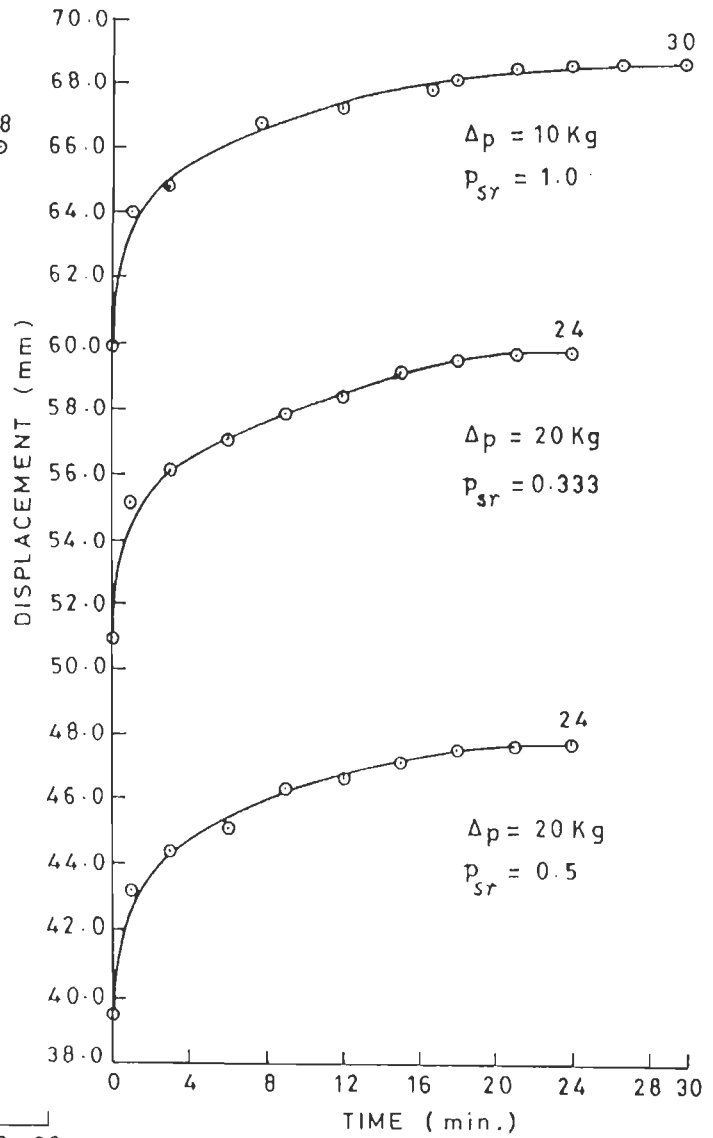
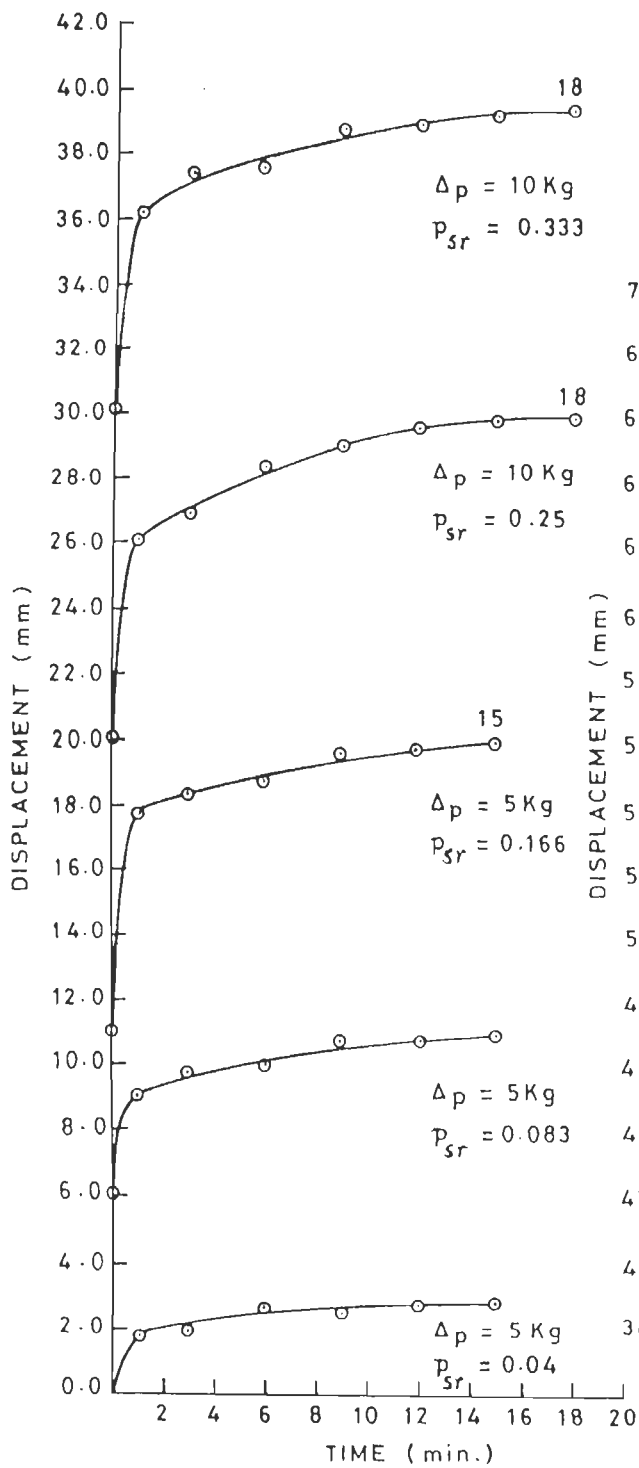


FIG.4.3.12 INFLUENCE OF THE TIME ON PULLOUT DISPLACEMENT USING NONWOVEN GEOTEXTILES REINFORCEMENT (RE3)

Static pullout resistance tests were performed using relative densities of 59%, 62.2% and 70.14% for sand; normal stresses of 2.774, 3.52 and 4.35 t/m²; and geotextiles of length 295 mm with widths of 100, 200 and 290 mm.

Table 4.3.2 Results of Pullout Tests Using Geotextile, RE1

Sl. No.	Width of reinforcement B_r (mm)	Normal stress σ_v (t/m ²)	Maximum pullout displacement d_{pmax} (mm)	Maximum pullout stress, τ_{pmax} (t / m ²)	Average angel of pullout resistance ϕ_p (degree)	Maximum average of coefficient static pullout resistance μ_{avsmx}
$\gamma_d = 1.565 \text{ t/m}^3$, $D_r = 54\%$, $\phi = 33.424^0$ and length of reinforcement, $L_r = 295\text{mm}$						
1	200	2.774	15.10	1.1577	22.113	0.4129
2	"	3.520	16.80	1.4400	"	"
3	"	4.350	18.50	1.8266	"	"
4	100	2.774	16.70	0.8700	17.294	0.3113
5	"	3.520	17.80	1.1100	"	"
6	"	4.350	18.90	1.3615	"	"
$\gamma_d = 1.595 \text{ t/m}^3$, $D_r = 62.2\%$, $\phi = 35.445^0$ and length of reinforcement, $L_r = 295\text{mm}$						
7	200	2.774	15.30	1.2427	24.896	0.4512
8	"	3.520	17.20	1.6123	"	"
9	"	4.350	18.60	1.9471	"	"
10	100	2.774	16.90	1.0430	20.067	0.3653
11	"	3.520	17.90	1.2970	"	"
12	"	4.350	19.10	1.5905	"	"
$\gamma_d = 1.625 \text{ t/m}^3$, $D_r = 70.14\%$, $\phi = 44.44^0$ and length of reinforcement, $L_r = 295\text{mm}$						
13	200	2.774	15.50	1.5350	28.81	0.550
14	"	3.520	17.70	1.9300	"	"
15	"	4.350	9.500	2.4084	"	"
16	100	2.774	17.20	1.0821	21.933	0.402
17	"	3.520	18.20	1.4234	"	"
18	"	4.350	20.10	1.7527	"	"

Table 4.3.3 Results of Pullout tests Using Geotextiles, RE1, RE2 and RE3

Sl. No.	Width of reinforcement B_r (mm)	Normal stress σ_v (t/m^2)	Maximum pullout displacement d_{pmax} (mm)	Maximum pullout stress, τ_{pmax} (t / m^2)	Average angel of pullout resistance ϕ_p (degree)	Maximum average of coefficient static pullout resistance μ_{avsmx}
$\gamma_d = 1.625 t/m^3$, $D_r = 70.14\%$, $\phi = 44.44^\circ$ reinforcement length, L_r and width, $B_r = 295 \text{ mm} \times 290 \text{ mm}$						
1	RE2	2.774	53.30	0.86000	16.70	0.3000
2	"	3.520	60.50	1.03474	"	"
3	"	4.350	73.50	1.38151	"	"
4	RE3	2.774	68.80	0.44660	10.46	0.1846
5	"	3.520	75.30	0.68320	"	"
6	"	4.350	80.50	0.79450	"	"
$\gamma_d = 1.625 t/m^3$, $D_r = 70.14\%$, $\phi = 44.44^\circ$ reinforcement length, L_r and width, $B_r = 295 \text{ mm} \times 200 \text{ mm}$						
7	RE1	2.774	15.50	1.53500	28.810	0.5500
8	"	3.520	17.70	1.93000	"	"
9	"	4.350	19.50	2.40840	"	"
10	RE2	2.774	45.00	0.65440	14.340	0.2557
11	"	3.520	55.00	0.89880	"	"
12	"	4.350	69.40	1.16317	"	"
13	RE3	2.774	65.40	0.26692	5.31	0.0930
14	"	3.520	70.20	0.31960	"	"
15	"	4.350	75.30	0.44869	"	"
$\gamma_d = 1.625 t/m^3$, $D_r = 70.14\%$, $\phi = 44.44^\circ$ reinforcement length, L_r and width $B_r = 295 \text{ mm} \times 100 \text{ mm}$						
16	RE1	2.774	17.20	1.08213	21.930	0.4026
17	"	3.520	18.20	1.42340	"	"
18	"	4.350	20.10	1.75277	"	"

Three reinforcements: RE1, RE2 and RE3 were used. Ultimate pullout stress, τ_{pmax} , and the corresponding maximum pullout displacement, d_{pmax} , were obtained from tests. Table 4.3.2 and 4.3.3 give test results obtained.

Average coefficient of static pullout resistance, μ_{avs} , is defined as the ratio of average pullout stress, τ_p , along the interface of soil and reinforcement and the normal stress, σ_v . For a reinforcement of length, L_r , and width, B_r , subjected to a pullout force, P_s , pullout displacement, d_p , and effective length of the reinforcement, $(L_r - d_p)$, expressions for τ_p and μ_{avs} are given by:

$$\tau_p = P_s / [2B_r \cdot (L_r - d_p)] \quad (4.3.1)$$

$$\mu_{avs} = \tau_p / \sigma_v = P_s / [2B_r \sigma_v (L_r - d_p)] \quad (4.3.2)$$

Figure 4.3.13 shows variation of μ_{avs} with percentage pullout strain, ϵ_p , given by $(100 d_p / L_r)$ for woven geotextile, RE1 of size 295 mm x 200 mm. Upper and lower bound curves for results of the three tests show some scatter. This scatter leads to negligible error in μ_{avs} computed w.r.t. μ_{avs}

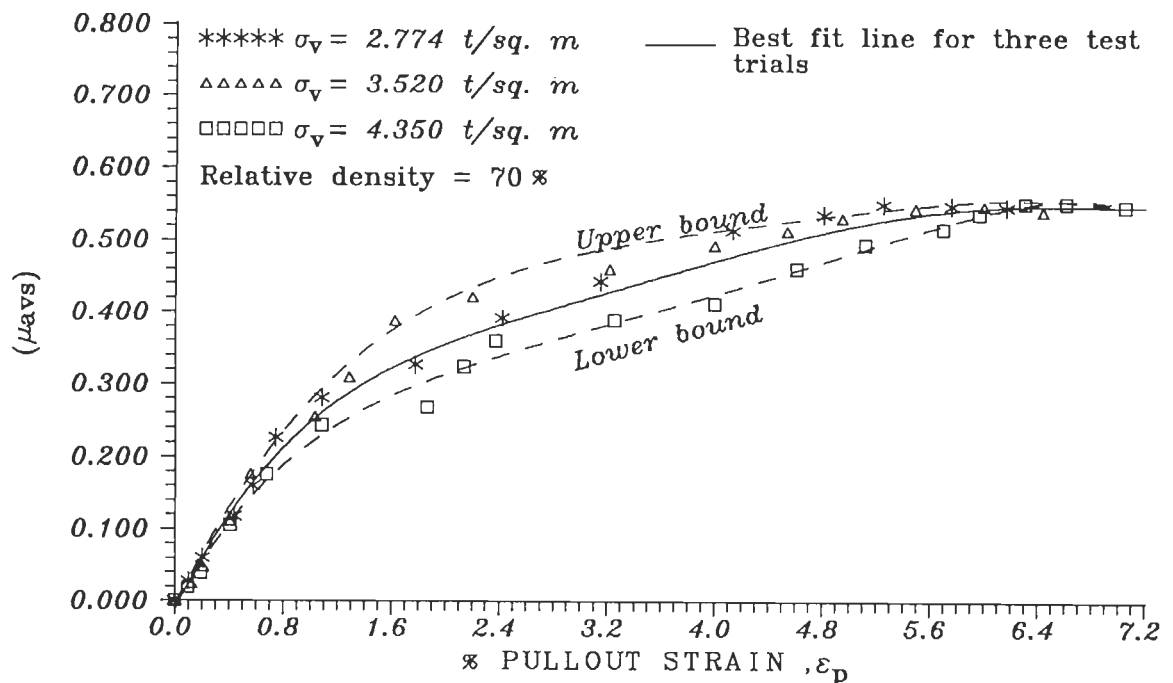


FIG.4.3.13 VARIATION OF % PULLOUT STRAIN, ϵ_p , WITH μ_{avs} FOR WOVEN GEOTEXTILE, RE1 (295 MM x 200 MM).

given by mean curve for ϵ_p upto 0.8% and also for $\epsilon_p > 6.2\%$ near failure. For range of ϵ_p in between, the corresponding error in μ_{avs} is less than 15% which is small. Hence, $\mu_{avs}-\epsilon_p$ relationship (Fig. 4.3.13) given by mean curve was adopted to make μ_{avs} independent of σ_v for range of σ_v considered.

Figure 4.3.14 and 4.3.15 show plot of μ_{avs} with ϵ_p for 290 mm wide nonwoven geotextiles RE2 and RE3. Error due to scatter of μ_{avs} w.r.t.mean μ_{avs} at any percentage pullout strain, ϵ_p , amounts to a maximum of 19% for RE2 and 22% for RE3. Ultimate pullout strain, ϵ_{pmax} , for RE1 is 6.4 % (Fig. 4.3.13), that for RE2 is 24.8 % (Fig. 4.3.14) and that for RE3 is 26.5 % (Fig. 4.3.15). As such, error appears to increase with ϵ_{pmax} for more extensible geotextiles. Hence, woven fabric with much smaller ϵ_{pmax} is desirable. Nonwoven geotextiles reinforcements with $\epsilon_{pmax} \geq 25\%$ are unsuitable as such ϵ_{pmax} is not be usually realised even under dynamic loads and the tolerable design ϵ_{pmax} is much smaller.

These figures indicate that when ϵ_{pmax} is reached, μ_{avs} nearly reaches its maximum value, μ_{avsmx} , and coefficient of residual μ_{avs} is very nearly equal to μ_{avsmx} . Hence, geotextiles show ductile behaviour in pullout test making them ideal for use in geotechnical earthquake engineering to avoid catastrophic failures (assuming no tension failure of reinforcements).

Figures 4.3.13, 4.3.14 and 4.3.15 show that $\mu_{avs}-\epsilon_p$ relationship may be assumed to be trilinear. First threshold strain, ϵ_{th} , is small compared to second threshold strain, ϵ_{pmax} , at failure. Upto ϵ_{th} , mobilisation rate of μ_{avs} is faster than the rate in the range of ϵ_p from ϵ_{th} to ϵ_{pmax} . For RE1, RE2 and RE3, ϵ_{th} is 1, 3 and 4 % respectively. For RE1, μ_{avs} at ϵ_{th} is about 55 % of μ_{avsmx} whereas ϵ_{th} is about 15% of ϵ_{pmax} only. This appears

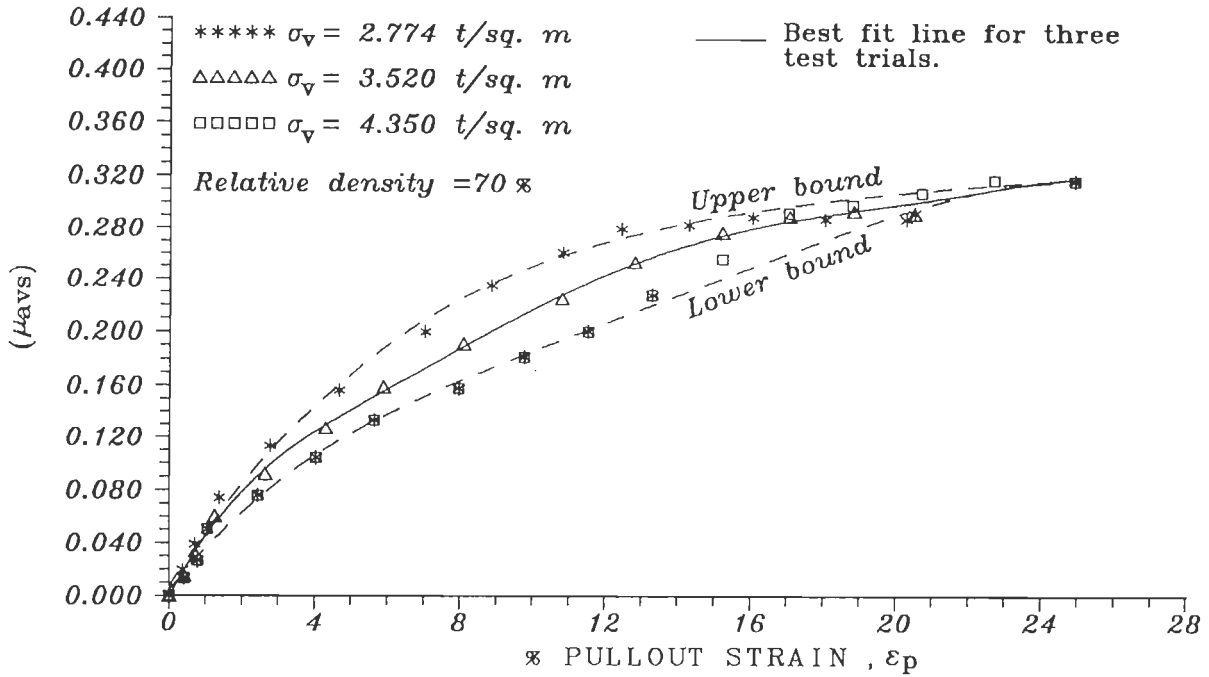


FIG.4.3.14 VARIATION OF %PULLOUT STRAIN, ϵ_p , WITH μ_{avs} FOR NONWOVEN GEOTEXTILE, RE2 (295 MM x 290 MM).

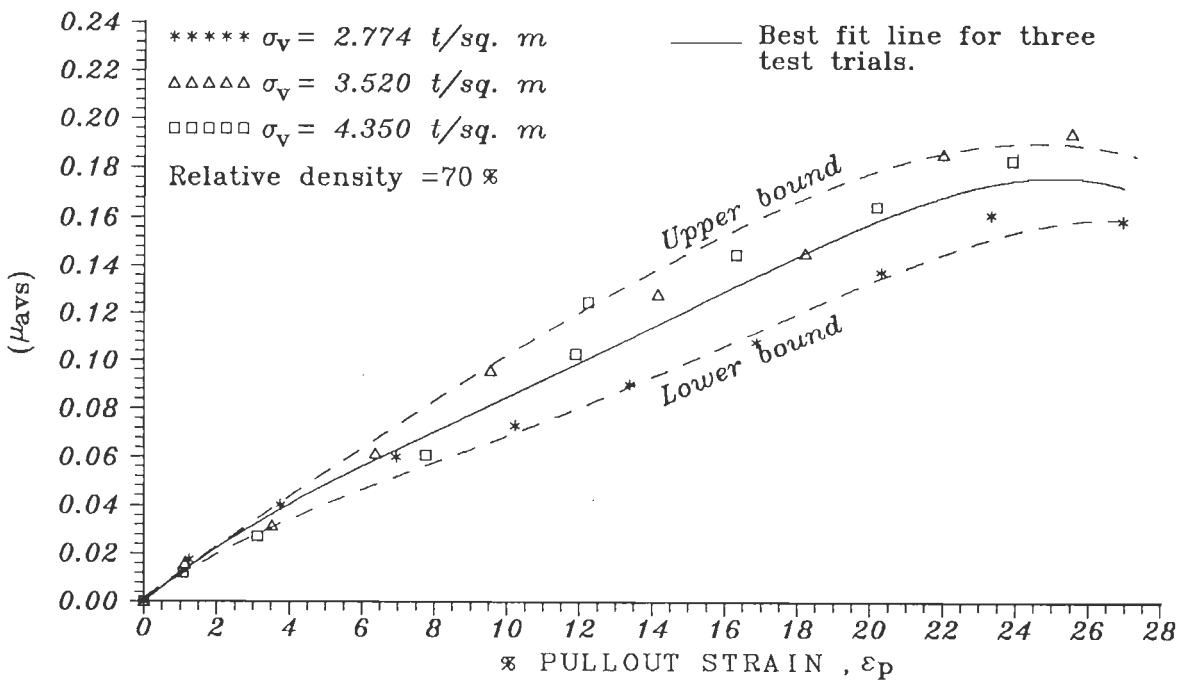


FIG.4.3.15 VARIATION OF %PULLOUT STRAIN, ϵ_p , WITH μ_{avs} FOR NONWOVEN GEOTEXTILE, RE3 (295 MM x 290 MM).

to be due to faster mobilisation of angle of shear resistance in soil at small initial strains equal to 10-15 % of failure strain of soil (supported by stress-strain characteristics of plain sands from direct shear tests). For $\varepsilon_p \geq \varepsilon_{pmax}$, μ_{avs} remains the same as failure is reached. Similar observations may be made for RE2 and RE3 also.

Relationship between μ_{avs} and ε_p (Fig. 4.3.13) is a useful design curve for obtaining displacement dependent or pullout strain dependent μ_{avs} which is useful in obtaining pullout resistance from the known value of σ_v at level of reinforcement. This relationship in dimensionless terms is very useful form of expression of material property of reinforcements.

Figure 4.3.16 shows effect of width of reinforcement, B_r , on μ_{avs} for various geotextiles for a normal stress, $\sigma_v = 0.2774 \text{ kg/cm}^2$. It may be noted that with increasing B_r , μ_{avs} increases initially sharply for small B_r values and then gradually to reach a constant maximum value at critical width, $B_{cr} = 290 \text{ mm}$ for three geotextiles tested. Normal stress environment within the box of test setup used is not similar to that prevailing in field. Hence, it is concluded that use of geotextile test specimen of width smaller than critical width leads to appreciable under-estimation of pullout resistance and tests with a larger box would be more desirable.

Table 4.3.4 shows settlements measured near front and rear diagonal ends of box in pullout tests. It also shows settlements as a percentage of initial soil depth. The settlements are quite small and decrease as relative density, D_r , increases, as expected. Maximum percentage settlement, S_{vpmx} , for soil obtained from void ratios at maximum and minimum densities,

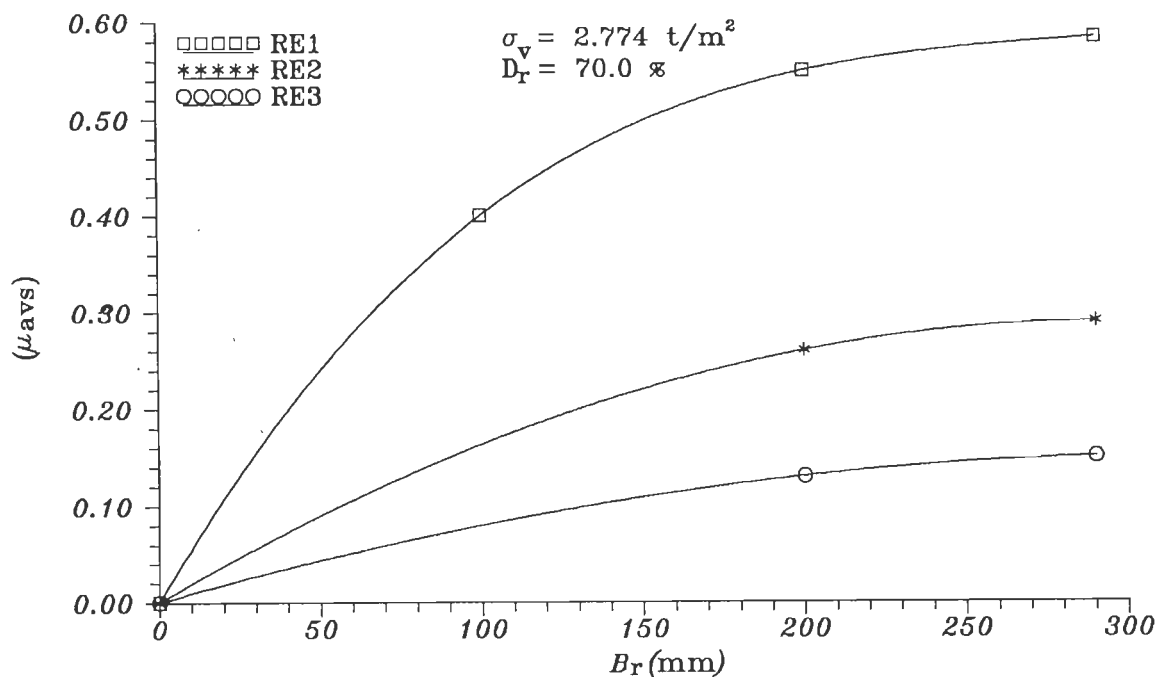


FIG.4.3.16 VARIATION OF AVERAGE COEFFICIENT OF PULLOUT RESISTANCE, μ_{avs} , WITH WIDTH OF REINFORCEMENT, B_r .

Table 4.3.4 Maximum Settlements of Soil Samples in Pullout Tests

Relative Density, D_r %	Settlements (mm)		Average Settlement, S_{av} (mm) $= (S_{fs} + S_{rs})/2$	$S_{avdp} = \frac{S_{avdp} \cdot 100}{S_{av} \cdot 100}$ Depth of soil	$\frac{S_{avdp} \cdot 100}{S_{avpmx}}$
	Front side (S_{fs})	Rear side (S_{rs})			
54	0.95	0.85	0.900	0.82950	3.230
62.2	0.85	0.78	0.815	0.75115	2.925
70	0.70	0.64	0.670	0.61750	2.400

is 25.67 % with reference to soil at its minimum density. Compared to this, observed settlement in any test is only 2.4 % to 3.23 % which is very small.

Proposed embankments, 0.9 m high, with a relative density of 70% and unit weight of 1.625 t/m^3 for sand, generate vertical stress $\sigma_v = 1.46 \text{ t/m}^2$ at base. The largest σ_v used in pullout tests is 4.35 t/m^2 equivalent to roughly 2.63 m deep soil cover. This is more than the range of σ_v in test embankments. Hence, σ_v range used in pullout tests is adequate. Woven geotextiles are better than nonwoven ones when they required to provide larger pullout resistance at any specified pullout strain. Hence, woven geotextile RE1 was selected for reinforcing test embankments.

4.3.4 Theoretical Model for Stress Distribution for Pullout Tests

For pullout test results cited above, uniform distribution of normal stress, σ_v , and stress, τ_p , at the soil-geotextile interface due to pullout resistance were assumed which does not represent actual conditions within test specimen. Maximum intensity of τ_p denoted by τ_{pmax} is given by:

$$\tau_{pmax} = 2 \cdot \sigma_v \cdot \tan \phi \quad (4.3.3)$$

Effective length of fabric, L_e , at ultimate pullout resistance, P_{rmax} , is given by $(L_r - d_{pmax})$ where d_{pmax} is the maximum pullout displacement at P_{rmax} . Actually, τ_p is zero at rear end of fabric and increases rapidly along its length to reach τ_{pmax} . As such, the curve representing variation of τ_p should begin with a near vertical tangent at the rear end and end with a horizontal tangent at the pulling end of the of the fabric. An elliptical variation of τ_p as shown in Fig. 4.3.17 satisfies this requirement.

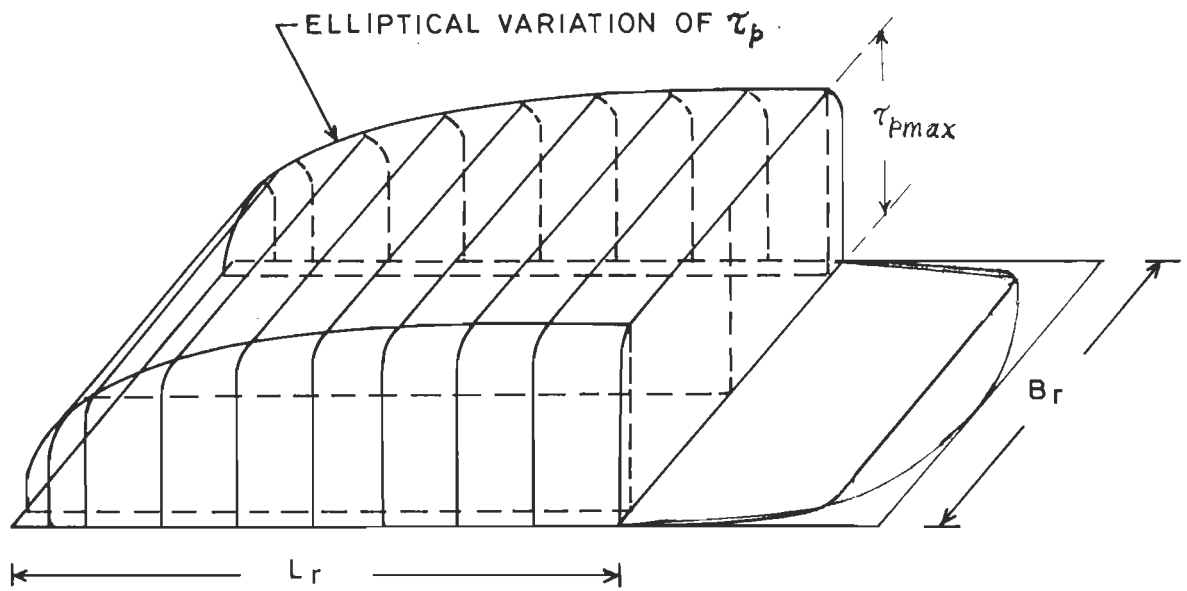


FIG.4.3.17 IDEALIZED INTENSITY OF PULLOUT RESISTANCE AND APPLIED PULLOUT FORCE CONSIDERED FOR THE PULLOUT TESTS.

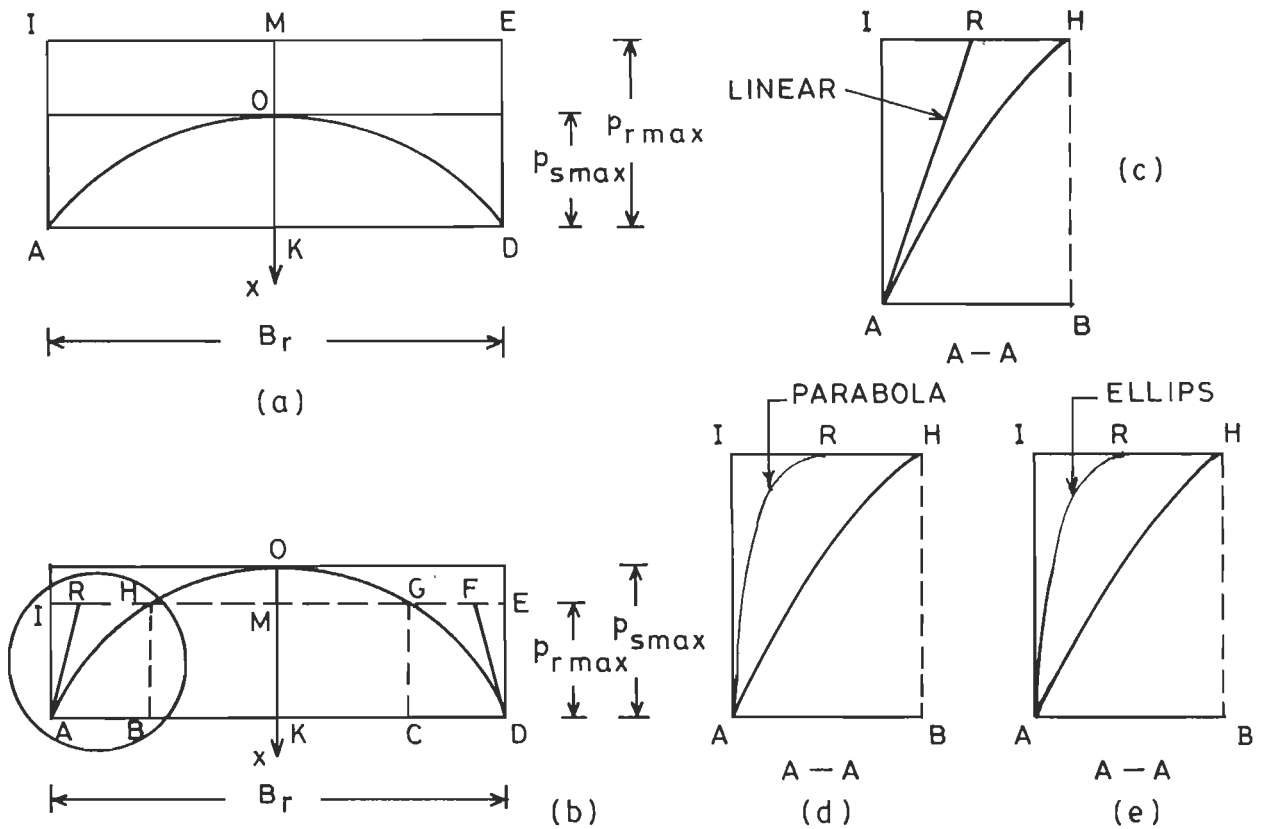


FIG.4.3.18 DIFFERENT TYPES OF IDEALIZED VARIATION OF PULLOUT RESISTANCE AFTER REDISTRIBUTION ALONG THE WIDTH OF REINFORCEMENT.

Intensity of pullout resistance, p_r , per unit width varies along the width of fabric. Its maximum value, p_{rmax} , is given by:

$$P_{rmax} = L_e \tau_{pmax} \pi/4 \quad (4.3.4)$$

If p_{rmax} is assumed to be mobilized throughout the width, B_r , the computed value of pullout resistance is larger than the applied pullout force, P_{smax} , obtained from tests. This is not admissible. However, at each free end of the width of fabric the intensity of pullout resistance p_r is zero. Therefore, it is necessary to obtain an appropriate variation of p_r along B_r to obtain maximum pullout resistance, P_{rmax} , equal to the maximum applied pullout force, P_{smax} , obtained from tests.

The mild steel grip used in tests for gripping the reinforcement is rigid compared to fabric. As such, the maximum applied pullout force, P_{smax} , generates a parabolic variation of intensity of pullout force, p_s , per unit width of fabric. The maximum value of p_s denoted by p_{smax} occurs at mid-width of the pulling end of fabric (Fig.4.3.18) and is given by:

$$p_{smax} = 3 P_{smax} / 2B_r \quad (4.3.5)$$

Pullout resistance intensity, p_r , at any point along width B_r should be equal and opposite to intensity of pullout force, p_s . If $p_{rmax} > P_{smax}$, no yielding occurs at interface of soil and fabric (Fig.4.3.18a). On the other hand, if $p_{smax} > p_{rmax}$ the yielding takes place (Fig.4.3.18b). Yielding along interface occurs all along width (HG) where p_s predicted by assuming parabolic variation exceeds p_{rmax} (Fig. 4.3.18b). Hence, the fraction of P_{smax} represented by area OHMG has to be redistributed to other parts (IH and GE) of B_r where fabric is subjected to $p_s < p_{rmax}$.

Intensity of pullout resistance generated at free ends A and D of the fabric (Fig. 4.3.18b) by applied pullout force is zero. Besides, it will not alter ultimate pullout resistance, p_{rmax} , which has already been reached within HBCG (Fig. 4.3.18b) for width BC of the fabric. As such, any further change in pullout resistance developed due to redistribution will have to be within areas IHBA and GEDC for the portion of widths AB and CD where p_r has not reached its maximum value. Different types of variations of p_r such as linear, parabolic and elliptical (Fig. 4.3.18 c, d and e) have been considered for this purpose. It is impossible to adopt elliptical variation under certain situations. Parabolic variation is desirable, because, it begins with a horizontal tangent at points R and F where it meets the p_{rmax} line RF. Linear variation is the simplest but gives rise to a sudden change in gradient of p_r at R and F where line AR and DF meet p_{rmax} line, RF, which is undesirable. Nevertheless, linear variation has also been considered in this study.

Variation of p_r along the width of fabric obtained by using linear variation (Fig.4.3.18b) is represented by the area ARFD. It may be observed that yield width B_{ry} (represented by RF) along the width has developed resistance equal to p_{rmax} . The dimensionless yield width, B_{rd} , is defined as (B_{ry}/B_r) . Figure 4.3.18 c, d and e show the enlarged view of linear, parabolic and elliptical variation of p_r with width obtained on similar lines and variation of $100B_{rd}$ obtained by these idealizations are shown in Fig. 4.3.19 as function of relative density, D_r . As D_r increases, B_{rd} reduces for all the three σ_v values considered. Elliptical variations could be considered only for two cases shown in Fig. 4.3.19 a and b for reasons cited earlier and leads to smaller B_{rd} compared to B_{rd} obtained by using

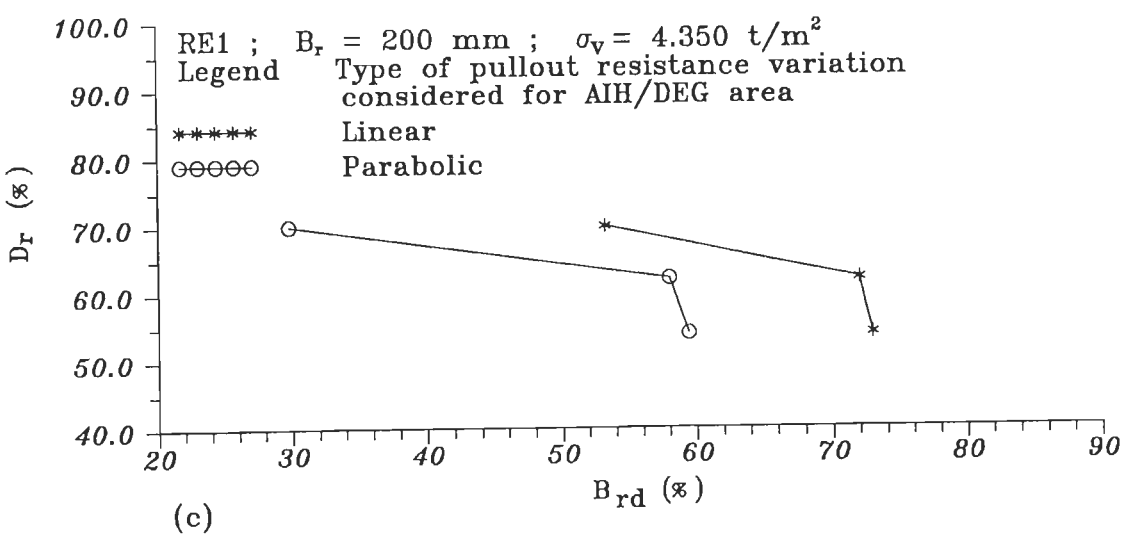
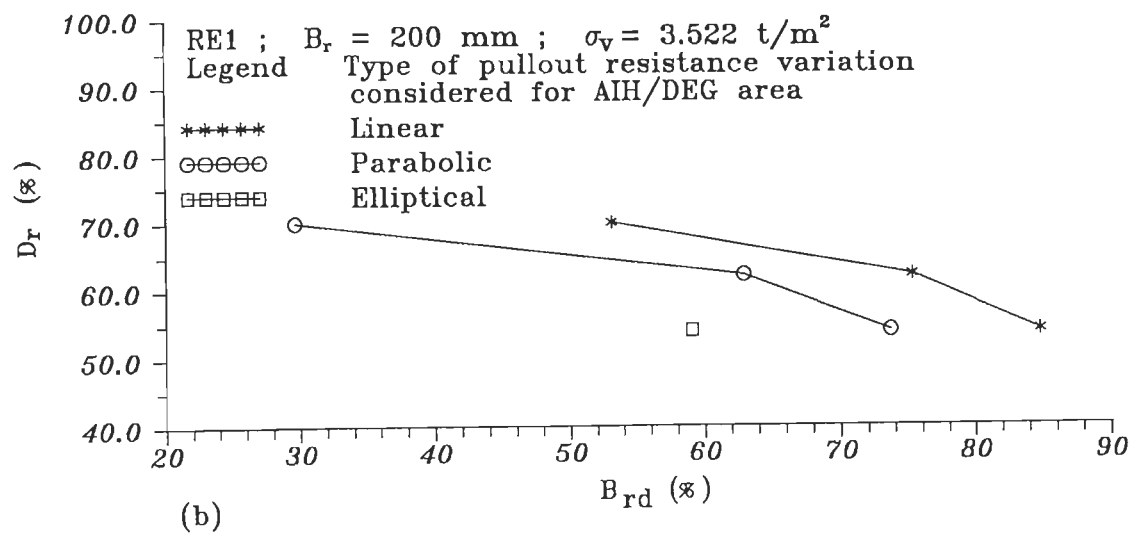
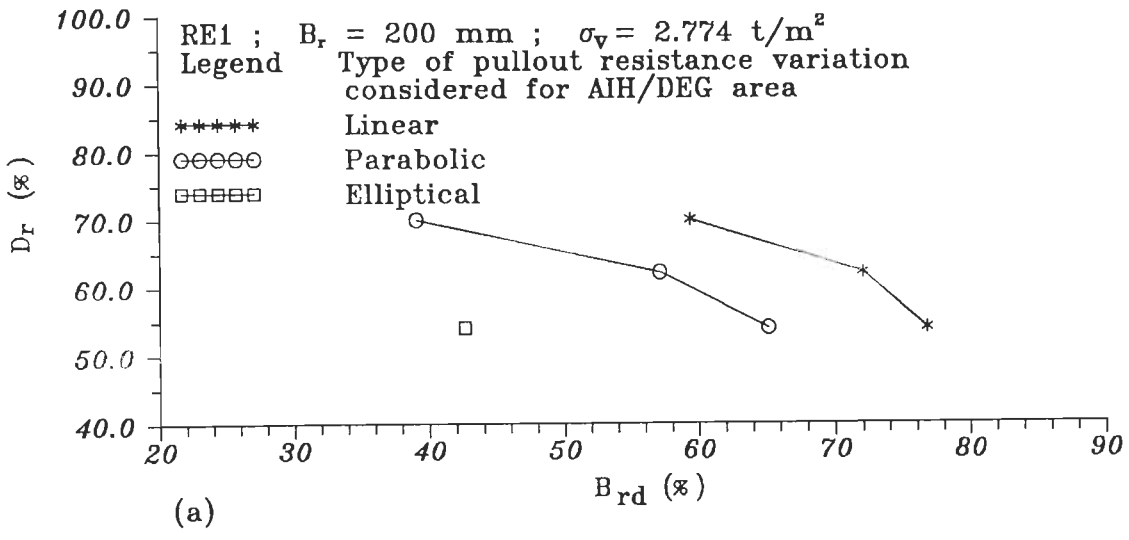


FIG.4.3.19 VARIATION OF % DIMENSIONLESS YIELD WIDTH, B_{rd} , WITH % RELATIVE DENSITY, D_r .

linear and parabolic variations. Linear variation results into larger B_{rd} compared to that obtained by using parabolic variation. Values of B_{rd} obtained for $D_r=62.2\%$ are close to B_{rd} obtained for D_r equal to 54% but are appreciably larger than B_{rd} values obtained for D_r equal to 70%. This expected, because, angle of shear resistance, ϕ , obtained are 33.424° , 35.445° and 44.44° for D_r equal to 54%, 62.2% and 70% respectively.

Another observation which can be made is that when such tests are carried out for pullout resistance, only a portion of the width reaches yield resistance and the remaining portion does not mobilize full pullout resistance. This reduces average value of pullout resistance attributed to fabric based on test results. However, in the field applied pullout force is not distributed using a rigid gripping element. As such, fabric under plain strain conditions existing in field is expected to develop pullout resistance more or less uniformly over entire width except for short width equal to half the critical width B_{cr} which is approximately given by $0.5(B_r - B_{ry})$ at each end. To that extent, test setup does not simulate field behaviour of reinforcement and underestimates resistance which is conservative. However, it is possible to obtain μ_{avs} corresponding to field conditions (which may be denoted by $\mu_{avsfield}$) by multiplying μ_{avs} obtained from laboratory tests by ratio of area ARFD to area AIED shown in Fig.4.3.18 cited earlier. The area ARFD corresponds to pullout resistance developed under laboratory conditions whereas area AIED corresponds to pullout resistance developed under field conditions. Therefore, correction factor C_μ and $\mu_{avsfield}$ may be obtained as:

$$C_\mu = (B_r + B_{ry})/2B_r \quad (4.3.6)$$

$$\mu_{avsfield} = \mu_{avs} \cdot C_\mu \quad (4.3.7)$$

These relationships are useful in obtaining designed pullout resistance parameters for field conditions based on laboratory tests whenever it is impossible to carryout pullout tests under field conditions.

TABLE 4.3.5 Dimensionless Yield Width Results from Pullout Tests Considering Linear Pullout Resistance Variation for AIH/DEG Area (RE1 Reinforcement; $B_r = 20$ mm)

σ_v (t/m^2)	B_{rd}			Average B_{rd} (B_{rd}) _{ave}	% Difference of (B_{rd}) _{max} /(B_{rd}) _{ave}	$(B_{rd})_{max}$ $(B_{rd})_{min}$
	$D_r = 70\%$	$D_r = 62.2\%$	$D_r = 54\%$			
2.774	0.593875	0.720217	0.767501	0.693864	10.612546	0.173626
3.520	0.531103	0.752858	0.847826	0.847826	19.312014	0.316723
4.357	0.532393	0.720001	0.729501	0.729501	10.257873	0.197108

Table 4.3.5 shows dimensionless yield widths for different normal stresses, σ_v , and relative densities by using woven geotextile (295 mm long x 200 mm wide). Spread of B_{rd} values range from 0.173626 to 0.316723 for different values of σ_v for D_r values considered. It appears that this spread in B_{rd} values is nearly independent of σ_v (with errors less than 10%). This is clear from Fig. 4.3.20 also. Figure 4.3.21 shows variation of B_{rd} with B_r from which it may be observed that as B_r increases value of B_{rd} also increases which is expected. The reduction in B_{rd} for smaller values of B_r is mainly due to a relatively small value of intensity of peak pullout force, p_s , per unit width when compared with intensity of maximum pullout resistance, p_{rmax} , per unit width (Fig.4.3.21). In fact, this effect is highlighted more dramatically in Fig.4.3.22 where B_{rd} is zero for all cases with B_r equal to 100 mm whereas the B_{rd} varies from 53.11% to 84.78% for different values of σ_v and D_r when B_r is 200 mm. For D_r equal to 70% and σ_v equal to 2.774 t/m^2 , B_{rd} increases from 59.38% to 63.06% when B_r increases

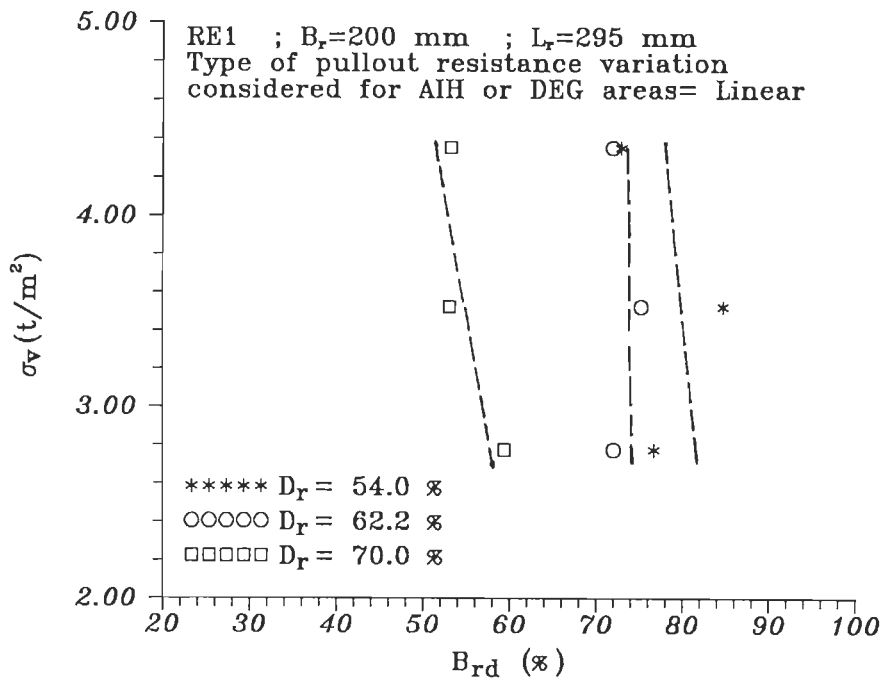
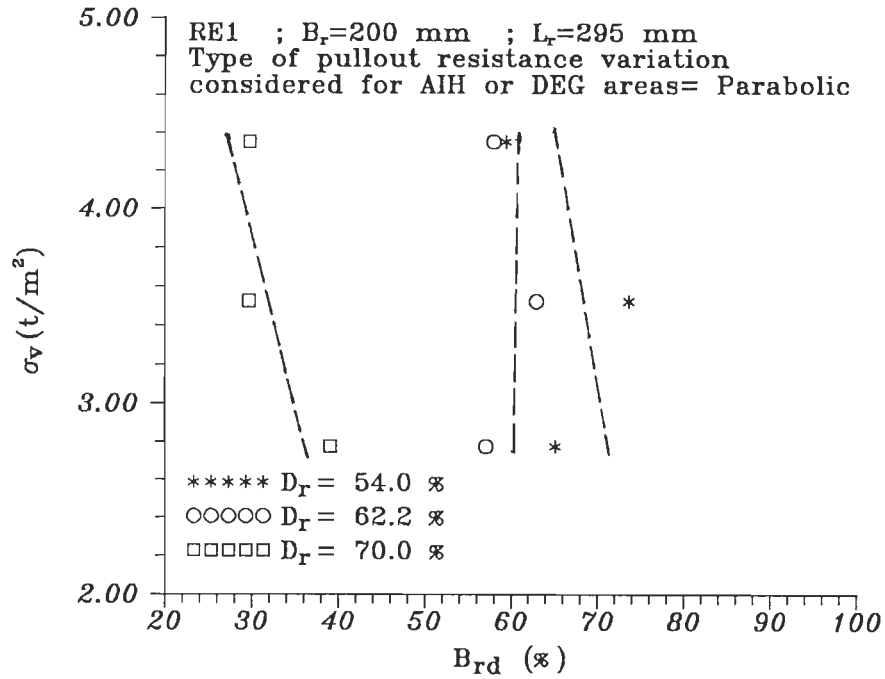


FIG.4.3.20 VARIATION OF % DIMENSIONLESS YIELD WIDTH, B_{rd} , WITH NORMAL STRESS , σ_v .

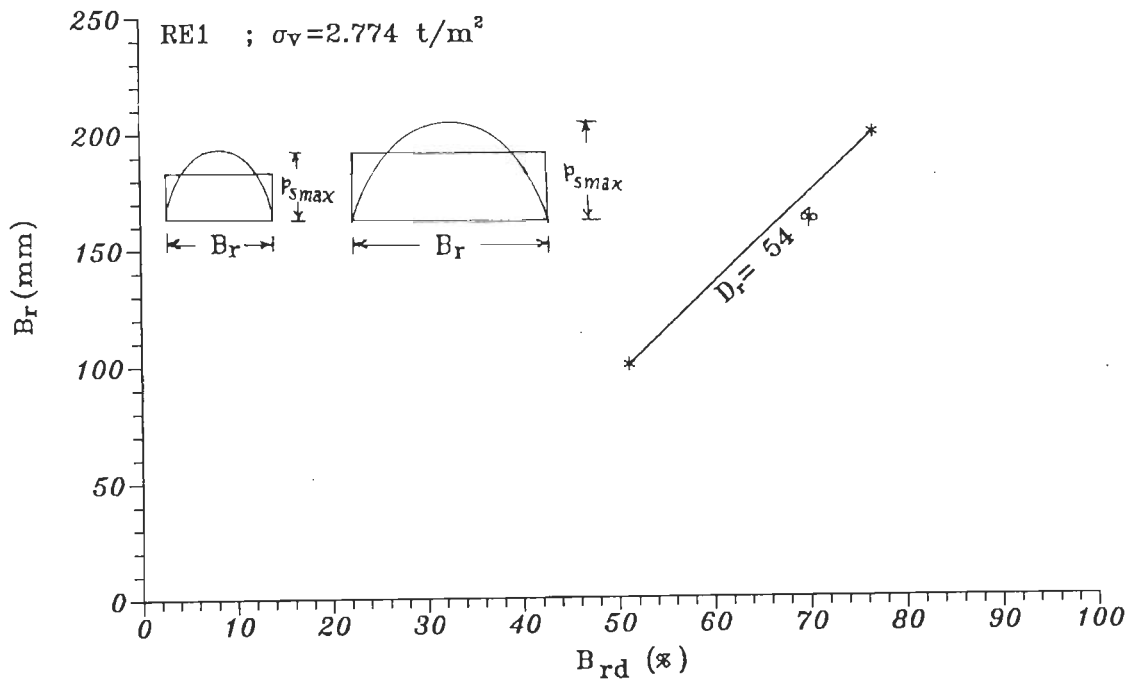


FIG.4.3.21 VARIATION OF % DIMENSIONLESS YIELD WIDTH, B_{rd} , WITH WIDTH OF REINFORCEMENT, B_r .

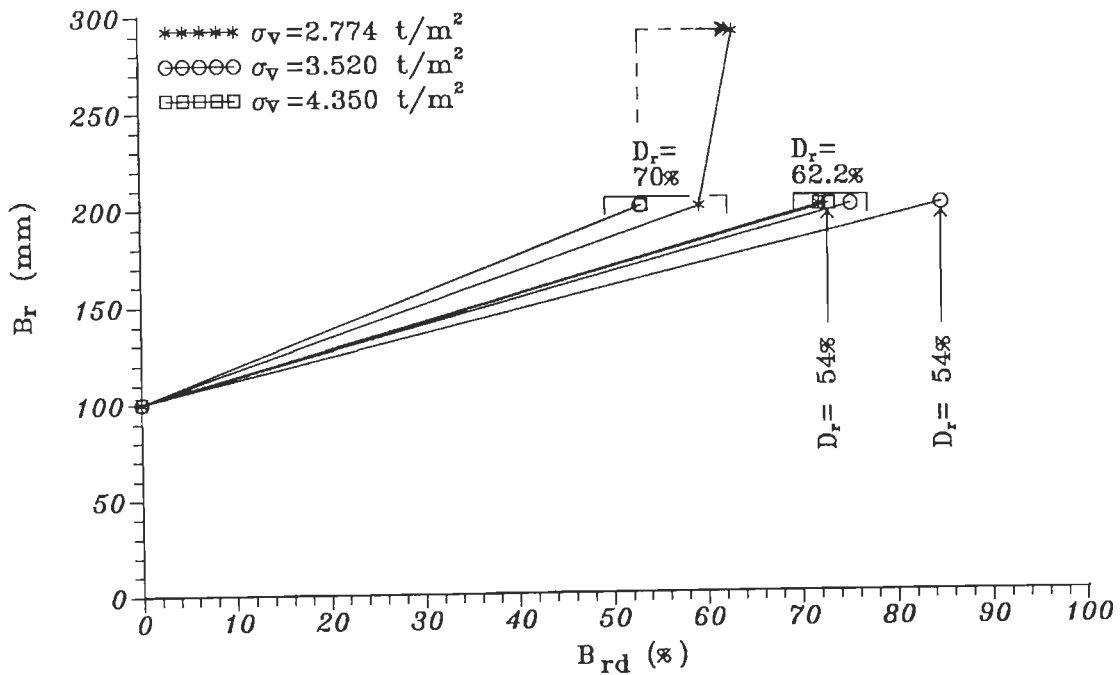


FIG.4.3.22 VARIATION OF % DIMENSIONLESS YIELD WIDTH, B_{rd} , WITH WIDTH OF REINFORCEMENT, B_r , WHEN B_{rd} IS ZERO FOR SMALLER WIDTH, $B_r = 100 \text{ MM}$.

from 200 mm to 290 mm. This increase in B_{rd} is insignificant compared to increase in B_{rd} from 0 to 59.38 when B_r increases from 100 mm to 200 mm. This conclusion is in agreement with the conclusion drawn from Fig. 4.3.16 cited earlier. Therefore, based on these results, it may be concluded that fabrics of shorter widths are uneconomical and relatively under stressed eventhough the fabric may be otherwise capable of mobilising higher intensity of pullout resistance for a given relative density and normal stress. Hence, B_r should be as large as possible in the field and should be at least equal to critical width B_{cr} in laboratory tests.

4.3.5 Effect of Arching Action on Pullout Resistance

When the reinforcement is pulled out using the test setup cited above, it creates a void at its buried end within the box while the pullout displacements occur. This leads to arching action. Figure 4.3.23 shows the void (denoted by A) created this way.

To facilitate the pulling out of reinforcement between upper and lower parts of the box, the two parts are separated by a gap, t_g , which is slightly larger than thickness, t_r , of the reinforcement. As a result, soil grains may escape through the clearance between lower end of the upper half of the box and top level of the reinforcement when the reinforcement is being pulled out. Volume of soil thus escaping is approximately equal to the product of the width of reinforcement, pullout displacement and the thickness of clear gap through which the soil grains escape out. This gives rise to a void denoted by B which is equal to volume of void A cited earlier (Fig.4.3.23). To fillup voids A and B thus created, the soil flows radially in the direction of centers of these voids. Consider an arc of soil element

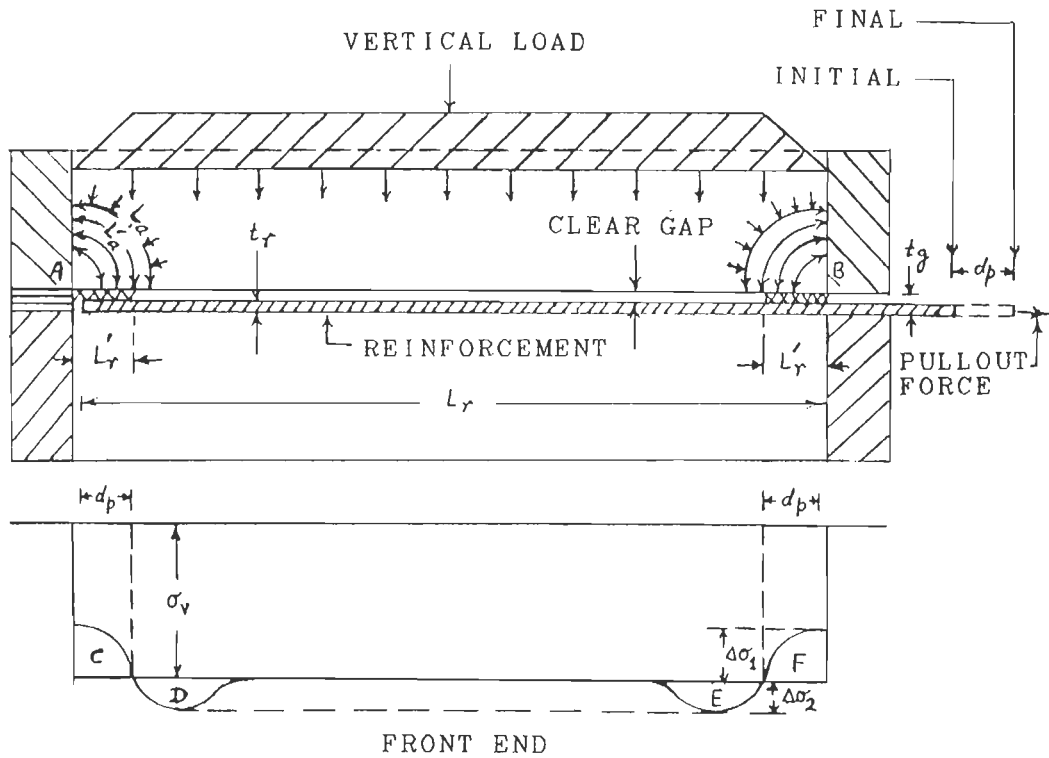


FIG. 4.3.23 DETAILS OF ARCHING ACTION ON PULLOUT RESISTANCE.

of initial length, L_a , moving towards the void A to reach, a new position of length L'_a . Change in the length is $(L_a - L'_a)$, which induces compressive strain $(L_a - L'_a)/L_a$. As a result, arc with L'_a as the length develops capacity to resist its further movement in the direction of center of void A. This is called as 'Arching action' (Terzaghi, 1960). As a result, the element at its position indicated by L'_a will be capable of shielding elements below it from experiencing the entire normal stress applied directly above void space. However, as a consequence of this arching action, the element at its position L'_a transfers the stress acting on it partly to vertical side of the box and partly to the soil elements adjacent to the void (Fig.4.3.23). Therefore, there will be a decrease in normal stress on elements within void and an increase in normal stress at elements adjacent to void as shown in

figure. Similar type of normal stress changes occur at the void B also. This changed stress environment is different from assumed stress environment of uniform intensity of normal stress along the length of reinforcement. The larger the thickness of reinforcement or the clear gap between above the reinforcement, the greater the arching action and corresponding deviation of stress environment from assumed uniform stress intensity (Fig.4.3.23).

In the test setup used, reinforcement losses its length, L_r , to the extent of the pullout displacement, d_p . As such, no portion of its length is situated within the void A to reduce its pullout resistance due to reduction of normal stress within the void. The effective length, L_e , defined as $(L_r - d_p)$ is used in computation of pullout resistance in analysis carried out. However, the reinforcement receives additional normal stress in the region D which leads to somewhat higher pullout resistance. At the void B, similar phenomenon takes place, but reinforcement is situated below the void. Hence, it is shield from normal stress in the region F due to arching action. However, it receives slightly larger normal stresses in the region E adjacent to void B. Therefore, increase in the normal stress in the region D and E tend to partly compensate the reduction in the normal stress in the region F of void B. The net effect of this phenomenon is to slightly reduce pullout resistance. However, this reduction in pullout resistance is small for very small clear gap between reinforcement and upper part of box as per the present state of the art. As such, no investigations and corrections to pullout resistance in this regard have been carried out.

4.4 TEST EMBANKMENTS FOR DYNAMIC INVESTIGATIONS

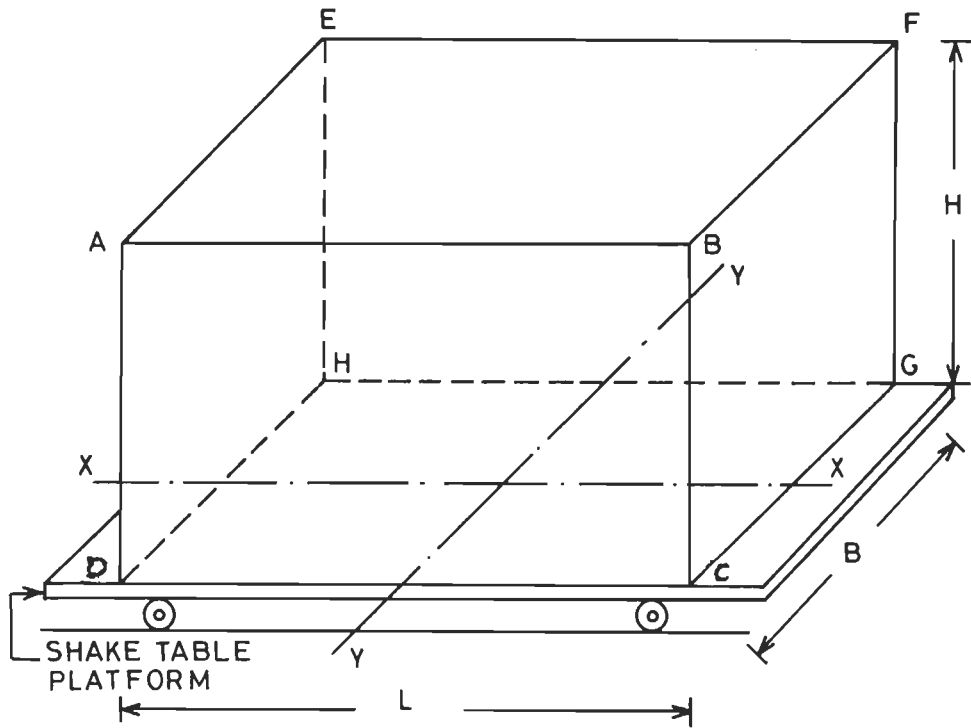
For dynamic investigations, embankments have been tested using shake table facility. In this article, details of working out dimensions and

components of embankment as well as measuring instrument for recording accelerations have been discussed. Procedure for preparation of embankment and procedure for conducting various dynamic tests using the shake table facility have also been discussed. Back-analyses of test results have also been carried out to evaluate dynamic parameters like shear modulus, G_r , shear strain, γ , and coefficient of average dynamic pullout resistance, μ_{avd} , and to correlate them with other parameters like frequency of excitation, F_{rq} , natural frequency of test embankment, F_n , and phase angle of vibrations, θ , etc. Based on analytical and experimental results obtained, suitable conclusions have been arrived at.

4.4.1 Fixing Dimensions of the Test Embankment

To ensure test embankment to behave like a shear beam in direction of excitation, embankment should have properly designed dimensions and its slenderness ratio should be less than or equal to 5 in direction of excitation (Krishna et.al., 1994). This has been adopted for fixing embankment dimensions

For a test embankment (Fig. 4.4.1) with a length of 1.5 m and width of 0.75 m, moment of inertia is 0.052 m^4 , and the area of the base is 1.125 m^2 . Therefore, the radius of gyration is 0.432 m. Using a slenderness ratio ($2H/\text{radius of gyration}$) equal to 5, the largest permissible height of the embankment, H , is evaluated to be 1.08 m. Hence, a test embankment of 1.5 m x 0.75 m x 0.9 (high) has been used for dynamic investigations. Slenderness ratio for this test embankment works to be 4.16 only.



AEFB – TOP FACE.
 ABCD AND EFGH – TRANSVERS FACES.
 AEHD AND BFGC – LONGITUDINAL FACES.
 DHGC – BOTTOM FACE.
 DIRECTION OF EXCITATION X – X

FIG. 4.4.1 SCHEMATIC DIAGRAM OF R.E. TEST EMBANKMENT.

4.4.2 Simulation of Plane Strain Conditions for Test Embankment

Embankments are typical examples of structures performing under plane strain conditions at all planes transverse to their longitudinal directions. Seismic vibrations are more critical when acting in transverse plane of the embankments. As such, it is necessary to create plane strain conditions in the lab test facility for obtaining proper results. To create plane strain conditions, following conditions have to be realised:

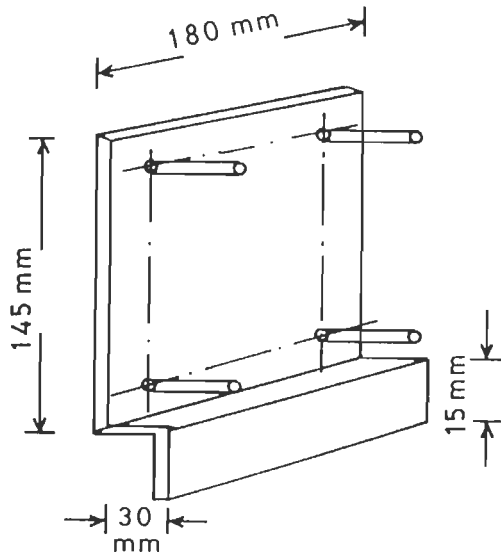
- i) Normal stress, σ_2 , acting on transverse plane should remain the same at all transverse planes.

- ii) Transverse plane should not move in the longitudinal direction.
- iii) No shear stress should develop along transverse planes during tests.

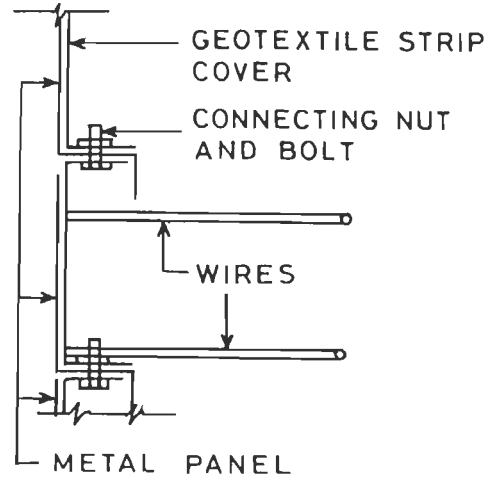
Usually, plane strain conditions are difficult to realise in the laboratory conditions. A common practice is to simulate plane strain conditions by placing glass sheets at transverse ends of the embankment and supporting them suitably. Even smooth glass surfaces have friction coefficient of 0.05 at the interfaces with embankment which vitiates plane strain conditions and tends to reduce embankment response (Fairless, 1989).

Proposed arrangement for creating plane strain conditions

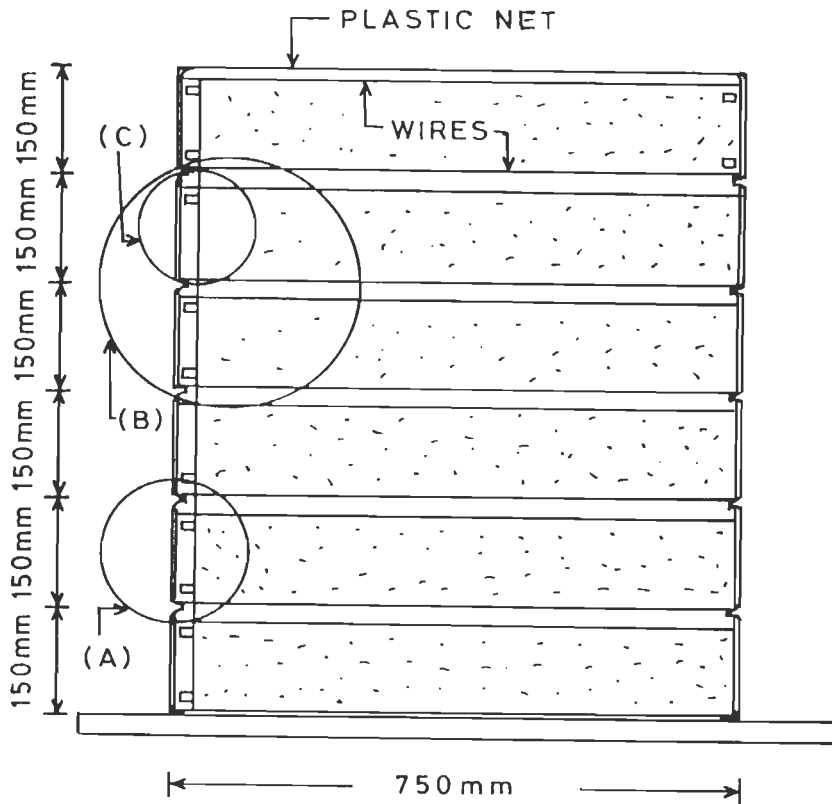
To overcome the difficulty cited above, transverse sides of test embankments were enclosed with flexible geotextile which facilitates the movement in transverse direction without any hindrance. Rough surfaces of geotextile are formally in contact with soil and move together with the soil at transverse ends. To prevent this transverse geotextile covering from undergoing longitudinal displacements under the influence of earth pressures, this covering is provided with eight panel of G.I. metal sheets (180 mm long, 145 mm high and 1 mm thick) in each of the six 150 mm high horizontal strips of the geotextile cover. Figure 4.4.2a shows a detailed schematic diagram of metal panels attached to geotextile cover. There is adequate gap between adjacent panels to allow free movements of panels in vertical and horizontal directions and rotations about longitudinal axis. Every panel at one transverse end of the embankment is connected to the corresponding panel on the other transverse end of the embankment by using four thin steel wires (one near each corner of the panel) of 0.5 mm diameter (Fig.4.4.2b). Figure 4.4.2c shows end view of arrangement consisting of



(a) METAL PANEL WITH WIRES



(b) DETAILS OF CONNECTION BETWEEN PANELS AND STRIPS OF GEOTEXTILES.



(c) END VIEW OF ARRANGEMENT FOR CREATING PLAIN STRAIN CONDITION.

FIG. 4.4.2 DETAILS OF THE ARRANGEMENT FOR CREATING PLANE STRAIN CONDITION.



FIG. 4. 4. 3 VIEW OF THE TRANSVERSE FACE OF RE-
TEST EMBANKMENT AT THE END OF
CONSTRUCTION AFTER REMOVAL OF
FORMWORK.

geotextile cover, metal panels, G.I. wires etc. Force of earth pressure acting on panels is resisted by tension in wires. Tensile deformation within wires for lower most panels is 2.411×10^{-7} mm, which is negligible for the soil fill used in the test embankments. Wires of 0.5 mm diameter offer negligible resistance to transverse movement of embankments as they practically move with adjacent soil mass.

The geotextile cover on transverse faces consists of 6 strips of same clothing, covering a depth of 150 mm (Fig.4.4.2(c)). Each strip is bolted to the corresponding rigid facing element at each end by using metal strips (Fig.4.4.2b). After completing construction of the test embankment, when the form work supporting transverse ends of the embankment are removed, the transverse sides covered with facing elements stand with vertical plane faces with no longitudinal movements and Fig. 4.4.3 shows a view of the same. These transverse sides remain vertical even after completing dynamic tests. Hence, it is concluded that the device developed for creating plane strain conditions has performed well.

4.4.3 Components of the Test Embankment

Fixity of the embankment at the base

The embankment is assumed to be fixed at base in the analysis. As such, its base should be firmly secured to shake table platform to disallow sliding between the table and the embankment. For this purpose, two pairs of metal strips (one at the base of each longitudinal end of embankment) are screwed to shake table platform. The bottom most longitudinal facing

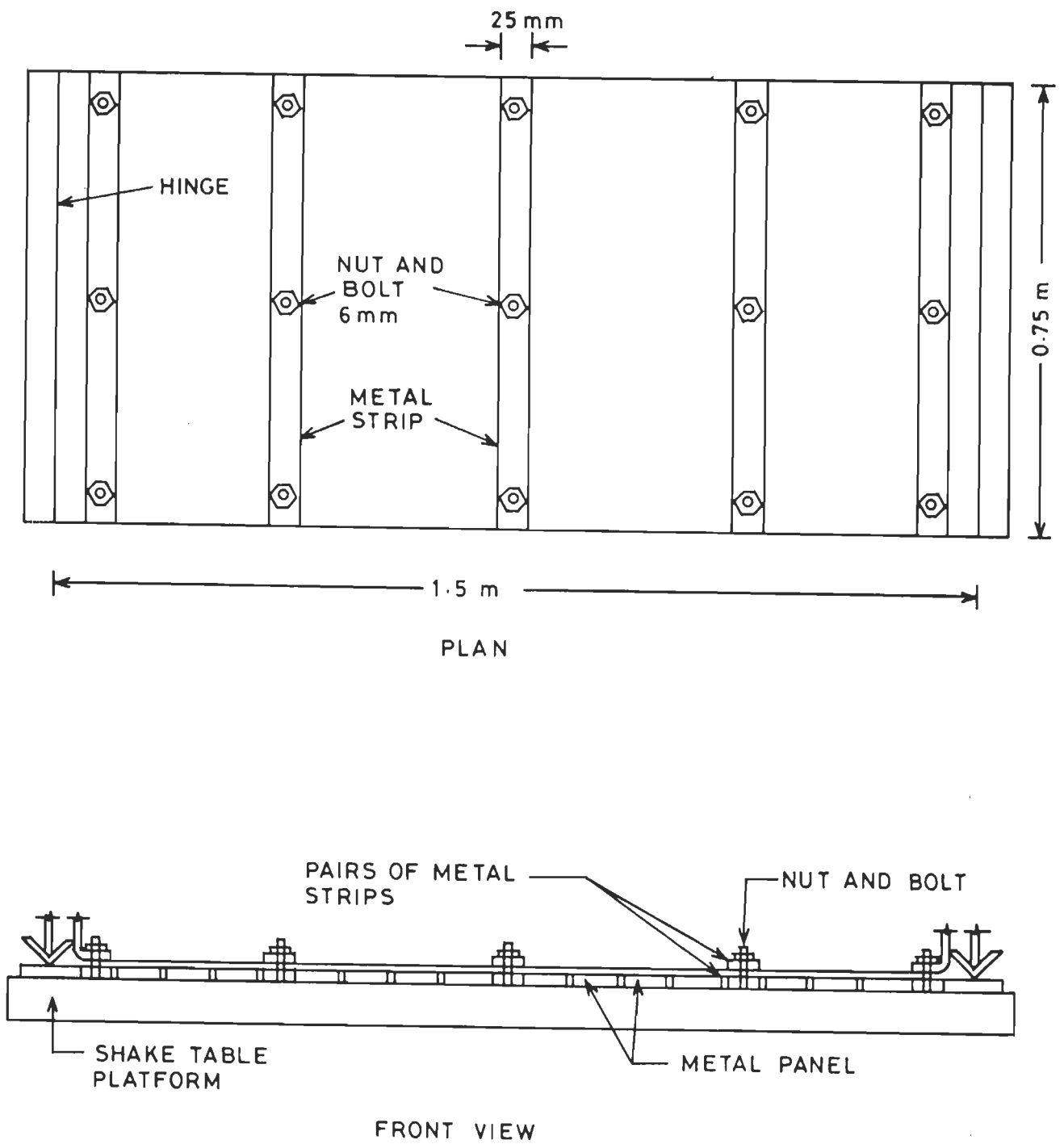


FIG. 4.4.4 ARRANGEMENT FOR FIXITY OF THE EMBANKMENT AT THE BASE.

element at each end is hinged to these metal strips. Besides, three more pairs of metal strips parallel to longitudinal faces are also screwed to shake table platform (Fig.4.4.4). The lower strip of each pair is first bolted to the platform. The horizontal leg of the lowest geotextile strip of transverse face is sandwiched between the upper and lower longitudinal strips and these two strips are bolted together to secure the lower end of geotextile to provide fixity at base. Besides, roughness of the table and interlocking between the table and the soil of the embankment due to these longitudinal strips provides sliding resistance to give fixity at the base. Inspection of transverse embankment faces at the end of dynamic tests showed that the arrangement worked satisfactory to provide fixity at base.

Hinging the bottom most facing element to shake table

The base of test embankment should be hinged to shake table platform to allow rotation of longitudinal face under dynamic loading. The hinge used for this purpose (Fig. 4.4.5) consists of an angle iron (A) welded to a metal strip which in turn is screwed to platform. In the V-groove of the angle iron, the vertical leg of another angle iron is positioned. The facing element rests directly over this angle iron (B). Another smaller aluminium angle (C) is used to screw facing element to this angle iron (B). The facing element with the angle iron (B) as its shoe resting in the V-groove of angle iron (A) provides the necessary hinge.

To prevent sand fill entering into V-groove of hinge, a geotextile piece is secured at its one end (D) to facing element by screwing. Its other end (E) is screwed to metal strip supporting the angle iron (A).

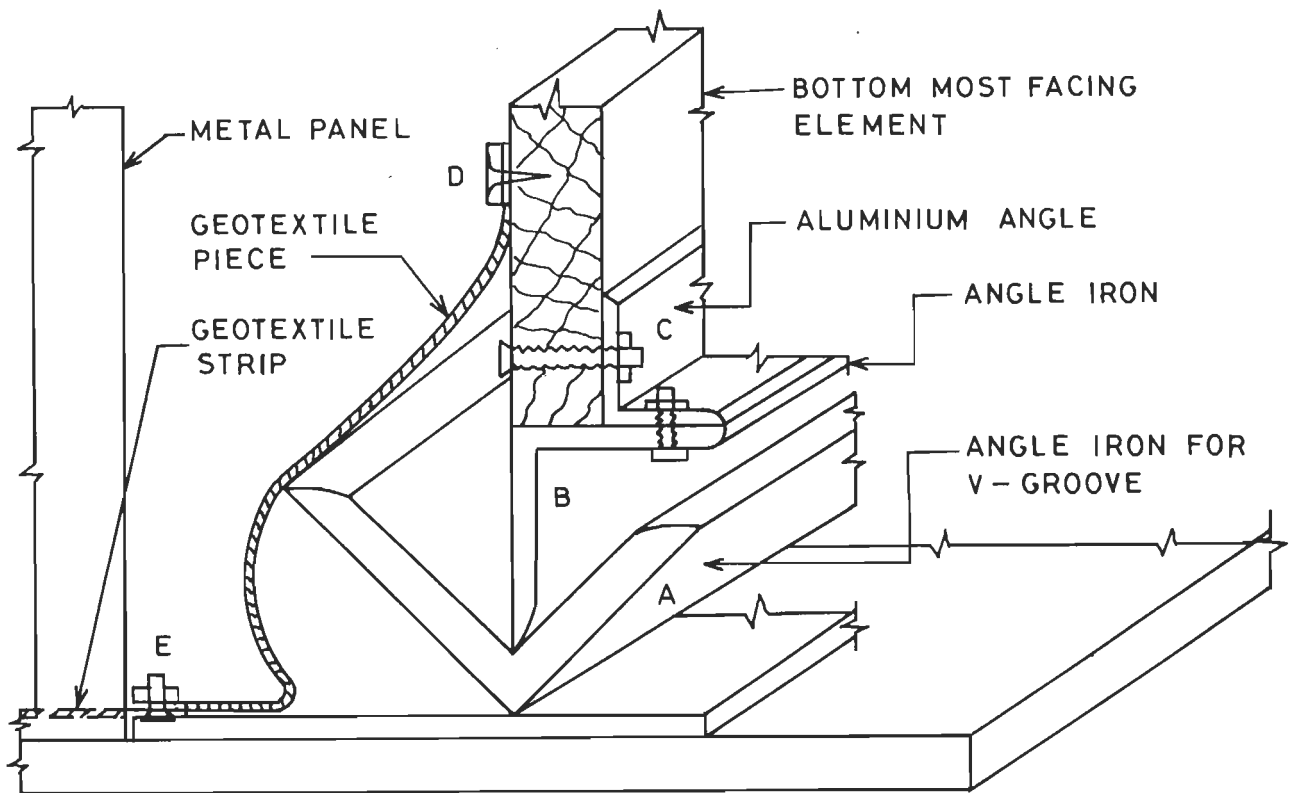


FIG. 4.4.5 DETAILS OF THE HINGE AT THE BASE OF THE LONGITUDINAL FACING.

Facing element

Each longitudinal vertical face of test embankments is provided with six separate plywood facing elements, 750 mm long, 49 mm high and 12 mm thick. For bottom layer, displacement of free end of facing element due to cantilever action is 0.00736 mm which is 0.16355% of maximum displacement of 4.5 mm needed at the top end of the embankment for reaching active state of failure. Actual displacements of facing elements situated above bottom layer will be subjected to much smaller earth pressures and hence will undergo much smaller deflections. Hence, bending displacements of these facing element have negligible effect on earth pressures developed in the

earth fill. Facing elements are stiffened in longitudinal direction by screwing them at mid depth to angle irons of 25 mm x 25 mm x 3 mm x 750 mm long size on outer face. Aluminium angles gripping the reinforcing geotextile are screwed to these facing elements on the inner face to further stiffen facing elements in longitudinal direction (Fig. 4.4.6). Hence, these facing elements were rigid for all practical purposes.

To reduce friction between adjacent facing elements, each facing element was wrapped with two layers of thin smooth plastic sheet.

Facing elements are connected to main reinforcements at their mid depth by using aluminium angle with its vertical screwed to facing element (Fig.4.4.6). Reinforcement was wrapped fully around a flat m.s. strip for getting good grip and strip was bolted to horizontal of aluminium angle.

The facing element is also connected to corresponding strip of transverse face geotextile cover. The geotextile strip is folded in the shape of a channel (Fig.4.4.6). The horizontal projections of such channels adjacent to each other are connected by using nuts and bolts. The longitudinal strip is bent at right angles at the end where it meets the facing element. At this junction, this bent portion of the strip is bolted to the facing element by using five clamps (Fig. 4.4.6). Clamp A was such that its outer edge coincided with outer edge of facing element to give proper finish at the vertical corner of the embankment.

To prevent leakage of sand at joints, special care was taken. A patch of 30 mm wide geotextile strip of transverse facing was bent to L-shape and stitched at lower corner of strip of longitudinal geotextile cover as shown

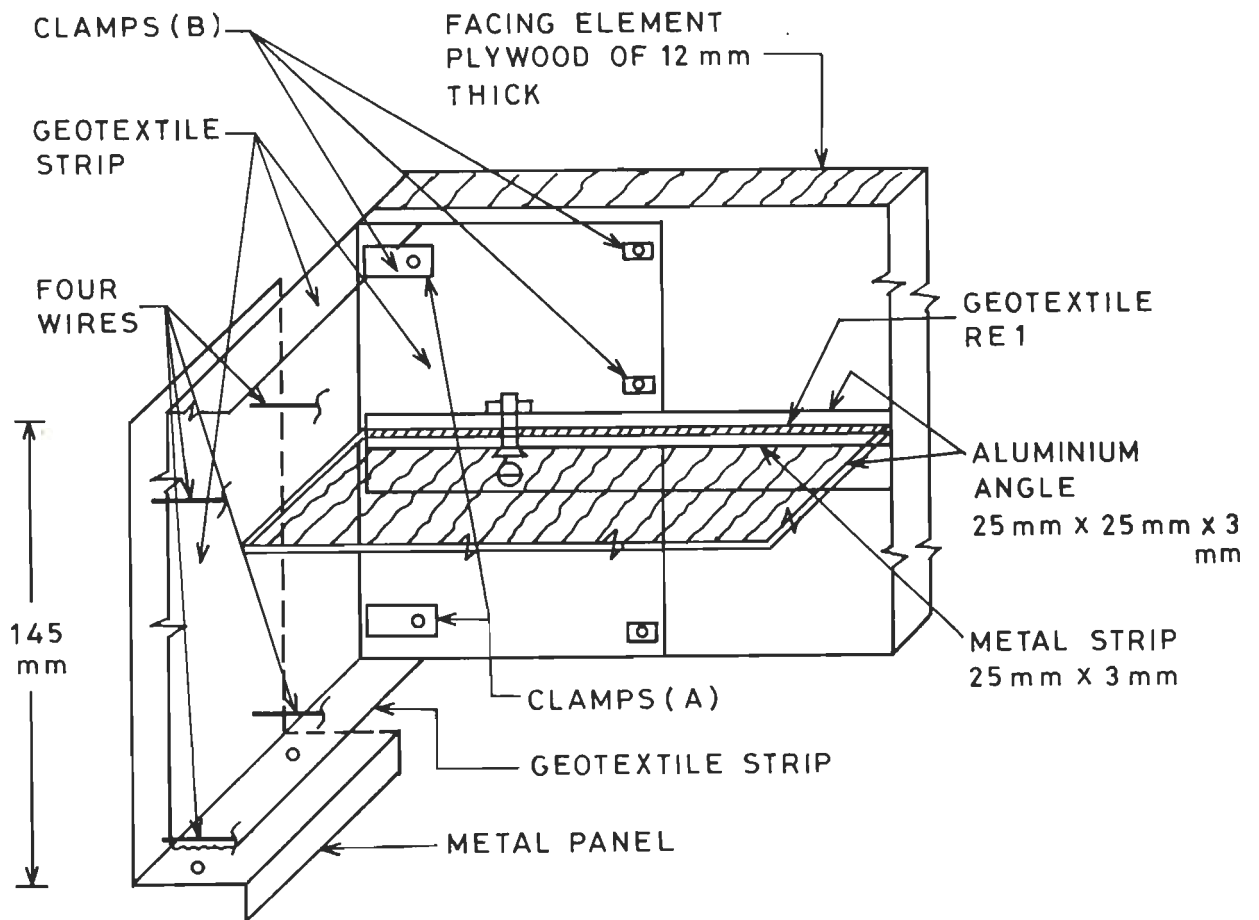


FIG. 4.4.6 DETAILS OF CONNECTIONS BETWEEN THE SOIL REINFORCEMENT, GEOTEXTILE STRIPS COVERING TRANSVERSE SIDE AND THE FACING ELEMENT.

in Fig. 4.4.7 at A. Besides, a thin angle of 25 mm x 25 mm x 1 mm thick, 148 mm long, was screwed on to plywood facing element along its inner vertical side. This angle supports vertical corner of geotextile and precludes its opening due to outward movement and hence spilling the sand. Such sealing of sand leakage at bottom of each layer precluded formation of funnel shaped leakage creators extending upto the top of embankment. Trial run of embankment construction was helpful in identifying such leakages and remedial measures. Arrangement cited above performed quite satisfactorily. Details shown in Fig. 4.4.7 were suppressed in Fig. 4.4.6 for clarity.

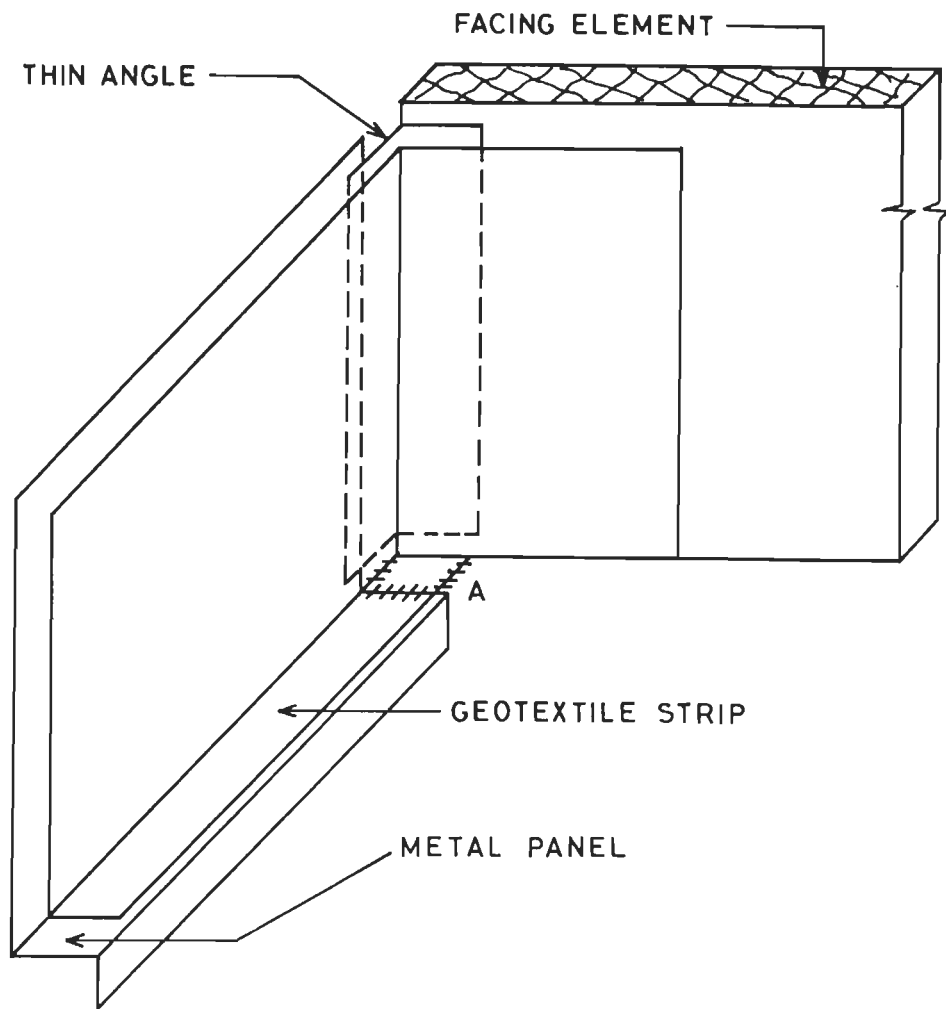


FIG.4.4.7 DETAILS OF MEASURES TAKEN TO AVOID LEAKAGE OF SAND AT CORNER JOINTS.

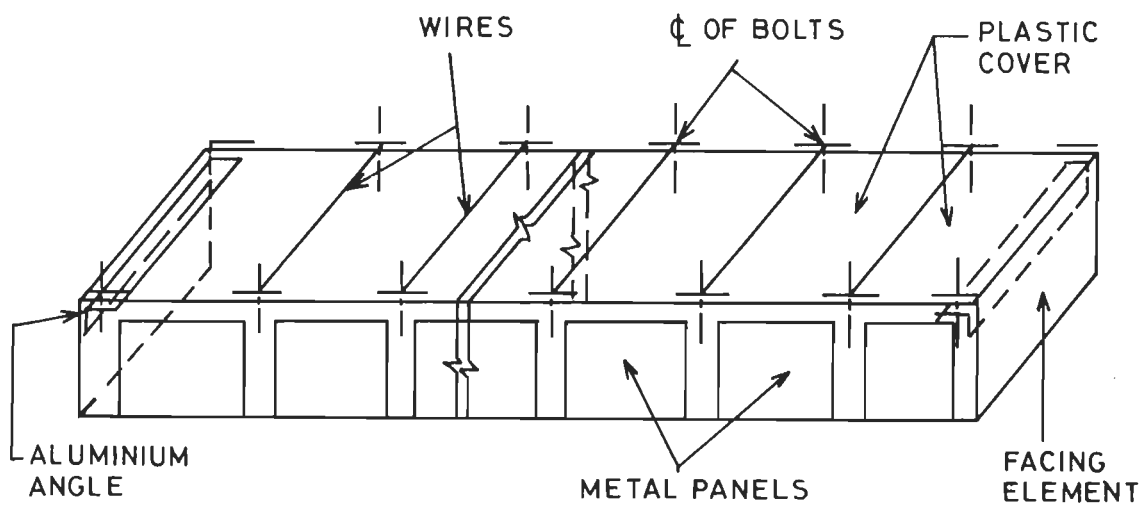


FIG.4.4.8 SCHEMATIC DIAGRAM OF DETAILS OF TOP COVER AND TOP LAYER OF THE EMBANKMENT.

Top Cover of the Embankment

To avoid sand flying out from top end, the top was covered with a plastic sheet, 1.5 mm long and 750 mm wide, connected to an aluminium angle at each 750 mm wide edge. Vertical legs of these angles, not connected to facing elements, are pressed into sand fill to hold the cover firmly in position. Sixteen wires at regular intervals running parallel to facing elements and connected to transverse geotextile covers assist the plastic cover in containing sand. This arrangement (Fig. 4.4.8) has worked well.

4.4.4 Preparation of Test Embankments

Step wise procedure for preparing embankments is discussed here. Two hinges and three longitudinal lower strips were first bolted to shake table platform. The rectangular box like plywood form work (150 mm deep) was placed in position on platform and held in position by connecting it to shake table frame at 3 places on each transverse side. The lowest transverse side strip of geotextile cover was now place in position. Transverse side metal panels for bottom layer were L-shaped and secured in proper position to geotextile cover from outside with adequate gap between adjacent panels. On placing geotextile strip together with these panels in position, the L-shaped panels rest on platform. The 30 mm wide horizontal folded projection of geotextile strip was sandwiched between upper and lower longitudinal metal strips and held securely by bolting. The upper 30 mm wide folded portion of geotextile strip is stretch outwards at top end of plywood form work and another 150 mm deep form work was placed over the form work already in position. The 750 mm wide geotextile piece is connected to inner face facing element at one end at D (Fig. 4.4.5) and to longitudinal metal strip at E to prevent sand from spilling into the hinge.

Each metal panel on transverse side was connected at the lower end to corresponding panel on opposite side by two longitudinal wires. Plywood strut placed between metal panels controlled the required length of wires.

Sand rain apparatus (SRA) was lowered to its position above the platform to obtain the height of fall for obtaining required density. The SRA was filled with 75 mm deep sand with all shutters closed (Fig. 4.4.9). Plastic sheet was wrapped around the outer periphery of SRA frame and shutters released to rain sand to form 75 mm deep lower half of bottom most layer of sand. The SRA was raised by 75 mm then..

Geotextile reinforcement of this layer, together with aluminium angles connected to it at each 75mm wide end was placed on surface of finished soil layer. Aluminium gripping angles were then connected to corresponding facing element at its mid height by bolting. Remaining two longitudinal metal wires connecting each pair of metal panels at their top ends were then tied up. Figure 4.4.10 shows a photograph of the setup at this stage.

The SRA, filled with sand, was then lowered to its proper position and the procedure for pouring sand was repeated to form another 75 mm thick sand deposit to finish formation of the bottom layer of embankment. The SRA was raised again and transverse strips of geotextiles together with metal panels were connected to corresponding geotextile strips of the lower layer by using nuts and bolts. The setup was then ready for repeating process on the lines indicated above for preparation of the second layer. The procedure was repeated till completion of top most layer. Plastic cover was then placed on top surface and tied with wires to finished construction of embankment. Figure 4.4.11 shows embankment with form work at this stage.



FIG. 4.4.9 VIEW OF THE SETUP AT THE BEGINNING OF PREPARATION OF RE TEST EMBANKMENT.

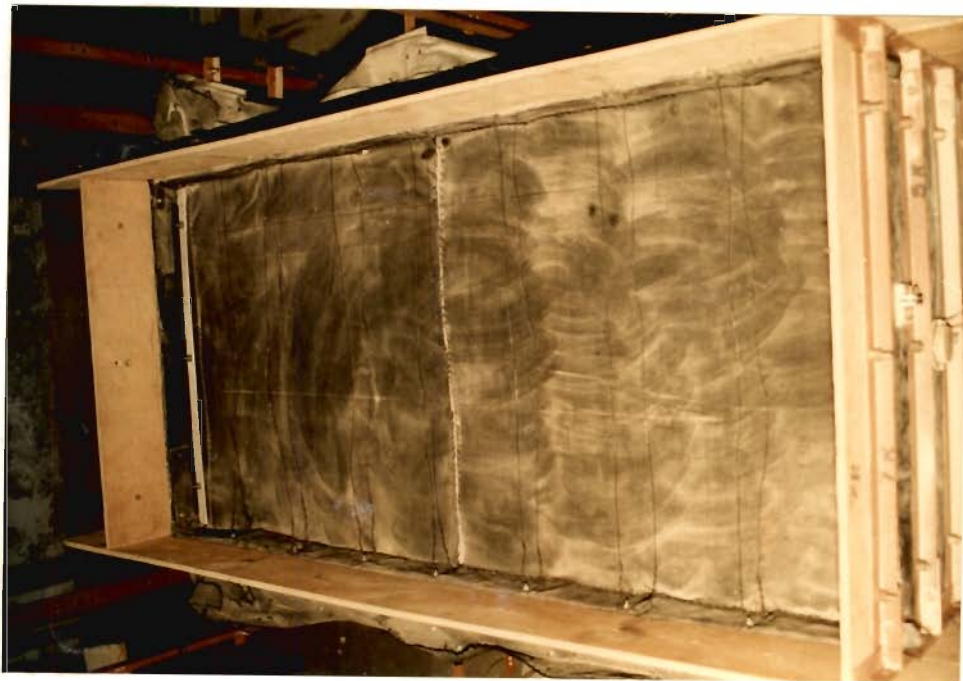


FIG. 4.4.10 VIEW OF THE TEST SETUP AFTER PLACING AND CONNECTING THE GEOTEXTILE REINFORCEMENT.

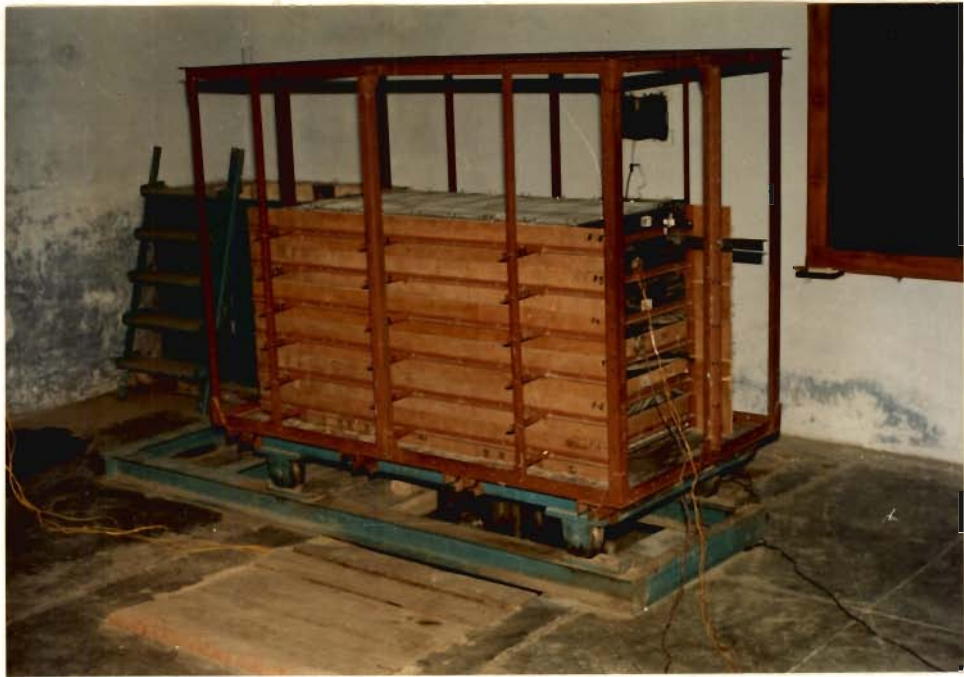


FIG. 4. 4. 11 VIEW OF RE- TEST EMBANKMENT WITH FORMWORK IN POSITION AT THE END OF CONSTRUCTION.



FIG. 4. 4. 12 VIEW OF THE LONGITUDINAL FACE OF THE EMBANKMENT WITH ACCELERATION PICKUPS IN POSITION.

Two acceleration pickups were fixed on facing elements at this stage, one at 0.425 m and the other at 0.875 m above base. Third pickup was fixed on vertical edge of shake table to measure response. All pickups monitor horizontal accelerations. Figure 4.4.12 shows a view of longitudinal face of test embankment with acceleration pickups in position at this stage.

On removing plywood form work planks covering transverse sides, test embankment stood freely. Diagonal elements of shake table frame were now assembled using nuts and bolts to stiffen the frame. Pickups were then connected to amplifiers and recorders and were calibrated just before starting and again, just after completing dynamic tests (Fig.4.4.13). Power connections were made for motor/power supply unit with mechanical oscillator set to position of zero OME. Set up was then ready for dynamic tests.

Three R.E. test embankments M1, M2 and M3 were prepared this way. M1 has all reinforcements running continuously from one longitudinal face to another in all layers which makes it the strongest of the 3 embankments. M2 has such continuous reinforcements in the top four layers. Reinforcements in bottom two layer are discontinuous at their mid-length which makes it weaker than M1. In Fig. 4.4.10, a view of discontinuous reinforcements in position during preparation of embankment is shown. For M3, continuous reinforcement is provided in top layer only and remaining reinforcements are discontinuous which makes it the weakest of the 3 embankments. This has been substantiated by test results presented in this chapter later.

4.4.5 Procedure for Dynamic Testing of Embankments

Free and forced vibration tests were carried on each test embankment. Sinusoidal base excitations using different values of oscillatory mass



FIG. 4.4.13 A VIEW OF THE FREE STANDING RE TEST EMBANKMENT ON SHAKE TABLE AND THE AMPLIFIERS AND RECORDERS JUST BEFORE THE DYNAMIC TESTING.



FIG. 4.4.14 A VIEW OF THE RE-TEST EMBANKMENT AFTER THE DYNAMIC TESTS IS COMPLETED.

eccentricity (OME) settings and different frequencies were employed. The step-wise test procedure is as explained below:

Free vibration tests using impact energy

Free vibration tests were carried out by giving impact of a sledge hammer on table in transverse direction of embankment. The embankment oscillated under the influence of impact. Response of embankment and the table was recorded using the fastest paper speed of 125 mm/sec. The test was repeated three times and acceleration records were obtained.

Forced vibration tests

Forced vibration tests were conducted with low OME settings. Each test began with a frequency of 5 Hz and frequencies were scanned at short interval increments till the fundamental frequency of embankment was exceeded. At each frequency with the same OME, accelerations using three pickups were recorded along with the chart multiplier values.

At the end of force vibration test for a particular OME, DC motor of the oscillator was switched off. When system came to rest, next higher value of OME setting was chosen and the test was repeated. This was repeated at intervals of 6 OME setting intervals till the maximum OME setting of 36 was reached. Figure 4.4.14 shows a view of the transverse face of the test embankment after the dynamic testing was completed.

4.5 PROCESSING AND BACK-ANALYSES OF EXPERIMENTAL DATA

Acceleration and frequency are dynamic parameters which were measured directly. Other dynamic parameters of interest were obtained from back-

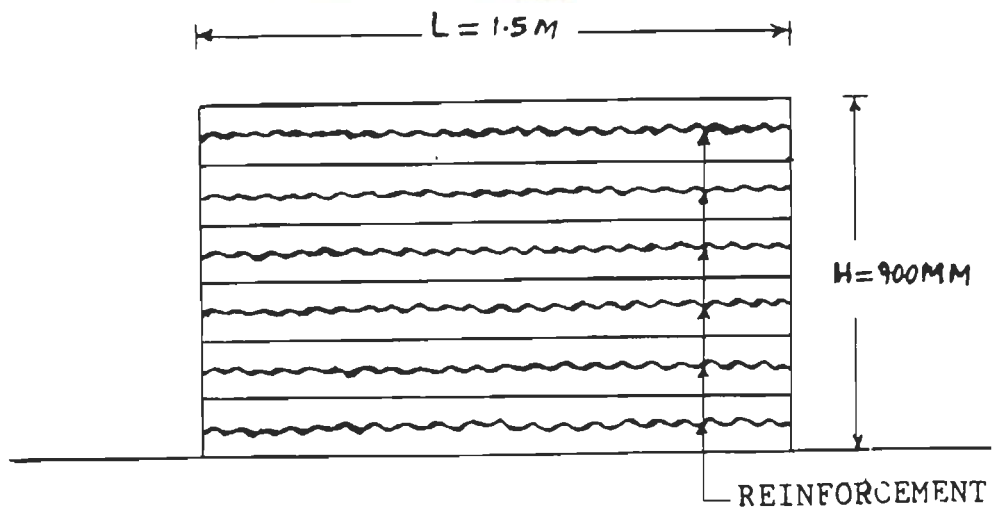
analyses of test data knowing dynamic behaviour of embankments. In this article, processing and back-analyses of test data is dealt with.

For analytical and experimental study, embankment of length, $L=1.5$ m, width, $B=750$ mm and height, $H=900$ mm, was considered which ensured that the model behaved like a shear beam. Hence, bending stresses were negligible. The embankment was fixed at the base and free at the top. Figure 4.5.1a shows embankment M1 with six layers, each with thickness, $H_L=150$ mm. These layers were numbered serially. The first layer was at top and sixth layer was at the base. For i 'th layer, X_i is depth from embankment top upto bottom of i 'th layer. Each layer had a reinforcement at mid depth. Reinforcements were also numbered serially with first one in top later. For the i 'th reinforcement, depth from the top of the model is H_{ri} .

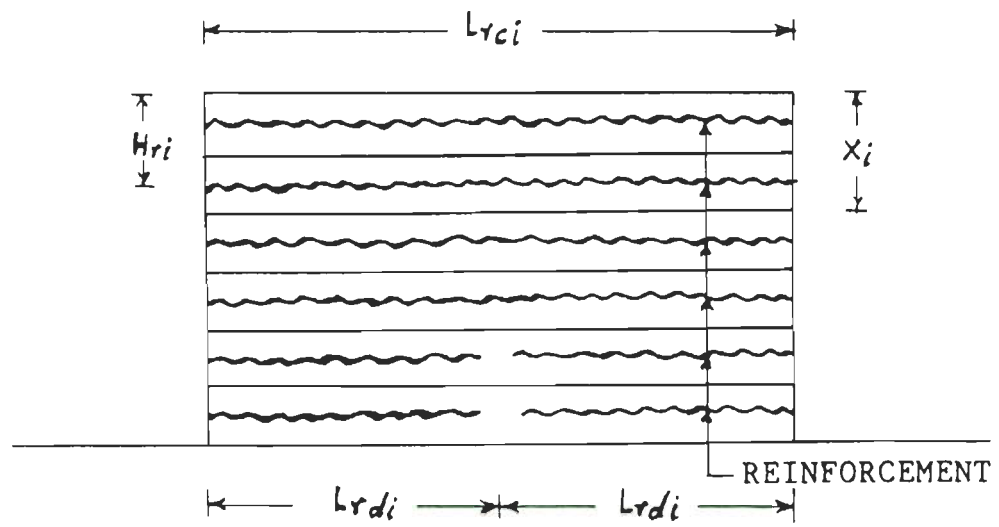
Three types of embankments were studied. Embankment M1 (Fig. 4.5.1a) had only reinforcements. Embankment M2 (Fig. 4.5.1b) had continuous reinforcements in top four layers. The remaining two were discontinuous. Embankment M3 (Fig. 4.5.1c) had continuous reinforcement only in the top layer. Remaining reinforcements were discontinuous. The length of i 'th reinforcement, L_{rci} , is equal to 1.50 m if it is a continuous element and equal to 0.75 m if it is discontinuous.

The dynamic parameters dealt with in this article are :

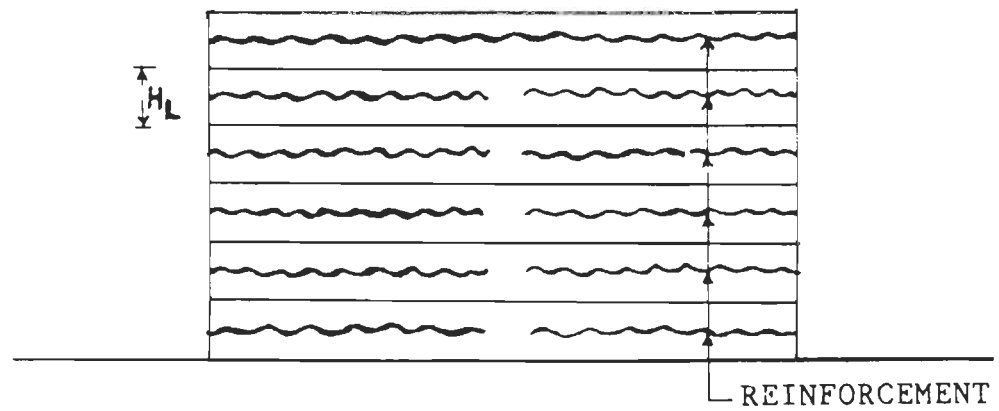
- i) Fundamental frequency, average shear strain and shear modulus
- ii) Variation of acceleration
- iii) Disturbing force
- iv) Shear resistance due to plain sand
- v) Displacement dependent dynamic pullout resistance
- vi) Coefficient of average dynamic pullout resistance



(a) TEST EMBANKMENT M1



(b) TEST EMBANKMENT , M2



(c) TEST EMBANKMENT , M3

FIG. 4.5.1 SCHMETIC DIAGRAMS OF TEST EMBANKMENTS.

First four parameters cited above refer to whole embankment. Parameters cited under v and v_i refer to components of the embankment.

4.5.1 Fundamental Frequency, Shear Strain and Shear Modulus

Dynamic parameters for the whole embankment are obtained from results of free and forced vibration tests dealt with in detail in this article.

Processing data from impact type of free vibration tests

Acceleration was obtained as a function of time from free vibration tests with impact. Three acceleration peaks in one direction and two in opposite direction could be measured with reasonable accuracy. Mean position of pen before and after impact was also available. With respect to this mean, acceleration amplitude for three peaks on the same side of mean pen position were measured and their average amplitude was obtained. Fundamental frequency was also obtained from the record of accelerations.

The embankment is assumed to vibrate with natural frequency, F_n , obtained this way and with mean single acceleration amplitude, a_{free} , obtained as explained above. Using this information, the single amplitude of the mean displacement, d_{free} , may be obtained as :

$$d_{free} = a_{free} / (4\pi^2 F_n^2) \quad (4.5.1)$$

Mean or average shear strain, γ_r , is obtained as (d_{free}/H) where H is height of the embankment. From fundamental vibrations of shear beam, the circular frequency, ω_n , is obtained as :

$$\omega_n = \sqrt{\frac{K_s G_{rn}}{\rho} \frac{(2r-1)\pi}{2H}}, \quad \text{i.e.,} \quad G_{rn} = \frac{\omega_n^2 \cdot \rho \cdot 4H^2}{K_s (2r-1)^2 \pi^2} \quad (4.5.2)$$

where, G_{rn} is shear modulus of R.E. embankment, ρ is mass density and $r=1$ for fundamental mode of vibration. Constant shape factor $K_s=5/6$ (Krishna et.al., 1994). Using this relationship, value of shear modulus is evaluated using value of $\omega_n=2\pi F_n$. Values of γ_r and G_{rn} thus obtained for test embankments are reported in Article 4.6 later in this Chapter.

Processing data from forced Vibration Tests

For each OME setting, values of steady state acceleration at different frequencies were obtained from recorded acceleration. Knowing the acceleration and the corresponding frequency, the frequency response curves were obtained. The displacement, d_{fq} , for any sinusoidal excitation of a given frequency, F_{rq} , associated with acceleration, a_{fq} , is given by :

$$d_{fq} = a_{fq} / (4\pi^2 F_{rq}^2) \quad (4.5.3)$$

From frequency response relationships obtained for a given OME setting and for a given test embankment, resonance frequency, F_n , may be obtained which is associated with maximum response. The shear modulus of R.E. embankment, G_{rn} , corresponding to the resonant frequency for first mode may be obtained by using Eq. (4.5.2). The average shear strain, γ_r , may be obtained as the ratio (d_{fq}/H) at resonant frequency. Acceleration and frequency values obtained from force vibration tests using the two acceleration pickups on longitudinal face of embankment are cited in Article 4.6 in this chapter.

4.5.2 Variation of Acceleration

Variation of acceleration along the height of embankment is needed for computing inertia forces. But accelerations are measured only at the top, middle and bottom pickup levels. As such it is necessary to devise a method for predicting variation acceleration with height based on measured accelerations at these three points.

Shear waves generated by table excitation propagate vertically with frequency equal to excitation frequency. Velocity of propagation, V_s , may be evaluated from known shear modulus, G_r , for R.E. and shear strain, γ_r , for the test under consideration. The expression for the V_s is given by:

$$V_s = \sqrt{G_r/\rho} \quad (4.5.4)$$

where ρ is mass density of sand. Using values of, V_s , the time lag, Δt , and corresponding phase difference, $\delta\theta$, between instant of arrival of shear wave at any two points may be obtained. Expressions for Δt and $\delta\theta$ are:

$$\Delta t = X/V_s \quad (4.5.5)$$

$$\delta\theta = 2\pi\Delta t/T \quad (4.5.6)$$

where T is period of table excitation and X is vertical distance between two points being considered. Using these expressions, the phase difference, $\delta\theta_t$, for top position of acceleration pickup, $\delta\theta_m$ for the middle position pickup and $\delta\theta_b$, for the bottom pickup w.r.t. phase angle for the top of embankment are computed. Phase angle, θ , at any instant of time at top, middle and bottom pickup positions and at top end of model are respectively denoted by θ_t , θ_m , θ_b and θ_{top} where :

$$\theta_t = \theta_{top} + \delta\theta_t \quad (4.5.7)$$

$$\theta_m = \theta_{top} + \delta\theta_m \quad (4.5.8)$$

$$\theta_b = \theta_{top} + \delta\theta_b \quad (4.5.9)$$

The θ_{top} values varies from zero to 2π in the Eq. 4.5.7., 4.5.8 and 4.5.9.

Figure 4.5.2 shows these details. Knowing measured amplitudes of acceleration a_t , a_m and a_b at the top, middle and bottom pickup positions, magnitudes of accelerations Y_{tt} , Y_{mt} and Y_{bt} at the given instant, t , are:

$$Y_{tt} = a_t \cdot \sin \theta_{tt} \quad (4.5.10)$$

$$Y_{mt} = a_m \cdot \sin \theta_{mt} \quad (4.5.11)$$

$$Y_{bt} = a_b \cdot \sin \theta_{bt} \quad (4.5.12)$$

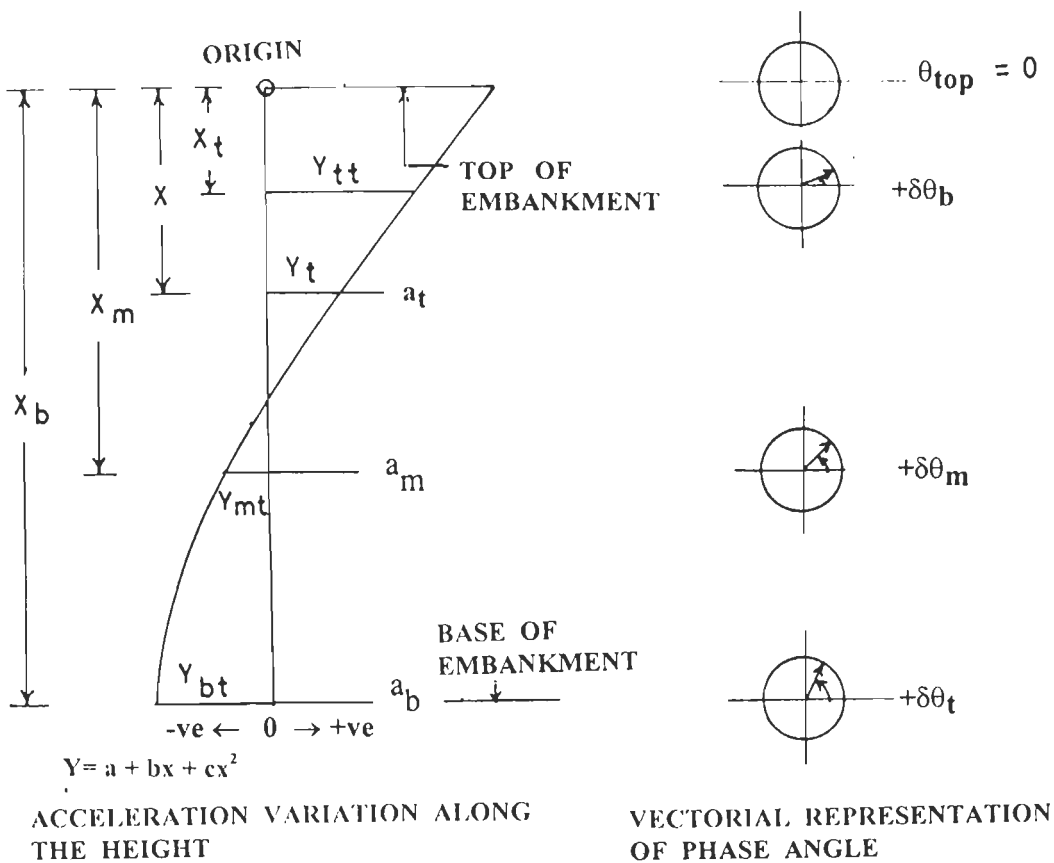


FIG. 4.5.2 ACCELERATION AND PHASE ANGLES ALONG THE HEIGHT OF THE EMBANKMENT.

For computation of disturbing inertia forces, it is necessary to evaluate acceleration vectors at each level of reinforcing elements. For this purpose a polynomial of the second degree is used and given by :

$$y = a + bx + cx^2 \quad (4.5.13)$$

Constants a, b and c are evaluated by known values of Y_{tt} , Y_{mt} and Y_{bt} and the corresponding distances x_t , x_m and x_b measured from the top.

4.5.3 Disturbing Forces

Disturbing forces are generated by inertia of different embankment layers. Since accelerations are only in horizontal directions, inertia forces are also in horizontal direction. The acceleration vector at any instant of time varies along the height of embankment. As such, to obtain net horizontal force, it is necessary to integrate the same numerically by considering a number of horizontal elements (layers) of embankment. For convenience, embankment is divided into six horizontal elements of 150 mm thickness. A horizontal reinforcing element is situated at the mid height of each element. Inertia force, F_{dk} generated by k'th element is given by:

$$F_{dk} = m_k \cdot Y_k \quad (4.5.14)$$

where m_k is mass of k'th element and Y_k is acceleration at the mid height of k'th element. Inertia force acting on reinforcing element in top layer is equal to inertia generated by that element. Net disturbing force, F_{di} , on i'th reinforcing element situated in i'th element is obtained as:

$$F_{di} = \sum_{k=1}^i F_{dk} \quad (4.5.15)$$

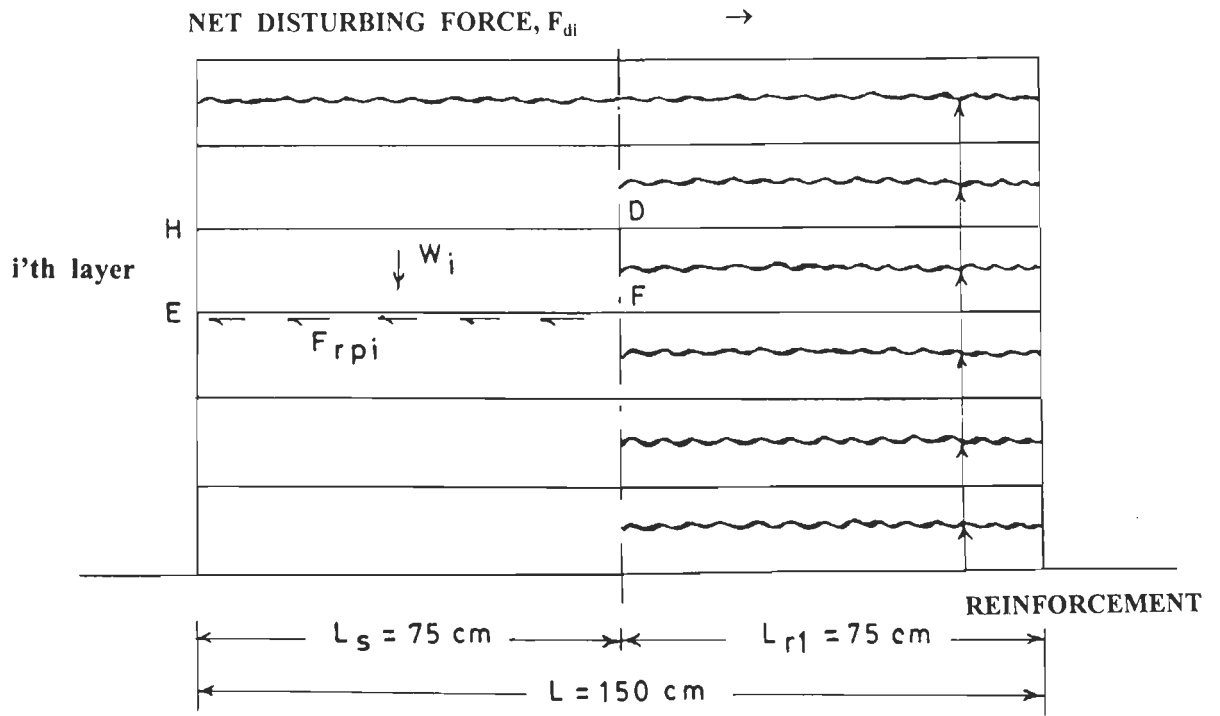
Net disturbing force, F_{di} , acting in forward direction on any reinforcing element is overcome by pullout resistance offered by that

reinforcing elements r_1 of length L_{r1} and the shear resistance offered by plain sand of length equal to L_s (Fig. 4.5.3a) for the first half cycle of vibration where the net length of embankment is given by $(L_{r1} + L_s)$. This is obvious from the fact that reinforcing element offers resistance only when disturbing force causes tension in it. Similarly, when disturbing force, F_{di} , acts in reverse direction (Fig. 4.5.3b), the reinforcing element, r_2 of length L_{r2} offers pullout resistance to overcome this disturbing force and which is supplemented by resistance offered by plain sand over the length equal to L_s .

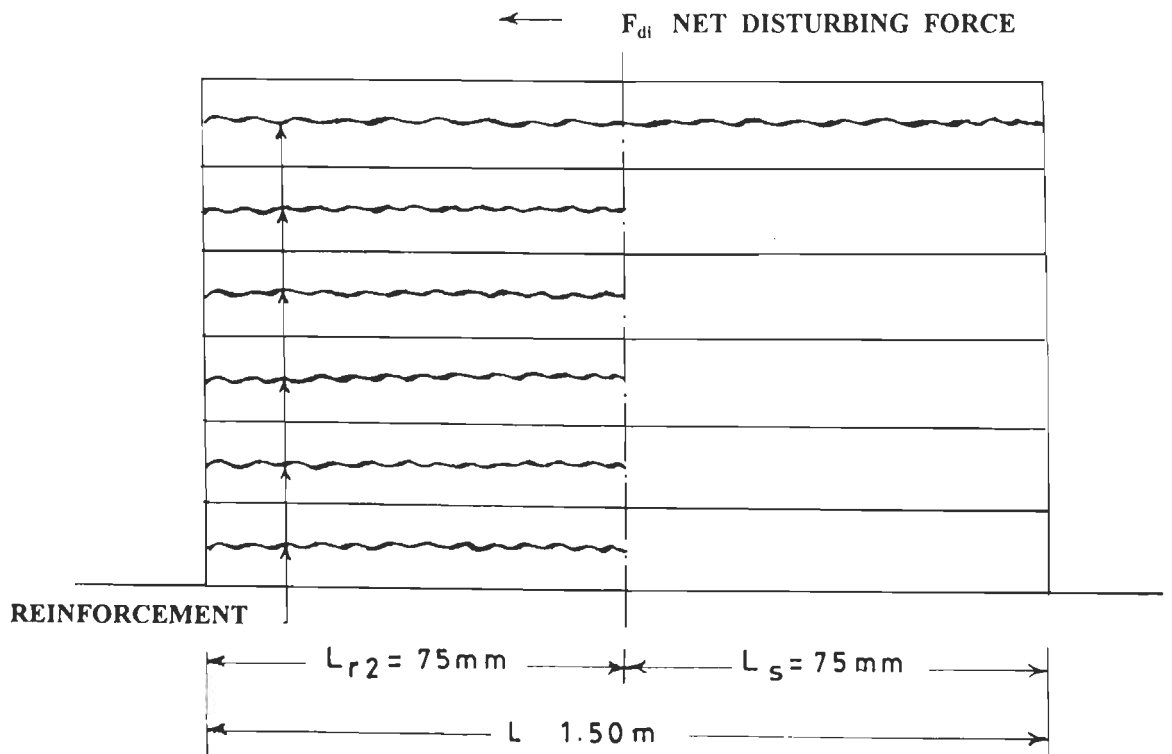
4.5.4 Shear Resistance Due to Plain Sand

Embankment excited sinusoidally suffers deformations mainly in shear mode. As cited earlier, resistance is developed due to shearing of plain sand and the pullout resistance of reinforcement (Fig. 4.5.3a). For top layer, reinforcement extends for the entire length. As such, plain sand develops no shear resistance for this layer. For second layer, shearing of plain sand occurs along HD and for third layer along EF (Fig. 4.5.3a) and soon for the remaining layers also. Angle of shear resistance mobilised, ϕ_m , in any layer depends on average mobilised shear strain, γ_m . As such, a relationship between ϕ_m and γ_m is needed to evaluate shear resistance due to plain sand, which has been obtained from test results (Fig. 4.2.2a).

Results of the investigation indicate that contribution of resistance by plain sand computed for the worst condition associated with severe most disturbing forces is very negligible (Table 4.5.1). As such, more accurate computation of γ_m and the associated value of ϕ_m is unnecessary. If a_t is maximum acceleration at embankment top with frequency, F_{rq} , the maximum displacement, d_t , at embankment top and shear strain, γ_m , are given as :



(a) FORWARD DIRECTION OF LOADING



(b) REVERSE DIRECTION OF LOADING

FIG. 4.5.3 SCHEMATIC DIAGRAMS OF EMBANKMENT INDICATING PARTICIPATING REINFORCEMENTS WHEN SUBJECTED TO FORWARD AND REVERSE DIRECTION LOADING.

$$d_t = a_t / (4\pi^2 F_{rq}^2) \quad (4.5.16)$$

$$\gamma_m = d_t / H \quad (4.5.17)$$

Figure 4.2.2a Shows the relationship between $\tan\phi_m$ and γ_m for plain sand. It is clear from the figure that for value of γ_m upto 0.266, $\tan\phi_m$ varies linearly with γ_m . Slope, C_s of lower bond curve from this figure is

Table 4.5.1 Percentage Resisting Force Contribution by Plain Sand for R.E. Test Embankment, M3.

OME	F_n (Hz)	F_{rq} (Hz)	F_{rq}/F_n	F_{dmx} (t)	F_{rpmx} (t)	$(F_{rpmx}/F_{dmx}) \times 100$
24	13.5	9.540	0.7066	0.32593	5.74112E-03	1.761458
		11.475	0.8500	0.49630	6.39963E-03	1.289468
		12.250	0.9074	0.63539	6.86751E-03	1.080830
		12.825	0.9500	0.98758	0.010092100	1.021902
		13.095	0.9700	1.20728	0.011241100	0.931109
		13.500	1.0000	1.44400	0.015314300	1.060547
36	13.15	9.290	0.7071	0.4079	6.39981E-03	1.569000
		11.177	0.8500	0.66505	6.79758E-03	1.022115
		11.835	0.90000	0.89240	7.48926E-03	0.839220
		12.500	0.95000	1.29675	0.013771500	1.062001
		12.755	0.97000	1.5474	0.016391200	1.059287
		13.150	1.00000	1.7353	0.018327800	1.056187

Note: F_{dmx} is maximum inertia force generated by mass of embankment layers for phase angle varying from 0 to 2π .

F_{rpmx} is maximum restoring force due to shearing mobilised due to plain sand layers of embankment.

obtained as 2.63157 which gives conservative estimates of $\tan\phi_m$ for use in this analysis. Hence, value of $\tan\phi_m$ in this analysis may be expressed as:

$$\tan\phi_m = \gamma_m \cdot C_s \quad (4.5.18)$$

If weight W_i is standing above EF (Fig. 4.5.3 a), shear resistance offered by plain sand, F_{rpi} , at the base of slice is given by:

$$P_{pri} = W_i \tan\phi_m = W_i C_s \gamma_m \quad (4.5.19)$$

4.5.5 Displacement Dependent Dynamic Pullout Resistance of a Reinforcement

As cited earlier, resistance to overcome dynamic distributing forces is mainly developed as pullout resistance of geotextile. However, for mobilization of this dynamic pullout resistance, P_{dr} , some pullout displacement, d_{pd} , should take place and P_{dr} increases with increasing d_{pd} . If embankment is to behave within elastic domain only, it is necessary to limit coefficient of dynamic pullout resistance, μ_{avd} , to be acceptably small. However, in reality, the performance criteria of structures such as embankment is often specified in terms of allowable displacement which depends on importance of the structure. Therefore, it is very logical and desirable to propose a relationship between mobilised μ_{avd} and associated d_{pd} for this purpose. This is useful in design of individual reinforcements to satisfy tolerance limit specified for the case under consideration.

Dynamic pullout resistance, P_{dri} , developed by i 'th reinforcement may be evaluated by equating disturbing and resistance forces as shown below :

$$F_{di} = \sum_{k=1}^i F_{dk} = P_{pri} + P_{dri} = P_{pri} + 2\sigma_v \mu_{avdi} \cdot L_{ri} \quad (4.5.20)$$

$$\begin{aligned} \text{i.e., } \mu_{avdi} &= \frac{F_{di} - P_{pri}}{2 W_i} \\ &= \frac{m_i \cdot Y_i - W_i C_s \gamma_m}{2 W_i} \end{aligned} \quad (4.5.21)$$

Where σ_v is normal stress, Y_i is acceleration vector at the level of i 'th reinforcement and μ_{avdi} is coefficient of average dynamic friction developed along i 'th reinforcement. Knowing value of μ_{avdi} , average pullout resistance angle, ϕ_{avpi} , developed for i 'th reinforcement is defined as:

$$\phi_{avpi} = \tan^{-1} (\mu_{avdi}) \quad (4.5.22)$$

Evaluation of μ_{avdi} , ϕ_{avpi} , disturbing force, F_{di} , shearing resistance due to plain sand, F_{rpi} etc. (all for i 'th reinforcement) is useful for understanding behaviour of various components of R.E. embankment under earthquake loading conditions.

4.5.6 Average Dynamic Pullout Resistance for the Whole Embankment

As cited earlier, if individual layers of R.E. forming the embankment are quite small compared to embankment height, the embankment may be considered to be homogeneous throughout. As such, it is desirable to obtain average material properties and average behaviour of test embankment to obtain equivalent material properties for assumed homogeneous embankment.

Using accelerations and strains varying from layer to layer, μ_{avdi} for i 'th layer may be obtained. Weighted average coefficient of dynamic pullout resistance, μ_{avd} , for the entire embankment may be obtained by employing standard analytical methods which is attempted in this article.

If for each layer, frequency, eccentricity and embankment type, μ_{avdi} is given separately data would be inconveniently large to present. The study aims to understand behaviour of R.E. conceived to be homogeneous. So, presenting weighted μ_{avdi} denoted by μ_{avd} and computed for whole embankment is appropriate, convenient and helpful to overcome difficulty cited above.

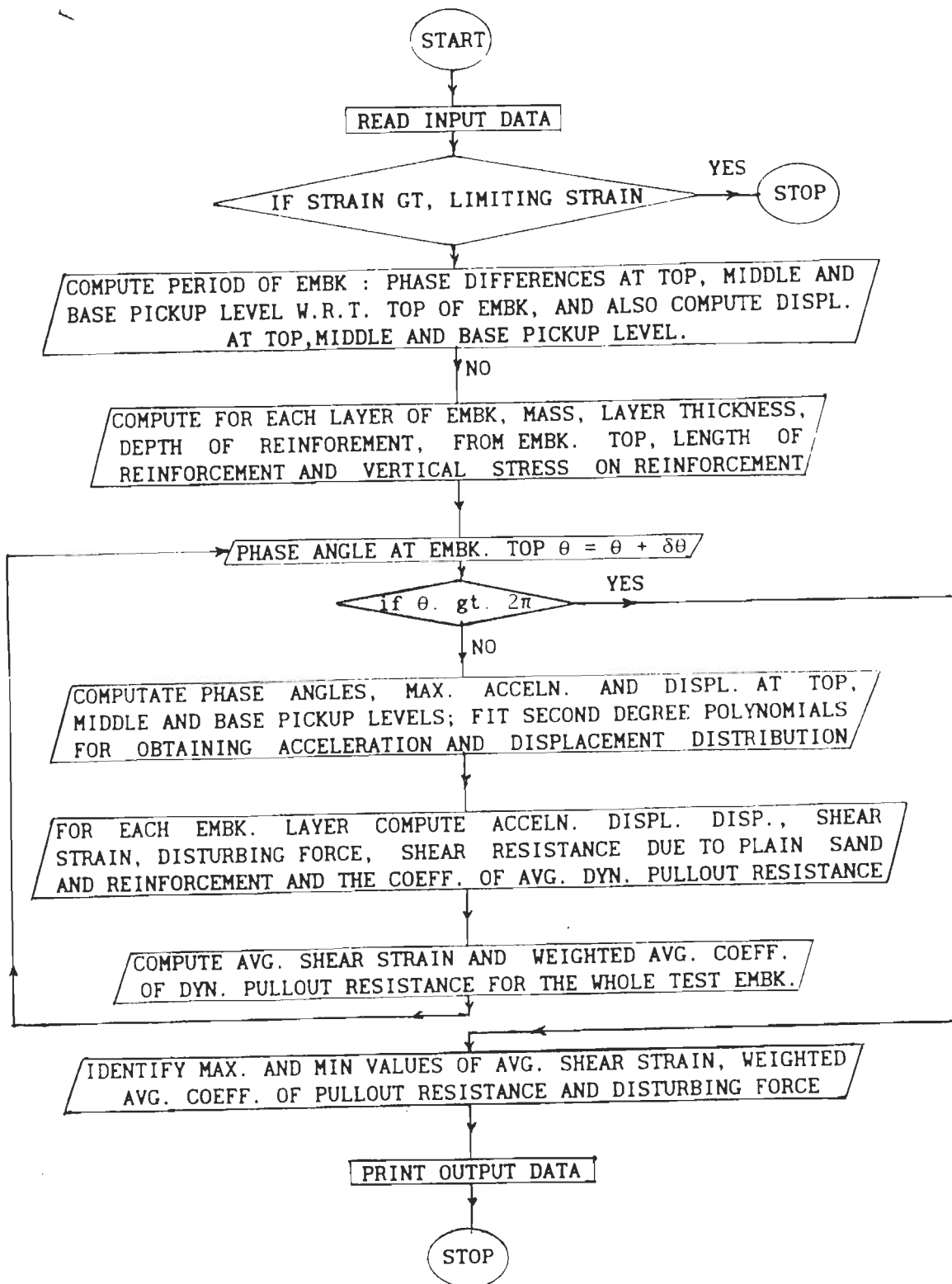
Evaluation of μ_{avdi} for each reinforcement for various phase angles was explained earlier. Layer thickness, H_{Li} , and active reinforcement length, L_{ri} , may vary from layer to layer. Hence, it is essential to assign proper weights to these factors in computing μ_{avd} which is given as :

$$\mu_{avd} = \frac{\sum_{i=1}^6 \mu_{avdi} L_{ri}}{\sum_{i=1}^6 H_{Li} \cdot L_{ri}} \quad (4.5.23)$$

Averaging of pullout resistance in a given zone of R.E. indicated by Eq. 4.5.23 above is very useful in obtaining this material property for different R.E. zones of the same embankment, if warranted.

4.5.7 Computer Software 'DYMU' for the Back-Analyses

For carrying out back-analyses on the lines indicated above to compute acceleration, displacement and strain distribution over embankment height, the disturbing forces, resisting forces due to plain sand and reinforcement, the value of μ_{avdi} in any i'th layer as well as for obtaining the μ_{avd} for the whole embankment, maximum and minimum values of average shear strain and disturbing forces within the embankment, a software 'DYMU' has been developed. This software employs acceleration, frequency, shear wave



ABBREVIATIONS USED:

ITEM	ABBREVIATION	ITEM	ABBREVIATION
ACCELERATION	ACCELN.	DYNAMIC	DYN.
AVERAGE	AVG.	EMBANKMENT	EMBK.
COEFFICIENT	COEFF.	MAXIMUM	MAX.
DISPLACEMENT	DISPL.	MINIMUM	MIN.

FIG. 4.5.4 FLOW DIAGRAM FOR THE COMPUTER SOFTWARE "DYMU".

velocity etc. obtained from tests as input data. Figure 4.5.4 shows the flow diagram for DYMU and abbreviations used in it

The compact software, written in fortran IV language, has about 700 statements only. Computational effort for each run is quite small. It may be run on PC-486 commonly available. Output from this program is useful in studying relationship between dynamic parameters discussed in this article and their comparison with results reported in the state of the art.

4.6 PRESENTATION OF RESULTS

Results are presented with dimensionless parameters (Table 4.6.1) as far as possible to make presentation independent of units and size.

4.6.1 Damping Ratios from Free Vibration Tests

Damping is an important material properties of embankments required for dynamic analysis. It depends on shear strain. A standard method is to determine it from data of free vibration tests explained earlier. Amplitude of acceleration, a_{free} , in free vibration tests decreases with increasing time after initial impact due to damping in the embankment. Knowing successive a_{free} and by using Eq. 4.5.1, corresponding displacement amplitudes, d_{free} , for successive peaks of free vibrations and their logarithmic decrement, δ_1 , can be obtained. Damping coefficient, ζ , is obtained as $\{\delta_1/2\pi\}$. Table 4.6.2a gives a typical free vibration record, displacements, shear strains and damping ratios obtained for M1 and M3.

For stiffer M2, damping ratio vary from 0.0196 to 0.042 and from 0.022 to 0.045 for softer M3. For associated strain levels, these damping ratios

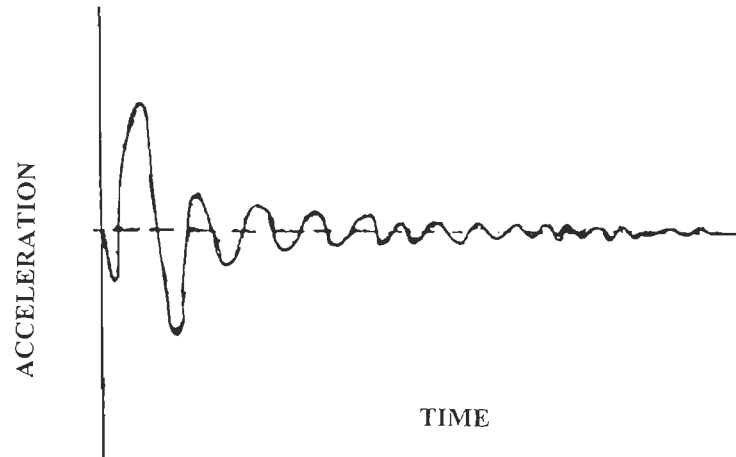
Table 4.6.1 Parameters for Presentation of Results of Back-Analysis

S.No.	Parameter	Symbol	Definition
1.	Frequency of excitation (Hz)	F_{rq}	
2.	Natural frequency (Hz)	F_n	
3.	Frequency ratio	r_f	F_{rq}/F_n
4.	Acceleration (m/sec)		
	From free vibration tests at top pickup	a_{free}	
	From forced vibration tests at top pickup level	a_t	
	at middle pickup level	a_m	
	at base pickup level	a_b	
5.	Magnification factor	M_f	a_t/a_b
6.	Displacements (mm)		
	From free vibration tests at top pickup	d_{free}	See Eq. 4.5.1
	From forced vibration tests	d_t	See Eq. 4.5.3
7.	Shear Strains		
	From free vibration tests at top pickup at a distance H_t above base	ξ_{free}	d_{free}/H_t
	From force vibration tests at top pickup For plain sand.	γ_r	d_t/H_t
		γ_s	
8.	Maximum average shear strain for embankment (when θ varies from θ to 2π)	γ_{avdmx}	
9.	Shear Moduli		
	For R.E. test embankment	G_r	See Eq. 4.5.2
	For plain sand of test embankment	G_s	
10.	Ratio of Shear Moduli	r_G	G_r/G_s

with damping reported by Seed et al (1984) for same strains. Hence, damping obtained from free vibration tests of this study are reasonably good.

4.6.2 Frequency-Acceleration Response.

Table 4.6.2b shows natural frequencies and accelerations from free vibration tests and displacements, average shear strain, γ_r , shear modulus,



Typical Free Vibration Record.

Table 4.6.2a Damping Ratios Obtained from Free Vibration Tests on R.E. Embankments.

R.E Embankment	M2					M3				
Displacement (mm)	0.1059	0.0867	0.0766	0.0587	0.0485	0.2703	0.21947	0.1908	0.1431	0.1145
Shear Strain $\times 10^{-4}$	1.2100	0.9080	0.8750	0.6708	0.5543	3.0890	2.50800	2.1810	1.6350	1.3080
Damping Ratio, ζ	0.0320	0.0196	0.0420	0.0300		0.0330	0.0220	0.0450	0.0350	

Table 4.6.2b Data From Free Vibration Tests on R.E. Embankments.

R.E Embankment	Natural Frequency F_n (Hz.)	Horizontal Acceleration at Top pickup Level Coeff. in a_t in (α_{ht}) (m/sec ²)	Displacement $d_{free} = \frac{a_{free}}{4\pi^2 F_n^2}$ (mm)	Average Shear Strain $\gamma_r = \frac{d_{free}}{H}$	Shear Modulus of R.E. Embankment G_r (t/m ²)	Shear Velocity of R.E. Embankment V_s (m/sec)
M2	23.250	0.2522 2.47417	0.11593	1.325×10^{-4}	1316.278	89.1418
M3	20.833	0.4928 4.83508	0.28218	3.225×10^{-4}	1056.8304	79.8750

G_r , and shear wave velocity, V_s , in embankments computed as cited earlier. Values of γ_r are of the order of 1×10^{-4} which are small and reasonable due to relatively small applied forces. They will be used to obtain G_r - γ_r relationship. Embankment, M3, with only one continuous reinforcement is weaker than M2 with four continuous reinforcements. Applied force being nearly the same, it is logical that $\gamma_r = 1.325 \times 10^{-4}$ of M2 is smaller than the $\gamma_r = 3.225 \times 10^{-4}$ of M3. Similar are observations for G_r and V_s of M2 and M3.

Table 4.6.3 to Table 4.6.8 show data from forced vibration tests on M1, M2 and M3. Table 4.6.9 gives data from these tests at resonance. From the tables, excitation frequency, F_{rq} , accelerations, displacements, OME value, γ_r , G_r , magnification factor, M_f , and V_s are obtained. Using this, frequency-response curves (Fig. 4.6.1 to Fig. 4.6.8) were prepared for the three embankments to obtain fundamental frequencies, F_n , at the first peak of response. Values of F_n have also been listed in these tables.

Frequency-response curves are flatter for lower F_{rq} values. Response increases with F_{rq} nonlinearly. Near resonance for increasing F_{rq} , response increases very sharply on rising flank and decreases also very sharply on falling flank as expected. Falling flank beyond F_n may rise again when second natural frequency begins to dominate. However, second natural frequency is not included in this study. These observations are similar to those from test results reported by Richardson and Lee (1975).

Excitation force obtained by using mechanical oscillators is given by $(m_e \cdot e \cdot \omega^2)$ where m_e is eccentric mass, e is its eccentricity and ω is the angular velocity in radian per second. Eccentricity e may be expressed as

Table 4.6.3 Accelerations, Displacements and Strains at Top Pickup Level of R.E. Embankment M1 Using Shake Table Tests.

$$H_t = 875 \text{ mm}$$

Run No.	Frequency, F_{rq} in Hz	Horizontal acceleration amplitude α_{ht} a_t (m/sec ²)		Displacement $d_t = a_t / (4\pi^2 F_{rq}^2)$ (mm)	Average Shear Strain $\gamma_r = (d_t / H_t)$ (multiplied by 10^4)
OME = 24		$F_n = 16.9 \text{ Hz}$			
1.	7.37	0.1108	1.087129	0.522725	5.79400
2.	8.50	0.1539	1.509944	0.529375	6.05000
3.	10.50	0.2500	2.452500	0.563469	6.43965
4.	12.70	0.3900	3.825900	0.596147	6.81311
5.	14.70	0.6900	6.768900	0.793450	9.06808
6.	16.90	1.3577	13.31900	1.181240	13.50000
7.	18.00	0.6000	5.886000	0.460167	5.25905
OME = 36		$F_n = 16.5 \text{ Hz}$			
8.	14.50	0.75	7.3575	0.886409	10.13030
9.	16.50	1.540	15.1074	1.405600	16.10000
10.	17.00	1.29	12.6549	1.109177	12.67630
11.	17.50	1.05	10.3005	0.851966	9.73675
12.	19.50	0.57	5.5917	0.372490	4.25703

**Table 4.6.4 Accelerations and Displacements at Mid Pickup Level of
R.E. Embankment M1 Using Shake Table Tests**

Run No.	Frequency F_{rq} in Hz	Horizontal acceleration amplitude α_{hm} a_m in m/sec^2		Displacement $d_m = a_m / (4\pi^2 F_{rq}^2)$ (mm)
OME = 24		$F_n = 16.9$ Hz		
1.	7.37	0.04200	0.412020	0.1921425
2.	8.50	0.06000	0.588600	0.2063580
3.	10.50	0.10560	1.035936	0.2380090
4.	12.70	0.16000	1.569600	0.2445730
5.	14.70	0.23500	2.305350	0.2702350
6.	16.90	0.42688	4.187695	0.3714000
7.	18.00	0.27153	2.663723	0.2082500
OME = 36		$F_n = 16.5$ Hz		
8.	14.50	0.30000	2.94300	0.3545600
9.	16.50	0.48000	4.70880	0.4381094
10.	17.00	0.43000	4.21830	0.3697250
11.	17.50	0.41600	4.08096	0.3375409
12.	19.50	0.32500	3.18825	0.2123847

Table 4.6.5 Accelerations, Displacements and Strains at Top Pickup Level of R.E. Embankment M2 Using Shake Table Tests.

$H_t = 875 \text{ mm}$

Run No.	Frequency, F_{rq} in Hz	Horizontal acceleration amplitude α_{ht} a_t (m/sec ²)		Displacement $d_t = a_t / (4\pi^2 F_{rq}^2)$ (mm)	Average Shear Strain $\gamma_r = (d_t / H_t)$ (multiplied by 10^4)
OME = 12 $F_n = 16 \text{ Hz}$					
1.	5.00	0.0350	0.34335	0.347886	3.97584
2.	7.00	0.0800	0.78480	0.405696	4.63655
3.	8.437	0.1200	1.17720	0.418903	4.78747
4.	10.00	0.2420	2.37402	0.566826	6.47801
5.	12.37	0.4200	4.12020	0.682054	7.79490
6.	14.00	0.5960	5.85625	0.756875	8.65000
7.	14.90	0.7000	6.86700	0.783492	8.95419
8.	16.75	1.1781	11.55720	1.043450	1.19250
9.	18.50	0.3500	3.43350	0.254117	2.90419
OME = 24, $F_n = 15.65 \text{ Hz}$					
10.	14.75	0.8500	8.3385	0.970832	11.0952
11.	15.65	1.7674	17.3380	1.569000	20.493
12.	18.00	0.7500	7.3525	0.575209	6.57381
13.	20.00	0.3000	2.9430	0.284054	3.24632
OME = 36, $F_n = 15.20 \text{ Hz}$					
14.	8.375	0.1850	1.81485	0.655407	7.49037
15.	10.350	0.2934	2.87891	0.680750	7.78000
16.	11.875	0.4090	4.01870	0.721875	8.25000
17.	12.625	0.5000	4.90500	0.779500	8.90857
18.	14.125	0.6900	6.76890	0.859372	9.82139
19.	15.000	1.4500	14.22450	1.601400	1.83015
20.	15.200	2.4406	23.94230	2.625000	3.00000
21.	17.250	1.2750	12.50775	1.064734	1.21683
22.	18.500	0.7000	6.86700	0.508234	5.80839

**Table 4.6.6 Accelerations and Displacements at Mid Pickup Level
of R.E. Embankment M2 Using Shake Table Tests.**

Run No.	Frequency F_{rq} in Hz	Horizontal acceleration amplitude α_{hm} a_m in m/sec^2		Displacement $d_m = a_m / (4\pi^2 F_{rq}^2)$ (mm)
OME = 12, $F_n = 16.75 H_z$				
1.	5.00	0.01368	0.134220	0.136000
2.	7.000	0.04090	0.401220	0.161261
3.	8.437	0.05113	0.501619	0.178510
4.	10.000	0.08100	0.794610	0.189720
5.	12.370	0.12363	1.212872	0.200770
6.	14.000	0.16818	1.649860	0.213222
7.	14.900	0.19540	1.917409	0.218767
8.	16.750	0.43100	4.228100	0.381729
9.	18.500	0.18000	1.765500	0.130680
OME=24, $F_n = 15.65 H_z$				
10.	14.75	0.27000	2.648700	0.308380
11.	15.65	0.54030	5.300450	0.548182
12.	18.00	0.36600	3.590460	0.280702
13.	20.00	0.26000	2.550600	0.161518
OME = 36, $F_n = 15.20 H_z$				
14.	8.375	0.0669	0.656290	0.237009
15.	10.350	0.1100	1.079100	0.255165
16.	11.875	0.1600	1.569600	0.281943
17.	12.625	0.1950	1.912950	0.304005
18.	14.125	0.3200	3.139200	0.398549
19.	15.000	0.4363	4.280700	0.481920
20.	15.200	0.6486	6.356800	0.696930
21.	17.250	0.4818	4.726600	0.402350
22.	18.500	0.4550	4.463550	0.330350

Table 4.6.7 Accelerations, Displacements and Strains at Top Pickup Level of R.E. Embankment M3 Using Shake Table Tests.

$$H_t = 875 \text{ mm}$$

Run No.	Frequency, F_{rq} in Hz	Horizontal acceleration amplitude α_{ht} a_t (m/sec ²)		Displacement $d_t = a_t / (4\pi^2 F_{rq}^2)$ (mm)	Average Shear Strain $\gamma_r = (d_t / H_t)$ (multiplied by 10 ⁴)
OME = 6, $F_n = 16.30$ Hz					
1.	11.50	0.2180	2.13858	0.409609	4.68125
2.	12.50	0.3620	3.55122	0.575702	6.57945
3.	14.25	0.6780	6.65118	0.829677	9.48202
4.	15.00	0.7875	7.72537	0.869710	9.93960
5.	15.80	1.0000	9.81000	0.995400	11.37590
6.	16.00	1.0437	10.23870	1.013080	11.57800
7.	16.30	1.0875	10.68370	1.017100	11.62390
8.	17.25	0.8250	8.09325	0.689000	7.84280
9.	18.50	0.9500	9.31950	0.689740	7.88281
10.	19.50	1.0550	10.34950	0.689430	7.87924
11.	12.00	0.3900	3.82590	0.672994	7.69136
12.	13.50	0.6140	6.02334	0.837163	9.56757
13.	14.50	0.8187	8.03193	0.967660	11.05900
14.	15.00	0.9470	9.29007	1.045868	11.95270
15.	16.00	1.1268	11.05396	1.093750	12.50000
16.	16.20	1.1200	10.98720	1.060467	12.11960
17.	17.50	0.9400	9.22140	0.762713	8.71671
18.	18.00	0.9600	9.41760	0.736267	8.41448
19.	19.00	1.0350	10.15335	0.712430	8.14206
20.	19.50	1.1100	10.88910	0.725375	8.29000
OME = 12, $F_n = 14.50$ Hz.					
21.	4.875	0.0425	0.41690	0.444370	5.07856
22.	7.500	0.1050	1.03005	0.463848	5.30112
23.	9.500	0.2160	2.11896	0.594720	6.79685
24.	12.250	0.6100	5.98410	1.010100	11.54400
25.	13.000	0.7343	7.20422	1.079800	12.34040
26.	14.000	0.8906	8.73730	1.129000	12.90440
27.	14.500	1.4060	13.79500	1.662000	18.99440
28.	15.000	1.1250	11.03625	1.242400	14.19940
29.	15.500	1.0625	10.04231	1.098940	12.55930
30.	16.000	0.9406	9.22753	0.913031	10.43500
31.	17.000	1.0300	10.10430	0.885620	10.12140
32.	18.000	1.1250	11.03625	0.862813	9.86072
33.	18.500	1.1875	11.64937	0.862183	9.85352
34.	20.500	1.2344	12.10927	0.729875	8.34143

Table 4.6.7 Continued

Run No.	Frequency, F_{rq} in Hz	Horizontal acceleration amplitude α_{ht} a_t (m/sec ²)		Displacement $d_t = a_t / (4\pi^2 F_{rq}^2)$ (mm)	Average Shear Strain $\gamma_r = (d_t / H_t)$ (multiplied by 10^4)
OME = 18, $F_n = 14.00$ Hz.					
35	10.50	0.43500	4.26737	0.980437	11.205
36	11.50	0.5500	5.39550	1.033418	11.804
37	12.50	0.6950	6.81795	1.105284	12.6318
38	14.00	1.6218	15.90986	1.916772	21.9059
39	14.50	1.3750	13.48875	1.625084	18.5723
40	15.00	1.1500	11.28150	1.270061	14.5149
41	15.25	1.0750	10.54575	1.148624	13.1271
42	16.00	1.2000	11.77200	1.164797	13.3119
43	16.50	1.2562	12.32320	1.146569	13.1036
44	17.00	1.3430	13.17480	1.154750	13.1971
45	18.00	1.3875	13.61130	1.193000	13.6344
46	19.00	1.4250	13.97920	0.980880	11.21
47	19.50	1.4750	14.46970	0.963900	11.016
OME = 24, $F_n = 13.5$ Hz					
48	7.00	0.2206	2.16408	1.187100	12.7852
49	9.75	0.4558	4.47220	1.191660	13.6189
50	12.00	0.7794	7.64600	1.344900	15.3710
51	12.25	0.8443	8.28280	1.456900	16.6512
52	13.50	2.2700	22.26900	3.095000	35.3719
53	13.75	1.1000	10.79100	1.445700	16.5229
54	14.50	1.1125	10.91362	1.314840	15.0267
55	15.00	1.1750	11.52675	1.297671	14.8305
56	16.00	1.2812	12.56906	1.243660	14.2133
57	17.00	1.4312	14.04056	1.230620	14.0643
58	18.00	1.5687	15.38943	1.203145	13.7502
59	20.00	1.8625	18.27112	1.157030	13.2232
60	20.50	1.9500	19.12950	1.153018	13.1773
OME = 36, $F_n = 13.15$ Hz					
61	4.375	0.0713	0.70000	0.926360	10.5870
62	7.875	0.3166	3.10625	1.268750	14.5000
63	11.50	0.7500	7.35750	1.409200	16.1052
64	13.15	2.5770	25.28030	3.704000	42.3324
65	14.00	1.1760	11.54110	1.491530	17.0460
66	15.80	1.4430	14.63188	1.437100	16.4240
67	17.00	1.5560	15.26436	1.337900	15.2901
68	20.00	1.9062	18.69980	1.184180	13.5334

**Table 4.6.8 Accelerations and Displacements at Mid Pickup Level
of R.E. Embankment M3 Using Shake Table Tests.**

Run No.	Frequency F_{rq} in Hz	Horizontal acceleration amplitude α_{hm} a_m in m/sec^2		Displacement $d_m = a_m / (4\pi^2 F_{rq}^2)$ (mm)
OME = 6, $F_n = 16.30$ Hz				
1.	11.50	0.1280	1.25568	0.24050
2.	12.50	0.1800	1.76580	0.28626
3.	14.25	0.2852	2.79780	0.34900
4.	15.00	0.3451	3.38440	0.38102
5.	15.80	0.4000	3.92400	0.39815
6.	16.00	0.4250	4.16925	0.41253
7.	16.30	0.4500	4.41450	0.42087
8.	17.25	0.3150	3.09015	0.25305
9.	18.50	0.3650	3.50650	0.26500
10.	19.50	0.4000	4.92400	0.26139
OME = 9, $F_n = 16.00$ Hz				
11.	12.00	0.20370	1.99833	0.351510
12.	13.50	0.31500	3.09015	0.429490
13.	14.50	0.37250	3.65420	0.443500
14.	15.00	0.43000	4.21830	0.474890
15.	16.00	0.52315	5.13210	0.507800
16.	16.20	0.50000	4.90500	0.473420
17.	17.50	0.35400	3.47270	0.287230
18.	18.00	0.39800	3.90538	0.305357
19.	19.00	0.45900	4.50280	0.315947
20.	19.50	0.47500	4.65750	0.310400
OME = 12, $F_n = 13.50$ Hz				
21.	4.875	0.03058	0.30000	0.319751
22.	7.500	0.07500	0.73575	0.331320
23.	9.500	0.13000	1.27530	0.357936
24.	12.250	0.25400	2.49174	0.420601
25.	13.000	0.31070	3.04820	0.456875
26.	14.000	0.47000	4.61070	0.595870
27.	14.500	0.63880	6.26750	0.755090
28.	15.000	0.43520	4.26735	0.480410
29.	15.500	0.38000	3.72700	0.393000
30.	16.000	0.41890	4.11020	0.406690
31.	17.000	0.45000	4.41450	0.386920
32.	18.000	0.49530	4.85958	0.379900
33.	18.500	0.51600	5.06396	0.374800
34.	20.500	0.54160	5.31375	0.320280

Table 4.6.8 Continued

Run No.	Frequency F_{rq} in Hz	Horizontal acceleration amplitude		Displacement $d_m = a_m / (4\pi^2 F_{rq}^2)$ (mm)
		α_{hm}	a_m in m/sec^2	
OME = 18, $F_n = 14.00$ Hz				
35	10.50	0.17125	1.679962	0.385976
36	11.50	0.22250	2.182720	0.418065
37	12.50	0.30100	2.952810	0.478691
38	14.00	0.69400	6.808140	0.879858
39	14.50	0.43840	4.300704	0.518136
40	15.00	0.40040	3.927920	0.442202
41	15.25	0.42000	4.120200	0.448764
42	16.00	0.45800	4.492980	0.444560
43	16.50	0.48500	4.757850	0.442670
44	17.00	0.56500	5.542650	0.485802
45	18.00	0.60100	5.895810	0.460933
46	19.00	0.62500	6.131251	0.430211
47	19.50	0.64500	6.327450	0.421500
OME = 24, $F_n = 13.50$ Hz				
48	6.625	0.07250	0.711225	0.410464
49	9.75	0.18000	1.765800	0.470513
50	12.00	0.30100	2.952800	0.519410
51	12.25	0.35650	3.488400	0.588800
52	13.50	0.75000	7.357500	1.022600
53	13.75	0.35000	3.433500	0.460015
54	14.50	0.42500	4.169250	0.502298
55	15.00	0.44500	4.365400	0.491458
56	16.00	0.50250	4.929520	0.487760
57	17.00	0.57000	5.591700	0.490101
58	18.00	0.63950	6.273490	0.490460
59	20.00	0.70400	6.906240	0.437340
60	20.50	0.74000	7.259400	0.437500
OME = 36, $F_n = 13.15$ Hz				
61	4.375	0.04534	0.444780	0.588620
62	7.875	0.14900	1.461600	0.596990
63	11.50	0.48055	4.714250	0.902900
64	13.15	0.93930	9.215124	1.349800
65	14.00	0.57870	5.677000	0.733600
66	15.80	0.540	5.297400	0.537512
67	17.00	0.645	6.327450	0.554580
68	20.00	0.824	8.084100	0.511930

($e' \cdot OME$), e' being constant of proportionality. Excitation force ratio, r_e , may be defined as ratio of excitation force to the reference excitation force with same mass, same e' but OME value equal to unity and ω corresponding to one Hz and is expressed as:

$$r_e = (m_e \cdot e' \cdot OME \cdot 4\pi^2 F_{rq}^2) / (m_e \cdot e' \cdot 1 \cdot 4\pi^2 \cdot 1^2) = OME \cdot F_{rq}^2 \quad (4.6.1)$$

TABLE 4.6.9 Data from Forced Vibration Tests on Embankments at Resonance.

OME	Embankment no.	Fundamental frequency F_n (Hz)	Coeff. of horizontal acceleration (top pickup)	Average shear strain $\gamma_r \times 10^3$	Excitation force ratio, $r_e = OME F_{rq}^2$	Shear modulus G_r (t/m^2)	Shear wave Velocity V_s (m/sec^2)
6	3	16.30	1.08750	1.16239	1594	684.456	64.280
9	3	16.00	1.12680	1.25000	2304	659.493	63.09
12	2	16.50	1.17811	1.19250	3366	722.770	66.055
12	3	14.50	1.40600	1.89940	2533	541.635	57.182
18	3	14.00	1.62180	2.35000	3528	504.925	55.210
24	1	16.90	1.35770	1.35000	6854	735.773	66.469
24	2	15.65	1.76740	2.04930	5878	630.956	61.717
24	3	13.50	2.27000	3.53710	4374	469.503	53.238
36	1	16.50	1.54000	1.61000	9801	701.356	65.069
36	2	15.20	2.44060	3.00000	8317	595.193	59.943
36	3	13.15	2.57700	4.23320	6225	445.473	51.858

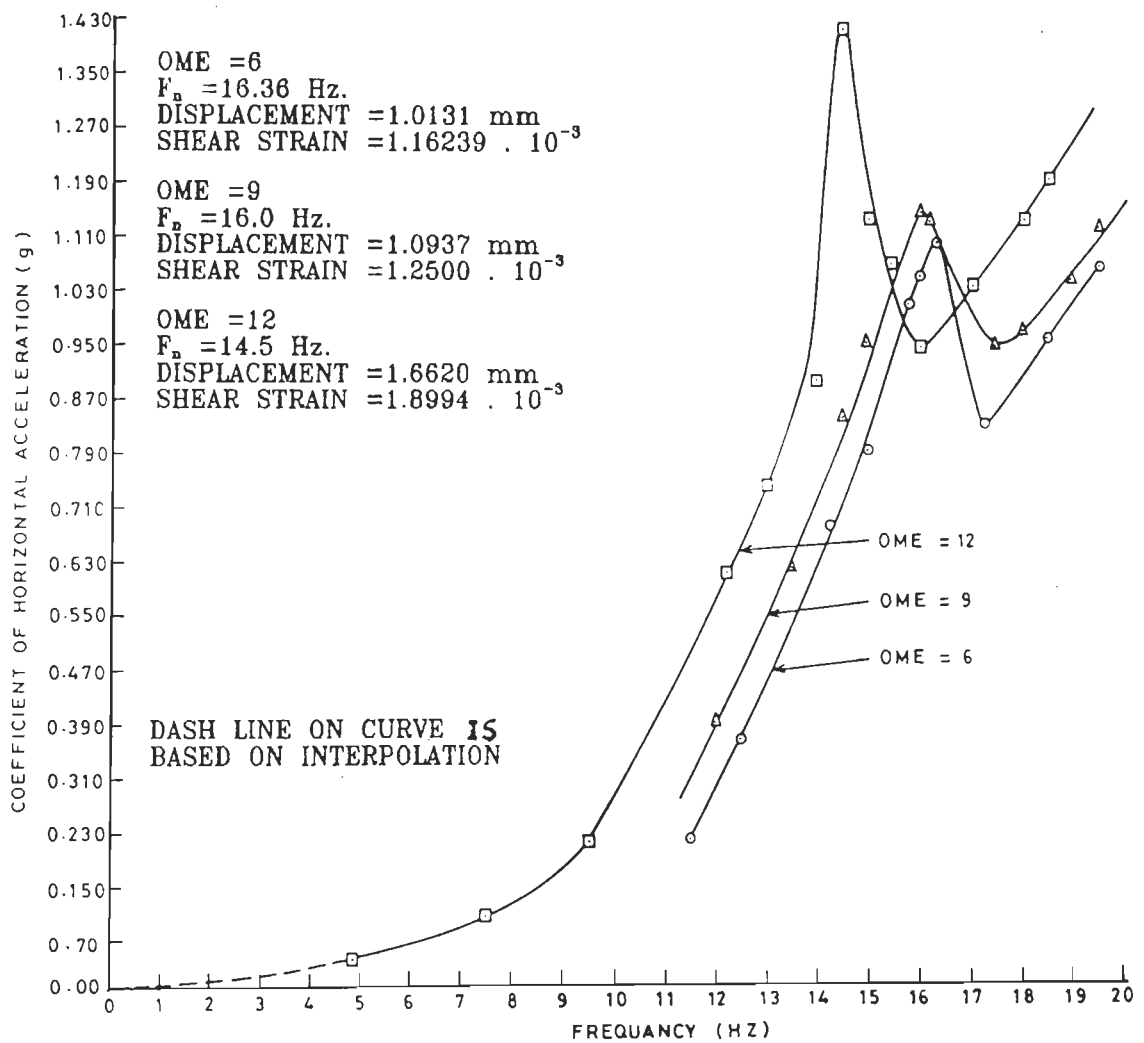


FIG. 4.6.1 FREQUENCY-RESPONSE CURVES FOR EMBANKMENT M3 MEASURED AT TOP PICKUP (OME= 6, 9 AND 12).

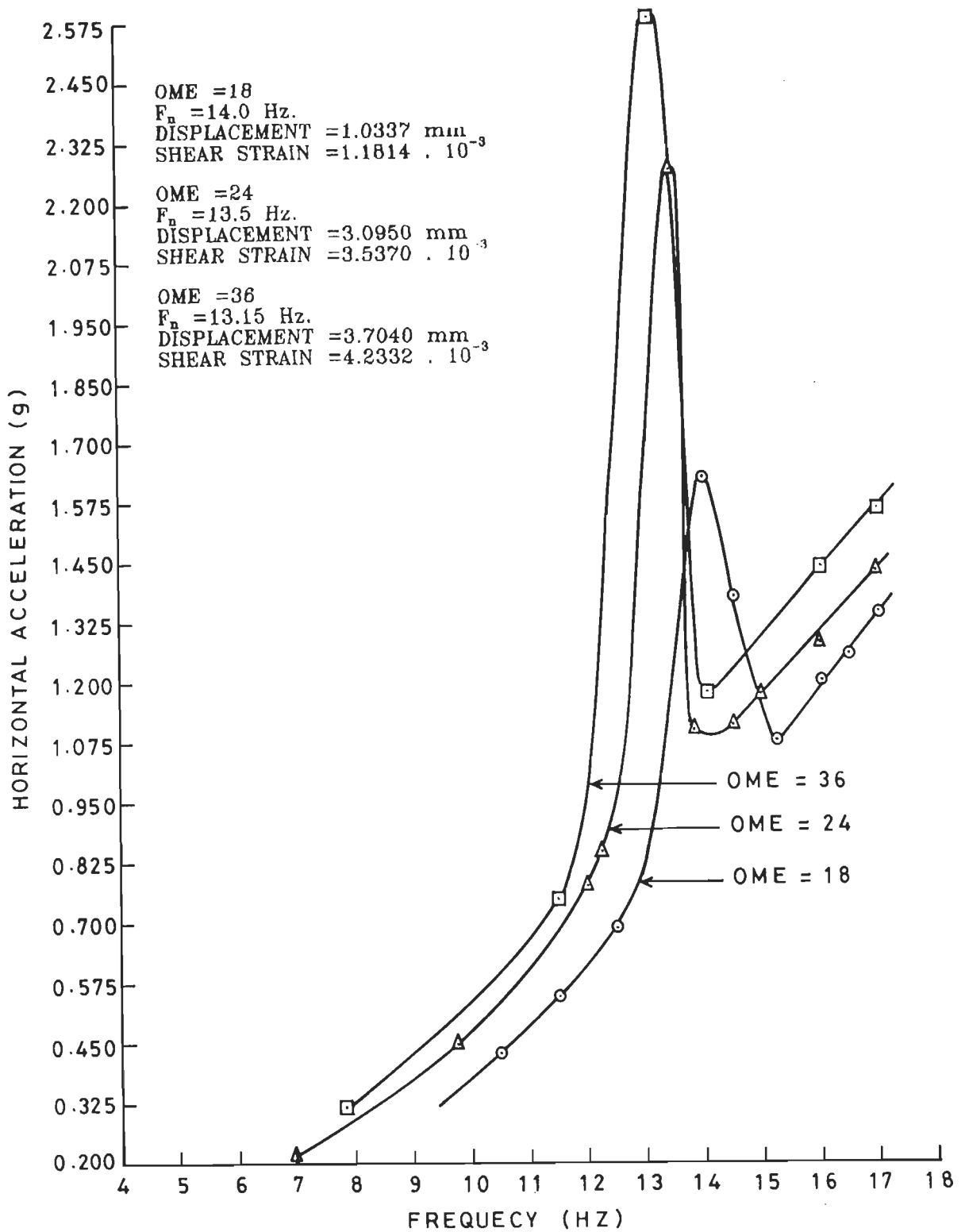


FIG. 4.6.2 FREQUENCY-RESPONSE CURVES FOR EMBANKMENT M3 MEASURED AT TOP PICKUP (OME= 18, 24 AND 36).

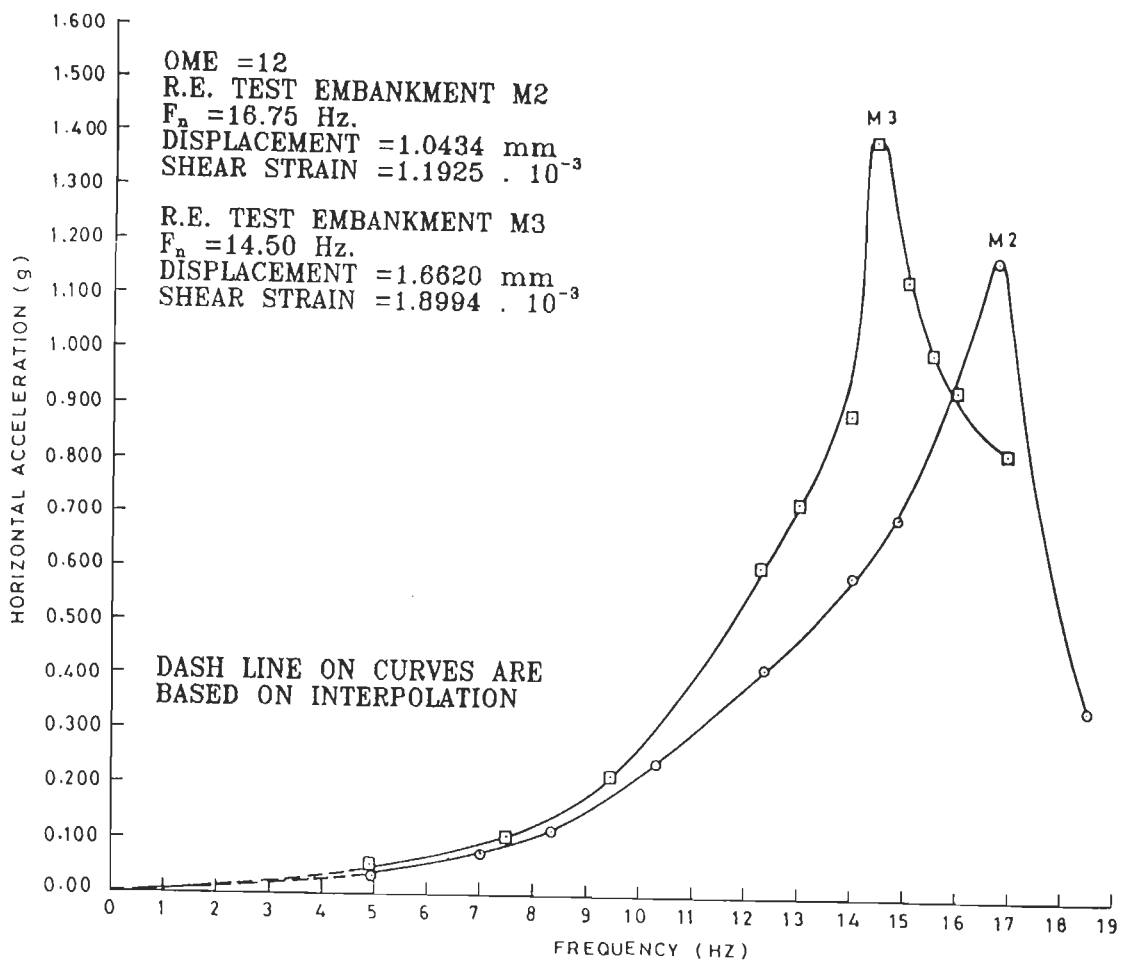


FIG. 4.6.3 FREQUENCY - RESPONSE CURVES FOR EMBANKMENTS M2 AND M3 MEASURED AT TOP PICKUP.

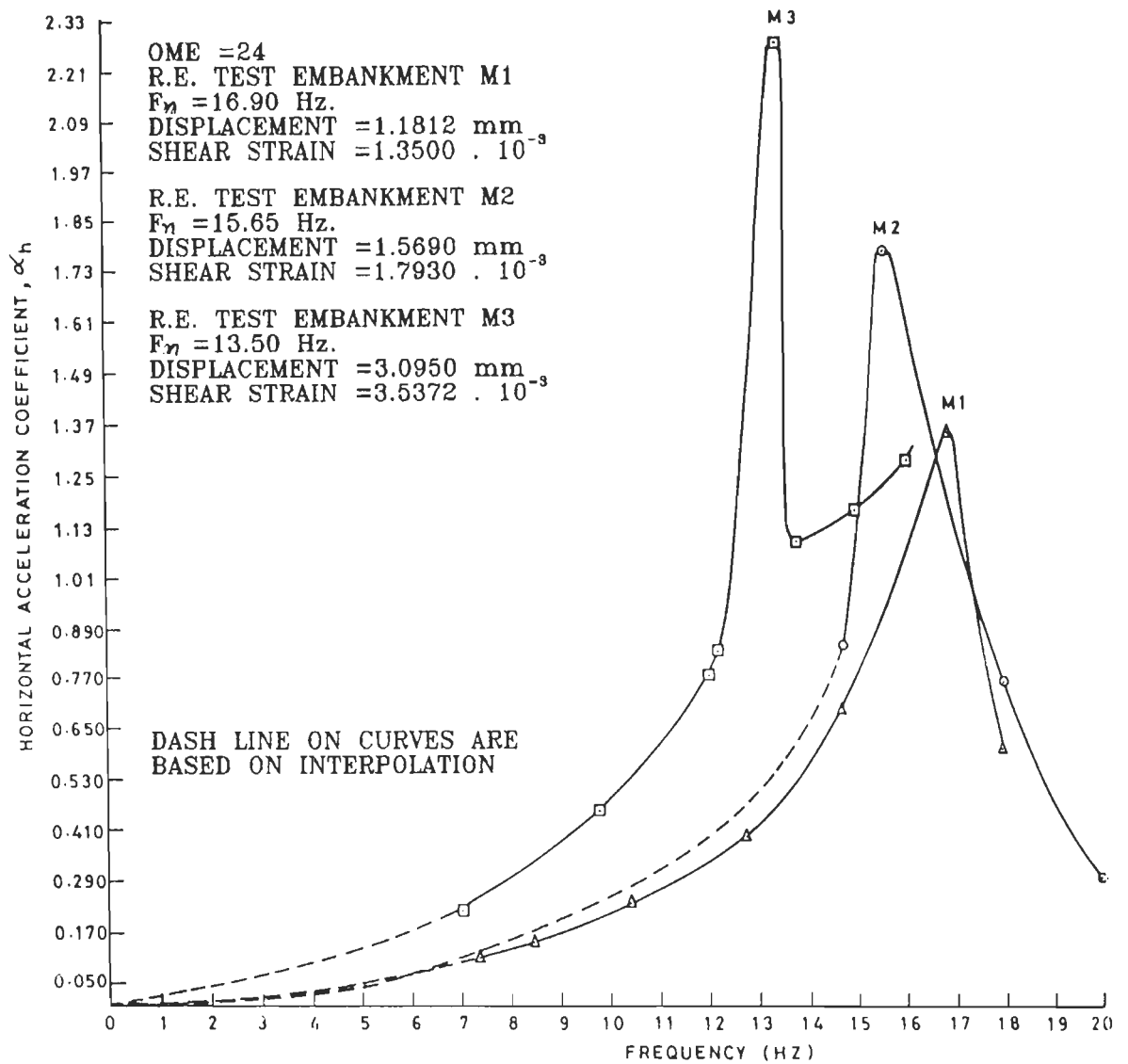


FIG. 4.6.4 FREQUENCY-RESPONSE CURVES FOR EMBANKMENTS M1, M2 AND M3 MEASURED AT TOP PICKUP (OME=24).

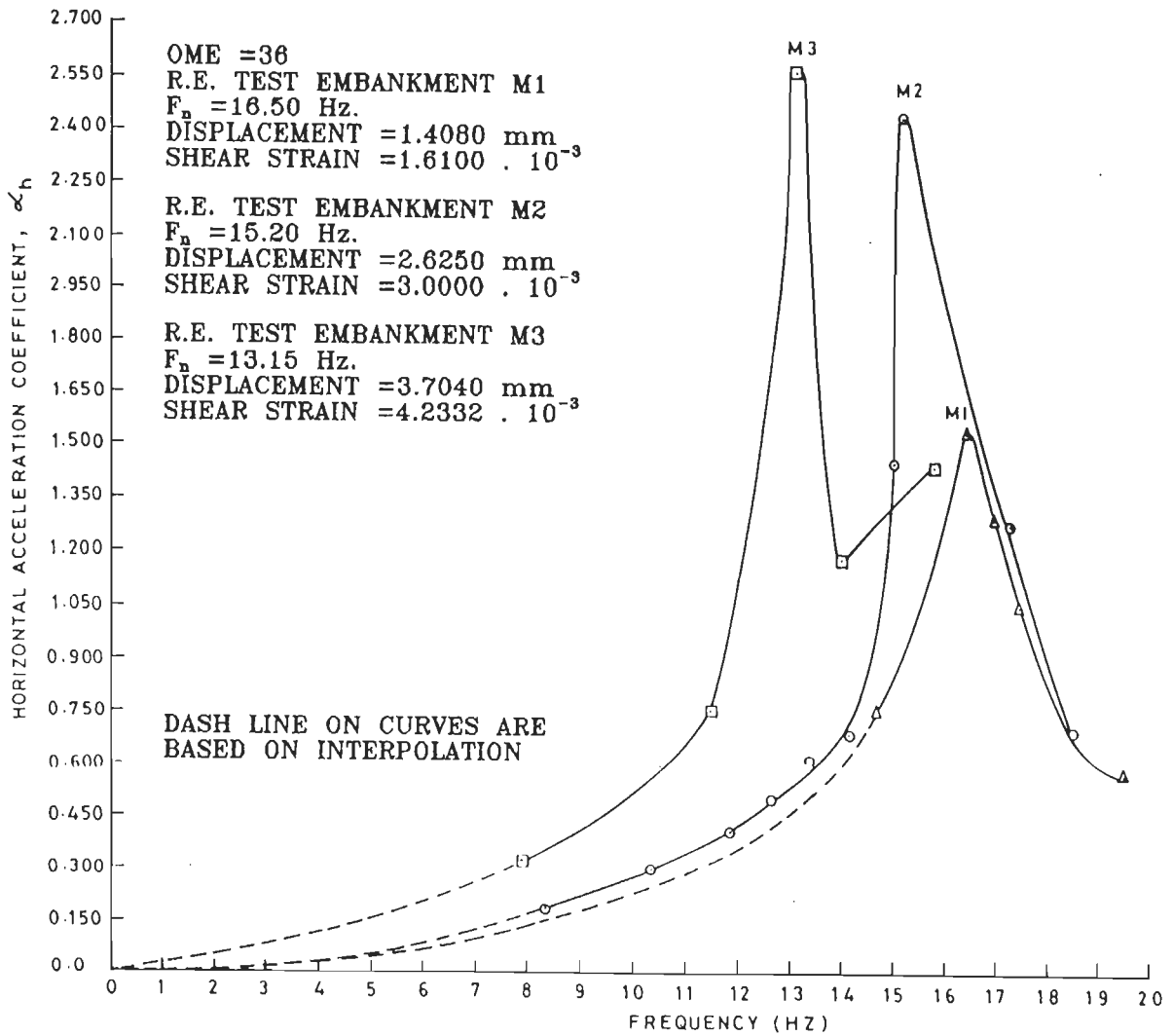


FIG. 4.6.5 FREQUENCY-RESPONSE CURVES FOR EMBANKMENTS M1 , M2 AND M3 MEASURED AT TOP PICKUP (OME=36).

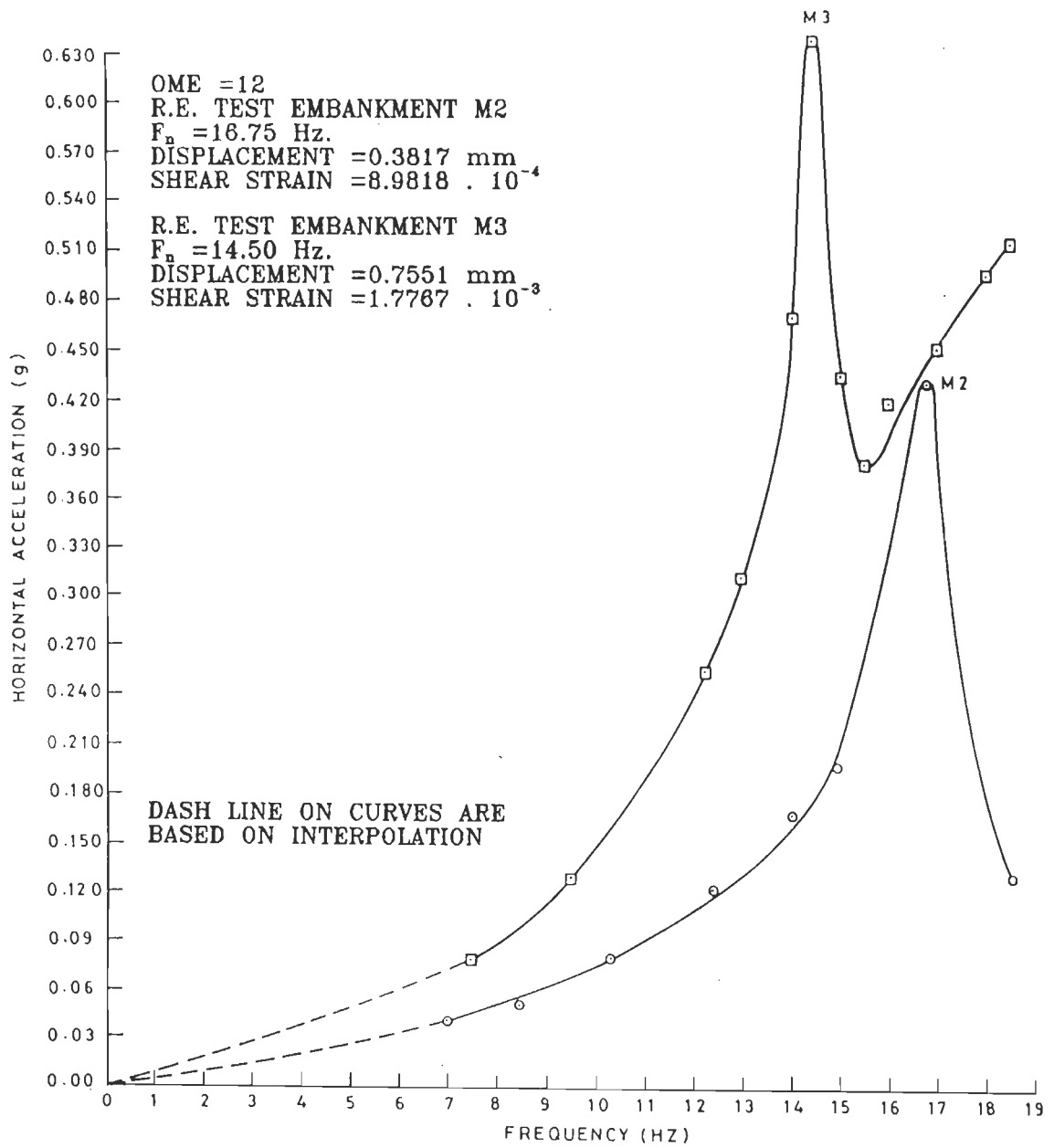


FIG. 4.6.6 FREQUENCY - RESPONSE CURVES FOR EMBANKMENTS M2 AND M3 MEASURED AT MIDDLE PICKUP.

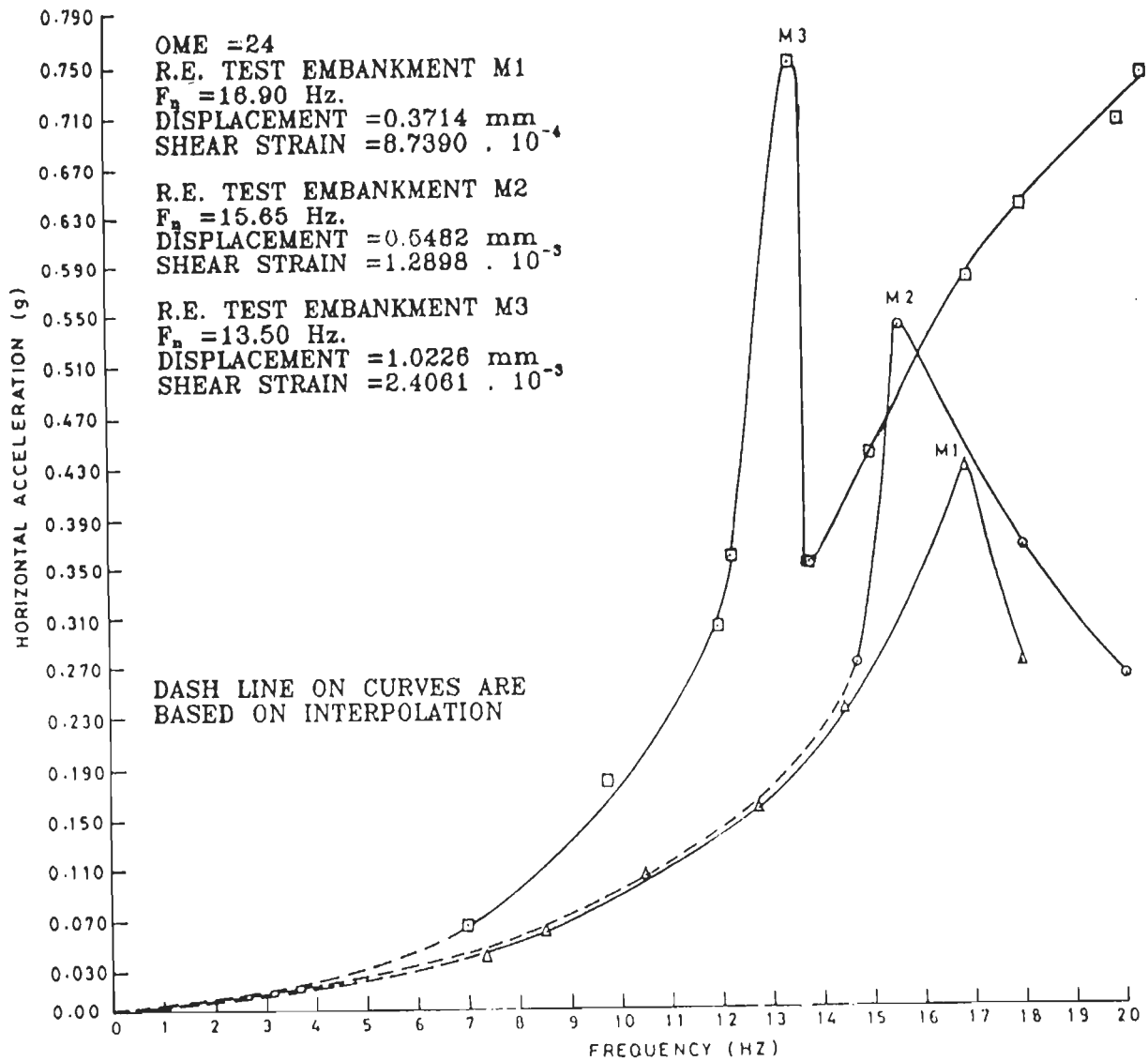


FIG. 4.6.7 FREQUENCY-RESPONSE CURVES FOR EMBANKMENTS M1 , M2 AND M3 MEASURED AT MIDDLE PICKUP (OME=24).

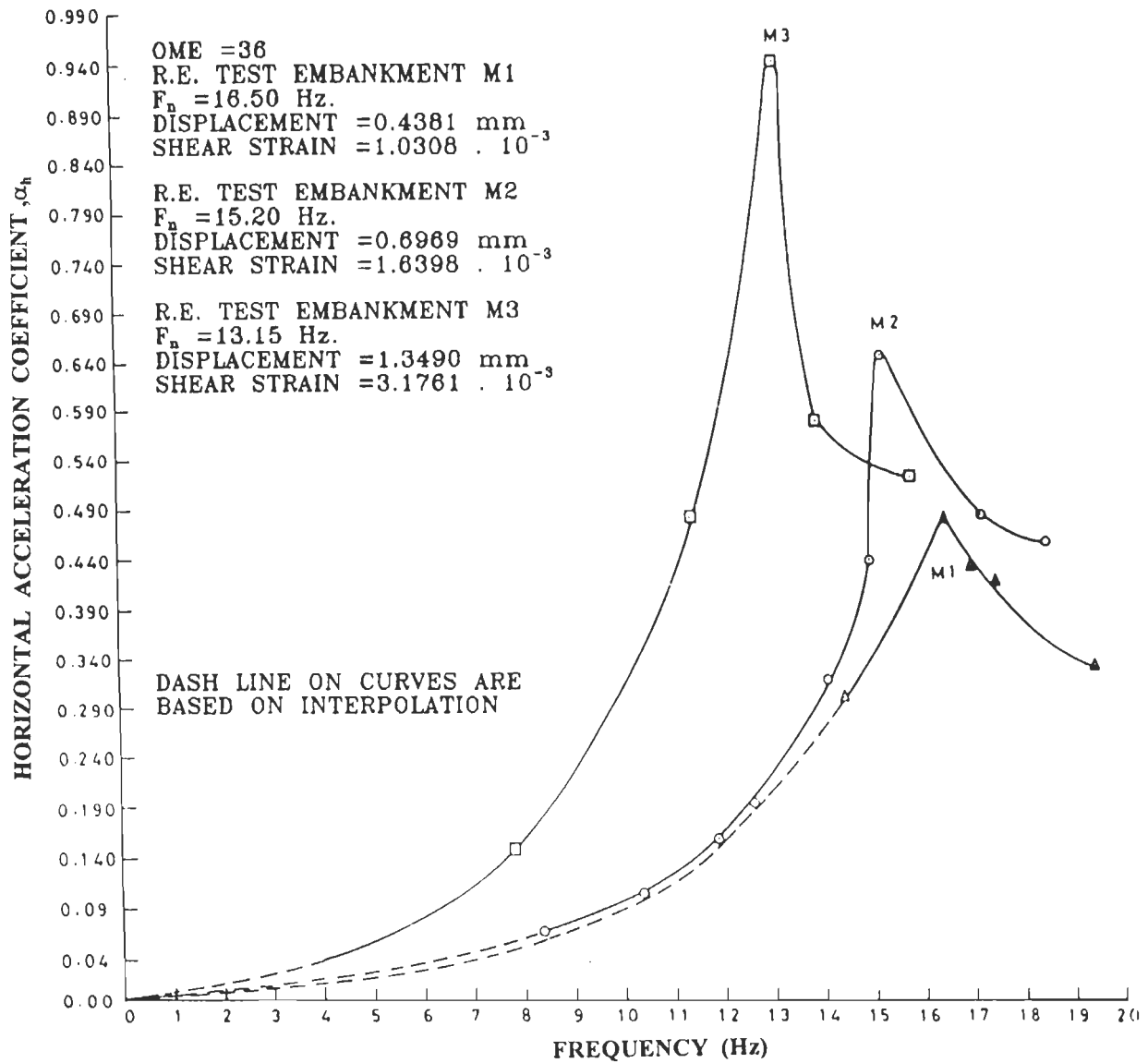


FIG. 4.6.8 FREQUENCY-RESPONSE CURVES FOR EMBANKMENTS M1, M2 AND M3 MEASURED AT MIDDLE PICKUP (OME=36).

Figure 4.6.9 shows variation of F_n with r_e . As expected, F_n decreases with increasing r_e , because, increasing forces result into higher shear strains and lower shear moduli which in turn lead to reduced F_n . The figure

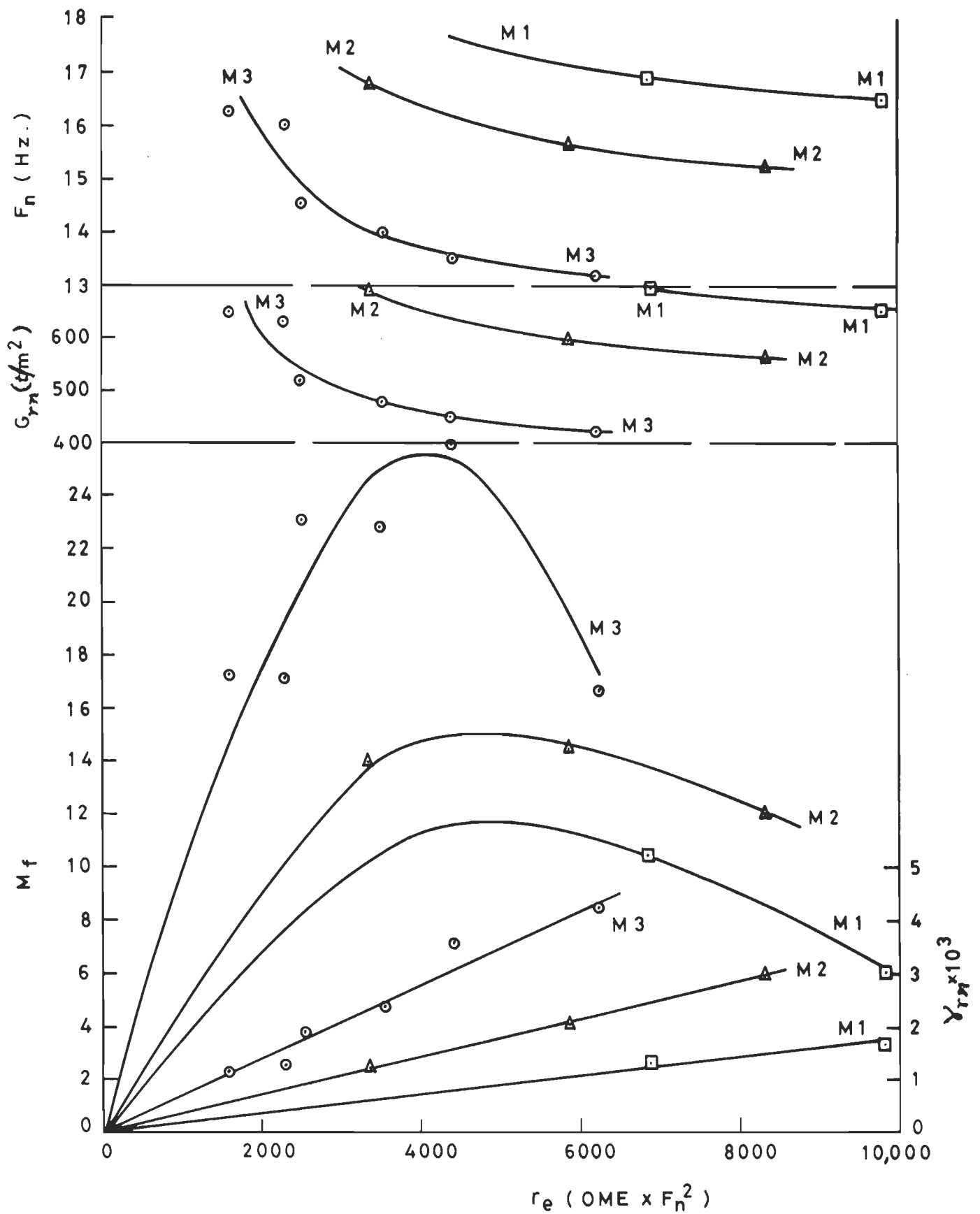


FIG. 4.6.9 VARIATION OF FUNDAMENTAL FREQUENCY OF VIBRATION, F_n , SHEAR MODULUS, G_{rn} , SHEAR STRAIN, γ_{rn} , AND MAGNIFICATION FACTOR, M_f , WITH EXCITATION FORCE RATIO, r_e , FOR R.E. EMBANKMENTS AT RESONANCE.

also shows variation of shear modulus at resonance, G_{rn} , with r_e which are similar to those between F_n and r_e . The figure also shows a linear relationship between shear strain at resonance, γ_{rn} , and r_e for all the three embankments. Hence, it is concluded that even after experiencing resonant vibrations at different frequencies, R.E. embankments show predominantly elastic behaviour though accelerations at top pickup level were as large as 2.577g (Table 4.6.9). This important positive indication highlights ability of R.E. to exhibit elastic behaviour over a much wider range of accelerations, stresses and strains, which is an advantage.

4.6.3 Magnification Factor

Figure 4.6.9 shows magnification factor, M_f , at top pickup w.r.t. base excitation. The M_f rises rapidly with r_e to reach a peak and then falls with further increasing r_e . The M_f - r_e relationship shows a sharp peak for the weakest embankment M3. The peak is much flatter and smaller for embankment M2 which is stiffer than M3. Three points available for embankment M1 are inadequate to draw the curve. Nevertheless, an anticipated curve is shown which is flatter with a shorter peak compared to that for M2, because, M1 is stiffer than M2. Increasing peak amplification with increasing softness of embankments is expected. Ground response amplification is also larger with softer surface layers (Okamoto, 1973).

At $r_e=0$, $\gamma_{rn}=0$ and increases linearly with r_e . For smaller r_e , though F_n is large, large F_n^2 does not generate large α_h and M_f due to small strains. At higher strains, α_h and, hence, M_f increases to peak. At r_e higher than that at peak M_f , F_n and F_n^2 reduce and, hence, decrease α_h and

For all R.E. embankments, Richardson and Lee (1975) recommend an equivalent design seismic coefficient, α_{hav} , to be 1.4 times the α_{hb} of base excitation (Fig. 4.6.10). However, it should really be a function of excitation force level, material properties as well as size and geometry of embankment. Multiplier constant 1.4 was based on earth pressures observed experimentally and the best fit equivalent seismic coefficient was worked back using these pressures (Fig 2.4.1). In this study, α_{hav} based on measured accelerations at base, middle and top pickups was obtained as :

$$\alpha_{hav} = (\alpha_{hb} \cdot H_x + \alpha_{hm} \cdot H_y + \alpha_{ht} \cdot H_z) / H \quad (4.6.1)$$

where H_x , H_y and H_z are the depths of influence attributed to base, middle and top pickups respectively (Fig. 4.6.10). The figure also shows α_{hav} obtained from this study as well as those recommended by Richardson and Lee as function of α_{hb} . It may be observed that α_{hav} recommended by Richardson and Lee is much smaller than those obtained for the three embankments tested in this study. Their recommendation fails to reflect nonlinearity of the relationship at higher levels of excitation as well as the stiffness (i.e. material property) of the embankment. As such, it may be concluded that their generalized recommendation for use for all R.E. embankments may be unsafe. Therefore, their recommendations may be considered valid only for embankments comparable to their test embankment. Figure 4.6.11 shows first natural frequency, F_n of embankment obtained from test results for M1, M2 and M3 of height, $H=0.9$ m. This figure also shows $F_n=(38/H)$ expressed in Hz as proposed by Richardson et al. (1977) where H is embankment height in meters. It may be observed that eleven points representing measured values of F_n range from 13.15 Hz to 16.9 Hz which is much lower than $F_n=42.2$ Hz obtained for M1, M2 and M3 by using above expression for F_n recommended by

Richardson et. al. (1977). The F_n predicted by above expression is 176% higher than average of 11 values of F_n obtained from tests. Hence, it is concluded that expression for F_n proposed by Richardson et al.(1977) and recommended by Richardson (1978) for universal application to all R.E. embankments is not a valid statement.

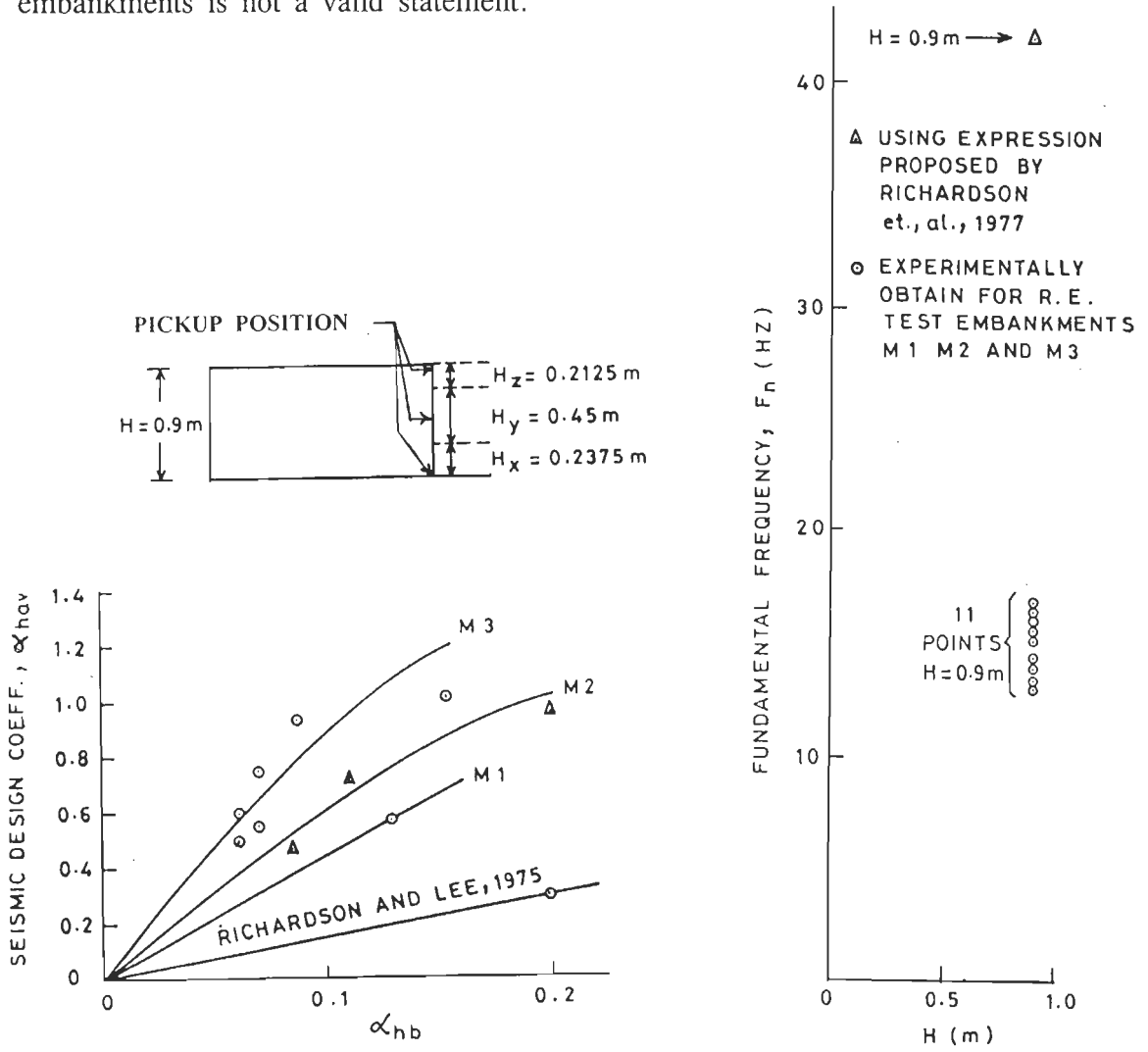


FIG. 4.6.10 VARIATION OF EQUIVALENT DESIGN SEISMIC COEFFICIENT, α_{hav} , WITH COEFF. OF BASE ACCELERATION, α_{hb} FOR R.E. EMBANKMENT.

FIG. 4.6.11 RELATIONSHIP OF F_n WITH EMBANKMENT HEIGHT, H.

4.6.4 Shear Modulus

Shear modulus, G_r , is dependent on shear strain, γ_r , and is important for earthquake resistance design of structures. As γ_r increases, G_r reduces

and G_r - γ_r relationship is an ideal way to provide this material property of idealized homogeneous reinforced earth.

At different strains, G_{rn} obtained from free and forced vibration tests explained in Article 4.5 are listed in Table 4.6.2b and Table 4.6.9 cited earlier. Shear modulus, G_{rn} , and shear strain, γ_{rn} , computed at resonance are convenient and computed by Standard methods available in the state of the art (Article 4.5). Shear modulus is shear strain dependent and not resonant frequency dependent. Hence, G_r - γ_r relationship (Fig. 4.6.12) thus obtained is valid for whole range of γ_r and not just at resonance.

In the above figure, at $\gamma_r = 3.225 \times 10^{-4}$, the G_r - γ_r curves for M2 and M3 are very close. Difference between G_r values from these two curves is 0.95% only at $\gamma_r = 3.225 \times 10^{-4}$ which is negligible. It further reduce to be even more negligible at $\gamma_r = 1.325 \times 10^{-4}$ at A where practically all G_r - γ_r curves merge into a single curve. Therefore, G_r - γ_r relationships for M3 and M1 are obtained by extending them upto A.

In above figure, G_r reduces from M1 to M2 to M3 at any given γ_r . This is logical as M2 is weaker than M1 and M3 is weaker than M2. The G_r - γ_r relations for $\gamma_r < 1.325 \times 10^{-4}$ are of no practical interest as for such small strains the reinforcing action is insignificant. For reinforcement to significantly contribute resisting forces, higher γ_r should be mobilised. The largest $\gamma_r = 4.2332 \times 10^{-3}$ mobilized for the largest possible base excitation from test facility available was incorporated in this figure.

Figure 4.6.12 also shows shear modulus, G_s , of plain sand with 70% D_r obtained by the method given by Seed and Idriss (1970). At shear strain for

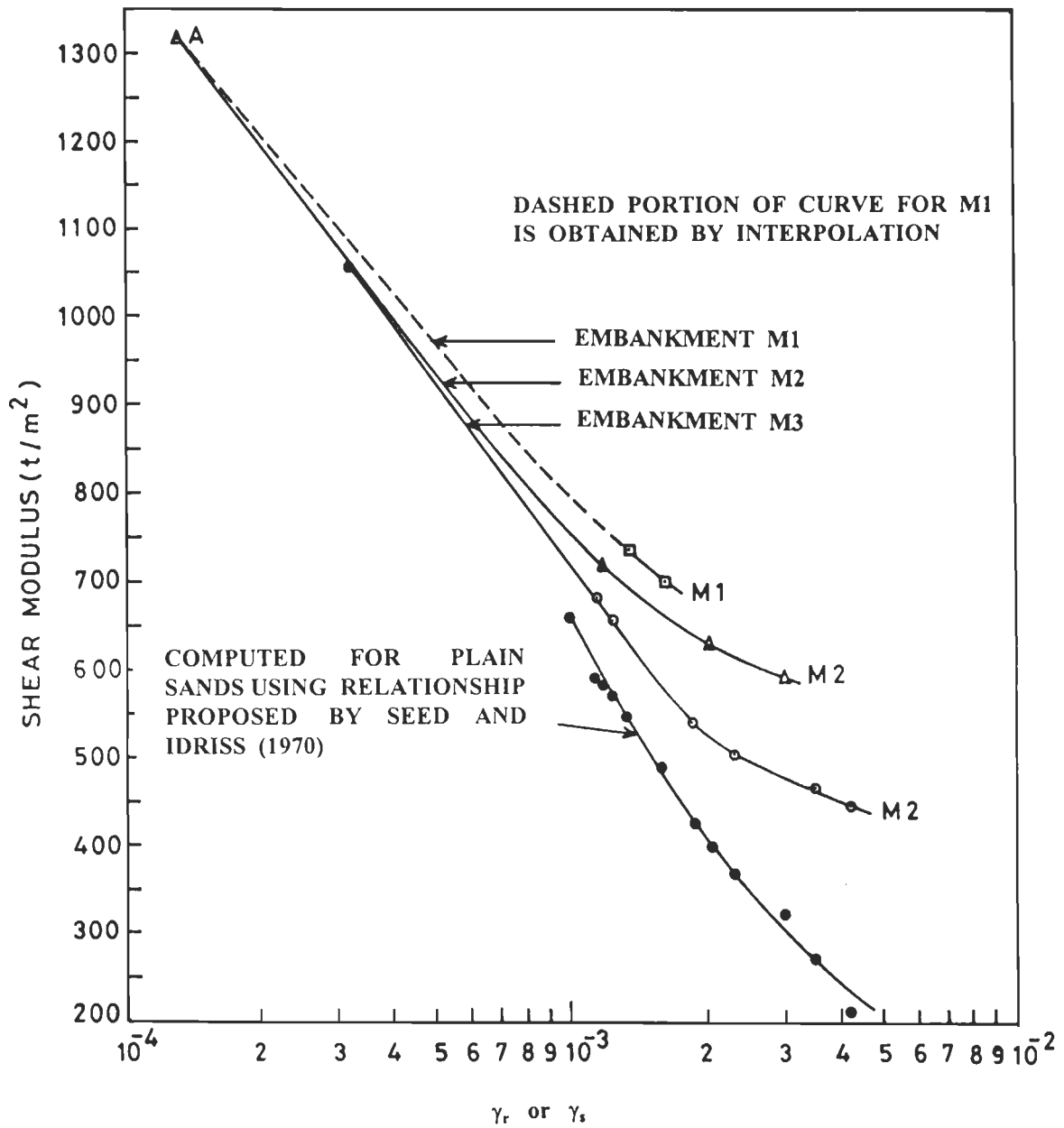


FIG. 4.6.12 VARIATION OF SHEAR MODULUS, G_r , WITH SHEAR STRAIN, γ_r , FOR R.E. EMBANKMENTS AND SHEAR MODULUS, G_s , AND SHEAR STRAIN, γ_s , FOR PLAIN SAND.

plain sand, $\gamma_s = 10^{-3}$, G_s is 12.2% smaller than G_r of M1 which is small. The comparison is much better with G_r of M2 and M3 with the percentage difference being only 3.87% for M3. As strain level increases, difference between G_s and G_r for any embankment increases. This highlights advantage of R.E. to improving soil properties. The ratio of shear modulus, r_G , is defined as (G_r/G_s) . Figure 4.6.13 shows r_G for M1, M2 and M3 for $\gamma \geq 10^{-3}$. Value of $r_G > 1$ and for $\gamma > 10^{-3}$ and r_G increases with increasing γ which highlights advantage of R.E. particularly at larger strain levels.

Many investigators have recommended elastic domain for soil at strains $\gamma \leq 10^{-6}$ due to very low levels of strain at which soil loses its

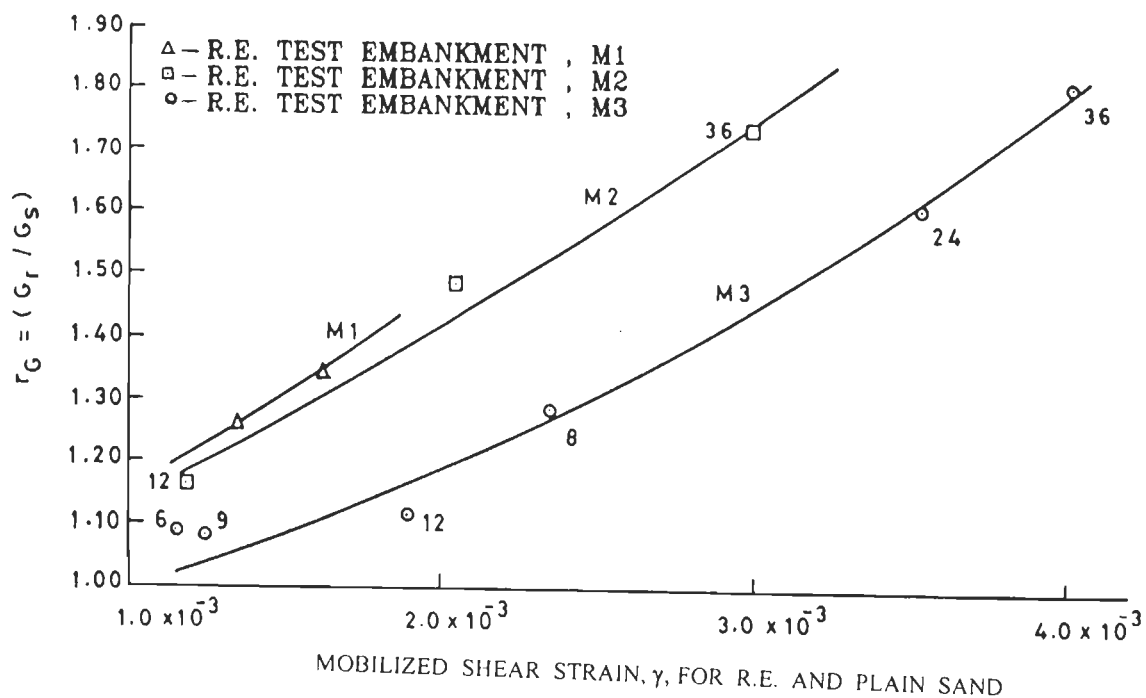


FIG. 4.6.13 RELATIONSHIP BETWEEN SHEAR STRAIN, γ , AND THE RATIO, r_G , OF SHEAR MODULUS OF R.E. TO THAT OF PLAIN SAND.

elasticity and exhibits nonlinearity (Seed and Idriss, 1970; Kuribayashi, 1974, Moore, 1985 and Saxena & Reddy, 1989). As such, many have suggested normalisation of G of soil w.r.t. its G at $\gamma=10^{-6}$. However, R.E. is very different from plain sand. It exhibits elastic behaviour over a much wider range of strains, at least upto $\gamma=10^{-3}$ (Fig. 4.6.12). Besides, shear strains of the order of 10^{-6} are of no interest when dealing with R.E., because, reinforcements do not contribute significant resisting forces at such low strain levels. Moreover, R.E. being significantly stronger, resisting forces mobilised will be too small to be measure accurately for γ of the order of 10^{-6} . This may pose some problem in conducting desired tests. Therefore, it is more reasonable and logical to normalise G_r w.r.t. reference modulus, G_{rf} , at $\gamma=10^{-3}$ instead of at γ equal to 10^{-6} .

Figure 4.6.14 shows relationship between shear strain, γ_r , and normalised shear modulus, G_n , obtained by normalising G_r w.r.t. G_{rf} at the $\gamma_r=10^{-3}$. All γ_r - G_n curves cross each other at one point at $\gamma_r=10^{-3}$ which is due to normalisation. Curves of γ_r - G_n for M1 and M2 practically merge with each other for $\gamma_r \geq 10^{-3}$ in view of G_r for M1 and M2 being very close and also due to a very small range of $\gamma_r \geq 10^{-3}$ for which the G_n values are available for M1. Embankment M3 being much weaker than M2, its G_n is much smaller that that for M2 and hence, γ_r - G_n curve for M3 is situated much below the curve for M2 for $\gamma_r \geq 10^{-3}$. The above figure also shows G_n - γ_r relationships worked out for data reported by Shewbridge and Sousa (1991) for uniaxially and biaxially reinforced earth specimens using cyclic torsional tests. The relationship is linear upto $\gamma_r=10^{-3}$ which is in very close agreement with results of tests of this investigation. The linear relationship for their results extends beyond $\gamma_r \geq 10^{-3}$ also, because, they employed steel bars as

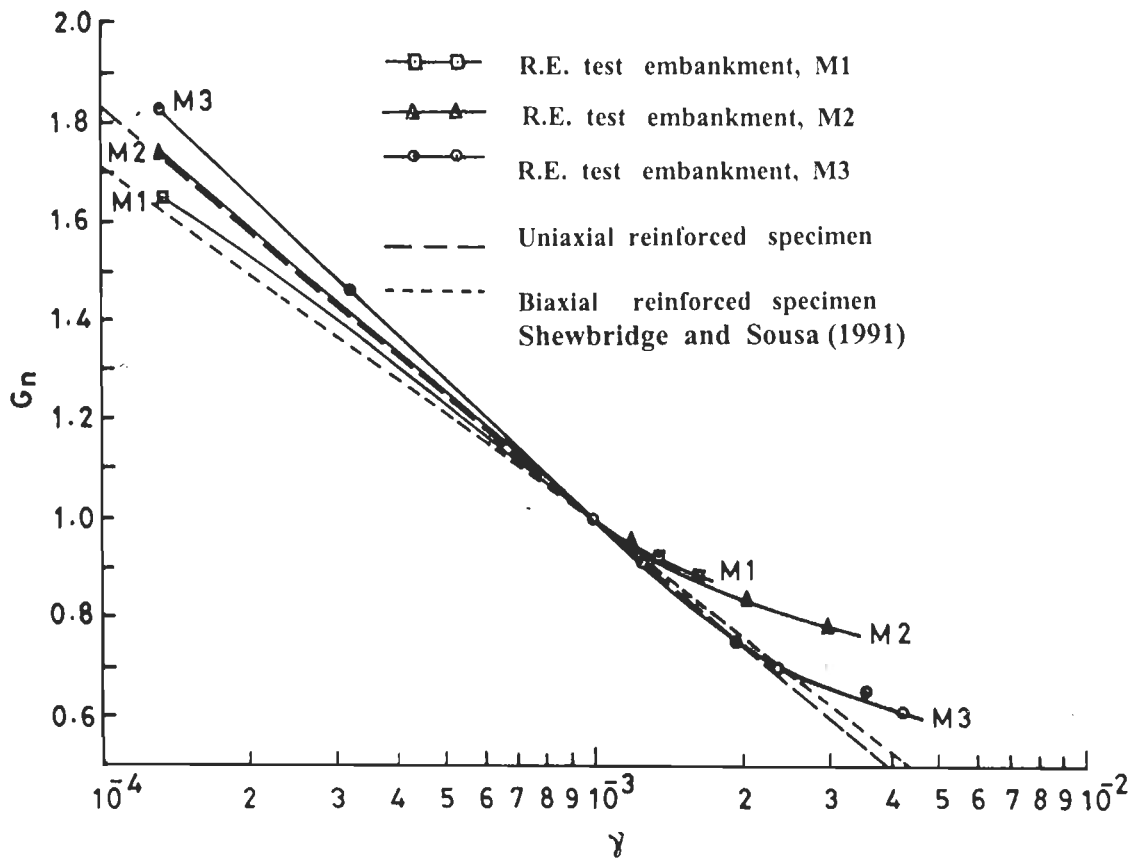


FIG. 4.6.14 RELATIONSHIP BETWEEN NORMALIZED SHEAR MODULUS, G_n , AND SHEAR STRAIN, γ , FOR R.E. EMBANKMENTS AND REINFORCED SPECIMENS.

as reinforcement which is much stiffer than the geotextile reinforcements used in this investigation. Smith and Segrestin (1992) have also reported similar observations based on analytical results for R.E. embankments with High Adherence Steel Strips with very high stiffness and Oriented Polyethylene Grids as reinforcements.

Near resonance, the excitation frequency, F_{rq} , strongly affects G_r since vibration amplitudes and associated strains are large. Figure 4.6.15

to 4.6.17 show G_r - F_{rq} plots for M1, M2 and M3 at different OME values. For M1, curves for OME equal to 24 and 36 are very close. Moreover, G_r very much reduces with increasing F_{rq} approaching resonant frequency to reach its minimum value at resonance. Even a small increase in F_{rq} beyond resonance, G_r increase sharply. Similar observation may be made from curves for M2 and M3 also. However, for M3 curves are well separated for different OME values, particularly for lower values of OME equal to 6 and 12. This is due to greatly different buildup of displacements and, hence, of shear strains in view of the relatively low stiffness of the embankment M3.

Frequency ratio, r_f , is defined as (F_{rq}/F_n) . The r_f - (G_r/G_{rn}) relationships (Figures 4.6.18 to 4.6.20) give $(G_r/G_{rn})=1$ at resonance for all embankments and for all OME values. The (G_r/G_{rn}) reaches a minimum value of unity at resonance and increases sharply with change in r_f on either side of resonance. Table 4.6.10 presents percentage differences in (G_r/G_{rn}) computed w.r.t. mean value of (G_r/G_{rn}) for different OME at r_f values of 0.6, 0.707, 0.9 and 0.95 for M1, M2 and M3. The largest difference is 12.79% and in most cases it is much smaller which is tolerable. Hence, it is concluded that a single r_f - (G_r/G_{rn}) relationship may be considered adequate for computing (G_r/G_{rn}) for different r_f values.

It is clear from Fig.4.6.17 and Fig.4.6.20 that (G_r/G_{rn}) - r_f relationship is much more advantageous than G_r - F_{rq} relationship. The spread between curves in Fig.4.6.17 is much larger and difficult to correlate.

4.6.5 Acceleration Variation with Phase Angle

Theory of shear wave propagation through embankment of height, H, due to base excitation was cited in Article 4.5.2 earlier. Time lag between

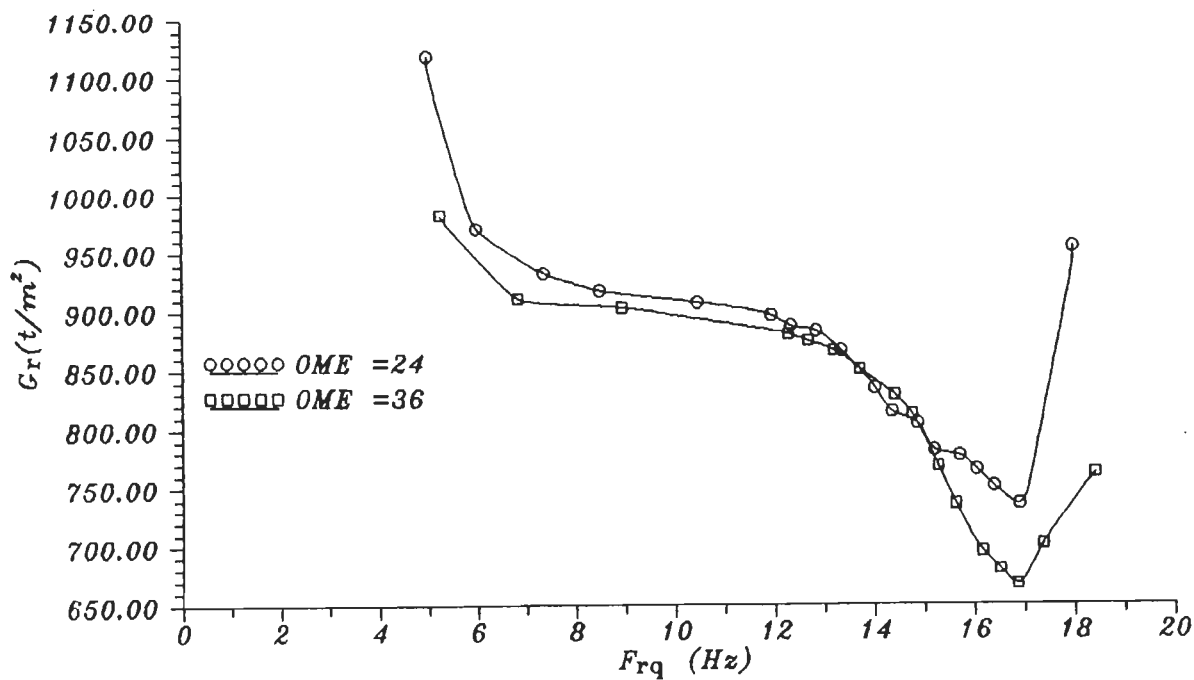


FIG.4.6.15 VARIATION OF SHEAR MODULUS, G_r , WITH FREQUENCY OF EXCITATION, F_{rq} , FOR R.E. TEST EMBANKMENT, M1.

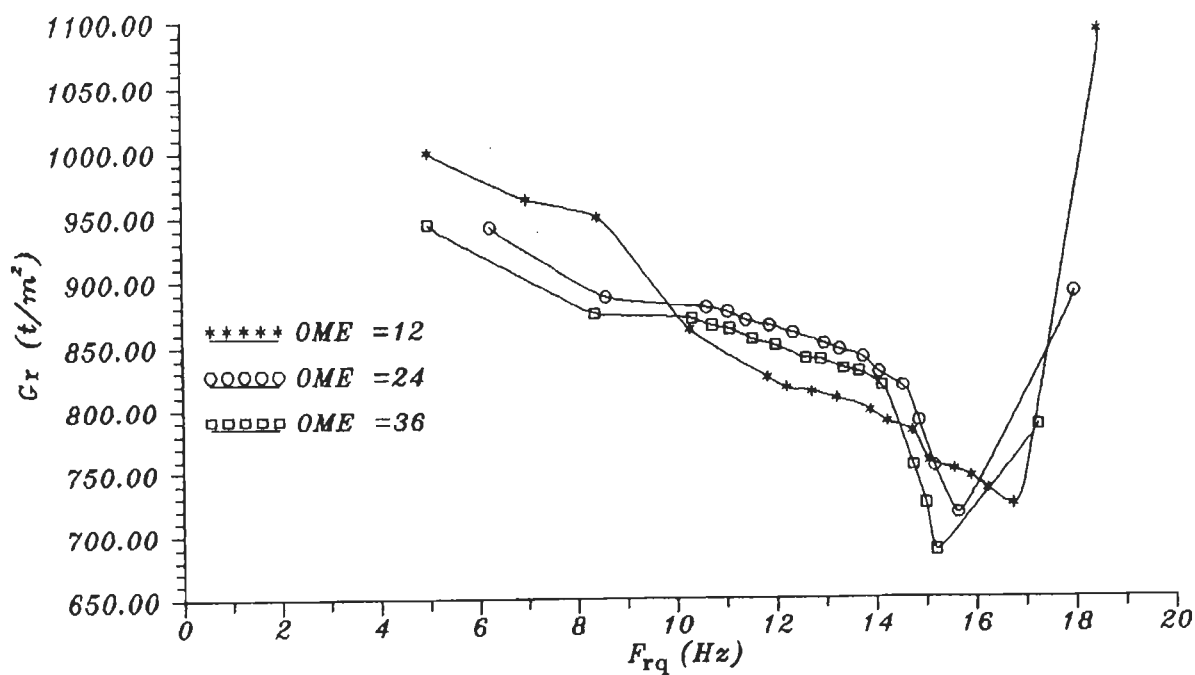


FIG.4.6.16 VARIATION OF SHEAR MODULUS, G_r , WITH FREQUENCY OF EXCITATION, F_{rq} , FOR R.E. TEST EMBANKMENT, M2.

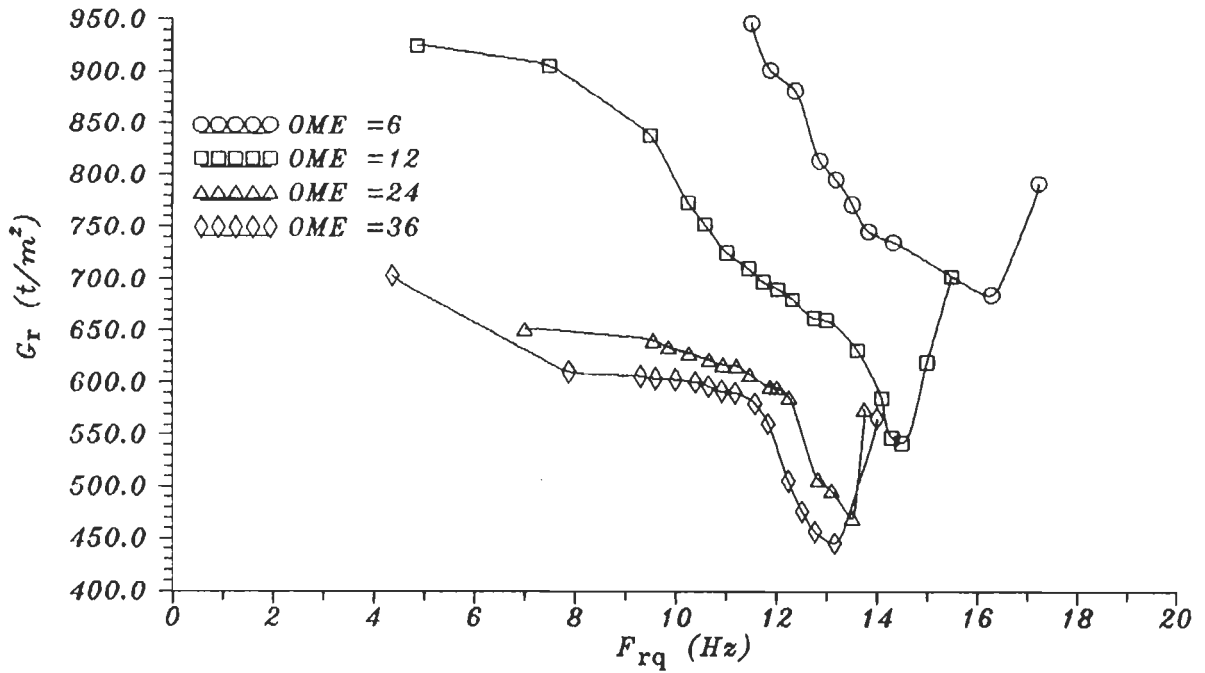


FIG.4.6.17 VARIATION OF SHEAR MODULUS, G_r , WITH FREQUENCY OF EXCITATION, F_{rq} , FOR R.E. TEST EMBANKMENT, M3.

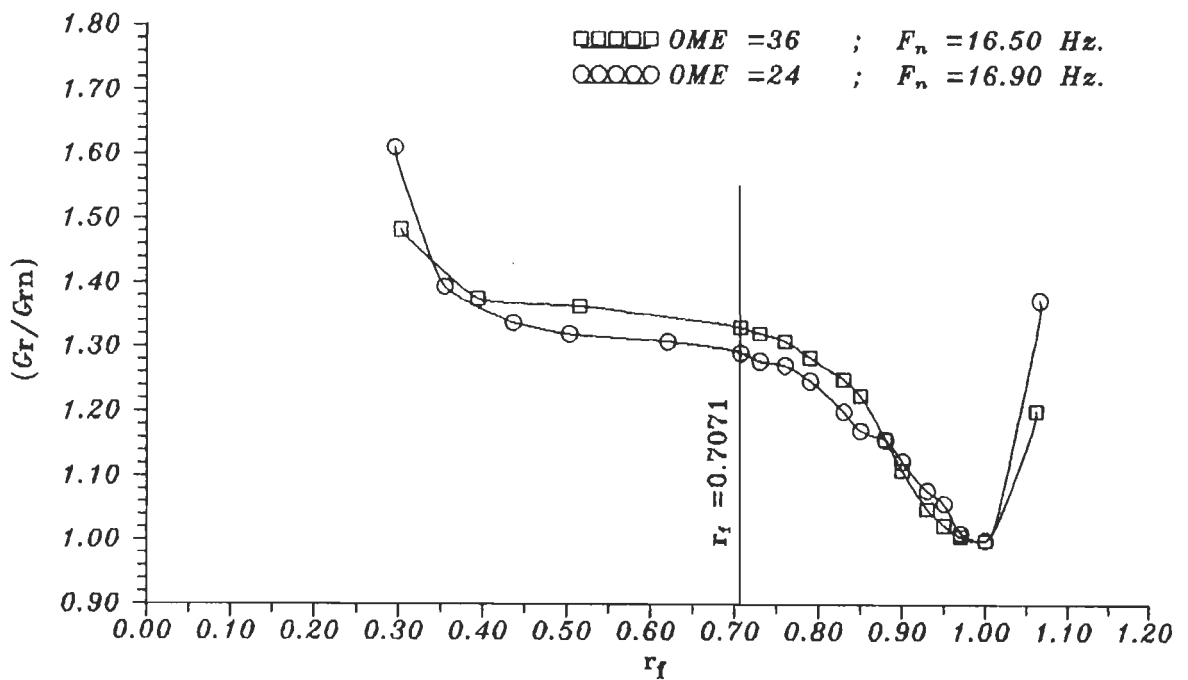


FIG.4.6.18 VARIATION OF DIMENSIONLESS SHEAR MODULUS (G_r/G_{rn}) WITH FREQUENCY RATIO, r_f , FOR R.E. TEST EMBANKMENT M1.

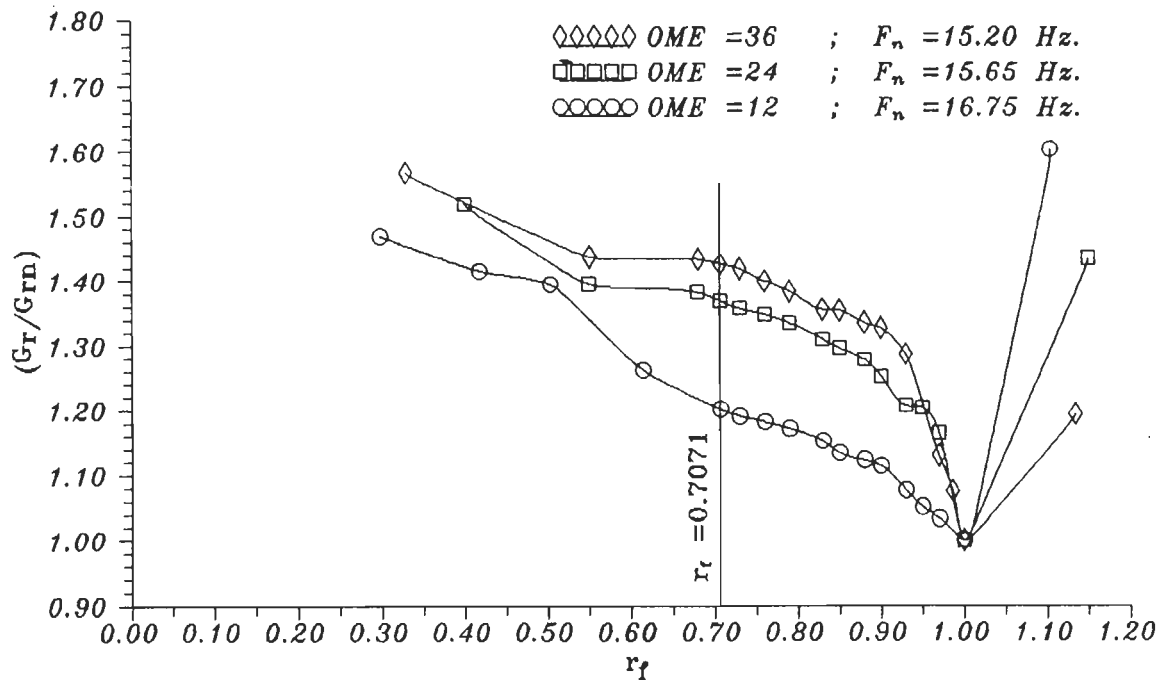


FIG.4.6.19 VARIATION OF DIMENSIONLESS SHEAR MODULUS (G_r/G_{rn}) WITH FREQUENCY RATIO, r_f , FOR R.E. TEST EMBANKMENT M2.

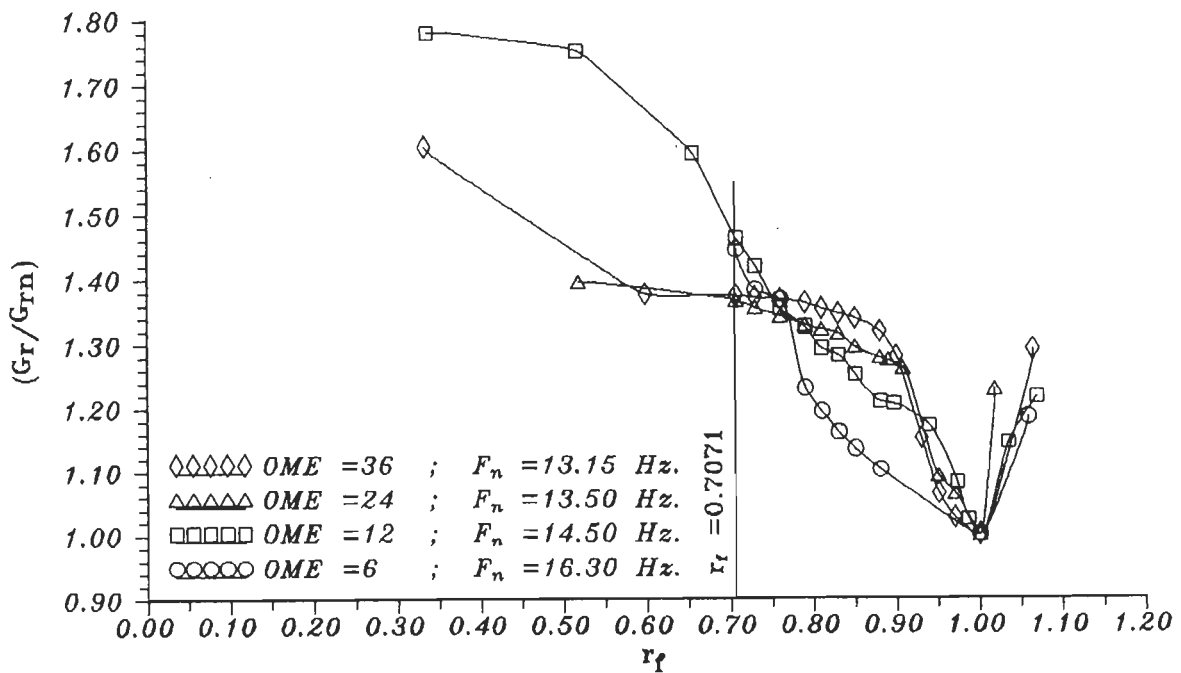


FIG.4.6.20 VARIATION OF DIMENSIONLESS SHEAR MODULUS (G_r/G_{rn}) WITH FREQUENCY RATIO, r_f , FOR R.E. TEST EMBANKMENT M3.

Table 4.6.10 Percentage Differences in (G_r/G_{rn}) Values Computed w.r.t. the Mean Value of (G_r/G_{rn}) at Different r_f Values for R.E. Test Embankments.

R.E. Test Embankment, M1				
OME	(G_r/G_{rn})			
	$r_f = 0.6$	$r_f = 0.707$	$r_f = 0.90$	$r_f = 0.95$
24	1.31	1.295	1.115	1.0275
36	1.35	1.33	1.12	1.0550
mean	1.33	1.3125	1.1175	1.0412
% deviation from mean	1.50%	1.33%	0.223%	1.32%
R.E. Test Embankment, M2				
OME	(G_r/G_{rn})			
	$r_f = 0.6$	$r_f = 0.707$	$r_f = 0.90$	$r_f = 0.95$
12	1.280	1.20	1.130	1.0575
24	1.375	1.37	1.255	1.2075
36	1.435	1.43	1.330	1.2075
mean	1.3633	1.3333	1.2383	1.1575
% deviation from mean	-6.11% 5.25%	-10% 7.25%	-8.748% 7.402%	-8.639% 4.3196%
R.E. Test Embankment, M3				
OME	(G_r/G_{rn})			
	$r_f = 0.6$	$r_f = 0.707$	$r_f = 0.90$	$r_f = 0.95$
6	-	1.44	1.09	1.04
12	1.65	1.46	1.33	1.06
24	1.39	1.37	1.27	1.092
36	1.39	1.38	1.28	1.15
mean	1.485	1.4125	1.2425	1.0855
% deviation from mean	-6.39% 12.79%	-3.00% 3.36%	-12.273% 7.042%	-4.1916% 5.94%

arrival times of shear waves propagating with velocity, V_s , at any two points separated by a distance, X , causes a phase difference, $\delta\theta$, and results into different accelerations. In this article, variation of acceleration and phase angle, θ , with dimensionless depth, X/H , is studied.

Figure 4.6.21 and 4.6.22 show acceleration variation with (X/H) for OME value of 36 and $r_f=0.7071$ for embankments M1 and M2 respectively. Different shapes of acceleration variation are obtained for different values of θ considered at the embankment top. These shapes are similar to different shapes of the embankment expected under influence of sinusoidal excitation. Hence, obtaining a smooth acceleration variation along (X/H) knowing accelerations measured by three pickups at different phase angles has been accomplished. It is required to compute inertia in different layers of embankment to obtain coefficient of dynamic pullout resistance.

4.6.6 Shear Strains

Average dynamic shear strain, γ_{avd} , varies with phase angle, θ . The maximum value of γ_{avd} is denoted as γ_{avdmax} . The $\gamma_{avdmax}-r_f$ relationship obtained for M1, M2 and M3 for different OME values are presented in Fig.4.6.23 to 4.6.25 respectively. As expected, the largest value of γ_{avdmax} occurs at resonance. Value of γ_{avdmax} reduces sharply with change in r_f on either side of resonance. For M1, curves for different OME values are close to each other for r_f upto 0.9, because, M1 is stiff and γ_{avdmax} is not affected significantly by change in force levels due to change in OME range under consideration. Nevertheless, it is prudent to limit the validity of this observation for $r_f \leq 0.7071$ only to be on safer side. These observations are true for M2 also. For the weakest embankment M3, the curves show appreciable difference in γ_{avdmax} at different OME values as expected.

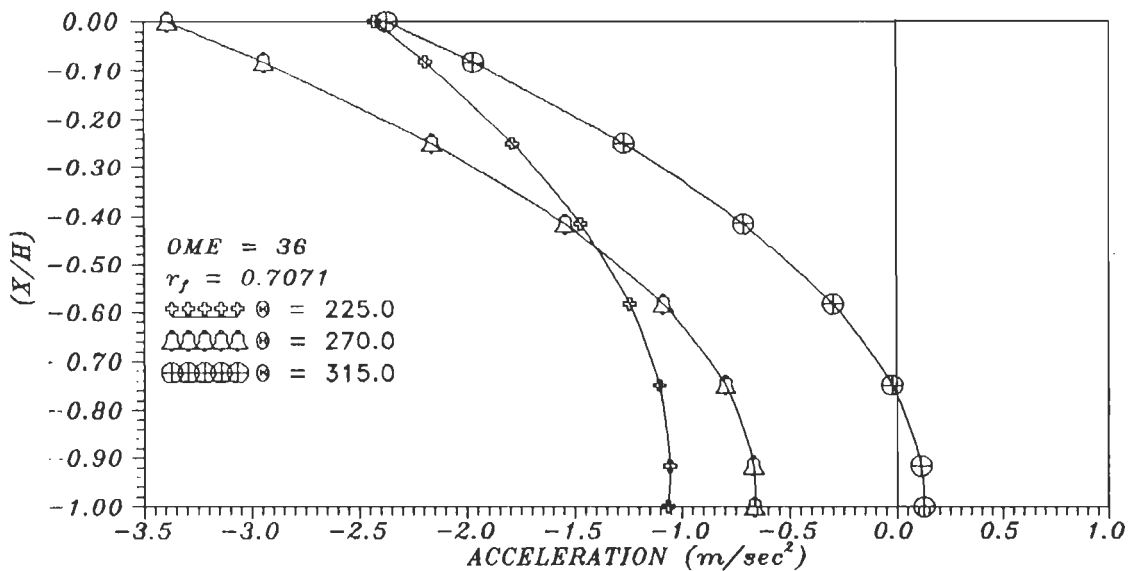
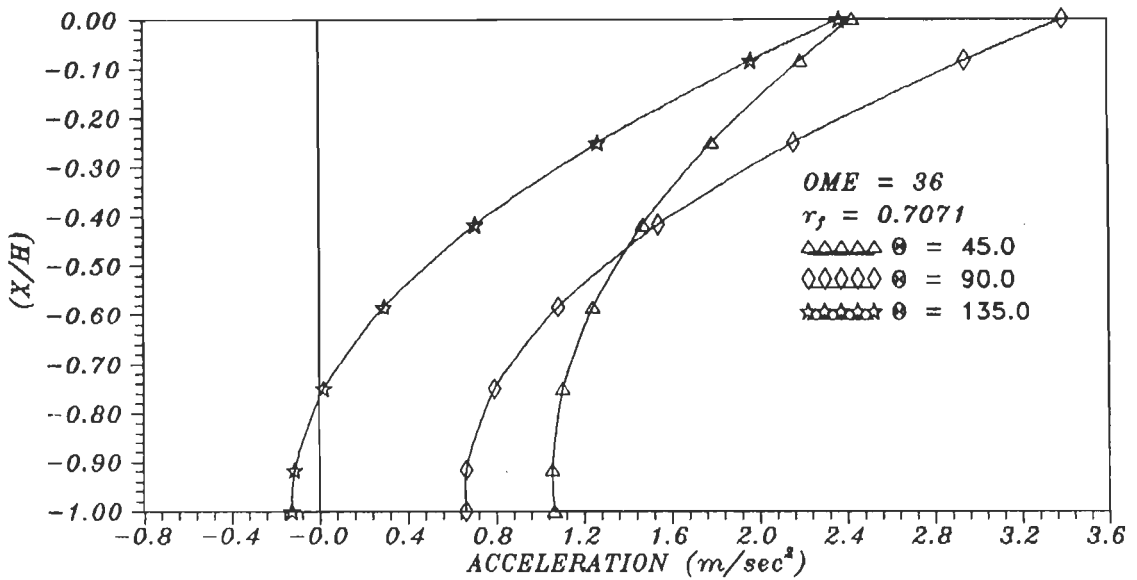
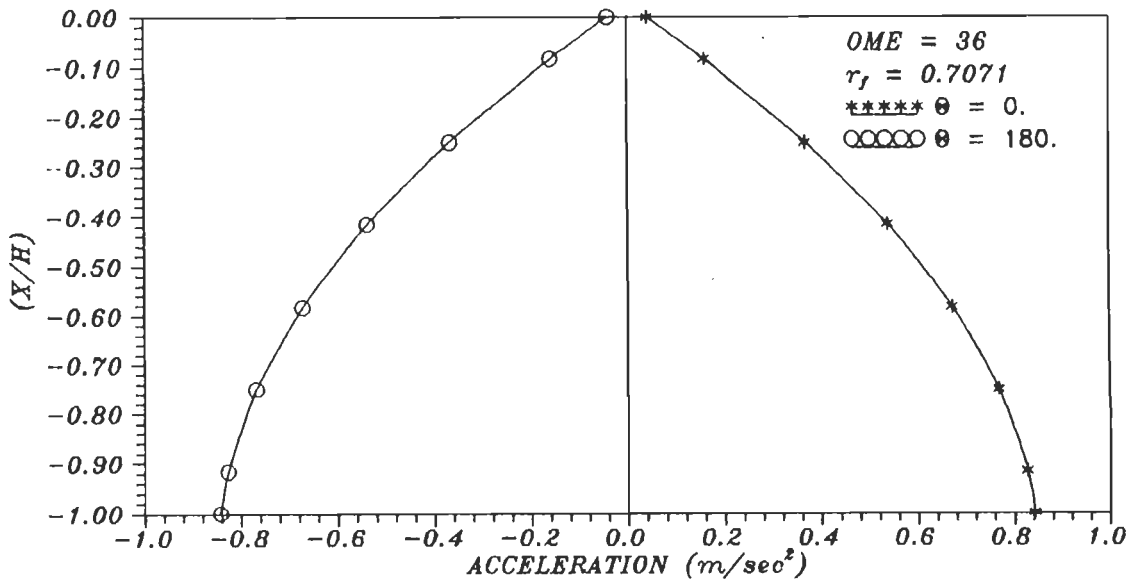


FIG.4.6.21 VARIATION OF ACCELERATION WITH DIMENSIONLESS DEPTH (X/H) AT DIFFERENT PHASE ANGLE, θ , FOR R.E. TEST EMBANKMENT M1.

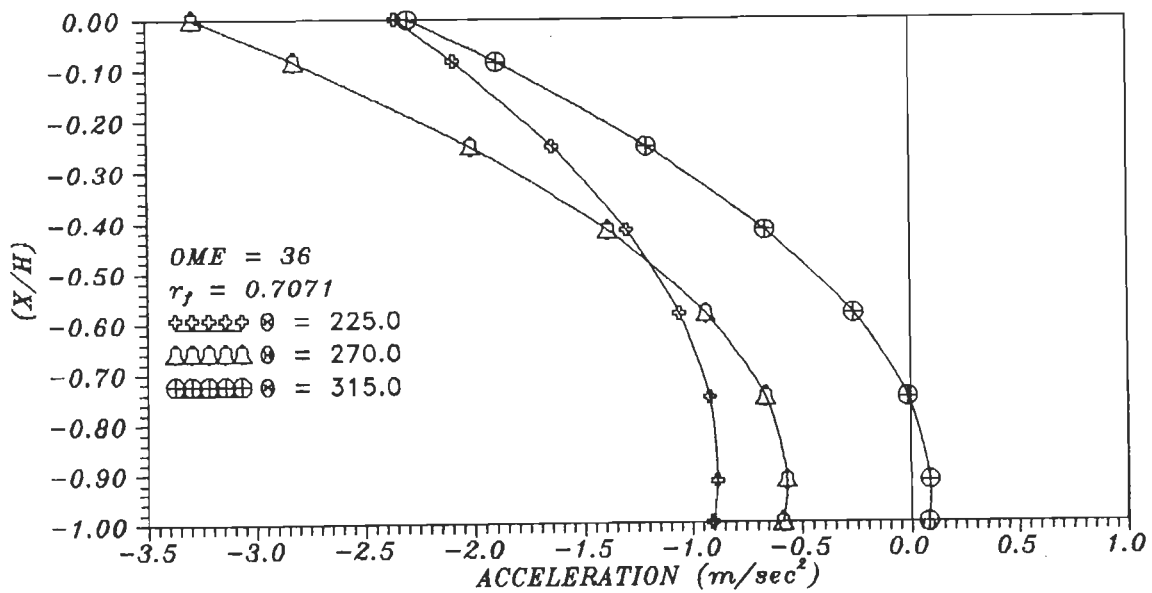
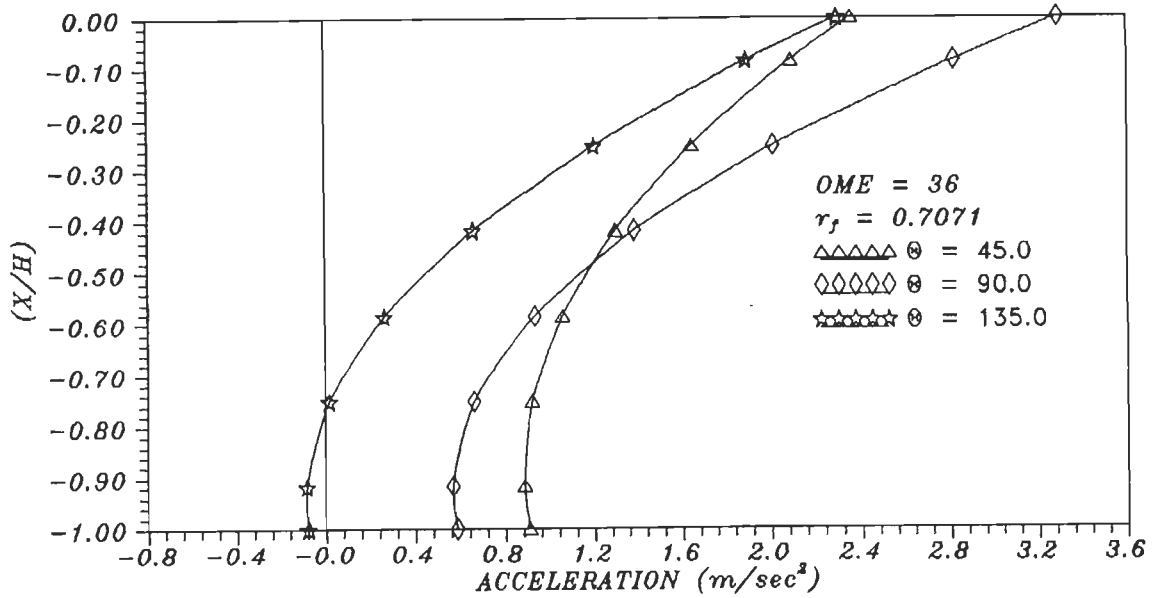
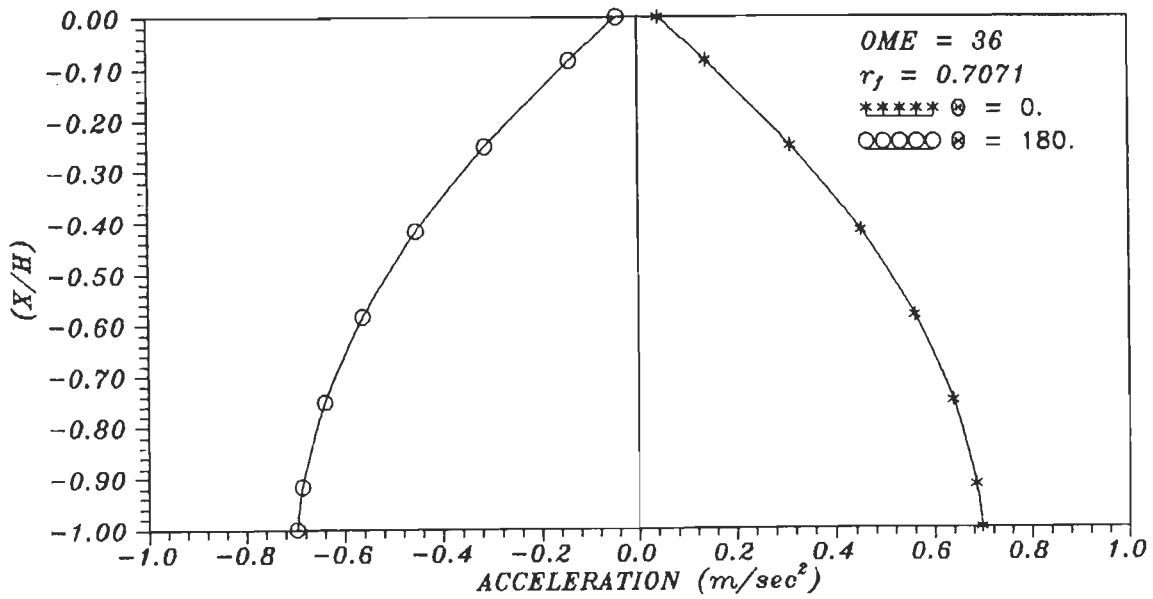


FIG.4.6.22 VARIATION OF ACCELERATION WITH DIMENSIONLESS DEPTH (X/H) AT DIFFERENT PHASE ANGLE, θ , FOR R.E. TEST EMBANKMENT M2.

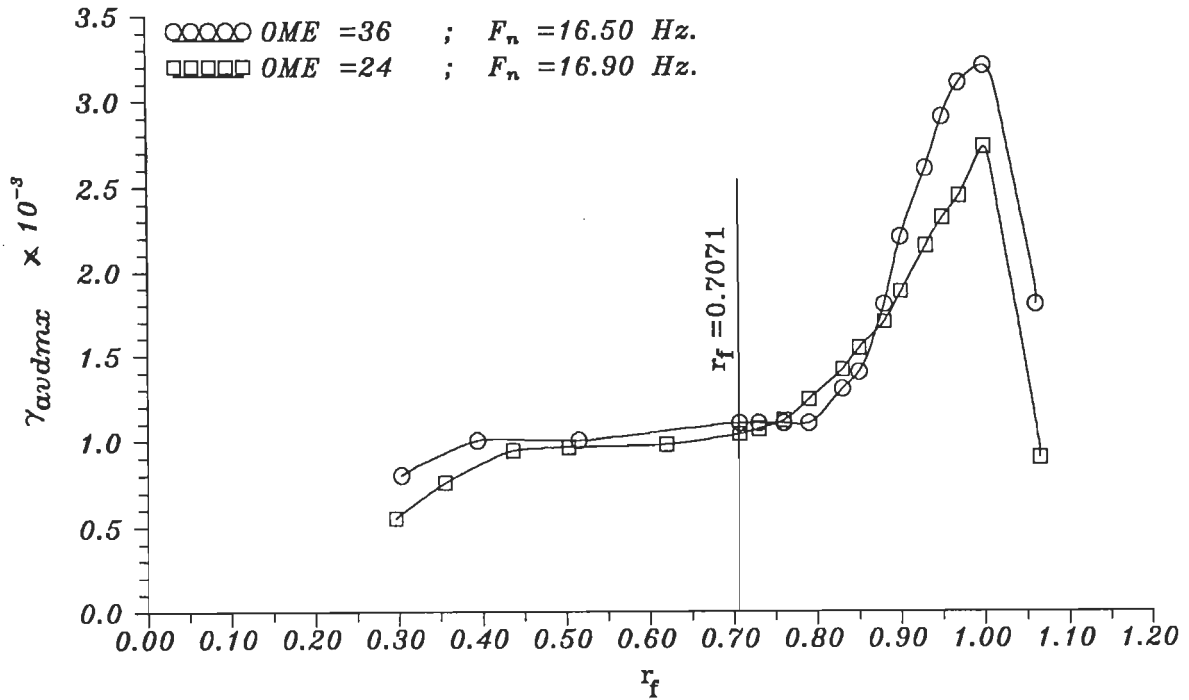


FIG.4.6.23 VARIATION OF MAXIMUM AVERAGE SHEAR STRAIN , γ_{avdmax} , WITH FREQUENCY RATIO, r_f , FOR R.E. TEST EMBANKMENT M1.

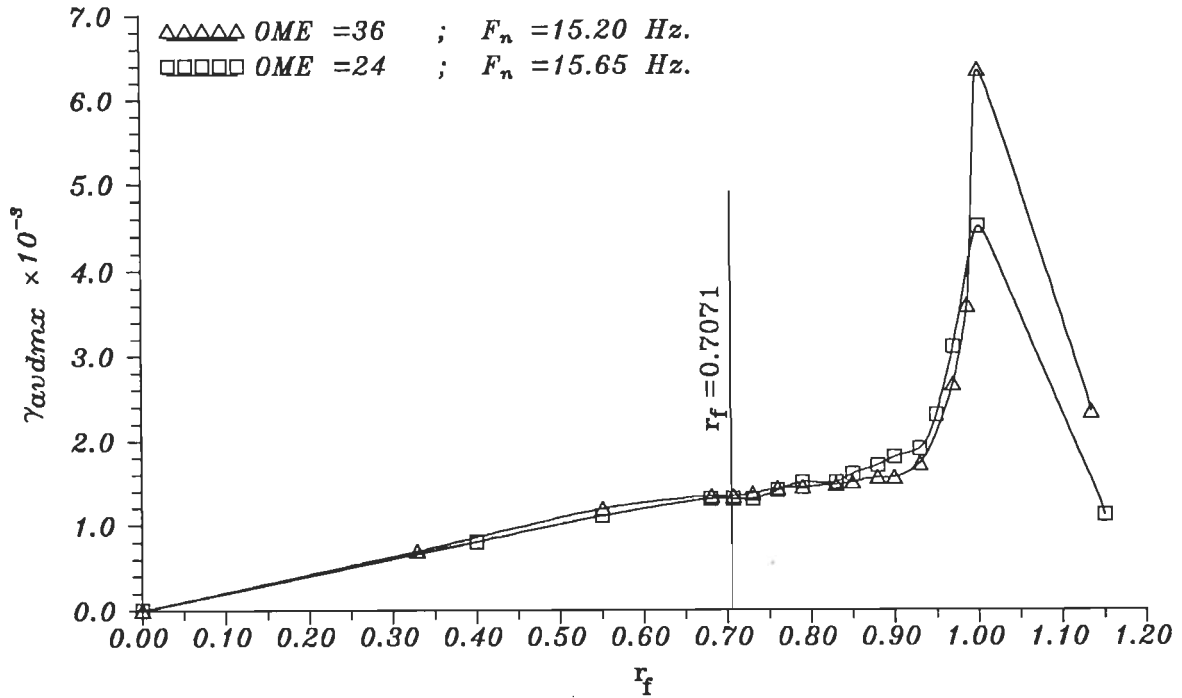


FIG.4.6.24 VARIATION OF MAXIMUM AVERAGE SHEAR STRAIN , γ_{avdmax} , WITH FREQUENCY RATIO, r_f , FOR R.E. TEST EMBANKMENT M2.

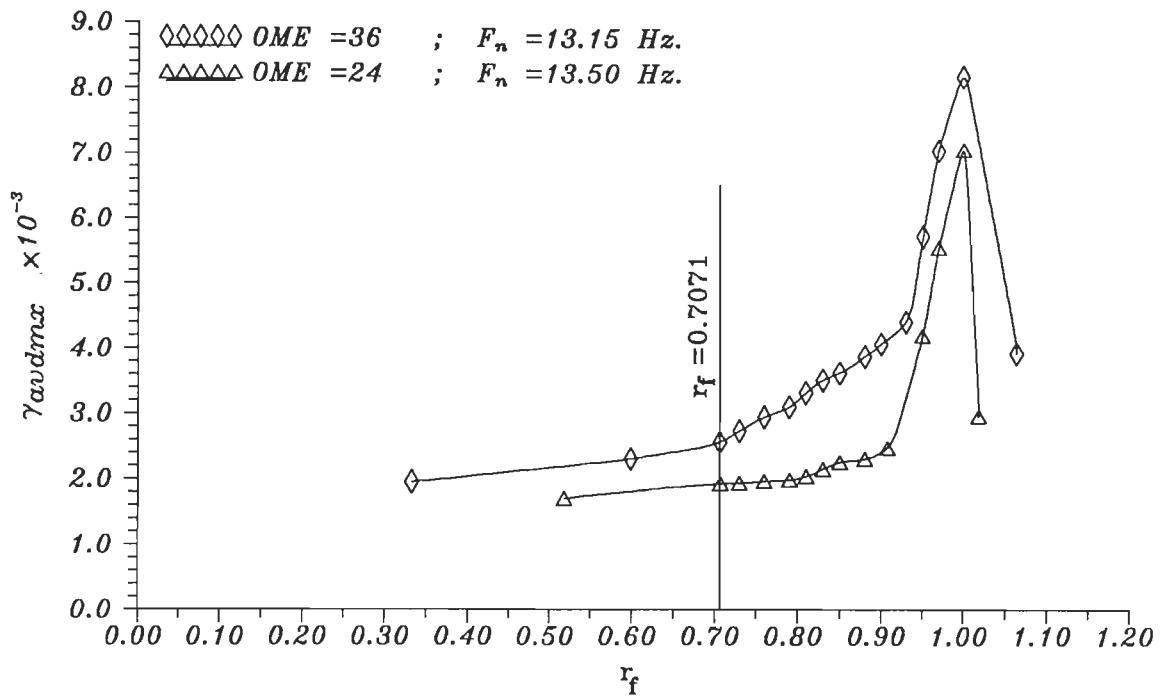


FIG.4.6.25 VARIATION OF MAXIMUM AVERAGE SHEAR STRAIN , $\gamma_{ave\max}$, WITH FREQUENCY RATIO, r_f , FOR R.E. TEST EMBANKMENT M3.

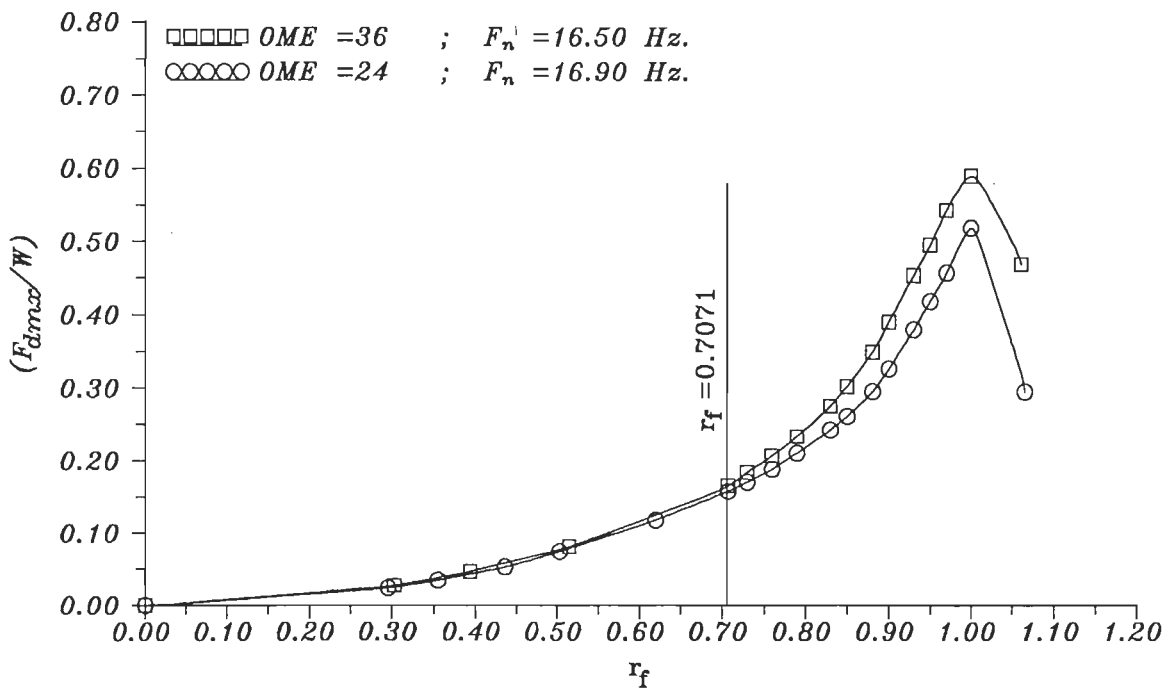


FIG.4.6.26 VARIATION OF DIMENSIONLESS DISTURBING FORCE ($F_{d\max}/W$) WITH FREQUENCY RATIO, r_f , FOR R.E. TEST EMBANKMENT M1.

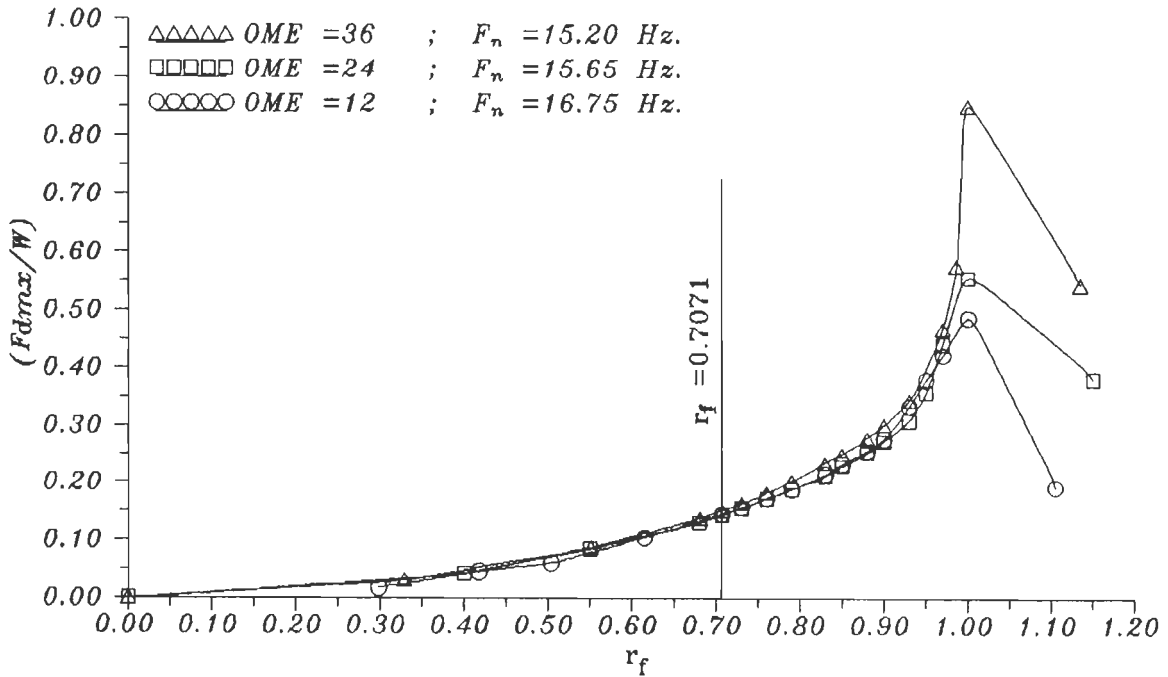


FIG.4.6.27 VARIATION OF DIMENSIONLESS DISTURBING FORCE (F_{dmx}/W) WITH FREQUENCY RATIO, r_f , FOR R.E. TEST EMBANKMENT M2.

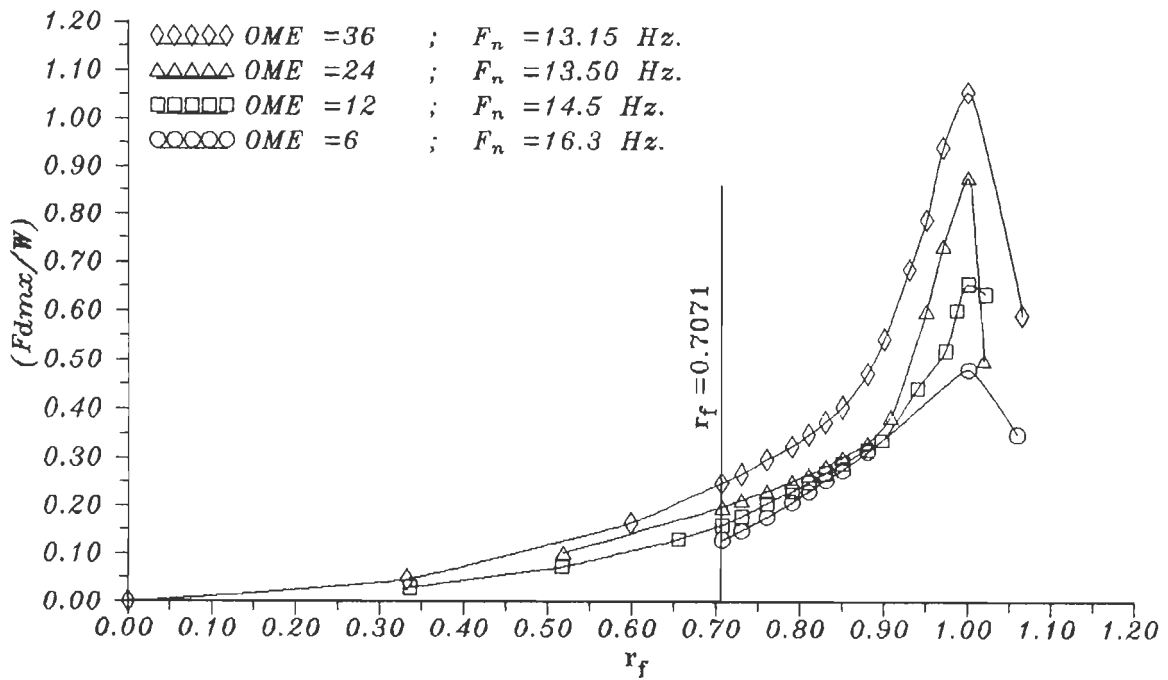


FIG.4.6.28 VARIATION OF DIMENSIONLESS DISTURBING FORCE (F_{dmx}/W) WITH FREQUENCY RATIO, r_f , FOR R.E. TEST EMBANKMENT M3.

4.6.7 Disturbing Inertia Forces

On excitation, different layers of embankment experience different horizontal accelerations which generate disturbing/destabilizing inertia force, F_d varying with phase angle. Its maximum value, F_{dmx} , is rendered dimensionless w.r.t. embankment weight, W . Variation of (F_{dmx}/W) with frequency ratio, r_f , at different OME are given in Fig.4.6.26 to 4.6.28 for M1, M2 and M3 respectively. As expected, (F_{dmx}/W) reaches peak at resonance for a given OME. For M1 the curves for different values of OME are close to each other for r_f upto 0.7071, because, M1 is stiff and accelerations generated are not significantly affected by change in force levels due to change in OME in the range under consideration. These observations are true for M2 also. For the weakest embankment M3, the curves show appreciable difference in (F_{dmx}/W) at different OME values as expected.

4.6.8 Coefficient of Dynamic Pullout Resistance

Disturbing inertia are resisted mainly by pullout resistance of reinforcements. Based on resistances generated by all reinforcements, coefficient of average dynamic pullout resistance, μ_{avd} , is obtained by using Eq. 4.5.23 cited earlier. Figure 4.6.29 to 4.6.36 show variation of μ_{avd} with θ at embankment top for different r_f and different OME values for M1, M2 and M3. It may be observed that μ_{avd} varies sinusoidally with θ , because, inertia generated by sinusoidal excitations is also sinusoidal. As r_f increase, peak value of μ_{avd} also increases to reach its maximum value at $r_f=1$ (resonance). For $r_f>1$ and $r_f<1$, the peak value of μ_{avd} reduces. It is expected, because, accelerations and, hence, disturbing forces reduce sharply with change in r_f leading to reduced need for pullout resistance.

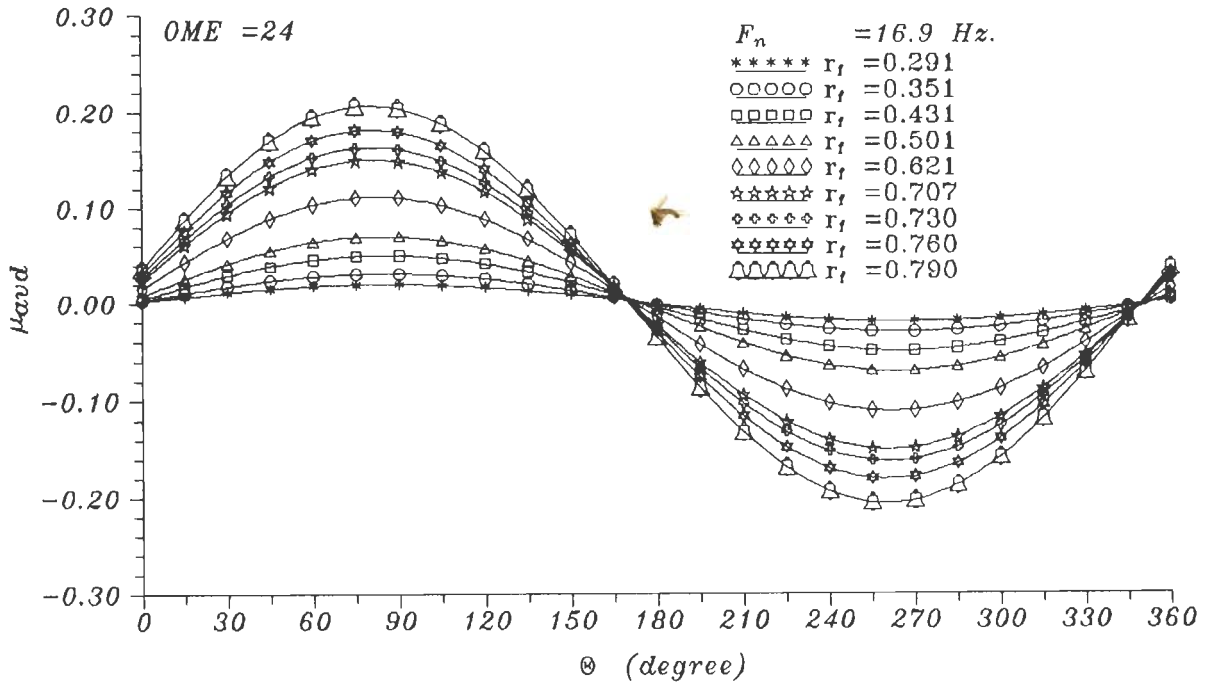


FIG.4.6.29 VARIATION OF AVERAGE COEFFICIENT OF PULLOUT RESISTANCE, μ_{avd} , WITH PHASE ANGLE, θ , FOR R.E. TEST EMBANKMENT, M1.

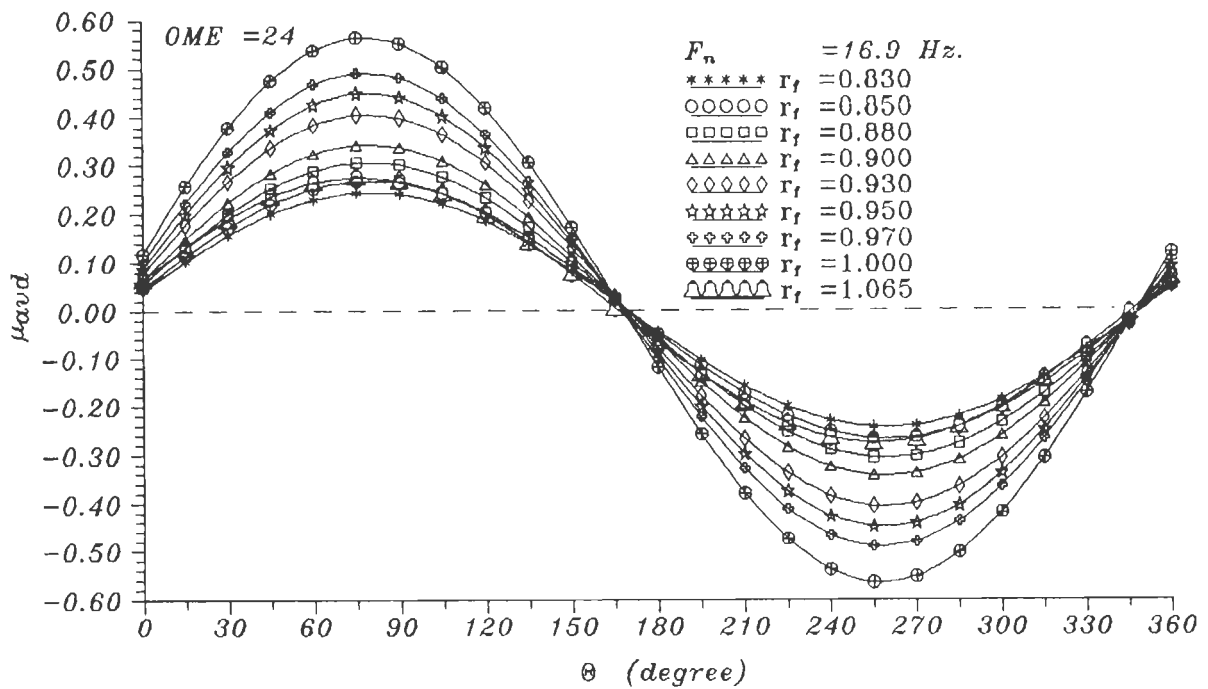


FIG.4.6.30 VARIATION OF AVERAGE COEFFICIENT OF PULLOUT RESISTANCE, μ_{avd} , WITH PHASE ANGLE, θ , FOR R.E. TEST EMBANKMENT, M1.

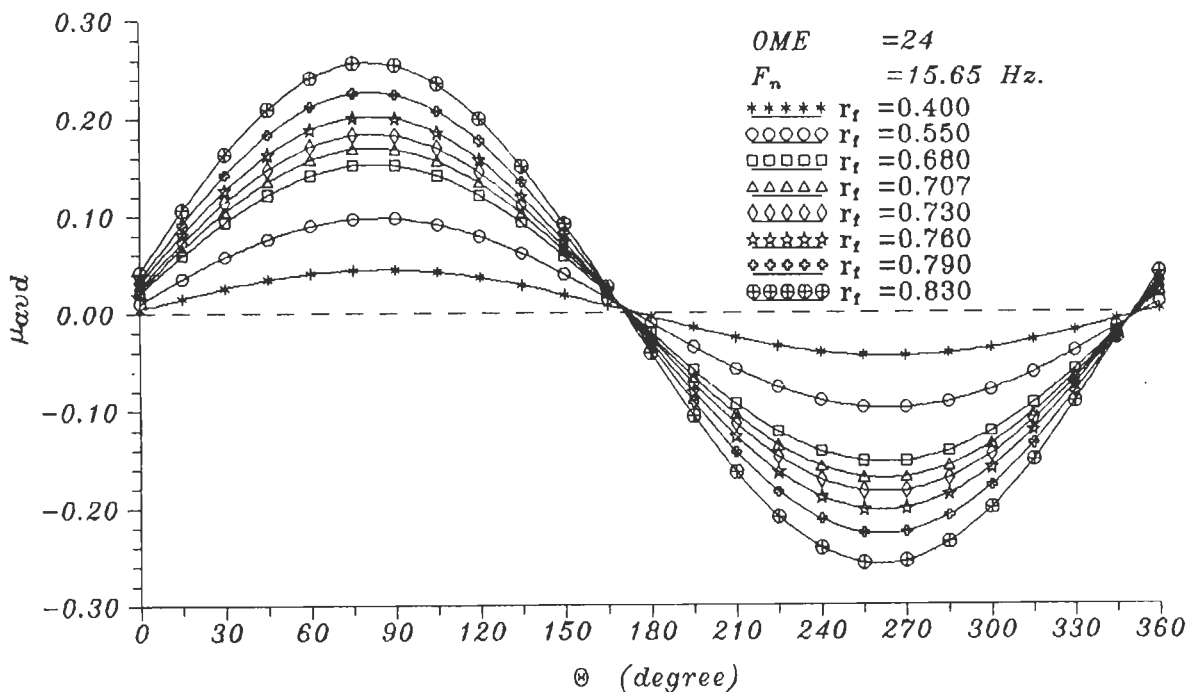


FIG.4.6.31 VARIATION OF AVERAGE COEFFICIENT OF PULLOUT RESISTANCE, μ_{avd} , WITH PHASE ANGLE, θ , FOR R.E. TEST EMBANKMENT, M2.

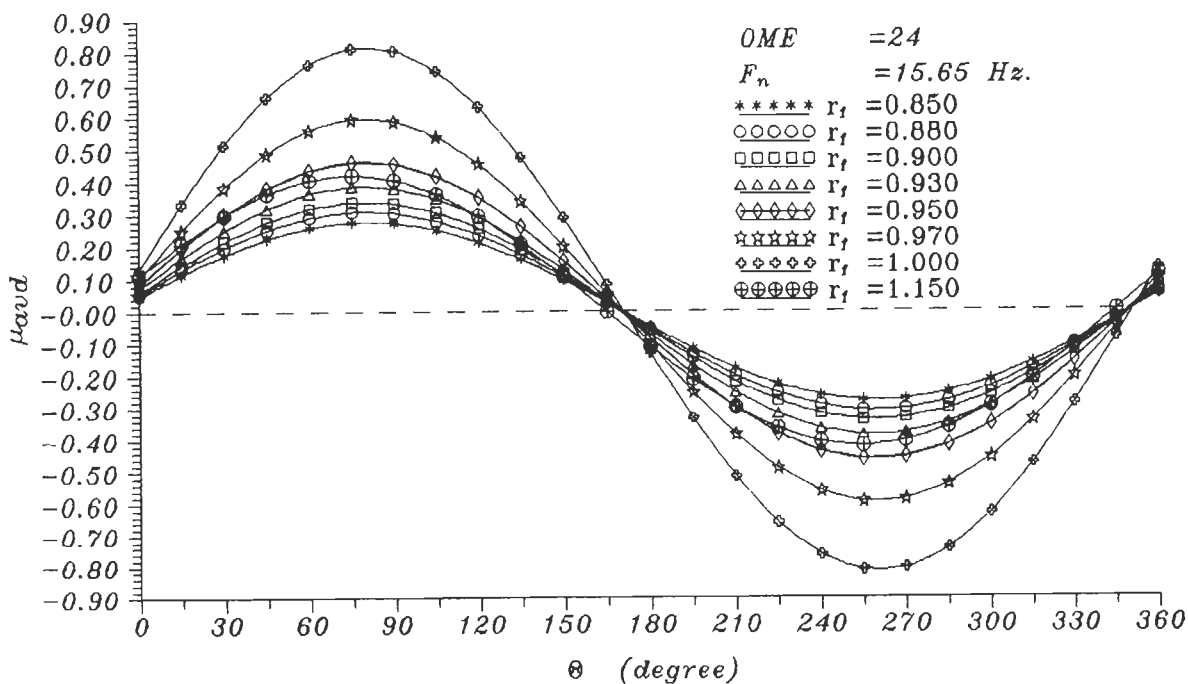


FIG.4.6.32 VARIATION OF AVERAGE COEFFICIENT OF PULLOUT RESISTANCE, μ_{avd} , WITH PHASE ANGLE, θ , FOR R.E. TEST EMBANKMENT, M2.

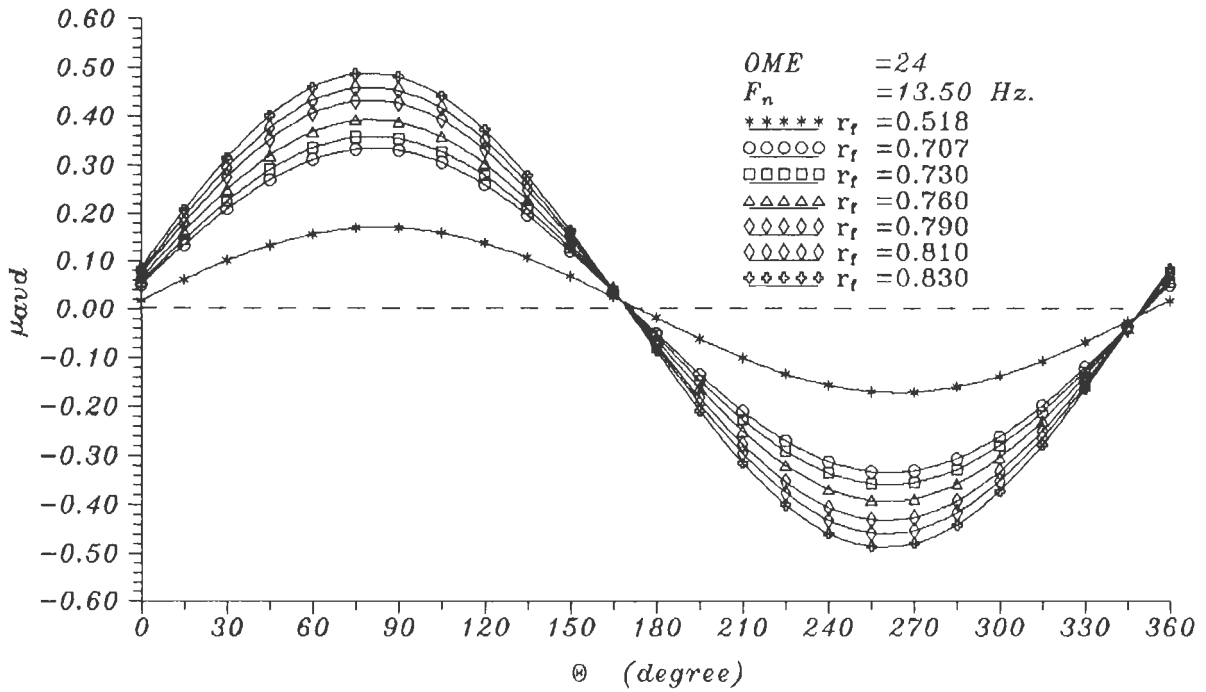


FIG.4.6.33 VARIATION OF AVERAGE COEFFICIENT OF PULLOUT RESISTANCE, μ_{avd} , WITH PHASE ANGLE, θ , FOR R.E. TEST EMBANKMENT, M3.

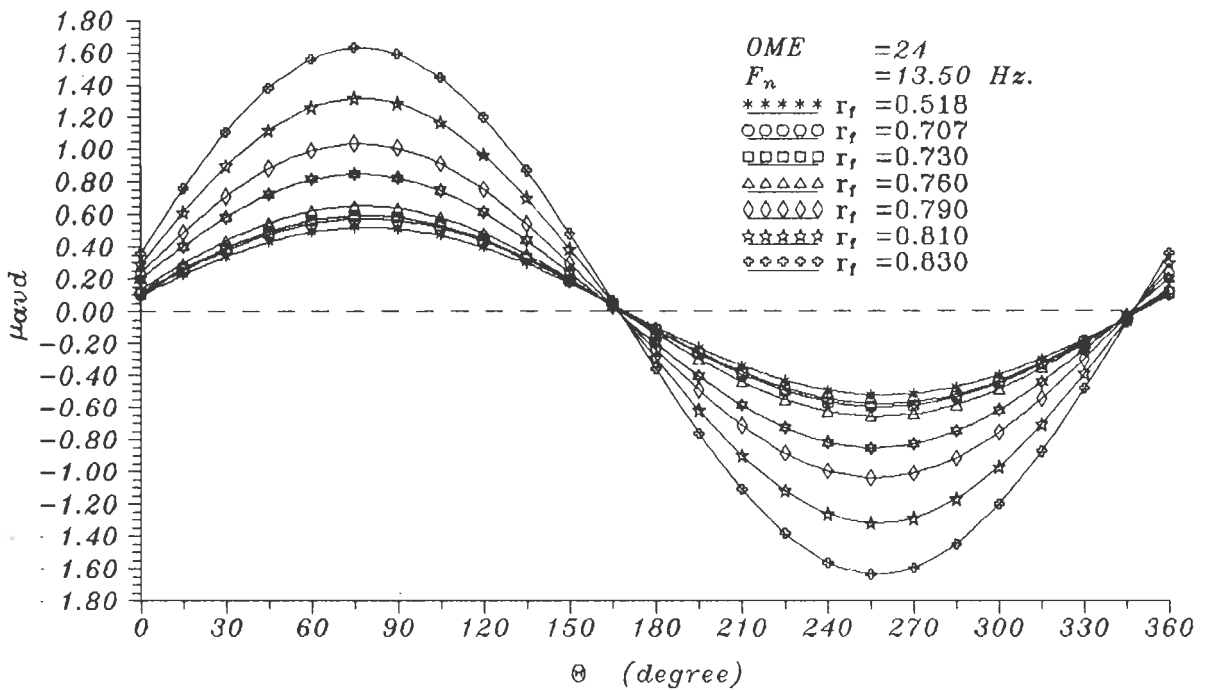


FIG.4.6.34 VARIATION OF AVERAGE COEFFICIENT OF PULLOUT RESISTANCE, μ_{avd} , WITH PHASE ANGLE, θ , FOR R.E. TEST EMBANKMENT, M3.

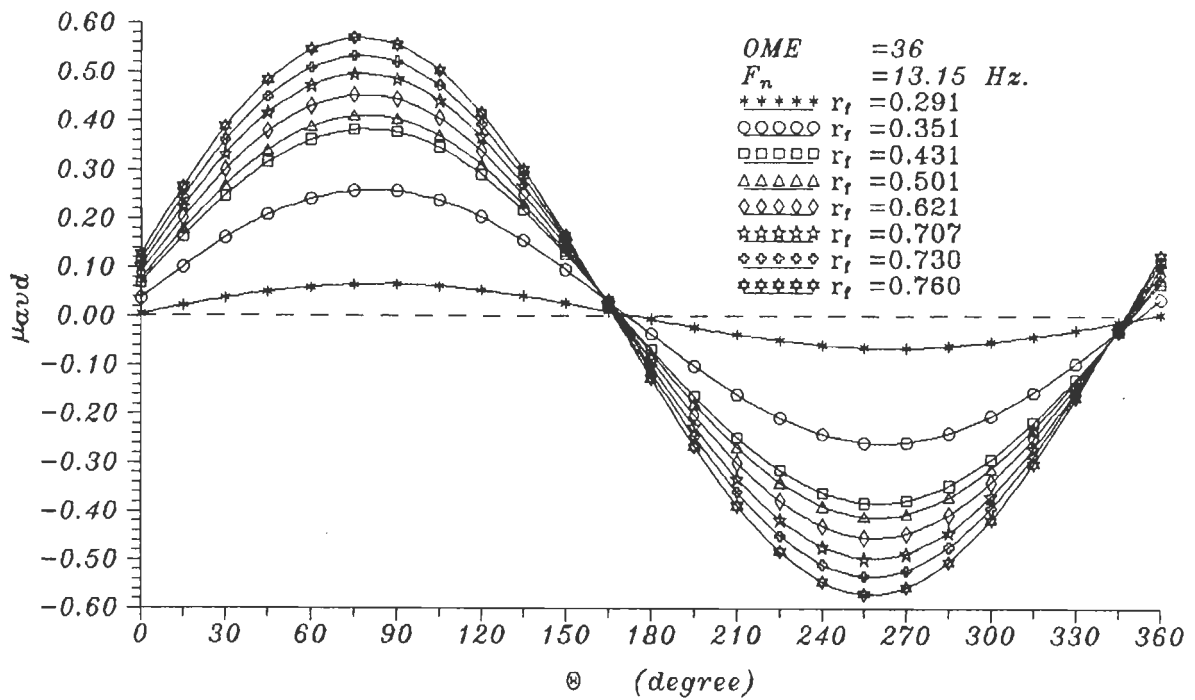


FIG.4.6.35 VARIATION OF AVERAGE COEFFICIENT OF PULLOUT RESISTANCE, μ_{avd} , WITH PHASE ANGLE, θ , FOR R.E. TEST EMBANKMENT, M3.

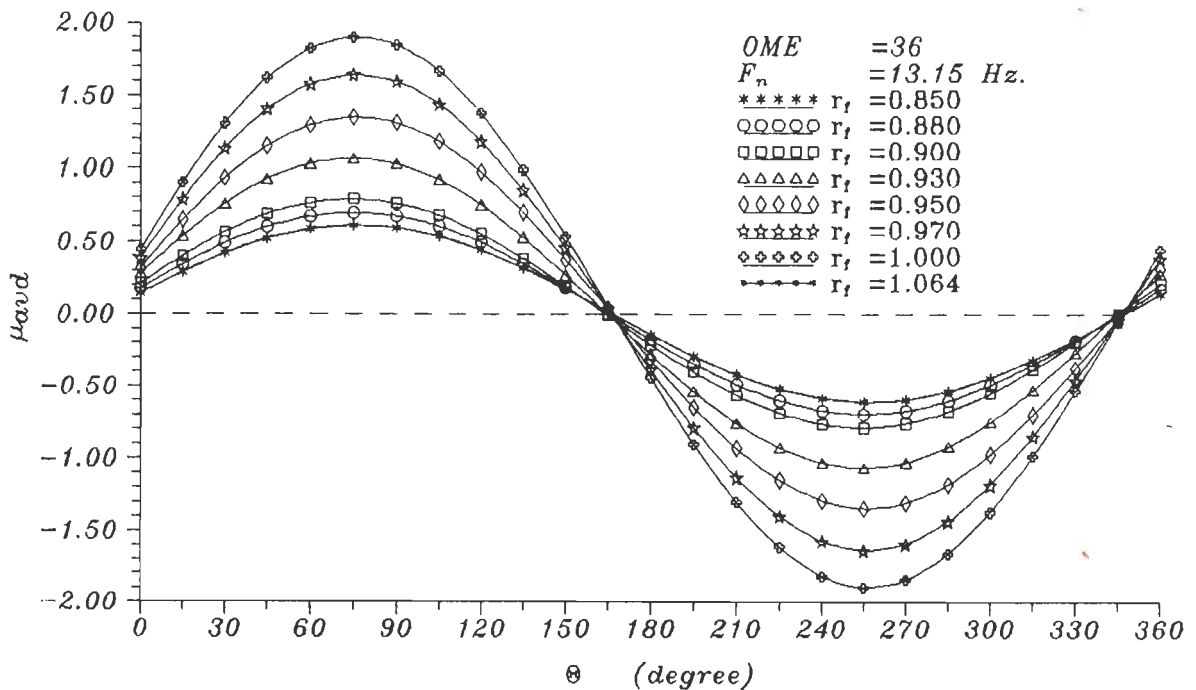


FIG.4.6.36 VARIATION OF AVERAGE COEFFICIENT OF PULLOUT RESISTANCE, μ_{avd} , WITH PHASE ANGLE, θ , FOR R.E. TEST EMBANKMENT, M3.

When θ at embankment top is zero, curves in above figures show a non-zero value of μ_{avd} , because, for $\theta=0$ the acceleration may be zero only at the top. At other levels, accelerations will not be necessary zero due to phase difference existing between points at different elevations. This leads to a finite disturbing force and a finite μ_{avd} value at $\theta=0$. At some θ , the net disturbing forces may be rendered zero resulting into $\mu_{avd}=0$.

Value of μ_{avd} depends upon disturbing force, F_d , at reinforcement level. Since F_d depends on θ , μ_{avd} also depends on θ . Its maximum value, μ_{avdmax} , is obtained by varying θ from zero to 2π . Figures 4.6.37 to 4.6.39 show $\mu_{avdmax}-r_f$ relationships for different values of OME and for M1, M2 and M3. Both, μ_{avd} and μ_{avdmax} are dimensionless. Curves for M1 and M2 are closely spaced for different OME values for $r_f \leq 0.8$ due to relatively smaller levels of stresses and strains caused by excitations and due to relatively large stiffnesses of M1 and M2. But, it is prudent to limit this observation to $r_f \leq 0.7071$ only to be on safer side. Nevertheless, curves are noticeably separated near resonance. As expected at resonance, μ_{avdmax} reaches the maximum value and reduces sharply with small changes in r_f on either side of resonance. Weakest embankment M3 shows more μ_{avdmax} variation at different OME values due to noticeably different values of forces, stresses and strains generated by excitation at these OME values.

Figures 4.6.38 and 4.6.39 show that for some range of r_f near resonance for certain OME values, $\mu_{avdmax} > \tan\phi$, where $\phi=44.44^\circ$ is the angle of shear resistance of plain soil of embankment. Line A-A represents $\mu_{avdmax} = \tan\phi$. Besides for such cases near resonance, $\mu_{avdmax} > \mu_{avsmx}$ where $\mu_{avsmx}=0.55$ is the largest coefficient of static pullout resistance obtained from tests

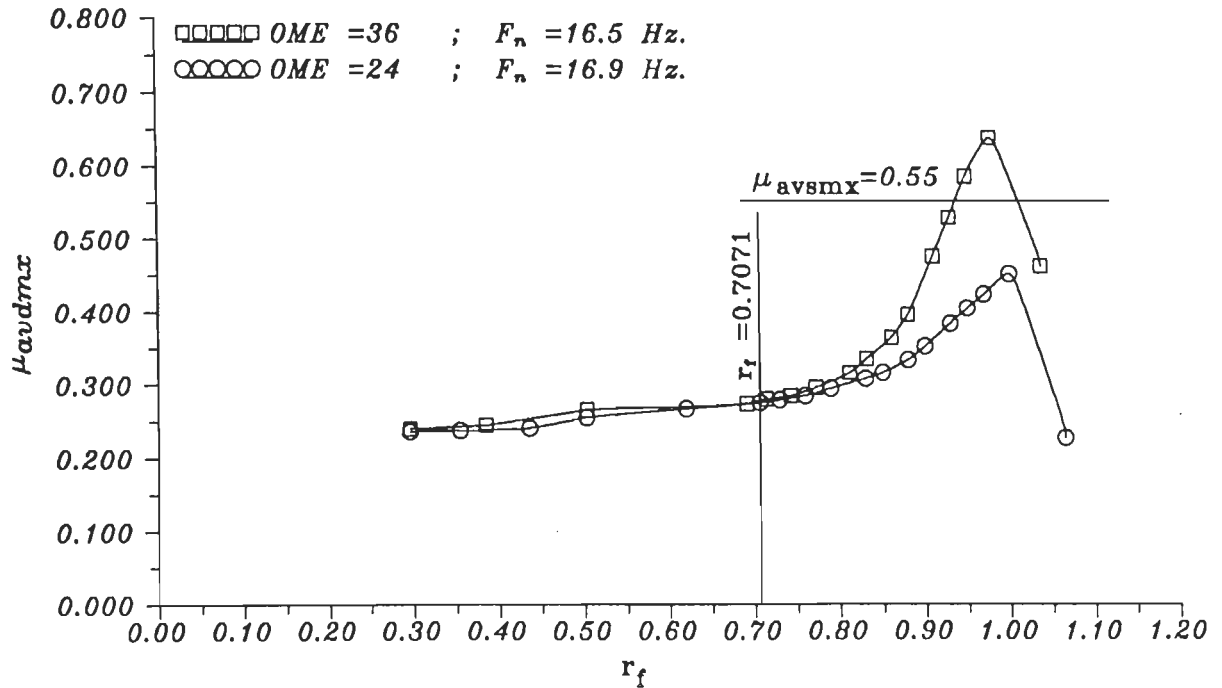


FIG.4.6.37 VARIATION OF MAXIMUM AVERAGE COEFFICIENT OF DYNAMIC PULLOUT RESISTANCE, μ_{avdmax} , WITH FREQUENCY RATIO, r_f , FOR R.E. TEST EMBANKMENT, M1.

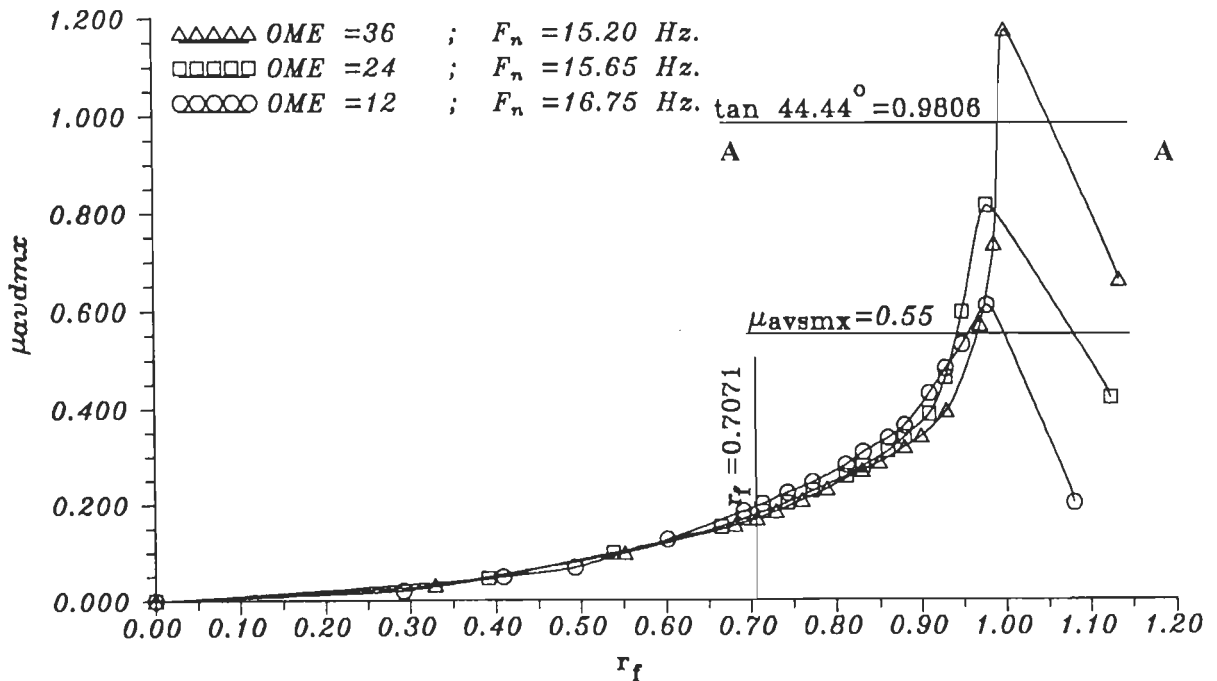


FIG.4.6.38 VARIATION OF MAXIMUM AVERAGE COEFFICIENT OF DYNAMIC PULLOUT RESISTANCE, μ_{avdmax} , WITH FREQUENCY RATIO, r_f , FOR R.E. TEST EMBANKMENT, M2.

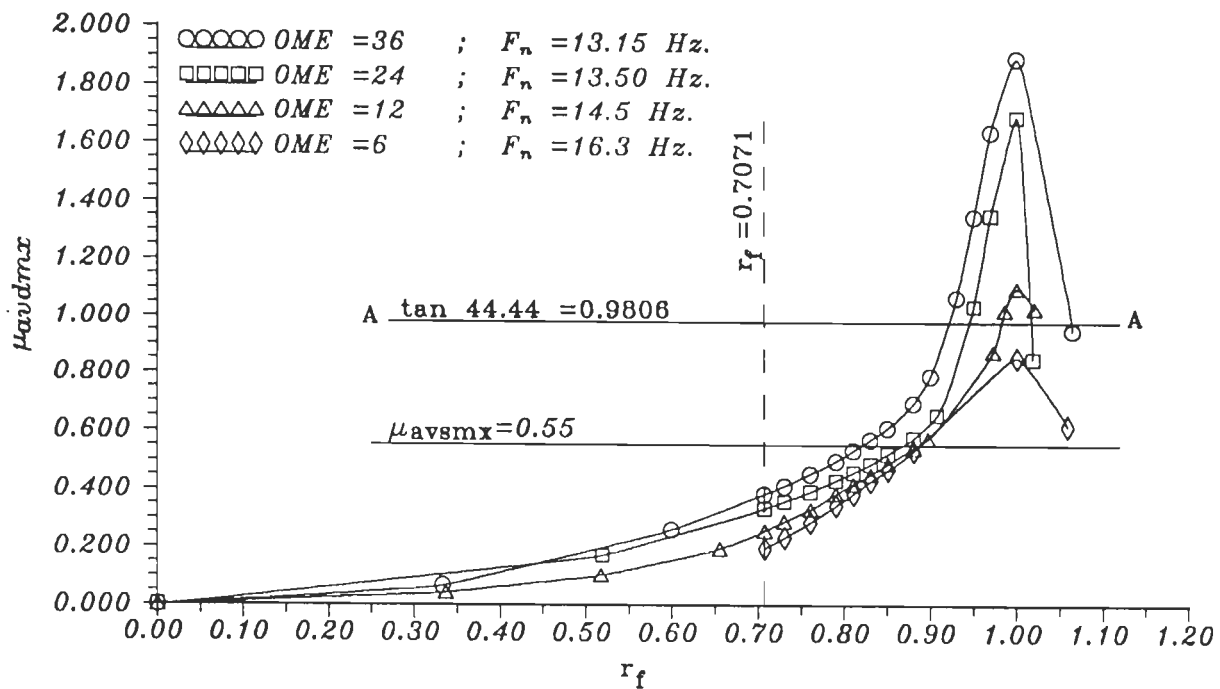


FIG. 4.6.39 VARIATION OF MAXIMUM AVERAGE COEFFICIENT OF DYNAMIC PULLOUT RESISTANCE μ_{avdmax} , WITH FREQUENCY RATIO, r_f , FOR R.E. TEST EMBANKMENT, M2.

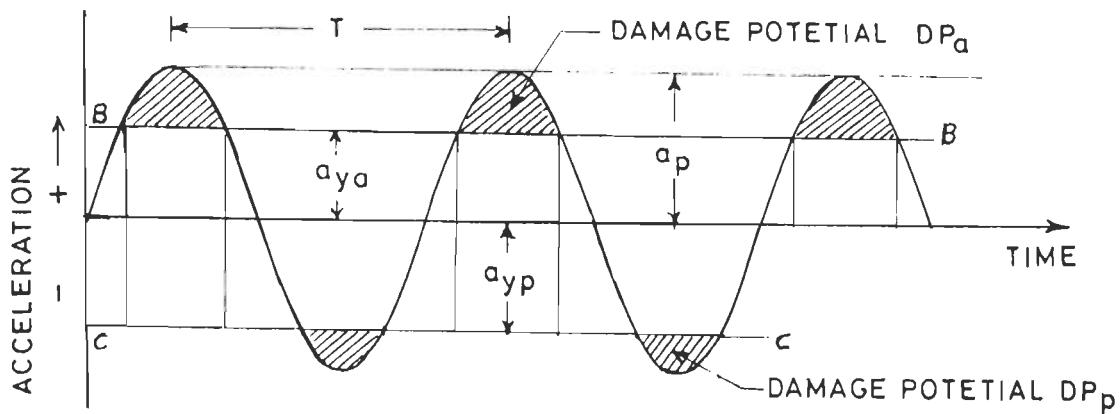


FIG. 4.5.2 ACCELERATIONS AND PHASE ANGLES ALONG THE HEIGHT OF THE EMBANKMENT.

(Table 4.3.2). Similar observation has been reported by Fairless (1989). This appears to be impossible. However, mobilization of $\mu_{avdmax} > \mu_{avsmx}$ means the dynamic disturbing force is larger than the force required for failure under static condition. Such a case does not mean a failure under dynamic condition, if failure is defined in terms of displacements. This is explained in greater detail in the next paragraph.

Figure 4.6.40 shows sinusoidal acceleration experienced by the embankment. Yield acceleration, a_{ya} , is acceleration causing plastic or yield displacement of reinforcement in active direction or direction away from embankment. Negative yield acceleration, a_{yp} , is defined similarly for yield displacements in passive direction or direction towards embankment. Normally, $a_{yp} > a_{ya}$. Active yield displacements occur only when embankment acceleration is greater than a_{ya} . Area of positive lobe of acceleration beyond line BB (defined by a_{ya} and shown as hatched area in Fig. 4.6.40) is the damage potential, DP_a , having units of velocity. Double integration of positive lobe of acceleration beyond line BB in time domain gives plastic displacement, d_{pa} , of embankment in active direction as a function of time for that acceleration lobe. Similarly, when negative lobe of embankment acceleration exceeds line CC (defined by a_{yp} and shown as hatched area), plastic displacement, d_{pp} , occurs in negative or passive direction due to damage potential, DP_p , for that acceleration lobe.

Each complete acceleration cycle causes net plastic embankment displacement ($d_{pa} - d_{pp}$). Magnitudes of DP_a and d_{pa} increase with peak acceleration, a_p , and period of vibration, T . Higher frequencies lead to smaller displacements per cycle due to short time duration for which forces generated by acceleration act.

Figures 4.6.38 and 4.6.39 show that $\mu_{avd_{mx}} > \mu_{av_{smx}}$ only for a short range of r_f near resonance. For rest of the range of r_f , $\mu_{avd_{mx}} < \mu_{av_{smx}}$. Seismic vibrations have many frequencies. Hence, resonance during earthquakes is rare and does not last long. Hence, reinforcements of embankments are unlikely to experience many acceleration pulses at resonant frequency. A few acceleration pulses at resonant frequency, if any, may not necessarily cause failure in view of short durations of acceleration pulses. This explains why test embankments in this study withstood very high accelerations without experiencing large displacement constituting failure.

If yield acceleration concept proposed by Newmark (1965) were used to compute dynamic pullout displacements, then, a more realistic pullout resistance coefficient closer to μ_{avs} would be used which in turn is based on $\tan\phi$ of soil which is frequency independent. As such, μ_{avd} is purely a number and not a physical quantity such that $\mu_{avs} \leq \mu_{avd}$.

Figures 4.6.41 to Fig. 4.6.43 show $\mu_{avd_{mx}} - \gamma_{avd_{mx}}$ relationship for different OME values for M1, M2 and M3. Since stiffer M1 does not get significantly deformed by forces generated at different OME adopted, curves are closely spaced. Initially for low values of $\gamma_{avd_{mx}}$, $\mu_{avd_{mx}}$ increases slowly till slackness in fabric is overcome. As $\gamma_{avd_{mx}}$ further increase, $\mu_{avd_{mx}}$ increases sharply to reach another threshold beyond which it increase with flatter gradient upto resonance. This may be approximated to be trilinear. The largest $\mu_{avd_{mx}}$ for each curve corresponds to resonant frequency at that excitation. For M1 at $\gamma_{avd_{mx}} = 10^{-3}$, slackness is overcome and $\mu_{avd_{mx}}$ is almost strain-independent for $\gamma_{avd_{mx}} \leq 10^{-3}$. For M2 also similar observations may be made. However for weak M3, $\mu_{avd_{mx}} - \gamma_{avd_{mx}}$ plots are

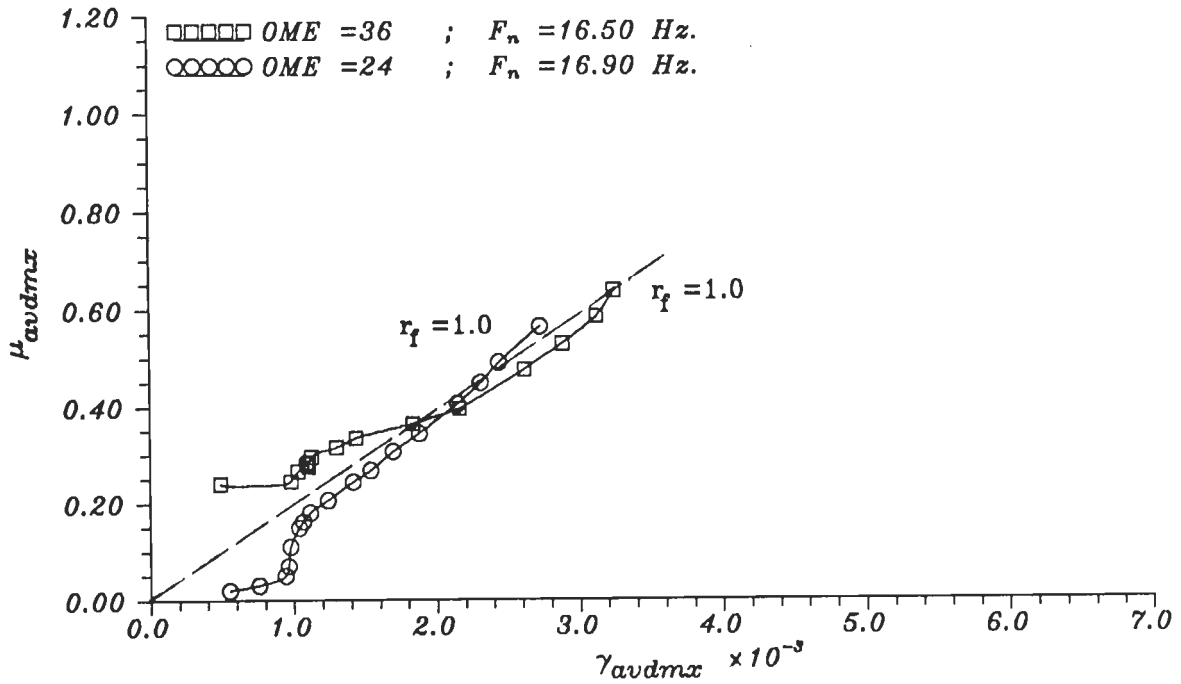


FIG.4.6.41 VARIATION OF MAXIMUM AVERAGE COEFFICIENT OF DYNAMIC PULLOUT RESISTANCE, μ_{avdmax} , WITH MAXIMUM SHEAR STRAIN, γ_{avdmax} , FOR R.E. TEST EMBANKMENT, M1.

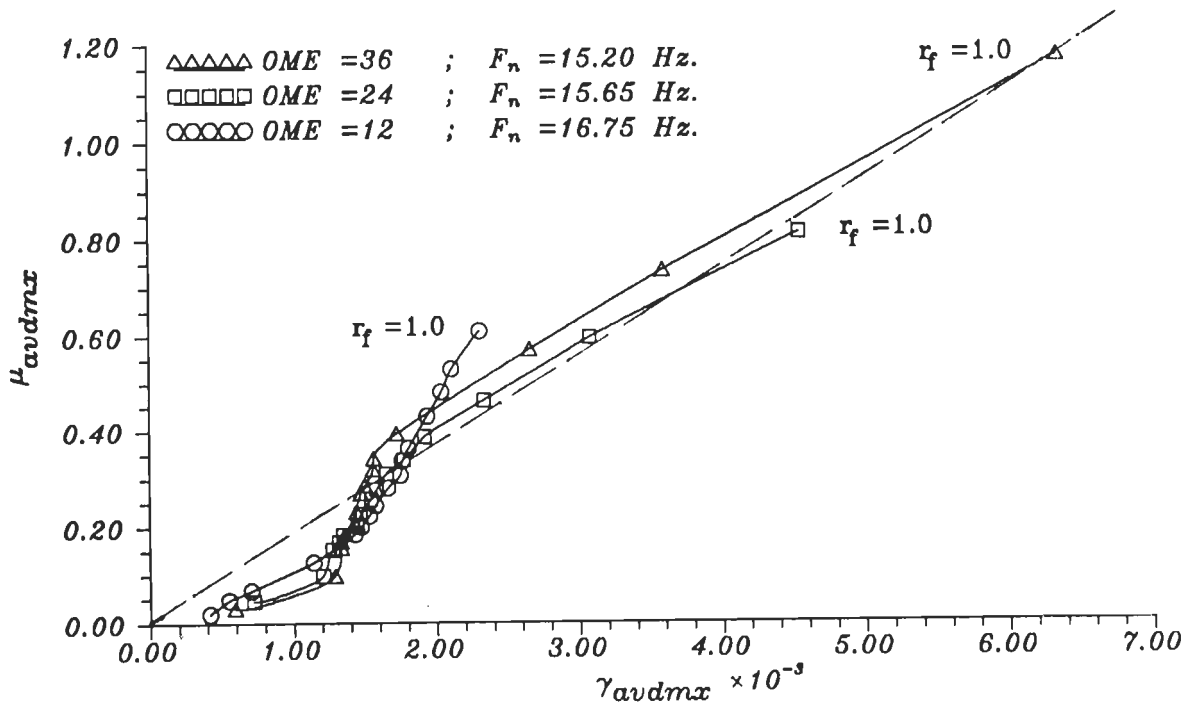


FIG.4.6.42 VARIATION OF MAXIMUM AVERAGE COEFFICIENT OF DYNAMIC PULLOUT RESISTANCE, μ_{avdmax} , WITH MAXIMUM SHEAR STRAIN, γ_{avdmax} , FOR R.E. TEST EMBANKMENT, M2.

distinctly apart at different OME as expected. For all embankments, μ_{avdmx} at resonance at any OME is higher than that for any higher OME for same strain level due to easy build up of very large response at resonance.

Reinforcing action is not significant at low strains for which μ_{avdmx} is not of practical interest. For higher strains, μ_{avdmx} plots for different OME tend to get closer and reach a stable slope with a much larger range of γ_{avdmx} . In this range of γ_{avdmx} , reinforcements contribute resisting forces significantly which is very desirable. It would be highly uneconomical to adopt much smaller limiting strains. If 10% discrepancy in μ_{avdmx} is tolerable, then μ_{avdmx} may be considered to be independent of OME values for $\gamma_{avdmx} \geq 1.75 \times 10^{-3}$, 2×10^{-3} and 5×10^{-3} for M1, M2 and M3 respectively. Infact, for each embankment a (dashed) straight line passing

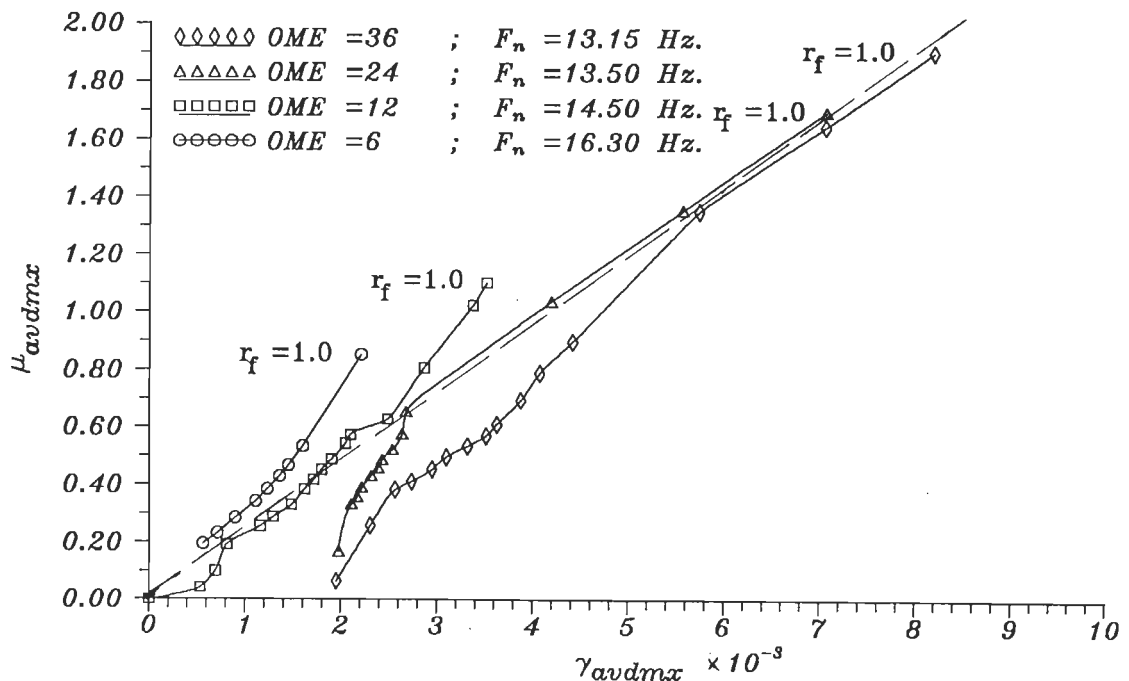


FIG.4.6.43 VARIATION OF MAXIMUM AVERAGE COEFFICIENT OF DYNAMIC PULLOUT RESISTANCE, μ_{avdmx} , WITH MAXIMUM SHEAR STRAIN, γ_{avdmx} , FOR R.E. TEST EMBANKMENT, M3.

through the origin may be drawn to represent average $\mu_{avdmx} - \gamma_{avdmx}$ plots for higher strains of practical interest (Fig. 4.6.41 to 4.6.43). When slackness of reinforcement is overcome, rate of build up of μ_{avdmx} with strains is faster, because, ϕ is mobilized faster at initial low strains.

Coefficients of average dynamic pullout resistance mobilized at various reinforcements for the 3 test embankments are worked out on lines explained in Article 4.5.5 earlier. Figure 4.6.44 shows these coefficients (μ_{avdi} for i'th reinforcement) as functions of dimensionless depth for different OME values. As OME increases, μ_{avdi} increases for all reinforcements and for M2 and M3. This is expected, because, disturbing force at these reinforcements increases with increasing OME. This observation is true for M1 below dimensionless depth of 0.4. In the remaining small portion near top, the trend reverses slightly and curves are very close to each other. The curves for M1 and M2 for different OME are closely spaced, because, M1 and M2 are stronger and experience smaller displacement variations. On the other hand, μ_{avdi} for the weak M3 shows greater variations at different OME values because of wider variations of displacements generated by these OME values.

Curves for M1 and M2 at different OME are close to each other in view of continuous reinforcements in top 4 layers. Reinforcements are discontinuous in 5'th and 6'th layer for M2 resulting into larger displacements at these reinforcements compared to those of M1. This leads to increased μ_{avdi} mobilisation for these reinforcements for M2 as shown in figure which is expected. With increasing dimensionless depth from top, μ_{avdi} reduces due to acceleration reduction upto 4'th reinforcement. For 5'th reinforcement,

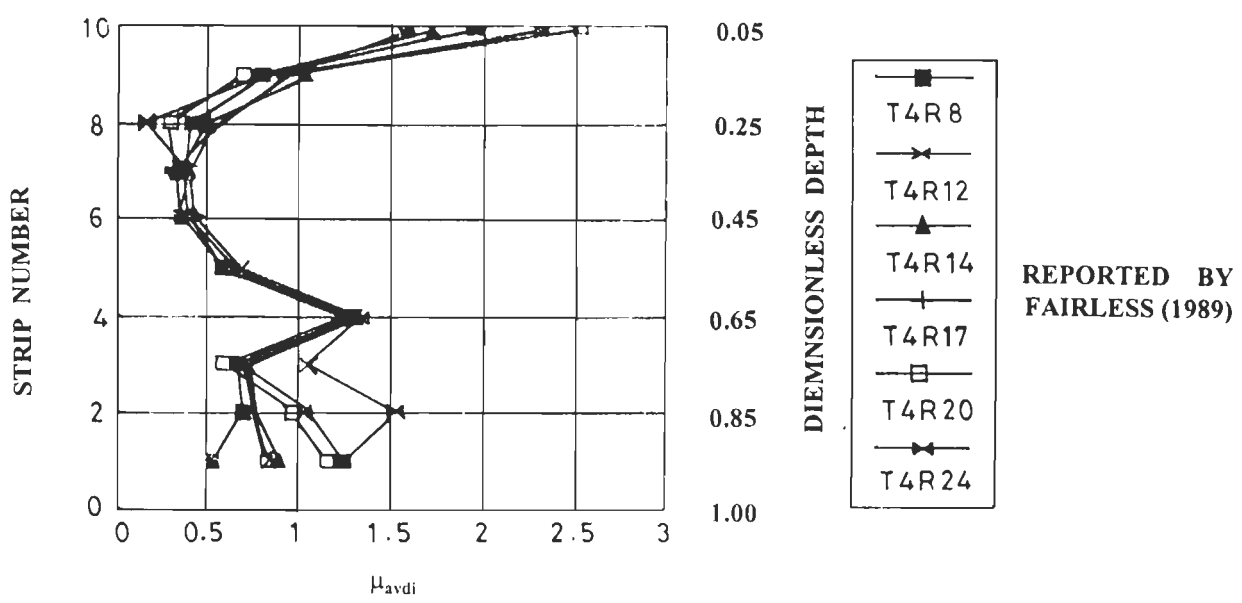
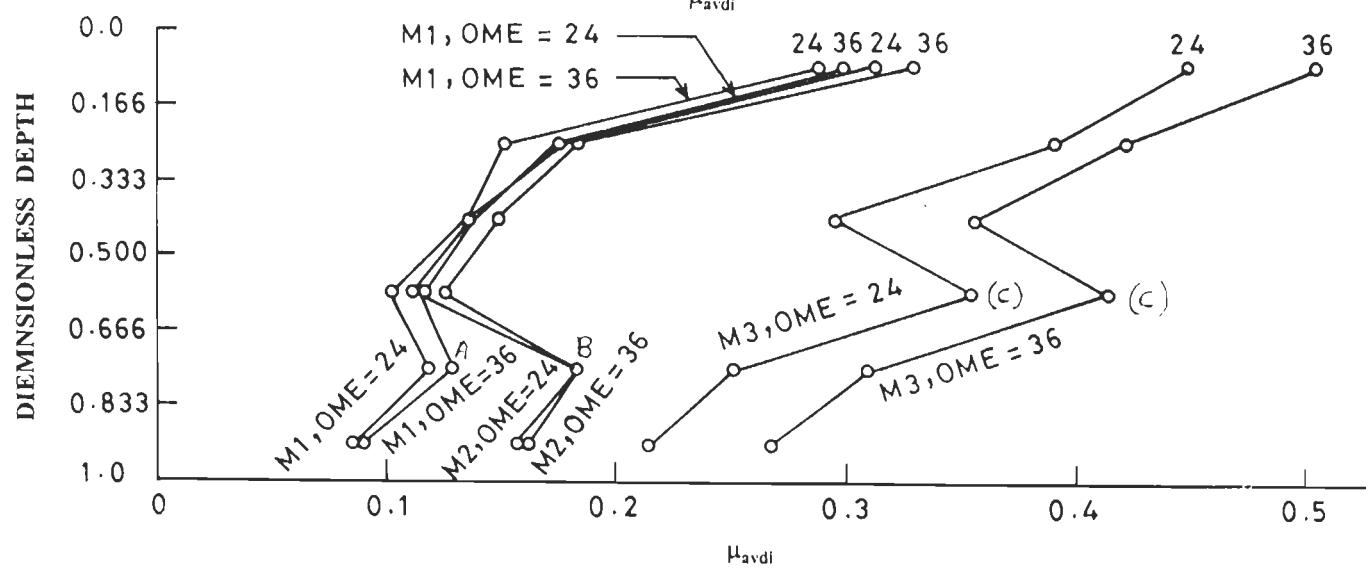
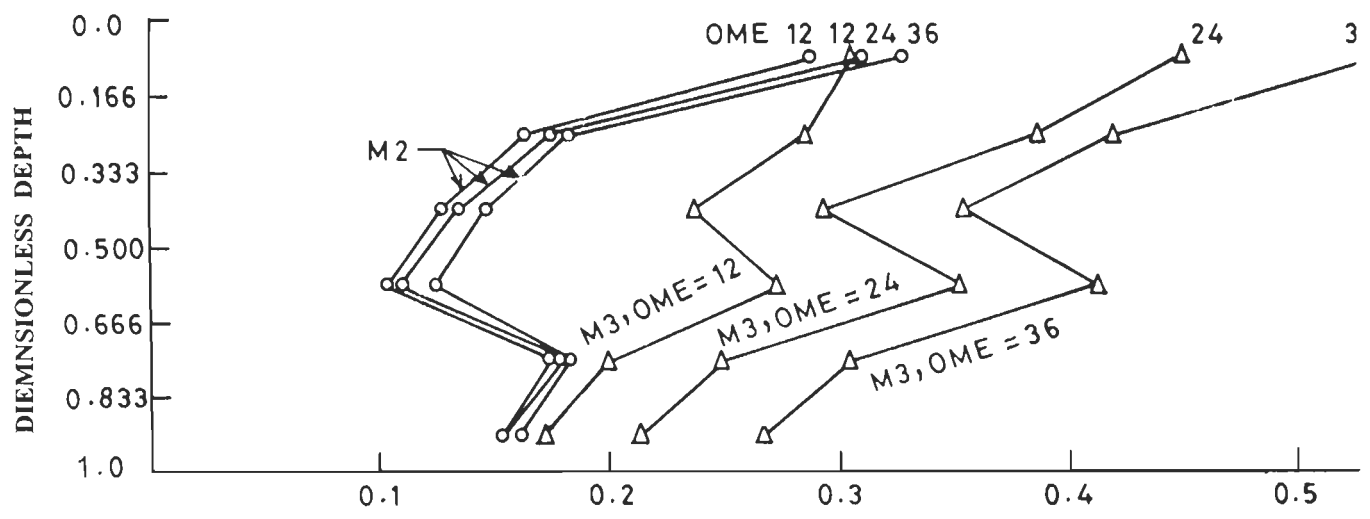


FIG. 4.6.44 VARIATION OF COEFFICIENT OF AVERAGE DYNAMIC PULLOUT RESISTANCE, μ_{avdi} , FOR R.E. TEST EMBANKMENT, WITH DIMENSIONLESS DEPTH (X/H).

μ_{avdi} increases due to increase in disturbing earth pressures though disturbing inertia reduces due to reduced acceleration. For the lowest reinforcement, μ_{avdi} reduces w.r.t. μ_{avdi} for 5'th reinforcement because of further reduction in acceleration and reduced displacements due to embankment being hinged at base (Fig. 4.6.44). For increasing distance from top for M3, μ_{avdi} decreases upto 3'rd reinforcement and then increases for the 4'th reinforcement (C) and then onwards again decreases. Point C of M3 is situated higher than the corresponding point B of M2 and A of M1. This is because of M3 being weaker and the discontinuous fourth reinforcement of embankment M3 suffers greater outward displacement and hence, mobilizes larger μ_{avdi} when compared with that for M1 and M2, which is reasonable.

Figure 4.6.44 shows μ_{avdi} -dimensionless depth relations obtained from tests by Fairless (1989) which are similar to those obtained from this investigation. Near top end μ_{avdi} is large. With increasing depth, it decreases, reaches its minimum and then increases to reach a peak and then again reduces towards base. Fairless obtained μ_{avdi} are based on measured tie forces whereas those of this investigation are based on measured accelerations. This indicates that the mechanics of back-analyses presented in this Chapter is reasonable.

4.6.9 Lateral Displacements of Longitudinal Faces

On exciting R.E. embankment of height H, its vertical longitudinal faces experience outward movements. These movements along the height of M2 and M3 (Fig. 4.6.45) are stepped in nature at junctions between adjacent facing elements where elements are free to move laterally. It may be observed from Fig.4.6.45 that the bottom hinge of lowest facing element

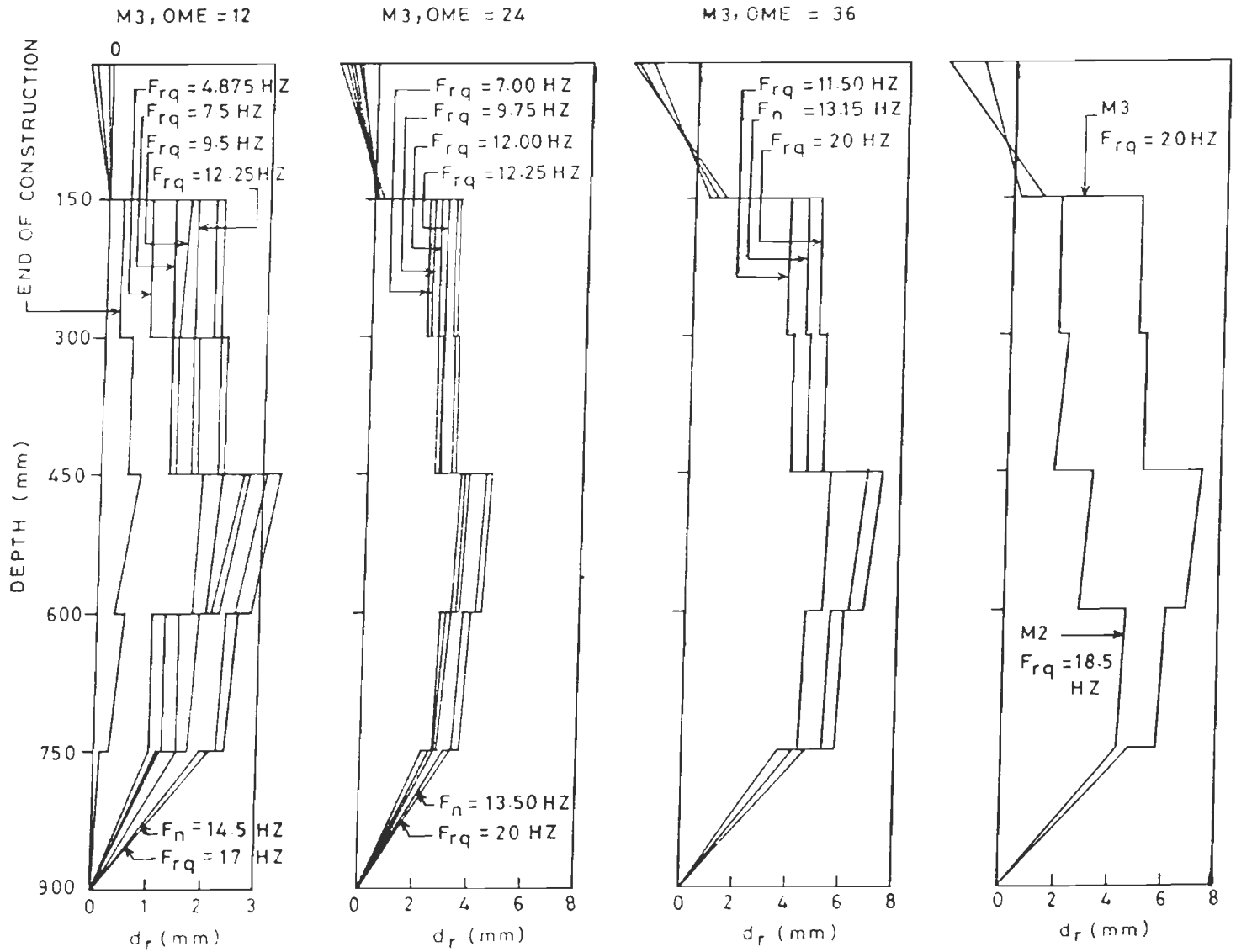


FIG. 4.6.45 RESIDUAL DISPLACEMENT OF R.E. EMBANKMENTS M3 AND M2 AT END OF TESTS AT DIFFERENT EXCITATION FREQUENCIES.

performed well in allowing rotational displacements. For M3, the maximum displacement is 0.78333% of H which is more than 0.5% H movement required to mobilise active state of earth pressures. (Ishii, et.al., 1960 and Sarma-Thakur, 1984). In spite of reaching active state, embankment did not fail catastrophically. This highlights the advantage of using R.E..

The top facing at its mid-depth moved inward approximately by 1 mm and experienced rotational movement. This is expected as earth pressure on its lower half is much larger than that on its upper half. Mobilisation of pullout resistance for top reinforcement is low due to low normal stress. Hence, residual earth pressures are more prominent than inertia forces. Continuous top reinforcement partly transfers inertia and earth pressures acting on connected facing element to the element on opposite end which resists transferred forces by developing passive earth resistance. This results into small displacement of top facing element. Hence, continuous reinforcements inter-connecting upper end facing elements are effective in restricting their outward movements. Embankments without such continuous reinforcements near top end is expected to experience large displacements.

Facing elements standing vertically when form work is in position at the end of construction, experience some outward movement (Fig. 4.6.45) on removing the form work. The largest outward movement of 0.62 mm occurred at 4'th facing element from top end which is much less than 0.5% of H needed to realise active earth pressures. Therefore, the embankment experiences at rest earth pressures at the end of construction. However, embankment experienced outward movement some what more than $(0.5\% H)/10$ for 20% of H and outward movement was less than $(0.5\% H)/10$ for remaining 80% of H. For

M2 and M3, outward movements increase with depth from top end and reach their maximum at 4'th facing element for all tests. Due to rigidity of the shake table steel platform and the hinge, the displacement decreases towards the base below the 4th facing element, which is expected.

Movements of all facing elements increase with increasing OME of base excitation, because, forces generated by excitation increase with increasing OME values. For OME=36, movement for M2 is less than that at corresponding element for weaker M3 which is expected.

Design engineers are interested in earth pressures acting at the end of dynamic tests which is sum of earth pressure mobilized for displacement experienced by facing element at that location and the additional confining pressure caused by reinforcing action there. Earth pressures are dependent on displacements (Lamb and Whitman, 1969 ; Joshi and Sarma-Thakur, 1984). Mobilized earth pressure coefficients and corresponding earth pressures may be obtained using properties of fill and displacement of facing element.

Table 4.6.11 shows displacements of various facing elements at their mid-depths at the end of tests for M2 and M3. It also shows displacement, Δ_a , required at each reinforcement to reach active state of earth pressure assuming a displacement of 0.5% of the depth of that reinforcement below the embankment top. If displacement of facing element is zero, coefficient of at rest earth pressure, $K_0=(1-\sin\phi)$, is assumed (Jaky, 1944). If outward displacement is larger than or equal to Δ_a , Rankine coefficient of active earth pressure, K_a , is assumed. If outward displacement of facing element is greater than zero but less than Δ_a , the mobilized coefficient of active earth pressure is obtained by bilinear interpolation curve (Fig. 4.6.46a).

TABLE 4.6.11 Displacements and Corresponding Coefficient of Earth Pressures at End of Shake Table Tests.

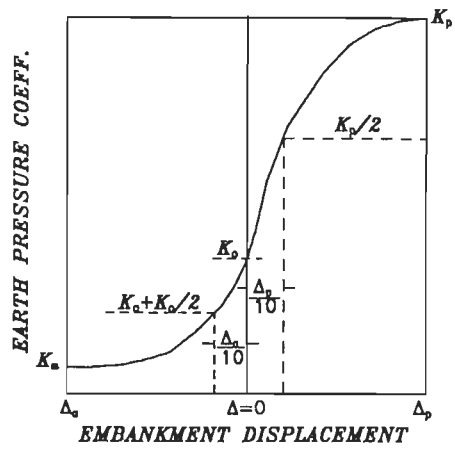
Panel no.	Depth H_i (m)	Δ_a 0.5% of H_i (mm) or Δ_p 0.5% of H_i (mm)	$\Delta_a/10$ or $\Delta_p/10$ (mm)	Embankment M2		Embankment M3	
				Absolute displacement (mm)	Coefficient of earth pressure	Absolute displacement (mm)	Coeff. of earth pressure
1	0.075	-3.750	-0.3750	-0.5	$K_{pm} = 1.61712$	-0.9	$K_{pm} = 1.74364$
2	0.225	1.125	0.1125	1.8	$K_a = 0.17636$	4.8	$K_a = 0.17636$
3	0.375	1.875	0.1875	2.0	$K_a = 0.17636$	5.1	$K_a = 0.17636$
4	0.525	2.625	0.2625	3.0	$K_a = 0.17636$	7.0	$K_a = 0.17636$
5	0.675	3.375	0.3375	4.4	$K_a = 0.17636$	5.8	$K_a = 0.17636$
6	0.825	4.125	0.4125	2.0	$K_{am} = 0.13200$	2.3	$K_{am} = 0.23835$

- Note:
- Δ_a = Displacement require for reaching active state.
 - Δ_p = Displacement require for reaching passive state.
 - K_a = Coefficient of active earth pressure.
 - K_{am} = Coefficient of mobilised earth pressure.
 - K_o = Coefficient of at rest earth pressure.
 - K_p = Coefficient of passive earth pressure.
 - K_{pm} = Coefficient of mobilised passive earth pressure.

If movement is inward (towards the fill), passive pressures will be mobilized behind facing elements. If such displacement is greater than zero but less than the displacement for reaching passive state, Δ_p , (equal to 5% of depth of reinforcement from top) then the mobilized passive coefficient of earth pressure, K_{pm} , is also obtained by using bilinear interpolation (Fig. 4.6.46a). Table 4.6.11 shows mobilized earth pressure coefficients based on displacements at various reinforcement.

Outward displacements of facing elements cause tensile strains for continuous reinforcements and pullout strains for discontinuous ones. Tensile or pullout force (as the case may be) generate different confining pressures on embankment in different layers which may be obtained knowing tension per unit width-tensile strain relationship of the reinforcement, or, pullout resistance Versus pullout strain relationship for reinforcement obtained from tests. These incremental pressures are added to earth pressures cited above to obtain the net earth pressures at the end of test.

Distribution of net confining earth pressure along depth at the end of tests is shown in Fig. 4.6.46b for M2 and M3. Increase in net confining pressure is very large compared to active/at rest pressures upto 4'th reinforcement from top for M2, because, top 4 reinforcements are continuous. Largest net pressure occurs at 4'th reinforcement, because, tension in it generated by displacement at that location is very large compared to earth pressures for that location. For the 5'th reinforcement, net confining pressure falls drastically to values close to active earth pressures. This is due to mobilized pullout resistance in the reinforcement which is much smaller than mobilized tension in 4'th reinforcement. This shows high confining pressures obtainable for continuous reinforcements.



(a)

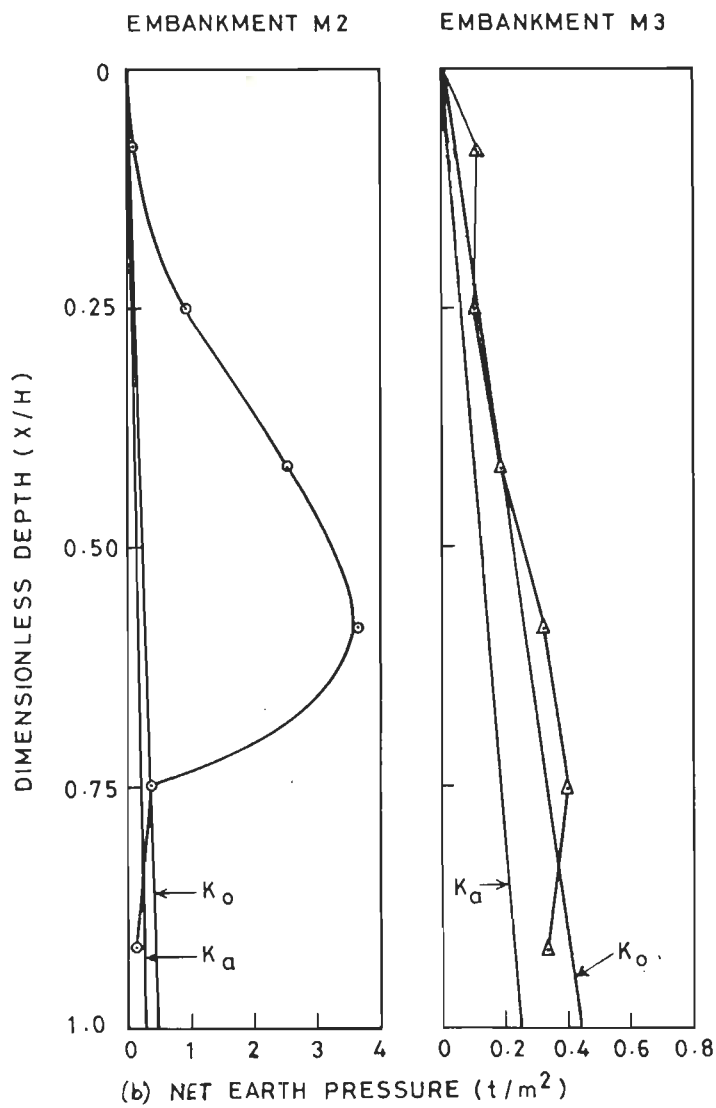
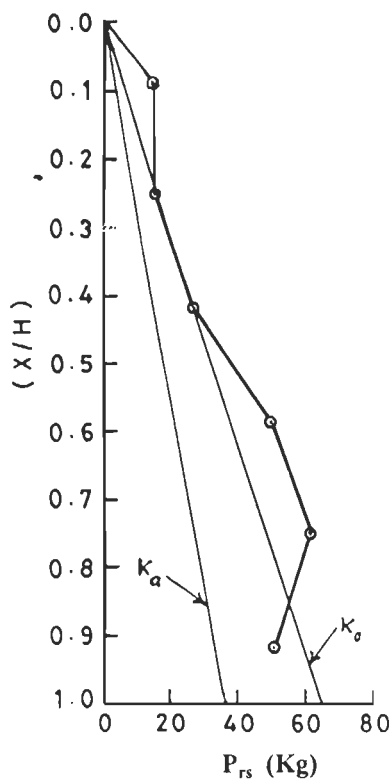


FIG. 4.6.46 NET CONFINING PRESSURE DISTRIBUTION ALONG THE DIMENSIONLESS DEPTH FOR EMBANKMENTS M2 AND M3.

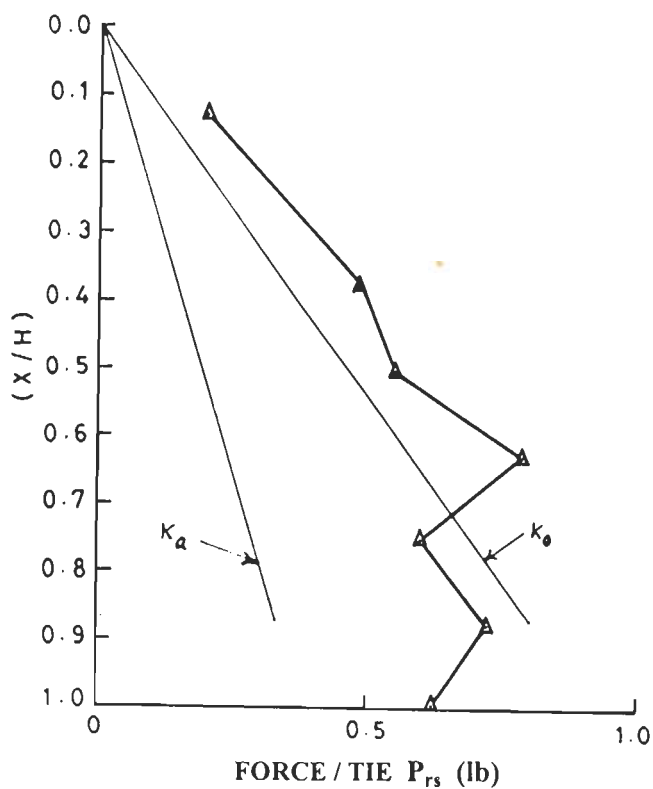
Figure 4.6.46b also shows variation of net confining pressure along depth at the end of tests for M3. Net confining pressure increases with depth to reach its maximum at 5'th reinforcement and then reduces somewhat at 6'th reinforcement. Near the top end, net confining pressure initially increases quickly and then more gradually further below. This is due to inward movement of upper half of top facing element due to rotation of element which tends to mobilize earth pressures larger than active/at rest pressures. Net confining pressures for M3 are much smaller than corresponding values for M2. This is so, because, all reinforcements except the top one are discontinuous for M3. Besides, the mobilized pullout resistance in M3 is much smaller than mobilized tension in the corresponding reinforcement in M2 for the same outward movement.

Therefore, use of continuous reinforcements capable of withstanding tensile forces with adequate safety margin are more effective than use of discontinuous reinforcements performing under pullout resistance only.

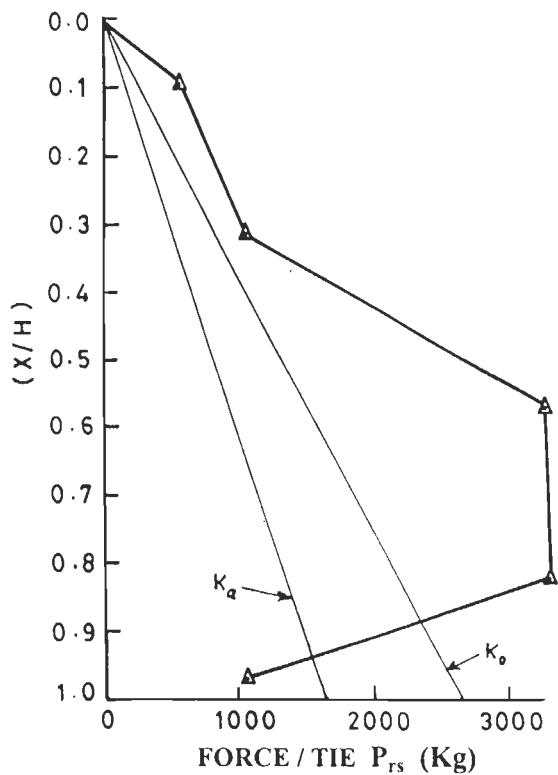
Figure 4.6.47 shows variation of residual force obtained from net confining pressures cited above at the end of dynamic test for M3. It is similar to variation of net confining pressure for M3 (Fig. 4.6.46b) as expected. It is also similar to variation of residual earth forces in strip reinforcements reported by Richardson and Lee (1975), Richardson et.al. (1977) and by Fairless (1989) (Fig. 4.6.47). It is, again, similar to variation pattern obtained from field data for 15 m high R.E. embankment (Richardson and Lee, 1975). Near the top end, earth force obtained from this investigation initially increases quickly and then more gradually further below for reasons cited earlier in this article. This is supported by similar observation from Fig. 4.6.47 c and d.



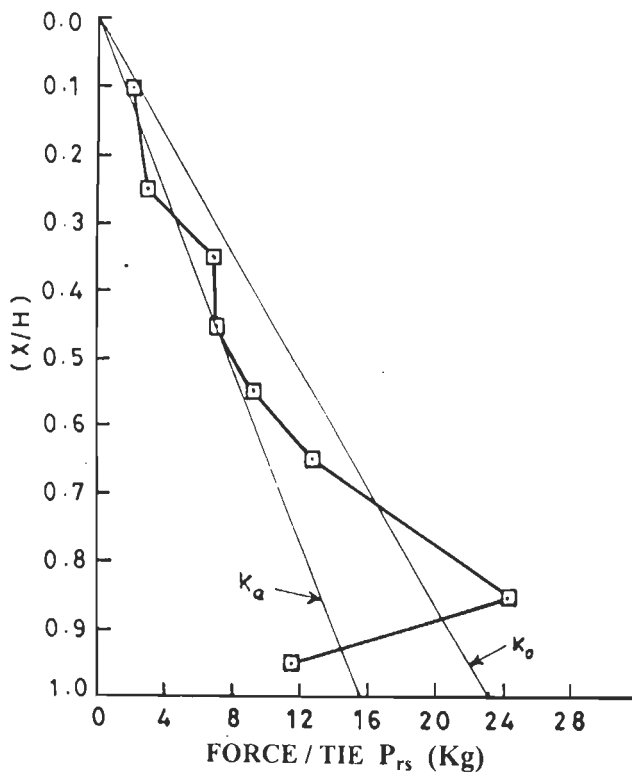
(a) PRESENT INVESTIGATION



(b) RICHARDSON AND LEE (1975)



(c) RICHARDSON ET. AL. (1977)



(d) FAIRLESS (1989)

FIG. 4.6.47 RESIDUAL FORCE, P_{rs} , IN REINFORCEMENT WITH DIMENSIONLESS DEPTH (X/H) AT THE END OF DYNAMIC TEST ON M3 AND P_{rs} PER REINFORCEMENT REPORTED BY OTHER INVESTIGATORS.

In all these cases, residual forces, P_{rs} , larger than earth forces developed due to at rest condition have been mobilized. This is so, because, residual forces comprise of earth forces and forces due to mobilization of additional confining pressures due to reinforcing action. For M3, additional confining pressures are smaller. Hence, mobilization of P_{rs} in excess of earth forces is not significant and is observed for a limited depth. Breakup of residual forces into mobilized earth pressures and mobilized additional confining pressures has not been given by other investigators. Nevertheless, outward displacements of the order of 2%, 0.9% and 1.7% reported for their investigations indicate that fairly large additional confining pressures may have been mobilized as is indicated by the figure. More precise analysis of their test data on lines cited above is not possible due to lack of appropriate data for this purpose.

From above discussions, it may be concluded that computing residual forces based on net confining pressures (comprising of mobilized earth forces and mobilized additional confining pressures due to reinforcing action) using the methodology proposed in this chapter is reasonable.

4.6.10 Settlements

Cohesionless soils tend to get compacted when vibrated. As such, embankment settlements occurred which were measured along three lines obtained by joining mid-point and quarter points of top edge of top facing element on one side to corresponding points on facing element on the other side. Since settlements along these lines were almost identical (maximum difference being only 4.5% from mean value) only average of the three settlements at a given distance from a facing element have been presented.

This indicated that embankment showed almost identical behaviour at all points in a given horizontal level, which is desirable and that the embankment behaved under plain strain condition.

Figure 4.6.48 shows average settlements of the top of M2 and M3 in the middle transverse vertical plane. Settlements are 2.15% of H for M2 and 2.46% of H for M3 which is tolerable. Besides, the settlement adjacent to top facing element is zero and increases rapidly upto a distance of 100 mm from the facing. Thereafter, it increases very gradually upto the mid span of top surface. The slope of top surface is 0.7° for M2 and 0.88° for M3 in the middle segment of the embankment A-A shown in the figure. This may be considered to be negligible for all practical purposes.

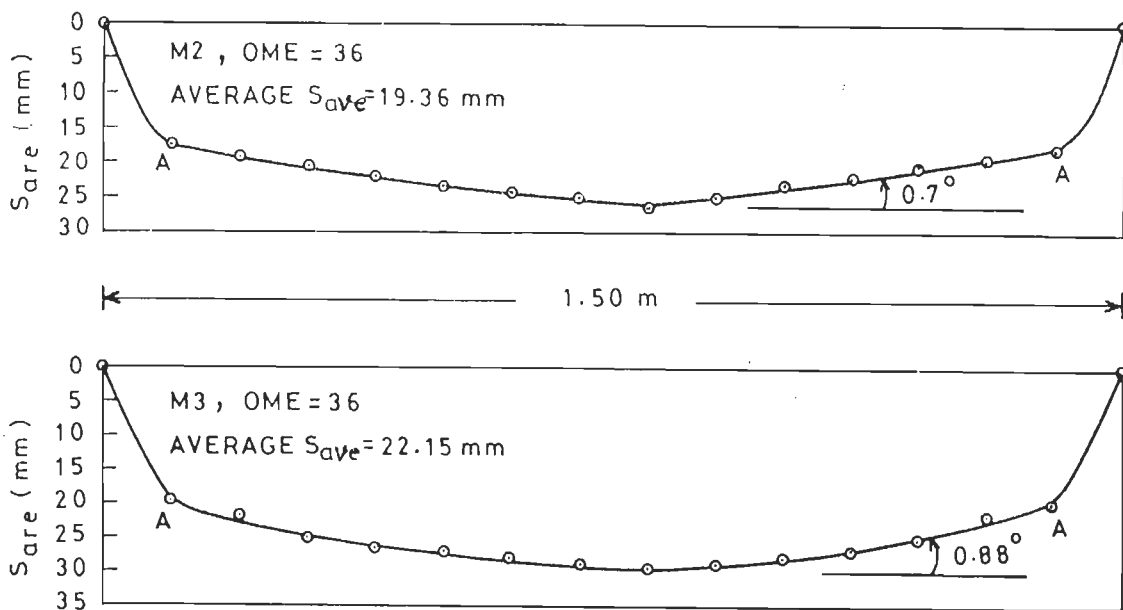


FIG. 4.6.48 AVERAGE SETTLEMENT, S_{ave} , PROFILE OF R.E. TEST EMBANKMENTS M2 AND M3 AT TOP AT END OF DYNAMIC TESTS.

Settlement was more at mid span compared to that adjacent to facing elements because of resistance to settlement offered by friction between

soil and facing elements. Shake table tests on the same Solani river plain sand with comparable relative density in a tank indicated that settlement decreases with increasing distance from inner vertical face of the tank to reach its maximum value at a distance of 100 mm (Kulshreshtha, 1991) which is identical to that observed for M3 at the end of forced vibration tests. Besides, the differential settlement between the settlement of plain sand at inner face of the tank and interior point at the top surface of soil is 8 mm per meter depth of the fill (Kulshreshtha, 1991).

For M3, continuous reinforcement in top layer, firmly connected to facing elements at their mid depth, does not allow settlement of soil adjacent to facing elements below the reinforcement. This is indicated by settlements recorded (Fig. 4.6.49). Top facing element rests firmly on the facing element immediately below. Top most reinforcement loses contact with soil immediately below, because, the soil settles down whereas the facing element and, hence, the reinforcement does not. However, this takes place upto a distance of about 100 mm only from the facing as may be observed from the figure cited above.

Reinforcement and soil come in contact with each other at A where the upward support exerted on soil by tension in reinforcement comes to an end and indicated by sharp change in gradient of settlements w.r.t. distance from facing element. The settlement very gradually increases with further increase in distance from facing element. Knowing the differential settlement per meter depth of plain sand as 8 mm, net settlement at facing works out to be 12.8 mm if no reinforcement were present (Fig. 4.6.49). Based on this, settlement per m depth works out to be 14.222 mm at the facing. As such, settlement for 75 mm soil depth work out to be 1.0666 mm.

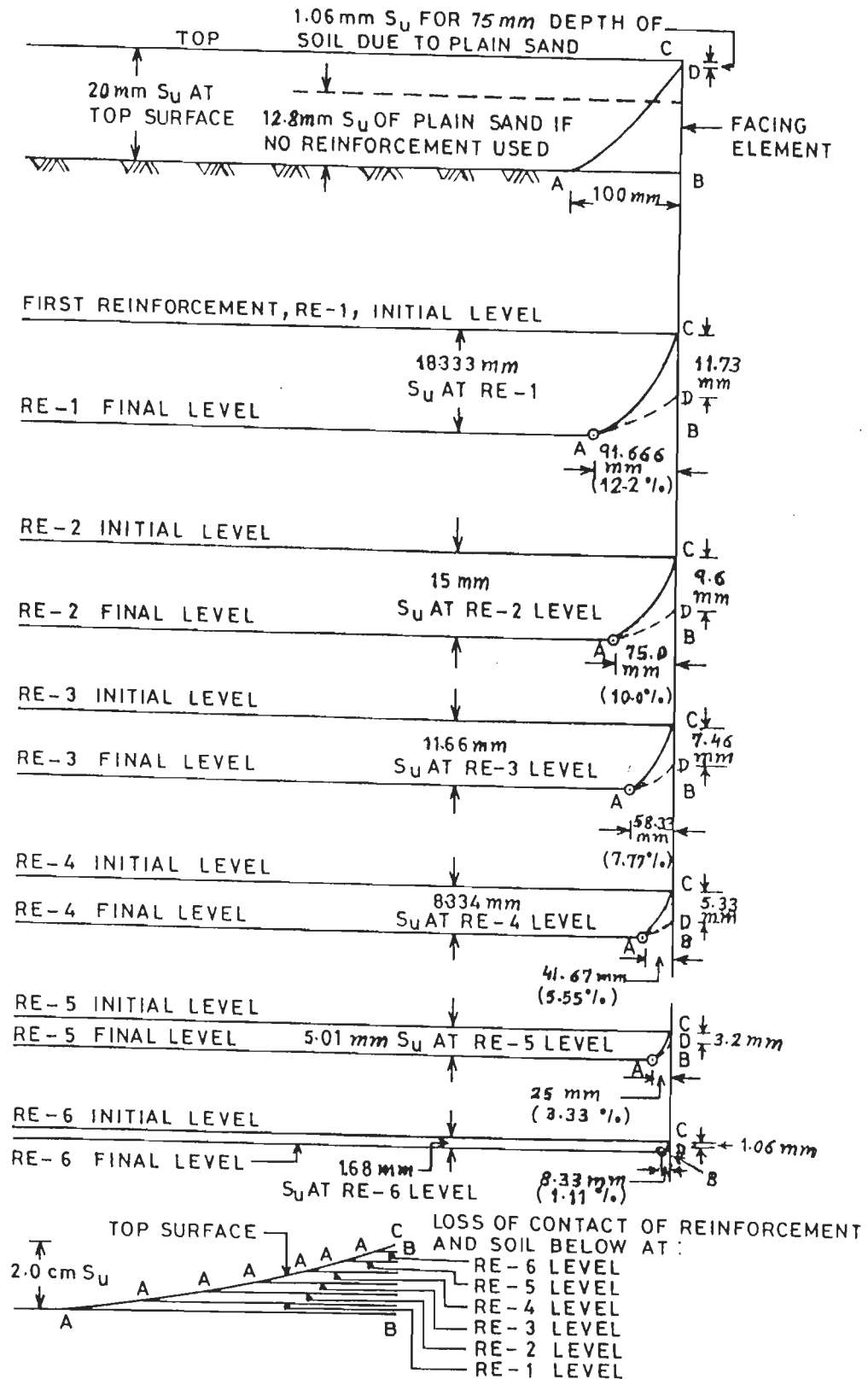


FIG. 4.6.49 MAXIMUM SETTLEMENT, S_u , AND LOSS OF CONTACT AT DIFFERENT REINFORCEMENT LEVELS OF EMBANKMENT M3.

The figure also shows settlements at the top upto a distance 100 mm from facing. Settlement of 20 mm at A leads to a settlement of 22.222 mm/m depth of soil. As such, settlements of 18.333, 15, 11.666, 8.334, 5.01 and 1.68 mm occur at first to 6th reinforcement respectively. For plain sand at the top, settlement gets almost stabilized to CB=20 mm at AB=100 mm from facing. At the first reinforcement, the settlement is CB=18.333 mm and the distance AB along which it is not in contact with soil below was 91.666 mm obtained from proportionate reduction of AB for top level. Similarly, AB for 2nd to 6th reinforcement work out to be 75, 58.33, 41.67, 25 and 8.33 mm respectively, i.e., 12.22, 10, 7.77, 5.55, 3.33 and 1.11% of half width (750 mm) of embankment. Line, AC, represents profile of reinforcement and the dotted line, AD, represents surface of soil fill not in contact with the portion of reinforcement, AC. Largest gap CD=11.73 mm occurred at the top reinforcement. Such gaps were 9.6, 7.46, 5.33, 3.2 and 1.06 mm at 2nd to 6th reinforcements respectively.

Maximum percentage length of reinforcement (w.r.t. half width of embankment) losing contact with soil below is 12.2% at the top reinforcement. The minimum is 1.11% at the bottom reinforcement. Average percentage is 6.66% only and, as such, neglected in all back-analyses carried out in this investigation.

Loss of contact of reinforcement with soil below near the facing occurs when facing elements are rigid and fill settles due to base excitations. This was so for tests carried out by Richardson and Lee (1975) and by Fairless (1989) who reported settlements similar to those obtained in this investigations. However, they did not analyse settlements on lines

cited above. Above discussion highlights need to device suitable facing elements which allow free field settlements near facing elements also.

Figure 4.6.50 shows shape of the reinforcement connected to top most facing element after the settlement. For static case, over turning moment, m_o , about mid point of facing element is generated by earth force P_1 acting on upper half of facing element and P_2 on lower half. This is balanced by equal and opposite moment due to tension in reinforcement, T_2 , with lever arm equal to differential settlement, s_{er} , between outer end of reinforcement and mid point of embankment width. This counter-balancing

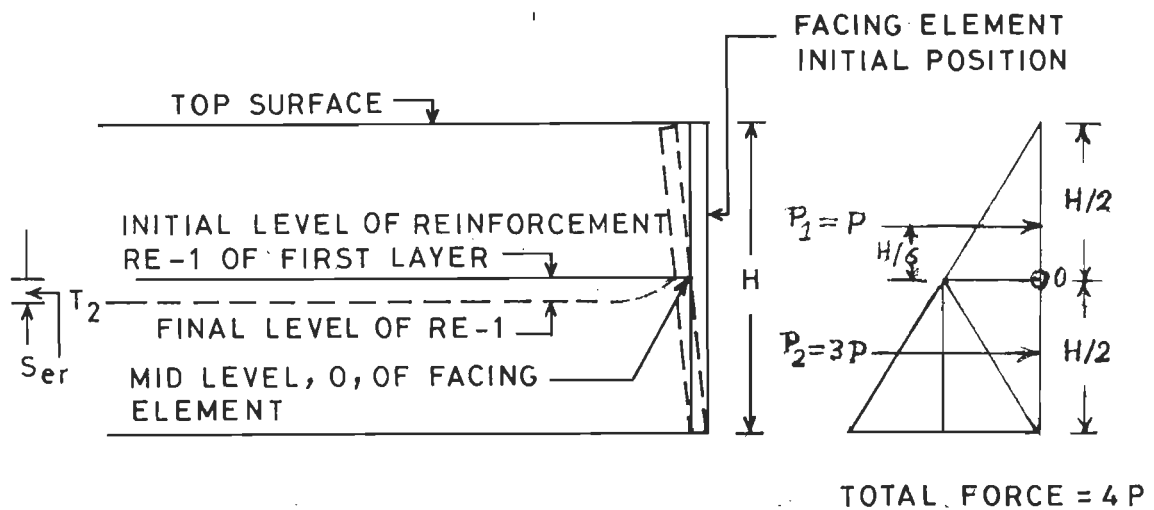


FIG. 4.6.50 MECHANICS OF FORCES GENERATED DUE TO SETTLEMENT AND EARTH PRESSURE.

moment increases with increasing s_{er} . For case with no settlement, the rotational movement of top facing element will be such that the mobilized earth force on the upper half of element and moment generated by it are counter-balanced by force mobilized on lower half of top element and the moment generated by it. In case some portion of reinforcement loses contact

with soil, its pullout resistance gets suitably reduced. This increases lateral displacement of facing element which in turn suitably reduces earth forces to be equal and opposite to this reduced pullout force.

For top facing element, similar overturning moments due to dynamic earth forces acting on facing elements are larger than those for static case. This induces larger tension and correspondingly larger counterbalancing moments. Any loss of contact of reinforcement with soil and resulting reduced pullout resistance suitably increase lateral movements which suitably reduces dynamic earth forces to maintain equilibrium.

Compared to continuous reinforcements, tension in discontinuous ones gets modified in light of pullout resistance mobilised. Extent of loss contact of discontinuous reinforcement with soil depends on length of reinforcement. Discontinuous reinforcement is relatively more free to move laterally to a larger extent to reduce lateral earth forces suitably to match the reduced pullout resistance due to loss of contact.

4.7 Closure

Time dependent pullout displacement can not be studied using strain control setup. To overcome the problem, stress control setup was developed which is superior to strain control setup. Technique developed for creating plane strain conditions is an important experimental research contribution. Based on studies presented in this chapter, following conclusions are drawn.

Conclusions based on pullout test results

Relationship between coefficient of static pullout resistance (defined as ratio of pullout stress to normal stress), μ_{avs} , with pullout strain, ϵ_p ,

at different normal stresses is represented by a single best fit curve. Woven geotextiles are better reinforcements than nowoven type as they provide more pullout resistance at a given ϵ_p . Besides, scatter in results obtained for woven geotextile is lesser. With increasing width of reinforcement, μ_{avs} increases nonlinearly and gets stabilised at critical width of 290 mm. For smaller widths (upto 200 mm) the increase is rapid. Testing specimen with small widths (less than 200 mm) leads to appreciable error in pullout resistance and, hence, should be avoided. Critical width of specimen may be obtained by determining μ_{avs} by testing specimens of various widths. Only μ_{avs} for specimen wider than or equal to critical width is useful for designed purposes. Correlation factor, C_μ , has been proposed based on test results to obtain μ_{avs} under field conditions.

Time to reach maximum pullout displacement, d_p , increases nonlinearly with increasing ratio of pullout force, P_r , to reach its maximum value at $P_r=1$ when pullout force equals the ultimate pullout force. With increasing time, d_p increases to reach its maximum after a while and not immediately. Soil settlements in pullout tests were small and decreased with increasing relative density. Normal stresses equal to that of height of embankment is recommended for pullout tests to obtain good design data.

Pullout stress, τ_p , is zero at free edges of test specimens and its variation along length should begin with a near vertical tangent and end with a horizontal tangent at pulling end. Elliptical variation satisfies this requirement and, hence, recommended for back-analysis of test data.

Concentrated pullout force on gripping device is transferred to fabric. It is assumed to varies parabolically along width with its maximum at mid-

width (if mobilized strength is less than yield strength). If it exceeds yield strength, yield strength mobilization spreads along width towards both ends to provide resistance equal to applied pullout force.

Variation of dimensionless width, B_{rd} , defined as (B_{ry}/B_r) , B_r being width and B_{ry} being yield width of reinforcement, at various D_r , σ_v and B_r was studied. With decreasing D_r , B_{rd} increases and is nearly independent of σ_v for a given D_r (with errors $< 10\%$). With increasing B_r , B_{rd} increases for range of B_r tested. However, at B_r equal to critical width, B_{cr} , B_{rd} reaches its maximum. Widths smaller than B_{cr} lead to under utilization of strength of fabric though fabric may be capable of mobilising higher pullout resistance for a given D_r and σ_v . Therefore, test specimens wider than or equal to B_{cr} should be used.

Conclusions based on results of shake table tests and back-analyses

For back-analyses of shake table test results on R.E. embankments, software 'DYMU' was developed to evaluate dynamic parameters and correlate them. Embankments were designed to be shear beams with slenderness ratio less than five in excitation direction.

Techniques developed for creating plane strain conditions in transverse planes of embankment and for providing mechanical hinges at base of embankment worked satisfactorily. These are important experimental research contributions for static and dynamic studies.

Analysis results of free vibration tests (using sledge hammer) on R.E. embankments treated as homogeneous indicate that stiffer embankment show

smaller shear strain of 1.325×10^{-4} compared to larger strain of 3.225×10^{-4} for weaker one. The opposite is true for shear moduli and velocity of shear waves for embankments.

Similar are observations for shear strains, shear moduli and shear wave velocities obtained from forced vibration tests on M1, M2 and M3. With increasing excitation frequency, F_{rq} , acceleration initially increases slowly at low F_{rq} and then rapidly to reach a peak at resonant frequency, F_n , and then fall sharply. Sudden acceleration fall immediately after crossing F_n is due to larger reinforcing action which overcomes inertia.

R.E. embankments with base excitations amplitude from 0.0061 to 0.319 g experienced very high peak accelerations from 1.0875 to 2.577 g which were withstood with insignificant permanent deformation and damage. Hence, R.E. embankments show a predominantly elastic dynamic behaviour.

Plots $\gamma_{rn} - r_e$ are linear for R.E. embankments. Even at resonance, R.E. embankments exhibited elastic behaviour over a wide range of stresses, strains and accelerations, which is important.

Embankment softness and magnification factor, M_f , increase together. Increase in peak M_f with increasing embankment softness is expected. Effect of F_n on M_f is high at low excitation force ratio, r_e , and reduces nonlinearly with increasing r_e due to high damping at high excitation force.

Seismic coefficient, α_{hav} , proposed by Richardson and Lee (1975) is smaller than that obtained from tests of this study. It fails to predict

its nonlinear variation with base acceleration at stronger excitations and lower embankment stiffness. Prediction of F_n as $38/H$ by Richardson et. al. (1977) and recommended by Richardson (1978) for all R.E. embankments are higher than those obtained from tests in this study. Hence, the expression is not valid for all R.E. embankments.

Shear modulus decreases with decreasing embankment stiffness at any γ_r as expected. Plots of G_r - γ_r at $\gamma_r=1.325 \times 10^{-4}$ almost merge. Hence, these plots were obtained by extending them upto this γ_r . At $\gamma_r \leq 1.325 \times 10^{-4}$, G_r is not of much interest as reinforcing action at such low strains is insignificant.

At strain of 10^{-3} , difference between G_r of R.E. and shear modulus, G_s , of plain sand at same D_r is small. At higher strains, $G_r > G_s$. Hence, R.E. has advantage over plain earth only at high strains.

For elastic behaviour, range of shear strain, γ , is upto 10^{-3} for R.E. in this study and upto much smaller $\gamma=10^{-6}$ for plain sand. Hence, it is logical to normalize G_r w.r.t. G_r at $\gamma=10^{-3}$ and not w.r.t. G_r at $\gamma=10^{-6}$.

Frequency, F_{rq} , strongly affects G_r . With increasing F_{rq} , G_r decreases to reach its minimum at resonance and then increases sharply for all embankments. For stiffer embankments G_r - F_{rq} curves for different OME values are closely spaced. The opposite is true for softer embankments.

For R.E. embankment, a single best-fit r_f -(G_r/G_{rn}) relationship may be adequate to compute (G_r/G_{rn}) at different r_f with a small discrepancy $\leq 12.79\%$. Hence, it is recommended for design.

Accelerations along dimensionless depth at various phase angles w.r.t. embankment top at a given OME is needed to compute inertia forces.

For safety, μ_{advmx} , γ_{advmx} and dimensionless disturbing force (F_{dmx}/W) may be obtained for $r_f \leq 1/\sqrt{2}$ at different OME. All these variables for stiffer R.E. embankment is lower from those for weaker R.E. embankment. At resonance, γ_{advmx} reduces sharply with change in r_f .

Inertia generated by sinusoidal excitation causes sinusoidal coefficient of average dynamic pullout resistance, μ_{avd} , with phase angle, θ , at different r_f and OME for R.E. embankments. As r_f increases, peak μ_{avd} increases to its peak at $r_f=1$. For $r_f > 1$ or $r_f < 1$ peak μ_{avd} reduces.

For M2 and M3, $\mu_{advmx} > \tan\phi$ and $\mu_{advmx} > \mu_{avsmx}$ near resonance does not necessarily mean a displacement dependent failure. Higher F_{rq} leads to smaller displacements per cycle due to short duration of inertia forces. Typical resonance during earthquakes is rare and does not last long. Many acceleration pulses at resonance are rare. Even if a few such pulses occur, it may not necessary lead to failure as indicated by test results.

Near resonance, large $\mu_{advmx} \geq \mu_{avsmx}$ obtained from back analysis is due to definition of μ_{avd} using shear stress due to disturbing inertia which could be larger than soil strength without always leading to displacement at failure. If Newmark's method to compute plastic displacements under dynamic loads is used to interpret pullout resistance, actual pullout resistance coefficient may be close to μ_{avsmx} based on $\tan\phi$. Hence, μ_{advmx} is just a number and not a physical quantity.

For stiffer R.E. embankments with many continuous fabrics and with γ_{avdmx} upto 10^{-3} at which slackness in fabric is overcome, μ_{avdmx} is almost strain-independent due to high tensile modulus of fabric and mobilization of required tension for stability at very low strains. Buildup of μ_{avdmx} with strain is faster when slackness is overcome. It is invalid for more flexible embankment, because, all fabrics except one are discontinuous and displacements mobilized for developing requisite pull-out resistance are relatively larger. At high strains, μ_{avdmx} is OME-independent if error less than or equal to 10% is tolerable.

Variation of μ_{avd} and γ_{avdmx} with r_f is similar to that of μ_{avdi} with (X/H). Continuous reinforcements lead to higher μ_{avdi} compared to the discontinuous ones. Variation of μ_{avdi} with (X/H) in this analysis is similar to those obtained from tests by Fairless (1989).

Active state of earth pressure was reached when maximum observed displacement of 0.78333% of embankment height was realized. In spite of this, catastrophic failure was precluded which highlights advantage of R.E. Continuous fabrics give advantage of low displacements also.

Post construction displacements showed near-mobilization of at rest pressures. Post vibration maximum displacement was at about 0.6H from top which agrees with that reported by others. Displacement increases with increasing OME and decreasing embankment stiffness.

Computed post vibration net confining pressures along depth indicate that continuous reinforcements designed to withstand tensile force with adequate margin of safety are more effective than discontinuous one.

Computed post vibration net residual force, P_{rs} , for M3 at first increases quickly with depth and then more gradually to peak at 0.675 H. Further below, it decreases. This conforms with experimental and field data reported by others. Values of P_{rs} for M3 and those reported by others are larger than at rest earth forces, because, P_{rs} comprises of earth forces and forces due to mobilization of additional confining pressures due to reinforcing action. For M3, additional confining pressures are smaller. Hence, mobilized P_{rs} in excess of at rest earth forces is insignificant and occurs for a limited depth.

Compaction settlement measured at the end of dynamic tests is zero at facing and stabilizes at a short distance from facing. Average settlement at the top is $\leq 2.46\%$ H which is small. Settlements decrease linearly with depth. Fabrics at facing end do not settle, because, rigid facing elements resting one over the other do not permit it. Resulting average loss of contact of reinforcement with soil below is 6.66% only which is small. Hence, results of this analysis are not seriously affected by it. However, it is desirable and possible to employ facing elements which settles along with embankment soil to precluded such loss of contact.

DYNAMIC ANALYSIS OF REINFORCED EARTHEN EMBANKMENTS

5.1 PREAMBLE

Objective of the study is to establish suitability of idealizing reinforced earth as homogeneous material in dynamic analysis by comparing analytically obtained response of R.E. embankments subjected to sinusoidal base excitations with response obtained experimentally for same embankments. The response is also compared with computed response of plain sand embankment of same height to highlight merits of reinforced earth.

FEM analysis in time domain was used to analyze R.E. Embankments idealized to be homogeneous and represented by four noded isoparametric elements. General concepts of FEM with special emphasis on isoparametric elements has been briefly dealt with herein. Equation of motion was solved in time domain by using direct step by step numerical integration proposed by Newmark which is unconditionally stable. Computer software FE95 was developed for this purpose and its flow diagram has been presented. The required material properties were obtained from tests cited in Chapter IV.

Embankments M1 and M3 have been considered for this study and the results obtained have been presented as far as possible in terms of dimensionless parameters which is desirable. In this chapter, the term amplitude stands for single amplitude of any dynamic quantity such as acceleration, displacement, shear stress etc., unless explained otherwise.

5.2 FINITE ELEMENT METHOD OF ANALYSIS IN TIME DOMAIN

5.2.1 Finite Element Method

General concepts of linear 2D FEM analysis are discussed briefly here. FEM analysis uses discretization of a continuum into finite numbers of elements. Nodes of elements are assigned finite degrees of freedom of movement. Simple displacement functions are chosen for appropriate distribution of displacements over each element in conformity with compatibility at element boundaries. This powerful analytical tool can account for different geometries of structure and different properties of each element. Banded stiffness matrix permits economical computations.

Isoparametric elements

An element whose geometry and displacements can be described by same parameter is the isoparametric element for which displacements within the element may be computed with help of shape function itself. Shape functions shall be dealt with a little later in this article. It allows variation of linear displacement within element. Hermann and Al-Yassin (1978) reported representation of R.E. as homogeneous material using 4-noded isoparametric elements to be adequate. In this analysis also, four noded quadrilateral isoparametric elements have been employed (Fig. 5.2.1).

For a point within the element, (x, y) are Cartesian global coordinates. This point is mapped and transferred into nonorthogonal system of local (natural) coordinates. The corresponding points in local coordinates is in ξ - η plane. The advantages of above transformation are:(1) In local coordinate system a better accuracy will be arrived while performing integration as ξ - η coordinates vary between -1 and +1, (2)

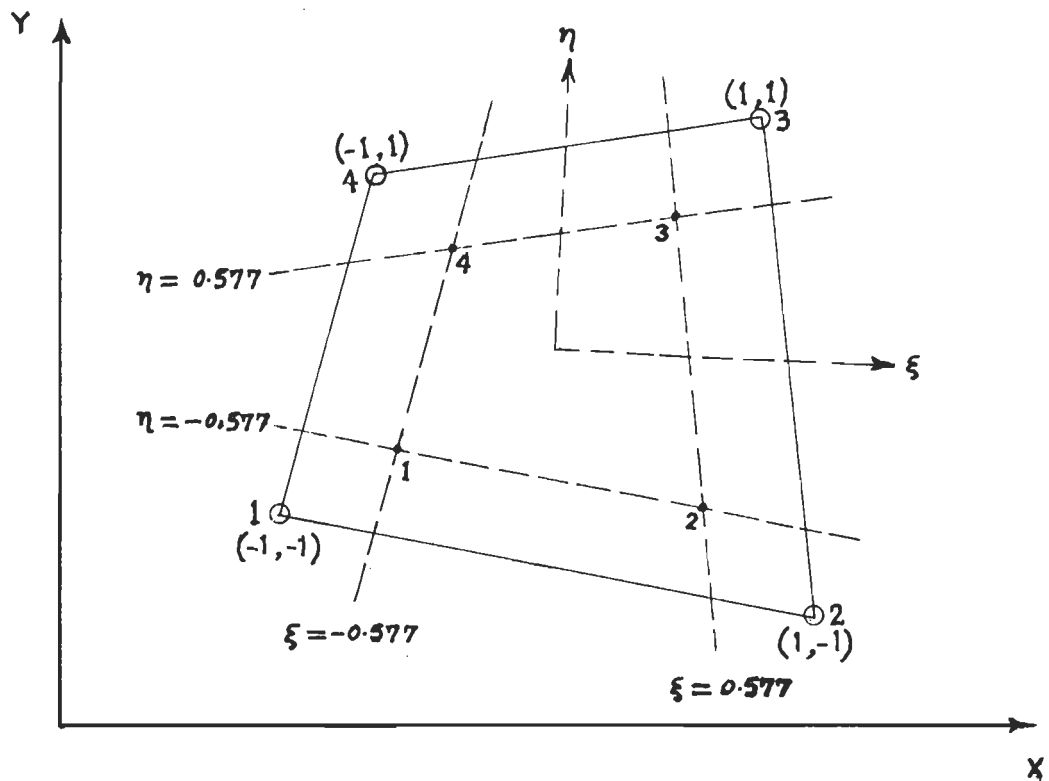


FIG. 5.2.1 FOUR NODED ISOPARAMETRIC QUADRILATERAL ELEMENT AND LOCATION OF GAUSS INTEGRATION POINTS.

shape and elements of higher order will be transferred to simple geometric forms permitting easier and accurate integration and (3) Derivation of required matrices is simple and independent of shape of element and its orientation in nonorthogonal system. The coordinates of nodes in local coordinates are $(-1,-1)$, $(1,-1)$, $(1,1)$ and $(-1,1)$ respectively. Global coordinates of any point are expressed in terms of shape functions and local coordinates of element nodes. Displacements u and v of a point within element are also expressed in terms of shape functions of nodes and nodal displacements. Expressions for x , y , u and v will be given later. Element nodes are denoted by 1,2,3 and 4 or by $i,j,m,..$ etc. numbered in counterclockwise fashion, where $i=1$, $j=2$, $m=3,..etc.$

Shape functions

For the four noded quadrilateral element considered, shape functions in terms of local coordinates for nodes 1 to 4 are :

$$\begin{aligned} N_1 &= \frac{1}{4} (1-\xi) (1-\eta) & N_3 &= \frac{1}{4} (1+\xi) (1+\eta) \\ N_2 &= \frac{1}{4} (1+\xi) (1-\eta) & N_4 &= \frac{1}{4} (1-\xi) (1+\eta) \end{aligned} \quad (5.2.1)$$

Displacement functions

For element 'e' with nodes i,j,m.. etc., the general displacement matrix, $\{U\}$, for any point within the element is :

$$\{U\} = [N] \{\delta\}^e \quad (5.2.2)$$

$$\text{where } [N] = [N_i \ N_j \ N_m \dots] \quad (5.2.3)$$

$$\text{and } \{\delta\}^e = \begin{pmatrix} u_i \\ v_i \\ u_j \\ v_j \\ \vdots \\ \vdots \\ \vdots \end{pmatrix} \quad (5.2.4)$$

Components of $[N]$ such as N_i, N_j, \dots are shape functions for nodes of the element and $\{\delta\}^e$ is nodal displacement vector. In case of a two dimensional element, horizontal and vertical displacements of a typical point inside element are given by $\{U\}$ and which is expressed as :

$$\{U\} = \begin{Bmatrix} u \\ v \end{Bmatrix} = \begin{bmatrix} N_1 & 0 & N_2 & 0 & \dots & N_4 & 0 \\ 0 & N_1 & 0 & N_2 & \dots & 0 & N_4 \end{bmatrix} \begin{Bmatrix} u_1 \\ v_1 \\ u_2 \\ v_2 \\ \vdots \\ u_4 \\ v_4 \end{Bmatrix} \quad (5.2.5)$$

The expressions for u and v are :

$$u = N_1 u_1 + N_2 u_2 + \dots + N_4 u_4 \quad (5.5.6)$$

$$v = N_1 v_1 + N_2 v_2 + \dots + N_4 v_4 \quad (5.2.7)$$

Strains

Strains at any point within the 2D element are the two normal strains and one shear strain component. The strain matrix, $\{\epsilon\}$, is expressed as :

$$\begin{aligned} \{\epsilon\} &= \begin{Bmatrix} \epsilon_x \\ \epsilon_y \\ \gamma_{xy} \end{Bmatrix} = \begin{Bmatrix} \frac{\partial u}{\partial x} \\ \frac{\partial v}{\partial y} \\ \frac{\partial u}{\partial y} + \frac{\partial v}{\partial x} \end{Bmatrix} = \begin{Bmatrix} \frac{\partial}{\partial x} & 0 \\ 0 & \frac{\partial}{\partial y} \\ \frac{\partial}{\partial y} & \frac{\partial}{\partial x} \end{Bmatrix} \cdot \begin{Bmatrix} u \\ v \end{Bmatrix} \\ &= [B_i \ B_j \ B_m \ \dots] \{\delta\}^e = [B] \cdot \{\delta\}^e \end{aligned} \quad (5.2.8)$$

$$\text{where } [B_1] = \begin{Bmatrix} \frac{\partial N_1}{\partial x} & 0 \\ 0 & \frac{\partial N_1}{\partial y} \\ \frac{\partial N_1}{\partial y} & \frac{\partial N_1}{\partial x} \end{Bmatrix} \quad (5.2.9)$$

In derivation of stiffness matrix later, [B] matrix is used. Global coordinates x and y as well as displacement u in the x direction and v in the y direction for any point within the isoparametric quadrilateral element are expressed as:

$$x = \sum N_i x_i = N_1 x_1 + N_2 x_2 + N_3 x_3 + N_4 x_4 \quad (5.2.10)$$

$$y = \sum N_i y_i = N_1 y_1 + N_2 y_2 + N_3 y_3 + N_4 y_4 \quad (5.2.11)$$

$$u = \sum N_i u_i = N_1 u_1 + N_2 u_2 + N_3 u_3 + N_4 u_4 \quad (5.2.12)$$

$$v = \sum N_i v_i = N_1 v_1 + N_2 v_2 + N_3 v_3 + N_4 v_4 \quad (5.2.13)$$

Nodel displacements are formulated in terms of local coordinates (ξ, η) which are functions of global coordinates (x, y). Using the chain rule of partial differentiation, we may write:

$$\frac{\partial N_i}{\partial \xi} = \frac{\partial N_i}{\partial x} \cdot \frac{\partial x}{\partial \xi} + \frac{\partial N_i}{\partial y} \cdot \frac{\partial y}{\partial \xi} \quad (5.2.14)$$

$$\frac{\partial N_i}{\partial \eta} = \frac{\partial N_i}{\partial x} \cdot \frac{\partial x}{\partial \eta} + \frac{\partial N_i}{\partial y} \cdot \frac{\partial y}{\partial \eta} \quad (5.2.15)$$

$$\text{i.e., } \begin{Bmatrix} \frac{\partial N_i}{\partial \xi} \\ \frac{\partial N_i}{\partial \eta} \end{Bmatrix} = \begin{bmatrix} \frac{\partial x}{\partial \xi} & \frac{\partial y}{\partial \xi} \\ \frac{\partial x}{\partial \eta} & \frac{\partial y}{\partial \eta} \end{bmatrix} \begin{Bmatrix} \frac{\partial N_i}{\partial x} \\ \frac{\partial N_i}{\partial y} \end{Bmatrix} = [J] \cdot \begin{Bmatrix} \frac{\partial N_i}{\partial x} \\ \frac{\partial N_i}{\partial y} \end{Bmatrix} \quad (5.2.16)$$

where $[J]$ is the Jacobian square matrix. Since shape functions are derivatives w.r.t. local coordinates (ξ, η) , the Jacobian matrix may be used to convert them into derivatives w.r.t. global coordinates (x, y) and which is given by:

$$\begin{Bmatrix} \frac{\partial N_i}{\partial x} \\ \frac{\partial N_i}{\partial y} \end{Bmatrix} = [J]^{-1} \begin{Bmatrix} \frac{\partial N_i}{\partial \xi} \\ \frac{\partial N_i}{\partial \eta} \end{Bmatrix} \quad (5.2.17)$$

By substituting expressions for global coordinates (x, y) into the expression for the Jacobian matrix cited above $[J]$ may be rewritten as :

$$[J] = \begin{bmatrix} \sum x_i \frac{\partial N_i}{\partial \xi} & \sum y_i \frac{\partial N_i}{\partial \xi} \\ \sum x_i \frac{\partial N_i}{\partial \eta} & \sum y_i \frac{\partial N_i}{\partial \eta} \end{bmatrix} \quad (5.2.18)$$

The above expression for $[J]$ for four noded element is:

$$[J] = \begin{bmatrix} \frac{\partial N_1}{\partial \xi} & \frac{\partial N_2}{\partial \xi} & \frac{\partial N_3}{\partial \xi} & \frac{\partial N_4}{\partial \xi} \\ \frac{\partial N_1}{\partial \eta} & \frac{\partial N_2}{\partial \eta} & \frac{\partial N_3}{\partial \eta} & \frac{\partial N_4}{\partial \eta} \end{bmatrix} \begin{Bmatrix} x_1 & y_1 \\ x_2 & y_2 \\ x_3 & y_3 \\ x_4 & y_4 \end{Bmatrix} \quad (5.2.19)$$

To transform variables and region w.r.t. which the integration is made, a standard process will be used which involves the determinant of Jacobian matrix. For instance, area of an element becomes:

$$\text{Area} = dx \, dy = \det[J] \, d\xi \, d\eta \quad (5.2.20)$$

This will be used later in derivation of the stiffness matrix.

Stresses

Stresses are functions of strains and material properties of element. Stress matrix, $[\sigma]$, consists of normal stresses, σ_x and σ_y , as well as shear stress, τ_{xy} , and is expressed as:

$$\{\sigma\} = \begin{Bmatrix} \sigma_x \\ \sigma_y \\ \tau_{xy} \end{Bmatrix} = [D] \left[\{\epsilon\} - \{\epsilon_0\} \right] + \{\sigma_0\} \quad (5.2.21)$$

where $[D]$ is elasticity matrix, $\{\epsilon_0\}$ is initial strain vector and $\{\sigma_0\}$ is initial stress vector. For plane strain condition, $[D]$ matrix is given by:

$$[D] = \frac{E}{(1+\nu)(1-2\nu)} \begin{bmatrix} 1-\nu & \nu & 0 \\ \nu & 1-\nu & 0 \\ 0 & 0 & \frac{1-2\nu}{2} \end{bmatrix} \quad (5.2.22)$$

where E is Young's modulus and ν is Poisson's ratio of the element. Stresses and strains are related by the $[D]$ which will be used in derivation of stiffness matrix which follows.

Stiffness matrix

For an element in equilibrium the nodal Force matrix $\{F\}^e$ is related to the nodal displacement matrix $\{\delta\}^e$ by:

$$\{F\}^e = [K]^e \{\delta\}^e \quad (5.2.23)$$

where $[K]^e$ is stiffness matrix of the element. The stiffness matrix for the element can be derived based on the principle of Virtual Work. Let $\{\delta\}^{*e}$ be the virtual displacement applied to an element in equilibrium under the influence of external force $\{F\}^e$. Therefore, expressions for internal and external work done is expressed as:

$$\text{Work done by internal stresses} = \int_V \{\epsilon\}^T \{\sigma\} d(\text{Vol}) \quad (5.2.24)$$

$$\text{Work done by external forces} = \{\delta\}^{*eT} \{F\}^e \quad (5.2.25)$$

Based on principle of virtual work, work done by internal stresses should be equal to work done by external forces, i.e.,

$$\{\delta\}^{*eT} \{F\}^e = \int_V \{\epsilon\}^T \{\sigma\} d(\text{Vol}) \quad (5.2.26)$$

according to the principle of virtual work, the work done by external forces when the system is subjected to a virtual displacement, is equal to the work done by internal stresses caused by the external forces, i.e.,

$$\{\delta\}^{*eT} \{F\}^e = \int_v ([B] \{\delta\}^{*e})^T ([D] [B] \{\delta\}^e) d(\text{Vol}) \quad (5.2.27)$$

$$\{\delta\}^{*eT} \{F\}^e = \int_v \{\delta\}^{*eT} [B]^T [D] [B] \{\delta\}^e d(\text{Vol}) \quad (5.2.28)$$

$$\{\delta\}^{*eT} \{F\}^e = \{\delta\}^{*eT} \left(\int_v [B]^T [D] [B] d(\text{Vol}) \right) \{\delta\}^e \quad (5.2.29)$$

$$\{F\}^e = \int_v [B]^T [D] [B] \{\delta\}^e d(\text{Vol}) = [K]^e \{\delta\}^e \quad (5.2.30)$$

$$[K]^e = \int_v [B]^T [D] [B] d(\text{Vol}) \quad (5.2.31)$$

When thickness, t , of an element is constant, integration over volume may be replaced by integration over area as follows:

$$[K]^e = t \int_A [B]^T [D] [B] \cdot d(\text{Area}) \quad (5.2.32)$$

As explained earlier, the term $d(\text{Area})$ may be expressed as:

$$d(\text{Area}) = dx dy = \det[J] d\xi d\eta \quad (5.2.33)$$

Using above expression, $[K]^e$ may be rewritten as:

$$[K]^e = t \int_{-1}^{+1} \int_{-1}^{+1} [B]^T [D] [B] \det[J] d\xi d\eta \quad (5.2.34)$$

The above equation is integrated numerically. Gaussian integration is popularly used for this purpose which involves summation of functions evaluated at specific points. The number of points used for this purpose depends upon the order of integration and accuracy required. For the whole structure with a total of N_e elements, the relationship between global nodal force matrix $[F]$ and global nodal displacement matrix, $\{\delta\}$, is:

$$[F] = [K] \{\delta\} \quad (5.2.35)$$

where $[K]$ is global stiffness matrix obtained directly by adding individual stiffness terms and expressed as:

$$[K] = \sum_{e=1}^{Ne} [K]^e \quad (5.2.36)$$

5.2.2 Equation of motion

The general equation of motion for a multi-degree freedom system subjected to dynamic external loads is expressed as:

$$[M]\{\ddot{u}(t)\} + [C]\{\dot{u}(t)\} + [K]\{u(t)\} = \{F(t)\} \quad (5.2.37)$$

where $[M]$, $[C]$ and $[K]$ are mass, damping and stiffness matrices respectively; $\{\ddot{u}(t)\}$, $\{\dot{u}(t)\}$ and $\{u(t)\}$ are acceleration, velocity and displacement vector matrices respectively (all being relative to ground and time dependent) and $[F(t)]$ is time dependent force vector. It may be noted that displacement vector $\{u(t)\}$ in this article 5.2.2 comprises of displacements in vertical and horizontal directions and is different from displacement u in the x direction explained in article 5.2.1 earlier. If entire base of embankment is subjected to same excitation at any time, the load vector $[F(t)]$ associated with that excitation is given by:

$$\{F(t)\} = - [M]\{S_x\}\ddot{X}_g - [M]\{S_y\}\ddot{Y}_g \quad (5.2.38)$$

where $\ddot{X}(g)$ and $\ddot{Y}(g)$ are base excitations in the horizontal and vertical directions respectively; S_x and S_y are matrices describing degrees of freedom in X and Y directions. Transposes of these matrices are given as:

$$\{S_x\}^T = \{1 \quad 0 \quad 1 \quad 0 \dots 1 \quad 0\} \quad (5.2.39)$$

$$\{S_y\}^T = \{0 \quad 1 \quad 0 \quad 1 \dots 0 \quad 1\} \quad (5.2.40)$$

In these equations, 1 indicate freedom of movement, zero indicates no freedom of movement. Term X stands for horizontal direction and Y for vertical direction. After substituting these terms, the final form of equation of motion may be given as:

$$[M]\{\ddot{u}(t)\} + [C]\{\dot{u}(t)\} + [K]\{u(t)\} = -[M]\{S_x\}\ddot{X}_g - [M]\{S_y\}\ddot{Y}_g \quad (5.2.41)$$

Details of computing [K] matrix were discussed earlier and those regarding [M] and [C] matrices are discussed in this article.

Mass matrix [M]

Mass matrices are of two types: consistent mass matrix and lumped mass matrix. For obtaining consistent mass matrix, usually interpolation functions used are same as those in deriving element stiffness matrix which lead to non-zero cross diagonal terms in mass matrix. Lumped mass matrix is a diagonal matrix and is its simplest form. The simplest procedure for defining mass is to assume that mass is concentrated or lumped at discrete points forming nodes of the element. This mass matrix is given by:

$$[M] = \begin{bmatrix} M_{11} & 0 & 0 & 0 \\ 0 & M_{22} & 0 & 0 \\ 0 & 0 & M_{33} & 0 \\ 0 & 0 & 0 & M_{nn} \end{bmatrix} \quad (5.2.42)$$

where n is total number of degrees of displacement freedom of FEM grid considered. At any node same lumped mass will be associated with all degrees of displacement at that node.

Disadvantage associated with this matrix is that the large storage and computational effort required compared with that when lumped mass matrix is used in dynamic analysis. Moreover, rotational degrees of freedom can be eliminated from lumped mass analysis (by static condensation) whereas all rotational/translational degrees of freedom must be included while using consistent mass matrix (Clough and Penzien, 1986). As such, in absence of significant advantages arising out of using consistent mass matrix, simple lumped mass matrix is popularly favoured and, hence, adopted for this study.

Damping matrix [K]

Damping of the system represents the resistance to movement of nodes. It is rather difficult to represent damping in the system appropriately. However, it is customary to assume damping to be viscous. This simplifies solution of equation of motion. Rayleigh has recommend an expression for obtaining damping matrix which has been considered in this analysis and which is given by (Bathe, 1990):

$$[C] = \alpha[M] + \beta[K] \quad (5.2.43)$$

Where α and β constants to be determined from two damping ratios corresponding to any two natural frequencies of vibration. In the proposed analysis, damping in first and second natural frequencies have been considered for evaluation of α and β for which, the relationship between α , β , ω_1 and ζ_1 for i th mode is given by :

$$\alpha + \beta \omega_1^2 = 2 \omega_1 \zeta_1 \quad (5.2.44)$$

More details about choice of damping shall be given later in this chapter.

5.2.3. Solution of the Equation of Motion

Equation of motion cited above may be solved by following methods:

1. Mode superposition method
2. Analysis in frequency domain
3. Direct step-by-step numerical integration in time domain.

For a linear elastic analysis, all the three are equally good. However, the third is useful even for nonlinear analysis. Mode superposition method is effective if a few of low frequency modes are adequate to describe the response. If all modes are needed, extraction of complete set of eigen vectors needs a large computational effort. The step-by-step integration is better suited to structures subjected to short duration loads that excite many modes. Besides, integration techniques may be applied to nonlinear structures also whereas mode superposition method assumes only linearity (Krishnamoorthy, 1987). In this investigation, the analysis in time domain by direct step-by-step numerical integration has been adopted.

Direct step-by-step numerical integration methods

Such methods may be broadly grouped into two categories:

1. Explicit integration method (i.e. central difference method)
2. Implicit integration methods
 - (a) Newmark's method
 - (b) Wilson's θ method
 - (c) Houbolt's method
 - (d) Hilbev's α method

In either categories, the coupled equation of motion are integrated directly without any initial modal uncoupling (i.e. no transformation of equation of motion into a different form is carried out). In the explicit integration method, expressions for new vectors contain terms involving vectors known for the preceding time stations. Such integration is conditionally stable and requires very small time steps for integration. This make the analysis expensive. For the analysis in time domain, all the natural frequencies of the system are automatically considered.

Implicit methods cited above are useful for solving the equation of motion in time domain and which are unconditionally stable. However, Newmark's method is superior compared to other methods because of the smallest numerical errors when compared with other methods (Bathe ,1990). As such, in the proposed analysis, Newmark's method has been been adopted and which is explained briefly below.

Newmark's method

In the newmark's integration scheme, expressions for velocity and displacement vectors ${}^{t+\Delta t}\dot{u}$ and ${}^{t+\Delta t}u$ at time station $(t+\Delta t)$ are given by :

$${}^{t+\Delta t}\dot{u} = \dot{u}^t + \left[(1-\delta)\ddot{u}^t + \delta {}^{t+\Delta t}\ddot{u} \right] \Delta t \quad (5.3.45)$$

$${}^{t+\Delta t}u = u^t + \dot{u}^t \Delta t + \left[(0.5 - \alpha)\ddot{u}^t + \alpha {}^{t+\Delta t}\ddot{u} \right] \Delta t^2 \quad (5.3.46)$$

where δ and α are parameters to be chosen appropriately. The integration scheme is unconditionally stable provided $\delta \geq 0.5$ and $\alpha \geq 0.25 (0.5 + \delta)^2$ (Bathe, 1990). If $\delta=0.5$, value of α is very close to 0.25 when evaluated this way. In the proposed analysis, $\delta=0.5$ and $\alpha=0.25$ have been adopted.

5.3 IDEALIZATION OF REINFORCED EARTH

Soil having three phases (soil, water and air) is considered homogeneous, because, phases repeat at small intervals. This may be extended to micro-reinforced earth with reinforcements repeating at small intervals (Rao, 1995). Hermann and Al-Yassin (1978) reported representation of R.E. as homogeneous material to be adequate. Shewbridge and Sousa (1991) idealized composite R.E. test specimen (477 mm high, 204 mm diameter) as homogeneous to evaluate dynamic properties. In proposed study, by adopting adequately small ratio of reinforcement spacing to embankment height, R.E. may be assumed as homogeneous. Analytical studies are proposed to validate this idealization and results obtained by such analysis are compared with test results on same R.E. embankments with same base excitation. Hermann and Al-Yassin (1978) have reported representation of R.E. as homogeneous material by using 4-noded isoparametric elements to be adequate. Therefore, this has been considered for the proposed investigation.

Damping

Hardin and Drnevich (1970) reported that damping in sands is strongly influenced by shear strain, effective mean principal stress, void ratio and number of loading cycles; to a lesser extent by saturation degree, angle of shearing resistance and octahedral shear; and to the least extent by grain size characteristics. After reviewing their test results and those reported by others, Seed et.al. (1984) stated that even with procedure, apparatus and sand used for tests being the same, test results obtained showed appreciable scatter. They proposed a range of damping with upper/lower bounds and the mean at any shear strain (Fig. 5.3.1).

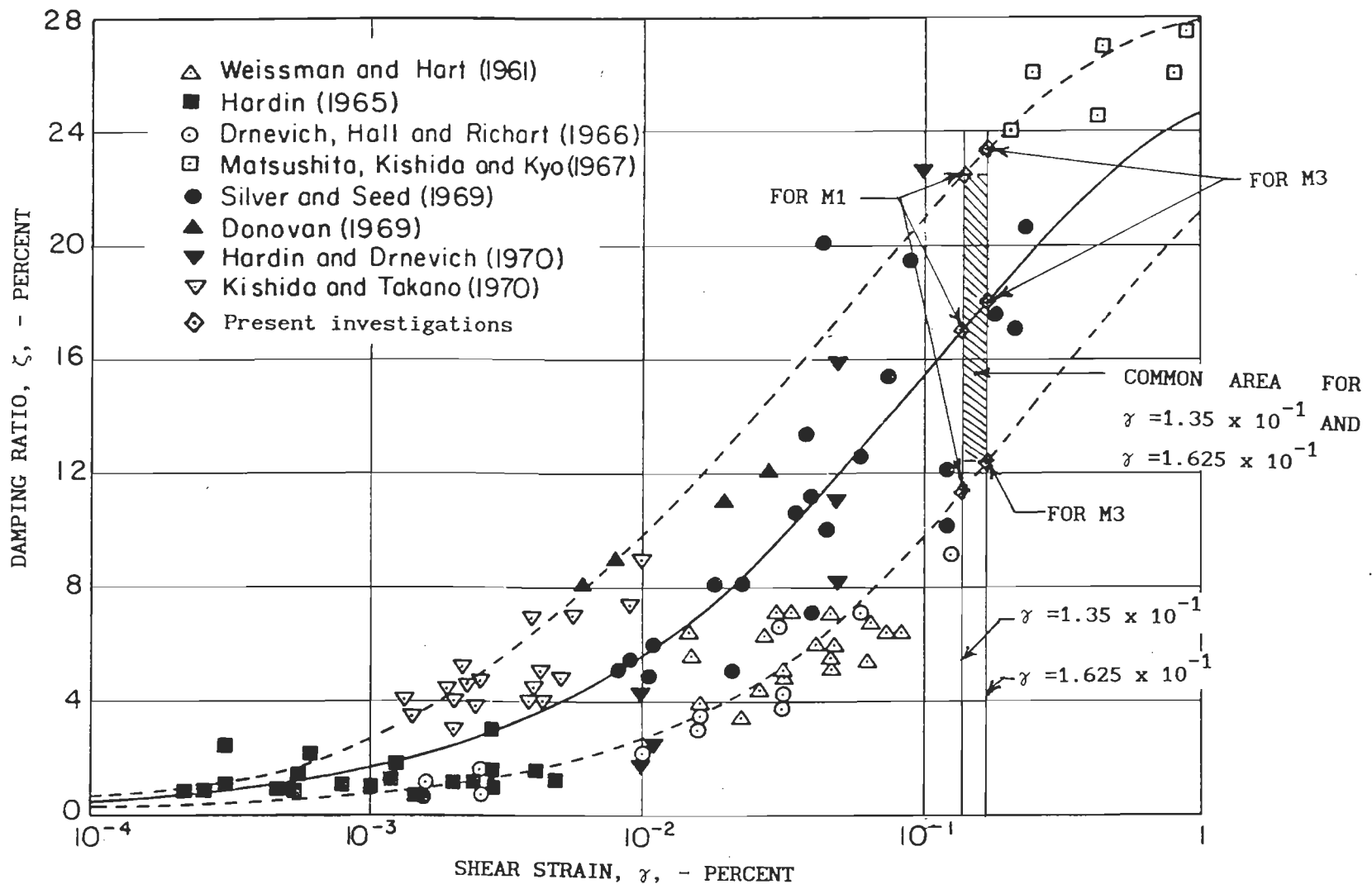


FIG.5.3.1 DAMPING RATIOS FOR SANDS (AFTER SEED ET.AL., 1984)

Plane sand is similar to R.E. as far as damping is considered since reinforcements form negligible fraction of R.E. volume. Besides, effect of reinforcements is to increase effective confining pressure on sand. Hence, damping recommended for plain sands by Seed et.al. (1984) were considered to be valid for R.E. also and has been adopted in the proposed analyses.

The proposed analysis makes following assumptions:

- i) R.E. is homogeneous and linear elastic.
- ii) R.E. embankment is a shear beam and is rigidly fixed at the base.
- iii) Structure-Foundation interaction is not considered.
- iv) Plane strain conditions exist in transverse planes.
- v) Excitation is the same at all points on embankment base at any time.

5.3.1 Details of R.E. Embankments Analysed

Test embankments are shear beams (with slenderness ratio of 4.16). Embankments M1 and M3 were each represented by 120 isoparametric four noded quadrilateral elements with 120 nodes and 286 displacement degrees freedoms. There were 12 elements along height and 10 along length. Each element was 75 mm deep. Velocity of shear wave and wave length, λ , for test embankment M1, are 66.469 m/sec and 3.933 m respectively. Corresponding values for M3 are 57.412 m/sec and 4.1754 m respectively. Ratio of wave length to thickness of element were 52.44 and 55.672 for M1 and M3 which are adequate. Element thickness of the order of $\lambda/8$ to $\lambda/10$ are usually adequate to make FEM grid adequately flexible (Bathe and Wilson, 1976).

Each element is numbered and defined by numbered nodal points. Node numbering is done in counter clockwise direction for each element.

Numbering scheme of nodal points determines the band width of stiffness matrix. Therefore, numbering scheme adopted is such that band width of stiffness matrix is minimised. Figure 5.3.2 and Table 5.3.1 show details of the FE idealization as well as the numbering of elements.

Horizontal sinusoidal base excitations A1 (Fig.5.3.3, Table 5.3.1) and A3 (Fig.5.3.4, Table 5.3.1) along BC (Fig.5.3.2) of these embankments were considered for dynamic analyses.

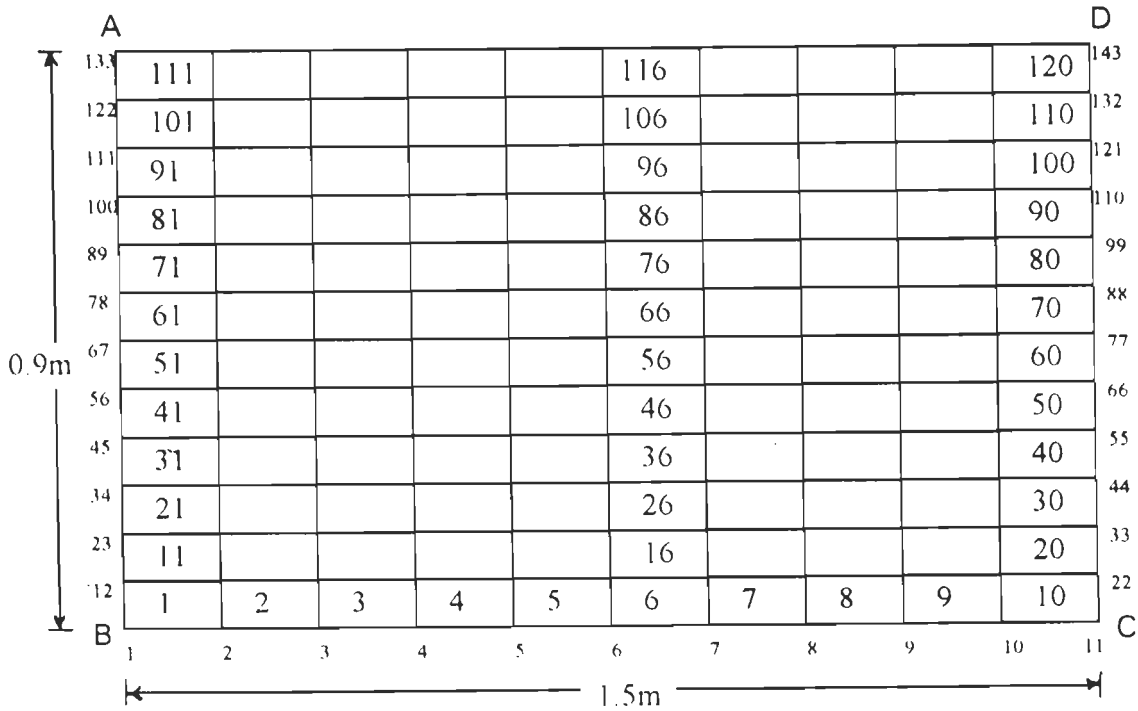


FIG. 5.3.2 IDEALIZED R.E. EMBANKMENT FOR 2D FEM ANALYSIS.

Acceleration amplitude for A1 is same as that obtained from tests carried out on M1 at $\text{OME}=24$ at fundamental frequency, F_n . Weaker embankment M3 may show nonlinear behaviour when excited at resonance. Besides, chances of resonance with design base excitation are remote and do not last long. Moreover, excitation at F_n for significant duration leads to unrealistically

Table 5.3.1 Details of Input Data for Single Layer Idealization of Embankments.

Details	R.E. embankment M1	R.E. embankment M3	Plain sand embankment P1	Plain sand embankment P2
1. Geometry				
i. Length (m)	1.50	1.50	4.44	6.18
ii. Width (m)	0.75	0.75	0.75	0.75
iii. Height (m)	0.90	0.90	0.90	0.90
iv. Top length (m)	1.50	1.50	1.50	1.50
v. Top width (m)	0.75	0.75	0.75	0.75
2. Material properties				
i. Dry density, γ_d (t/m ³)	1.625	1.625	1.625	1.625
ii. Mass density ρ (t.s ² /m ⁴)	0.16564	0.16564	0.16564	0.16564
iii. Relative density D_r	70%	70%	70%	70%
iv. Poisson's ratio, ν	0.25	0.25	0.25	0.25
v. Shear modulus, G (t/m ²)	735.773	546.00	592.038	592.038
vi. Shear velocity, V_s	66.469	57.412	59.784	59.784
vii. Wave length, λ (m)	3.9330	4.1754	3.5375	3.5375
viii. Modulus of Elasticity E (t/m ²)	1839.432	1365.0	1480.095	1480.095
3. Base excitations				
i. Nature	A1	A3	A1	A1
ii. Frequency of vibration (Hz)	Sinusoidal	Sinusoidal	Sinusoidal	Sinusoidal
iii. Single amplitude of vibration (g)	16.90	13.75	16.90	16.90
	0.152	0.1	0.152	0.152

Table 5.3.1 Continued

Details		R.E. embankment M1	R.E. embankment M3	Plain sand embankment P1	Plain sand embankment P2
iv.	Duration of excitation (sec)	4.0	4.0	4.0	4.0
4.	Fundamental frequency (Hz)	16.9	13.5	15.16	15.16
5.	Shear strain ($\times 10^{-3}$)	1.35	1.625		
6.	Damping ratio				
i.	First mode, ζ_1	0.115 0.17 and 0.225	0.124 0.151 and 0.179	0.05	0.05
ii.	Second mode, ζ_2	0.175 0.255 and 0.337	0.186 0.227 and 0.268	0.05	0.05
7.	Details of finite element grid				
i.	No. of isoparametric four noded quadrilateral element	120	120	120	120
ii.	Number of nodes	143	143	143	143
iii.	Total number of degree of freedom	286	286	286	286
iv.	Element thickness, t_e (mm)	75	75	75	75
v.	λ/t_e ratio	52.44	55.672	47.167	47.167
vi.	Element length, l_e (mm)	150	150	444	618
vii.	l_e/t_e ratio	2.00	2.00	5.92	8.24

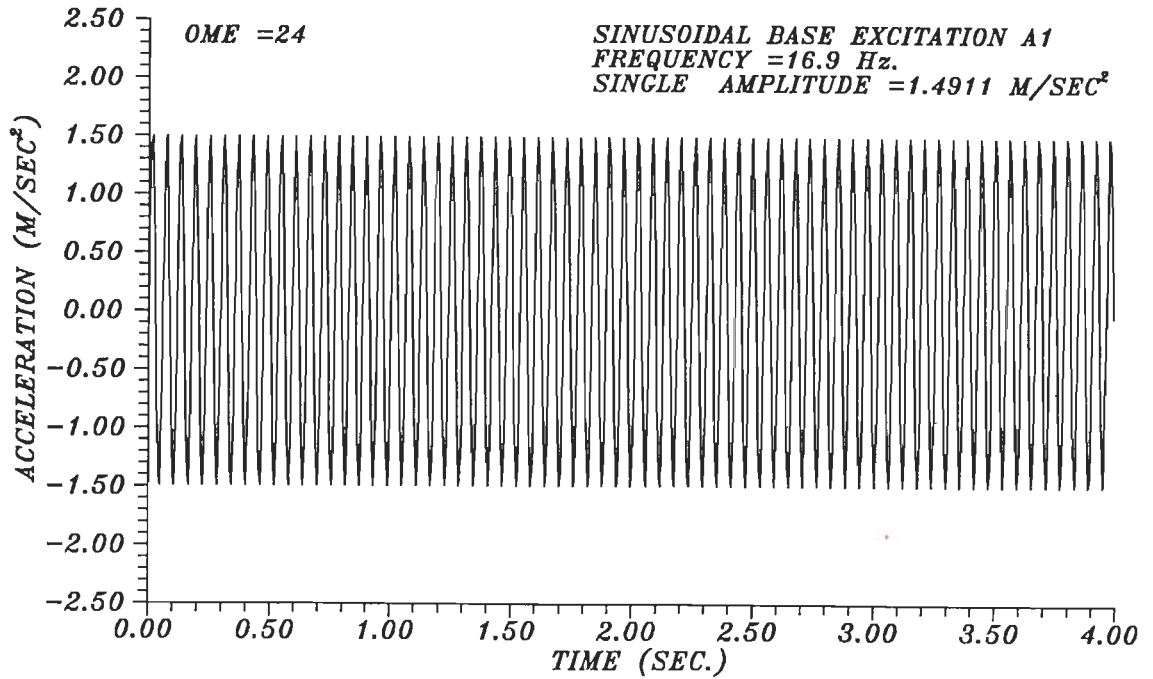


FIG.5.3.3 BASE EXCITATION A1 GENERATED BASED ON PEAK AMPLITUDE OF ACCELERATION RECORDED FOR R.E. EMBANKMENT M1.

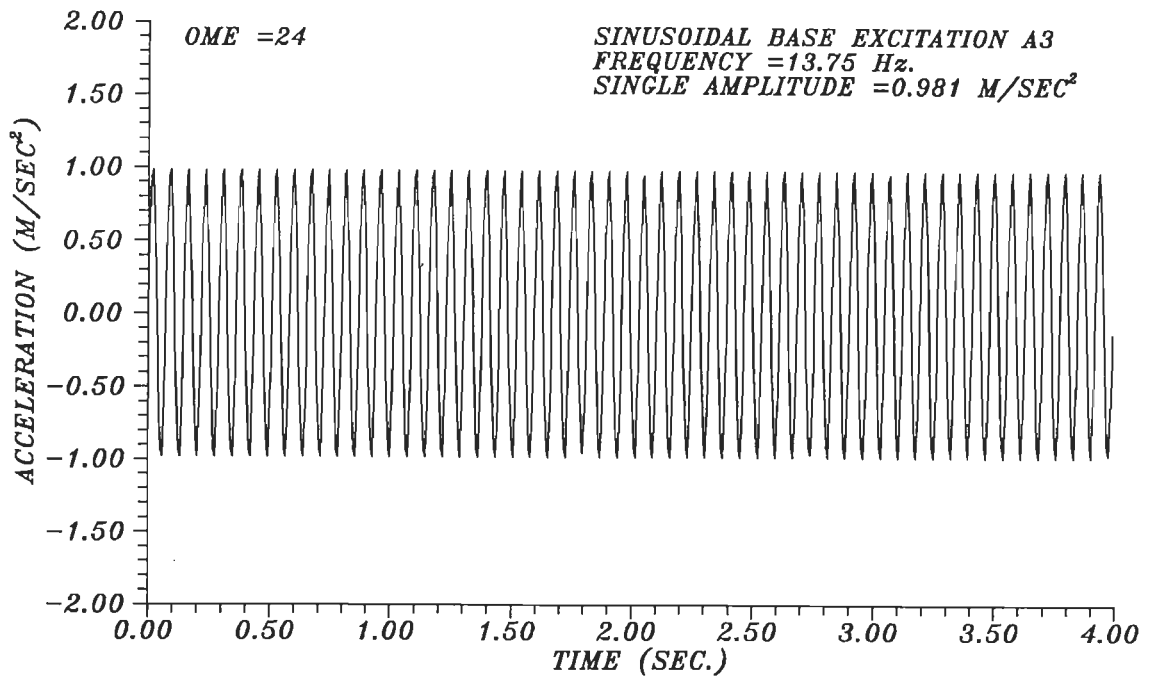


FIG.5.3.4 BASE EXCITATION A3 GENERATED BASED ON PEAK AMPLITUDE OF ACCELERATION RECORDED FOR R.E. EMBANKMENT M3.

large deformations. With very small change in excitation frequency at $F_n=13.5$ Hz, embankment response decreases significantly. As such, excitation A3 at OME=24 with acceleration amplitude of 0.981 m/sec^2 and frequency of $13.75 \text{ Hz} > F_n$ obtained from tests was chosen.

Air dry fine Solani sand with dry density of 1.625 t/m^2 , relative density of 70%, mass density of $0.1656 \text{ t sec}^2/\text{m}^4$ and Poisson's ratio, ν , of 0.25 was used to construct M1 and M3. This value of ν is the largest recommended for fine sand (Barkan, 1962). For dynamic analysis, shear modulus obtained from tests at OME=24 was 735.77 t/m^2 for M1 (Table 4.6.9) and 546 t/m^2 for M3 (Fig. 4.6.17) were used. Knowing shear modulus, G , and by using theory of elasticity, Young's modulus, E , is obtained as:

$$E = 2G (1 + \nu) \quad (5.3.1)$$

Table 5.3.1 gives damping ratios obtained from Fig. 5.3.1, based on shear strains of 1.35×10^{-3} and 1.625×10^{-3} obtained from tests for M1 excited at A1 and M3 excited at A3 respectively. In addition, damping ratio of 0.288 (which is greater than the upper bound value) and damping ratios of 0.05, 0.07 and 0.075 (which are smaller than lower bound values) were also used in the analyses of M1 to study effect of damping and which are also listed in the table. The R.E. embankments behaved predominantly in elastic domain in forced vibration tests. Hence, smaller damping ratios comparable to those obtained from free vibration tests (Table 4.6.2a) were also included in the range of damping used for this study.

In the proposed study, ratio of reinforcement spacing to embankment height was 0.16 is adequately small to facilitate idealization of the entire R.E. embankment to be a single homogeneous material. The above details were

used to analyze M1 and M3. Details of analysis of M1 and M3 by idealizing them with two layers of homogeneous materials with appropriate material properties will be discussed later in this chapter.

5.3.2 Details of Plain Sand Embankments Analysed

To highlight advantages of R.E., dynamic analysis was also carried out for plain sand embankments P1 and P2 with same height and top width as those for M1 and M3 (Table 5.3.1). Vertical side slopes being inadmissible for plain sand embankments, slopes were obtained by adopting static factors of safety of 1.6 and 2.5 for P1 and P2 respectively. Using pseudo-static analysis (Hirschfeld and Poulos, 1973), safety factors for P1 and P2 were obtained as 1.16 and 1.69 respectively when subjected to base excitation A1 (Table 5.3.1). This resulted into base widths 4.44 m and 6.18 m respectively for P1 and P2 (Fig. 5.3.5 and 5.3.6). Excitation A1 is considered for plain sand embankments, because, it is more severe than A3.

Embankments P1 and P2 were idealized by using same number and type of finite elements as those for M1 and M3. Table 5.3.1 gives dimensions, discretizations and base excitation for P1 and P2. Type of sand, dry density, relative density and Poisson's ratio for fill material of P1 and P2 were same as those for M1 and M3 cited earlier. Shear modulus was obtained by method of Seed and Idriss (1970) (explained in Article 2.4.2 and 4.6.2) at shear strain obtained for M1 excited with A1. Knowing G , Eq. 5.3.1 is used to evaluate Young's modulus, E . In absence of availability of strains for P1 and P2 based on tests, values of damping ratio of 0.05 was chosen for the first and second modes. Table 5.3.1 also gives values of damping ratios, V_s , E and G of P1 and P2.

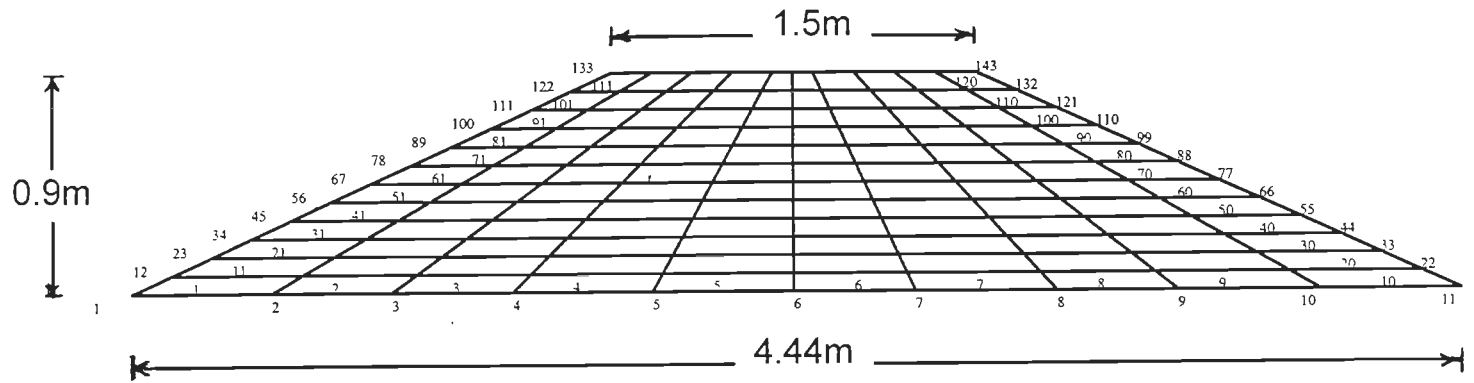


FIG. 5.3.5 IDEALIZED PLAIN SAND EMBANKMENT P1 FOR 2D FEM ANALYSIS.

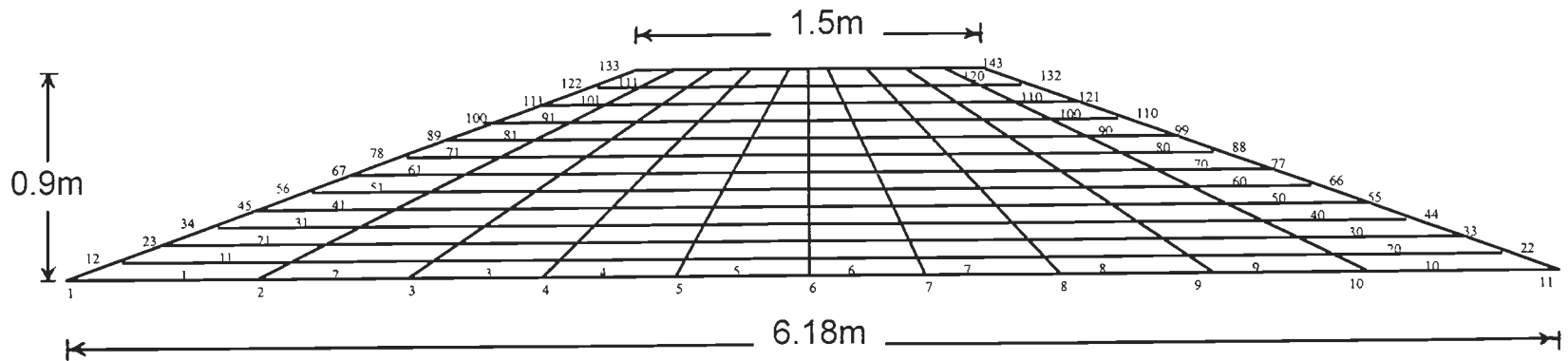


FIG. 5.3.6 IDEALIZED PLAIN SAND EMBANKMENT P2 FOR 2D FEM ANALYSIS.

5.3.3 Embankment Analysis Using Two Layer Idealization

Shear modulus, G , varies from its value of zero at the top of the embankment to its maximum value at the base. As such, assigning uniform value of G for the entire embankment results into discrepancy in assumed and actual values of G at any point. To reduce this discrepancy, the embankment may be idealized by more than one layer of homogeneous material. In the proposed analysis, the embankment is assumed to be represented by two homogeneous layers of equal depth. Seed and Idriss (1970) have indicated that shear modulus is proportional to square root of the octahedral stress at the point under consideration. If G_m is shear modulus corresponding to octahedral stress, σ_{octm} , at mid-depth of entire embankment, then, shear modulus, G_1 , at mid-depth of top layer corresponding to octahedral stress, σ_{oct1} , and G_2 at mid-depth of bottom layer corresponding to octahedral stress, σ_{oct2} , are given as:

$$G_1 = G_m (\sigma_{oct1}/\sigma_{octm})^{0.5} \quad (5.3.2)$$

$$G_2 = G_m (\sigma_{oct2}/\sigma_{octm})^{0.5} \quad (5.3.3)$$

Figure 5.3.7 shows idealization of embankment by a single layer and by two layers. Knowing G_1 and G_2 , properties E , V_s etc. can be obtained for the two layers. This may be further extended to system with more than two layers also for better representation of the embankment.

For better idealization of M1 and M3, the proposed analyses represents each of them by two homogeneous layers. Table 5.3.2 shows material properties of such layers for M1 and M3.

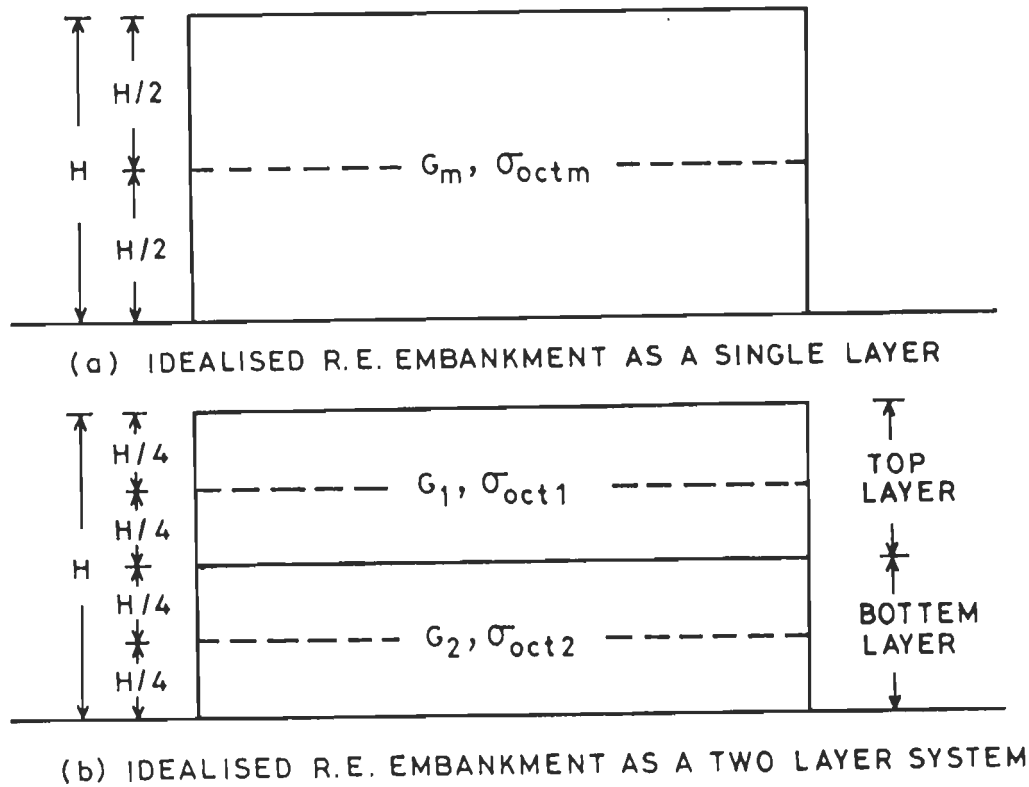


FIG.5.3.7 TYPE OF IDEALIZATION FOR R.E. EMBANKMENTS.

Table 5.3.2 Material Properties For M1 and M3 With Two Layer Idealization

S.No. Details	Top layer		Bottom layer	
	M1	M3	M1	M3
1. Dry density, γ_d (t/m^3)	1.625	1.625	1.625	1.625
2. Mass density, ρ (t/m^3)	0.16564	0.16564	0.16564	0.16564
3. Relative density D_r %	70	70	70	70
4. Poisson's ratio, ν	0.25	0.25	0.25	0.25
5. Shear modulus (t/m^2)	520.241	386.080	901.108	668.710
6. Shear velocity (m/sec)	56.042	48.280	73.760	63.540
7. Modulus of elasticity (t/m^2)	1300.604	965.200	2252.771	1671.777
8. Damping ratio				
First mode ζ_1	0.170	0.124	0.170	0.124
Second mode ζ_2	0.255	0.186	0.255	0.186

5.3.4 Computer Software FE95

Earlier version of FE95 developed for performing static 2D linear analysis and for eigen solutions (Pandey, 1995) was modified to perform linear dynamic 2D analysis in time domain under plane stress/plane strain conditions. Bathe (1990) has reported that for 4-noded quadrilateral isoparametric elements, the 2 x 2 Guassion point integration is adequate to compute stresses and, hence, employed in proposed study also. Mass is represented by lumped mass approach. FE95 carries out analysis either under static or dynamic conditions. Guassian elimination method was used to solve matrix equation employing Newmark's direct step-by-step numerical integration method in time domain.

The software has facility for checking errors in feeding data, if any. The program stops with an appropriate error message stored in the file 'a.err' if input data is erroneous. The software is supplemented by another one to optimise numbering sequence of nodes to minimise storage for stiffness matrix and computational effort for the solution. Figure 5.3.8 show flow diagram of software FE95.

5.4 RESULTS OF THE INVESTIGATION

Embankments M1 and M3 were analyzed by treating them to be homogeneous (also referred to as 1-layer representation). Results of analysis are presented and discussed in detail. Plain sand embankments P1 and P2 of same height and top width were also analyzed by treating them to be homogeneous and with excitation A1 and results of analyses compared with those of M1 to highlight advantages of using reinforced earth.

Using two layers of equal depths is a better representation of embankment and, hence, expected to improve results. To highlight this, M1 and M3 were analyzed by such representation. For further improvement of results, embankment may be represented by more than two layers.

5.4.1 Acceleration Response

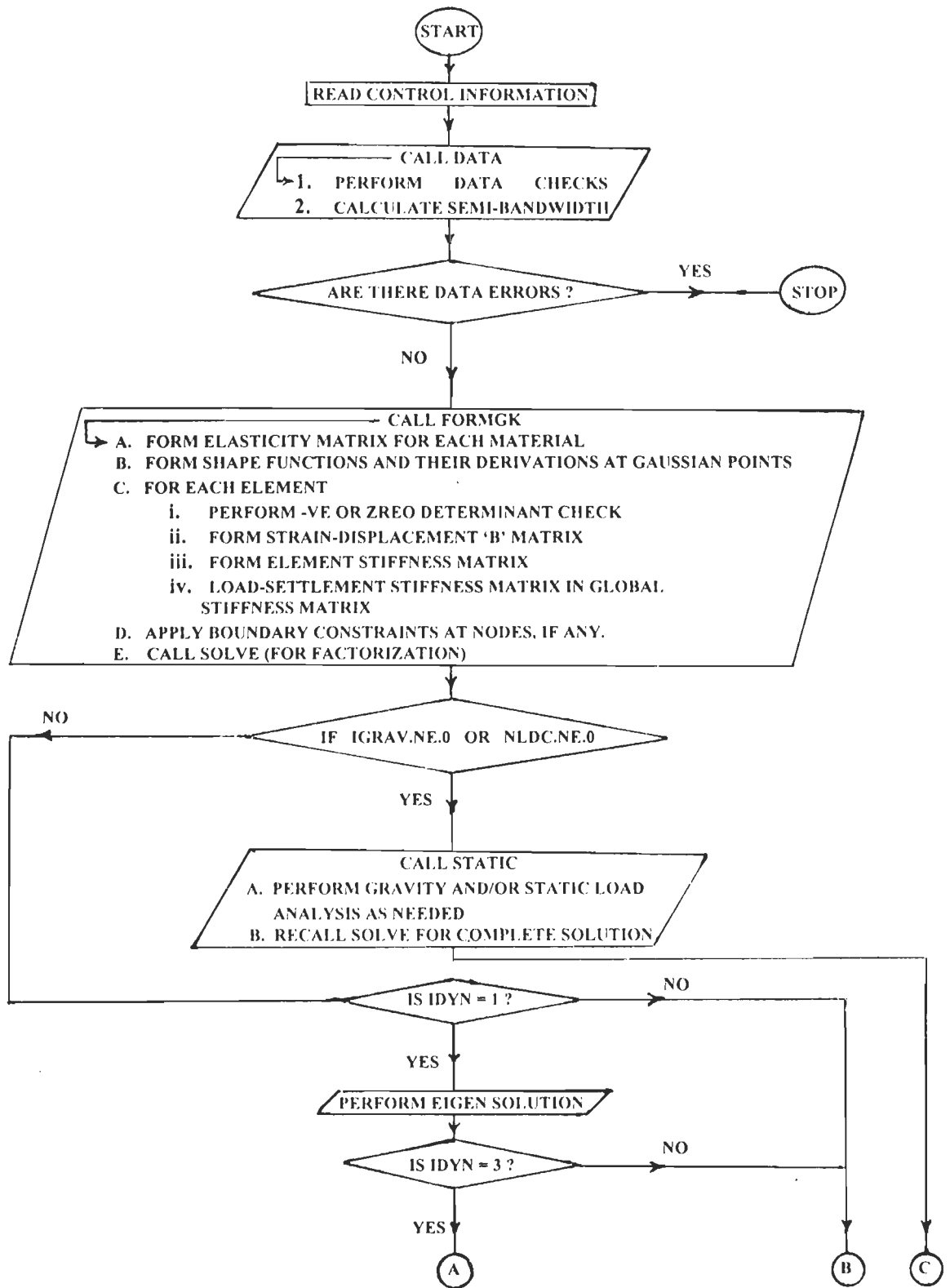
If $a_p(t)$ and $a_b(t)$ are accelerations at time t at any point p and at embankment base respectively, relative acceleration, $a_{rp}(t)$, at any point p is given by:

$$a_{rp}(t) = a_p(t) - a_b(t) \quad (5.4.1)$$

Accelerations of M1

Figure 5.4.1a shows a_{rp} at nodes 22, 66, 88 and 132 situated along vertical longitudinal face of M1 with single layer idealization and for excitation A1 and with damping ratios, ζ_1 and ζ_2 for the first and second modes equal to 0.05 each. Response is plotted only for first two seconds for clarity of figure. Transient vibrations die completely within initial 0.637 s duration followed by steady state vibrations at frequency of excitation. With increasing distance from base, a_{rp} increases due to amplification of motion. Peak transient acceleration is 1.49 times that for steady state. Above observations are as expected.

Figure 5.4.1b shows similar plot for M1 with $\zeta_1=0.17$ and $\zeta_2=0.255$ and excited with A1. Transient vibrations die completely within first 0.336 s. Transient vibration peaks are smaller than steady state peak acceleration. Amplification of response also increases with distance from base. Frequency



(Continued on pp.332)

FIG. 5.3.8 FLOW DIAGRAM OF SOFTWARE FE95.

(Continued from pp.331)

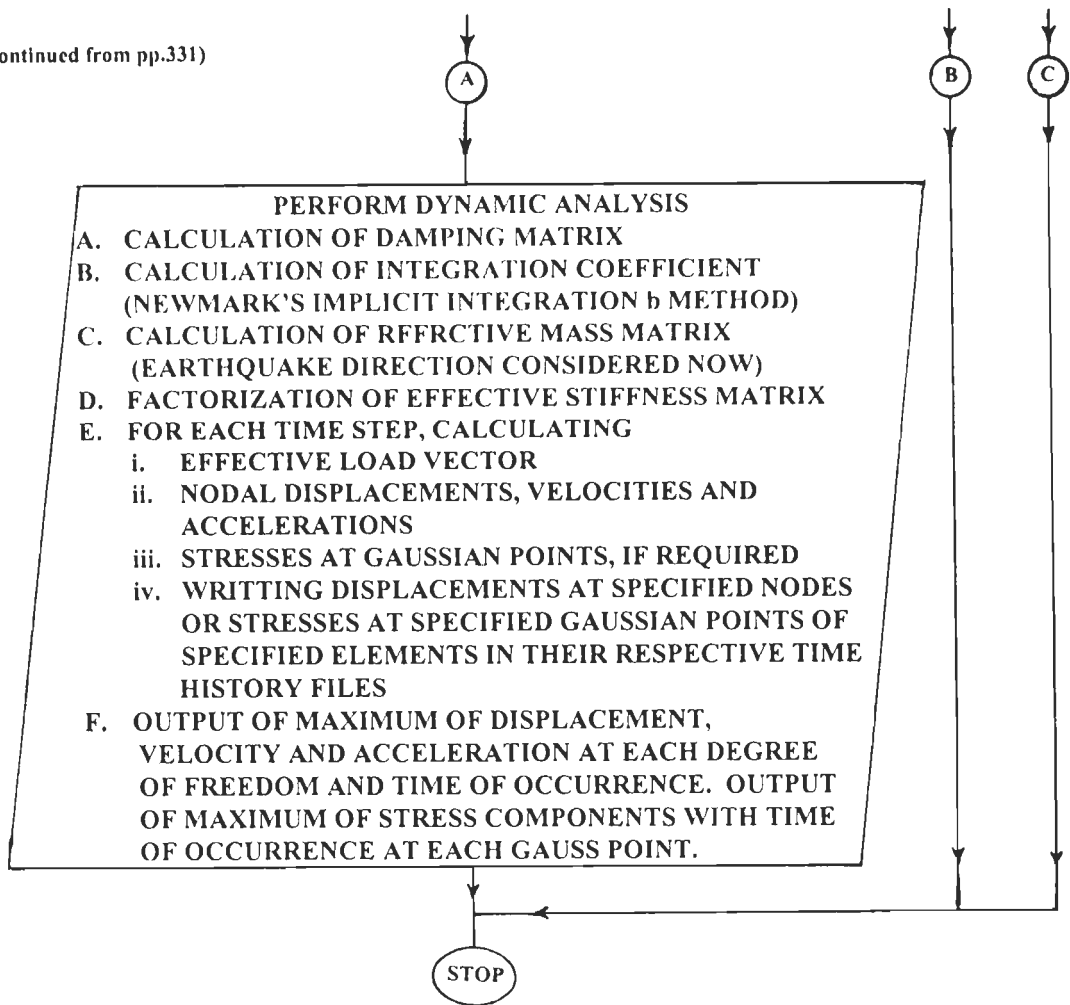


FIG. 5.3.8 FLOW DIAGRAM OF SOFTWARE FE95.

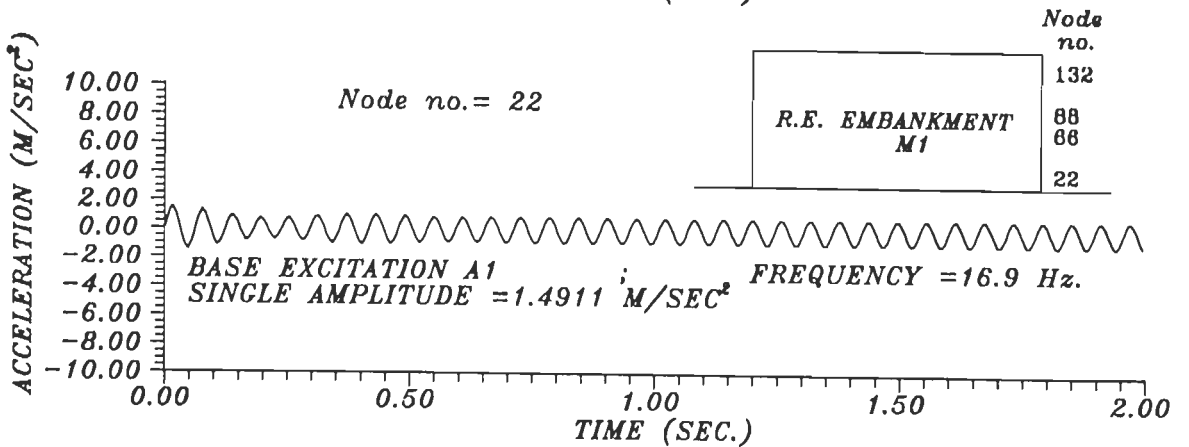
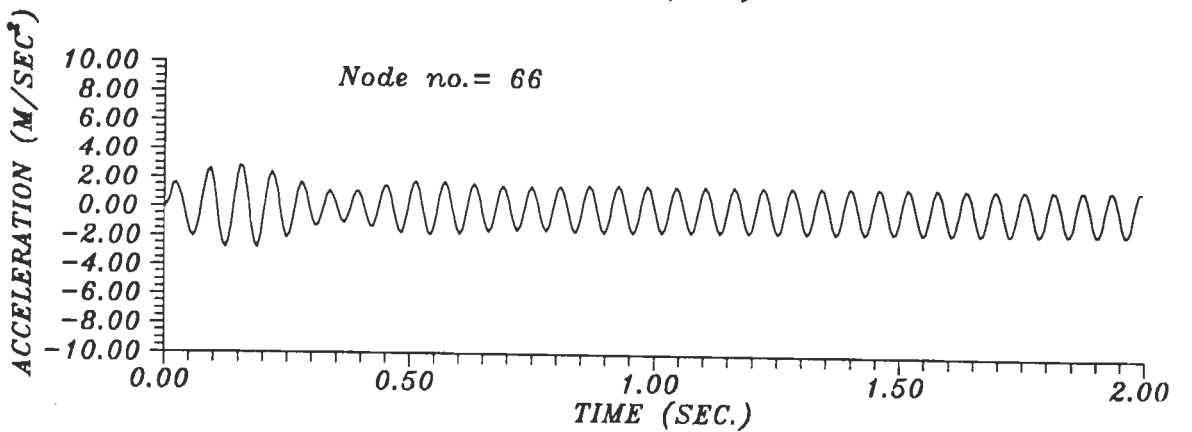
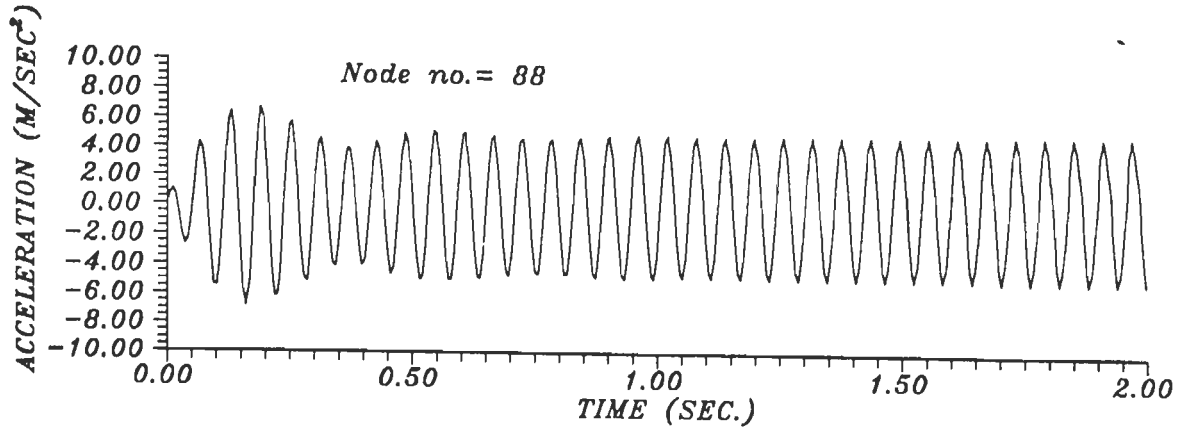
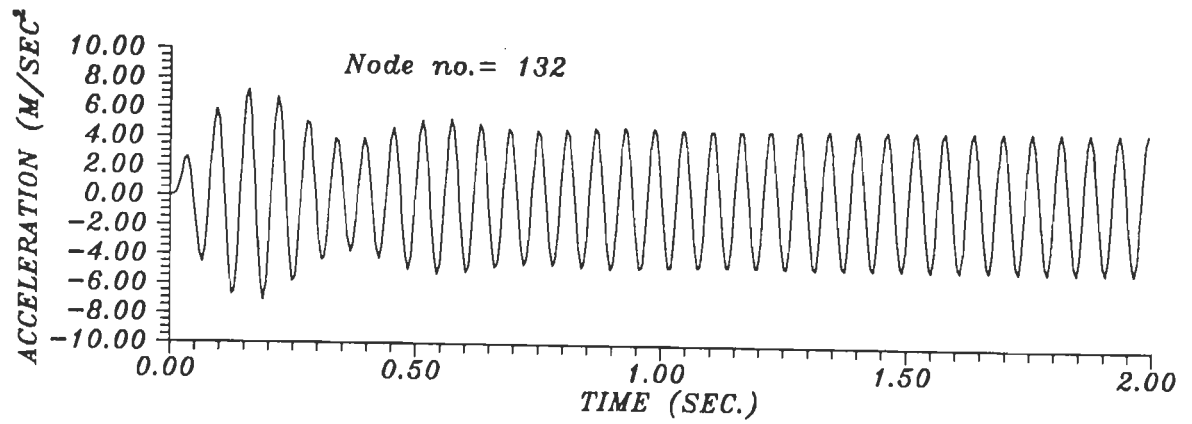


FIG.5.4.1a COMPUTED RELATIVE ACCELERATION OF EMBANKMENT M1, EXCITED AT BASE EXCITATION A1 (OME =24) FOR $\zeta_1 = 0.05$.

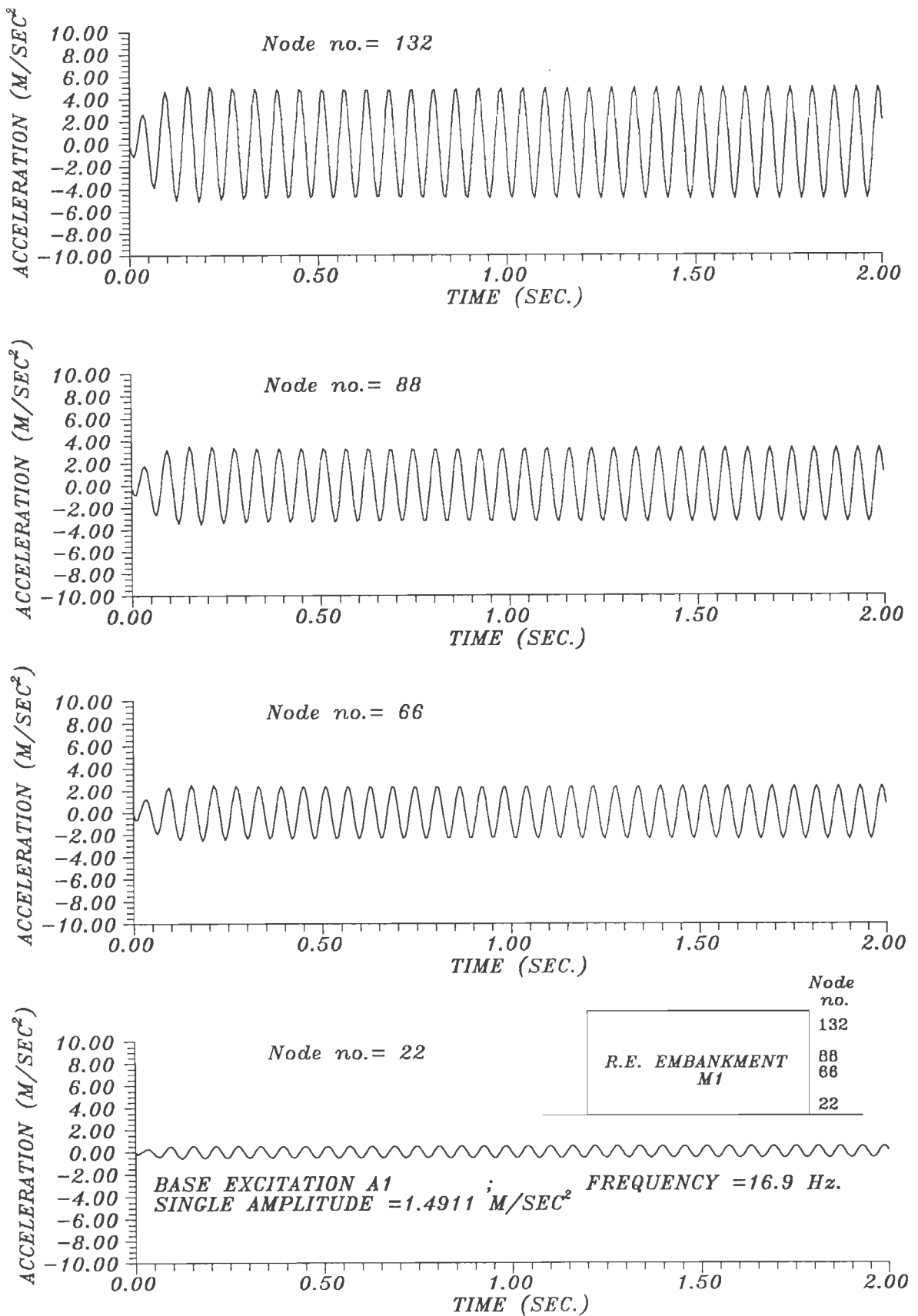


FIG.5.4.1b COMPUTED RELATIVE ACCELERATION OF EMBANKMENT M1, EXCITED AT BASE EXCITATION A1 (OME =24) FOR $\zeta_1 = 0.17$.

of steady state vibrations are at that for base excitation as in the previous case. Increased damping reduced large acceleration peak of transient vibrations by 71% and duration of transient vibrations by almost 50% w.r.t. those for the case with $\zeta_1=0.05$ and $\zeta_2=0.05$ as expected.

Accelerations of M3

Results of analysis of M3 with excitation A3 using $\zeta_1=0.05$ and $\zeta_2=0.05$ by employing 1-layer idealization are not plotted, because, they showed characteristics similar to those for M3 with 2-layer idealizations under same conditions. Figure 5.4.2a shows results for 2-layer idealization of M3 with $\zeta_1=0.05$ and $\zeta_2=0.05$ and excited with A3. For this case, transient vibrations die completely within initial 0.479 s followed by steady state vibrations at excitation frequency. There are no peak transient vibration acceleration larger than peak steady state acceleration. With increasing distance from base a_{rp} increases as was the case with M1.

Figure 5.4.2b shows results of analysis with 2-layer idealization of M3 with $\zeta_1=0.124$ and $\zeta_2=0.186$ and excited with A3. For this case, transient vibrations die down after 0.341 s with no peak transient vibration accelerations larger than steady state peak. Steady state acceleration amplitude gets reduced by 53.33% and duration of transient vibration by 28.8% w.r.t. those for the case with $\zeta_1=0.05$ and $\zeta_2=0.05$. These results indicate that ζ_1 has very strong influence on response of embankment. Hence, it is important to choose its values very carefully.

Accelerations of plain sand embankments

Duration of transient vibrations of P1 with excitation A1 is 0.56 s followed by steady state vibrations at excitation frequency (Fig.5.4.3).

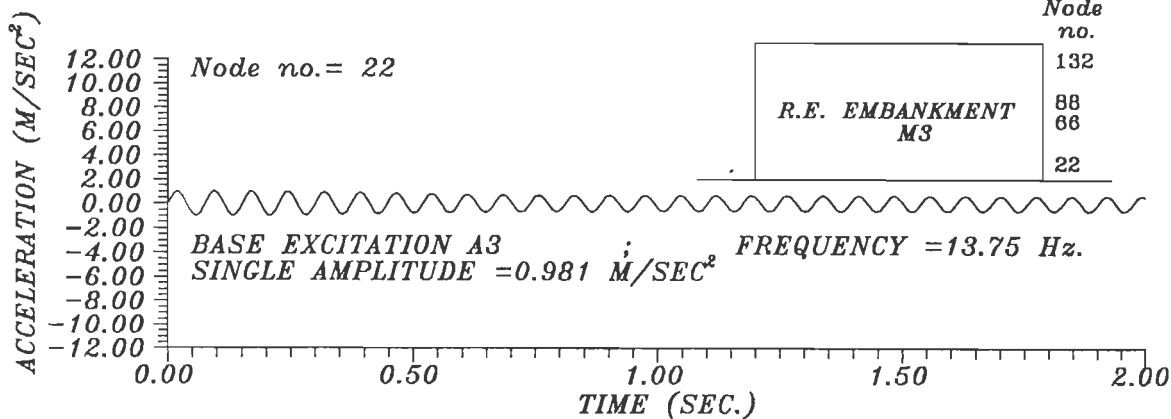
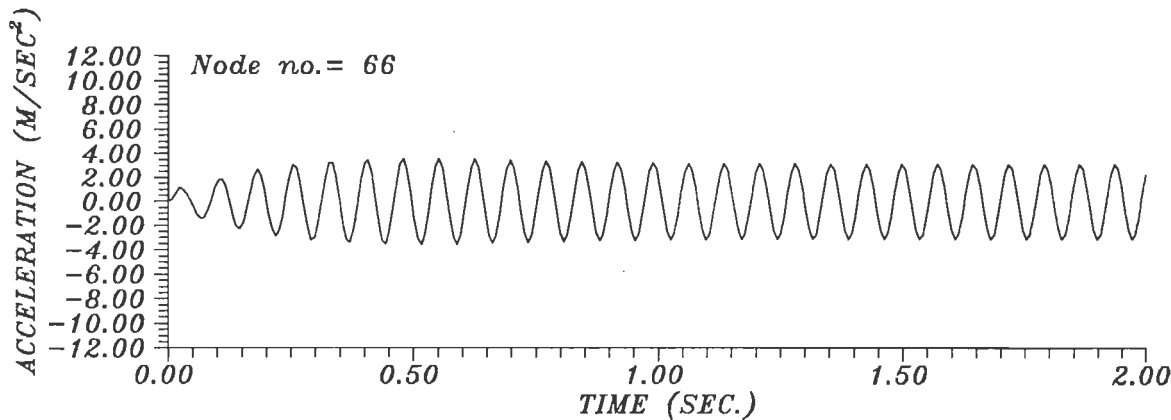
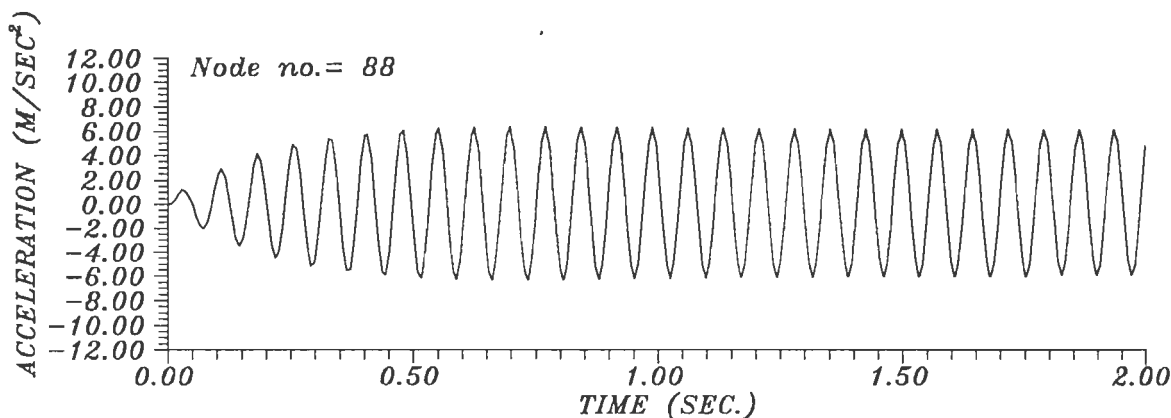
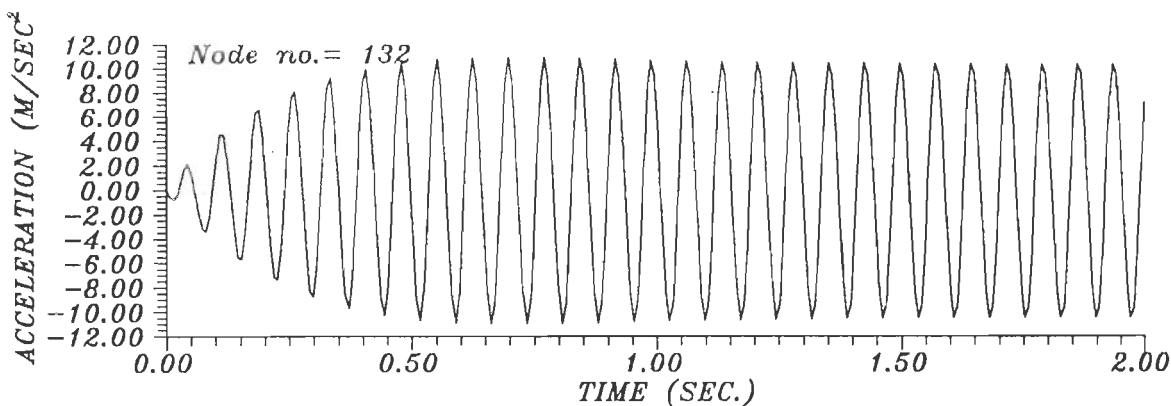


FIG.5.4.2a COMPUTED RELATIVE ACCELERATION OF EMBANKMENT M3, EXCITED AT BASE EXCITATION A3 (OME =24) FOR $\zeta_1 = 0.05$

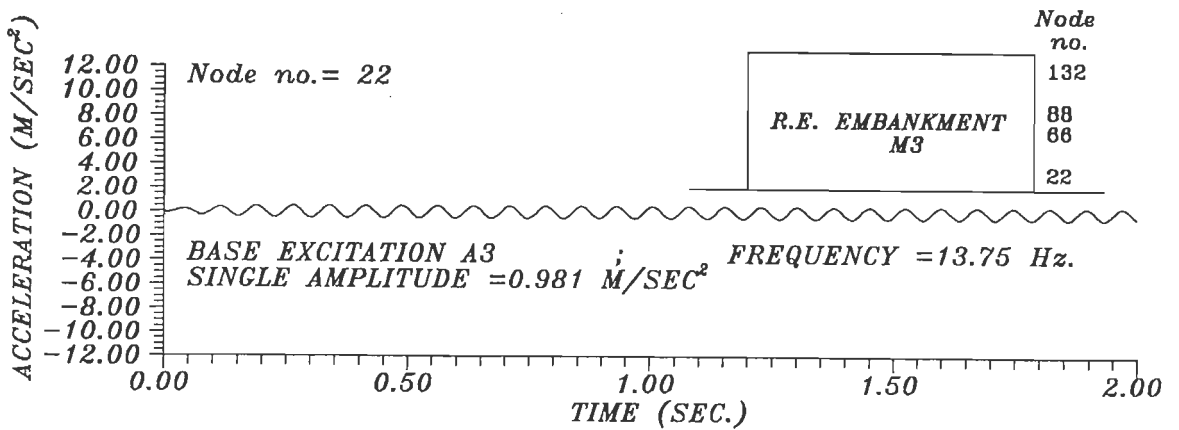
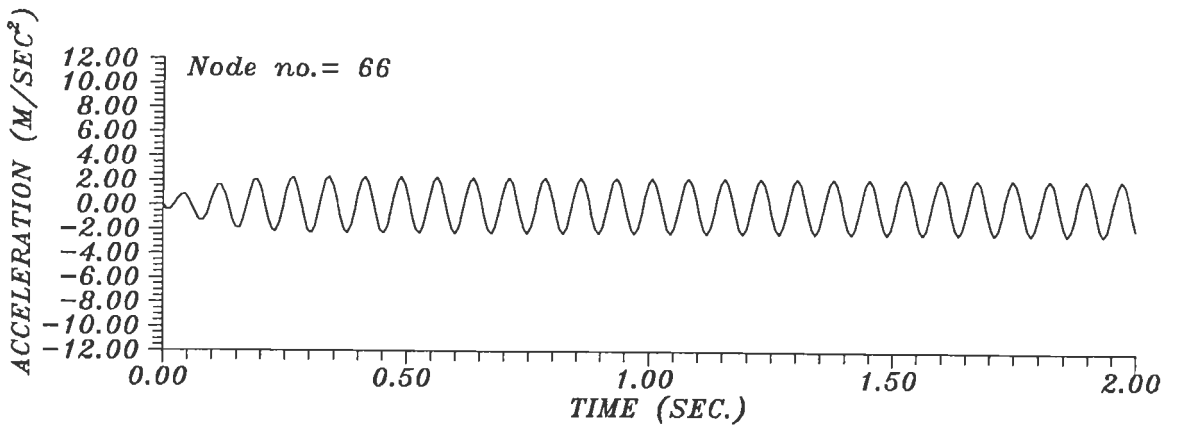
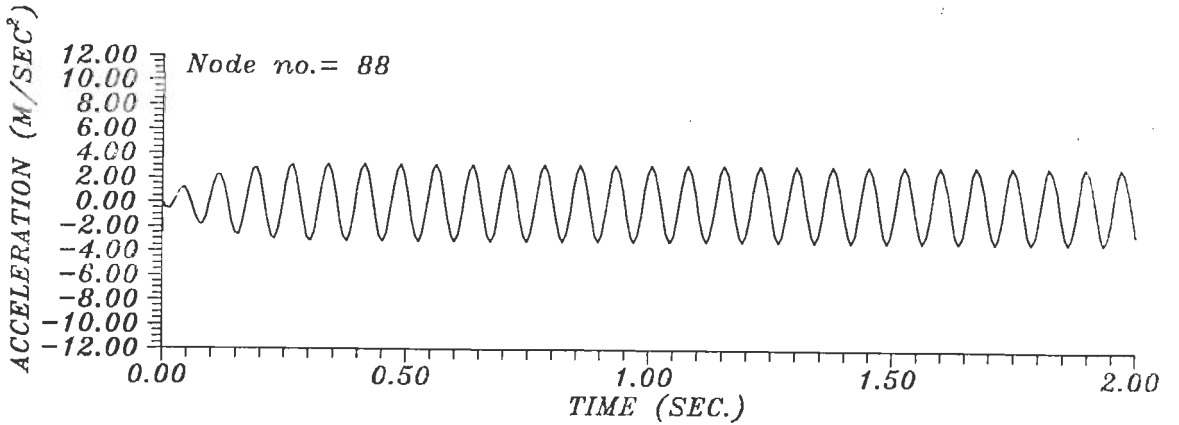
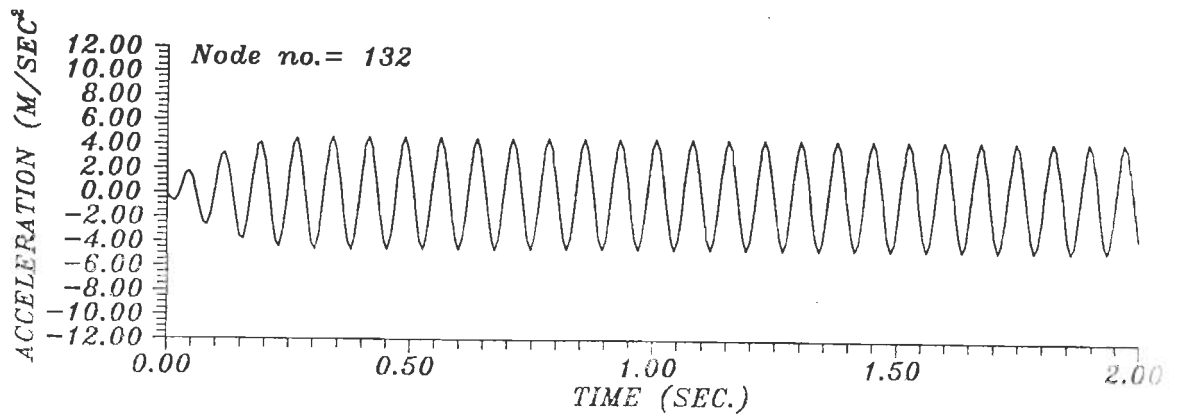


FIG.5.4.2b COMPUTED RELATIVE ACCELERATION OF EMBANKMENT M3, EXCITED AT BASE EXCITATION A3 ($\omega = 24$) FOR $\zeta_1 = 0.124$.

This duration is shorter than that for M1 since strain levels and damping are higher than those for M1. At peak transient acceleration at node no. 132 of P1, a_{rp} is 12 where as that for M1 is 7.17 only for same excitation indicating that with increasing distance from base, a_{rp} for weaker P1 increases at a faster rate compared to that for M1. Similar observations were made from results of analysis of P2 with same excitation, ζ_1 and ζ_2 . Acceleration amplitudes obtained for P2 were smaller than those for P1, because, base width of P2 is larger than that of P1. As such, similar plots of results obtained for P2 are not presented.

Comparison of analytical and experimental accelerations

Knowing computed maximum absolute accelerations, a_{cM1} and a_{cM3} , for M1 and M3 respectively and those obtained from tests (a_{eM1} and a_{eM3} for M1 and M3 respectively), the acceleration ratio, r_a , is defined as:

$$r_a = a_{cM1} / a_{eM1} \quad (5.4.2)$$

Ideal value of r_a denoted by, r_{aideal} , is unity. Percentage discrepancy between r_a and r_{aideal} is denoted by, r_{ad} , and expressed as:

$$r_{ad} = 100(r_a - r_{aideal}) / r_{aideal} \quad (5.4.3)$$

Figure 5.4.4 shows r_{ad} at 0.527H below top end on longitudinal face of embankment obtained with various damping ratios for M1 excited with A1 and M3 with A3. It indicates that for the ideal case of $r_{ad}=0$ with no discrepancy between analytical and experimental responses, $\zeta_1=0.1275$ for M3 and $\zeta_1=0.18$ for M1 which are plotted on Fig. 5.3.1 also. For M1, ζ_1 is slightly larger than damping given by average damping curve. For M3, ζ_1 is slightly larger than damping given by lower bound damping curve. As such,

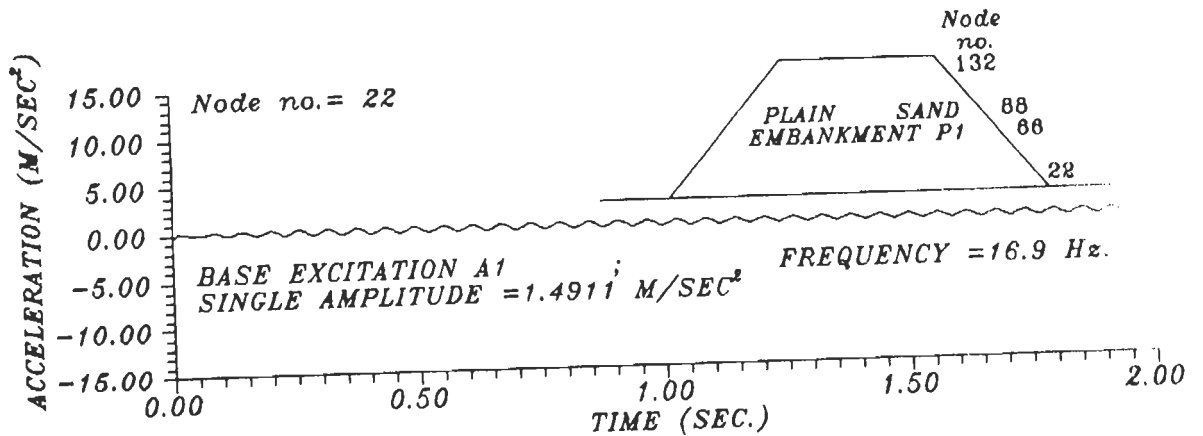
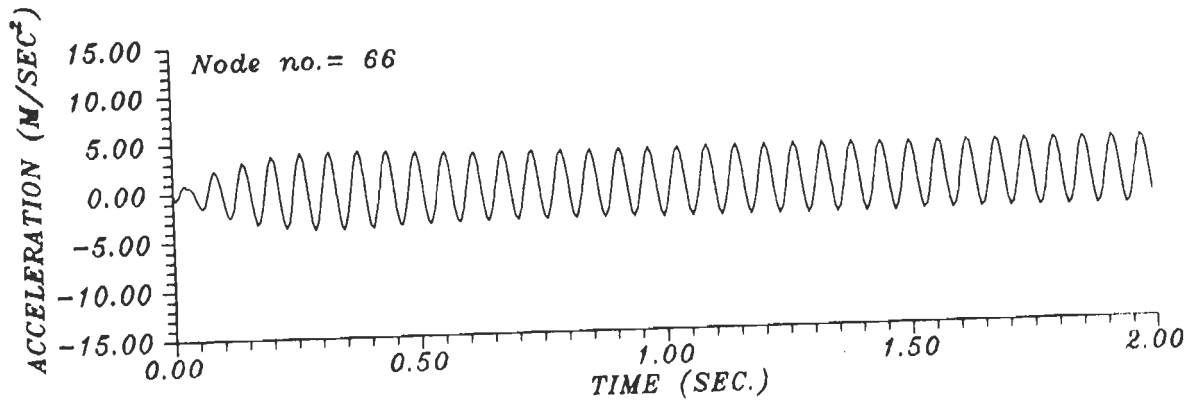
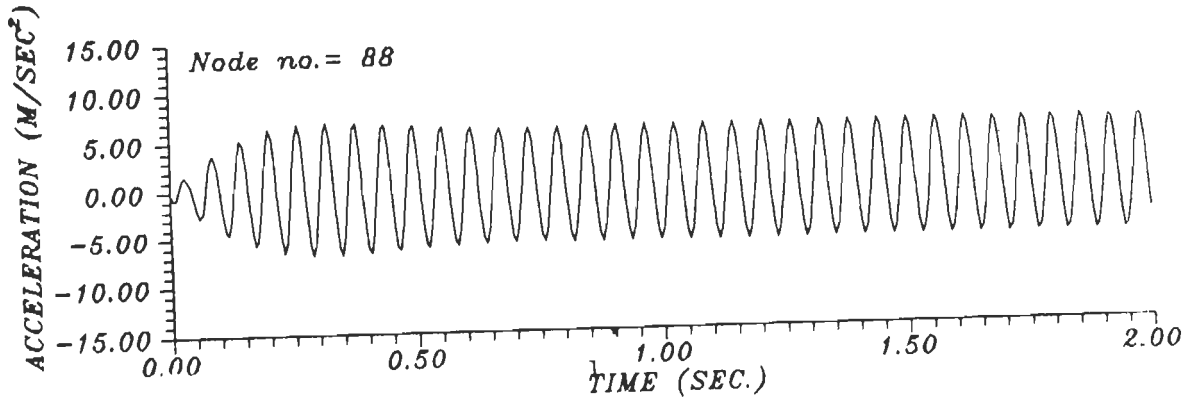
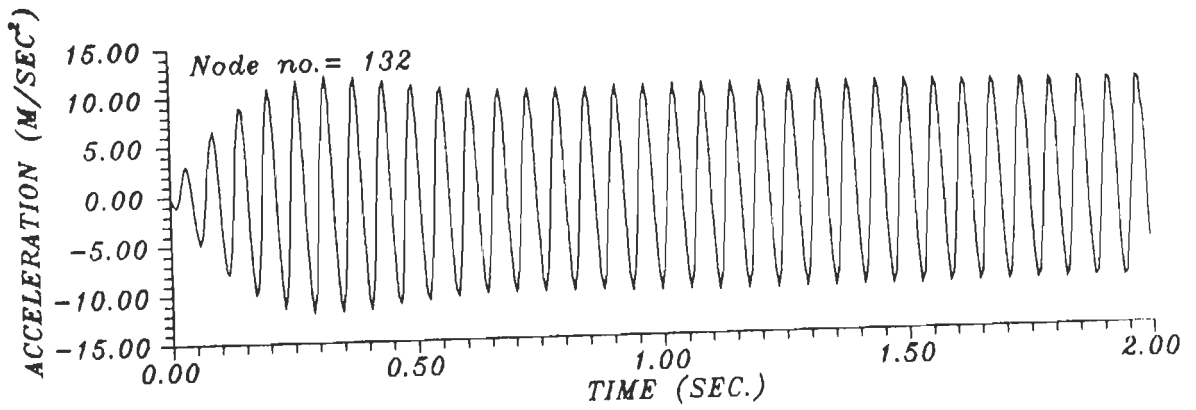


FIG.5.4.3 COMPUTED RELATIVE ACCELERATION OF PLAIN SAND EMBANKMENT P1, EXCITED AT BASE EXCITATION A1 ($\omega = 24$).

ζ_1 values obtained from present investigation are within limits suggested by Seed et. al. (1984). In this study, damping for plain sand was assumed to be same as that for R.E. in which it is used as a fill (Article 5.3). This is confirmed from the above finding.

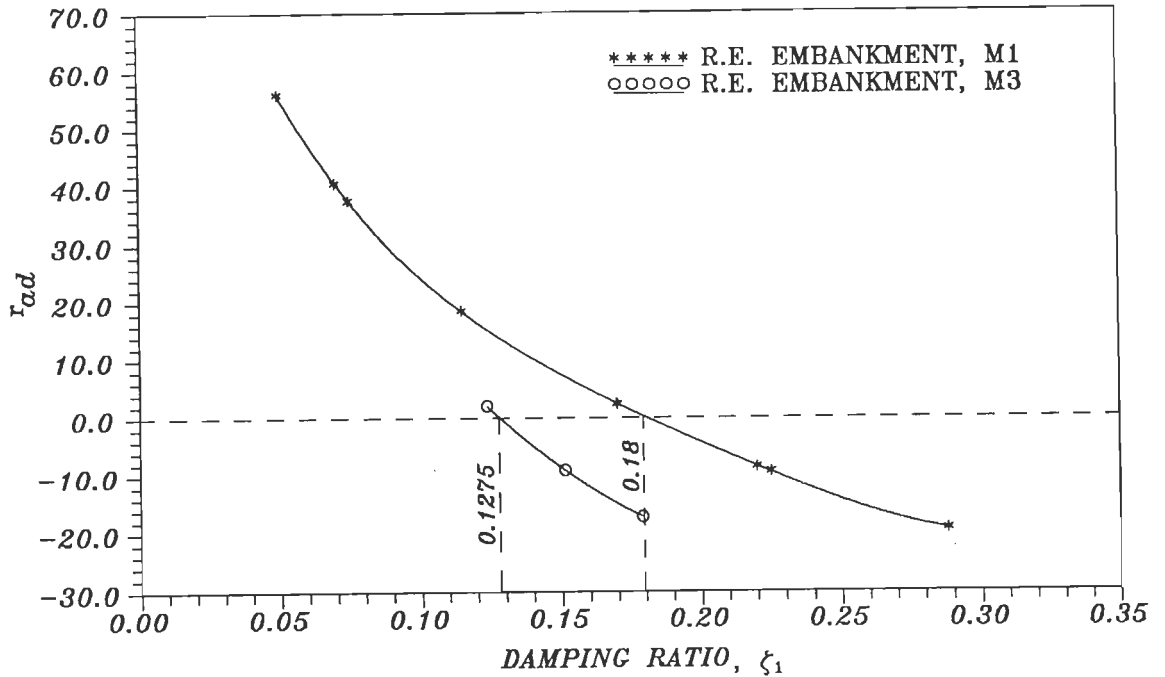


FIG.5.4.4 VARIATION OF DAMPING RATIO, ζ_1 , WITH PERCENTAGE DISCREPANCY IN ACCELERATION, r_{ad} , AT MID-DEPTH OF R.E. EMBANKMENTS M1 AND M3 IDEALIZED AS HOMOGENEOUS SINGLE LAYER.

It looks ironical that $\zeta_1=0.18$ for M1 at $\gamma=1.35 \times 10^{-3}$ is higher than $\zeta_1=0.1275$ for M3 at $\gamma=1.625 \times 10^{-3}$, because, ζ_1 normally increases with γ . However, present day state of art indicates that ζ_1 is influenced strongly by σ_{oct} , γ , void ratio and number of loading cycles and to a lesser extent by degree of saturation, octahedral shear stress and ϕ of soil. Range of ζ_1 at these γ values is so large that upper bound of ζ_1 is about 187 to 196% of the corresponding lower bound ζ_1 . Besides, 89.3% of the range of variation of damping for these two strain levels is common to both these strain levels (Fig. 5.3.1). From the present study, $\zeta_1=0.18$ at $\gamma=1.35 \times 10^{-3}$ for M1 is only 41% larger than $\zeta_1=0.1275$ at $\gamma=1.625 \times 10^{-3}$ for M3. This discrepancy of 41%

is less than the range of 89% variation of damping at these strains recommended by Seed et. al. (1984). From Fig. 5.3.1, it may be observed that in the range of shear strained from 10^{-4} to 2×10^{-3} the lower bound curve proposed by Seed et. al. (1984) is some what above the the lower bound curve if equal weightage is given to density of data plotted. This makes ζ_1 values obtained from the present investigation to be even more respectable. Clearly, better methods of evaluation of damping are urgently needed. In view of the large number of factors influencing damping, the values of damping obtained from the present investigation may be considered to be reasonably acceptable.

It is very much desirable that exact value of damping is determined by minimising discrepancy between experimental and analytical response for large R.E. embankments on the lines described in this investigation. However, in absence of the experimental data of this kind, evaluation of proper value of damping will be a difficult task indeed. This also highlights the need for facilities for testing large R.E. embankments in laboratory under dynamic loads.

For M1, Fig. 5.4.5 compares computed maximum absolute acceleration (a_{c1M1}) obtained with 1-layer idealization and the computed maximum absolute acceleration (a_{c2M1}) obtained with 2-layer idealization with maximum absolute acceleration (a_{eM1}) obtained from tests at different dimensionless depths (X/H). The figure also shows variation of acceleration ratio, r_a , with (X/H). Value of $\zeta_1=0.17$ used in this analysis is very close to $\zeta_1=0.18$ obtained from Fig. 5.4.4 for $r_{ad}=0$ for ideal case. Figure 5.4.6 shows variation of r_a and percentage discrepancy in acceleration, r_{ad} , with (X/H) for M1 for the above two idealizations.

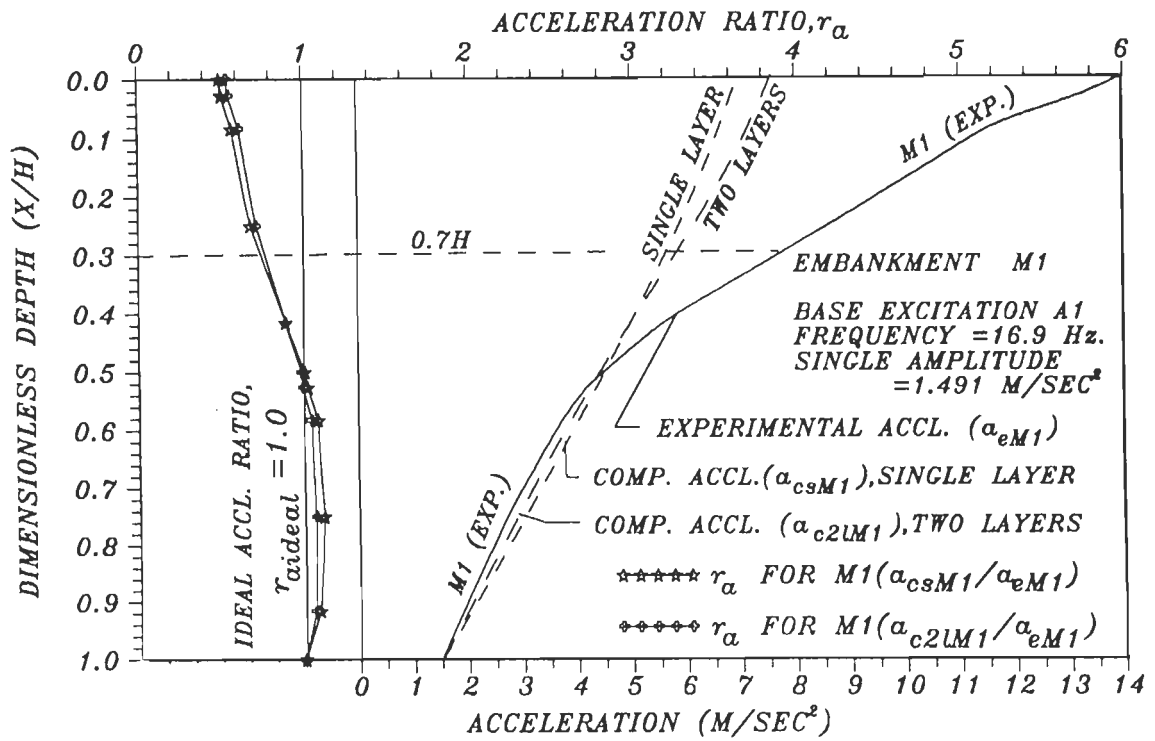


FIG.5.4.5 COMPUTED AND EXPERIMENTALLY RECORDED MAXIMUM ACCELERATION WITH DIMENSIONLESS DEPTH (X/H) FOR R.E. EMBANKMENT M1 EXCITED AT ITS FUNDAMENTAL FREQUENCY ($\omega_{ME} = 24$).

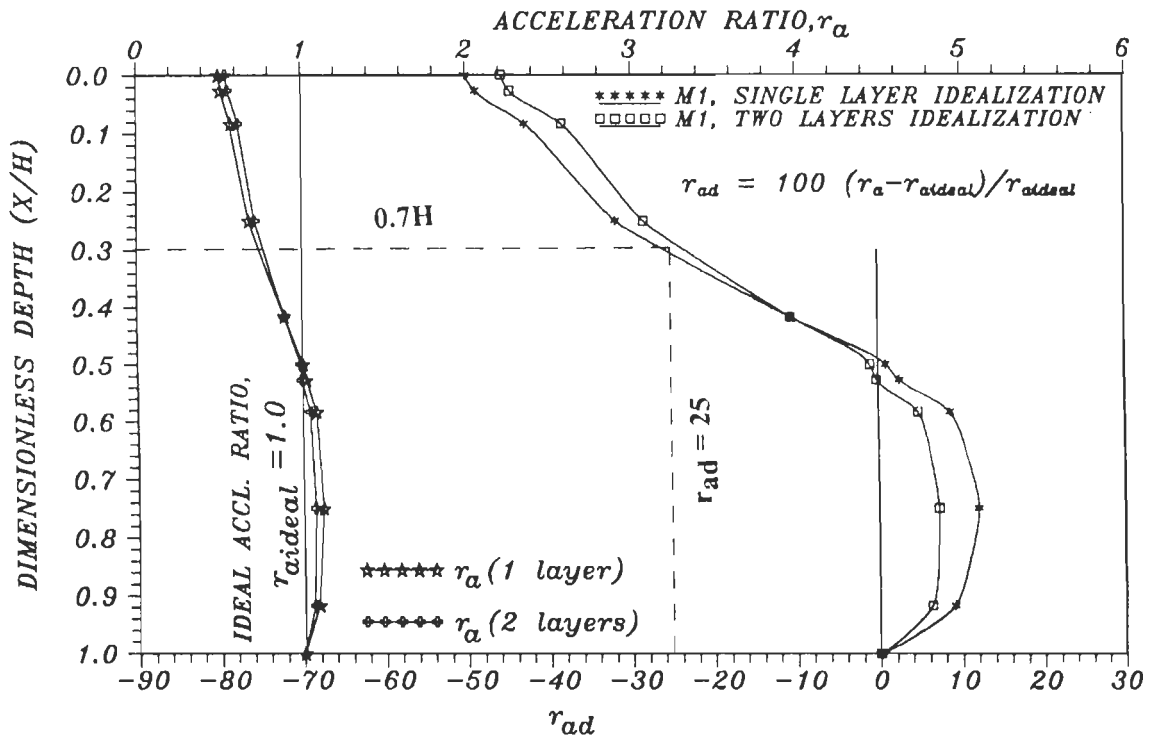


FIG.5.4.6 VARIATION OF PERCENTAGE DISCREPANCY IN ACCELERATION, r_{ad} , WITH DIMENSIONLESS DEPTH (X/H) FOR R.E. EMBANKMENT M1 IDEALIZED AS HOMOGENEOUS SINGLE AND TWO LAYERS.

In above figures, computed response is in good agreement with that obtained from tests upto 0.61H above base. The largest r_{ad} is only 12% which is small. If $r_{ad}=\pm 25\%$ is tolerable, this good agreement extends upto 0.7H above base. For entire depth, average $r_a=0.8626$ and corresponding $r_{ad}=-13.74\%$ which too is small. In top 0.3H depth, measured response is larger than computed responses. Measured response is closer to computed one for the superior 2-layer idealization than that for 1-layer idealization.

Figure 5.4.7 and Fig. 5.4.8 show similar plots for M3. Value of $\zeta_1=0.124$ used in this analysis is very close to $\zeta_1=0.1275$ obtained from Fig. 5.4.4 for $r_{ad}=0$ for the ideal case. In above figures, computed response is in good agreement with that obtained from tests upto 0.62H above embankment base, because, $-12.8\% < r_{ad} < 12.8\%$ which is quite tolerable. If $r_{ad}=\pm 25\%$ is considered tolerable, then this good agreement extends upto 0.72H above base. For the entire depth, the average $r_a=0.879$ and corresponding $r_{ad}=-12\%$ only which is also small. In the top 0.28H depth, measured response is larger than computed responses. However, computed response with 2-layer idealization is closer to measured response than that from 1-layer idealization, which is expected due to better idealization.

Discrepancy between measured and computed responses for M1 and M3 is larger near embankment top, because, shear modulus in that region is close to zero and smaller than uniform shear modulus assigned to homogeneous layer idealizing that region. Further improvements in computed response in top portion can be achieved by considering larger number of homogeneous layers in that portion of embankment.

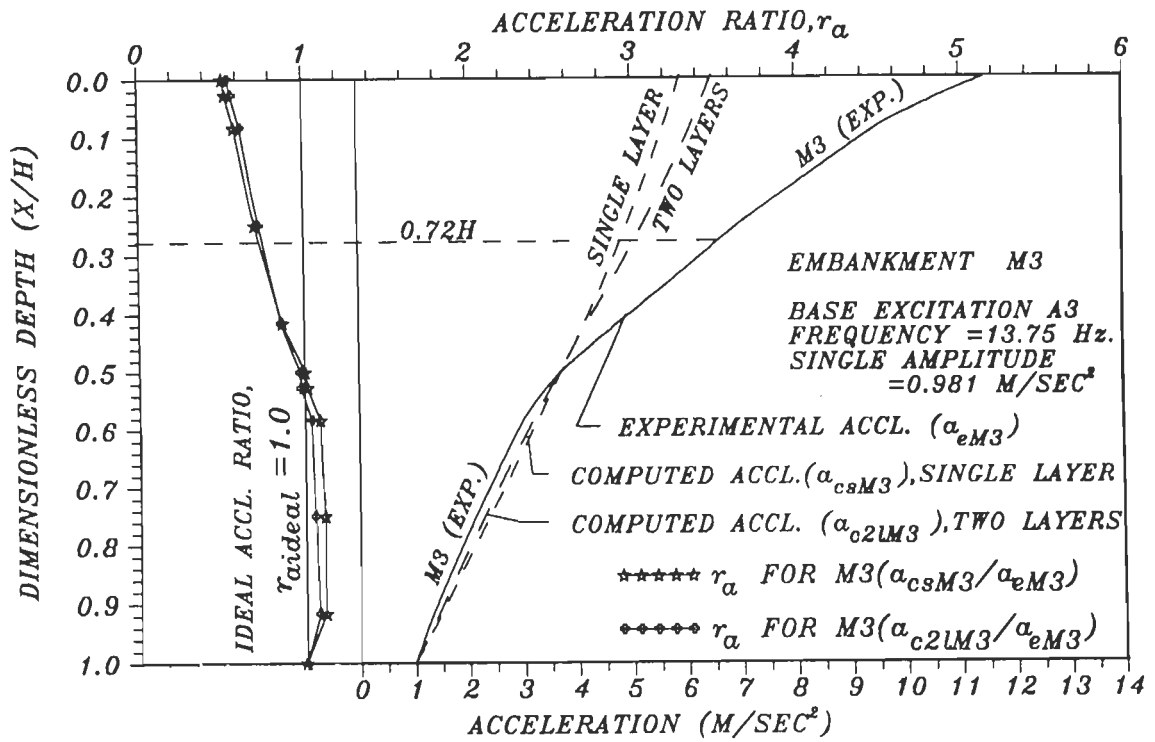


FIG.5.4.7 COMPUTED AND EXPERIMENTALLY RECORDED MAXIMUM ACCELERATION WITH DIMENSIONLESS DEPTH (X/H) FOR R.E. EMBANKMENT M3 (OME =24).

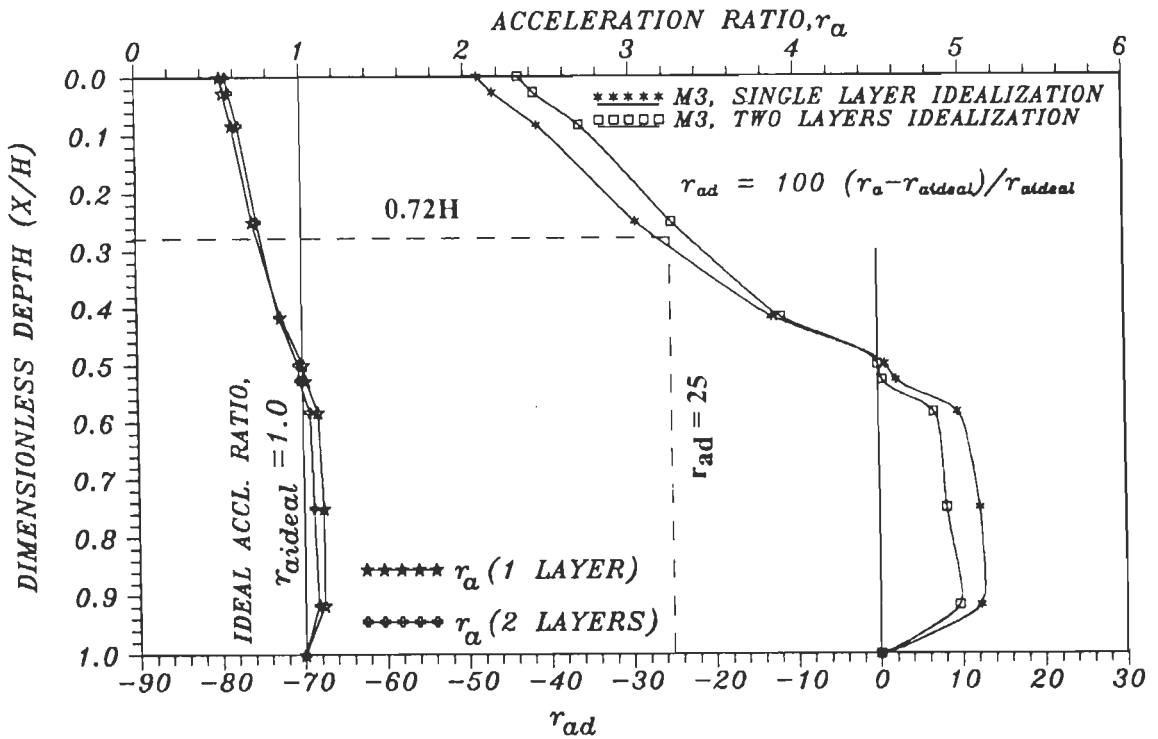


FIG.5.4.8 VARIATION OF PERCENTAGE DISCREPANCY IN ACCELERATION, r_{ad} , WITH DIMENSIONLESS DEPTH (X/H) FOR R.E. EMBANKMENT M3 IDEALIZED AS HOMOGENEOUS SINGLE AND TWO LAYERS.

Figure 5.4.9 shows computed absolute accelerations of P1 and P2 excited with A1. Accelerations for P1 were larger than those for P2 with flatter slopes as expected. The figure also shows accelerations from tests on M1 which are nearly equal to those of P1 and P2 close to base, because, influence of lower shear moduli of P1 and P2 w.r.t. that of M1 is nearly compensated by their larger base width compared to that of M1. As expected, acceleration of P2 is less than that of P1 for almost entire depth since P2 with a wider base is stiffer than P₁. In spite of much larger base widths, P1 and P2 show larger accelerations compared to those of M1 from tests upto 0.6H below top. This shows advantage of R.E. embankments for a given H and top width. This is even more pronounced for embankments with larger H.

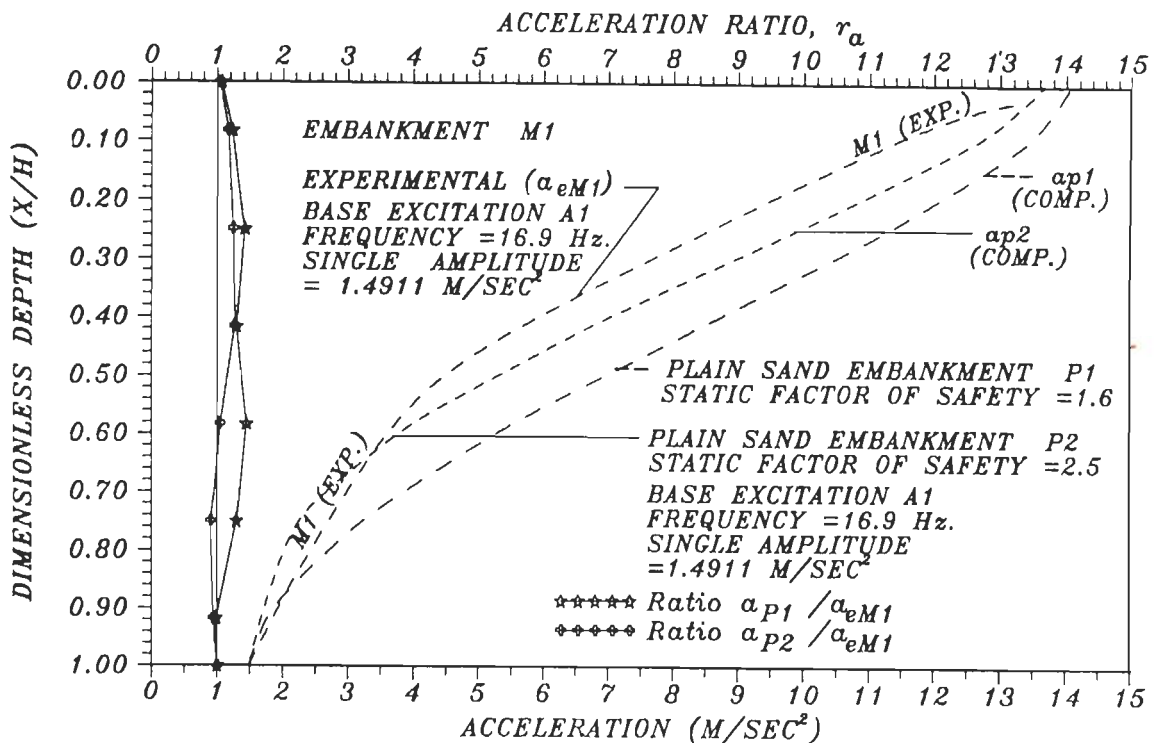


FIG.5.4.9 COMPARISON OF COMPUTED MAXIMUM ABSOLUTE ACCELERATION FOR PLAIN SAND EMBANKMENTS P1 AND P2 WITH THAT OF M1 FROM TEST.

Figure 5.4.10 shows acceleration amplification of M1, P1 and P2 excited with A1. Amplification increases almost linearly with distance from base for

M1. For P1 and P2, amplifications are nonlinear with much larger rate of increase near top end compared to that in lower half. This is expected. Amplification at top end of P1 and P2 are much larger since top widths of all embankments are equal and shear moduli of P1 and P2 are much smaller than that of M1. On the other hand, in lower half of embankment amplification for P1 and P2 are smaller than that for M1 inspite of their lower shear moduli, because, increase in base width has a greater influence compared to lower moduli.

Ratio of amplification factor of P1 or P2 to that of M1 excited with A1 is defined as r_{am} . Figure 5.4.11 shows r_{am} for P1 and P2. For P1 and P2 for $(X/H) > 0.5$, $r_{am} < 1$, i.e., amplification of P1 and P2 is much lower than that for M1. This is in view of larger base width of P1 and P2. For top 40% of depth for P1 and P2, $r_{am} > 1$, i.e., amplification of P1 and P2 are larger than that for M1 due to lower shear moduli for same top width. This is expected as plain sand embankments are more prone to damage in top quarter height due to earthquakes. This is supported by field observations of many earthquakes. Therefore, R.E. embankment with lesser quantity of fill performs far better than plain sand embankments having larger section.

5.4.2. Displacement Response

If $d_p(t)$ and $d_b(t)$ are displacements at time t at any point p and at embankment base respectively, relative displacement, $d_{rp}(t)$, at any point p is given by $\{d_p(t) - d_b(t)\}$.

Analytical displacements of embankments

Figure 5.4.12a shows d_{rp} with $\zeta_1 = 0.05$ and Fig. 5.4.12b shows d_{rp} with $\zeta_1 = 0.17$ for nodes on longitudinal face of M1 excited with A1. With

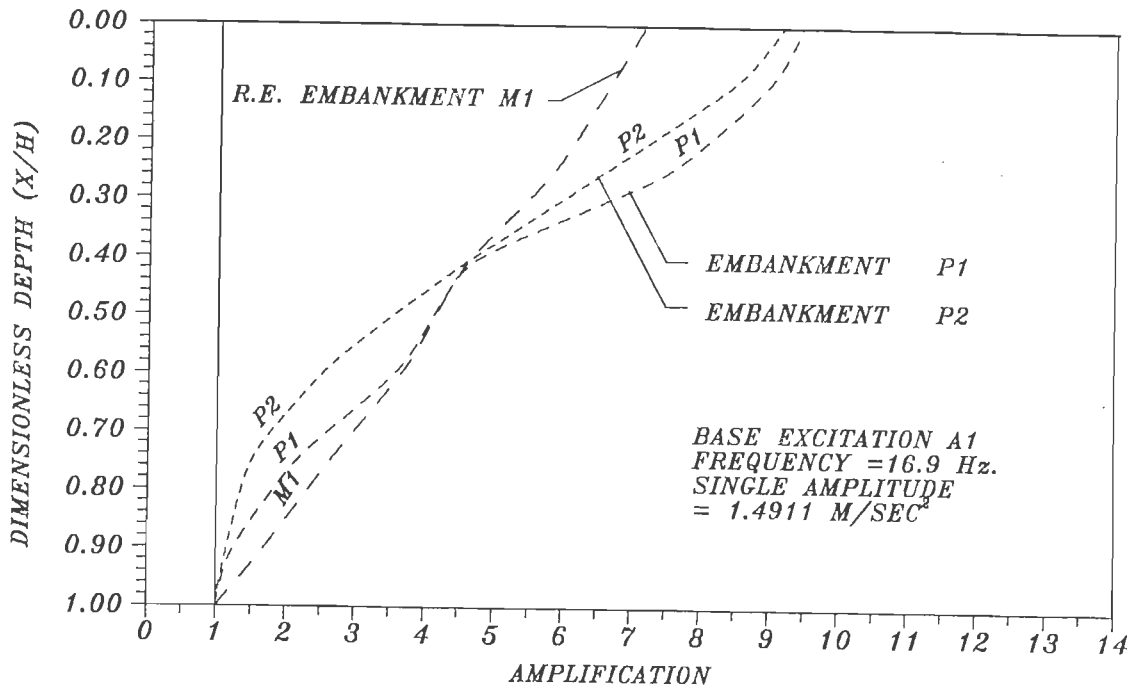


FIG.5.4.10 COMPARISON OF COMPUTED AMPLIFICATION FOR R.E. EMBANKMENT M1 AND PLAIN SAND EMBANKMENTS P1 AND P2.

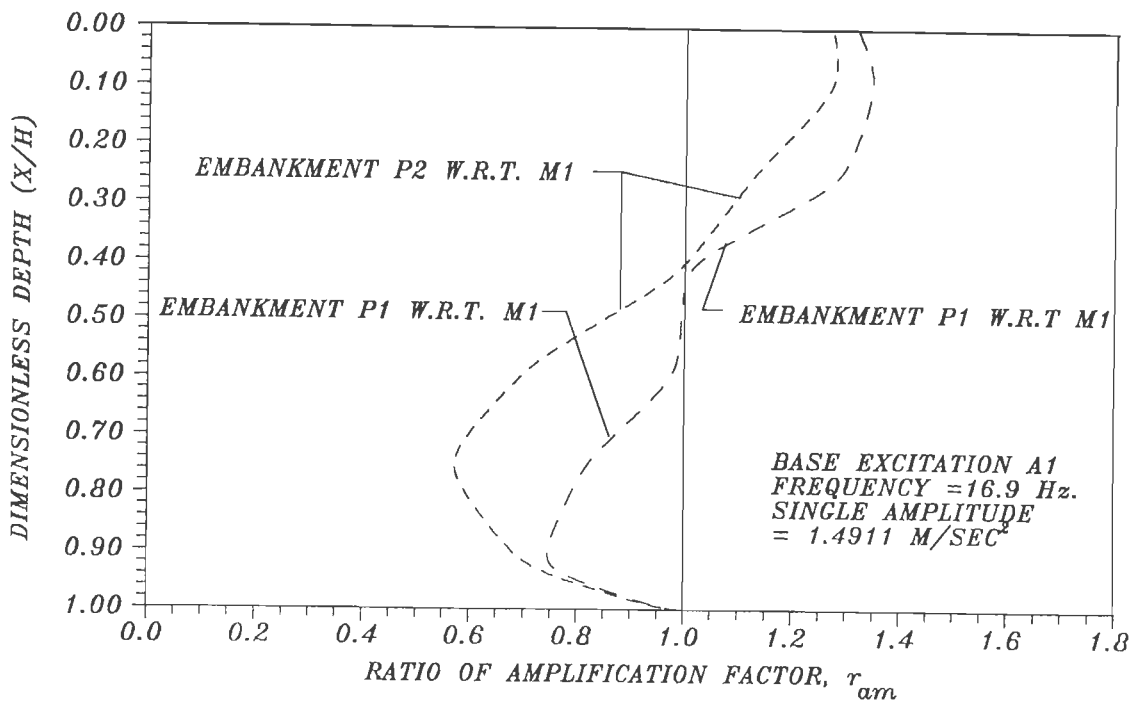


FIG.5.4.11 RATIO OF COMPUTED AMPLIFICATION FACTOR, r_{am} , OF EMBANKMENTS P1 AND P2 W.R.T. THAT OF M1.

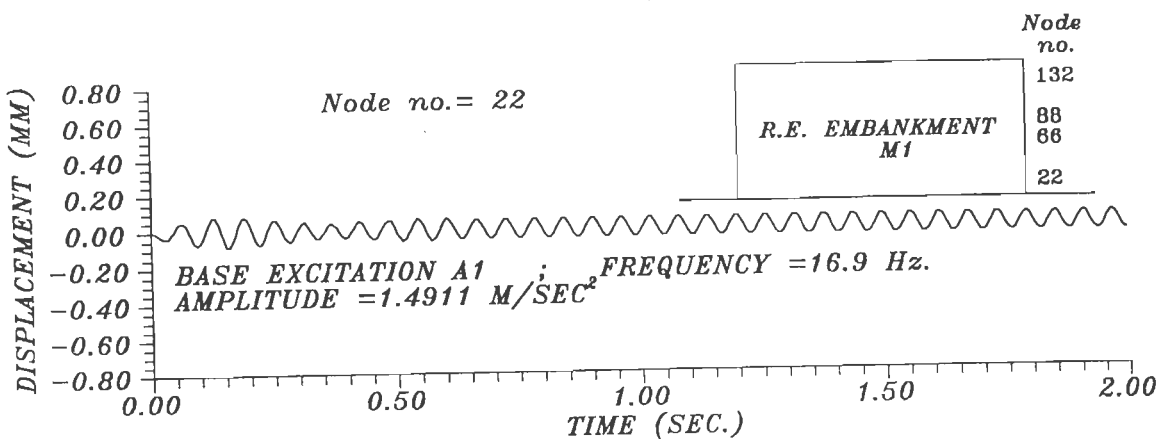
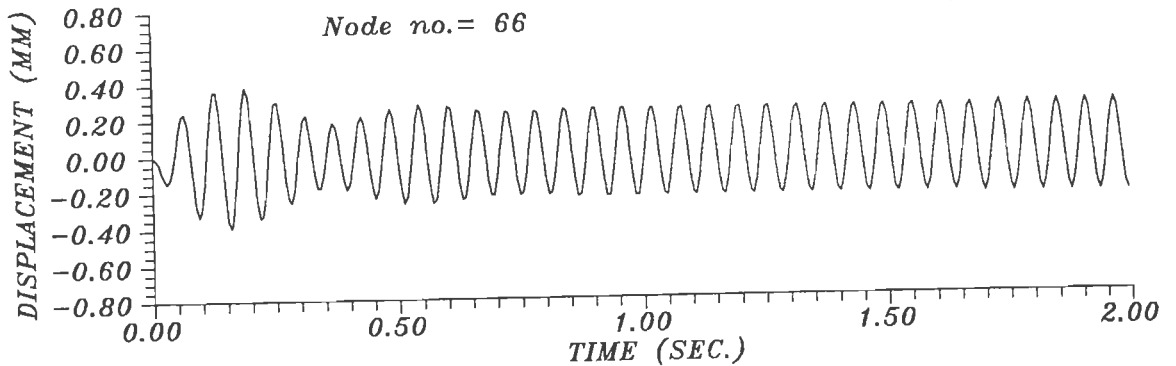
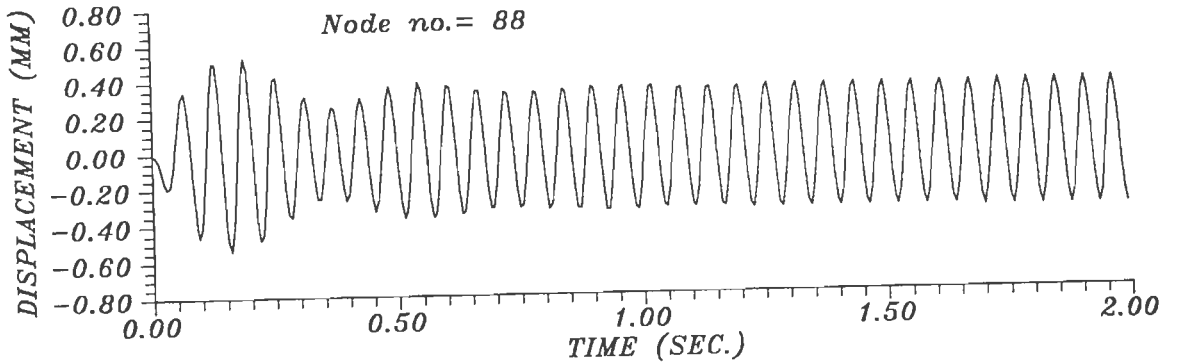
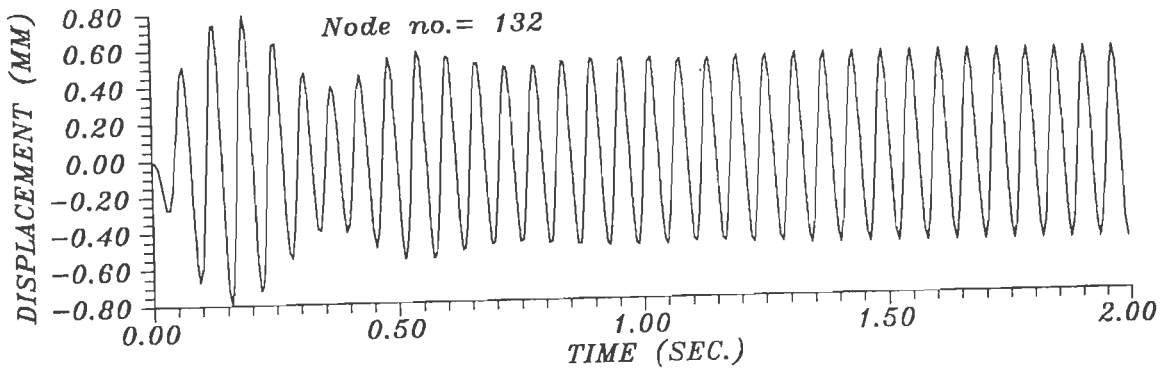


FIG.5.4.12a COMPUTED RELATIVE DISPLACEMENT OF R.E. EMBANKMENT M1 EXCITED AT BASE EXCITATION A1 ($\omega = 24$) FOR $\zeta_1 = 0.05$.

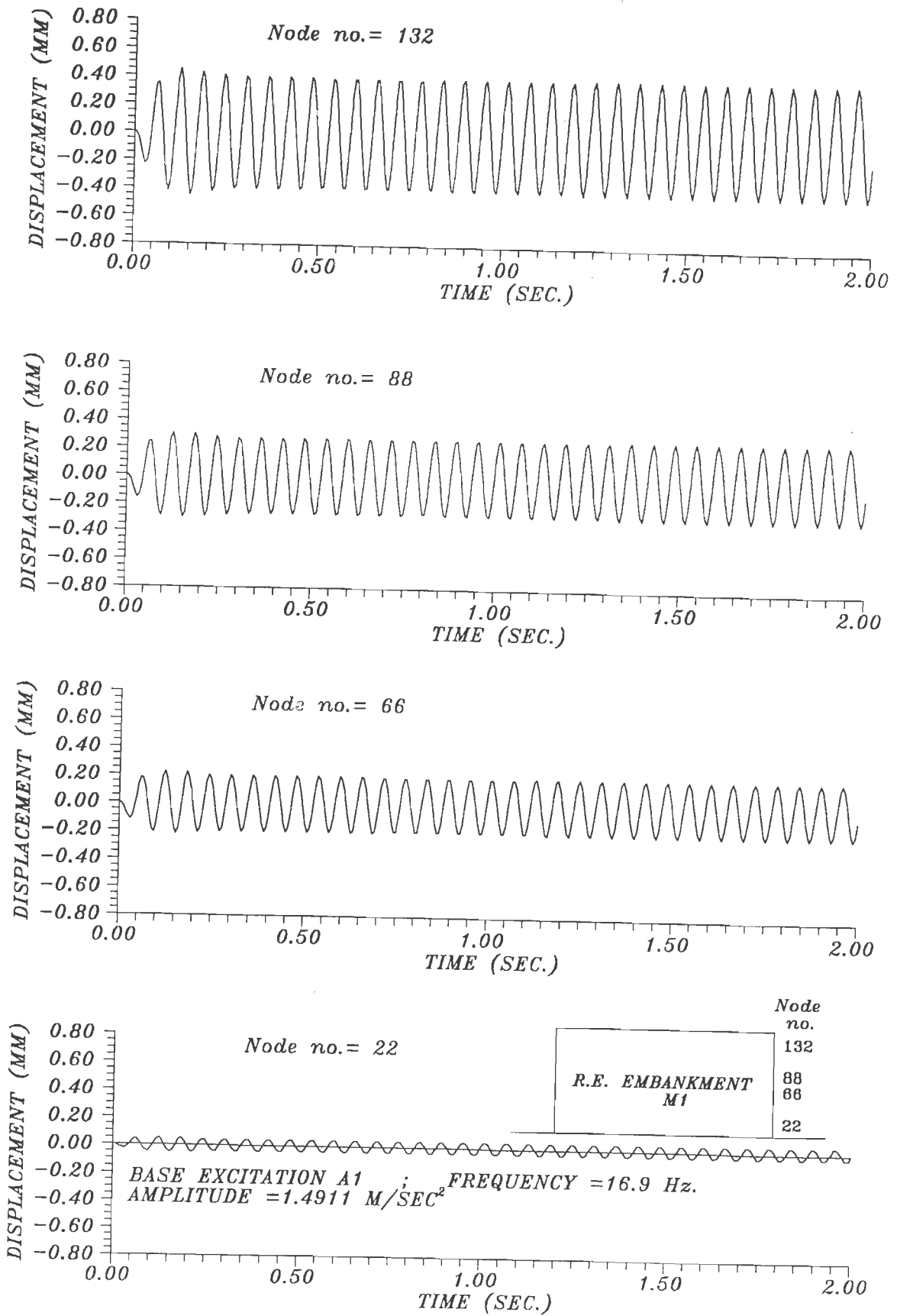


FIG.5.4.12b COMPUTED RELATIVE DISPLACEMENT OF R.E. EMBANKMENT M1 EXCITED AT BASE EXCITATION A1 ($\omega = 24$) FOR $\zeta_1 = 0.17$.

increasing distance from base, d_{rp} increases as expected. Observations about duration of transient vibrations, ratio of transient displacement peak to steady state displacement peak and frequency of steady state vibrations are same as those for relative accelerations (Fig. 5.4.1a and b) as expected. Similar plot for M3 excited with A3 with $\zeta_1=0.05$ is shown in Fig. 5.4.13a and that for $\zeta_1=0.124$ is shown in Fig. 5.4.13b. Observations from these figures are similar to those from Fig. 5.4.2a and b for relative accelerations cited earlier. For P1 excited with A1, Fig. 5.4.14 shows d_{rp} for nodes along side slopes. Observations from this figure are similar to those from Fig. 5.4.3 for relative accelerations for P1. Similar observations were made from results of analysis of P2 with same excitation, ζ_1 and ζ_2 . Displacement amplitudes obtained for P2 were smaller than those for P1, because, base width of P2 is larger than that of P1. As such, similar plots of results obtained for P2 are not presented.

Comparison of analytical and experimental displacements

Knowing computed maximum absolute displacements, d_{cM1} and d_{cM3} , for M1 and M3 respectively and those obtained from tests (d_{eM1} and d_{eM3} for M1 and M3 respectively), the displacement ratio, r_d , is defined as:

$$r_d = d_{cM1} / d_{eM1} \quad (5.4.4)$$

Ideal value of r_d denoted by, r_{dideal} , is unity. Percentage discrepancy between r_d and r_{dideal} is denoted by, r_{dd} , and expressed as:

$$r_{dd} = 100(r_d - r_{dideal}) / r_{dideal} \quad (5.4.5)$$

For M1, Fig. 5.4.15 compares computed maximum absolute displacement (d_{c1M1}) obtained with 1-layer idealization and the computed maximum absolute displacement (d_{c2M1}) obtained with 2-layer idealization with maximum

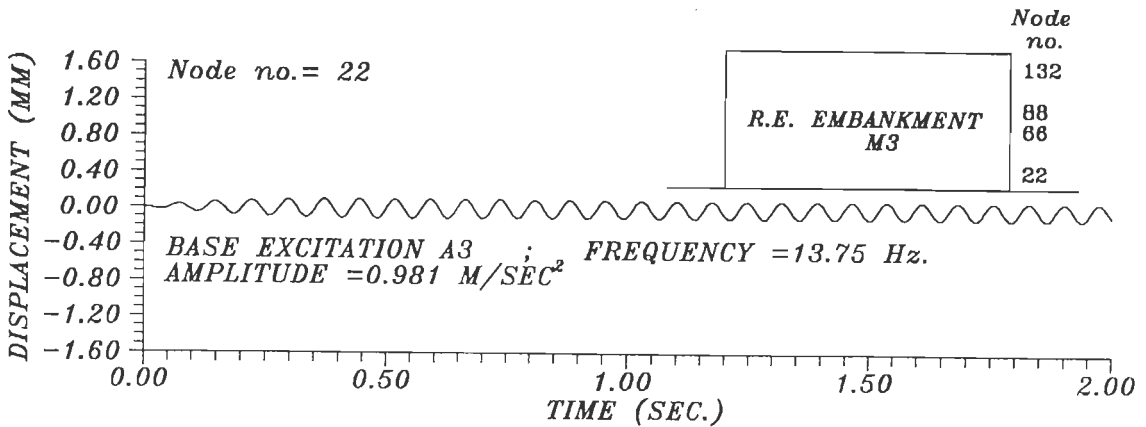
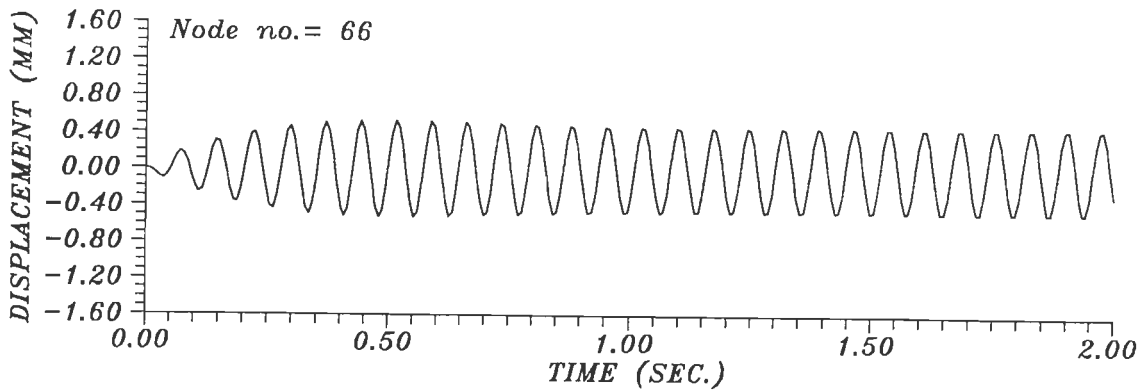
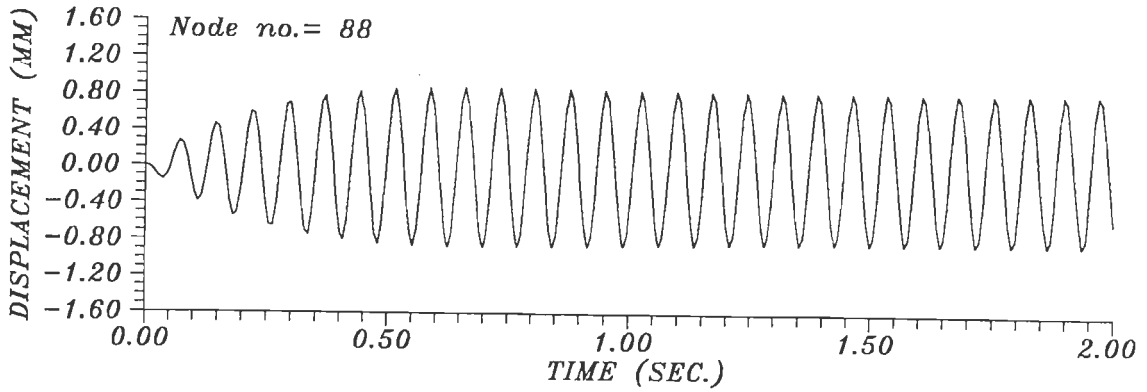
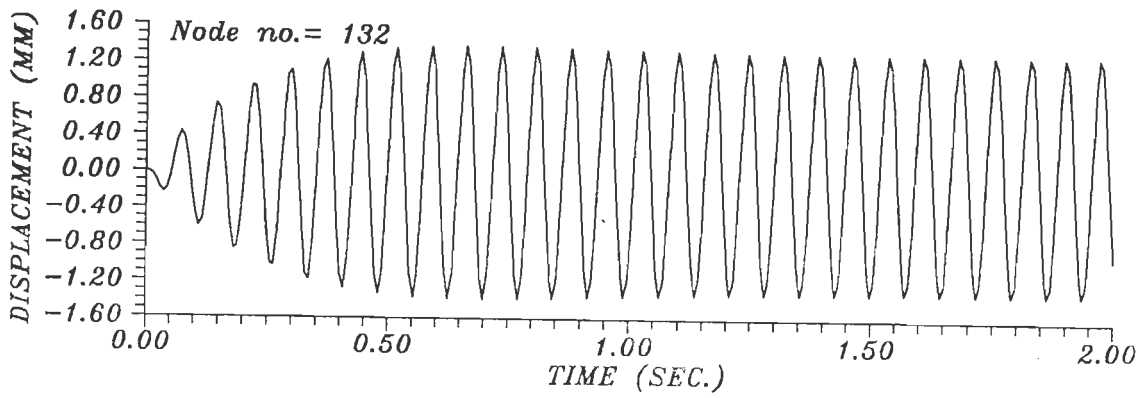


FIG.5.4.13a COMPUTED RELATIVE DISPLACEMENT OF R.E. EMBANKMENT M3 EXCITED AT BASE EXCITATION A3 ($\omega = 24$) FOR $\zeta_1 = 0.05$.

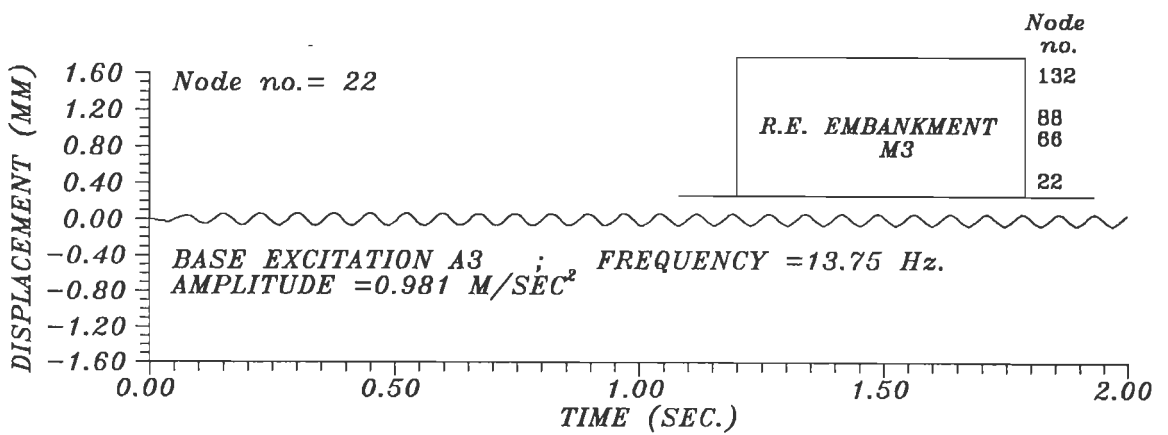
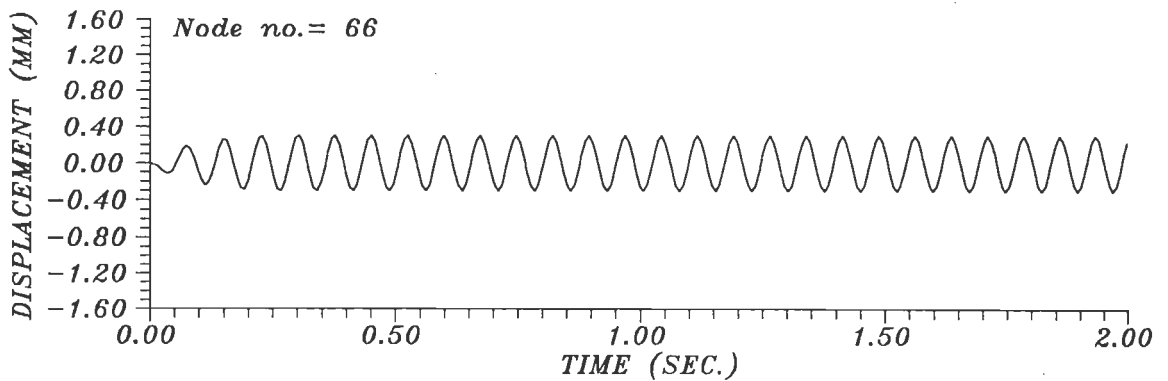
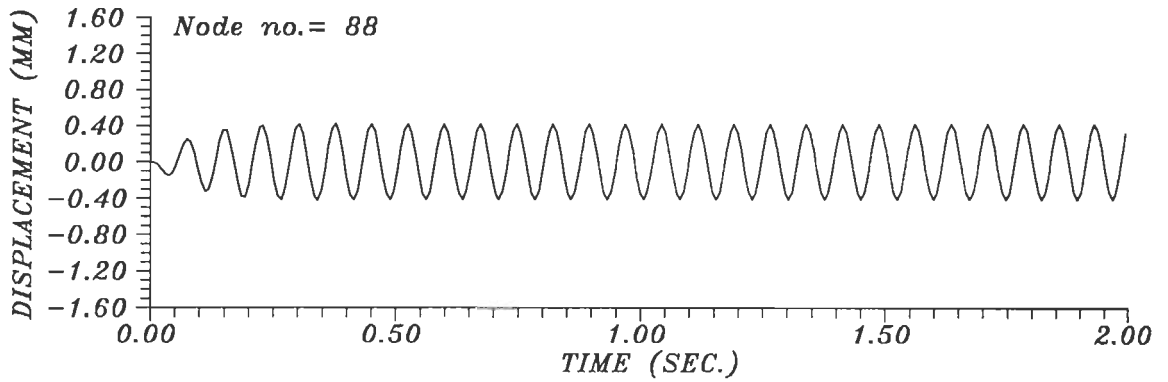
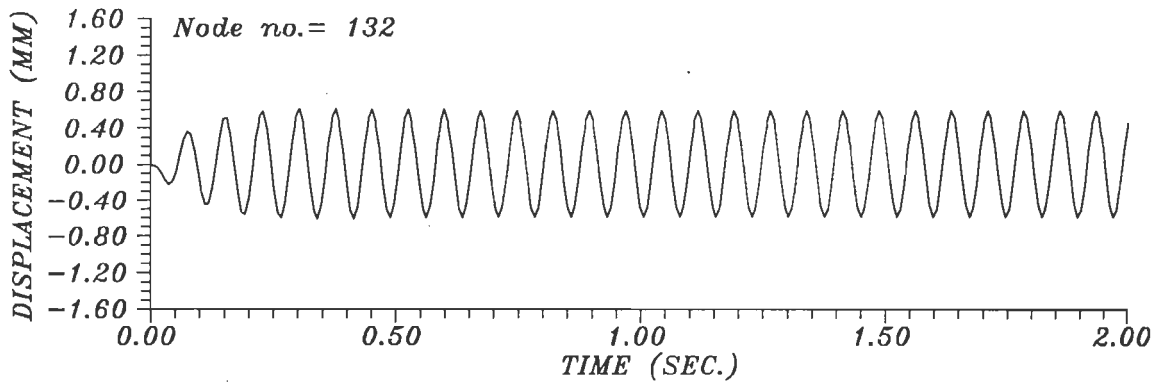


FIG.5.4.13b COMPUTED RELATIVE DISPLACEMENT OF R.E. EMBANKMENT M3 EXCITED AT BASE EXCITATION A3 (OME =24) FOR $\zeta_1 = 0.124$.

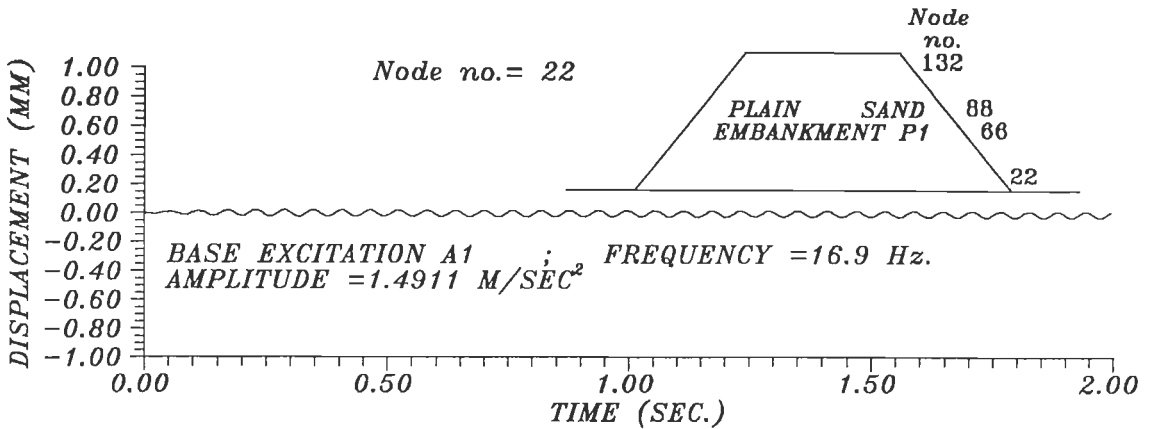
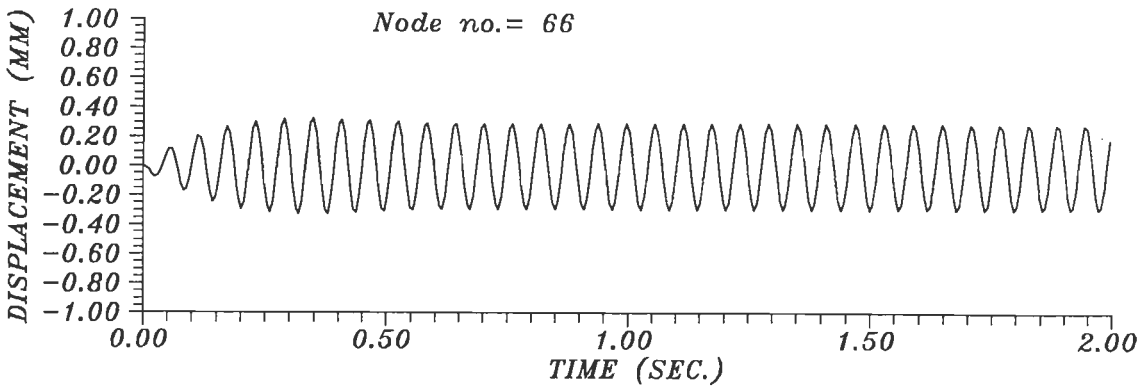
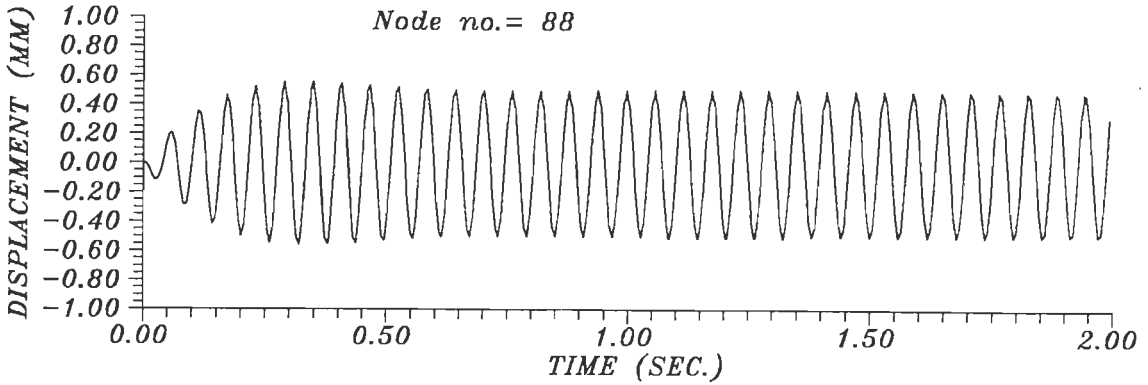
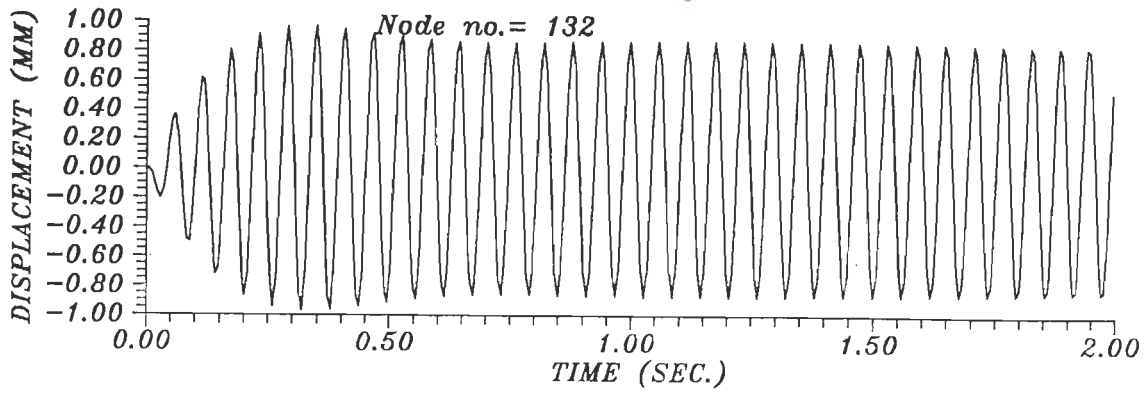


FIG.5.4.14 COMPUTED RELATIVE DISPLACEMENT OF PLAIN SAND EMBANKMENT P1 EXCITED AT EXCITATION A1 ($\omega = 24$).

absolute displacement (d_{eM1}) obtained from tests at different dimensionless depths (X/H). The figure also shows r_d values. Value of $\zeta_1=0.17$ used in this analysis as explained earlier. Figure 5.4.16 shows variation of r_d and r_{dd} with (X/H) for M1 for the above two idealizations.

In above figures, computed response is in good agreement with that obtained from tests upto $0.59H$ above base. The largest r_{dd} is 12.2% only which is quite small. If $r_{dd}=\pm 25\%$ is considered tolerable, then this good agreement extends upto $0.69H$ above base. For the entire depth, the average $r_d=0.8513$ and corresponding $r_{dd}=-14.87\%$ only which is also small. In top $0.3H$ depth, measured response is larger than computed responses. Measured response is closer to computed response with the superior 2-layer idealization than to that from 1-layer idealization which is expected.

Figure 5.4.17 and Fig. 5.4.18 show similar plots with $\zeta_1=0.124$ for M3. Upto $0.57H$ above base, $-14.22\% < r_{dd} < 14.22\%$ which is a small discrepancy, and hence, computed response is in good agreement with that obtained from tests. If $r_{dd}=\pm 25\%$ is tolerable, this good agreement extends upto $0.71H$ above base. For whole depth, average $r_d=0.86$ and corresponding $r_{dd}=-13.98\%$ which are small. Measured response is larger than computed responses in top $0.29H$ depth. However, computed response with superior 2-layer idealization is closer to measured one than that from 1-layer idealization, as expected.

Discrepancy between measured and computed displacements for M1 and M3 is larger near top, because, shear modulus in that region is nearly zero and smaller than uniform shear modulus assigned to homogeneous layer idealizing that region. Computed response can be further improved in top portion by idealizing it with larger number of thin homogeneous layers.

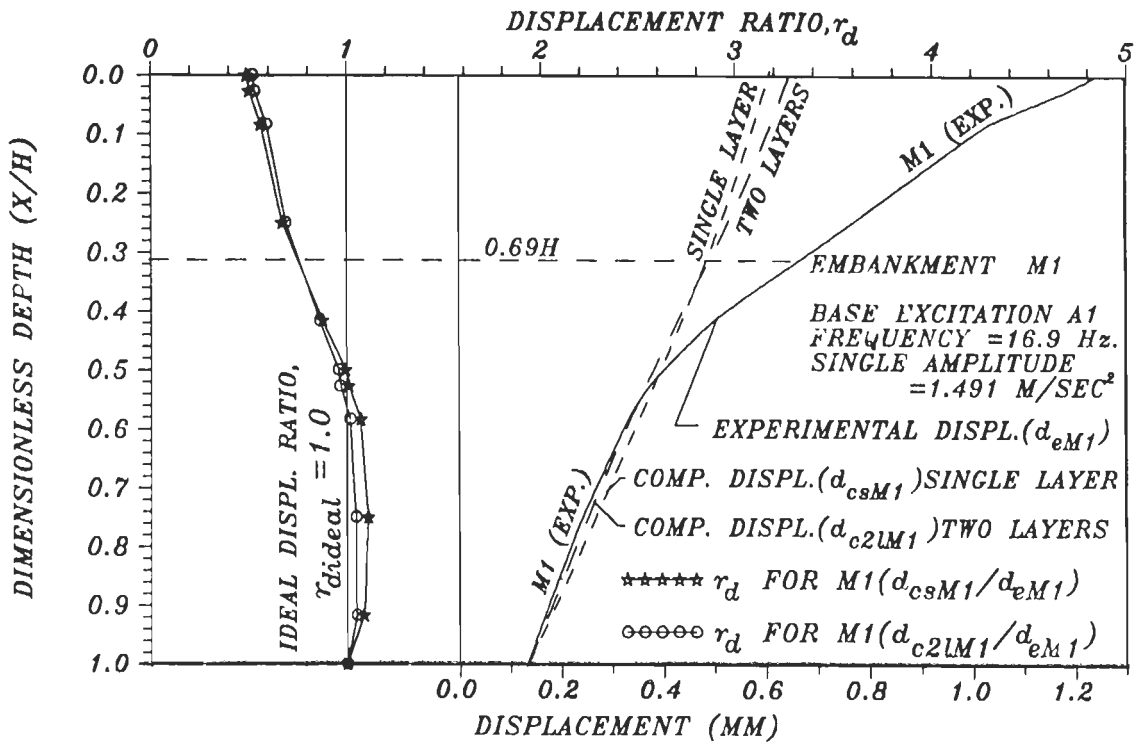


FIG.5.4.15 COMPUTED AND EXPERIMENTALLY RECORDED MAXIMUM DISPLACEMENT WITH DIMENSIONLESS DEPTH (X/H) FOR R.E. EMBANKMENT M1 EXCITED AT ITS FUNDAMENTAL FREQUENCY ($\omega = 24$).

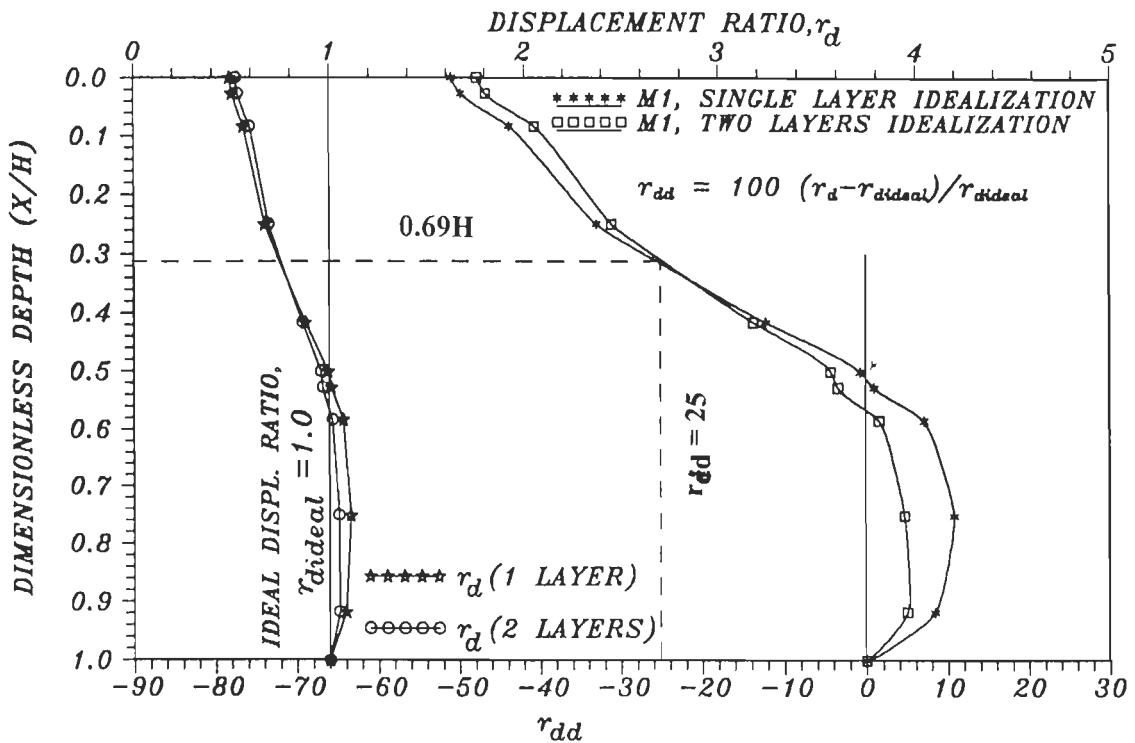


FIG.5.4.16 VARIATION OF PERCENTAGE DISCREPANCY IN DISPLACEMENT, r_{dd} , WITH DIMENSIONLESS DEPTH (X/H) FOR R.E. EMBANKMENT M1 IDEALIZED AS HOMOGENEOUS SINGLE AND TWO LAYERS.

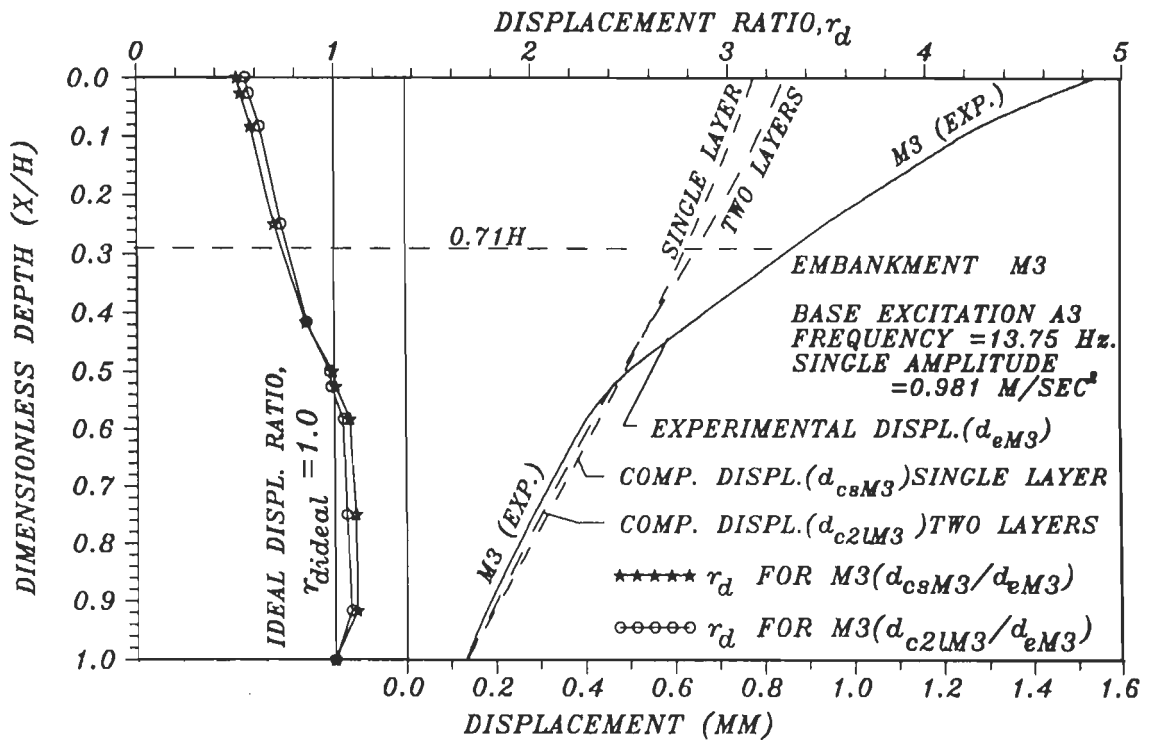


FIG.5.4.17 COMPUTED AND EXPERIMENTALLY RECORDED MAXIMUM DISPLACEMENT WITH DIMENSIONLESS DEPTH (X/H) FOR R.E. EMBANKMENT M3 (OME = 24).

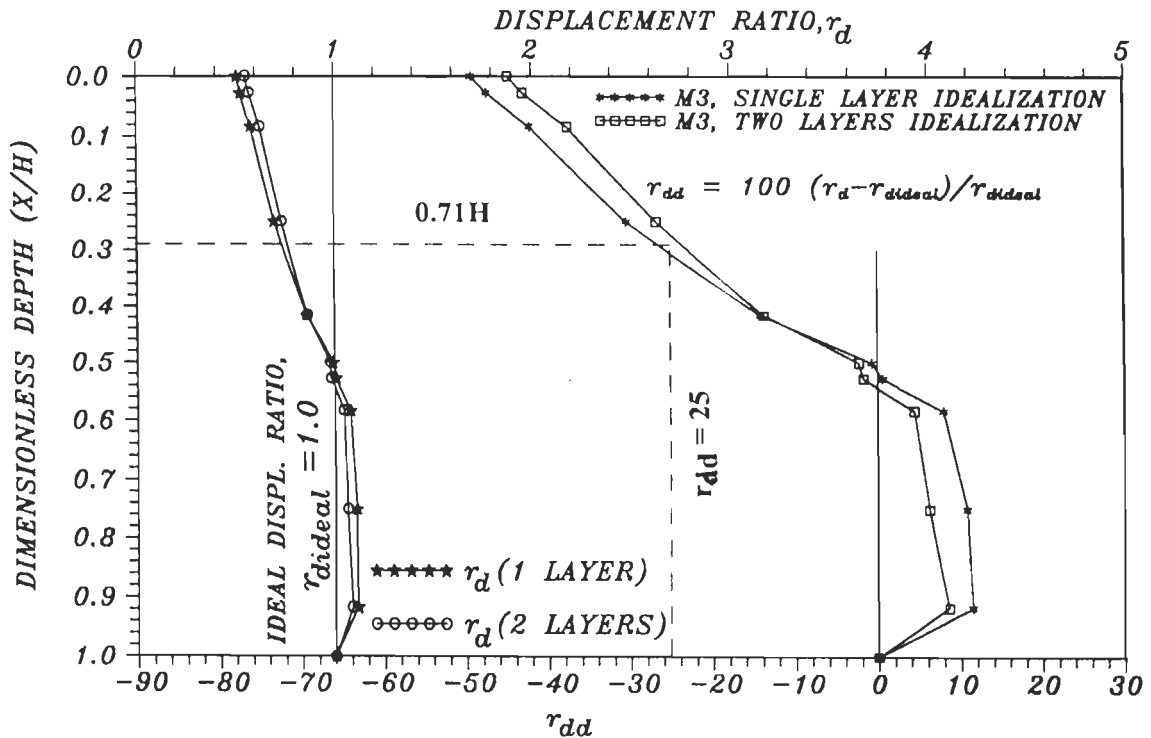


FIG.5.4.18 VARIATION OF PERCENTAGE DISCREPANCY IN DISPLACEMENT, r_{dd} , WITH DIMENSIONLESS DEPTH (X/H) FOR R.E. EMBANKMENT M3 IDEALIZED AS HOMOGENEOUS SINGLE AND TWO LAYERS.

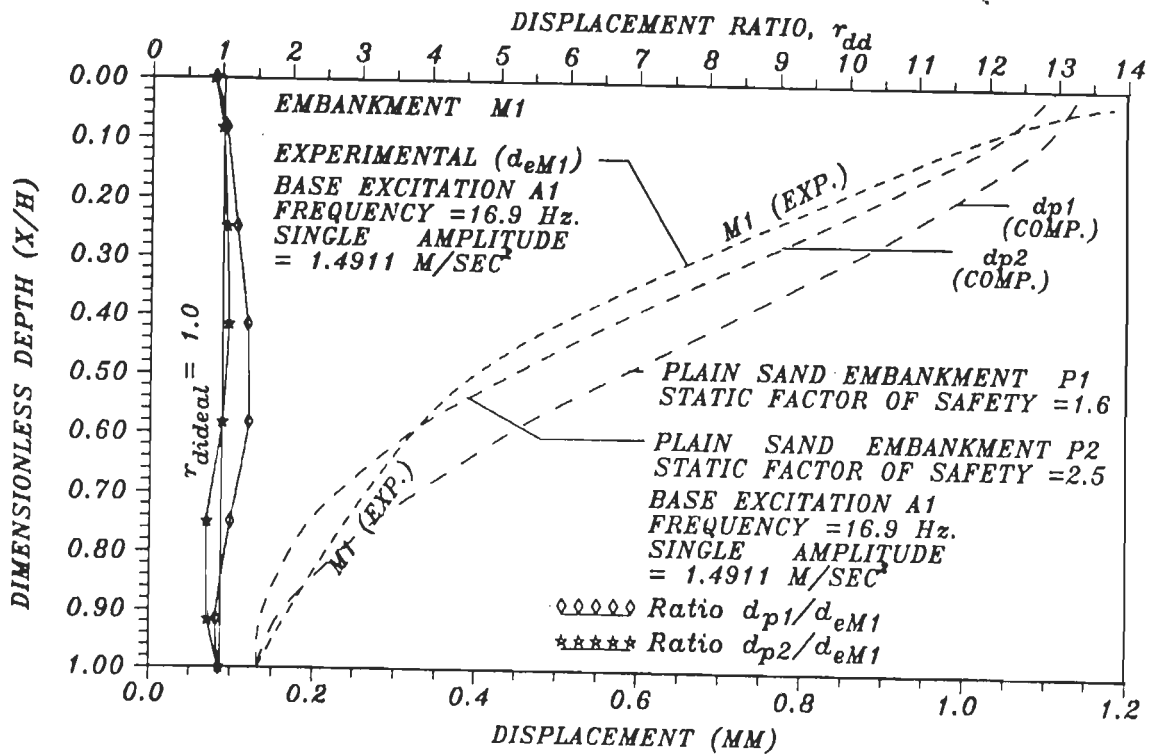


FIG.5.4.19 COMPARISON OF COMPUTED MAXIMUM ABSOLUTE DISPLACEMENT FOR PLAIN SAND EMBANKMENTS P1 AND P2 WITH THAT OF M1 FROM TEST.

For excitation A1, Fig. 5.4.19 shows r_d and computed maximum absolute displacements for P1 and P2 and maximum absolute displacements for M1 obtained from tests. Maximum displacement of P1 with steeper slopes is larger than that for P2 with flatter slopes as expected. For depths $\geq 0.84H$ from top for P1 with shorter base width and for depths $\leq 0.58H$ from top for P2 with larger base width, $r_d < 1$ as expected. For remaining depth, displacements of P1 and P2 are larger than those for M1 obtained from tests. This highlights advantage of using R.E. embankments instead of plain sand embankments of same top width and height.

5.4.3 Dynamic Shear Stresses

As cited in Article 5.3.2 dynamic shear stress, τ_D , at Gauss points of elements was computed from FEM analysis of M1, M3, P1 and P2. For ease of

presentation, average of τ_D for Gauss points of each element is presumed to act at centre of that element. Figure 5.4.20 shows τ_D -time relation for element no. 6, 26, 46 and 66 on vertical transverse cross section of M1 with 1-layer idealization, $\zeta_1=0.05$ and excitation A1. Observations about duration of transient vibrations, ratio of transient peak τ_D to steady state peak τ_D and frequency of steady state vibrations are same as those for relative accelerations and displacements as expected.

For M3 idealized by 2-layers, excited with A3 similar plot are given for $\zeta_1=0.05$ and 0.124 in Fig. 5.4.21a and Fig. 5.4.21b respectively. Observations from these figures are similar to those from relative accelerations and displacements of M3 cited earlier.

For P1 with excitation A1, τ_D -time relationship for element No.6, 26, 46 and 66 on vertical transverse cross section (Fig. 5.4.22) indicates that τ_D increases with depth below top of embankment to reach its maximum at element no. 6 near base. Other observations from this figure are similar to those for relative accelerations and displacements for P1. From results of analysis of P2 with same excitation, ζ_1 and ζ_2 , amplitudes of τ_D were smaller than those for P1, because, base width of P2 is larger than that of P1. Besides, other observations regarding duration of transient vibrations and frequency of steady state vibrations are similar to those for P1. As such, similar plots of results for P2 are not presented.

For M1, Fig.5.4.23 shows τ_D -time relationships for element no. 56, 57, 58 and 60 situated close to mid-depth and spaced horizontally 150 mm C/C. Element no. 56 is close to centre, element no. 60 is close to vertical face and remaining two are in between. Value of τ_D is maximum at element no.56

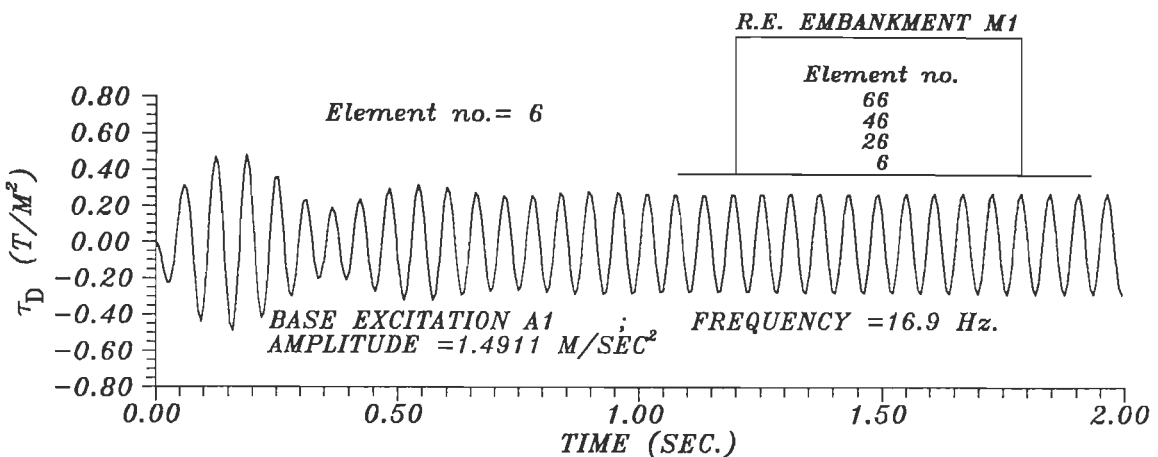
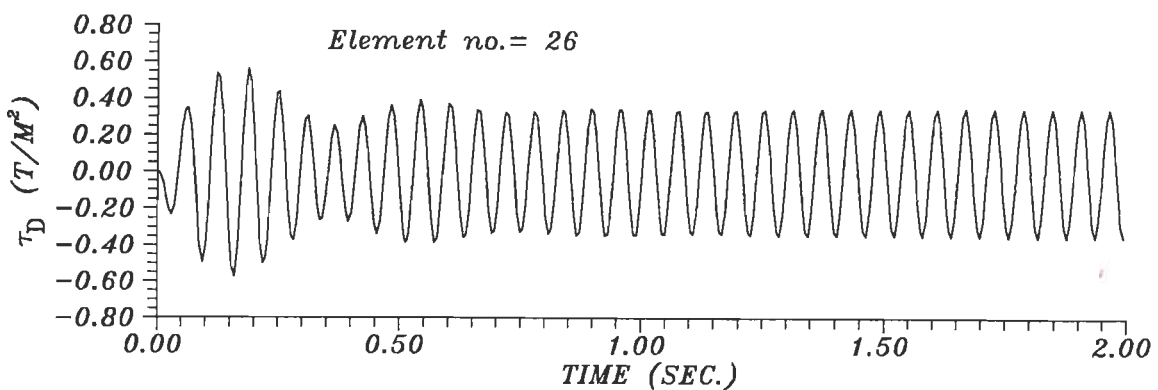
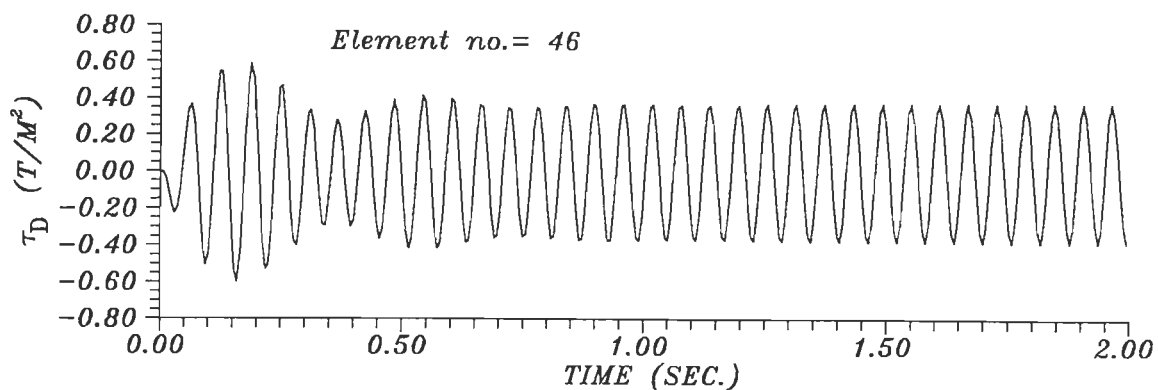
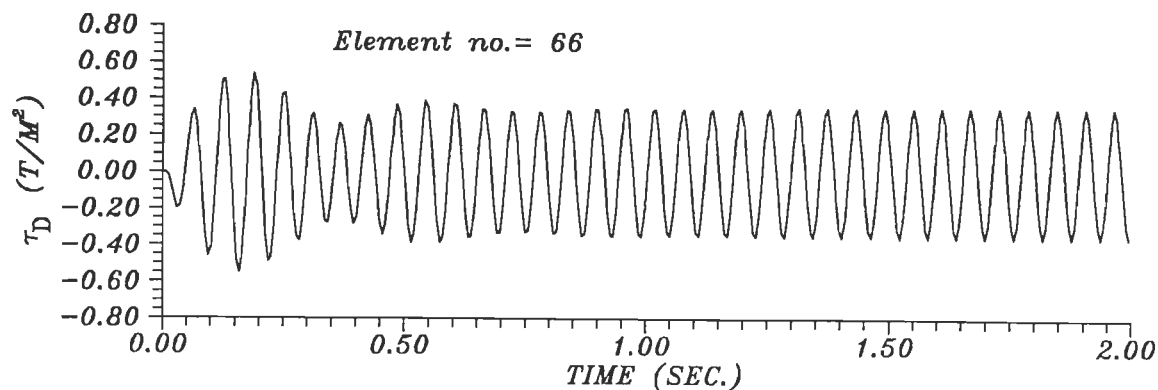


FIG.5.4.20 VARIATION OF COMPUTED DYNAMIC SHEAR STRESS, τ_D , OF R.E. EMBANKMENT M1 EXCITED AT BASE EXCITATION A1 (OME =24) FOR $\zeta_1=0.05$.

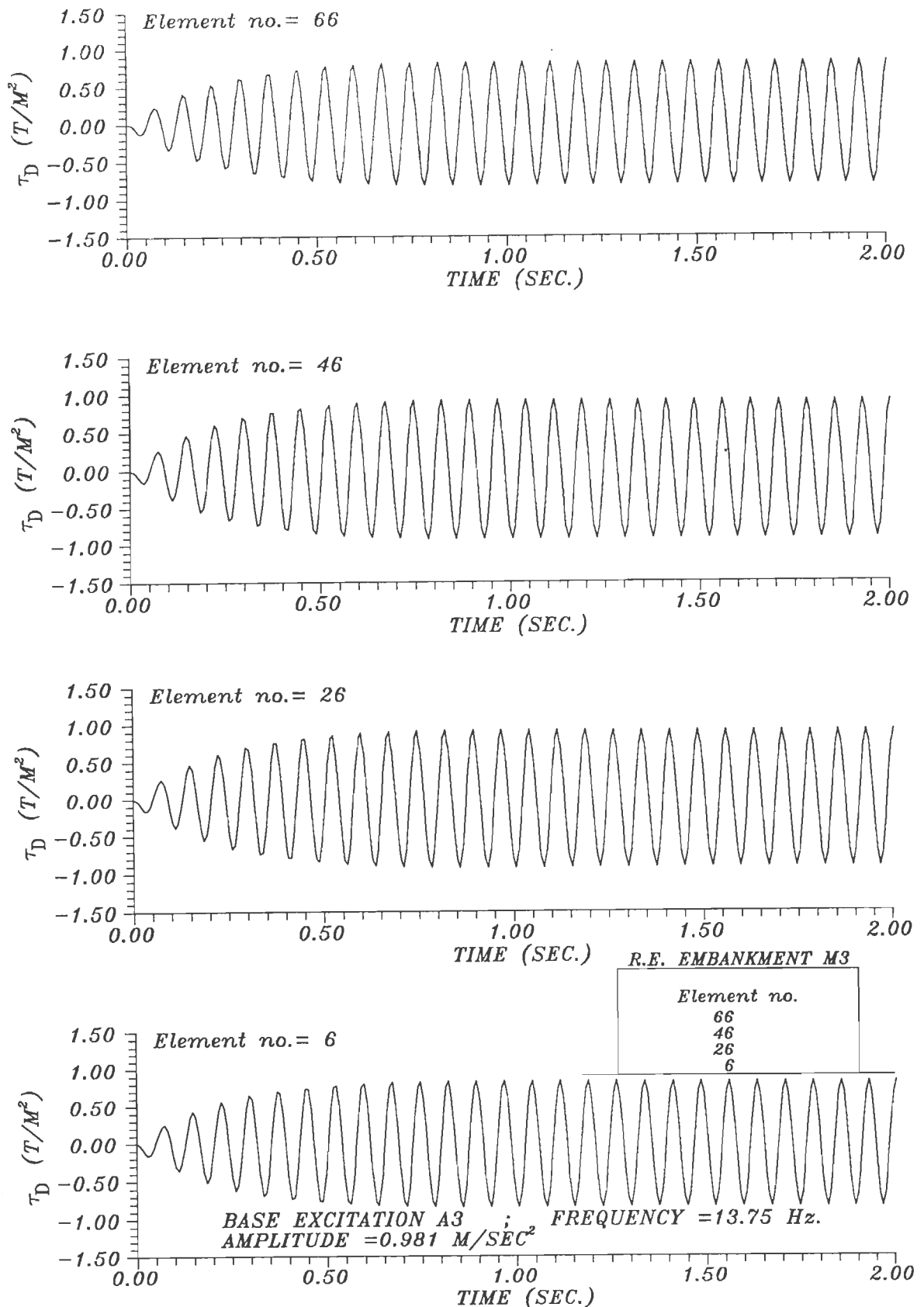


FIG.5.4.21a VARIATION OF COMPUTED DYNAMIC SHEAR STRESS, τ_D , OF R.E. EMBANKMENT M3 EXCITED AT BASE EXCITATION A3 (OME = 24) FOR $\zeta_1 = 0.05$.

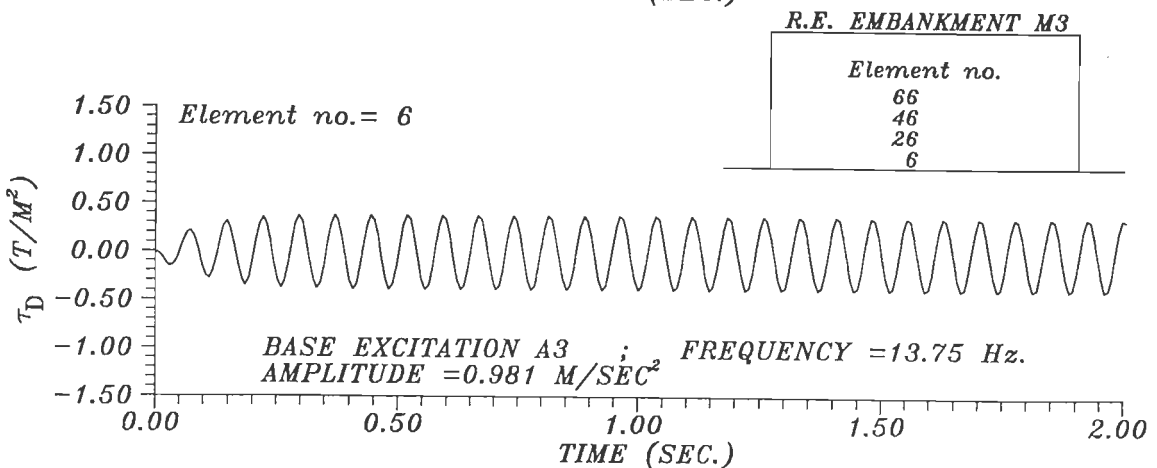
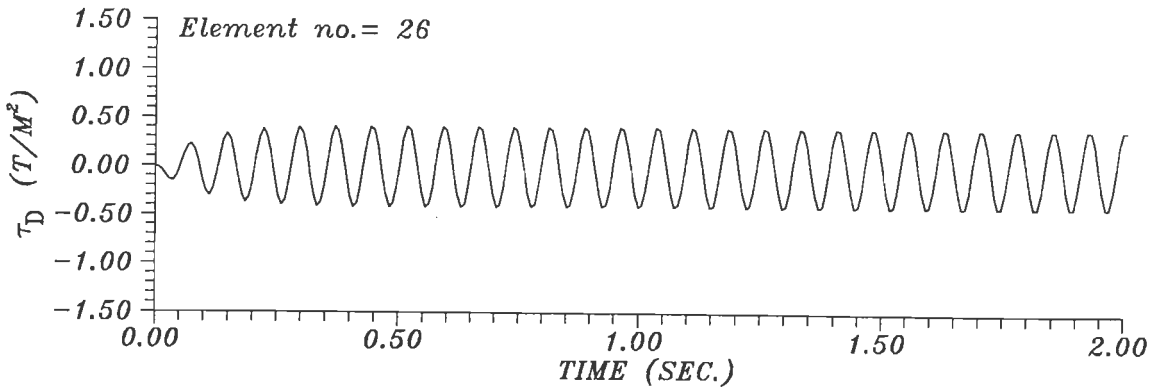
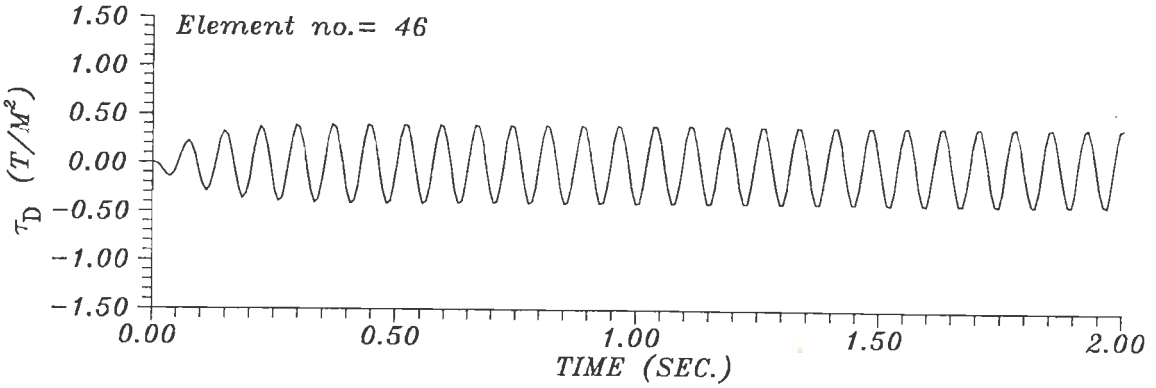
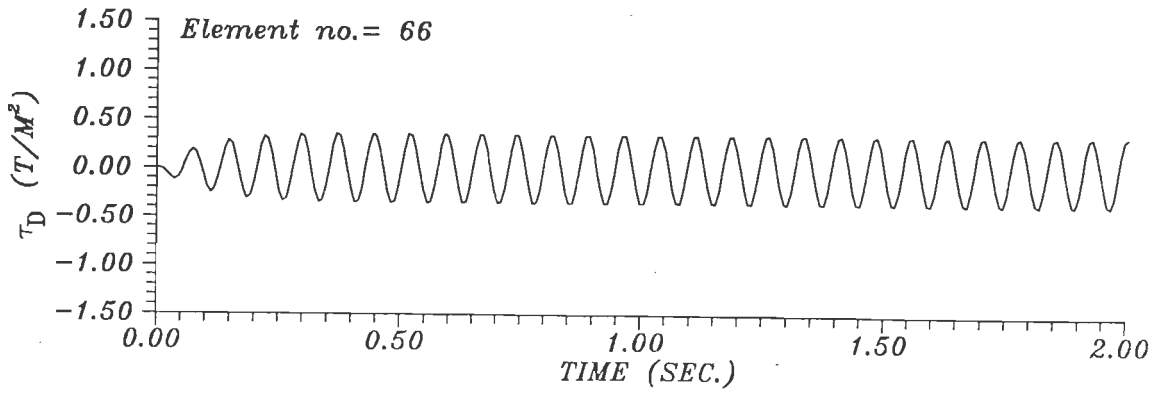


FIG.5.4.21b VARIATION OF COMPUTED DYNAMIC SHEAR STRESS, τ_D , OF R.E. EMBANKMENT M3, EXCITED AT BASE EXCITATION A3 (OME = 24) FOR $\zeta_1 = 0.124$.

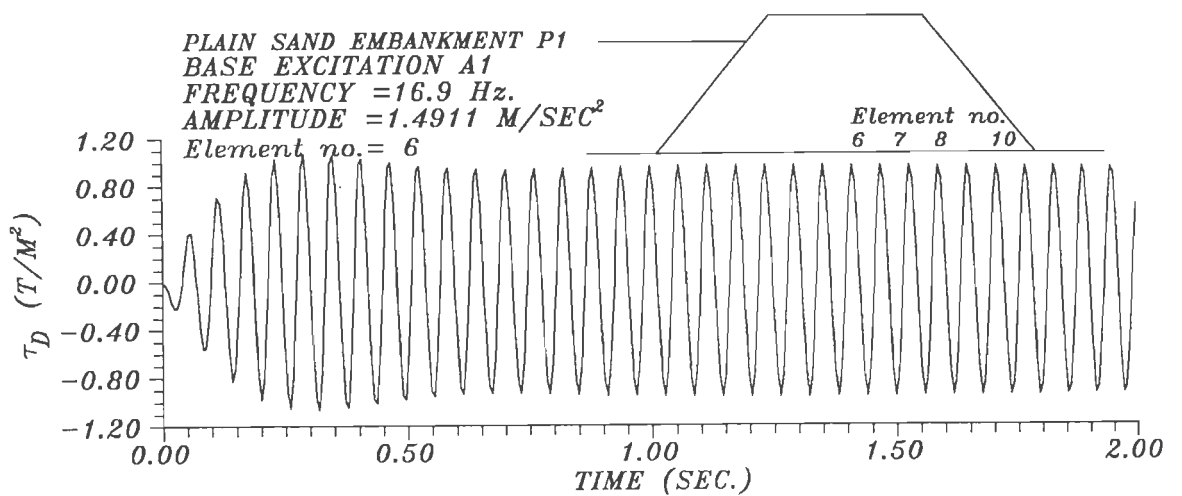
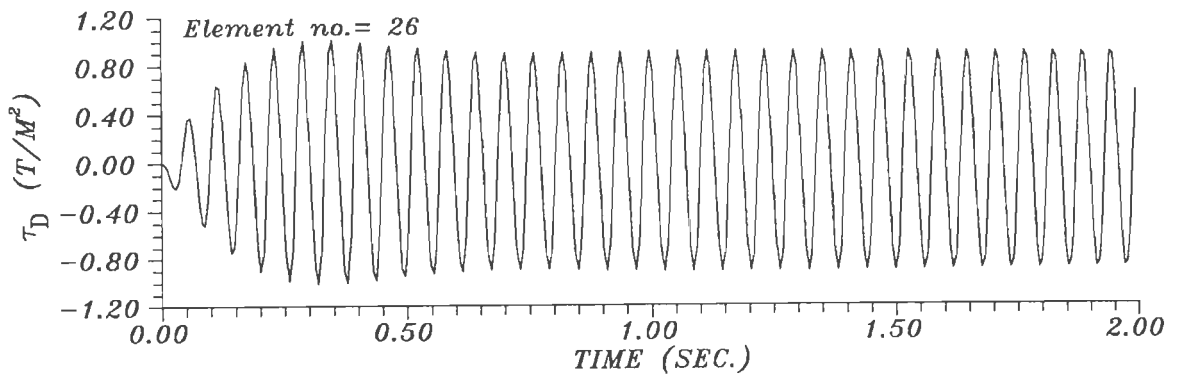
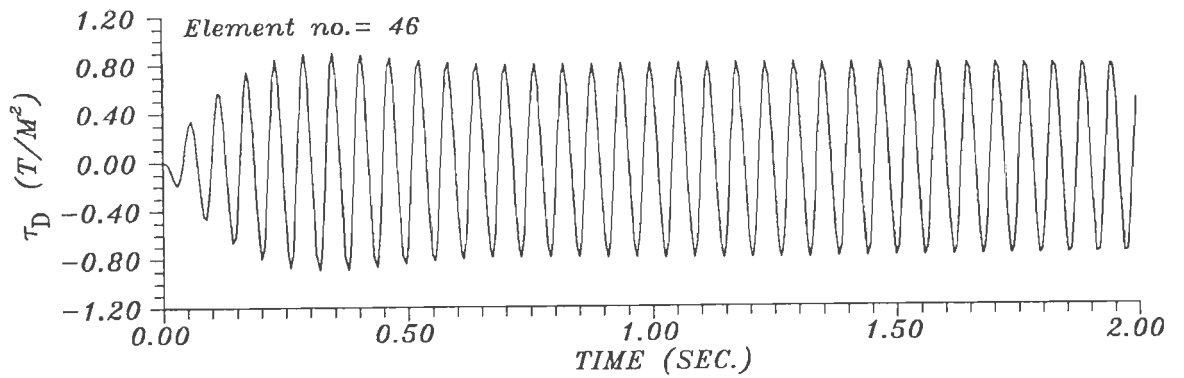
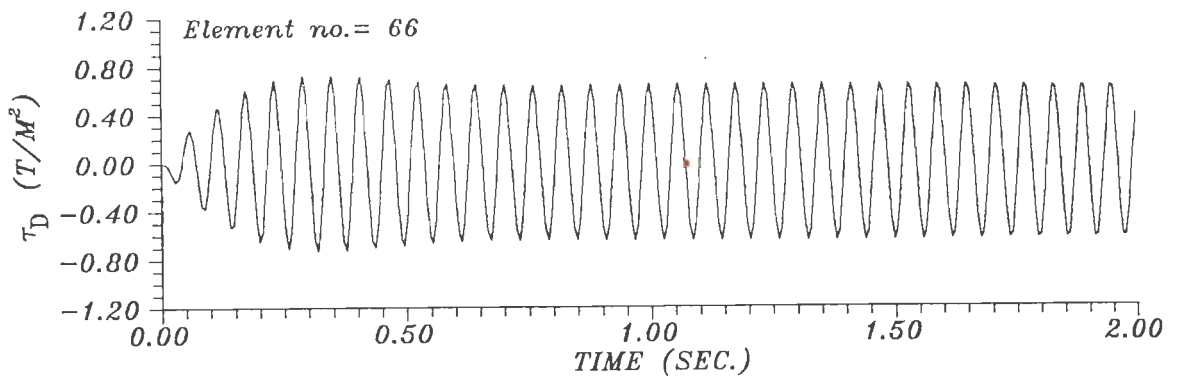


FIG.5.4.22 VARIATION OF COMPUTED DYNAMIC SHEAR STRESS, τ_D , OF PLAIN SAND EMBANKMENT P1 EXCITED AT BASE EXCITATION A1.

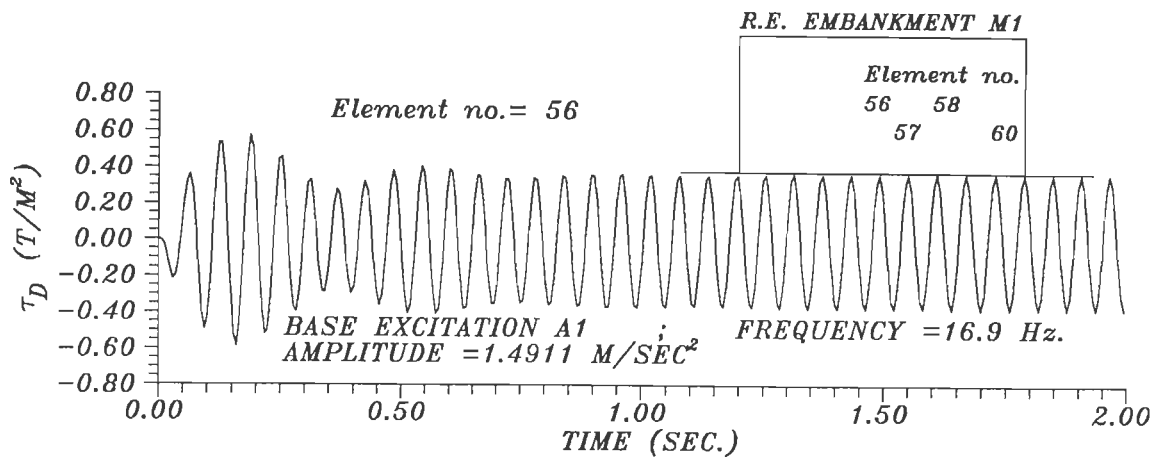
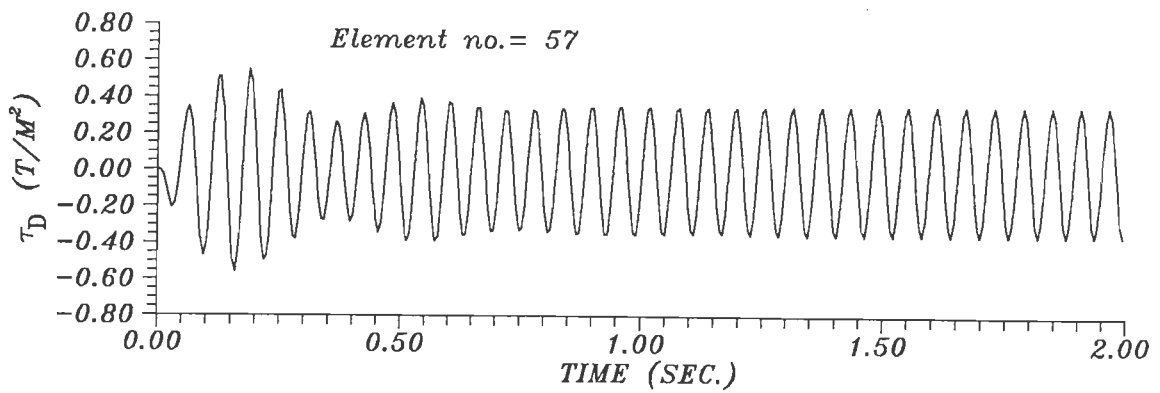
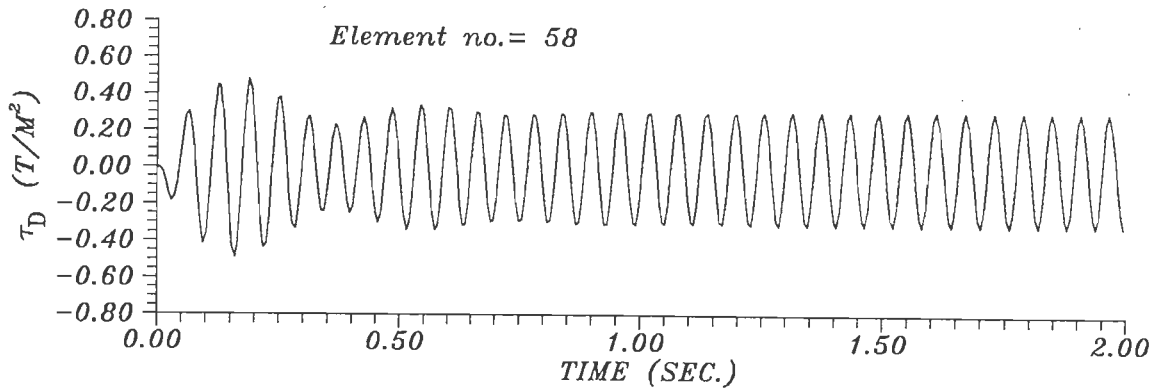
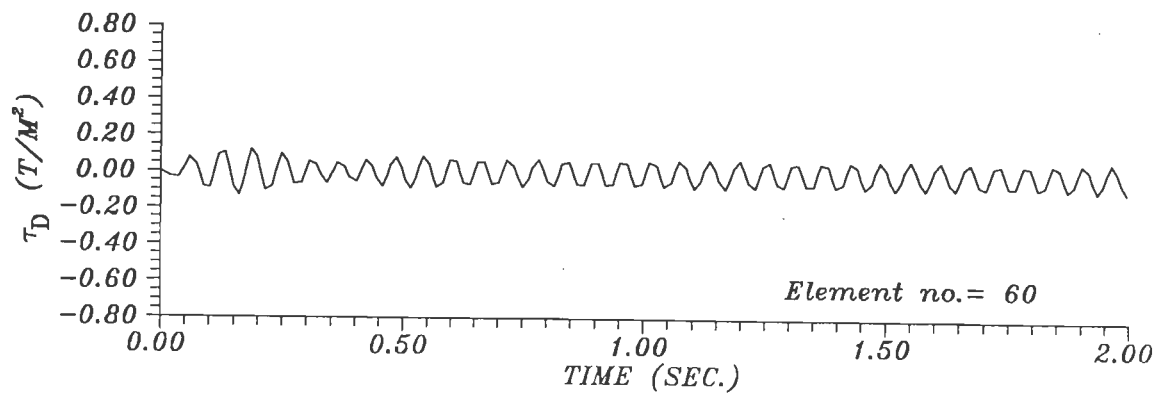


FIG.5.4.23 VARIATION OF COMPUTED DYNAMIC SHEAR STRESS, τ_D , OF R.E. EMBANKMENT M1, EXCITED AT BASE EXCITATION A1 (OME =24) FOR $\zeta_1 = 0.05$.

near mid-width and decreases to its minimum at element no.60 near vertical face. This shows nonuniformity of τ_D on horizontal section of M1 at any depth. This observation is valid for M3 also (Fig. 5.4.24).

For P1, Fig.5.4.25 shows τ_D -time relationship for element no. 6, 7, 8 and 10 at 37.5 mm above base in transverse plane and spaced horizontally at 444 mm C/C. Element no. 6 is close to mid-width, element no. 10 close to side slope and remaining are in between. Value of τ_D is maximum at element no. 6 near mid-width and decreases to reach the minimum at element no. 10 near side slope. This shows nonuniformity of τ_D on horizontal section. These observations may be expected to be valid for P2 also.

Figure 5.4.26 shows maximum dynamic shear stress, τ_{Dmax} , along depth in transverse plane for M1 excited with A1 using 1 and 2-layer idealizations. Damping ratios of 0.05 and 0.17 were used. For all cases, τ_{Dmax} increases with depth to peak at 0.625H below top. This is reported by Richardson and Lee (1975) also based on test results. Further below it gradually reduces upto element no. 6 near base due to increase in confining pressure and embankment fixity at base. Peak τ_{Dmax} of transient state for 2-layer idealization with $\zeta_1=0.05$ is 20% larger than that for steady state following transient state. This is expected. With $\zeta_1=0.17$, peak τ_{Dmax} for transient state larger than that for steady state were not observed. This is also expected at higher damping. Peak τ_{Dmax} for steady state with $\zeta_1=0.05$ is 67.8% larger than that for $\zeta_1=0.17$ which is also expected. Peak τ_{Dmax} with $\zeta_1=0.17$ for steady state with 1-layer idealization is 11.86% smaller than that for same case with 2-layer idealization. However for steady state with $\zeta_1=0.05$, peak τ_{Dmax} with 2-layer idealization is 43% larger than that for 1-

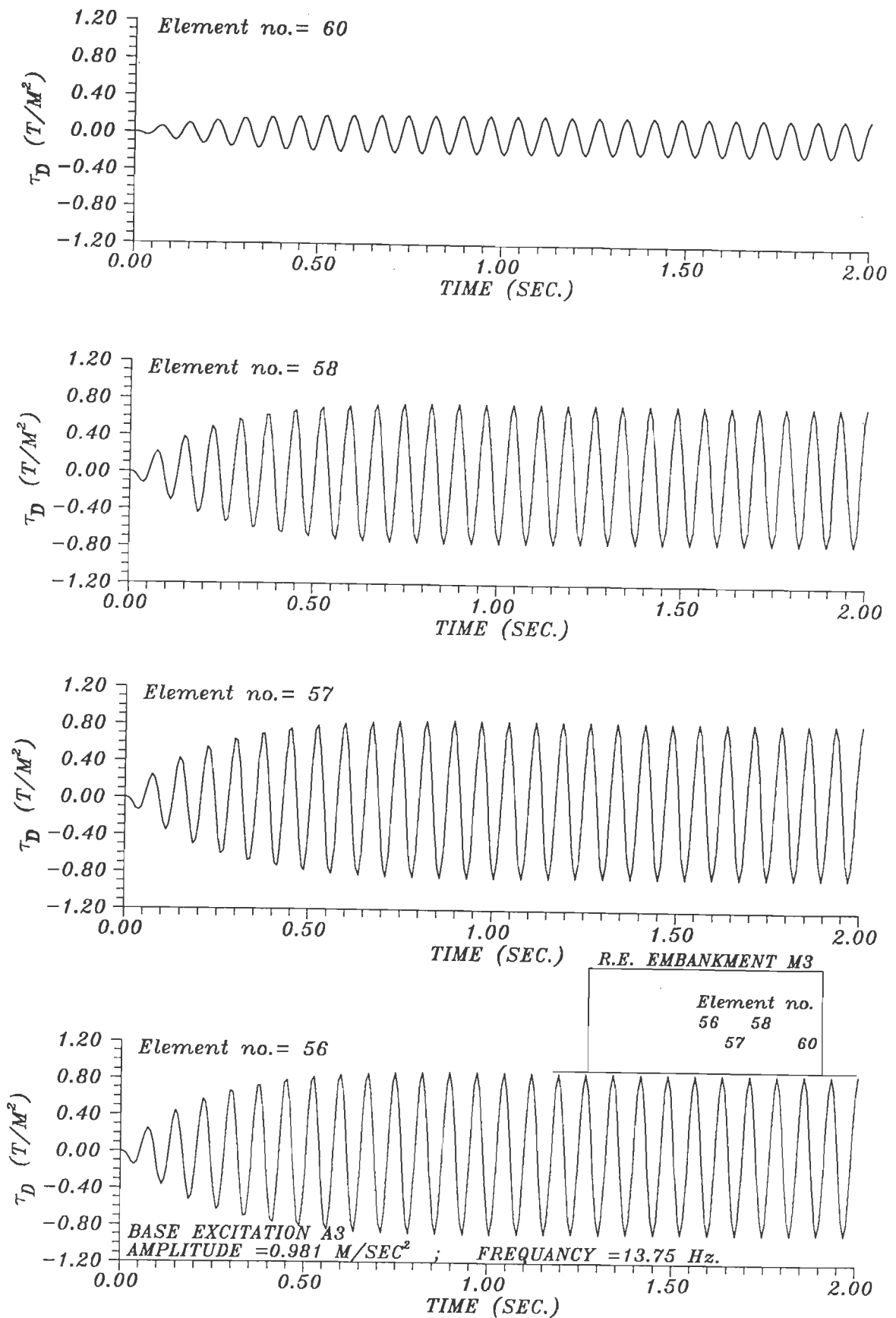


FIG.5.4.24 VARIATION OF COMPUTED DYNAMIC SHEAR STRESS, τ_D , OF R.E. EMBANKMENT M3 EXCITED AT BASE EXCITATION A3 (OME =24) FOR $\zeta_1 = 0.05$.

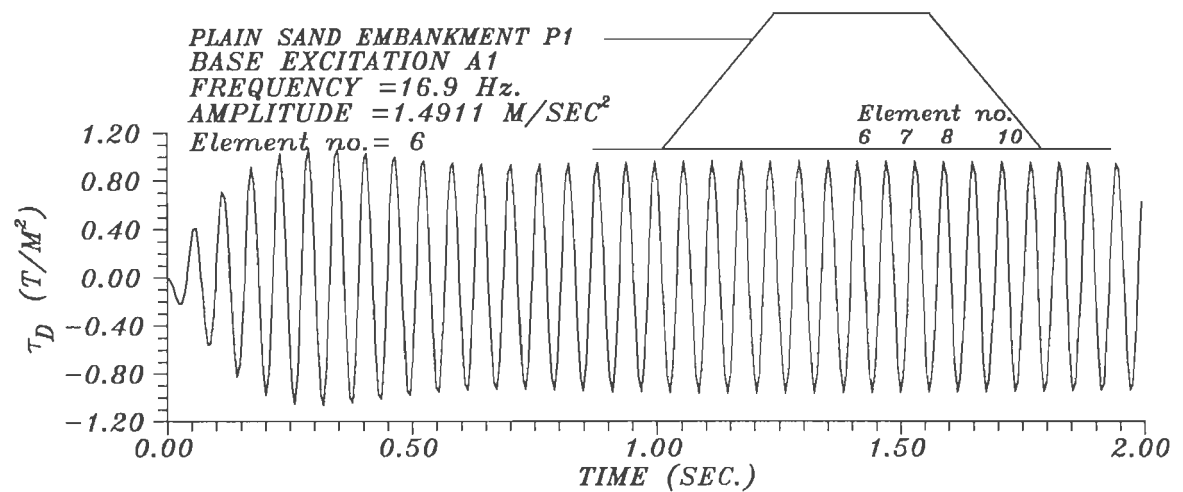
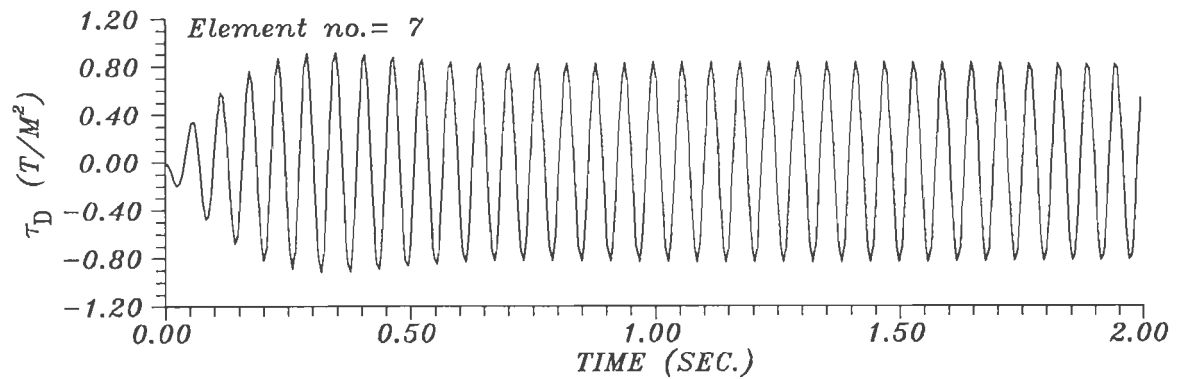
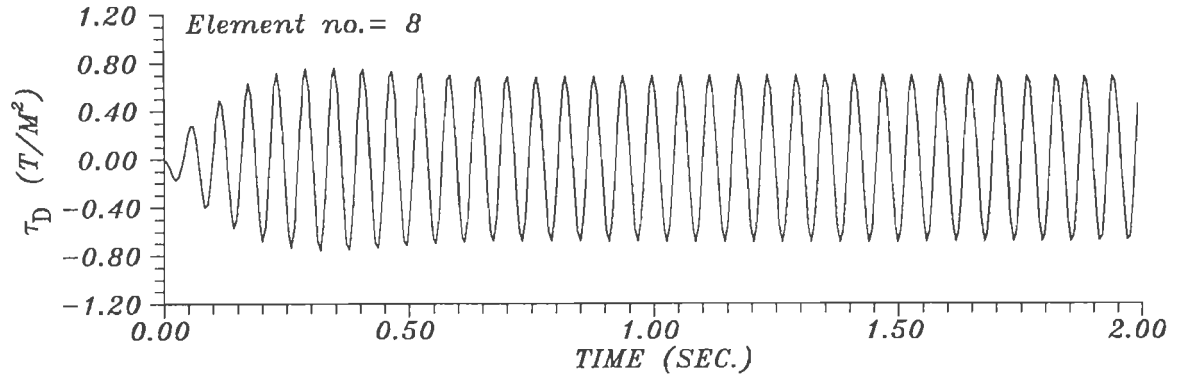
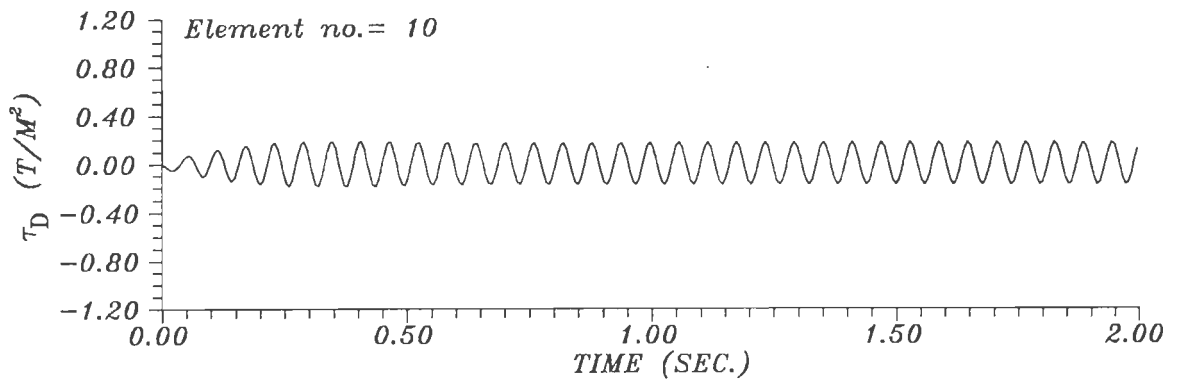


FIG.5.4.25 VARIATION OF COMPUTED DYNAMIC SHEAR STRESS, τ_D , OF PLAIN SAND EMBANKMENT P1. EXCITED AT BASE EXCITATION A1.

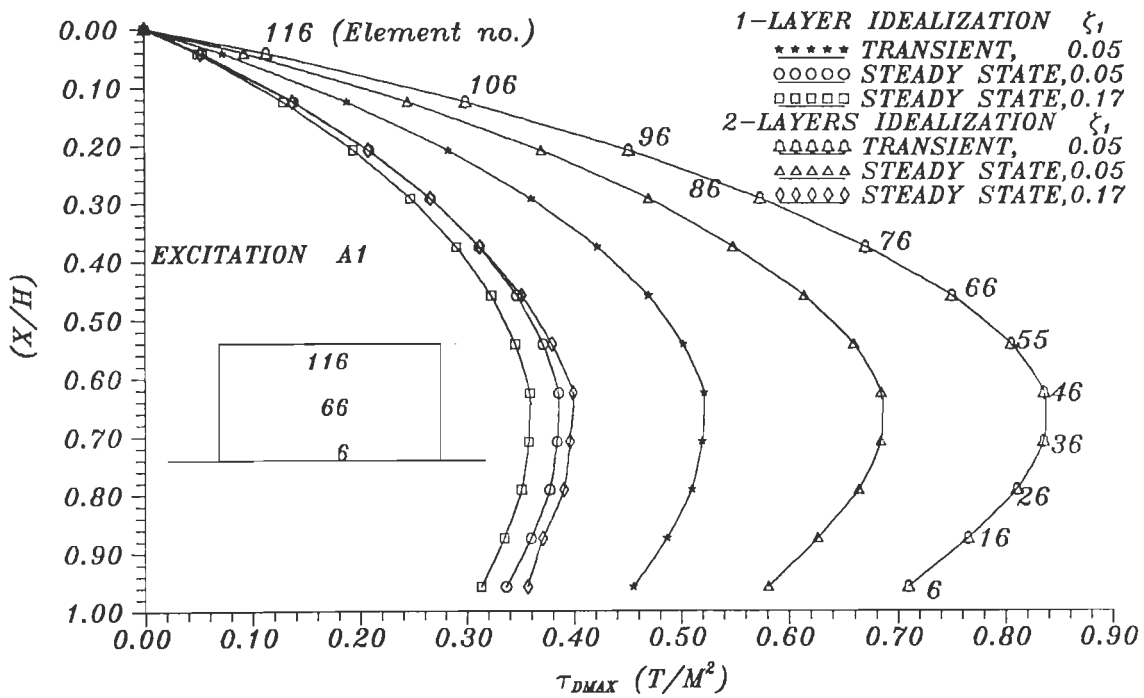


FIG.5.4.26 VARIATION OF COMPUTED MAXIMUM DYNAMIC SHEAR STRESS, τ_{DMAX} , WITH DIMENSIONLESS DEPTH (X/H) FOR R.E. EMBANKMENT M1.

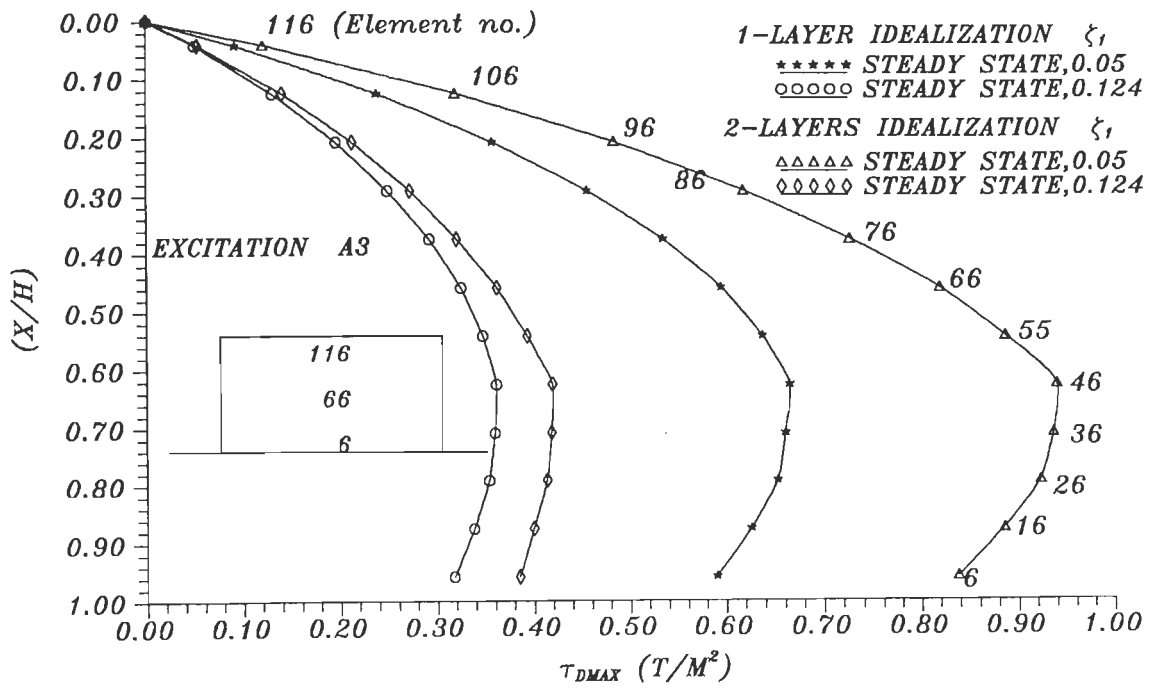


FIG.5.4.27 VARIATION OF COMPUTED MAXIMUM DYNAMIC SHEAR STRESS, τ_{DMAX} , WITH DIMENSIONLESS DEPTH (X/H) FOR R.E. EMBANKMENT M3.

layer idealization. Hence, in addition to using appropriate damping, it is very important to properly idealize embankment by using more homogeneous layers to improve estimates of τ_{Dmax} , particularly when lower values of damping are used.

Figure 5.4.27 shows similar plot for M3 excited with A3 using $\zeta_1=0.05$ and 0.124 with 1-layer and 2-layer idealizations. For this case, there were no transient peaks larger than those of steady state. The trend of these plots are similar to those given for M1 cited above.

From above discussion, it is clear that damping is a very important parameter and which affects shear stresses significantly. Allowing higher strain levels in R.E. embankments is of great advantage since it results into mobilization of higher damping with out losing elasticity leading to much reduction in shear stresses. This is highly desirable. It is impossible to have this advantage with plain sand embankments as it is not possible to allow such strain levels with out causing failure.

For P1 and P2, Fig. 5.4.28 shows similar plots together with shear strength envelopes of plain sand with factor of safety, $F_s=1$ and 1.2 (shown by solid and broken lines respectively). For top 60% depth with $F_s=1$, $\tau_{Dmax} > \tau_u$ indicating failure where τ_u is ultimate shear strength of sand. Further below, $\tau_{Dmax} < \tau_u$. For element no.6 near base, $\tau_{Dmax} = 0.774 \tau_u$. Similarly for $F_s=1.2$, P1 and P2 practically fail for the entire depth indicating that static $F_s=1.16$ and 1.69 and dynamic $F_s=1.6$ and 2.5 adopted for P1 and P2 respectively are inadequate to ensure safety which is partially due to neglecting frequency, frequency ratio and duration of dynamic loading in computing dynamic F_s .

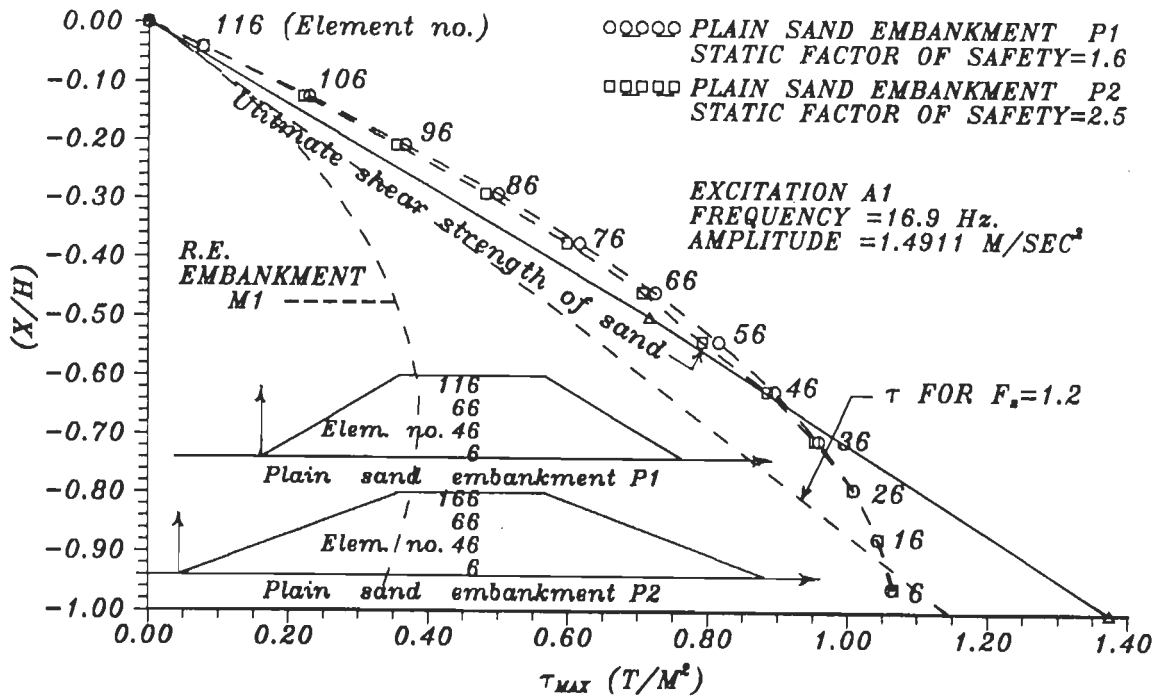


FIG.5.4.28 VARIATION OF COMPUTED MAXIMUM DYNAMIC SHEAR STRESS, τ_{DMAX} , WITH DIMENSIONLESS DEPTH (X/H) FOR M1 AND PLAIN SAND EMBANKMENTS P1 AND P2 FOR $\zeta_1=0.05$.

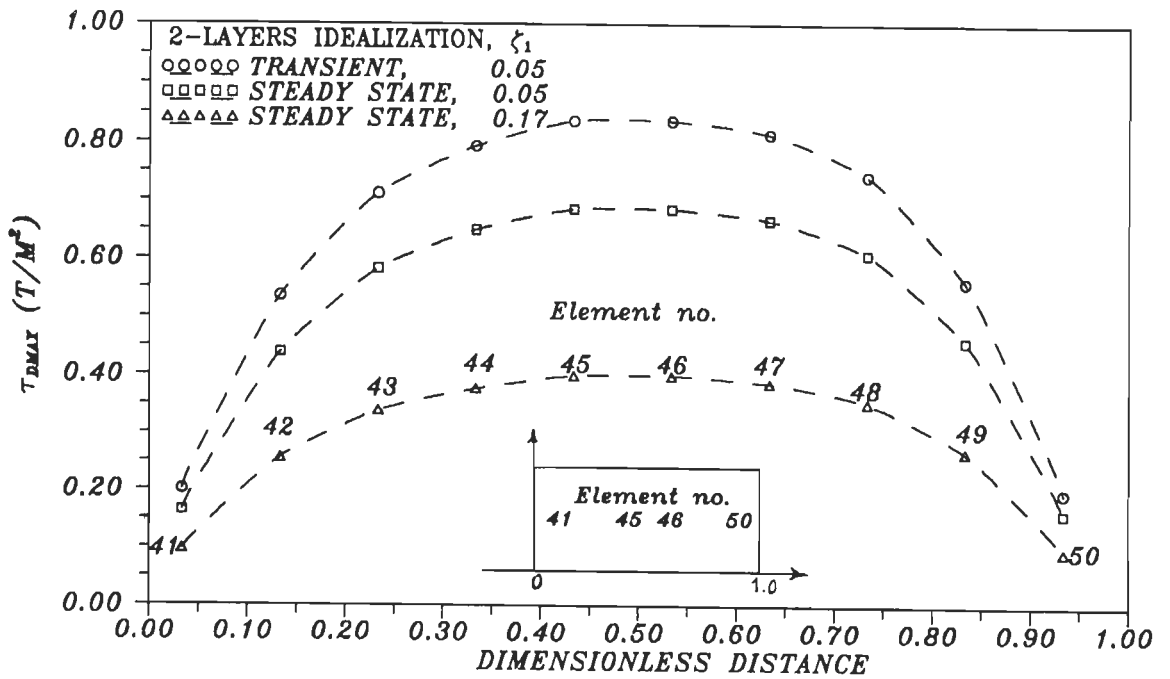


FIG.5.4.29 VARIATION OF COMPUTED MAXIMUM DYNAMIC SHEAR STRESS, τ_{DMAX} , WITH DIMENSIONLESS DISTANCE FROM LEFT TRANSVERSE END FOR R.E. EMBANKMENT M1.

To compare performance of P1 and P2 with that of M1 (as they are all excited with A1), τ_{Dmax} along depth is also plotted in this figure. Shear stresses for M1 are far below allowable τ of sand for whole depth when $F_s=1$ and 1.2 indicating a much better performance. Maximum τ_{Dmax} for P1 and P2 are 2.323 and 2.295 times more than that for M1. Besides, increasing embankment width from P1 to P2 does not indicate a noticeable improvement in shear stresses mobilised indicating that increasing width of plain sand embankment (with same D_r) is not a practical solution to withstand dynamic forces. R.E. embankment with same top width and considerably reduced base width results into much smaller shear stresses which is preferable.

For M1 and P1, travel time from base to top for shear wave is nearly $T/4$, T being period of fundamental vibration. As such, when peak acceleration occurs at top end, base acceleration is nearly zero and inertia forces over entire depth are added to get base shear. Throughout height, width of M1 is uniform. As such for simplicity, peak acceleration may be presumed to decrease linearly with depth below top. For P1, width at any depth from top increases to reach base width 2.96 times the top width. Inertia force (generating shear force) also increase with base width. As such with depth below top, rate of increase in τ_D is faster than rate of decrease in acceleration. Hence, net base shear for P1 increases leading to higher τ_D at base when compared with τ_D at top. For uniformly wide M1, rate of increase of τ_D with depth is slower than that for P1.

Figure 5.4.29 shows τ_{Dmax} in a transverse plane along horizontal defined by element no. 41 to 50 at which maximum τ_{Dmax} occurs with $\zeta_1=0.05$ and 0.17 and with 2-layer idealization. Dimensionless distance from left end of M1 is ratio of distance of centre of element to width of M1. Close to

both vertical longitudinal faces, lowest $\tau_{Dmax} \approx$ zero occurs. Towards the centre from either end of M1, τ_{Dmax} increases to peak at element no. 46 and 45. Plots show parabolic distribution of τ_{Dmax} , as expected. For $\zeta_1=0.05$, peak τ_{Dmax} for transient state is 1.2307 times that for steady state, as expected. Similarly, for steady state, τ_{Dmax} for $\zeta_1=0.05$ is 1.733 times than that for $\zeta_1=0.17$, as expected. Figure 5.4.30 shows similar plots for M3 with $\zeta_1=0.05$ and 0.124 and with 2-layer idealization. Observations from this figure are similar to those from Fig. 5.4.29 cited above.

Similar plots are shown in Fig. 5.4.31 for P1 and P2 $\zeta_1=0.05$ and with 1-layer idealization. They show lowest τ_{Dmax} close to sloping faces of P1 and P2. Towards the centre from either end, τ_{Dmax} increases to peak at element no. 6 for P1 and P2. For P1 τ_{Dmax} is higher than that for P2 since base width of P1 is lesser than that for P2.

5.9 CLOSURE

In Chapter-V, results of 2D linear FEM analyses of M1 and M3 in time domain with sinusoidal base excitations were compared with test results. Computed and test results of M1 were compared with computed results of P1 and P2 with same height, top width and material properties as those for M1 (except for shear modulus) but with different side slopes. Single layer idealization for M1, M2, P1 and P2 and 2-layer idealization for M1 and M3 were used. Damping strongly affects response and, hence, be obtained by reducing discrepancy between analytical and test results.

Parametric study with damping ratio for first mode, ζ_1 , from 0.05 to 0.288 showed that for $\zeta_1=0.18$ for M1 and $\zeta_1=0.1275$ for M3, responses from

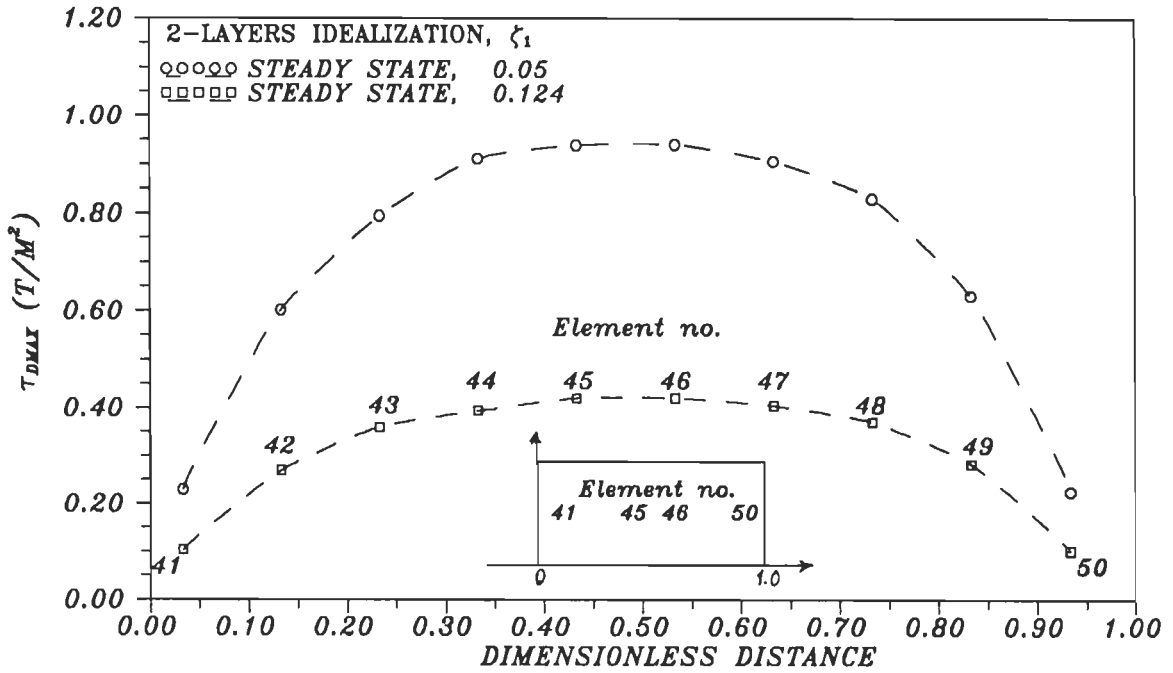


FIG.5.4.30 VARIATION OF COMPUTED MAXIMUM DYNAMIC SHEAR STRESS, $\tau_{D\text{MAX}}$, WITH DIMENSIONLESS DISTANCE FROM LEFT TRANSVERSE END FOR R.E. EMBANKMENT M3.

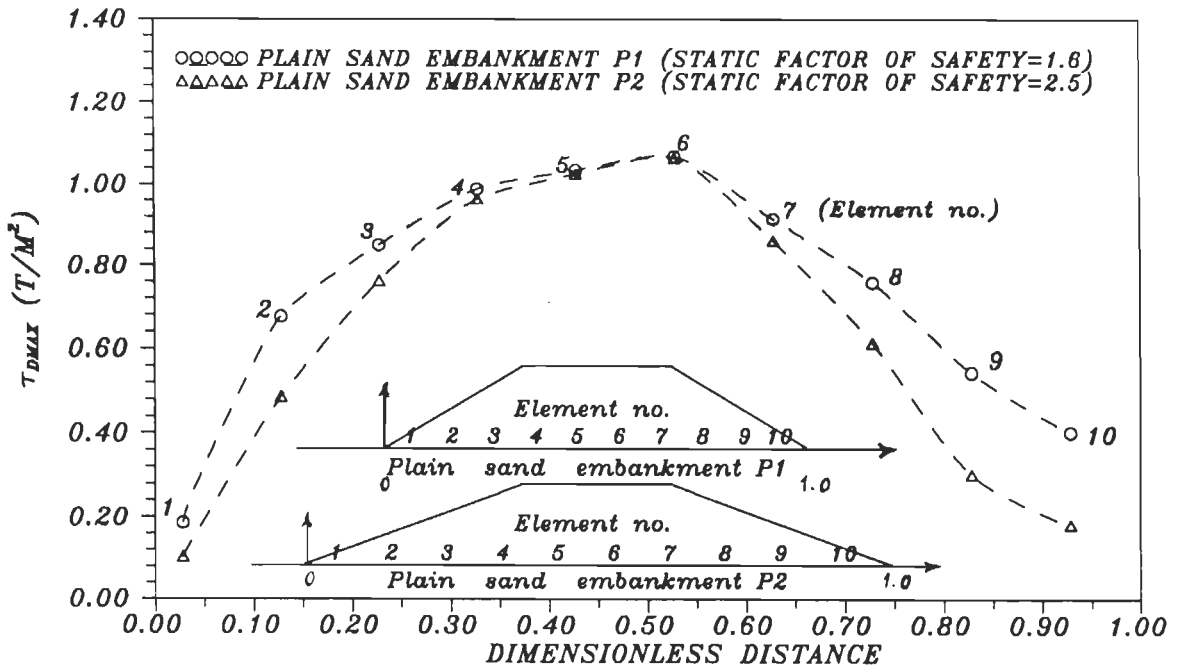


FIG.5.4.31 VARIATION OF COMPUTED MAXIMUM DYNAMIC SHEAR STRESS, $\tau_{D\text{MAX}}$, WITH DIMENSIONLESS DISTANCE FROM LEFT TRANSVERSE END FOR PLAIN SAND EMBANKMENTS P1 AND P2.

analysis and tests are identical. For M1 $\zeta_1=0.18$ and for M3 $\zeta_1=0.1275$ are within limits of damping recommended by Seed et al (1984) for plain sands at corresponding shear strain. Hence, damping ratio-shear strain relation may be considered to be the same for plain sands and reinforced earth.

For M1, $\zeta_1=0.17$ suppressed peak computed relative accelerations, a_{rp} , displacements, d_{rp} , and duration of transient state observed when $\zeta_1=0.05$ was used. For M3, $\zeta_1=0.124$ suppressed duration of transient state observed when $\zeta_1=0.05$ was used. For both M1 and M3 for steady state, amplitudes of a_{rp} and d_{rp} reduce with depth below top, frequency equal to excitation frequency and amplitudes of a_{rp} and d_{rp} reduce with increasing damping for same shear strain. This is expected.

Vertical shear wave propagation through embankment considered in back-analyses is correct, because, time lag obtained from recorded acceleration and those obtained from FEM analysis tally with each other.

Computed absolute accelerations and displacements for M1 with $\zeta_1=0.17$ and M3 with $\zeta_1=0.124$ are in very good agreement with test data upto $0.61H$ above base with discrepancy of $\pm 13.72\%$ or less. If $\pm 25\%$ discrepancy is tolerable, then this good agreement extends upto $0.7H$ from base. For whole depth, average discrepancy is of the order of -13.74% only. Near top, computed responses show more discrepancy due to difference between actual and assumed shear moduli in top portion. Measured responses are closer to computed ones with 2-layer idealization which is better. Discrepancy between measured and computed responses may be further reduced by employing more homogeneous layers in top $0.3H$ portion of embankments.

Spacing ratio of fabrics in R.E. embankments is a small 0.16 in this study which makes it a micro-reinforced earth. Hence, R.E. embankments are treated as homogeneous material in this study. It is confirmed by good agreement between computed and measured response of R.E. embankments and between computed and measured travel time of shear wave through embankment.

Computed responses of P1 and P2 were nearly identical for 0.1H near base. For remaining depth, response of P2 is less than that of P1 with smaller base, as expected. Near base, responses of P1 and P2 were almost identical to those measured for M1 due to large base widths of P1 and P2 compensating effect of their lower shear moduli. P1 and P2 being weaker than M1 in upper part, showed larger amplification upto 0.4H from top than those for measured response for M1 showing merit of using R.E. embankment.

For M1 and M3 maximum dynamic shear stress, τ_{Dmax} , is zero at top and peaks at 0.625H from top. This is reported by Richardson and Lee (1975) also based on test results. Further below, τ_{Dmax} slowly reduces due to increasing confining pressure and fixity at base. For stiffer embankment (M1) with low damping ($\zeta_1=0.05$), peak τ_{Dmax} of transient state may be more than that for steady state which gets suppressed by suitably large damping ($\zeta_1=0.17$). For M1 in steady state ($\zeta_1=0.05$), peak τ_{Dmax} for 2-layer idealization is 43% larger than that for 1-layer idealization. It is only 11.86% larger when correct $\zeta_1=0.17$ is used. So, besides using proper damping, proper idealization of embankments with more homogeneous layers near top is also important particularly when damping is low.

For R.E. embankments, ζ_1 and γ are of the order of 0.18 and 10^{-3} which are much higher than 0.05 and 10^{-6} for plain sands for elastic behaviour.

Since damping greatly affects shear stresses, this helps to reduce τ_{Dmax} in R.E. within elastic domain. This is a great advantage of reinforced earth.

For P1 and P2, τ_{Dmax} increases from zero at top to peak near base. Besides, $\tau_{Dmax} > \tau_u$ showing failure upto 0.6H from top for $F_s = 1$. For $F_s = 1.2$, $\tau_{Dmax} > \tau_{allowable}$ for nearly entire depth. Hence, concept of F_s does not ensure safety under dynamic loads as it fails to consider frequency, frequency ratio, duration of loading, damping etc. For same loading, height and top width with $F_s = 1.2$, $\tau_{Dmax} < \tau_{allowable}$ for entire depth of M1. Peak τ_{Dmax} for P1 and P2 with larger base width are 2.323 and 2.295 times that for M1 respectively. This highlights advantage of R.E.

Variation of τ_{Dmax} in a transverse plane along horizontal for M1 and M3 is parabolic with its maximum at the centre as expected. For P1, $\tau_{Dmax} > \tau_{Dmax}$ for P2 with flatter slopes as expected.

CONCLUSIONS AND SUGGESTIONS FOR FUTURE RESEARCH

6.1 PREAMBLE

This study entitled "Behaviour of reinforced earthen embankments during earthquakes", consists of laboratory and analytical work. Facilities and techniques developed for experimental investigations to improve quality of results are significant contributions to present day state of the art. They are briefly summarized in this article.

i. Sand rain apparatus rains sand over entire test bed of 1.5m x 0.75m size, simultaneously using rainfall technique to obtain more uniform spatial distribution of density throughout. Mean standard deviation of 1.08% in density obtained is better than 1.47% reported by Passalaqua (1991) and 2.39% by Fairless (1989) using motorized setup with electronic controls. So, the setup is very good for preparation of large embankments.

ii. Stress control apparatus to determine pullout resistance which is a critical material property in design of R.E. structures. Facilities reported in state of the art are mostly inferior strain control type which do not allow enough time to mobilize displacements fully and hence record smaller displacements at a given stress which is unsafe. Stress control facility designed and developed for this purpose worked satisfactorily and is the only of its size and kind.

iii. **Technique for creating plane strain conditions** for laboratory studies currently available are not good. The technique developed to create such conditions in transverse planes to restrain strains in longitudinal direction worked well for large R.E. embankments used in this study.

iv **Shake table test facility** with table of 2m x 1m size supports R.E. embankments, 1.5m x 0.75m x 0.9 m (high), and is excited with mechanical oscillators. These are some of the largest embankments used in research which themselves may be treated as prototypes to get reliable results for better understanding of behaviour of even larger prototypes. Such test results help in development and verification of better methods of analysis.

v. **Softwares developed** perform back-analyses of test data and FEM analysis of test embankments to compare analytical and test results. Software 'DYMU' utilises data from embankment tests to evaluate dynamic pullout resistance as a function of time and other parameters to carryout parametric studies. Software 'FE95' performs static/dynamic 2D linear analysis in time domain and obtains eigen solutions.

6.2 CONCLUSIONS

Laboratory and analytical studies were carried out to obtain material properties of components of R.E. as well as of R.E. as a whole. Results are used to perform dynamic analysis of R.E. and plain sand embankments of same top width, height and material properties except for shear modulus. Seismic motion are of many types and results vary with type and nature of base excitation. Sinusoidal base excitation was considered in study as it is possible to represent seismic excitation by its sinusoidal equivalent. As

far as possible, results are presented in terms of dimensionless parameters. Significant conclusions based on results are hereby presented.

6.2.1 Conclusions from Pullout Tests

- a. Ratio, μ_{avs} , of pullout stress to normal stress, σ_v , for woven geotextile is higher than that for nonwoven type for the same strain level. Results obtained for woven geotextile show lesser scatter.
- b. Static pullout resistance coefficient, μ_{avs} , at various pullout strains, ϵ_p , and normal stresses can be represented by a single best fit curve with less than 10% average errors. As width, B_r , of fabric increases, μ_{avs} increases nonlinearly to get stabilised at critical width, $B_{cr} = 290$ mm. For $B_r \leq 200$ mm μ_{avs} increases rapidly and leads to larger error in μ_{avs} which should be avoided. From tests specimen of various B_r , B_{cr} corresponding to largest μ_{avs} may be obtained. Only μ_{avs} for specimen with $B_r \geq B_{cr}$ should be used for designs. Correlation factor, C_μ , based on test results is used to get μ_{avs} for field conditions.
- c. Time to reach maximum pullout displacement, d_p , increases nonlinearly with increasing ratio of pullout force, P_r , to reach its maximum at $P_r = 1$ when pullout force equals ultimate pullout force. With increasing time d_p increases to reach its maximum and not instantaneously. Soil settlements in pullout tests were small and decreased with increasing relative density. Normal stresses comparable to that due to height of embankment should be used in pullout tests to obtain good design data.
- d. Pullout stress, τ_p , is zero at free edges of test specimens. Its variation along length should begin with a near vertical tangent and end

with a horizontal tangent at pulling end. Elliptical variation satisfying this condition suits back-analysis of test data.

- e. Dimensionless width, B_{rd} , defined as (B_{ry}/B_r) , B_{ry} being yield width of reinforcement, increases with decreasing relative density, D_r , and is nearly independent of σ_v for a given D_r (errors < 10%). It also increases with increasing B_r in range of B_r tested. It reaches its maximum at $B_r = B_{cr}$. For $B_r < B_{cr}$, fabric strength is under-utilized for a given D_r and σ_v . Hence, specimen with $B_r \geq B_{cr}$ should only be tested.

6.2.2 Conclusions based on results of shake table tests and back-analyses

- a. Analysis results of free vibration tests (using sledge hammer) on R.E. embankments treated as homogeneous indicate that stiffer embankment show smaller shear strain of 1.325×10^{-4} compared to larger strain of 3.225×10^{-4} for weaker one. The opposite is true for shear moduli and velocity of shear waves for embankments.
- b. Similar are observations for shear strains, shear moduli and shear wave velocities obtained from forced vibration tests on R.E. embankments. With increasing excitation frequency, F_{rq} , rate of increase in acceleration increases upto resonant frequency, F_n , and then reduces sharply. Sudden acceleration fall immediately after crossing F_n is due to larger reinforcing action which overcomes inertia.
- c. R.E. embankments with base excitation amplitude from 0.0061 g to 0.319 g experienced very high peak accelerations from 1.0875 g to 2.577 g which were withstood with insignificant permanent deformation and damage. Hence, R.E. embankments show a predominantly elastic dynamic behaviour.

- d. Plots $\gamma_{rn}-r_e$ are linear for R.E. embankments. Even at resonance, R.E. embankments exhibited elastic behaviour over a wide range of stresses, strains and accelerations, which is important.
- e. Embankment softness and magnification factor, M_f , increase together. Increase in peak M_f with increasing embankment softness is expected. Effect of fundamental frequency, F_n , on M_f is high at low excitation force ratio, r_e , and reduces nonlinearly with increasing r_e . This is due to higher damping associated with higher excitation force.
- e. Average seismic coefficient, α_{hav} , proposed by Richardson and Lee (1975) is smaller than that obtained from tests in this study. It fails to predict nonlinear variation of α_{hav} with base acceleration for stronger excitations and for lower embankment stiffness. Prediction of F_n as $38/H$ by Richardson et. al. (1977) and recommended by Richardson (1978) for all R.E. embankments is on higher than those obtained from tests in this study. Hence, the expression is not valid for all R.E. embankments.
- f. Shear modulus decreases with decreasing R.E. embankment stiffness at any γ_r as expected. Plots of $G_r-\gamma_r$ at $\gamma_r=1.325 \times 10^{-4}$ almost merge. Hence, these plots were obtained by extending them upto this γ_r . At $\gamma_r \leq 1.325 \times 10^{-4}$, G_r is of no interest as reinforcing action at such low strains is insignificant.
- g. At strain of 10^{-3} , difference between G_r of R.E. and shear modulus, G_s , of plain sand at same D_r is small. At higher strains, $G_r \gg G_s$. Hence, R.E. has advantage over plain earth only at high strains.

- h. For elastic behaviour, range of shear strain is upto 10^{-3} for R.E. in this study. It is upto much smaller $\gamma=10^{-6}$ for plain sands. Hence, it is logical to normalize G_r w.r.t. G_r at $\gamma=10^{-3}$ and not w.r.t. G_r at $\gamma=10^{-6}$.
- i. Frequency, F_{rq} , strongly affects G_r . With increasing F_{rq} , G_r decreases to reach its minimum at resonance and then increases sharply for all embankments. For stiffer embankments G_r - F_{rq} curves for different OME values are closely spaced. The opposite is true for softer embankments.
- j. For R.E. embankment, a single best-fit r_f - (G_r/G_{rn}) relationship may be adequate to compute (G_r/G_{rn}) at different frequency ratio, r_f , with a small discrepancy $\leq 12.79\%$. Hence, it is recommended for design.
- k. Accelerations along dimensionless depth at various phase angles w.r.t. embankment top at a given OME is needed to compute inertia forces.
- l. For safety, μ_{avdmx} , γ_{avdmx} and dimensionless disturbing force (F_{dmx}/W) may be obtained for $r_f \leq 1/\sqrt{2}$ at different OME. All these variables for stiffer R.E. embankment is lower from those for weaker R.E. embankment. At resonance, γ_{avdmx} reduces sharply with change in r_f .
- m. Inertia generated by sinusoidal excitation causes sinusoidal coefficient of average dynamic pullout resistance, μ_{avd} , with phase angle, θ , at different r_f and OME for R.E. embankments. As r_f increases, peak μ_{avd} increases to its peak at $r_f=1$. For $r_f > 1$ or $r_f < 1$ peak μ_{avd} reduces.
- n. For M2 and M3, $\mu_{avdmx} > \tan\phi$ and $\mu_{avdmx} > \mu_{avsmx}$ near resonance does not necessarily mean a displacement dependent failure. Higher F_{rq} leads to smaller displacements per cycle due to short duration of inertia forces. Typical resonance during earthquakes is rare and does not last long. Many

acceleration peaks at resonance are rare. Even if a few such peaks occur, it may not always lead to failure as indicated by test results.

- o. Near resonance, $\mu_{avdmx} \geq \mu_{avsmx}$ obtained from back analysis is due to definition of μ_{avd} using shear stress due to disturbing inertia which could be larger than soil strength without always leading to displacement at failure. If Newmark's method to compute plastic displacements under dynamic loads is used to interpret pullout resistance, actual pullout resistance coefficient may be close to μ_{avsmx} based on $\tan\phi$. So, μ_{avdmx} is just a number and not a physical quantity.
- p. For stiffer R.E. embankments with many continuous fabrics and with γ_{avdmx} upto 10^{-3} at which slackness in fabric is overcome, μ_{avdmx} is almost strain-independent. This is due to high tensile modulus of fabric and mobilization of required tension for stability at very low strains. Buildup of μ_{avdmx} with strain is faster when slackness is overcome. This is not valid for more flexible embankment, because, all fabrics except one are discontinuous and displacements mobilized for developing requisite pull-out resistance are relatively quite large. At high strains, μ_{avdmx} is independent of OME if error $\leq 10\%$ is tolerable.
- q. Variation of μ_{avd} and γ_{avdmx} with r_f is similar to $\mu_{avdi}^{-(X/H)}$ relationship. Continuous fabrics lead to higher μ_{avdi} compared to discontinuous ones. Variation of μ_{avdi} with (X/H) in this analysis is similar to that obtained from tests reported by Fairless (1989).
- r. Active state of earth pressures was reached when maximum observed displacement of 0.78333% of embankment height was realized. In spite of

this, catastrophic failure was precluded which highlights advantage of R.E. Continuous fabrics give advantage of low displacements also.

- s. Post construction displacements showed near-mobilization of at rest pressures. Post vibration maximum displacement was at about $0.6H$ from top which agrees with that reported by others. Displacement increases with increasing OME and decreasing embankment stiffness.
- t. Computed post vibration net confining pressures along depth indicate that continuous reinforcements designed to withstand tensile force with adequate margin of safety are more effective than discontinuous one.
- u. Computed post vibration net residual force, P_{rs} , for weaker M3 at first increases quickly with depth and then more gradually to its peak at $0.675 H$. Further below, it decreases. This conforms with lab and field test data reported by others. Values of P_{rs} for M3 and those reported by others are larger than at rest earth forces, because, P_{rs} comprises of earth forces and forces due to mobilization of additional confining pressures due to reinforcing action. For M3, additional confining pressures are smaller. Hence, mobilized P_{rs} in excess of at rest earth forces is insignificant and occurs for a limited depth.
- v. Compaction settlement at the end of dynamic tests is zero at facing and almost reaches its maximum at a short distance from facing. Average settlement at top is $\leq 2.46\%$ of H which is small. Settlements decrease linearly with depth. Fabrics at facing do not settle, because, rigid facing elements resting one over the other do not permit it. Resulting average loss of contact of fabric with soil below is 6.66% only which is small. Hence, results of this analysis are not seriously affected by it.

However, it is desirable and possible to employ facing elements which settles along with embankment soil to precluded such loss of contact.

6.2.3 Conclusions based on FEM dynamic analysis of embankments

Results of dynamic 2D linear analyses of R.E. embankments in time domain with sinusoidal base excitations were compared with results of tests on same embankments as well as with computed results of plain sand embankments with same height, top width and material properties (except for shear modulus) but with different side slopes. Single layer idealization for M1, M2, P1 and P2 and 2-layer idealization for M1 and M3 were used. Damping strongly affects response. Hence, it was obtained by reducing discrepancy between analytical and test results.

- a. Vertical shear wave propagation through embankment considered in back-analyses is correct, because, time lag obtained from recorded acceleration and those obtained from FEM analysis tally with each other.
- b. Parametric study with damping ratio for first mode, ζ_1 , ranging from 0.05 to 0.288 showed that for $\zeta_1=0.18$ for M1 and $\zeta_1=0.1275$ for M3, responses from analysis and tests are identical. For M1 $\zeta_1=0.18$ and for M3 $\zeta_1=0.1275$ are within limits of damping recommended by Seed et al (1984) for plain sands at corresponding shear strain. Hence, damping ratio-shear strain relation may be considered to be the same for plain sands and reinforced earth.
- c. For R.E. embankments, higher damping reduces duration of transient vibrations, peak computed relative acceleration, a_{rp} , and displacement, d_{rp} , compared to those obtained for low damping. For steady state,

amplitudes of a_{rp} and d_{rp} reduce with depth below top, frequency of response is equal to excitation frequency and amplitudes of a_{rp} and d_{rp} reduce with increasing damping for same shear strain.

- d. Computed absolute accelerations and displacements for M1 with $\zeta_1=0.17$ and M3 with $\zeta_1=0.124$ are in very good agreement with test data upto $0.61H$ above base with discrepancy of $\pm 13.72\%$ or less. If $\pm 25\%$ discrepancy is tolerable, then this good agreement extends upto $0.7H$ from base. For whole depth, average discrepancy is about -13.74% only. Near top, computed responses show more discrepancy due to difference between actual and assumed shear moduli in top portion. Measured responses are closer to computed ones with the better 2-layer idealization. Discrepancy between measured and computed responses may be further reduced by employing more homogeneous layers in top $0.3H$ portion of embankments.
- e. Spacing ratio of fabrics in R.E. embankments is a small 0.16 in this study which makes it a micro-reinforced earth. Hence, R.E. embankments are treated as homogeneous material in this study. It is confirmed by good agreement between computed and measured response of R.E. embankments (as cited in conclusion d) and between computed and measured travel time of shear wave through embankment (as cited in conclusion a).
- f. Computed responses of P1 and P2 were nearly identical for $0.1H$ near base. For remaining depth, response of P2 is less than that of P1 with smaller base, as expected. Near base, responses of P1 and P2 were almost identical to those measured for M1 due to large base widths of P1 and P2 compensating effect of their lower shear moduli. Plain sand embankments being weaker than M1 in upper part, showed larger response amplification

in 0.4H depth from top than those for measured response for M1. This highlights advantage of using R.E. embankments.

- g. For R.E. embankments, maximum dynamic shear stress, τ_{Dmax} , is zero at top and peaks at 0.625H from top. This is also reported by Richardson and Lee (1975) based on tests. Further below, τ_{Dmax} slowly reduces due to increasing confining pressure and fixity at base. For stiffer embankment with low damping, peak τ_{Dmax} of transient state may be more than that for steady state. This gets suppressed by suitably large damping. For stiffer R.E. embankment in steady state with low damping, peak τ_{Dmax} for 2-layer idealization is 43% larger than that for 1-layer idealization. It is only 11.86% larger when very nearly correct damping is used. So, besides using proper damping, proper idealization of embankments with more homogeneous layers near top is also important particularly when damping is low.
- h. For R.E. embankments, ζ_1 and γ are of the order of 0.18 and 10^{-3} which are much higher than 0.05 and 10^{-6} for plain sands for elastic behaviour. Since damping greatly affects shear stresses, this helps to reduce τ_{Dmax} in R.E. within elastic domain. This is a great advantage of reinforced earth.
- i. For plain sand embankments, τ_{Dmax} increases from zero at top to peak near base. They fail upto 0.6H from top when factor of safety is unity and for entire depth when factor of safety is 1.2 only. Concept of factor of safety does not ensure safety under dynamic loads as it fails to consider frequency, frequency ratio, duration of loading, damping etc. For same loading, height and top width with $F_s=1.2$, R.E. embankment show

$\tau_{Dmax} < \tau_{allowable}$ for entire depth with peak τ_{Dmax} being only about 43% of that of plain sand embankments which highlights advantage of R.E.

- j. Variation of τ_{Dmax} in a transverse plane along horizontal for R.E. embankments is parabolic with its maximum at the centre as expected.

6.3 Suggestions for Future Research

Experimental and analytical investigations carried out to understand behaviour of R.E. embankments indicated many research gaps to be filled up by further research in this field which are cited below:

- i. Experimental studies on prismatic R.E. embankments larger than that used in this study to understand effect of size of embankment on dynamic parameters.
- ii. Employing different types of reinforcements for R.E. embankment.
- iii. To study the effect of different reinforcement spacing.
- iv. Effect of prestretching of reinforcing elements.
- v. Development of an apparatus for determination of coefficient of dynamic pullout resistance.
- vi. Role of different types of facing element with different rigidities.
- vii. Effect of moisture content and drainage.
- viii. Effect of different types of soils and their densities.
- ix. Effect of surcharge on R.E. embankment when subjected to different level of base excitation.

The area to be explored analytically are:

- i. For determination of coefficient of dynamic pullout resistance, μ_{avd} , in back-analysis of experiment data, incorporating displacements associated with value of μ_{avd} by employing Newmark's method for computing plastic displacements.
- ii. Extending the limit of strains upto which validity of the concept of idealization of R.E. embankments to be homogeneous may hold good.
- iii. Optimizing the number of homogeneous layers needed for idealization of R.E. embankments.

REFERENCES

1. **Aggour, M.S. and Brown, C.B.** (1974), "The Prediction of Earth Pressure on Retaining Walls due to Compaction", *Jl. Geotechnique*, Vol.24, No. 4, pp. 489-502.
2. **Alimi, I. , Bacot, J., Lareal, P. Long, N.T. and Schlosser, F.** (1977), "Adherence between Soil and Reinforced Insitu and in the Laboratory", *Proc. IX ICSMFE*, Vol. 1, pp. 11-14.
3. **Al-Hussaini, M. and Johnson, L.D.** (1978), "Numerical Analysis of Reinforced Earth Wall", *Proc. Symp. on Earth Reinforcement*, ASCE, Pittsburgh, pp. 98-126.
4. **Al-Hussaini, M. and Perry, B.B.** (1978a), "Field Experiment of Reinforced Earth Wall," *Jl. of Geotech. Engg. Div., ASCE*, Vol. 104, GT3, pp.307-322.
5. **Al-Hussaini, M. and Perry, B.B.** (1978b), "Analysis of a Rubber Membrane Strip Reinforced Earth Wall", *Proc. Symp. on Soil Reinforcing and Stabilising Techniques in Engg. Practice*, Sydney, pp.59-72.
6. **Al-Hussaini, M.M. and Perry, E.B.** (1978c), "Field Experiment of Reinforced Earth Wall," *Proc. Symp. on Earth Reinforcement*, Pittsburgh, ASCE, pp.127-156.
7. **Antia, A.E. and Whitman, R.V.** (1982), "Predicting Relative Displacement for Limited - Slip Seismic Design of Gravity Retaining Walls with Non-liquefying Backfills", *Res. Rep. R82-34*, Dept. of Civil Engg., Massachusetts Inst. of Tech., Cambridge, Massachusetts.
8. **Bacot, J. and Lareal, P.** (1976), "Theoretical Study of Calculations Made at the Point of Failure of Retaining Walls of Reinforced Earth", *Proc. 5 Conf. ICSMFE*, Budapest.

9. **Banerjee, P.K.** (1975), "Principles of Analysis and Design of Reinforced Earth Retaining Walls," Highway Engineer, Vol.22, No.1, pp.13-18.
10. **Barkan, D.D.** (1962), "Dynamic of Bases and Foundations", McGraw-Hill Book Co., New York.
11. **Bathe, K.J.** (1990), "Finite Element Procedures in Engineering Analysis", Prentice-Hall of India.
12. **Bathe, K.J. and Wilson, E.L.** (1976), "Numerical Methods in Finite Element Analysis", Prentice-Hall of India.
13. **Bolton, M.D. and Choudhury, S.P. and Pang, P.L.R.**(1978), "Reinforced Earth Walls: A Centrifugal Model Study", Proc. of Symp. on Earth Reinforcement, ASCE, Pittsburgh, pp.252-261.
14. **Bolton, M.D. and Pang, P.L.R.**(1982), "Collapse Limit States of Reinforced Earth Retaining Walls", Jl. of Geotechnique, Vol. 32, No. 4, pp. 349-367.
15. **Bonaparte, R., Shmerstman, G.R. and Williams, N.D.** (1986), "Seismic Design of Slopes Reinforced with Geogrids and Geotextiles", Proc. of IIIrd Int. Conf. on Geotextiles. Vienna, Austria, Vol. I, Session 3A/1, pp. 273-278.
16. **Boyd, M.S.** (1985), "Reinforced Earth Bridges", Seminar notes, Reinforced Earth Limited, New Zealand (Quoted by Fairless, 1989).
17. **Bracegirdle, A.** (1979), "Reinforced Earth Walls: Static and Dynamic Consideration", M.Sc. Rep., Imperial College, Dept. of Civil Engg., London, England (Quoted by Fairless, (1989).
18. **Broms, B.B.** (1988), "Fabric Reinforced Retaining Walls", Proc. of Int. Geotechnical Symposium on Theory and Practice of Earth Reinforcement, Fukuoka, Japan, pp. 3-31.

19. **Chakrabarty, R.K.** (1989), "An Experimental Study for Earth Pressure at Rest in Reinforced Earth", M.E. Thesis, Dept. of Earthq. Engg., Univ. of Roorkee, India.
20. **Chang, J.C. and Forsth, R.** (1974), "Performance of a Reinforced Earth Fill", Transportation Research Record, No.510, Soil Mechanics, Transportation Research Board, National Research Council, Washington, D.C., 1974.
21. **Clough, R.W. and Penzien, J.** (1986), "Dynamics of Structures", McGraw Hill International Editions, Singapore.
22. **Donovan, N.C.** (1973), "A Statistical Evaluation of Strong Motion Data Including the February 9, 1971, San Fernando Earthquake", Proc. V WCEE Rome, Italy, Vol. I, pp. 1252-1261.
23. **Fairless, G.J.** (1989), "Seismic Performance of Reinforced Earth Walls", Res. Rep. No. 89-8, Dept. of Civil Engg., Univ. of Canterbury, Christchurch, New Zealand.
24. **Fang, H.Y.** (1978), "Reinforced Earth with Sulphur-Sand Treated Bamboo Earth Mat", Proc. of Symp. on Soil Reinforcing and Stabilising Techniques, Sydney, Australia, pp.191-200.
25. **Finlay, T.W.** (1977), "Performance of a Reinforced Earth Structure at Granton", Proc. Symp. on Reinforced Earth and Other Composite Soil Techniques, Heriot-Watt University (Quoted by Naresh et.al., 1990).
26. **Finlay, T.W., and Sutherland, H.B.** (1977), "Field Measurement on a Reinforced Earth Wall at Granton", Proc. IX ICSMFE, Tokyo, Vol.1, pp.511-516.
27. **Garde, R.J. and Mirajgaonker, A.B.** (1977), "Engineering Fluid Mechanics", Nemchand Bros., Roorkee, India.

28. **Garg, K.G.** (1988), "Earth Pressure behind Retaining Wall with Reinforced Backfill", Ph.D. Thesis, Dept. of Civil Engg., Univ. of Roorkee, Roorkee, India.
29. **Guilloux, A. Schlosser, F. and Long, N.T.** (1979), "Etude du Frottement Sable-Armature En Laboratoire", Proc. Int. Conf. Soil Reinforcement, Paris, Vol.I, pp. 35-40 (Quoted by Ingold, 1982).
30. **Gupta, M.K.** (1977), "Liquefaction of Sands During Earthquakes", Ph.D. Thesis, Dept. of Civil Engg., Univ. of Roorkee, Roorkee, India.
31. **Gutierrez, V. and Tatsuoka, F.** (1988), "Role of Facing in Reinforcing Cohesionless Soil Slopes by Means of Metal Strips", Proc. Int. Geotechnical, Symp. on Theory and Practice of Earth Reinforcement, Fukuoka, Japan, 5-7, Oct., pp.289-294.
32. **Hardin, B.O. and Drnevich, V.P.**(1970), "Shear Modulus and Damping in Soils: I. Measurement and Parameter Effects, II. Design Equations and Curves", Technical Rep. UKY 27-70-CE 2 and 3, College of Engg, Univ. of Kentucky, Lexington, Kentucky, July (Quoted by Seed and Idriss, 1970).
33. **Herrmann, L.R. and Al-Yassin, Z.** (1978), "Numerical Analysis of Reinforced Soil System", Proc. ASCE Symp. on Earth Reinforcement, Pittsburgh, April 27, pp. 428-457.
34. **Hirschfeld, R.C. and Poulos, S.J.** (1973), "Embankment - Dam Engineering, Casagrande Volume, John Wiley and Sons, Paper by Seed, H.B., pp.239-269.
35. **Hoshiya, M.** (1978), "Strength of Reinforced Earth Retaining Walls", Proc. of Symp. on Earth Reinforcement, ASCE, Pittsburgh, pp. 458-472.
36. **Housner, G.W. and Hudson, D.E.** (1963), "Applied Mechanics Dynamics", Affiliated East-West Press, New Delhi, India.
37. **Ingold, T.S.** (1982), "Reinforced Earth", Thomas Telford Ltd., London.

38. **IS: 1948** (1970): "Classification and Identification of Soils for General Engineering Purposes", Indian Standards Bureau, New Delhi, India.
39. **IS: 2720-III** (1964) : "Determination of Specific Gravity", Indian Standard Bureau, New Delhi, India.
40. **IS: 2720-IV** (1975): "Grain size Analysis", Indian Standards Bureau, New Delhi.
41. **IS: 2720 - XIII** (1972): "Direct Shear Test", Indian Standards Bureau, New Delhi.
42. **Ishii, Y.H., Arai, H. and Tsuchida, H.** (1960), "Lateral Earth Pressure in an Earthquake", Proc. II WCEE, Japan, Vol.I, pp. 211-230.
43. **Iwasakai, K. and Watanabe, S.** (1978), "Reinforcement of Railway Embankments in Japan", Proc. ASCE Symp. on Earth Reinforcement, Pittsburgh, U.S.A., pp. 473-500.
44. **Jaky, J.** (1944), "The Coefficient of Earth Pressure at Rest", Jl. Of the Society of Hungarien Architects and Engineers, Budapast, Hungary, pp. 355-358.
45. **Jewell, R.A.** (1990), "Revised Design Charts for Steep Reinforced Slopes", Proc. Symp. on Reinforced Embankment - Theory and Practice, Ed. Shercliff, Thomas Telford, London, pp. 1-40.
46. **John, N.W.M.** (1979), "Some Considerations on the Reinforced Earth Design in U.K.", Proc. Int. Conf. on Soil Reinforcement, Paris, pp.71-76.
47. **Jones, C.J.F.P.** (1978), "The York Method of Reinforced Earth Construction", Proc. ASCE Symp. on Earth Reinforcement, Pittsburgh, pp. 501-527.

48. **Jones, C.J.F.P.** (1979), "Lateral Earth Pressure Acting on the Facing Units of Reinforced Earth Structures", Proc. of Int. Conf. on Soil Reinforcement, Paris, pp. 445-449.
49. **Jones, C.J.F.P.** (1985), "Earth Reinforcement and Soil Structures", Butterworths, Advanced Series in Geotech. Engg.
50. **Joshi, V.H. and Parajapati, G.I.** (1982), "Active Pressure Distribution due to Cohesionless Fills", Proc. VII Symp. on Earthq. Engg, Univ. of Roorkee, Roorkee, Vol.1, pp.469-475.
51. **Joshi, V.H. and Sarma-Thakur, L.P.** (1984), "Seismic Displacement Analysis of Hydel Power Houses", Proc. of Symp. on Earthquake Effects on Plant and Equipment, Dec., pp.91-98.
52. **Khan, I.N.** (1991), "Engineering Behaviour of Reinforced Earth Wall", Ph.D. Thesis, Dept. of Civil Engg., Univ. of Roorkee, Roorkee, India.
53. **Koga, Y., Taniguchi, E., Itoh, Y., Sukaguchi, M. and Sakemi, T.** (1986), "Small Scale Shaking Test of the Embankment Reinforced by Geotextile", Proc. 1st. Nat. Symp. on Geotextile, Japan Chapter of Int. Geotextile Society, Dec., pp. 57-60 (In Japanese).
54. **Koga, Y., Ito, Y., Washida, S. and Shimazu, T.** (1988), "Seismic Resistance of Reinforced Embankment by Model Shaking Table Test", Proc. Int. Geotech. Symp. on Theory and Practice of Earth Reinforcement, Fukuoka, Japan, October, pp. 413-418.
55. **Koga, Y., Washida, S. and Ito, Y.** (1992), "Report of the Experiment as to the Seismic Stability of Reinforced Embankment", Rep. of Public Works Res. Inst., No. 3066, Ministry of Construction (In Japanese, quoted by Tatsuoka, 1992).
56. **Kolbuszewski, J.J.** (1948), "General Investigation of the Fundamental Factors Controlling Loose Packing of Sands", Proc. 2nd ICSMFE, Vol.7.

57. **Korner, R.M. and Welsh, J.P.** (1980), "Construction and Geotechnical Engineering Using Synthetic Fabric", John Wiley, New York.
58. **Krishna, J., Chandrasekaran, A.R. and Chandra, B.** (1994), "Elements of Earthquake Engineering", 2nd Ed., South Asian Publishers, New Delhi.
59. **Krishnamoorthy, C.S.** (1987), "Finite Element Analysis-Theory and Programming", Tata McGraw-Hill, New Delhi.
60. **Kulshreshtha, V.** (1991) "The Effect of Vertical Geo Membrane on Liquefaction", M.E. Dissertation, Dept. of Earthquake Engg. Univ. of Roorkee, Roorkee, India.
61. **Kuribayashi, E., Iwasaki, T. and Tatsuoka, F.** (1974), "Stress Condition Effects on Dynamic Properties of Soils", Proc. 5 Symp. on Earthq. Engg. Roorkee, India, Nov., Section c., pp. 135-144.
62. **Lamb, T.W. and Whitman, R.V.** (1969), "Soil Mechanics", John Wiley and Sons, New York.
63. **Lee, K.L., Adams, B.D. and Vajneron, J.J** (1973), "Reinforced Earth Retaining Walls", Jl. of ASCE, SMFD, Sm10, Oct., pp. 745-763.
64. **Lin, J.S. and Whitman, R.V.** (1986), "Earthquake - Induced Displacements of Sliding Blocks", Jl. ASCE,GTD, Vol.112, GT1, pp.44-59.
65. **Matyas, E.L. and Davis, J.B.** (1982), "Experimental Study of Earth Loads on Rigid Pipes", Jl. ASCE,GTD, Vol.109, No.2, Feb., pp. 202-209.
66. **McGuire, R.K.** (1977), "Seismic Design Spectra and Mapping Procedures Using Hazard Analysis Based Directly on Oscillator", Earthq. Engg. and Structural Dynamics, Vol. 5, No.3, pp. 211-234 (Quoted by Paul, et.al., 1978).
67. **McKittrick, D.P.** (1978), "Reinforced Earth : Application of Theory and Research to Practice," Proc. Symp. on Soil Reinforcing and Stabilising Technique in Engg Practice, Sydney, Australia (Quoted by Ingold, 1982).

68. **Mitchell, J.K.** (1981), "Soil Improvement State of the Art Report", Proc. X ICSMFE, Stockholm, Vol.4, pp. 509-565.
69. **Moore, P.J.** (1985), "Analysis and Design of Foundations for Vibrations", A.A. Balkema Publisher, Netherlands.
70. **Mulilis, J.P., Chan, C.K. and Seed, H.B.** (1975), "The Effects of Method of Sample Preparation on the Cyclic Stress Strain Behaviour of Sands", EERC, Univ. of California, Berkeley, Rep. No. 75-18, July.
71. **Murata, O., Tateyama, M. and Tatsuoka, F.** (1992), "Loading Tests of Geosynthetic-Reinforced Soil Retaining Walls and Their Stability Analyses", Proc. Int. Geotech. Symp. on Theory and Practice of Earth Reinforcement, I.S. Kyushu, 92, Fukuoka, Japan (Personal communication).
72. **MWD** (1973), "Retaining Wall Design Notes", NZ Ministry of Works and Development, Civil Div. Publication CDP 702/C, Wellington (Quoted by Fairless, 1989).
73. **MWD** (1980), "Reinforced Earth: Notes on Design and Construction", Supplement to CDP 702/C, 1973: Retaining Wall Design Notes, NZ Ministry of Works and Development, Wellington (Quoted by Fairless, 1989).
74. **Nagel, R.B.** (1985), "Seismic Behaviour of Reinforced Earth Walls," Res. Rep. No. 85-4 Dept. of Civil Engg., Univ. of Canterbury, Christchurch, New Zealand (Quoted by Fairless, 1989).
75. **Nakamura, K., Tamura, Y., Tatsuoka, F., Iwasaki, K. and Yamauchi, H.** (1988), "Roles of Facing in Reinforcing Steep Clay Slopes with a Non-Woven Geotextile", Proc. Int. Geotech. Symp. on Theory and Practice of Earth Reinforcement, I.S. Kyushu 88, Fukuoka, Japan, pp.553-558.
76. **Naresh, D.N., Venkataratnam, M., Bhalabhadra Rao, M. and Subrahmanyam, G.** (1989), "Performance Study of a Prototype Reinforced

- Earth Embankment", Proc. XII ICSMFE, Rio de Janeiro, Brazil, Vol.II, pp. 1295-1298.
77. **Naresh, D.N., Venkataratnam, M., Bhalabhadra Rao, M. and Subrahmanyam, G.** (1989)," Field Experiment on Reinforced Soil Embankment", Indian Geotechnical Jl., July, Vol.22, No.3, pp. 175-205.
 78. **Newmark, N.M.** (1965), "Effect of Earthquakes on Dams and Embankments", Geotechnique, Vol.15, No.2, pp.139-160.
 79. **Oda, M., Koishikawa, L. and Higuchi, T.** (1978), "Experimental Study of Anisotropic Shear Strength of Sand by Plain Strain Tests", Soils and Foundations, Vol.18, No.1, PP. 25-38.
 80. **Okamoto, S.** (1973), "Introduction to Earthquake Engineering", University of Tokyo Press, Japan, 567 pp.
 81. **Orphal, D.L. and Lahoud, J.A.** (1974),"Prediction of Peak Ground Motion from Earthquakes", Jl. of Bull. of. Soc. of Soismology American, Vol. 64, No. 5, pp. 1563-1574.
 82. **Pandey, A.D.** (1995), Reader Earthquake Engg. Dept., Univ. of Roorkee, Roorkee, Personal Communication.
 83. **Pandey, U.K.** (1995), "Dynamic At Rest Earth Pressure for Cohesionless Fills", M.E. Thesis, Dept. of Earthquake Egg., Univ. of Roorkee, Roorkee, India.
 84. **Parasad, C.D.** (1989), "Displacement Dependent Dynamic Active Earth Pressures", M.E. Thesis, Dept. of Earthq. Engg., Univ. of Roorkee, Roorkee, India.
 85. **Passalacqua, R.** (1991), "A Sand-Spreader Used for the Reconstitution of Granular Soil Models", Jl. Soils and Foundations, Vol. 31, No.2, pp.175-180.

86. **Paul, D.K., Singh, V.N. and Kumar, N.** (1978), "A Guide to Acceleration Velocity and Displacement Relationships with Distance and Magnitude". Bull. of the Indian Society of Earthquake Technology, Vol. 15, No. 4, pp. 73-88.
87. **Phan, T.L., Segrestin, P., Schlosser, F. and Long, N.T.** (1979), "Etude de la Stabilité Interne et Externe des Ouvrages en Terre Armée par Deux Méthodes de cercles de Ruptures", Proc. Int. Conf. on Soil Reinforcement, Paris, pp.119-123.
88. **Rankilor, P.R.** (1981), "Membranes in Ground Engineering", Jone Wiley.
89. **Rao, G.V.** (1995), Prof. of Civil Engg. Dept., I.I.T, New Delhi, India, Personal Communication.
90. **Rao, G.V. and Raju, G.V.S.S.,** (1990), "Engineering with Geosynthetics", Tata Mc-Graw Hill Publishing Co. Ltd., New Delhi.
91. **Rea, D. and Wolfe, W.E.** (1980), "Earthquake-Induced Permanent Displacement in Model Reinforced Earth Walls", Proc. 7 WCEE, Istanbul, Turkey, Vol. 7, pp. 273-280.
92. **Richards, R. Jr. and Elms, D.G.** (1979), "Seismic Behaviour of Gravity Retaining Walls", Jl. ASCE, GTD, Vol. 101, GT2, pp.167-188.
93. **Richardson, G.N.** (1978), "Earthquake Resistance Reinforced Earth Walls", Proc. ASCE Symp. on Earth Reinforcement", Pittsburgh, April, 27, pp.664-684.
94. **Richardson, G.N., Feger, D., Fong, A. and Lee, K.L.** (1977), "Seismic Testing of Reinforced Earth Walls", Jl. ASCE, GTD., Vol.103, No. GT1, Jan. pp.1-17.
95. **Richardson, G.N., and Lee, L.** (1975), "Seismic Design of Reinforced Earth Walls", Jl., ASCE, GTD, Vol.101, No. GT2, pp. 167-188.

96. **Romstad, K.M., Al-Yassin, Z., Herrmann, L.R. and Shen, C.K.** (1978), "Stability Analysis of Reinforced Earth Retaining Structures", Proc. ASCE Symp. on Earth Reinforcement, Pittsburgh, April 27, pp. 685-713.
97. **Sabhahit, N. and Madhav, M.R.** (1996), "Seismic Design of Reinforced Wall", Proc. Indian Geotech. Conf., Madras, Dec., Vol. I, pp. 338-341.
98. **Sabhahit, N., Madhav, M.R. and Basudhar, P.K.**(1996), "Seismic Analysis of Nailed Soil Slopes-a Pseudo-Dynamic Approach", Proc. Int. Symp. on Earth Reinforcement Practice, IS-Kyushu'96, Fukuoka, Japan, Nov., pp. 4
99. **Sakagachi, M., Muramatsu, M. and Nagura, K.** (1992), "A Discussion on Reinforced Embankment Structures Having High Earthquake Resistance", Proc. Symp. on Reinforced Earth Practice, Fukuoka, Japan, pp.287-292.
100. **Sarma, S.K.** (1975), "Seismic Stability of Earth Dams and Embankments", Jl. Geotechnique, Vol.25, No.4, pp.743-761.
101. **Sarma Thakur, L.P.** (1984), "Seismic Displacement Analysis of Earth Retaining Structures", M.E. Thesis, Dept. of Earthquake Engg., Univ. of Roorkee, 89 pp.
102. **Saran, S. and Khan, I.N.** (1990), "Seismic Design of Reinforced Earth Wall", Proc. 9 Symp. on Earthquake Engg., Univ. of Roorkee, Vol. I, pp. 5-63-5-82.
103. **Saxena, S.K. and Reddy, K.R.** (1989), "Dynamic Moduli and Damping Ratios for Monterey No. 0 Sand by Resonant Column Tests", Jl. Soils and Foundation JSSMFE, Vol.29, No.2, June, pp.37-51.
104. **Schlosser, F.** (1972), "La Terre Armée et Realisations", Bull.de Liais, LCPC, No. 33 (Quoted by Ingold, 1982).
105. **Schlosser, F.** (1978), "History, Current and Future Developments of Reinforced Earth", (In French), Keynote Address, Proc. Symp. on Soil Reinforcing and Stabilising Techniques in Engineering Practice, Sydney, pp.5-28.

106. **Schlosser, F.** (1982), "Reinforced Earth Mechanism Behaviour and Design Methods", Proc. Symp. on Soil and Rock Improvement Techniques, Including Geotextiles, Reinforced Earth and Modern Pilling Methods, Bangkok, pp. C-1-1-C-1-20.
107. **Schlosser, F.** (1990), "Mechanically Stability Earth Retaining Structures in Europe", Design and Performance of Retaining Structure, Geotechnical Special Publication No.25, ASCE, Lambe and Hansen (ed.), pp. 347-378.
108. **Schlosser, F.** (1994), "Utilisation of Geosynthetic and Natural Fibers in Geotechnical Engineering", Proc. ICSMFE, New Delhi, January,10-15, Vol.6, pp.89-98.
109. **Schlosser, F. and Elias, V.** (1978), "Friction in Reinforced Earth", Proc. Symp. on Reinforced Earth, Pittsburgh, ASCE, pp.735-763.
110. **Schlosser, F. and Long, N.T.** (1974), "Recent Results in French Research on Reinforced Earth", Jl., ASCE,Construction Div.,Vol. 100, No.CO3, pp.223-237.
111. **Schlosser, F. and Vidal, H.** (1969), "Reinforced Earth", Bull. de Liaison des Laboratoire Central des Ponts et Chaussées, No.41, Paris.
112. **Seed, H.B. and Idriss, I.M.** (1970): "Soil Moduli and Damping Factors for Dynamic Response Analyses", Rep. No. EERC 70-10, Earthq. Engg. Res. Ctr., Berkeley, California.
113. **Seed, H.B. and Idriss, I.M.** (1971), "Simplified Procedure for Liquefaction Potential"., Jl., ASCE, SMFD, Vol. 93, SM3, pp. 83-108.
114. **Seed, H.B. and Mitchell, J.K.** (1980), Unpublished Rep. Prepared for the Reinforced Earth Company, USA, and Summarised by Tai (1985).
115. **Seed, H.B., Wong, R.T., Idriss, I.M. and Tokimatsu. K.** (1984): "Moduli and Damping Factors for Dynamic Analyses of Cohesionless Soils", Rep. No. EERC 84-14, Earthq. Engg. Res. Ctr., Berkeley, California.

116. **Sharda, S.** (1975), "Response of Well Foundations Under Horizontal Loads", Ph.D. Thesis, School of Res. and Training Earthq. Engg., Univ. of Roorkee, Roorkee, India.
117. **Shewbridge, S.E. and Sousa, J.B.** (1991), "Dynamic Properties of Reinforced Sand", *Jl. , ASCE, GTD*, Vol. 117, No.9, pp. 1402-1422.
118. **Smith, A.K.C. and Bransby, P.L.** (1976), "The Failure of Reinforced Earth Walls by Overturning", *Geotechnique*, Vol.26, pp.376-361.
119. **Smith, I.M. and Segrestin, P.** (1992), "Inextensible Reinforcements Versus Extensible Ties - FEM Comparative Analysis of Reinforced or Stabilised Earth Structures", *Proc. Earth Reinforcement Practice*, Ochiai, Hayashi and Otani (eds.) Balkema, Rotterdam, pp. 425-430.
120. **Smith, A.K.C. and Wroth, P.C.** (1978), "The Failure of Model Reinforced Earth Walls", *Proc. Symp. on Earth Reinforcement*, ASCE, Pittsburgh, pp. 794-855.
121. **Sommers, S.A. and Wolfe, W.E.** (1984), " Earthquake Induced Responses of Model Retaining Walls", *Proc. 8 WCEE*, San Francisco, Vol. III, pp. 517-524.
122. **Steedman, R.S. and Zheng, X.** (1990), "The Influence of Phase on the Calculation of Pseudo-Static Earth Pressure On a Retaining Wall", *Jl. of Geotechnique*, Vol. 40, No.1, pp. 101-112.
123. **Sud, V.K.** (1984), "Behaviour of Shallow Foundations Adjacent to Slopes", Ph.D. Thesis, Dept. of Civil Engg., Univ. of Roorkee, Roorkee, India.
124. **Tai** (1985), "Seismic Design of Reinforced Earth Walls", *Terre Armée Internationale*, Informative Report No. 14 (Quoted by Fairless, 1989).
125. **Talwar, D.V.** (1981), "Behaviour of Reinforced Earth in Retaining Structures and Shallow Foundations", Ph.D. Thesis, Univ. of Roorkee, Roorkee, India.

126. **Tatsuoka, F.**(1992), "Roles of Facing Rigidity in Soil Reinforcing", Proc. Int. Symp. on Earth Reinforced Practice, Is Kyushu, 1992, Fukuoka, Japan, pp. 298-336.
127. **Tatsuoka, F., Tateyama, M. and Murata, O.** (1989), "Earth Retaining Wall with a Short Geotextile and a Rigid Facing", Proc. XII ICSMFE Rio de Janeiro, Brazil, pp. 935-946.
128. **Terzaghi, K.** (1960), "From Theory to Practice in Soil Mechanics", John Wiley and Sons, New York.
129. **Tso, Y.H.** (1988), "Investigation of Soil-Reinforcement Interaction in Reinforced Earth Structures", Research Report 88-5, Dept. of Civil Engg. Univ. of Canterbury, Christchurch, NZ (Quoted by Fairless, 1989).
130. **Uezawa, H. and Nasu, K.** (1973),"Anti-Earthquake Measures for Embankment on a Weak Ground", 7 WCEE, Rome, Italy, Vol.I, pp.346-355.
131. **Wood, J.H.** (1982), "Unpublished Test Proposal for Reinforced Earth Walls," Ph.D. Thesis, Univ. of California, Los Angeles (Quoted by Fairless, 1989).
132. **Vaid, Y.P. and Negusse, N.** (1984), "Relative Density of Pulviated Sand Samples", Soils and Foundations JI., Vol.24, No.2, pp.101-105.
133. **Verma, A.** (1991) "Reinforced Earth Retaining Structures Subjected to Earthquakes", M.E. Dissertation, Dept. of Earthq. Engg. Univ. of Roorkee, Roorkee, India, 93 pp.
134. **Vidal, H.** (1969), "The Principle of Reinforced Earth", Highway Research Record, No.282, pp. 1-16.
135. **Vidal, H.** (1966),"La Tterre Armée Annles Inst. Tech. du Batim. Suppl., Vol. 22, No. 223-224, Serie Materiaux 38 (Quoted by Ingold, 1982).
136. **Vidal, H.** (1978), "Development and Future of Reinforced Earth", Keynote Address, Proc. Symp. on Earth Reinforcement, ASCE, pp.1-61.

137. **Wolfe, W.E., Lee, K.L. Rea, D. and Yourman** (1978), "The Effect of Vertical Motion on the Seismic Stability of Reinforced Earth Walls", Proc. Symp. on Earth Reinforcement, Pittsburgh, ASCE, pp. 856-879.
138. **Wood, J.H.** (1982), "Unpublished Test Proposal for Reinforced Earth Walls", Ph.D. Thesis, Univ. of California, Los Angeles (Quoted by Fairless, 1981).
139. **Yourmann, A.M.** (1978), "Determination of Soil-Tie Friction for Reinforced Earth Structures", M.S. Thesis, Univ. of California, Los Angeles (Quoted by Fairless, 1989).
140. **Youssef, Z.T.** (1995), "Investigations of Plane Frame-Footing-Reinforced Soil Interaction", Ph.D. Thesis, Dept. of Civil Engg., Univ. of Roorkee, Roorkee, India.